

**Springer Theses**

Recognizing Outstanding Ph.D. Research

Amit Agarwal

# Simulation Studies of Recombination Kinetics and Spin Dynamics in Radiation Chemistry



Springer

# **Springer Theses**

Recognizing Outstanding Ph.D. Research

For further volumes:  
<http://www.springer.com/series/8790>

## **Aims and Scope**

The series “Springer Theses” brings together a selection of the very best Ph.D. theses from around the world and across the physical sciences. Nominated and endorsed by two recognized specialists, each published volume has been selected for its scientific excellence and the high impact of its contents for the pertinent field of research. For greater accessibility to non-specialists, the published versions include an extended introduction, as well as a foreword by the student’s supervisor explaining the special relevance of the work for the field. As a whole, the series will provide a valuable resource both for newcomers to the research fields described, and for other scientists seeking detailed background information on special questions. Finally, it provides an accredited documentation of the valuable contributions made by today’s younger generation of scientists.

### **Theses are accepted into the series by invited nomination only and must fulfill all of the following criteria**

- They must be written in good English.
- The topic should fall within the confines of Chemistry, Physics, Earth Sciences, Engineering and related interdisciplinary fields such as Materials, Nanoscience, Chemical Engineering, Complex Systems and Biophysics.
- The work reported in the thesis must represent a significant scientific advance.
- If the thesis includes previously published material, permission to reproduce this must be gained from the respective copyright holder.
- They must have been examined and passed during the 12 months prior to nomination.
- Each thesis should include a foreword by the supervisor outlining the significance of its content.
- The theses should have a clearly defined structure including an introduction accessible to scientists not expert in that particular field.

Amit Agarwal

# Simulation Studies of Recombination Kinetics and Spin Dynamics in Radiation Chemistry

Doctoral Thesis accepted by  
University of Oxford, UK

 Springer

*Author*

Dr. Amit Agarwal  
Reactor Chemistry and Materials  
National Nuclear Laboratory  
Oxon  
UK

*Supervisor*

Dr. Nicholas Green  
Physical and Theoretical Chemistry  
Laboratory  
University of Oxford  
Oxford  
UK

ISSN 2190-5053

ISBN 978-3-319-06271-6

DOI 10.1007/978-3-319-06272-3

Springer Cham Heidelberg New York Dordrecht London

ISSN 2190-5061 (electronic)

ISBN 978-3-319-06272-3 (eBook)

Library of Congress Control Number: 2014936852

© Springer International Publishing Switzerland 2014

This work is subject to copyright. All rights are reserved by the Publisher, whether the whole or part of the material is concerned, specifically the rights of translation, reprinting, reuse of illustrations, recitation, broadcasting, reproduction on microfilms or in any other physical way, and transmission or information storage and retrieval, electronic adaptation, computer software, or by similar or dissimilar methodology now known or hereafter developed. Exempted from this legal reservation are brief excerpts in connection with reviews or scholarly analysis or material supplied specifically for the purpose of being entered and executed on a computer system, for exclusive use by the purchaser of the work. Duplication of this publication or parts thereof is permitted only under the provisions of the Copyright Law of the Publisher's location, in its current version, and permission for use must always be obtained from Springer. Permissions for use may be obtained through RightsLink at the Copyright Clearance Center. Violations are liable to prosecution under the respective Copyright Law. The use of general descriptive names, registered names, trademarks, service marks, etc. in this publication does not imply, even in the absence of a specific statement, that such names are exempt from the relevant protective laws and regulations and therefore free for general use.

While the advice and information in this book are believed to be true and accurate at the date of publication, neither the authors nor the editors nor the publisher can accept any legal responsibility for any errors or omissions that may be made. The publisher makes no warranty, express or implied, with respect to the material contained herein.

Printed on acid-free paper

Springer is part of Springer Science+Business Media ([www.springer.com](http://www.springer.com))

**Parts of the thesis have been published in the following journal articles:**

1. Agarwal, Amit; Green, Nicholas. "Photodissociation of H<sub>2</sub>O<sub>2</sub>: singlet or triplet precursor?" *Phys. Chem. Chem. Phys.* (publication pending).
2. Agarwal, Amit; Green, Nicholas. "Competition between geminate ion recombination and scavenging in low-permittivity solvents" *Phys. Chem. Chem. Phys.* (publication pending).
3. Agarwal, Amit; Green, Nicholas. "Simulating the exchange interaction in the IRT framework: Slice package" *Phys. Chem. Chem. Phys.* (publication pending).
4. Agarwal, Amit; Green, Nicholas. "Reactive products in the IRT algorithm" *Phys. Chem. Chem. Phys.* (publication pending).

*To my parents, Raj and Neeru*

# Supervisor's Foreword

Radiation damage is important in a wide range of areas, from medicine and biology to material science, and has obvious applications in nuclear power generation, radiation detection and quantification, waste treatment, polymer curing, and nuclear medicine. Radiation chemistry is concerned with the molecular understanding of the physical and chemical transformations that take place during the course of radiation damage. Because the damage is highly localized along radiation tracks, and microscopically clustered within these tracks, there are challenging theoretical problems. The scope of radiation chemistry encompasses the physical interactions between ionizing radiation and the molecule (femtosecond timescale), the dynamics of molecular fragmentation and solvation (sub picosecond timescale) and the fast combination of radical fragments within the track (picosecond–nanosecond timescale), as well as the subsequent radical chemistry. Radiation chemistry uses a combination of theory and computer modeling, together with available experimental results, to interpret the chemical nature of radiation damage in terms of the underlying physicochemical processes, and to elucidate the fundamental physics from the earliest chemical observations.

Amit Agarwal's thesis reports a substantial contribution to the microscopic simulation of radiation chemical reactions, extending the models in several areas, including scavenging, spin, and relaxation effects. This thesis has made advances in developing both the Monte Carlo Random Flights and the Independent Reaction Times (IRT) simulation tools. Particular highlights are the extension of these methods to include both the spin-exchange interaction and spin relaxation, both of which are influential in radiolytic systems where many reactions are spin-controlled. In addition, the study has discovered a novel correlation of the scavenging rate on the recombination time in low permittivity solvents. This is a fundamental breakdown of the assumptions underlying the theory of diffusion kinetics, but can still be accommodated in the IRT method, demonstrating the power of this unconventional approach.

In conclusion, Amit Agarwal's work allows one to model complex radiation track structures and spur reactions with an explicit treatment for spin dynamics, without compromising computational resources. The predictive capabilities gained

by such an understanding have important applications in radiation protection, and in the various areas of technology where radiation is used, such as the nuclear industry, medicine, sterilization, food treatment, polymer curing, the preparation of nano-colloids, power generation, and nuclear waste disposal.

Oxford, March 2014

Dr. Nicholas Green

# Preface

Radiation chemistry is concerned with understanding the chemical kinetics following the application of ionising radiation. There are two main methods for modeling recombination and spin dynamics in radiation chemical systems: The Monte Carlo random flights algorithm, in which the trajectories of the diffusing species are followed explicitly and the Independent Reaction Times (IRT) algorithm, where reaction times are sampled from appropriate marginal distribution functions. This thesis reports developments to both methods, and applies them to better understand experimental findings, particularly spin relaxation effects.

**Chapter 4** introduces current simulation techniques and presents newly developed algorithms and simulation programs (namely *Hybrid* and *Slice*) for modeling spatially dependent spin effects. A new analytical approximation for accurately treating ion-pair recombination in low-permittivity solvents is also presented in this chapter.

**Chapter 5** explores the photodissociation of  $\text{H}_2\text{O}_2$ , where there is some controversy in the literature on the spin state of the precursor. This chapter explores the possibility of reproducing the observed spin polarization phase using the Radical Pair Mechanism.

**Chapter 6** presents two new algorithms for treating reactive products in the IRT framework. These have been tested for two chemical systems: (i) photodissociation of  $\text{H}_2\text{O}_2$  where the  $\cdot\text{OH}$  are scavengeable; (ii) water photolysis which produces  $\text{H}^+$ ,  $\cdot\text{OH}$  and  $e_{\text{aq}}^-$ . In the latter case a careful handling of three body correlations is required.

**Chapter 7** presents simulation results, which suggest a strong correlation between scavenging and ion recombination in low permittivity solvents (a fundamental breakdown of the assumptions underlying the theory of diffusion kinetics). A path decomposition method has been devised that allows IRT simulations to be corrected for this effect.

**Chapter 8** presents evidence for spin-entanglement and cross-recombination to act as an extra source of spin relaxation for ion-recombination in low permittivity solvents. It is hypothesized that this effect contributes to the anomalous relaxation times observed for certain cyclic hydrocarbons.

[Chapter 9](#) presents an extension of the IRT simulation method to micelles. The kinetics are shown to be accurately described using the mean reaction time and the exponential approximation.

# Acknowledgments

I would like to thank the following people for all their help and support, without which this thesis would not have been possible:

**Dr. Green:** Thank you so much for supervising me at Oxford and for providing the necessary support, encouragement, and challenging discussions. I would like to especially thank you for your immense help in the mathematics underlying this work.

**Prof. Pimblott:** I am extremely grateful to you for allowing me to make use of your computational resources at Manchester University.

**Pen Richardson:** Thank you for all your technical support in using the computational resources at Manchester University.

**Prof. Hore:** I am very grateful for the helpful discussion concerning the work described in [Chap. 5](#) of this thesis.

**Dr. Timmel:** Thank you so much for allowing me to work with your research group after my migration from the Central Chemistry Laboratory.

**Nina Jupp:** I am especially grateful to you for keeping me updated on Dr. Green's availability and for taking time to listen to my concerns, especially during the latter part of my studies. A big thank you.

Lastly, I am eternally indebted to my parents and sister for their love, support, encouragement, and prayers.

# Contents

<b>1</b>	<b>Introduction to Radiation Chemistry</b>	1
1.1	Aims and Motivation	1
1.2	Ionising Radiation and Energy Loss	2
1.2.1	Charged Particles	2
1.2.2	Electromagnetic Radiation	7
1.2.3	Neutrons	8
1.3	Radiolysis of Water	8
1.3.1	Physico-Chemical Stage	9
1.3.2	Chemical Stage in Water	10
1.4	Radiolysis of Hydrocarbons	12
1.4.1	Electron Mobility	13
1.4.2	Hole Mobility	14
1.4.3	Scintillator Species	15
1.4.4	Non-random Bond Rupture	16
1.5	Macroscopic Theory of Spur Kinetics	16
1.5.1	Problems with the Deterministic Theory	19
	References	19
<b>2</b>	<b>Theory of Scavenging and Recombination Kinetics</b>	23
2.1	Introduction	23
2.2	Homogeneous Kinetics	23
2.2.1	Neutral Species in Solution	24
2.2.2	Ions in Solution	33
2.3	Diffusion as a Stochastic Process	35
2.3.1	Introduction	35
2.3.2	One Dimensional Diffusion Process	36
2.3.3	Three Dimensional Diffusion	40
2.3.4	Other Models of Molecular Motion	40
2.4	Geminate Recombination	43
2.4.1	Diffusion Controlled Reactions	44
2.4.2	Partially Diffusion Controlled Reactions	47

2.5	Bulk Recombination Rate Constant . . . . .	49
2.5.1	Independent Pairs Approximation . . . . .	49
2.6	Scavenging Kinetics. . . . .	52
2.6.1	Scavenger Concentration and the Inverse Laplace Transform Relationship . . . . .	52
2.6.2	Competition Between Scavenging and Recombination. . .	53
2.7	Spin-Controlled Reactions . . . . .	55
2.7.1	Recovering Boundary Model . . . . .	56
	References . . . . .	58
<b>3</b>	<b>Spin Dynamics</b> . . . . .	<b>61</b>
3.1	Introduction . . . . .	61
3.2	Stochastic Liouville Theory . . . . .	62
3.3	Coherent Spin Evolution . . . . .	63
3.3.1	Zeeman Interaction . . . . .	63
3.3.2	Hyperfine Interaction. . . . .	65
3.3.3	Exchange Interaction. . . . .	67
3.4	Incoherent Spin Evolution . . . . .	68
3.4.1	Bloch Equations . . . . .	68
3.4.2	Solomon Equations . . . . .	69
3.4.3	Redfield Theory . . . . .	70
3.4.4	Measuring Spin Relaxation . . . . .	72
3.4.5	Spin-Locking . . . . .	73
3.5	Radical Pair Mechanism. . . . .	73
3.5.1	Introduction . . . . .	73
3.5.2	Radical-Triplet Pair Mechanism . . . . .	74
3.5.3	Zero Field Splitting. . . . .	75
3.5.4	Chemically Induced Dynamic Nuclear Polarisation . . . .	75
3.5.5	Chemically Induced Dynamic Electron Polarisation . . . .	78
3.5.6	$S - T_0$ Mixing . . . . .	79
3.5.7	$S - T_{-1}$ Mixing . . . . .	81
3.6	Triplet Mechanism. . . . .	82
3.7	Magnetic Field Effect . . . . .	84
3.7.1	Low Field Effect. . . . .	85
3.7.2	Quantum Beats . . . . .	85
3.7.3	Magnetic Effect on Reaction Yield . . . . .	86
3.7.4	Optically Detected Magnetic Resonance . . . . .	87
3.7.5	Reaction Yield Detected Magnetic Resonance . . . . .	87
3.8	Summary . . . . .	87
	References . . . . .	88

<b>4</b>	<b>Simulation Techniques and Development</b>	91
4.1	Introduction	91
4.2	Random Number Generation	91
4.3	Monte Carlo Random Flights Simulation	92
4.3.1	Introduction	92
4.3.2	Brownian Bridge Probability	93
4.3.3	Reflection	94
4.3.4	New Variable Time Step Algorithm	96
4.3.5	Partially Diffusion Controlled Reactions	98
4.3.6	Exact Simulation of Sample Paths	99
4.4	Independent Reaction Times	100
4.4.1	Introduction	100
4.4.2	Diffusion Controlled Reactions: Neutral Species	101
4.4.3	Partially Diffusion Controlled Reactions: Neutral Species	109
4.4.4	Ionic Species	110
4.5	Hybrid Simulation Package	116
4.5.1	Choice of the Critical Boundary	118
4.6	Slice Simulation Package	118
4.6.1	Situation 1: Mean Exit Time Between Slices for Neutral Species	120
4.6.2	Situation 3: Time to Hit the Boundary	123
4.6.3	Situation 4: Mean Exit Time to One of the Slices	124
4.6.4	Probability of Exit Boundary: Neutral Species	124
4.6.5	Slice: Partially Diffusion Controlled Reactions	125
4.6.6	Situation 2: Mean Exit Time After Reflection for Neutral Species	130
4.6.7	Situation 1: Mean Exit Time for Charged Species	130
4.6.8	Probability of Exit Boundary: Charged Species	132
4.7	Summary	132
	References	133
<b>5</b>	<b>Photodissociation of Hydrogen Peroxide Solution: Singlet or Triplet Precursor?</b>	135
5.1	Introduction	135
5.2	Spin Relaxation of $\cdot\text{OH}$	138
5.3	Computational Model of the Kinetics	139
5.3.1	Diffusion Controlled	139
5.3.2	Partially Diffusion Controlled	141
5.4	Computational Model for the Spin Dynamics	142
5.4.1	Singlet–Triplet Probabilities	143
5.4.2	Spin Evolution and Relaxation: The Wavefunction Approach	144

5.4.3	Spin Evolution and Relaxation: The Density Matrix Approach . . . . .	148
5.4.4	Spin Dependent Reactivity . . . . .	151
5.5	Simulation Parameters . . . . .	153
5.5.1	Kinetic Parameters: Diffusion Controlled Conditions. . . . .	153
5.5.2	Photochemistry . . . . .	154
5.5.3	Spin Parameters . . . . .	154
5.5.4	Scaled 2-Propanol Parameters: Diffusion Controlled . . . . .	155
5.5.5	Scaled 2-Propanol Parameters: Partially Diffusion Controlled Conditions . . . . .	156
5.5.6	Variable Parameters . . . . .	157
5.6	Kinetics . . . . .	157
5.6.1	Kinetics with no Spin Dynamics Incorporated . . . . .	157
5.6.2	Kinetics with Spin Dynamics Incorporated. . . . .	159
5.7	Electron Polarisation Using Slice and Hybrid . . . . .	159
5.8	CIDEP Spectrum: Escaped 2-Propanolyl Radicals . . . . .	162
5.8.1	Diffusion Controlled Reactivity . . . . .	163
5.8.2	Partially Diffusion Controlled Reaction . . . . .	173
5.8.3	Symmetrical and Non-symmetrical Encounters. . . . .	173
5.9	Discussion . . . . .	176
	References . . . . .	178
<b>6</b>	<b>Reactive Products: New IRT Algorithm . . . . .</b>	<b>181</b>
6.1	Introduction . . . . .	181
6.2	Photodissociation of H <sub>2</sub> O <sub>2</sub> . . . . .	182
6.2.1	Reactive Products Algorithm . . . . .	182
6.2.2	Simulation Results . . . . .	183
6.3	Radiolysis of Water . . . . .	186
6.3.1	Diffusion Controlled Reactions. . . . .	186
6.3.2	Partially Diffusion Controlled Reactions . . . . .	188
6.3.3	Simulation Results . . . . .	189
6.3.4	Centre of Diffusion Vector Method. . . . .	194
6.3.5	Discussion and Further Work . . . . .	197
	References . . . . .	198
<b>7</b>	<b>Correlation Between Scavenging and Recombination Times for Ions in Low Permittivity Solvents . . . . .</b>	<b>201</b>
7.1	Introduction . . . . .	201
7.2	One Scavengeable Species . . . . .	201
7.2.1	Understanding the Nature of the Fast Scavenging Kinetics . . . . .	204
7.2.2	Steady State Scavenging Rate for Charged Species. . . . .	205
7.2.3	Rate Constant Extracted from Simulations. . . . .	209
7.2.4	Kac Functional . . . . .	210

7.2.5	Effect of Encounter Radius and Onsager Distance . . . . .	212
7.2.6	Conditioned Diffusion Process . . . . .	213
7.2.7	Correcting the IRT Algorithm Using a Predefined Deterministic Time . . . . .	219
7.2.8	Deterministic Region . . . . .	220
7.2.9	Correcting the IRT Algorithm for Any Given Parameter Space . . . . .	223
7.3	Two Scavengeable Species . . . . .	224
7.4	Discussion . . . . .	230
	References . . . . .	232
<b>8</b>	<b>Correlation Between Spin Entanglement and the Spin Relaxation Time.</b> . . . . .	233
8.1	Introduction . . . . .	233
8.2	Theory of Quantum Beats in Recombination Luminescence of Spin-Correlated Radical Ion Pairs . . . . .	234
8.2.1	Time Resolved Magnetic Field Effect . . . . .	235
8.3	Electron Exchange in Spurs . . . . .	238
8.3.1	Singlet and Triplet Frequency. . . . .	239
8.4	Computational Model. . . . .	240
8.4.1	Projection Operator . . . . .	240
8.4.2	Spin-Correlation Following Cross Recombination . . . . .	241
8.4.3	Spin Relaxation: Boltzmann Distribution . . . . .	242
8.4.4	Spin-Dependent Reactivity . . . . .	245
8.4.5	Simulation Flow Diagrams . . . . .	245
8.5	Radiolysis of <i>n</i> -Hexane Containing a Solution of Hexafluorobenzene and Cyclohexane . . . . .	246
8.5.1	Scavenging Kinetics and Diffusion Parameters . . . . .	247
8.5.2	Recombination Kinetics and Spin Dynamics . . . . .	247
8.5.3	Quantum Beats in the Singlet Probability. . . . .	248
8.5.4	TR MFE Decay Curves . . . . .	249
8.5.5	Explicit Treatment of the Hyperfine Coupling . . . . .	252
8.5.6	Discussion . . . . .	254
8.6	Radiolysis of <i>n</i> -Dodecane Containing a Solution of Tetramethyl- <i>p</i> -Phenylenediamine . . . . .	255
8.6.1	Spur Structure . . . . .	255
8.6.2	Reaction Scheme . . . . .	256
8.6.3	Spin Exchange Reactions . . . . .	258
8.6.4	Kinetics . . . . .	259
8.6.5	Time-Resolved Magnetic Field Effect . . . . .	261
8.7	IRT Algorithm: <i>Stealing Reactivity</i> . . . . .	266
8.8	Discussion and Further Work . . . . .	270
	References . . . . .	271

<b>9</b>	<b>Extending the IRT for Micelles</b>	273
9.1	Parameter Space	274
9.2	Reflective Outer Boundary with Geminate Recombination	274
9.3	Partially Absorbing Outer Boundary with No Geminate Recombination	277
9.3.1	Monte Carlo Random Flights Algorithm	278
9.3.2	Analytical Formula and Mean Reaction Time	280
9.4	Partially Absorbing Outer Boundary with Geminate Recombination	281
9.5	Randomly Distributed Radical Pairs Inside a Micelle	283
9.5.1	Reflecting Outer Boundary	283
9.5.2	Elastic Outer Boundary	285
9.5.3	Scavenging of Neutral Species: Reflecting Outer Boundary	287
9.5.4	Modelling Scavenging Inside a Micelle: Reflecting Outer Boundary	293
9.6	Diffusion on the Surface of a Micelle	294
9.6.1	Diffusion on a Sphere: Monte Carlo Random Flights Algorithm	295
9.6.2	Diffusion on a Sphere: IRT Algorithm	296
9.7	Reversible Reactions in the IRT Model	300
9.8	Conclusion and Further Work	303
	References	304
<b>Appendix A:</b>	<b>Theoretical Details</b>	305
<b>Appendix B:</b>	<b>Random Number Statistical Test</b>	319
<b>Appendix C:</b>	<b>Simulation Flow Diagrams</b>	321
<b>Appendix D:</b>	<b>Micelle Results</b>	331

# Symbols and Abbreviations

## Constants

Quantity	Symbol	Numerical	Unit
Avogadro constant	$N_A$	$6.0221415(1) \times 10^{23}$	$\text{mol}^{-1}$
Bohr magneton $e\hbar/2m_e$	$\mu_B$	$927.400949(80) \times 10^{-26}$	$\text{J T}^{-1}$
Boltzmann constant $R/N_A$	$k_B$	$1.3806505(24) \times 10^{-23}$	$\text{J K}^{-1}$
Electron $g$ – factor	$g_e/2$	1.0011596567(35)	–
Electron gyromagnetic ratio $ g_e \mu_B/\hbar$	$\gamma_e$	$-1.76085974(15) \times 10^{11}$	$\text{rads}^{-1} \text{T}^{-1}$
Electron magnetic moment	$\mu_e$	$-928.476412(80) \times 10^{-26}$	$\text{J T}^{-1}$
Electron mass	$m_e$	$9.1093826(16) \times 10^{-31}$	kg
Elementary charge	$e$	$1.602176565 \times 10^{-19}$	C
Magnetic constant	$\mu_0$	$4\pi \times 10^{-7}$ (exact)	$\text{N A}^{-2}$
Molar gas constant	$R$	8.314472(15)	$\text{J mol}^{-1} \text{K}^{-1}$
Permittivity of free space	$\epsilon_0$	$8.8541878176\dots \times 10^{-12}$	$\text{F m}^{-1}$
Planck constant	$h$	$6.6260693(11) \times 10^{-34}$	J s
$h/2\pi$	$\hbar$	$1.05457168(18) \times 10^{-34}$	J s
Proton gyromagnetic ratio $2\mu_p/\hbar$	$\gamma_p$	$2.67522205(23) \times 10^8$	$\text{s}^{-1} \text{T}^{-1}$
Speed of light in vacuum	$c$	299 792 458 (exact)	$\text{m s}^{-1}$

## Nontrivial Functions

Function	Name	Definition
$C(z)$	Fresnel cosine integral	$\int_0^z \cos\left(\frac{t^2\pi}{2}\right) dt$
$\text{erfc}(z)$	Complementary error function	$\frac{2}{\sqrt{\pi}} \int_z^\infty e^{-t^2} dt$
$\text{erfcx}(z)$	Exponentially scaled complementary function	$e^{z^2} \frac{2}{\sqrt{\pi}} \int_z^\infty e^{-t^2} dt$

(continued)

(continued)

Function	Name	Definition
$Ei(z)$	Exponential integral	$\int_{-\infty}^z \frac{e^t}{t} dt$
$F_f(z)$	Auxiliary Fresnel integral	$(\frac{1}{2} - S(z)) \cos\left(\frac{z^2\pi}{2}\right) - (\frac{1}{2} - C(z)) \sin\left(\frac{z^2\pi}{2}\right)$
$S(z)$	Fresnel sine integral	$\int_0^z \sin\left(\frac{t^2\pi}{2}\right) dt$
$\psi'(z)$	Trigamma function	$\sum_{n=0}^{\infty} \frac{1}{(z+n)^2}$
$\Gamma(z)$	Gamma function	$\int_0^{\infty} t^z e^{-t} dt$

## Symbols

$a$	Encounter radius $\text{\AA}$
$a'_{\text{eff}}$	Effective encounter radius $\text{\AA}$
$a_i$	Hyperfine coupling constant on radical $i$ T
$a_{\text{eff}}$	Effective hyperfine coupling constant T
$a_H$	Hyperfine coupling constant T
$A_m$	Atomic mass of the absorbing medium kg
$B_0$	Static external field T
$B_1$	Rotating magnetic field T
$C_0$	Stopping power constant $\text{eV } \text{\AA}^2 \text{ mol}^{-1}$
$D'$	Mutual diffusion coefficient $\text{\AA}^2 \text{ s}^{-1}$
$D^0$	Zero field splitting parameter $\text{\AA}^{-1}$
$D_i$	Diffusion coefficient of species $i$ $\text{\AA}^2 \text{ s}^{-1}$
$D_m$	Diffusion coefficient for charge migration $\text{\AA}^2 \text{ s}^{-1}$
$E^0$	Zero field splitting parameters $\text{\AA}^{-1}$
$E_k$	Kinetic energy of the incoming charged particle J
$E_0$	Initial energy of the ionization particle J
$g_i$	$g$ -factor for radical $i$
$\hat{H}_0$	Static Hamiltonian $\text{rad s}^{-1}$
$\hat{H}_1$	Hamiltonian describing the perturbation $\text{rad s}^{-1}$
$I_i$	Nuclear spin of the $i$ th nucleus
$I_m$	Mean excitation/ionization potential J
$J_B$	Diffusive flux of B particles $\text{mol } \text{\AA}^{-2} \text{ s}^{-1}$
$J(r)$	Exchange interaction parameter T
$J_0$	Exchange strength T
$k_{\text{act}}$	Activation controlled rate constant $\text{M}^{-1} \text{ s}^{-1}$
$k_{\text{diff}}, k_{\text{smol}}$	Diffusion controlled rate constant $\text{M}^{-1} \text{ s}^{-1}$

$k_{\text{high}}$	High velocity scavenging rate constant $\text{M}^{-1} \text{s}^{-1}$
$k_{\text{obs}}$	Observed rate constant $\text{M}^{-1} \text{s}^{-1}$
$k_{\text{MC}}$	Rate constant extracted from random flights simulation $\text{M}^{-1} \text{s}^{-1}$
$k_q$	Scavenging rate constant inside a sphere $\text{M}^{-1} \text{s}^{-1}$
$k_{\text{ss}}$	Steady-state scavenging rate constant for ions $\text{M}^{-1} \text{s}^{-1}$
$m$	Mass of particle kg
$m_I$	Nuclear magnetic spin quantum number
$m_s$	Electron magnetic spin quantum number
$M_0$	Rest mass of heavy charged particle kg
$N_i$	Number of particles of species $i$ inside the spur
$N(\mu, \sigma)$	Gaussian distributed random number
$p(x, y, t)$	Transition density with no boundary
$p^\dagger(x, y, t)$	Transition density conditioned on hitting a boundary $\text{\AA}^{-1}$
$p_{\text{abs}}(x, y, t)$	Transition density with an absorbing boundary $\text{\AA}^{-1}$
$p_{\text{rad}}(x, y, t)$	Transition density with an elastic boundary $\text{\AA}^{-1}$
$p_{\text{ref}}(x, y, t)$	Transition density with a reflecting boundary $\text{\AA}^{-1}$
$p_a(x, y, t)$	Transition density for trajectories that go through $a$ and survive $\text{\AA}^{-1}$
$P_s$	Singlet probability at the point of recombination
$P_{\text{rad}}$	Probability of reacting subject to an inelastic boundary
$r$	Separation distance $\text{\AA}$
$r_c$	Onsager distance $\text{\AA}$
$r_{\text{centre}}$	Distance from center of spur $\text{\AA}$
$r_0$	Initial separation $\text{\AA}$
$s$	Laplace variable $\text{s}^{-1}$
$S^{\text{mass}}$	Mass stopping power $\text{MeV } \text{\AA}^2 \text{ kg}^{-1}$
$T$	Temperature K
$T_{\text{esc}}$	Particle escape time from the surface of the micelle s
$T'_0$	Spin relaxation time at zero field s
$T_{gi}$	Geminate recombination time for pair $i$ s
$T_{\text{recom}}$	Particle-micelle recombination time s
$T_s, S_i, T_{\text{scav}}$	Scavenging time for the radical s
$T_1$	Spin-lattice relaxation time s
$T_{1\rho}$	Spin-lattice relaxation time in the rotating frame s
$T_2$	Spin-spin relaxation time s
$\bar{T}$	Mean reaction time s
$U(r)$	Electrostatic potential energy at separation $r$ J
$U(0, 1]$	Uniformly distributed random number in the interval (0,1]
$v$	Surface reactivity $\text{\AA} \text{s}^{-1}$
$v_c$	Particle velocity $\text{\AA} \text{s}^{-1}$
$V$	Volume $\text{\AA}^3$
$w(t)$	First passage time density $\text{s}^{-1}$

$W(r)$	Reaction probability
$W_t$	Wiener process
$z_i e$	Charge on ion $i$ C
$Z_m$	Atomic number of the heavy charged particle kg
$\bar{Z}$	Mean number of spurs per unit length in the track
$Ze$	Charge on the nucleus C
$Z_m$	Atomic number of the absorbing material kg

## Greek Symbols

$\gamma_c$	Critical boundary (Hybrid) Å
$\gamma_F$	Friction coefficient N
$\epsilon_{\text{avg}}$	Average energy required to form one spur J
$\epsilon_r$	Dielectric constant of the solvent
$\epsilon_D$	Variable time step parameter
$\mu$	Mean of the process
$\mu_m$	Mobility Å <sup>2</sup> V <sup>-1</sup> s <sup>-1</sup>
$\xi'$	Fluctuating stochastic force (Langevin equation) N
$\rho$	Density matrix
$\rho_B$	Density distribution of B about A
$\sigma$	Standard deviation of the process
$\sigma_S$	Spin statistical factor
$\chi$	Velocity autocorrelation function Å <sup>2</sup> s <sup>-2</sup>
$\chi_N$	Nuclear spin state
$\Omega(r)$	Survival probability
$\omega_0$	Larmor frequency rad s <sup>-1</sup>
$\omega_{x,y}$	Fluctuating field along the $x, y$ direction rad s <sup>-1</sup>

## Abbreviations

AAS	Adjacent average smoothing
ARES	Adiabatic rotation of effective spin orientations
CIDEP	Chemically induced dynamic electron polarization
CIDNP	Chemically induced dynamic nuclear polarization
CM	Center of vector diffusion approach
CPMG	Carr-Purcell-Meiboom-Gill relaxation
EPR	Electron paramagnetic resonance
ERP	Einstein-Podolsky-Rosen
FD	Free diffusion
FDMR	Fluorescence detected magnetic resonance
FP	First passage approach
HCC	Hyperfine coupling constant

HFB	Hexafluorobenzene
HFCM	Hyperfine coupling mechanism
IRT	Independent reaction times
LCM	Level crossing mechanism
LET	Linear energy transfer
LFE	Low field effect
MARY	Magnetic field effect on reaction yield
MC	Monte Carlo random flights
MFE	Magnetic field effect
ODMR	Optically detected magnetic resonance
PP	Photolytic pair
RP	Radiolytic pair
RPM	Radical pair mechanism
RPTM	Radical pair triplet mechanism
RYDMR	Reaction yield detected magnetic resonance
SLE	Stochastic Liouville equation
TM	Triplet mechanism

# Chapter 1

## Introduction to Radiation Chemistry

### 1.1 Aims and Motivation

Radiation damage is important in a wide range of areas, from medicine and biology [1] to material science [2, 3], as well as having obvious applications in nuclear power generation [3], radiation detection and quantification, waste treatment [4] (and references therein), polymer curing and nuclear medicine [1]. Radiation chemistry is interested in the molecular mechanisms of radiation damage, which include the fundamental physical interactions between ionising radiation and the molecule (femtosecond time scale), the dynamics of molecular fragmentation and solvation (sub picosecond) and the fast recombination of radical fragments (picosecond to nanosecond time scale). Using a combination of theory and computer modelling, together with available experimental results, the motivation of this research is to (i) describe and interpret experimental results as realistically as possible; (ii) identify and analyse implicit assumptions; (iii) identify effects that are missing in current formulations and understand their importance and finally (iv) discover how the chemical nature of radiation damage can be understood in terms of the fundamental physical processes involved. The predictive capabilities gained by such an understanding are vital for the purposes of radiation protection, and for all the different areas of technology where radiation is used (for example, nuclear industry, medicine, sterilization, food treatment, the preparation of nano-colloids, power generation and waste disposal).

The fundamental processes involved in the physical formation of a radiation track and in its subsequent evolution by diffusion and reaction are stochastic in nature. Every track is unique and even identical tracks may evolve differently. Thus most recent simulation methods [5–8] are stochastic in these senses (i.e. for the underlying track and for the diffusion and reaction of the reactive particles that can take place). Unfortunately, these methods ignore the spin-dynamics because of the complexity it introduces. As most radicals in radiation chemistry are paramagnetic species, there is a possibility of spin-controlled reactions and other spin effects such as quantum beats [9], chemically induced dynamic nuclear polarisation (CIDNP) [10–13] and chemically induced dynamic electron polarisation (CIDEP) [11, 12], which would

not only govern the recombination kinetics, but also contain additional information about the underlying track. One of the roles of theory is to work out what information is available and how it may be extracted from experimental data.

Some work on spin effects and in particular, spin-controlled reactivity has already been presented in the literature [14–21] which have highlighted the importance of coherent and incoherent effects in the modelling of spur kinetics. As a result, one of the major aims of this work is to develop computationally efficient algorithms which are capable of modelling both the kinetics and spin-dynamics explicitly for any radiation chemical system. Using these simulation programs, this work then aims to:

1. Incorporate incoherent effects using the wavefunction of the system to investigate the spin-relaxation time of the hydroxyl radical.
2. Investigate the possibility of cross-recombination acting as an extra source of  $T_1$  spin relaxation time in hydrocarbons via the quantum phenomena known as the Einstein-Rosen-Podolsky effect.
3. Investigate the time-dependent scavenging of ions for low-permittivity solvents.
4. Extend currently used simulation programs to confined systems such as micelles and investigate the scavenging and recombination kinetics.

## 1.2 Ionising Radiation and Energy Loss

In radiation chemistry, the types of ionising radiation which are most commonly used can be classified according to their energy loss as: (i) electromagnetic radiation (e.g. X-rays and  $\gamma$ -rays), (ii) ‘heavy’ charged particles (e.g.  $\alpha$ -particles and protons), (iii) ‘light’ charged particles (e.g. electrons and positrons) and (iv) neutrons. In this section a brief description of the different processes of energy loss that commonly occur in radiation chemistry is presented. This section first considers the energy loss for charged particles, which is then followed by a review on electromagnetic radiation and neutrons.

### 1.2.1 Charged Particles

Charged particles can interact with matter and lose energy in two ways: (i) emission of electromagnetic radiation and (ii) inelastic collisions. A brief review of both processes is now presented.

#### 1.2.1.1 Energy Loss by Electromagnetic Radiation

The energy loss for high energy electrons (energy range between 10–1,000 MeV) and positrons occurs mainly through the formation of *Bremsstrahlung* (electromagnetic

radiation caused by the acceleration of a charged particle in the field of a nucleus). In this mechanism, the energy loss occurs at a rate proportional to  $(zZe^2/m)^2$ , with  $z$  and  $Z$  being the charges on the incident particle and nucleus respectively and  $m$  the mass of the incident particle. The energy of a Bremsstrahlung photon depends on how much the kinetic energy the incident electron has lost. If the electron has completely slowed down, then the maximum photon energy will be proportional to the initial kinetic energy of the incident electron. As the energy loss is inversely proportional to the square of the mass of the incident particle, it is not surprising that Bremsstrahlung is more important for light charged particles such as electrons than for other heavier particles such as  $\alpha$ -particles. In the case of electrons, Bremsstrahlung becomes important in the energy range of 10–100 MeV, however, for energies below 100 keV this source of energy loss becomes negligible. For heavier particles Bremsstrahlung only becomes important at very high energies  $\sim 1,000$  MeV.<sup>1</sup>

**Cherenkov radiation** Another interesting type of electromagnetic radiation is known as Cherenkov radiation. This type of radiation can occur when the speed of the charged particle (such as an electron) exceeds the speed of light for that material. This phenomenon was first discovered by Cherenkov in 1934 [22] and was studied from a theoretical perspective by Frank and Tamm in 1937 [23] and later by Ginsberg [24] in 1940. A charged particle can perturb the electromagnetic field as it travels through the medium, which causes polarisation of the orbital electrons. The relaxation of these polarised orbital electrons can subsequently emit a photon with wavelengths ranging from the infrared through to the ultraviolet region. In order to observe Cherenkov radiation in water the electrons need to have kinetic energies exceeding 0.775 MeV. This type of energy loss for charged particles is considered to only contribute a small part. For example, electrons in water lose  $\sim 2 \times 10^{-8}$  MeV  $\text{\AA}^{-1}$  through collisions (and other processes), but only  $4 \times 10^{-6}$  eV  $\text{\AA}^{-1}$  can be attributed to the Cherenkov radiation which is a factor of  $5 \times 10^3$  smaller [25].

### 1.2.1.2 Energy Loss by Inelastic Collisions

The electromagnetic interaction of the incident particle with the electrons of the stopping material can result in either excitation or ionisation of the atom, which in turn allows for many more inelastic collisions to occur within the stopping material. The average rate at which energy is transferred to the stopping material (and consequently, the density of ionisations) for a given incident particle is dependent on the stopping power of the medium. This is commonly referred to as the *linear energy transfer* (LET). More formally stated, LET is the *average* energy lost by the ionising radiation to the stopping material per unit distance. Mathematically, this can be stated as

$$\text{LET} = -\frac{dE}{dx} \quad (1.1)$$

---

<sup>1</sup> The main mechanism of energy loss below this energy occurs mainly by inelastic collision between the incident particle and the orbital electrons of the medium.

where  $dE$  is the energy lost by the charged particle during its passage  $dx$ . The stopping power of the medium is an important and widely used parameter in radiation chemistry, which can depend on many parameters of both the charged particle (such as mass, charge and velocity) and the absorbing medium (such as density and atomic number). The stopping power can generally be categorised into two parts [25]: (1) *collision stopping power*, which is interaction of the charged particle with the orbital electrons of the absorbing medium (applicable to both light and heavy charged particles) and (2) *radiation stopping power*, which is the interaction of the charged particle with the nucleus of the absorbing medium (applicable to light charged particles only). If Eq. (1.1) is divided by the density of the absorber then the stopping power becomes independent of the absorbing medium. Commonly this is called the *mass stopping power* ( $S^{\text{mass}}$ ) of the medium and has SI units  $\text{MeV m}^2 \text{ kg}^{-1}$ .

The main process of energy loss for heavy charged particle occurs via Coulomb interaction with the orbital electron of the stopping material.<sup>2</sup> In order to describe this form of energy loss, two theories were formulated in the 1900s, known as Bohr's and Bethe's theory. Before discussing these formulations in detail, it is important to first present the underlying assumptions inherent in both theories:

1. The heavy charged particle (i) moves much faster than the orbital electrons of the absorbing material and (ii) is much heavier than the orbital electron of the medium.
2. Interaction of the heavy charged particle occurs only through the Coulombic interaction of the orbital electron of the medium.
3. No energy loss is possible from elastic and inelastic collisions involving the nucleus of the absorbing medium and the heavy charged particle.

**Bohr theory for heavy charged particles** In 1913, Niels Bohr developed a classical expression [26] for calculating the mass stopping power for a particle with velocity ( $v_c$ ) as [25]

$$S^{\text{mass}} = 2\pi \frac{Z_m N_A}{A_m} \left( \frac{e^2}{4\pi\epsilon_0} \right)^2 \frac{z_m^2}{m_e v_c^2} \ln \frac{2m v_c^2}{I_m} \quad (1.2)$$

where  $N_A$  is Avogadro's number,  $A_m$  is the atomic mass of the absorbing medium,  $m_e$  the mass of the electron,  $I_m$  being the mean excitation potential of the absorbing medium,  $z_m$  and  $Z_m$  are the atomic number of the charged particle and the absorbing material respectively and  $v_c$  the velocity of the incident particle. In Bohr's formulation for the stopping power, there are two physical limitations which affect the energy transfer and the impact parameter  $b$  [25]: (i)  $b_{\text{max}}$  which corresponds to the minimum energy transfer ( $E_{\text{min}}$ ) cannot be less than the ionisation/excitation potential of orbital electrons of the medium; (ii) maximum energy transfer (corresponding to  $b_{\text{min}}$ ) cannot exceed  $E_{\text{max}}$  (equal to  $2m_e v_c^2$ ) on any collision. Unfortunately, because Bohr's theory neglected any quantum mechanical or relativistic effects, together with

---

<sup>2</sup> The inelastic Coulomb interaction of the heavy charged particle with the absorbing nucleus is negligible and as a result will not be considered in this section.

an unrealistic model to treat electron binding (through the parameter  $I_m$ ), the theory was found to disagree with experimental findings.

**Bethe theory for heavy charged particles** In 1932 Bethe [27–29] developed a new collision stopping power theory to take into consideration both quantum mechanical and relativistic effects. For heavy charged particles, Bethe found the non-relativistic expression for the mass stopping power to be [25]

$$S^{\text{mass}} = C_0 \frac{z_m^2 c^2}{A_m v_c^2} Z_m \ln \left( \frac{2m_e v_c^2}{I_m} \right) \quad (1.3)$$

where  $c$  is the speed of light and  $C_0$  is the stopping power constant with units  $\text{MeV m}^2 \text{mol}^{-1}$ , defined to be

$$C_0 = 4\pi N_A r_e^2 m_e c^2 \quad (1.4)$$

where  $r_e = e^2 / (4\pi \epsilon_0 m_e c^2)$  which takes a value of  $2.82 \times 10^{-5} \text{ \AA}$ . Equation (1.3) is double the result as obtained from Bohr's classical stopping power theory (Eq. 1.2), which is due to the fact that Bethe's formula does not impose any limitations on the impact parameter and explicitly treats both long distance and head-on collisions. The corresponding relativistic expression was found by Bethe to be

$$S^{\text{mass}} = C_0 \frac{z_m^2}{A_m \beta^2} Z_m \left[ \ln \frac{2m_e c^2}{I_m} + \ln \frac{\beta^2}{1 - \beta^2} - \beta^2 \right] \quad (1.5)$$

with  $\beta = v_c/c$ .

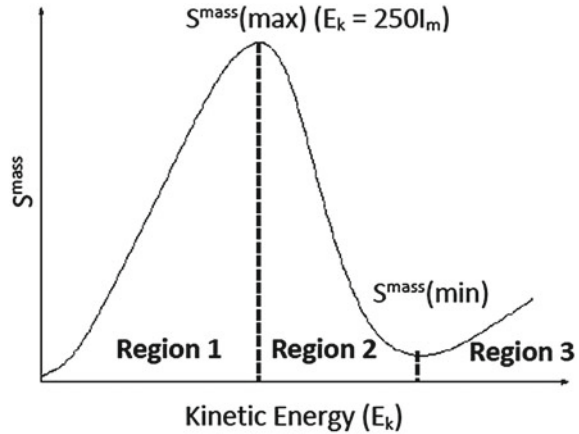
**Mass stopping power curve** Figure 1.1 shows the variation of  $S^{\text{mass}}$  as a function of the kinetic energy  $E_k$  for a heavy charged particle in the framework of Bethe's theory. In the first region,  $S^{\text{mass}}$  rises with  $E_k$  reaching a maximum value at approximately  $E_k = 250I_m$ . In region 2,  $S^{\text{mass}}$  decreases as  $1/v_c^2$  of the charged particle until it reaches a minimum at  $\sim 2.5M_0c^2$ , with  $M_0c^2$  representing the rest energy of the heavy charged particle (with rest mass  $M_0$ ). Within the last region,  $S^{\text{mass}}$  again slowly rises with  $E_k$  due to the relativistic term in Eq. (1.5) [25].

For low kinetic energies (within region 1 of Fig. 1.1), Bethe's theory fails to adequately describe the variation of  $S^{\text{mass}}$  because the orbital electrons of the medium fail to participate in energy transfer with the heavy charged particle. In the 1960s, Fano [30] introduced two corrections to Bethe's theory to help remove this discrepancy, known as the shell and polarisation correction.

In the shell correction [30], Fano introduced a correction term  $C/Z_m$  to Bethe's stopping formula, to account for the fact that at low kinetic energies, the velocity of the heavy charged particle is comparable to the electrons of the absorbing material. The  $C/Z_m$  term corrects for the overestimation of the mean excitation / ionisation potential ( $I_m$ ), which depends on both the velocity of the charged particle and the electron of the absorbing medium.

In the polarisation correction [30], Fano introduced a correction factor  $\delta_c$ , which recognises that at very high velocities of the incident particle, the polarisation

**Fig. 1.1** Variation of Bethe's stopping power ( $-dE/dx$ ) as a function of the charged particle kinetic energy  $E_k$  [25]



screening of the electron of the absorbing material prevents the energy transfer from the incident particle to distant electrons, thereby lowering the stopping power of the condensed medium. Utilising both of these correction factors, Fano found the expression for the mass stopping power to be

$$S^{\text{mass}} = 4\pi \frac{N_A}{A_m} \left( \frac{e^2}{4\pi\epsilon_0} \right) \frac{z_m^2}{m_e c^2 \beta^2} Z_m \left[ \ln \frac{2m_e c^2}{I_m} + \ln \frac{\beta^2}{1 - \beta^2} - \beta^2 - \frac{C}{Z_m} - \delta_c \right] \quad (1.6)$$

**Bethe theory for light charged particles** In contrast to heavy charged particles, the interaction of light charged particles with the orbital electrons of the absorber material deviates in two important ways: (1) relativistic effects need to be considered even at low kinetic energies and (2) both elastic and inelastic collisions can result in large energy transfers. The expression for the mass stopping power for light charged particles (i.e. electrons and positrons), employing Fano's shell and polarisation correction can be obtained in a similar manner to heavy charged particles and is found to be (D. K. Brice, unpublished)

$$S^{\text{mass}} = 2\pi r_e^2 \frac{Z_m}{A_m} N_A \frac{m_e c^2}{\beta^2} \left[ \ln \frac{E_k}{I_m} + \ln(1 + \tau/2) + F^\pm(\tau) - \delta_c \right] \quad (1.7)$$

with  $F^-(\tau)$  applying only to electrons and taking the form

$$F^-(\tau) = (1 - \beta^2)[1 + \tau^2/8 - (2\tau + 1) \ln 2] \quad (1.8)$$

and  $F^+(\tau)$  applying only to positrons which is defined as

$$F^+(\tau) = 2 \ln 2 - (\beta^2/12)[23 + 14/(\tau + 2) + 10/(\tau + 2)^2 + 4/(\tau + 2)^3] \quad (1.9)$$

with  $\tau = E_k/m_e c^2$ . As with heavy charged particles, it is found that  $S^{\text{mass}}$  decreases with increasing  $Z_m$  of the absorbing medium [25].

Bethe's general theory was extended by Møller in 1932 [31] for electrons, to account for the quantum mechanical effect of electron exchange. The expression found by Møller which incorporates these interactions is

$$-\frac{dE}{dx} = \frac{4\pi e^4 z_m^2 N_A}{mv_c^2} \left[ \ln \left( \frac{2mv_c^2}{I_m} \right) - \ln(1 - \beta^2) + \phi(\beta) \right] \quad (1.10)$$

with  $\phi(\beta)$  being defined as

$$\begin{aligned} \phi(\beta) = & \frac{1}{2} \ln \left[ \sqrt{1 - \beta^2} - 1 + \beta^2 \right] - \ln \beta - \left[ \sqrt{1 - \beta^2} + 1 + \frac{1}{2}\beta^2 \right] \ln 2 \\ & + \frac{1}{2} (1 - \beta^2) + \frac{1}{16} \left[ 1 - \sqrt{1 - \beta^2} \right] \end{aligned} \quad (1.11)$$

The spin-exchange contribution to the overall mass stopping power becomes important for energies below  $\sim 25$  eV.

**Track structure** The LET only shows the average energy loss of a charged particles during its passage through the medium. The energy is distributed in small clusters containing highly reactive particles which are commonly referred to as *spurs*. For energy losses greater than the ionisation potential, secondary electrons ( $\delta$ -rays) are ejected which are capable of further ionisation, creating a large number of clusters of ionisations and excitations along the radiation track. The random spacing between clusters is locally exponentially distributed<sup>3</sup> with a large spacing expected for low LET radiation. For heavy particles which possess a high LET, significant overlap of clusters occurs which allow the possibility of *intraspur* reactions.

The energy losses of a given type of radiation can be divided into three categories [32, 33]: (1) spurs (for energies up to 100 eV); (2) blobs (100–500 eV) and (3) short tracks (500–5000 eV). Spurs are formed by the ejection of  $\delta$ -rays (i.e. ionisation of the absorbing medium) which possess low energies with a short diffusion range. For example, the mean range of a 100 eV electron in liquid water is 115 Å [34], with secondary ionisation likely to produce a  $\delta$ -ray close to the primary event. Simulations [35] have shown that spurs account for 75% of the energy deposited by a 1 MeV electron in liquid water; the remaining energy is lost approximately equally between blobs and short tracks.

### 1.2.2 Electromagnetic Radiation

When photons interact with matter a fixed amount of energy is transferred to the matter, in contrast to the types of radiation discussed in the last section. There are

---

<sup>3</sup> The spacing between clusters is distributed according to the probability density function  $p(r) = \alpha^{-1} \exp(-r/\alpha)$ , where  $\alpha$  is the mean of the process.

three main types of processes by which photons lose their energy when interacting with matter:

(i) Photoelectric effect, which is the predominant mechanism for energy loss of low energy photons. In this mechanism, the complete photon energy is transferred to the atom. The ejected electron (known as a *photoelectron*) has energy equal to the difference in the photon energy and the electron binding energy. If the vacancy left by the photoelectron is filled by an upper shell electron of the atom, this results in the emission of a photon (X-ray fluorescence). If the emitted photon hits one of the valence electron of the atom, this then ejects another electron (known as an *Auger electron*) from the atom.

(ii) Compton effect: as the photon interacts with the electron of the material, it becomes scattered with a reduced energy. The scattered photon may then cause further interactions through either the photoelectric or Compton mechanism.

(iii) Pair production: if the photon energy is greater than 1.02 MeV, it can interact with the nucleus of the molecule during its passage. The photon is annihilated to produce an electron and a positron, and both can undergo further interactions as described earlier.

### 1.2.3 Neutrons

Since neutrons are neutral they interact differently to charged particles. The primary interaction occurs with the nucleus of the absorber and little interaction is present with its orbital electrons. Neutrons interact with the nucleus through elastic and inelastic scattering and neutron capture. In the latter mechanism, the neutron is absorbed by the nucleus which in turn excites the nucleus to higher energy levels. As the nucleus returns back to the ground state a particle is emitted (dependent on the incident energy this could be  $\alpha$ -particle, neutron etc), and a new radioactive nuclide is produced.

## 1.3 Radiolysis of Water

The radiolysis of water has been extensively studied both experimentally and theoretically over the past twenty years. A proper understanding of the different processes is important because of its application for example in the design of nuclear reactors, where water is used as a coolant and in biological systems, where the radiolysis of water makes it a primary event for radiation damage in living cells. It is customary to distinguish between the different chemical stages following radiolysis as: (1) the physical stage ( $<10^{-15}$  s); (2) the physico-chemical stage ( $<10^{-15}$ – $10^{-12}$  s) and (3) the chemical stage ( $<10^{-12}$ – $10^{-6}$  s). All three stages are now briefly discussed in this section.

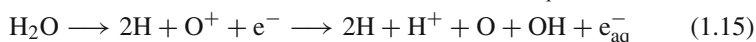
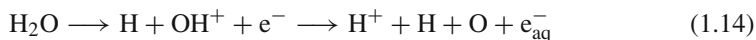
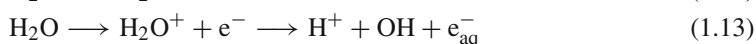
As a high energy radiation particle such as an electron interacts with matter, it loses its energy to the liquid water generating a track of events along its passage

of ionisation. This is the physical stage for the radiolysis of water. According to Turner et al. [36] the species  $\text{H}_2\text{O}^+$ ,  $\text{H}_2\text{O}^*$  and subexcitation electrons (*vide infra*) are produced in  $\leq 10^{-15}$  s in localised regions of a track structure. These portions of the same track structure then evolve independently of all other such clusters of ionisations until significant overlap occurs due to molecular diffusion.

During the passage of the ionising radiation, the mean energy transferred in any given event is found to be almost independent of the initial kinetic energy of the incident electron [35]. The distribution of ionised species along the radiation track is directly influenced by the type of radiation and the energy involved, since the rate of energy loss to the medium will occur at different rates. Different types of radiation can consequently form tracks which may either be densely or sparsely populated [37], leading to different observable chemical kinetics. However, all types of radiation lead to the formation of secondary electrons ( $\delta$ -rays) which in turn produce short electron tracks. For a 1 MeV electron (mean energy loss of 38 eV on every event), water has an LET of  $0.025 \text{ eV } \text{\AA}^{-1}$  [38] giving a mean spacing between events to be approximately  $3,600 \text{ \AA}$  [35, 39]. For an ionisation event to occur an energy of  $>8 \text{ eV}$  is required [40] for the process to occur with any significant probability.

### 1.3.1 Physico-Chemical Stage

The four main events which can occur during the radiolysis of water are



where  $\text{e}_{\text{aq}}^-$  is known as the hydrated electron, with its formation discussed later in this section. The last two reactions in the above reaction scheme are thought to be more rare than the first two. The production of O atoms in the radiation chemistry of water was postulated by Allen [41], and it is now commonly included in spur kinetic calculations [42]. The excited water molecule (which has a lifetime of  $\sim 0.1$  ps) can either return to the ground state without dissociating or fragment. Some of the other dissociation channels available for the excited water molecule include



with  $\text{O}(^1\text{D})$  and  $\text{O}(^3\text{P})$  being the singlet and triplet state of the atomic oxygen respectively. Reaction (1.16) is thought to be the main channel responsible for the production of molecular hydrogen at short times (on a longer timescale the main formation of  $\text{H}_2$  would occur by recombination).

Ionised water molecules (which avoid immediate geminate recombination with an electron) can also undergo proton transfer with other neighbouring water molecules in the picosecond timescale to form an oxonium ion and hydroxyl radical [43]

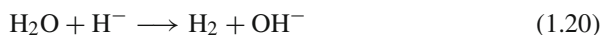


and is the primary mechanism responsible for the formation of OH.

Excited electrons can lose energy to electronic events (through a series of excitations and ionisations) until they no longer have sufficient subexcitation energy to produce further electronic transitions. They are then termed *subexcitation*. Subexcitation electrons may then lose their energy through vibrational and rotational excitations of the water molecule until they become thermalised (normally within  $\sim 10^{-12}$  s). The thermalised electron then rapidly attracts other water molecules (due to the water molecule being polar) which surround the electron; this is termed *hydrated electron* and is represented as  $e_{\text{aq}}^-$ . Experimental value of 0.3 ps [44] is suggested for this process, with simulations predicting a value of 0.2 ps [45]. The subexcitation electron can alternatively undergo dissociative electron attachment to a water molecule [46–48], which can then dissociate to give a hydride anion as



The hydride anion can then further react with a water molecule to give molecular hydrogen and a hydroxide anion



Alternatively, the water anion can self-decompose to yield molecular hydrogen by the reaction [49, 50]



It is found in the gas phase 99% of water anions formed by the electron attachment process dissociate via reaction (1.19) [51, 52]; the same is thought to be true for the liquid phase as well based on the observation of  $\text{H}^-$  by Rowntree et al. [49].

### 1.3.2 Chemical Stage in Water

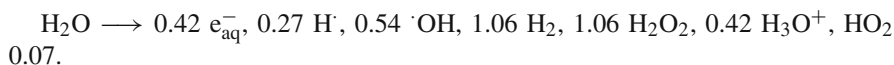
An exhaustive spur reaction scheme following the radiolysis of water is shown in Table 1.1 [53] together with their respective rate constants. Those species not reacting will eventually diffuse into the bulk and become homogeneously distributed, which is completed after  $\sim 10^{-7}$  s. The experimentally measured ‘primary’ G-yields (which are the number of molecules consumed or products formed per 100 eV of energy absorbed) for the different radiolytic species for an LET of  $0.023 \text{ eV } \text{\AA}^{-1}$  are found to be (in terms of molecules per 100 eV) [54]:

**Table 1.1** Reaction scheme for the radiolysis of water. For reaction between like species, the value of  $k$  and not  $2k$  is given [53]

No.	Reaction	$k / 10^{10} \text{ M}^{-1} \text{ s}^{-1}$
1	$e^- + e^- \rightarrow 2\text{OH}^- + \text{H}_2$	0.5
2	$e^- + \text{H}^+ \rightarrow \text{H}$	2.4
3	$e^- + \text{H} \rightarrow \text{OH}^- + \text{H}_2$	2.5
4	$e^- + \text{OH} \rightarrow \text{OH}^-$	3.0
5	$e^- + \text{O}_2 \rightarrow \text{O}_2^- + \text{H}_2$	1.9
6	$e^- + \text{O}_2^- \rightarrow \text{OH}^- + \text{OH}_2^-$	1.3
7	$e^- + \text{HO}_2 \rightarrow \text{HO}_2^-$	2.0
8	$e^- + \text{H}_2\text{O}_2 \rightarrow \text{OH}^- + \text{OH}$	1.2
9	$\text{H} + \text{H} \rightarrow \text{H}_2$	1.0
10	$\text{H} + \text{O} + \text{OH} \rightarrow \text{OH}$	2.0
11	$\text{H} + \text{OH} \rightarrow \text{H}_2\text{O}$	2.0
12	$\text{H} + \text{O}_2 \rightarrow \text{HO}_2$	1.9
13	$\text{H} + \text{O}_2^- \rightarrow \text{HO}_2^-$	2.0
14	$\text{H} + \text{HO}_2 \rightarrow \text{H}_2\text{O}_2$	2.0
15	$\text{H}^+ + \text{OH}^- \rightarrow \text{H}_2\text{O}$	14.3
16	$\text{H}^+ + \text{O}_2^- \rightarrow \text{HO}_2$	5.0
17	$\text{O} + \text{O} \rightarrow \text{O}_2$	2.2
18	$\text{O} + \text{OH} \rightarrow \text{HO}_2$	2.0
19	$\text{O} + \text{HO}_2 \rightarrow \text{HO} + \text{O}_2$	2.0
20	$\text{OH} + \text{OH} \rightarrow \text{H}_2\text{O}_2$	0.45
21	$\text{OH} + \text{O}_2^- \rightarrow \text{OH}^- + \text{O}_2$	1.2
22	$\text{OH} + \text{HO}_2 \rightarrow \text{O}_2 + \text{H}_2\text{O}$	1.9



On increasing the LET to  $10.8 \text{ eV } \text{\AA}^{-1}$  the frequency of reactions (1–4), (9), (11), (15) and (20) shown in Table 1.1 also increases, with the primary yields found to be [54] (in terms of molecules per 100 eV):



The initial  $G^0$ -yields obtained experimentally for the main products of the radiolysis of water are found to be [54] (in terms of molecules per 100 eV)[55–57]:



Primary yields can be determined either using steady-state scavenging experiments or pulse radiolysis. At low scavenger concentrations (which correspond to the later stages of spur chemistry), the yields of the molecular products are not affected since intraspur reactions occur on a much faster timescale. However, on increasing the scavenging concentration there is a significant decrease in the molecular yields as scavenging can now effectively compete on a comparable timescale with intraspur reactions. Most scavenging studies are not performed at high scavenger concentrations because: (i) the scavengers may absorb some of the incident particle energy

which would complicate the spur chemistry; (ii) the scavengers could form products that could interfere with the chemistry of the spur and (iii) other products of the radiolysis may react with the scavengers, complicating the reaction scheme. Usually the experimental results obtained at low scavenger concentrations can be extrapolated to high concentrations [58–62].

## 1.4 Radiolysis of Hydrocarbons

The primary process in alkane radiolysis has long been an intriguing subject of radiation chemistry, mainly because of the low dielectric permittivity of the solvent, where the Coulombic interactions are very strong and can influence the chemical kinetics. Furthermore, unlike the radiolysis of water,<sup>4</sup> spin-effects play a very important role, allowing the observation of magnetic field effects, quantum beats and recombination luminescence. Yields of stable products are known for some well-studied cases, but the detailed mechanism for their formation, including the number, identity and reactions of all the transient species involved is not yet known. A very general mechanism for the radiolysis of liquid alkanes can be found in the literature [63], but it must be stressed that these do vary for different organic systems and some stages might be negligible or become more complex.

In hydrocarbons, the ionising radiation interacts with the solvent to produce excited solvent molecules and electron-hole pairs. The ejected electrons normally have sufficient energy to further excite/ionise other solvent molecule during their passage, giving rise to a complicated track structure. The radiolysis of hydrocarbons is interesting for a number of reasons:

1. Hydrocarbon solvents have an important application in the field of high-energy physics for the design of new ionisation detectors.
2. Due to the low dielectric permittivity of the solvent, a large fraction of the ejected electrons thermalize before they escape the strong Coulomb attraction of the positive charges. In addition reaction between like charges in these chemical systems are impossible. Few of the thermalised electrons can escape beyond the Onsager radius ( $r_c \sim 300 \text{ \AA}$ ), which is defined as the distance at which the energy is equal to  $k_B T$  (with  $k_B$  being the Boltzmann constant and  $T$  the temperature). As a result the majority of electron-hole pairs recombine geminately. Geminately recombinations are usually important on the timescale  $\sim \frac{r_c^2}{4D}$  with diffusion and bulk recombination occurring on the  $\geq 10^{-8}$  s timescale.
3. In some solvents such as hexane, the mean free path is small and the diffusion model can be reliably used to model the system. However, in other hydrocarbons such as neopentane the escaped electrons are in a quasi-free state (*vide infra*), and the motion is not fully diffusive due to trapping by the solvent molecules.

---

<sup>4</sup> Spin effects for the hydroxyl radical can be neglected due to the fast spin relaxation time, which from this work is estimated to be  $< 20$  ps.

Various theoretical explanations have been proposed for the diffusive behaviour of the electron, such as quantum tunnelling [64] between solvent sites and the quasi-ballistic model [65].

4. The high mobility of cations due to the rapid resonant charge transfer and the dependence of the electron mobility on temperature, applied field and solvent / molecular structure [66].
5. Ultrafast  $T_1$  spin-lattice relaxation times observed for cyclic hydrocarbons such as cyclohexane [67], whose origin still remains unclear.

### 1.4.1 Electron Mobility

It was found in 1969 that excess electrons in some nonpolar solvents (such as neopentane) had mobilities significantly larger than ions formed in the same solvent [68–71]. As an electron constantly interacts with the solvent molecules, it is never entirely free. The term *quasi-free state* is usually given when the electron wavefunction is *delocalised* over the medium and there is minimal perturbation to the solvent structure. If however, the wavefunction is *localised*, the electron significantly perturbs the solvent structure and becomes self-trapped, greatly reducing its mobility. In some liquids the electron can create a cavity by repeated electron-solvent interactions and become self-trapped, or in other cases a pre-existing trapping potential may already exist.

For hydrocarbons, there appears to be a strong correlation between the electron mobility and the molecular and solvent structure. The electron mobilities for example in ethane, *n*-pentane and 2,2-dimethylpropane are  $2.8 \times 10^5$ ,  $1.5 \times 10^3$ ,  $7.0 \times 10^5$   $\text{\AA}^2 \text{ V}^{-1} \text{ ps}^{-1}$  respectively at room temperature [72]. This pattern suggests that for *n*-alkanes [54]: (1) the electron mobility decreases with increasing carbon number and (2) electron mobility is slower for linear alkanes. A possible explanation is because of irregularities of the potential in the liquid, the electron randomly scatters and becomes trapped.

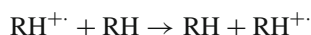
The mobility of the hydrated electron was found to be temperature dependent, with the mobility found to increase with increasing temperature and decreasing viscosity (for example in water  $e_{\text{aq}}^-$  has a mobility of  $0.19 \text{\AA}^2 \text{ V}^{-1} \text{ ps}^{-1}$ , whereas in ethane-1-2-diol it is  $2.8 \text{\AA}^2 \text{ V}^{-1} \text{ ps}^{-1}$  [54]). This suggests that for the hydrated electron, diffusion is the main model for the transport of the solvated electron (in contrast to the jump or quantum tunnelling models). A comprehensive list of the electron mobilities in low, intermediate and high mobility hydrocarbons can be found in the literature [73, 74].

**Table 1.2** Hole mobility in nonpolar dielectric liquids [93]

Liquid	$T$ (K)	Mobility ( $\text{\AA}^2 \text{V}^{-1} \text{ps}^{-1}$ )
Cyclohexane	292	$1.05 \times 10^2$
Methylcyclohexane	295	$5.8 \times 10^1$
Trans-decalin	292	$1.02 \times 10^2$
Methane	111	$2 \times 10^1$
Ethane	110	1.8
Tetramethylsilane	296	9
2,2,4,4-tetramethylpentane	296	4.3

### 1.4.2 Hole Mobility

Irradiation of a non-polar solvent (RH) generates an electron—hole pair ( $\text{RH}^+$ ,  $\text{e}^-$ ), which can transfer their charges to other molecules within the spur through reaction. These solvent holes can diffuse within a spur in two ways: (1) by molecular diffusion and (2) by molecular resonant charge transfer as



where the charge hops from the solvent molecule to a neighbouring alkane molecule. The latter process is highly efficient and can be substantially greater than the diffusion mobility of other molecular ions [75].

For hydrocarbons high-mobility ions are observable in cyclohexane, methylcyclohexane and cis and trans-decalin. In these liquids the hole mobilities were found to be roughly ten times greater than the mobility of ions (in the same liquid) [75–79]. If the charge resides on the solvent cation for a time  $\tau$ , then the apparent diffusion coefficient for the charge migration can be approximated as  $D_{m=} = \beta^2/6\tau$ , where  $\beta$  is the molecule diameter. It is found that for cyclohexane  $\tau \approx 0.5\text{--}1$  ps at 298 K [80],  $0.1\ \mu\text{s}$  for *n*-heptane and  $\approx 1\ \mu\text{s}$  for methylcyclohexane at 16 K [81], making the resonant charge transfer process detectable using time-resolved microwave [75, 79, 82] and dc conductivity techniques [83–92] for certain hydrocarbons. Typical experimental values [93] for the hole mobility are shown in Table 1.2 for a variety of different hydrocarbons.

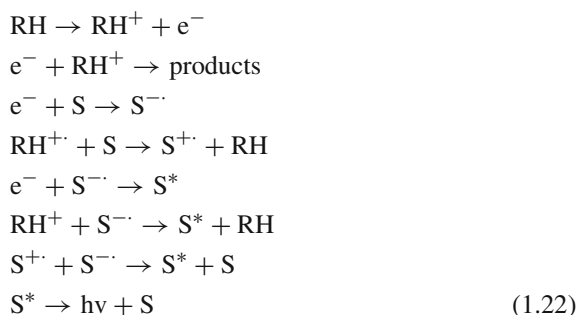
In order to experimentally observe the mobile hole, the charge hopping mechanism must be faster than molecular diffusion as otherwise the two mechanisms cannot be differentiated. Marcus theory [79, 80] predicts that for cyclohexane, the charge transfer mechanism is very efficient because of the low activation energy between different conformations, whereby the charge does not become ‘locked’ on a single conformation which corresponds to a minimum ionisation potential of the molecule. Experiments have confirmed this by diluting cyclohexane with a high ionisation potential alkane where a decrease in the hole mobility was found [79, 87].

The research group at Argonne [94] have highlighted the existence of high mobility ions in squalane and cyclo-octane as well, and have produced new theories to describe their motion. However, for squalane, the results obtained by Anisimov et al.

contradict the findings of the Argonne group. Anisimov et al. calculated a value of  $\tau \sim 1.7$  ns [95] for squalane at 293 K; assuming  $\beta = 6 - 9 \text{ \AA}$  [96],  $D_m = (4 - 6) \times 10^{-3} \text{ \AA}^2 \text{ ps}^{-1}$ , this value is very similar to the molecular diffusion coefficient of squalane ( $(5 - 15) \times 10^{-3} \text{ \AA}^2 \text{ ps}^{-1}$ ) which suggests that the hole in squalane moves at the normal diffusion rate, and the rapid resonant charge transfer mechanism to be negligible. Although the mobile hole was observed more than 20 years ago, its identity and the mechanism of migration are still a subject of investigation both experimentally and theoretically.

### 1.4.3 Scintillator Species

In radiation chemistry scavengers are often employed to intercept the fast kinetics to allow a better understanding of the chemical processes occurring within the radiation track. Unfortunately, this becomes necessary since both the electron and hole can have very fast diffusion coefficients and their diffusive behaviour cannot be monitored using current time-resolved experimental techniques. By using scavengers to intercept recombination, the same ( $e^- + h^+$ ) recombination will take place (since scavengers do not modify the charges of the chemical species) but on a much longer timescale. The general reaction scheme in the presence of a hole scavenger is shown in Eq. (1.22) [97]. With an added charge scavenger, the reaction scheme becomes much more complicated since there now exists four types of recombination pairs: (1) solvent cation + electron ( $\text{RH}^{+\cdot} + e^-$ ), (2) solvent cation + solute anion ( $\text{RH}^{+\cdot} + \text{S}^{-\cdot}$ ), (3) solute cation + electron ( $\text{S}^{+\cdot} + e^-$ ) and (4) solute cation + solute anion ( $\text{S}^{+\cdot} + \text{S}^{-\cdot}$ ).



The excited  $\text{RH}^*$  can be formed by the recombination of  $\text{RH}^{+\cdot} + e^-$  or directly through molecular excitation through secondary electrons. In the reaction scheme,  $\text{S}^*$  is a scintillator species, which can provide invaluable information about the distribution of the electron-hole distances and ion-pair singlet-triplet character (which itself is a function of the magnetic interactions and the applied field), by directly observing the time-dependence of the fluorescence.

Experimentally, the magnetic resonance spectrum can be detected using fluorescence detected magnetic resonance (FDMR) [98–106]. The FDMR technique works by altering the intensity of fluorescence using a resonant microwave ( $\mu\text{w}$ ) field (with amplitude  $B_1$ ) of typical duration 20–200 ns to induce spin transitions between  $T_0$  and  $T_{\pm 1}$  states. At strong magnetic fields ( $B_0$ ) of the spectrometer (where  $B_0 \gg a_{\text{H}}$  with  $a_{\text{H}}$  representing the hyperfine coupling constant), the  $T_{\pm 1}$  are decoupled (*Zeeman interaction*) which allows only  $S - T_0$  mixing to occur. The application of the  $\mu\text{w}$  field depletes the  $T_0$  states and shifts the singlet population towards the triplet  $T_{\pm 1}$  manifold. Therefore, the  $\mu\text{w}$  field reduces the singlet recombination and fluorescence yield for a singlet-correlated radical pair, which can be monitored to provide the magnetic resonance spectrum. In FDMR, only the species present during the microwave pulse, which recombine with their geminate partners to give  $^1\text{S}^*$  are observed. All other species present before or after the microwave pulse, or other radical ions that escape their geminate partners are not observed.

#### 1.4.4 Non-random Bond Rupture

From experimental data [107] it was found that the G-yields for  $\text{H}_2$  and  $\text{CH}_4$  are approximately proportional to the numbers of C–H and C– $\text{CH}_3$  bonds in the compounds, and that bond rupture is not random following the radiolysis of hydrocarbons. For example, tertiary C–C bonds are more readily broken than secondary or primary C–C bonds, which is consistent with the bond dissociation energy. Experimental data for neopentane and 2,2-dimethylbutane which both contain tertiary C– $\text{CH}_3$  bonds, both give a higher G-yield of  $\text{CH}_4$  suggesting that the tertiary C– $\text{CH}_3$  or C–H bonds are more readily broken. From EPR data for frozen alkanes irradiated at low temperatures, it was found that straight chain alkanes gave a spectrum which suggested the loss of hydrogen atom, with little evidence for any C–C bond rupture. However, the same is not true for branched-chain alkanes which suggest a greater probability for a C–C bond breakage [107]. The experimentally obtained G-yields for  $\text{H}_2$  and  $\text{CH}_4$  can be found in the literature [63].

### 1.5 Macroscopic Theory of Spur Kinetics

Conventional deterministic methods characterise a radiation track by an average spur, with concentration profiles for each species within the spur. A differential equation of the form

$$\frac{dc_i}{dt} = D_i \nabla^2 c_i - \sum_j k_{ij} c_i c_j + \sum_{j,k}^n k_{jk} c_j c_k \quad (1.23)$$

can be written for each species within the spur, with  $c_i$  representing the concentration of species  $i$  and  $D_i$  its diffusion coefficient. The first term represents the dissipation of the concentration by diffusion; the second and third terms in Eq. (1.23) represent the depletion and creation of species  $i$  respectively by chemical reaction. The summation in the third term runs across all pairs which can produce the species  $i$ . The rate constant  $k$  used in Eq. (1.23) is that obtained experimentally from the bulk, homogeneous kinetics.

**Prescribed Diffusion** In order to solve the coupled equations, Samuel and Magee [108] employed an approximate solution known as the *prescribed diffusion* (or Jaffé approximation [109]), in which the distribution of each species in the spur was assumed to be Gaussian distributed with mean zero and a variance which spreads linearly with time according to a prescribed amount. The form of  $c_i$  using the prescribed diffusion can then be expressed in the following form

$$c_i(t) = N_i(t) \left( \pi b_i^2 \right)^{-3/2} \exp \left( -r_{\text{centre}}^2 / b_i^2 \right) \quad (1.24)$$

with  $N_i$  representing the number of particles of species  $i$  inside the spur,  $r_{\text{centre}}$  the distance from the centre of the spur and  $b_i$  is a time-dependent parameter and is defined as  $b_i^2 = 4D_i(t + t_0)$  which models the spread of the Gaussian concentration by diffusion from time zero ( $t_0$ ) to time  $t$ . Magee et al. [108, 110] originally employed the prescribed diffusion method to describe the kinetics of overlapping spurs containing identical species. This was later extended using a time-dependent rate coefficient to spurs containing several different species. Schwarz [111] then improved the prescribed diffusion method by introducing a time-dependence to the evolution of the Gaussian variance of the form

$$\frac{d(b_i^2)}{dt} = 4D_i + \beta_i(t) \quad (1.25)$$

with  $\beta_i$  being the correction factor which is dependent on the geometry of  $c_i$ . This correction reduces the concentration at the centre of the spur faster than at the edges (due to the second order nature of reactions), leading to spreading of  $c_i$  of species  $i$  faster than diffusion alone. For spherical symmetry Schwarz found the expression for  $\beta_i$  to be

$$\beta_i(i, j) = -\frac{2}{3} \alpha b_i^2 k_{ij} N_j f_{jk} \left[ \left( 1 + \left( b_i^2 / b_j^2 \right) \right)^{3/2} - 1 \right] \quad (1.26)$$

with  $k_{ij}$  being the bulk homogeneous rate constant and  $\alpha$  being a factor which is determined by comparison with the numerical solution to equation (1.23). The term  $f_{jk}$  defined as

$$f_{jk} = \pi \left( b_j^2 + b_k^2 \right)^{-3/2} \times \left( 1 + \pi \left( b_j^2 + b_k^2 \right)^{1/2} \bar{Z} \right) \quad (1.27)$$

where  $\bar{Z}$  is the mean number of spurs per unit length in the track, given by the expression

$$\bar{Z} = \frac{1}{E_0 \epsilon_{\text{avg}}} \int_0^{E_0} \left( -\frac{dE}{dx} \right) dE \quad (1.28)$$

with  $E_0$  the initial energy of the ionisation particle,  $\epsilon_{\text{avg}}$  the average energy required to form one spur and  $-dE/dx$  is the rate of energy loss to the medium. For isolated spurs  $\bar{Z}$  is zero. If instead a cylindrical geometry for  $c_i$  is assumed (where  $\bar{Z}$  is very large), Schwarz [111] has found a simpler expression for  $\beta_i(ij)$  to be

$$c_i = -\alpha b_i^2 k_{ij} N_i f_{ij} \left( b_i^2 / b_j^2 \right) \quad (1.29)$$

If the species  $i$  can be formed by reaction of species  $j$  and  $k$ , Schwarz has found the correction for  $\beta$  to be

$$\beta_i(j, k) = -\alpha \left( b_i^2 / N_i \right) k_{jk} N_j N_k f_{jk} \times \left[ b_i^2 \left( b_j^2 + b_k^2 \right) / b_j^2 b_k^2 \right] - 1 \quad (1.30)$$

The species  $i$  can also be produced by the reaction of  $j$  with a solute particle, in which case  $\beta$  is given as

$$\beta_i(j, s) = -\alpha b_i^2 k_{js} C_s \left( N_j / N_i \right) \left[ b_i^2 / b_j^2 - 1 \right] \quad (1.31)$$

where  $C_s = N_s (\pi b_s^2)^{-3/2}$ . The reaction of species  $i$  with the solute does not affect  $\beta$  and no correction is therefore needed.

**FACSIMILE algorithm** In 1984, Burns [112] developed a numerical method using a differential equation solver, FACSIMILE to solve Eq. (1.23). This has the obvious advantage that the numerical solution does not require any explicit form of  $c_i$  except at the start. In this method the spur is divided into thin concentric shells and within each shell the concentration of each type of species is assumed constant (assuming each shell is sufficiently small). In this model reaction takes place with a local rate in each shell which depends on the concentration within each shell. The transport between adjacent shells is described by diffusion. The coupled differential equations are then subsequently solved using the FACSIMILE method which implements the Gear algorithm [113]. Although no explicit concentration profile is used in solving the coupled differential equations, it nonetheless uses the bulk rate constant based on homogeneous kinetics to describe the local reaction rates of non-homogeneously distributed species.

### 1.5.1 Problems with the Deterministic Theory

In the 1980s it was found that for the radiolysis of water, the deterministic method gives the wrong statistical weighting for small clusters [114], which is dependent on the number of particles of each type present. So for example, a system containing isolated clusters of  $N_A A$  particles and  $N_B B$  particles,<sup>5</sup> the products  $A_2$ ,  $AB$  and  $B_2$  are produced according to the ratio  $N_A(N_A-1)/2 : N_A N_B : N_B(N_B-1)/2$ ; the deterministic approach gives the ratio  $N_A^2 : 2N_A N_B : N_B^2$ . For  $N_A = N_B = 1$ , no  $A_2$  or  $B_2$  products are formed in the stochastic model, whereas the deterministic approach gives one of each. Similarly, for  $N_A = N_B = 2$  a ratio of 1:4:1 for  $A_2$ ,  $AB$  and  $B_2$  is expected respectively in the stochastic approach, whereas the deterministic treatment gives a ratio of 1:2:1. If the number of A and B particles becomes exceedingly large, then the ratio of 1:2:1 would be obtained and the deterministic theory would be correct. However, for small clusters the deterministic theory provides the wrong statistic weighting. In the case of the radiolysis of water, the deterministic treatment tends to overestimate the yields of  $H_2$  and  $H_2O_2$  and underestimates the yield of  $H_2O$  [114]. This coupled with the use of the homogeneous rate constant to describe non-homogeneous kinetics led to an alternative treatment for describing microscopic kinetics. This is now discussed in detail in the next chapter.

## References

1. G.B. Saha, *Physics and Radiobiology of Nuclear Medicine* (Springer, New York, 2003)
2. G.S. Was, *Fundamentals of Radiation Materials Science* (Springer, New York, 2007)
3. C.P. Race, *The Modelling of Radiation Damage in Metals using Ehrenfest Dynamics* (Springer, London, 2011)
4. B. Han, J. Ko, K. Kim, W. Chung, I.E. Makarov, A.V. Ponomarev, A.K. Pikaev, *Radiat. Phys. Chem.* **64**, 53 (2002)
5. P. Clifford, N.J.B. Green, M.J. Pilling, S.M. Pimblott, *J. Phys. Chem.* **91**, 4417 (1987)
6. N.J.B. Green, M.J. Pilling, S.M. Pimblott, P. Clifford, *J. Phys. Chem.* **93**, 8025 (1989)
7. N.J.B. Green, M.J. Pilling, P. Clifford, *J. Phys. Chem.* **86**, 1322 (1982)
8. N.J.B. Green, M.J. Pilling, S.M. Pimblott, P. Clifford, M.J. Oldfield, *J. Chem. Soc. Faraday Trans. I* **82**, 2673 (1986)
9. B. Brocklehurst, *Radiat. Phys. Chem.* **21**, 577 (1983)
10. K.M. Salikhov, Y.N. Molin, R.Z. Sagdeev, A.L. Buchachenko, *Spin Polarisation and Magnetic Field Effects in Radical Reactions* (Elsevier, Amsterdam, 1984)
11. L.T. Muus, P.W. Atkins, K.A. McLauchlan, J.B. Pedersen, *Chemically Induced Magnetic Polarisation* (Reidel, Dordrecht, 1977)
12. A.P. Lepley, G.L. Closs, *Chemically Induced Dynamic Nuclear Polarisation* (Wiley, New York, 1973)
13. R. Kaptein, *J. Amer. Chem. Soc.* **94**, 6251 (1972)
14. B. Brocklehurst, *J. Chem. Soc. Faraday Trans. II* **72**, 1869 (1976)
15. C.E. Bolton, N.J.B. Green, *J. Phys. Chem.* **100**, 8807 (1996)
16. C.E. Bolton, N.J.B. Green, *J. Phys. Chem.* **103**, 4446 (1999)
17. B. Brocklehurst, *Int. Rev. Phys. Chem.* **4**, 279 (1985)

---

<sup>5</sup> It is assumed that the encounter distances for A–A, A–B and B–B are identical.

18. N.J.B. Green, S.M. Pimblott, B. Brocklehurst, J. Chem. Soc. Faraday Trans. **91**, 223 (1995)
19. B. Brocklehurst, J. Chem. Soc. Faraday Trans. **93**, 1079 (1997)
20. B. Brocklehurst, S. Pimblott, N.J.B. Green, J. Chem. Soc. Faraday Trans. **87**, 3601 (1991)
21. B. Brocklehurst, S. Pimblott, N.J.B. Green, J. Chem. Soc. Faraday Trans. **87**, 2427 (1991)
22. A.P. Cherenkov, Dokl. Akad. Nauk SSSR **2**, 451 (1934)
23. I.E. Tam, I.M. Frank, Dokl. Akad. Nauk SSSR **14**, 107 (1937)
24. V.L. Ginsburg, Sv. J. Exp. Theor. Phys. **10**, 589 (1940)
25. E.B. Podgorsak, *Radiation Physics for Medical Physicists* (Springer, London, 2010)
26. N. Bohr, Kgl. Danske Videnskab. Selskab, Math-fys. Medd. **18**, 8 (1948).
27. H.A. Bethe, Ann. Physik **5**, 325 (1930)
28. H.A. Bethe, Z. Physik **76**, 293 (1932)
29. H.A. Bethe, Ann. Physik **24**, 273 (1933)
30. U. Fano, Ann. Rev. Nucl. Sci. **13**, 1 (1963)
31. C. Møller, Ann. Phys. **14**, 531 (1932).
32. A. Mozumder, J.L. Magee, Rad. Res. **28**, 203 (1966)
33. A. Mozumder, J.L. Magee, J. Chem. Phys. **45**, 3332 (1966)
34. J.A. LaVerne, A. Mozumder, J. Phys. Chem. **90**, 3242 (1986)
35. S.M. Pimblott, J.A. LaVerne, A. Mozumder, N.J.B. Green, J. Phys. Chem. **94**, 488 (1990)
36. J.E. Turner, J.L. Magee, H.A. Wright, A. Chatterjee, R.N. Hamm, R.H. Ritchie, Radiat. Res. **96**, 437 (1983)
37. J.A. LaVerne, Rad. Res. **153**, 487 (2000)
38. C.K. Bomford, I.H. Kunkler, J. Walter, *Textbook of Radiotherapy* (Churchill Livingstone, London, 2003)
39. J.A. LaVerne, S.M. Pimblott, Radiat. Res. **141**, 208 (1995)
40. S.M. Pimblott, A. Mozumder, J. Phys. Chem. **95**, 7291 (1991)
41. A. Allen, Radiat. Res. Suppl. **4**, 54 (1964)
42. A. Kuppermann, *Physical Mechanisms in Radiation Biology* (Springfield, Singapore, 1974)
43. I.G. Kaplan, A.M. Miterov, V.Y. Sukhonosov, Radiat. Phys. Chem. **36**, 493 (1990)
44. J.M. Wiesenfeld, E.D. Ippen, Chem. Phys. Lett **73**, 47 (1980)
45. A. Mozumder, J.L. Magee, J. Chem. Phys. **45**, 3332 (1966)
46. M. Faraggi, D. Zehavi, M. Anbar, Trans. Faraday Soc. **67**, 2057 (1971)
47. T. Goulet, J.P. Jay-Gerin, Radiat. Phys. Chem. **118**, 46 (1989)
48. V. Cobut, J.P. Jay-Gerin, Y. Frongilo, J.P. Patau, Radiat. Phys. Chem. **47**, 247 (1996)
49. P. Rowntree, L. Parenteau, L. Sanche, J. Chem. Phys. **94**, 8570 (1991)
50. G.A. Kaplan, T.M. Orlando, C. Vezina, L. Sanche, J. Chem. Phys. **101**, 3282 (1994)
51. C.E. Melton, J. Chem. Phys. **57**, 4218 (1972)
52. M.G. Curtis, I.C. Walker, J. Chem. Soc. Faraday Trans. **88**, 2805 (1992)
53. N.J.B. Green, M.J. Pilling, S.M. Pimblott, P. Clifford, J. Phys. Chem. **94**, 251 (1990)
54. M. Spothem-Mauizot, M. Mostafavi, T. Douki, J. Belloni, *Radiation Chemistry : from Basics to Applications in Material and Life Sciences* (EDP Sciences, France, 2008)
55. C.N. Trumbore, D.R. Short, J.E. Fanning, J.H. Olson, J. Phys. Chem. **82**, 2762 (1978)
56. C.N. Trumbore, W. Youngblade, D.R. Short, Radiat. Phys. Chem. **28**, 349 (1986)
57. C.N. Trumbore, W. Youngblade, D.R. Short, Radiat. Phys. Chem. **32**, 233 (1988)
58. A. Hummel, J. Chem. Phys. **48**, 3268 (1968)
59. A. Hummel, J. Chem. Phys. **49**, 4840 (1968)
60. J.M. Warman, K.D. Asmus, R.H. Schuler, J. Phys. Chem. **73**, 931 (1969)
61. S.J. RZad, P.P. Infelta, J.M. Warman, R.H. Schuler, J. Chem. Phys. **52**, 3971 (1970)
62. R.H. Schuler, P.P. Infelta, J. Phys. Chem. **76**, 3812 (1962)
63. J.W.T. Spinks, R.J. Woods, *Introduction to Radiation Chemistry* (John Wiley & Sons, London, 1990)
64. S.G. Fedorenko, A.I. Burshtein, J. Chem. Phys. **121**, 11876 (2004).
65. A. Mozumder, Chem. Phys. Lett. **207**, 245 (1993)
66. W.F. Schmidt, Can. J. Chem. **55**, 2197 (1977)
67. V.I. Borovkov, Y.N. Molin, Phys. Chem. Chem. Phys. **6**, 2119 (2004)

68. P.H. Tewari, G.R. Freeman, *J. Chem. Phys.* **49**, 4394 (1968)
69. R.M. Minday, L.D. Schmidt, H.T. Davis, *J. Chem. Phys.* **50**, 1473 (1969)
70. W.F. Schmidt, A.O. Allen, *J. Chem. Phys.* **50**, 5037 (1969)
71. E.E. Conrad, J. Silverman, *J. Chem. Phys.* **51**, 450 (1969)
72. R.A. Holroyd, *Radiation Chemistry, Principles and Applications* (VCH, New York, 1987)
73. Y. Tabata, Y. Ito, S. Tagawa, *CRCC Handbook of Radiation Chemistry* (Wiley-Interscience, New York, 1991)
74. A. Mozumder, *Fundamentals of Radiation Chemistry* (Academic Press, London, 1999)
75. M.P. de Haas, J. Warman, P.P. Infelta, A. Hummel, *Chem. Phys. Lett.* **31**, 382 (1975)
76. G. Beck, J.K. Thomas, *J. Phys. Chem.* **76**, 3856 (1972)
77. A. Hummel, L.H. Luthjens, *J. Chem. Phys.* **59**, 654 (1973)
78. E. Zador, J.M. Warman, A. Hummel, *Chem. Phys. Lett.* **23**, 363 (1973)
79. J.H. Baxendale, *The Study of Fast Processes and Transient Species by Electron-Pulse Radiolysis* (Reidel, The Netherlands, 1982)
80. J.M. Warman, *The Dynamics of Electrons and Ions in Nonpolar Liquids* (Delft, The Netherlands, 1981)
81. I.A. Shkrob, D.W. Werst, A.D. Trifunac, *J. Phys. Chem.* **98**, 13262 (1994)
82. J.M. Warman, H.C. de Leng, M.P. Haas, O.A. Anisimov, *Radiat. Phys. Chem.* **36**, 185 (1990)
83. I.A. Shkrob, A.D. Liu, M.C. Sauer, K.H. Schmidt, A.D. Trifunac, *J. Phys. Chem.* **36**, 3363 (1998)
84. I.A. Shkrob, A.D. Liu, M.C. Sauer, K.H. Schmidt, A.D. Trifunac, *J. Phys. Chem.* **36**, 3371 (1998)
85. A.D. Liu, I.A. Shkrob, A.D. Trifunac, *J. Phys. Chem.* **51**, 273 (1998)
86. I.A. Shkrob, M.C. Sauer, K.H. Schmidt, A.D. Liu, J. Yan, A.D. Trifunac, *J. Phys. Chem.* **101**, 2120 (1997)
87. M.C. Sauer, I.A. Shkrob, J. Yan, K.H. Schmidt, A.D. Trifunac, *J. Phys. Chem.* **100**, 11325 (1996)
88. A.D. Liu, M.C. Sauer, A.D. Trifunac, *J. Phys. Chem.* **97**, 11265 (1993)
89. K.H. Schmidt, M.C. Sauer, Y. Lu, A. Liu, *J. Phys. Chem.* **94**, 244 (1990)
90. M.C. Sauer, K.H. Schmidt, *Radiat. Phys. Chem.* **32**, 281 (1988)
91. M.C. Sauer, K.H. Schmidt, A. Liu, *J. Phys. Chem.* **91**, 4836 (1987)
92. M.C. Sauer, A.D. Trifunac, D.B. McDonald, R. Cooper, *J. Phys. Chem.* **88**, 4096 (1984)
93. M.P. de Haas, A. Hummel, P.P. Infelta, J.M. Warman, *J. Chem. Phys.* **65**, 5019 (1976)
94. I.A. Shkrob, M.C. Sauer, A.D. Trifunac, *J. Phys. Chem.* **100**, 5993 (1996)
95. V.A. Veselov, V.L. Bizyaev, V.I. Melekhov, O.A. Anisimov, Y.N. Molin, *Radiat. Phys. Chem.* **34**, 567 (1989)
96. M. Ikazaki, K. Nunome, K. Tonyama, *Bull. Chem. Soc. Jpn.* **63**, 1396 (1990)
97. C.E. Bolton, Ph.D. thesis, King's College London, 1996.
98. J.P. Smith, S. Lefkowitz, A.D. Trifunac, *J. Phys. Chem.* **86**, 4347 (1982)
99. J.P. Smith, A.D. Trifunac, *J. Phys. Chem.* **85**, 1645 (1981)
100. D.W. Werst, A.D. Trifunac, *J. Phys. Chem.* **95**, 3466 (1991)
101. D.W. Werst, M.G. Bakke, A.D. Trifunac, *J. Phys. Chem.* **112**, 40 (1990)
102. A.D. Trifunac, D.W. Werst, L.T. Percy, *Radiat. Phys. Chem.* **32**, 209 (1988)
103. M.F. Desrosiers, A.D. Trifunac, *J. Phys. Chem.* **90**, 1560 (1986)
104. A.D. Trifunac, D.W. Werst, L.T. Percy, *Chem. Phys.* **153**, 45 (1988)
105. I.A. Shkrob, A.D. Trifunac, *J. Phys. Chem.* **97**, 13298 (1993)
106. I.A. Shkrob, A.D. Trifunac, *J. Phys. Chem.* **98**, 13249 (1994)
107. M.S. Matheson, *Nucleonics* **19**, 57 (1961)
108. A.H. Samuel, J.L. Magee, *J. Chem. Phys.* **21**, 1080 (1953)
109. G. Jaffe, *Ann. Phys. IV* **42**, 344 (1913)
110. A. Mozumder, J.L. Magee, *Radiat. Res.* **28**, 215 (1966)
111. H.A. Schwarz, *J. Phys. Chem.* **73**, 1928 (1969)
112. W.G. Burns, H.E. Sims, J.A. Goodall, *Radiat. Phys. Chem.* **23**, 143 (1984)
113. C.W. Gear, *Numerical Mathematics* **14**, 176 (1971)
114. P. Clifford, N.J.B. Green, M.J. Pilling, S.M. Pimblott, W.G. Burns, *Radiat. Phys. Chem.* **30**, 125 (1987)

# Chapter 2

## Theory of Scavenging and Recombination Kinetics

### 2.1 Introduction

This chapter sets out to introduce the theory of diffusion kinetics and its implementation in the simulation packages used as part of this work. Diffusion is the movement of particles from regions of high concentrations to regions of lower concentrations, driven by a concentration gradient which approaches steady state at long times. It is driven by entropy and the second law of thermodynamics which results in Fick's law (*vide infra*). As the spatial distribution of particles is non-homogeneous in nature within a spur, the recombination kinetics cannot be described by conventional theories of homogeneous reactions. This has led to the development of new theories which are able to describe the time-dependent intra-spur reactions, and are discussed in detail in this chapter.

Following the radiolysis of the solvent, localised clusters of highly reactive particles are formed which have a non-uniform distribution. After a short period of time, the clusters of ions spread by diffusion to form a uniform distribution which can be characterised by homogeneous theories of chemical kinetics. However, before scavenging steady state conditions can be achieved there is a transient period whose lifetime varies as  $a^2/(\pi D')$  where  $a$  is the encounter radius and  $D'$  the mutual diffusion coefficient.

In the subsections below, a detailed review of the theories which underlie the diffusive behaviour and the chemical kinetics for both neutral and charged species are now presented.

### 2.2 Homogeneous Kinetics

Theories of diffusion-controlled reactions were first studied by Smoluchowski [1, 2] and form the foundation of many standard theories today. Considering a simple bimolecular reaction between the species A and B of the form



where  $k_d$  is the second order rate constant to form the encounter pair  $AB^*$ , while  $k_{-d}$  and  $k_a$  are the first order rate constants for the dissociation of the encounter pair and formation of products respectively. The rate of change of the transient  $[AB]$  with respect to time can be expressed as

$$\frac{d[AB]}{dt} = k_d[A][B] - (k_{-d} + k_a)[AB] \quad (2.2)$$

Using the steady state approximation such that  $d[AB]/dt = 0$  (which is appropriate when the lifetime of the encounter pair is short on the timescale of the reaction so that the concentration of pairs remains very small), Eq. (2.2) reduces to the form

$$[AB] = \frac{k_d[A][B]}{(k_{-d} + k_a)} \quad (2.3)$$

with the experimentally observed rate constant being of the form

$$k_{\text{obs}} = \frac{k_d k_a}{(k_{-d} + k_a)} \quad (2.4)$$

If  $k_a \gg k_{-d}$ , then  $k_{\text{obs}} \approx k_d$  and the reaction is said to be *diffusion controlled*, and  $k_{\text{obs}}$  depends only on the relative rate of diffusion of species A and B. If however,  $k_{-d} \gg k_a$  then the reaction is said to be *activation controlled* as the species A and B must have enough energy to surpass the activation energy barrier ( $E_a$ ) threshold. In an intermediate region,  $k_{-d}$  and  $k_a$  may become comparable, in which case the rate of reaction is dependent on both the rate of diffusion  $k_d$  and the rate of crossing  $E_a$  and is termed *partly diffusion controlled*.

## 2.2.1 Neutral Species in Solution

In this section the foundations of the theory underlying chemical kinetics are presented. Based on the diffusion equation to describe Brownian motion together with Smoluchowski's theory [1, 2], a thorough derivation of the bulk reaction rate constant for neutral species for both diffusion and partially diffusion controlled reactions is presented. This theory is then extended for charged species in subsequent sections.

### 2.2.1.1 Diffusion Controlled Reactions

In the absence of any intermolecular forces, the diffusion of species B is considered random and can be characterised by its diffusion coefficient, which according to the

Stokes-Einstein relation is inversely proportional to the solvent viscosity. However, in Smoluchowski theory this independence is extended to the frame of reference on the A as well; each B particle diffuses relative to the A particle with a mutual diffusion coefficient  $D'$ . The flux of B particles per unit area ( $\mathbf{J}_B$ ) is known to be dependent on the gradient operator ( $\nabla c$ ) with respect to the coordinates relative to the position of A and mutual diffusion through the relation

$$\mathbf{J}_B = -D'\nabla c \quad (2.5)$$

where  $c$  is the concentration of B particles. In the above formulation, the motion of B particles relative to A is assumed to be independent and the negative sign simply implies that the diffusive flow is in the direction of lower concentration. *Fick's first law of diffusion* is of the same form as Eq. (2.5) but does not involve these extra assumptions, and is used to describe the diffusion of species in real space not the relative diffusion of two species. Smoluchowski recognised that Fick's first law might also be applicable in relative space as well.

For a steady state reaction, the rate of flow of B particles through any sphere of radius  $r$  containing the A particle (with a concentration gradient  $\partial c/\partial r$ ) is constant,<sup>1</sup> with the pseudo first order rate constant ( $\zeta$ ) given by the expression

$$\zeta = D'4\pi r^2 \frac{\partial c}{\partial r} \quad (2.6)$$

where it is assumed that the concentration of B reactants around any A reactant is spherically distributed. With this simplification, only the radial part of the diffusion equation needs to be considered without the need to explicitly take into account its angular dependence (this assumption is made throughout this section). Integrating the above equation gives

$$c(r) = c(\infty) - \frac{\zeta}{4\pi D'r} \quad (2.7)$$

and using the inner boundary condition such that  $c(a) = 0$ , (instantaneous reaction at the encounter distance  $a$ ) gives the well known solution for the steady state rate constant to be

$$\begin{aligned} k(\infty) &= \frac{\zeta}{c(\infty)} \\ &= 4\pi D'a \end{aligned} \quad (2.8)$$

If the encountering particles are of the same species, then the above equation becomes  $k(\infty) = 2\pi D'a$ , which avoids double counting every pair of reactants. Before steady state conditions can arise there is a period of transient kinetics which must be properly

---

<sup>1</sup> This assumes that the stationary A particle is at the centre of the sphere.

taken into account. This is because initially the inward diffusion of species B does not balance the rate of reaction of B at A and consequently the concentration gradient dynamically changes. More formally stated, the flux of B particles towards A ( $J_{B1}$ ) is less than the flux of B particles leaving the chemical system ( $J_{B2}$ ) via reaction. From the law of conservation of matter, the difference between  $J_{B1}$  and  $J_{B2}$  results in a change in the concentration. Using Fick's first law together with mass balance, the rate of change of the concentration in one dimension can be formally expressed as

$$\begin{aligned}\frac{\partial c}{\partial t} &= -\frac{\partial}{\partial x} J_B \\ &= \frac{\partial}{\partial x} \left( D' \frac{\partial c}{\partial x} \right)\end{aligned}\quad (2.9)$$

In the above formulation, it is again assumed that the motion of B particles relative to A is independent. If  $D'$  is constant then Eq. (2.9) simplifies to

$$\frac{\partial c}{\partial t} = D' \frac{\partial^2 c}{\partial x^2} \quad (2.10)$$

which is recognisable as *Fick's second law of diffusion* in one dimension.<sup>2</sup> For diffusion in three dimensions, Fick's second law becomes

$$\frac{\partial c}{\partial t} = D' \nabla^2 c \quad (2.11)$$

which is the three dimensional diffusion equation ( $\nabla^2$  being the Laplacian operator). For the case in which  $D'$  is not constant, Fick's second law must be modified to the form

$$\frac{\partial c}{\partial t} = \nabla \cdot (D' \nabla c) \quad (2.12)$$

**Probability distribution of B around A** Letting  $[B]_{\text{avg}}(r, t)$  represent the average concentration of B particles around the surviving A particles (normalised to the bulk concentration  $[B]_0$ ), the density distribution of B about A can be expressed as

$$\rho_B(r, t) = \frac{[B]_{\text{avg}}(r, t)}{[B]_0} \quad 0 \leq \rho_B \leq 1 \quad (2.13)$$

where  $r$  is the distance between an A and B particle. Rewriting Eq. (2.11) in terms of  $\rho_B(r, t)$  and considering only the radial dependence of the diffusion equation, one arrives at the expression for the distribution of B about A to be

$$\frac{\partial \rho_B(r, t)}{\partial t} = D' \left\{ \frac{\partial^2 \rho_B}{\partial r^2} + \frac{2}{r} \frac{\partial \rho_B}{\partial r} \right\} \quad (2.14)$$

---

<sup>2</sup> This equation is known as the diffusion equation in one dimension.

with  $2D'/r$  term modelling the drift of the two particles away from each other, which is a geometric feature in a three dimensional space (in two dimensional space this would be  $D'/r$  and in one dimension this would be zero). To solve Eq. (2.14), the initial condition required is of the form

$$\rho_B(r, 0) = \begin{cases} 0 & r \leq a \\ 1 & r > a \end{cases} \quad (2.15)$$

which simply states that at zero time particles A are removed by reaction when  $r < a$  or are uniformly distributed around A if  $r > a$ . The two other boundary conditions required are  $\rho_B(a, t) = 0$ , which is simply reasserting that two species react instantly on encounter at  $t$  (commonly referred to as *totally absorbing boundary*), and  $\rho_B(r \rightarrow \infty, t) = 1$  with  $t \geq 0$ , thus establishing that  $[B]_{\text{avg}}(r, t)$  approaches the bulk concentration  $[B]_0$  with increasing distance at all times. The solution to Eq. (2.14) is shown below, which can be obtained in a straightforward manner by using the Laplace transform method [3].

$$\rho_B(r, t) = 1 - \frac{a}{r} \operatorname{erfc} \left( \frac{r-a}{\sqrt{4D't}} \right) \quad (2.16)$$

The  $\operatorname{erfc}$  term arising in the above equation is the complementary error function which is defined as

$$\operatorname{erfc}(x) = \frac{2}{\sqrt{\pi}} \int_x^{\infty} e^{-t^2} dt \quad (2.17)$$

It can be seen that at long times such that  $t \rightarrow \infty$ , Eq. (2.16) reduces to  $\rho_B(\infty) = 1 - (a/r)$ , which gives the steady state distribution of B particles around any A particle. The time variation of this density distribution is shown in Fig. 2.1, which shows that with a given  $D'$ , the return to steady state is more rapid for regions close to A.

Using the spherical symmetry of the concentration of B about A, the inward flux towards the A particle can be described using Fick's law as

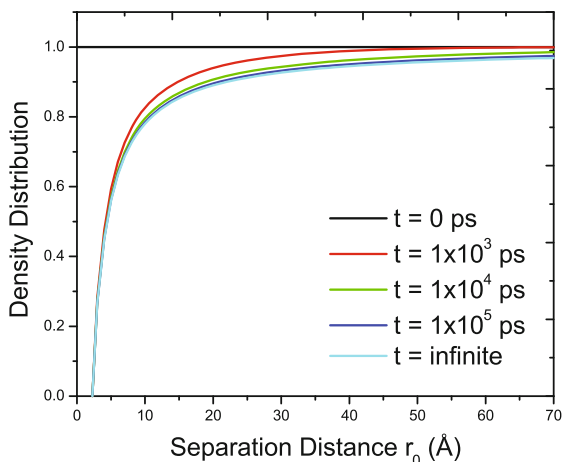
$$J_B(a) = D' \left. \frac{\partial [B]_{\text{avg}}}{\partial r} \right|_{r=a} = D' [B]_0 \left. \frac{\partial \rho_B}{\partial r} \right|_{r=a} \quad (2.18)$$

Differentiating Eq. (2.16) and taking the condition  $r = a$  (i.e. at the reactive boundary), the magnitude of the flux at  $a$  can be written in the form

$$J_B(a) = D' [B]_0 \left( \frac{1}{a} + \frac{1}{\sqrt{\pi D't}} \right) \quad (2.19)$$

The rate of reaction is then simply the magnitude of the inward flux of the B particle across a sphere of radius  $a$  containing the A particle, which is  $4\pi a^2 J_B(a)$ . Thus the

**Fig. 2.1** Density distribution of B species around an A species as a function of distance at five different time scales.  $D' = 0.44 \text{ \AA}^2 \text{ ps}^{-1}$  and encounter distance  $a = 2.2 \text{ \AA}$  (typical values for the  $\cdot\text{OH} + \cdot\text{OH}$  reaction)



overall reaction rate is given by

$$[A][B]_0 4\pi a^2 D' \left[ \frac{1}{a} + \frac{1}{\sqrt{\pi D' t}} \right] \quad (2.20)$$

with the second-order rate time dependent rate coefficient found to be

$$k(t) = 4\pi a D' \left( 1 + \frac{a}{\sqrt{\pi D' t}} \right) \quad (2.21)$$

The units of the second-order rate constant are  $\text{m}^3 \text{ s}^{-1}$  and should be converted to the more commonly used units of  $\text{M}^{-1} \text{ s}^{-1}$  by introducing a multiplicative factor  $10^3 N_A \text{ dm}^3 \text{ m}^{-3}$ , where  $N_A$  is Avogadro's constant. Equation (2.21) shows that the time-scale of the transient period is given by  $a/\sqrt{\pi D' t} \approx 1$ ; so for example using the parameters  $a = 2.52 \text{ \AA}$  and  $D' = 0.44 \text{ \AA}^2 \text{ ps}^{-1}$  (typical values for the  $\text{OH} + \text{OH}$  reaction) gives a transient period of  $\approx 4.5 \text{ ps}$ . The transient period using these parameters is shown diagrammatically in Fig. 2.2. It should be noticed that the timescale of the transient period scales with the square of the encounter radius ( $t = a^2/\pi D'$ ), highlighting the importance of the transient kinetics for chemical systems with larger reaction systems such as polymers and structures like micelles.

**Problems with Smoluchowski theory** Smoluchowski theory makes the assumptions such that: (1) the central particle A is fixed at the origin and (2) the central sink is indestructible. Many workers [4–6] have attempted to apply the theory where the central sink is destroyed by reaction or when the central A particle is not stationary. It is not immediately clear how the theory can describe either of these effects. The worst case scenario for Smoluchowski's theory is to consider the situation where the central A particle moves in a 'sea' of stationary B particles. Fixing on the frame of

**Fig. 2.2** Transient period of the kinetics for the  $\cdot\text{OH} + \cdot\text{OH}$  recombination in comparison with the steady state rate constant. The parameters used were  $a = 2.52 \text{ \AA}$  (encounter radius) and  $D' = 0.44 \text{ \AA}^2 \text{ ps}^{-1}$

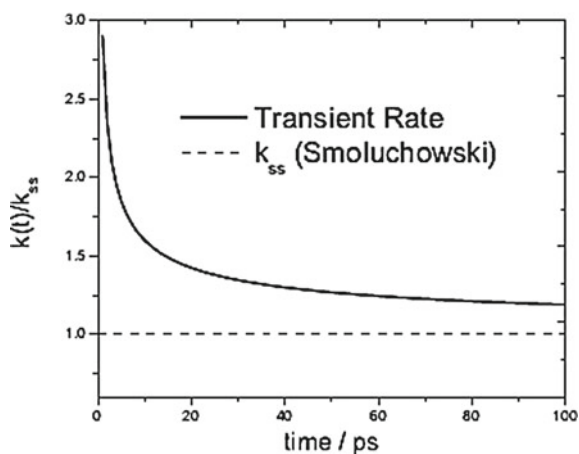
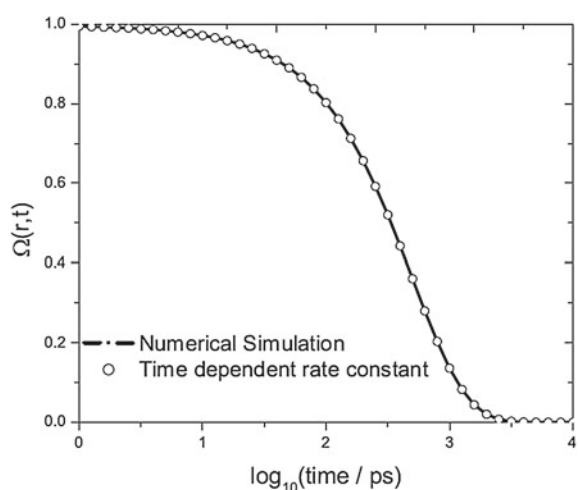


**Fig. 2.3** Survival probability of a hydroxyl radical in a concentration of 1 M of scavengers. Encounter radius was  $0.77 \text{ \AA}$  and the mutual diffusion coefficient ( $D'$ ) set to  $0.315 \text{ \AA}^2 \text{ ps}^{-1}$ . Scavenging rate constant was  $1.9 \times 10^{-3} \text{ M}^{-1} \text{ ps}^{-1}$



reference of the A particle, the relative movement of the B particles relative to A is *correlated*, whereas in Smoluchowski's theory the motion of the B particles is strictly *uncorrelated*. It is found that even with this neglect of the correlation between the A–B particles, the theory accurately predicts the survival probability of the A particle (as shown in Fig. 2.3), in comparison with numerical simulations, which treats the scavengers explicitly and takes into account the correlation of the B particles.

In the frame of reference of particle A, B particles diffusing into A are removed instantly by reaction, setting up a concentration gradient where inward diffusion balances reaction. Hence, the rate of reaction is equal to the rate of first encounter in solution, and the rate of flow into A is the rate of reaction per A molecule. In order to describe this from a theoretical point of view, one must set up a model of transport for Brownian motion. Although there are many models available (as discussed in

Sect. 2.3.4) currently the only solvable realistic model is the diffusion equation. From the viewpoint of spin dynamics, this theory is considered incomplete, since for a spin-controlled reaction the species are required to be in the correct spin state for reaction to occur. An alternative treatment for spin controlled reactions is presented later in this Sect. 2.7.1), which analytically treats re-encounters differently to first encounter and still retains the diffusion equation.

### 2.2.1.2 Partially Diffusion Controlled Reactions

Treating partially diffusion controlled reaction involves replacing the inner boundary condition such that  $\rho_B(a, t) = 0$  with a radiation boundary condition [7] of the form

$$k_{\text{act}}\rho_B(a) = 4\pi a^2 D' \left. \frac{\partial \rho_B}{\partial r} \right|_{r=a} \quad (2.22)$$

where  $k_{\text{act}}$  is the second-order rate constant, describing the rate at which the particle crosses the activation energy barrier to react. The right hand side of Eq. (2.22) is simply Fick's first law describing the flux of B particles towards a single A particle. The radiation boundary condition assumes that the rate of reaction is proportional to the concentration of B particles at the encounter distance ( $a$ ), where  $k_{\text{act}}$  is the constant of proportion. The relationship between  $k_{\text{act}}$  and the reactivity of the surface ( $v$ ) can be expressed through the equation  $k_{\text{act}} = 4\pi a^2 v$ , with  $v$  having units of velocity. Both  $k_{\text{act}}$  and  $v$  are simply alternative ways of parameterising the boundary rate; however it is more convenient to use the parameter  $v$ , as (i)  $k_{\text{act}}$  is second order and (ii) the effect of the encounter radius is factored out on the overall reactivity.

The probability distribution of the B particles around the A particle using this boundary condition can be obtained using the Laplace transform technique to give [3]

$$\begin{aligned} \rho_B(r, t) = & 1 - \frac{a}{r} \frac{k_{\text{act}}}{k_{\text{act}} + 4\pi a D'} \times \left[ \text{erfc} \left\{ \frac{r-a}{\sqrt{4D't}} \right\} \right. \\ & - \exp \left\{ \frac{(4\pi a D' + k_{\text{act}})(r-a)}{4\pi a^2 D'} \right\} \\ & \times \exp \left\{ \frac{(4\pi D'a + k_{\text{act}})^2 t}{(4\pi a^2)^2 D'} \right\} \\ & \left. \times \text{erfc} \left\{ \frac{4\pi a D' + k_{\text{act}}}{4\pi a^2 (D'/t)^{1/2}} + \frac{r-a}{\sqrt{4D't}} \right\} \right] \quad (2.23) \end{aligned}$$

where as before  $r$  is the separation distance of the A and B particle and  $D'$  is the mutual diffusion coefficient. As expected, for an infinitely fast reactivity boundary, it is seen that the solution reduces to Eq. (2.8) (Smoluchowski's totally absorbing boundary condition). Taking the limit  $t \rightarrow \infty$ , the steady state limit of  $\rho_B(r, \infty)$  can be found to be

$$\rho_B(r, t \rightarrow \infty) = 1 - \frac{a}{r} \left[ \frac{k_{\text{act}}}{k_{\text{act}} + 4\pi D'a} \right] \quad (2.24)$$

which shows that for a partially diffusion controlled reaction, there is a greater concentration of species B around A than what is predicted by Smoluchowski's totally absorbing boundary conditions.

The time dependent rate constant  $k(t)$  may be written in the form  $k(t) = k_{\text{act}}\rho_B(a, t)$ , which simply states that the rate is proportional to the concentration of B particles around the A particles multiplied by the reactivity of the surface. The explicit form for  $k(t)$  is then

$$k(t) = \frac{4\pi a D' k_{\text{act}}}{4\pi a D' + k_{\text{act}}} \left[ 1 + \frac{k_{\text{act}}}{4\pi a D'} \exp \left[ \frac{D't}{a^2} \left( 1 + \frac{k_{\text{act}}}{4\pi a D'} \right)^2 \right] \right] \\ \times \operatorname{erfc} \left\{ \frac{\sqrt{D't}}{a} \left( 1 + \frac{k_{\text{act}}}{4\pi a D'} \right) \right\} \quad (2.25)$$

which can be simplified by using the asymptotic form such that  $\lim_{x \rightarrow \infty} \exp(x^2) \operatorname{erfc}(x) = 1/x\sqrt{\pi}$  to give the rate at long times to be

$$k(t) = \frac{4\pi a D' k_{\text{act}}}{4\pi a D' + k_{\text{act}}} \left[ 1 + \frac{k_{\text{act}} a}{(4\pi D' a + k_{\text{act}})(\sqrt{\pi D' t})} \right] \quad (2.26)$$

For comparison with the diffusion controlled case, expressing Eq. (2.26) in the form of Eq. (2.21) gives

$$k(t) = 4\pi a'_{\text{eff}} D' \left[ 1 + \frac{a'_{\text{eff}}}{\sqrt{\pi D' t}} \right] \quad (2.27)$$

with the 'effective' encounter radius ( $a'_{\text{eff}}$ ) defined as

$$a'_{\text{eff}} = a \left( \frac{k_{\text{act}}}{4\pi a D' + k_{\text{act}}} \right) \quad (2.28)$$

The steady state rate constant is then simply

$$k(\infty) = 4\pi a'_{\text{eff}} D' \quad (2.29)$$

It can be seen that within the steady state limit the encounter distance is reduced by a factor of  $(k_{\text{act}} + 4\pi D'a)/k_{\text{act}}$  in comparison to Smoluchowski's totally absorbing boundary.

Equation (2.29) can be decomposed into two processes [8] as

$$k(\infty)_{\text{obs}}^{-1} = (k_{\text{diff}})^{-1} + (k_{\text{act}})^{-1} \quad (2.30)$$

which simply states that using the radiation boundary condition, the overall time required for species A and B to react involves: (i) the time required for diffusion [the first term in Eq. (2.30)] and (ii) time required to react once within this encounter distance [the second term in Eq. (2.30)]. If the condition  $k_{\text{act}} \gg 4\pi a D'$  is true, then the rate limiting step is diffusion towards the boundary and in this instance reactions are said to be *diffusion controlled*. If the converse is true, such that  $k_{\text{act}} \ll 4\pi a D'$ , then reaction on the boundary is the rate determining step (*kinetic control*) and the rate can be approximated as

$$k(t) = k_{\text{act}} \left[ 1 + \frac{k_{\text{act}}}{4\pi a D'} \frac{a}{\sqrt{\pi D' t}} \right] \quad (2.31)$$

**Problems with the radiation boundary** Some of the problems with using the radiation boundary condition to model chemical systems have been discussed in the literature [9]. The most important of these are (1) for particles close to the encounter distance, it is not possible to specify a non-zero probability for reaction, since an infinite number of encounters follow an unsuccessful first encounter resulting in reaction (as shown by Collins and Kimball [7]). (2) Schell and Kapral [10] have shown that the probability of reaction on encounter should scale with the ratio of  $D'$  and  $a$  ( $D'$  is the mutual diffusion coefficient and  $a$  the encounter distance) for radiation boundary condition to be applicable. (3) All re-encounters are treated in the same manner.

Sometimes for a spin controlled reaction, the probability of reaction of first encounter has a physical origin, and if this first encounter is unreactive then the spin state is also unreactive, and therefore all subsequent rapid re-encounters will not react either [due to condition (3)]. The radiation boundary condition is clearly not appropriate to use for such reactions, where an appropriate model for spin dynamics is not incorporated.

Noyes [8], Wilemski and Fixman [11] have pointed out that it is not strictly correct to apply Smoluchowski [1] or radiation [7] boundary conditions to the diffusion equation to model bimolecular chemical reactions. Both Teramoto and Shigesada [12] and Wilemski and Fixman [11] have proposed a modified diffusion equation by introducing a sink term to represent the reaction rate at a set of relative phase-space coordinates of two reacting species. Let a simple diffusive process be described as

$$\frac{\partial \rho_B}{\partial t} - D' \nabla^2 \rho_B = -\frac{k}{4\pi a^2} \delta(r - a) \rho_B \quad (2.32)$$

with  $k$  being a second order rate constant,  $\delta(x)$  the Dirac delta function and  $\nabla^2$  the Laplacian operator. Assuming spherical symmetry, Wilemski and Fixman [11] have shown that integrating Eq. (2.32) over the entire volume gives an expression for the rate of change for the total number ( $n$ ) of unreacted particles to be

$$\frac{dn}{dt} = -k \rho_B(a, t) \quad (2.33)$$

where the term  $\partial\rho_B/\partial t$  is required to vanish at the reactive surface  $a$  due to reaction. Integrating Eq. (2.32) again, but with  $r \geq a + \epsilon$ , Wilemski and Fixman [11] further obtain

$$\frac{dm}{dt} = -4\pi(a + \epsilon)^2 \left. \frac{\partial\rho_B}{\partial r} \right|_{r=a+\epsilon} \quad (2.34)$$

with  $m$  being the number of unreacted particles from a spherical surface of radius  $a + \epsilon$ , which is centered at the origin. By letting Eqs. (2.33) and (2.34) be equal and taking the limit  $\epsilon \rightarrow 0$  (such that there is no surface extending from  $a$ ), one retrieves the radiation boundary condition as given in Eq. (2.22). Clearly the radiation boundary is not appropriate to use if reaction is possible at multiple interparticle distances and one must instead use Wilemski and Fixman's method. Another important reason to use Wilemski and Fixman's method is that the Green's function can be more readily found (in comparison with the radiation boundary) which is described on the full configuration space, and can be used to solve the general diffusion equation.

## 2.2.2 Ions in Solution

In the analysis so far, it is assumed both particles A and B to be uncharged. If however, both the particles are now ions, the diffusion of B reactants about a given A particle has to be modified due to the drift exerted by the electrostatic forces. The steady state solution for both diffusion controlled and partially diffusion controlled reactions is now presented.

### 2.2.2.1 Diffusion Controlled Reactions

Diffusion controlled recombination of an ion pair is influenced by the random dispersive forces (also present for non-charged species) and the strong Coulombic electrostatic interactions. The diffusion equation [13, 14] governing the diffusive motion of charged species is known as the Debye-Smoluchowski equation [15], which can be expressed as

$$\frac{\partial\rho_B}{\partial t} = D'\nabla^2\rho_B + \frac{D'}{k_B T} \nabla \cdot (\rho_B \nabla U) \quad (2.35)$$

where as before  $\rho_B$  is the probability distribution of B about A, and  $U$  is the electrostatic potential energy at a separation  $r$ . The explicit form for  $U$  can be written as (in the absence of any screening potential)

$$U = \frac{k_B T z_i z_j r_c}{r} \quad (2.36)$$

with  $r_c$  representing the Onsager distance [14] (the distance at which the Coulombic interaction equals  $k_B T$ ), which is defined as

$$r_c = \frac{e^2}{4\pi\epsilon_0\epsilon_r k_B T} \quad (2.37)$$

In Eqs. (2.36) and (2.37)  $z_i e$  and  $z_j e$  are the charges on ion  $i$  and  $j$  respectively,  $\epsilon_0$  is the permittivity of free space,  $\epsilon_r$  is the relative permittivity of the solvent,  $k_B$  is the Boltzmann constant and  $T$  is the temperature. The sign of  $r_c$  is important and it depends on whether the encountering pair are of the same charge (in which case  $r_c > 0$ ) or of different charge (in which case  $r_c < 0$ ). In the absence of any external field, the diffusion tensor and potential energy of interaction is assumed to be spherically symmetrical, so the diffusive motion becomes independent of angles  $\phi$  and  $\theta$ . Substituting the expression for  $U$ , the radial part of Eq. (2.35) becomes

$$\frac{\partial \rho_B}{\partial t} = D' \left[ \frac{\partial^2 \rho_B}{\partial r^2} - \frac{\partial}{\partial r} \frac{(2r + r_c)\rho_B}{r^2} \right] \quad (2.38)$$

In the steady state limit ( $\partial \rho_B / \partial t = 0$ ) Eq. (2.38) can be reduced to

$$\frac{\partial}{\partial r} \left( r^2 \frac{\partial \rho_B}{\partial r} \right) - r_c \frac{\partial \rho_B}{\partial r} = 0 \quad (2.39)$$

which when integrated gives

$$\left( r^2 \frac{d\rho_B}{dr} \right) - \rho_B r_c = A \quad (2.40)$$

where  $A$  is the constant of integration. Using standard integration techniques together with boundary conditions  $\rho_B(a, t) = 0$  and  $\rho_B(r \rightarrow \infty, t)$ , the expression for the steady state distribution of B about A is then

$$\rho_B(r, \infty) = \frac{1 - \exp\left(\frac{r_c}{a} - \frac{r_c}{r}\right)}{1 - \exp\left(\frac{r_c}{a}\right)} \quad (2.41)$$

Fick's first law in the presence of electrostatic forces can be written as

$$\mathbf{J}_B = D' \left[ \nabla \rho_B + \frac{\rho_B}{k_B T} \nabla U \right] \quad (2.42)$$

which gives an expression for the steady state rate constant to be

$$k(\infty) = 4\pi a^2 D' \left[ \frac{\partial \rho_B}{\partial r} + \frac{\rho_B(a, \infty)}{k_B T} \frac{dU}{dr} \right] \quad (2.43)$$

Using the derivative of Eq. (2.41) and substituting into Eq. (2.43) finally gives the steady state rate constant for ions to be

$$k(\infty) = 4\pi r_c D' \left[ \exp\left(\frac{r_c}{a}\right) - 1 \right]^{-1}. \quad (2.44)$$

### 2.2.2.2 Partially Diffusion Controlled

Like the neutral case, the inner boundary condition must be replaced from Smoluchowski's condition to  $\rho_B(a) = k_{\text{act}}\rho_B$ . The required inner boundary condition for charged species then takes the form

$$4\pi a^2 D' \left[ \nabla \rho_B + \frac{\rho_B}{k_B T} \nabla U \right]_a = k_{\text{act}} \rho_B \quad (2.45)$$

where the left hand side of Eq. (2.45) simply representing the diffusive flux across a sphere of radius  $a$  (with the A particle located at the centre). Upon solving with the required boundary conditions one obtains an expression for the steady state rate constant to be  $k(\infty) = 4\pi a'_{\text{eff}} D'$ , with  $a'_{\text{eff}}$  representing

$$a'_{\text{eff}} = r_c \left[ \left( 1 + \frac{4\pi r_c D'}{k_{\text{act}}} \right) \exp(r_c/a) - 1 \right]. \quad (2.46)$$

## 2.3 Diffusion as a Stochastic Process

### 2.3.1 Introduction

Until now diffusion has been treated as a macroscopic physical process driven by entropy, however, the diffusion equation implies a microscopic interpretation in terms of stochastic trajectories. Since much of the work in this thesis uses and develops simulation methods at this microscopic level, it is necessary to introduce the fundamental concepts of this theory.

**Markov process** A stochastic process is a random process in which the evolution from a state  $X(t_n)$  to  $X(t_{n+1})$  is indeterminate (i.e. governed by the laws of probability) and can be expressed by a probability distribution function. Diffusion can be classified as a stochastic process in a continuous state space ( $\tau$ ) possessing the *Markov property* as

$$\begin{aligned} P(X(t_{n+1}) \in \tau | X(t_1) = x_1, X(t_2) = x_2, \dots, X(t_n) = x_n) \\ = P(X(t_{n+1}) \in \tau | X(t_n) = x_n) \end{aligned} \quad (2.47)$$

In diffusion terms of a stochastic process, the above equation simply states that the future trajectory of a particle is independent of the trajectory the particle followed to reach its current state.

**Strong markov process** For a diffusion process, the Markov property can be extended to a sequence of random times known as the *strong Markov property* and can be expressed as follows: let  $T_n, n = 1, 2, \dots$  be an increasing sequence of stopping times<sup>3</sup> for the process  $X(t), n \geq 0$ , and suppose  $X(T) = x_n$ ; the Markov chain  $X(T_{n+1}), X(T_{n+2}), \dots, X_{T+n}$  behaves as if the process had started anew at  $X(T_n) = x_n$ , and is independent of the Markov chain of events  $X(T_1), \dots, X(T_{n-1})$ . It should be noticed that a Markov process does not necessarily obey the strong Markov property because of subtle links between the random times. The converse is however true.

**Time homogeneous process** Finally a diffusion process is time-homogeneous in that the process is independent of the time origin. This can be written more formally as

$$P((X(T_n) = x_n)|X(T_{n-1}) = x_{n-1}) = P(X(T_n - T_{n-1}) = x_n|X(0) = x_{n-1}) \quad (2.48)$$

which simply states that the diffusion process starts afresh, and that the new position  $x_n$  only depends on the elapsed time since the most recently specified position  $x_{n-1}$ . A diffusion process is only time homogeneous if it obeys the above property. Not all diffusion process obey this property such as a conditioned diffusion process, where the time origin is of significant importance.

### 2.3.2 One Dimensional Diffusion Process

The mathematical model of a one dimensional diffusion is the Wiener process ( $W_t$ ), which satisfies the following three conditions: (1)  $W_0 = 0$ , (2)  $W_t$  is continuous with independent increments and (3) the trajectory of  $[W_{t+\delta t} - W_t]$  can be sampled from a normal distribution with mean ( $\mu$ ) of zero and variance ( $\sigma^2$ ) of  $\delta t$  (strong Markov property).

A Wiener process has the additional property  $\mathbb{E}(X(t_{n+1})|X_1 \dots X(t_n) = X(t_n))$  i.e. the expectation value for a future event  $X_{n+1}$ , conditioned on it having evolved to  $X(t_n)$  is  $\mathbb{E}[X(t_n)]$  and no information is needed regarding any previous or future events. In diffusion terms of a stochastic process, this means that the expectation value of a new position of the particle at  $X(t_{n+1})$  is equal to its position at  $X(t_n)$  and is known as the *martingale property*.

More generally, a diffusion process from a state  $X(t)$  to  $X(t + \delta t)$  of a particle in one dimension can be characterised by two parameters, namely  $\mu$  representing the

---

<sup>3</sup>  $T$  is said to be a stopping time for the sequence  $\{X(t_i)\}$ , if the event  $(X(T) = n)$  is independent of  $X(T_{n+1}), X(T_{n+2}), X(T_{n+3}) \dots$  for  $n = 1, 2, \dots$

mean (drift) and  $\sigma^2$  representing the variance (dispersion)

$$\begin{aligned}\mu &= \lim_{\delta t \rightarrow 0} \frac{\mathbb{E}(\delta X)}{\delta t} \\ \sigma^2 &= \lim_{\delta t \rightarrow 0} \frac{\mathbb{E}(\delta X^2)}{\delta t}\end{aligned}\quad (2.49)$$

All higher moments are zero for a diffusion process. The stochastic differential equation [16] which governs the change in the particle's position ( $dX$ ) in an infinitesimal time space ( $dt$ ) is well known to be

$$dX = \mu dt + \sigma dW_t \quad (2.50)$$

with  $dW_t$  representing the random increment of the standard Wiener process over the time interval  $dt$ . Analytical solution in terms of stochastic process that can be sampled exactly is only possible in some cases; where this is not possible, numerical simulations become necessary. There are many discretisation methods available [17], with the simplest being the Euler method (which is adopted for the purposes of this work). The solution to Eq. (2.50) is only possible when  $dt$  is infinitesimal, and must be approximated by time discretisation, which replaces  $dX$  and  $dt$  in Eq. (2.50) with  $\delta X$  and  $\delta t$ . Using the definition of a Wiener process [condition (3)],  $dW_t$  can be replaced with a normally distributed random variable with  $\mu = 0$  and  $\sigma = \delta t$  giving

$$\delta X = \mu \delta t + \sigma \sqrt{\delta t} N(0, 1) \quad (2.51)$$

For the Wiener process the transition density on going from a state  $x_0$  to  $y$  is a simple Gaussian of the form

$$p(x_0, y, t) = \frac{1}{\sigma \sqrt{2\pi t}} \exp \left[ -\frac{(y - x_0 - \mu t)^2}{2\sigma^2 t} \right] \quad (2.52)$$

A Wiener process  $\{X(t), t \geq 0\}$  with  $X(0) = 0$ ,  $\mu = 0$  and  $\sigma = 1$  is commonly referred to as the *standard Wiener process*. Using this transition density, both the *forward* and *backward* equations (see Sect. 2.3.2.1 for a detailed explanation) can be derived, for which Eq. (2.52) is a solution [18].

### 2.3.2.1 Kolmogorov Diffusion Equation

Defining  $p(x, y, t)$  as the probability (or more formally the transition density) of the particle diffusing from position  $x$  to  $y$  at a given time  $t$ , Kolmogorov [13] (and later by Cox and Miller [19]) has shown that  $p(x, y, t)$  satisfies Eqs. (2.53) and (2.54), formally known as the Kolmogorov forward and backward equations [13].

**Forward equation:**

$$\frac{\partial p}{\partial t} = \frac{\partial^2}{\partial y^2} \left( \frac{\sigma^2(y)p}{2} \right) - \frac{\partial}{\partial y} (\mu(y)p) \quad (2.53)$$

**Backward equation:**

$$\frac{\partial p}{\partial t} = \frac{1}{2} \sigma^2(x) \frac{\partial^2 p}{\partial x^2} + \mu(x) \frac{\partial p}{\partial x} \quad (2.54)$$

In the language of applied maths,  $p(x, y, t)$  is the Green's function for the diffusion process. It is important to note that in the forward equation, differentiation is carried out with respect to  $y$  (the current position) and with respect to  $x$  (the initial position) in the backward equation. In the simulation of chemical systems, the drift term ( $\mu$ ) arising in Kolmogorov's equation is normally due to the Coulombic interaction between charged species and can be expressed as

$$\mu(x) = -\frac{D'}{k_B T} \frac{\partial U}{\partial x} \quad (2.55)$$

with  $D'$  being the diffusion coefficient,  $k_B$  the Boltzmann constant,  $T$  the temperature and  $U$  the potential energy. If  $D'$  does not depend on either the position or time, then Eqs. (2.53) and (2.54) can be rewritten as the one dimensional Debye-Smoluchowski equation with variance  $2D'$  as

**Forward equation:**

$$\frac{\partial p}{\partial t} = D' \frac{\partial^2 p}{\partial y^2} + \frac{D'}{k_B T} \frac{\partial}{\partial y} \left( p \frac{\partial U}{\partial y} \right) \quad (2.56)$$

**Backward equation:**

$$\frac{\partial p}{\partial t} = D' \frac{\partial^2 p}{\partial x^2} - \frac{D'}{k_B T} \frac{\partial U}{\partial x} \frac{\partial p}{\partial x} \quad (2.57)$$

If both  $D'$  and  $\mu$  are constant then Eq. (2.53) can be re-expressed in the form

$$\frac{\partial p}{\partial t} = D' \frac{\partial^2 p}{\partial y^2} - \mu \frac{\partial p}{\partial y} \quad (2.58)$$

In order to numerically solve the stochastic differential equation, the constraint that  $\mu$  is constant is made, which is satisfactory so long as the time steps used in the simulation remain sufficiently small during interval  $t$  and  $t + \delta t$ . The solutions to Eq. (2.58) has been done by Kolmogorov [13] using different boundary conditions. Due to the extensive use of these Greens' functions in the simulation packages, they have been reproduced below using the four most common boundary conditions.<sup>4</sup>

---

<sup>4</sup> Proof of these are shown in the Appendix in Sects. A.4–A.7.

### 2.3.2.2 Transition Density with No Boundary

$$p(x, y, t) = \frac{1}{\sqrt{4\pi D't}} \exp\left[-\frac{(y-x-\mu t)^2}{4D't}\right]. \quad (2.59)$$

### 2.3.2.3 Transition Density with a Reflecting Boundary

*Boundary condition*

$$D' \frac{\partial p}{\partial y} \Big|_a - \mu p(a) = 0 \quad (2.60)$$

$$\begin{aligned} p_{\text{ref}}(x, y, t) &= \frac{1}{\sqrt{4\pi D't}} \exp\left[-\frac{(y-x-\mu t)^2}{4D't}\right] \\ &+ \frac{1}{\sqrt{4\pi D't}} \exp[-\mu(x-a)/D'] \exp[-(y+x-\mu t-2a)^2/4D't] \\ &+ \frac{\mu}{2D'} \exp[\mu(y-a)/D'] \operatorname{erfc}[(x+y+\mu t-2a)/\sqrt{4D't}]. \end{aligned} \quad (2.61)$$

### 2.3.2.4 Transition Density with an Absorbing Boundary

*Boundary condition*

$$p(a) = 0 \quad (2.62)$$

$$\begin{aligned} p_{\text{abs}}(x, y, t) &= \frac{1}{\sqrt{4\pi D't}} \left( \exp\left[-\frac{(y-x-\mu t)^2}{4D't}\right] \right) \\ &- \frac{1}{\sqrt{4\pi D't}} (\exp[\mu(a-x)/D'] - (y+x-\mu t-2a)^2/4D't). \end{aligned} \quad (2.63)$$

### 2.3.2.5 Transition Density with a Radiation Boundary

*Boundary condition*

$$D' \frac{\partial p}{\partial y} \Big|_a - \mu p(a) = vp(a) \quad (2.64)$$

Recalling  $v$  to measure the reactivity of the surface which has units of velocity, the solution is given as

$$\begin{aligned}
p_{\text{rad}}(x, y, t) = & \frac{1}{\sqrt{4\pi D't}} \exp\left[-\frac{(y-x-\mu t)^2}{4D't}\right] \\
& + \frac{1}{\sqrt{4\pi D't}} \exp[-\mu(y-a)/D'] \exp[-(y+x-\mu t-2a)^2/4D't] \\
& + \frac{2v+\mu}{2D'} \exp[v(x+y+\mu t-2a+vt) + \mu(y-a)/D'] \\
& \times \operatorname{erfc}\left(\frac{x+y-2a+(2v+\mu)t}{\sqrt{4D't}}\right). \tag{2.65}
\end{aligned}$$

### 2.3.3 Three Dimensional Diffusion

To model diffusion in three dimensions, the stochastic differential equation must be modified to the form

$$d\mathbf{r} = \boldsymbol{\mu}dt + \sigma\sqrt{dt}\mathbf{N}(0, 1) \tag{2.66}$$

with  $\boldsymbol{\mu}$  being the drift vector equalling to  $D\mathbf{F}/k_{\text{B}}T$  if the species are charged (in this expression  $D$  is the diffusion coefficient,  $\mathbf{F}$  the external force on the particle,  $k_{\text{B}}$  the Boltzmann constant and  $T$  the temperature). In three dimensional space, Kolmogorov's backward equation becomes

$$\frac{\partial p}{\partial t} = D'\nabla_x^2 p - \frac{D'}{k_{\text{B}}T} \nabla_x U \cdot \nabla_x p \tag{2.67}$$

with the adjoint forward equation taking the form

$$\frac{\partial p}{\partial t} = D'\nabla_y^2 p + \frac{D'}{k_{\text{B}}T} \nabla_y \cdot (p\nabla_y U). \tag{2.68}$$

### 2.3.4 Other Models of Molecular Motion

The modelling of Brownian motion for molecules in liquids is by no means limited to the Kolmogorov diffusion equation. There are many alternative algorithms available, which make use of the velocity and the force to explicitly calculate the trajectory of the particles. In this section, a brief discussion of the three most commonly used simulations in radiation chemistry are presented. A much more detailed explanation can be found in the references provided.

**Molecular dynamics** The most successful model which is able to describe molecular motion is molecular dynamics [20–23]. The foundation of molecular dynamics relies on the particles interacting using a predefined potential energy function, which itself is usually calculated from experimental data. The particles move according to the

laws of classical dynamics by integrating Newton's equations of motion. One of the most important functions which can be obtained from this type of simulation is the velocity autocorrelation function ( $\chi$ ) for a single particle, defined as

$$\chi = \frac{\langle \mathbf{v}_c(0) \cdot \mathbf{v}_c(t) \rangle}{\langle \|\mathbf{v}_c(0)\|^2 \rangle} \quad (2.69)$$

with  $\mathbf{v}_c(0)$  being the initial velocity and  $\mathbf{v}_c(t)$  the velocity at time  $t$ . Through the use of the Green-Kubo relation [24, 25],  $\chi$  can be related to the diffusion coefficient as

$$D = \frac{1}{3} \int_0^{\infty} \langle \mathbf{v}_c(t) \cdot \mathbf{v}_c(0) \rangle dt \quad (2.70)$$

Unfortunately, molecular dynamics are computationally very expensive which makes simulating radiation kinetics very difficult. This problem is further compounded by the necessity to perform many realisations to obtain statistically significant results; something which is not practical at present. In order to solve the ordinary differential equations of motion to generate a trajectory, a range of finite difference methods are available (for example the velocity Verlet algorithm [26]).

**Langevin equation** Although molecular motion can be entirely described using molecular dynamics, it does have the disadvantages of requiring small time steps and the necessity to model the solvent molecules explicitly. The Langevin equation [27] helps to circumvent these problems to a certain degree. Using Newton's second law of motion, the rate of change of the velocity for a single particle can be described using the relation

$$\frac{dv_c(t)}{dt} = -\frac{\gamma_F v_c(t)}{m} + \frac{1}{m} \xi'(t) \quad (2.71)$$

with  $v_c(t)$  being the velocity,  $m$  the mass,  $\gamma_F$  the friction coefficient as given by Stokes law and  $\xi'(t)$  a stochastic variable representing the collision between the particle and the solvent. The change in the particle's displacement is then simply

$$\frac{dx}{dt} = v_c(t) \quad (2.72)$$

Equation (2.71) is a linear equation whose solution is elementary such that

$$v_c(t) = e^{-t/\tau} v_c(0) + \frac{1}{m} \int_0^t e^{-(t-s)/\tau} \xi'(s) ds \quad (2.73)$$

with  $\tau = m/\gamma_F$ . The integral in the above equation gives an 'extra' velocity produced by the random noise to prevent the velocity decaying to zero. Unfortunately,  $\xi'(s)$  is a fluctuating function and it is not obvious whether any global solution to

Eq. (2.71) exists unless stronger conditions to  $\xi'(s)$  are imposed. It can be shown that  $\xi'(s)ds$  possesses the properties of a Wiener process  $d\mathbf{W}$ , which when substituted into Eq. (2.71) gives the stochastic differential equation of the form

$$d\mathbf{v}_c(t) = \frac{\gamma_F}{m}\mathbf{v}(t)dt + \frac{1}{m}d\mathbf{W} \quad (2.74)$$

with the solution to the above equation readily found to be

$$\mathbf{v}_c(t) = e^{-t/\tau}\mathbf{v}_c(0) + \frac{1}{m}\int_0^t e^{-(t-s)/\tau} d\mathbf{W} \quad (2.75)$$

where  $\mathbf{v}_c(0)$  is the initial velocity of the particle. The expression for the variance in the velocity is then

$$\langle v_c^2(t) \rangle_{\text{eq}} = \frac{k_B T}{m} \left( 1 - \exp\left(-\frac{2\gamma_F}{m}t\right) \right) + v_c^2(0) \exp\left(-\frac{2\gamma_F}{m}t\right) \quad (2.76)$$

where  $k_B$  is Boltzmann's constant and  $T$  the temperature. The solution for the variance in the position involves multiplying Eq. (2.71) by  $x$  and taking the ensemble average. Letting  $u = d\langle x^2 \rangle/dt$ , Eq. (2.71) can be re-written as<sup>5</sup>

$$\frac{m}{2} \frac{du}{dt} + \frac{\gamma_F}{2} u = k_B T \quad (2.77)$$

The general solution can be readily calculated to be

$$u = C e^{-\gamma_F t/m} + 2 \frac{k_B T}{\gamma_F} \quad (2.78)$$

with  $C$  being the constant of integration, which equals to  $k_B T/\gamma$ . Using the solution for  $u$ , the expression for  $\langle x^2 \rangle$  finally gives

$$\langle x^2(t) \rangle = \frac{2k_B T m}{\gamma_F^2} \left[ \frac{t\gamma_F}{m} - \left( 1 - \exp\left(-\frac{t\gamma_F}{m}\right) \right) \right]. \quad (2.79)$$

**Fokker-Planck equation** The Langevin equation describes the Brownian motion of a single particle which experiences a random force (due to collisions with the solvent particles) causing the velocity to behave in a stochastic way. The Fokker-Planck equation (also known as Kolmogorov forward equation) extends the Langevin equation to an ensemble of identical Brownian particles by finding the probability distribution  $P(v, t)$  of  $N$  particles in the ensemble having velocities in the interval  $(v, v + \delta t)$  at time  $t$ . The Fokker-Planck equation can be formally expressed as

<sup>5</sup> It should be recognised that  $\langle \dot{x}x \rangle = \frac{1}{2} \frac{dx^2}{dt}$  and  $\langle \ddot{x}x \rangle = \frac{1}{2} \frac{d^2x^2}{dt^2} - u^2$ .

$$\frac{\partial}{\partial t} P(v_c, t) = \gamma_F \frac{\partial}{\partial v_c} (v_c P(v_c, t)) + \frac{k_B T \gamma_F}{m} \frac{\partial^2}{\partial v_c^2} P(v_c, t) \quad (2.80)$$

The steady state solution to the Fokker-Planck equation can be readily found to be

$$P(v) = \left( \frac{\gamma_F}{\pi Q} \right)^{1/2} \exp \left( -\frac{\gamma_F v_c^2}{Q} \right) \quad (2.81)$$

with  $Q = 2\gamma_F k_B T / m$  which describes the strength of the stochastic force. The time dependence of  $P(v_c, t)$ , subject to the initial condition  $P(v_c, t_0) = \delta(v_c(t) - v_c(0))$  can be obtained using the method of Fourier transformation. A full derivation is not presented here, but can be found elsewhere [28]. The final result yields

$$P(v, t) = \sqrt{\frac{\gamma_F}{\pi Q [1 - \exp[1 - 2\gamma_F(t - t_0)]]}} \exp \left[ -\frac{\gamma_F [v_c(t) - v_c(0) \exp[-\gamma_F(t - t_0)]]^2}{Q [1 - \exp[-2\gamma_F(t - t_0)]]} \right] \quad (2.82)$$

**Diffusion model used in this work** For the purpose of this work the evolution of the particle position is described in terms of the stochastic differential equation. The major problem with using this technique is that the particle velocity cannot be described (since the diffusion sample paths are nowhere differentiable). The central limit theorem does however provide the reassurance that the diffusion equation accurately describes evolution of the transition density. For all chemical systems investigated as part of this work, the transient period occurs on a timescale of tens of picoseconds or possibly even longer. This value is much bigger than typical values of the velocity autocorrelation function, making the use of the diffusion equation justifiable.

## 2.4 Geminate Recombination

In diffusion controlled kinetics, two different types of reactions can take place, namely geminate recombination and bulk reactions. Geminate recombination arises in isolated spurs, before any significant diffusion has taken place and entails the reaction between isolated pairs of A and B particles. In this case it becomes meaningless to define their concentration. For geminate recombination, the survival probability  $\Omega(r, t)$  (or its complement  $W(r, t)$ ), which is the probability of surviving reaction to a time  $t$ , given an initial separation  $r$ , is one of the most important physical quantities in radiation chemistry.

In this section, the solution to the backward diffusion equation for  $\Omega(r, t)$  using two different types of boundary conditions for both neutral and charged species is presented. These solutions will then be used in the next section to demonstrate the link between the bulk reaction rate and the pair survival probability. Before presenting

the discussion, it is worth noticing why  $\Omega(r, t)$  (and by extension  $W(r, t)$ ) obeys only the backward diffusion equation rather than the forward diffusion equation.

The expression relating  $\Omega(r, t)$  and  $p(x, y, t)$  is given by

$$\Omega(r, t) = \int_a^{\infty} p(x, y, t) dy \quad (2.83)$$

which simply states that the probability of survival is an integral of the probability density function for the interparticle distance up to time  $t$ . This integral involves the variable  $y$ , so the backward diffusion equation is not affected. However, upon integrating the forward equation one obtains

$$\frac{\partial \Omega}{\partial t} = \left[ \frac{\partial}{\partial y} \left( \frac{1}{2} \sigma^2(y) p(x, y, t) \right) - \mu(y) p(x, y, t) \right]_a^b \quad (2.84)$$

which simply states that the rate of reaction is proportional to the diffusive flow over the two boundaries (essentially Fick's law). This is not an expression for the survival probability.

## 2.4.1 Diffusion Controlled Reactions

### 2.4.1.1 Neutral Species

In order to find the expression for the reaction probability of two neutral particles it is necessary to return to the backward diffusion equation

$$\frac{\partial W}{\partial t} = D' \left[ \frac{\partial^2 W}{\partial r^2} + \frac{2}{r} \frac{\partial W}{\partial r} \right] \quad (2.85)$$

with  $r$  being the separation of the pair and  $W$  is the reaction probability. Assuming spherical symmetry together with the boundary conditions<sup>6</sup>

$$W(a, t) = 1 \quad (t > 0) \quad (2.86)$$

$$W(r \rightarrow \infty, t) = 0 \quad (2.87)$$

$$W(r, 0) = 0 \quad (r > a) \quad (2.88)$$

the solution to Eq. (2.85) can be found using the Laplace transform method to give

---

<sup>6</sup> These boundary conditions are equivalent to Smoluchowski's boundary conditions as discussed earlier.

$$W(r, t) = \frac{a}{r} \operatorname{erfc} \left( \frac{r - a}{\sqrt{4D't}} \right) \quad (2.89)$$

where  $a$  is the encounter radius and  $D'$  is the mutual diffusion coefficient. The reaction probability  $W(r, t)$  is the complement of the survival probability  $\Omega(r, t)$  so Eq. (2.89) can be easily reformulated in terms of the survival probability using the relationship  $\Omega(r, t) = 1 - W(r, t)$ . The asymptotic recombination yield is then easily seen to be

$$W(r, \infty) = \frac{a}{r} \quad (2.90)$$

### 2.4.1.2 Charged Species

The time-dependent backward diffusion equation for the reaction probability of ions [29, 30] is known to be

$$\frac{\partial W}{\partial t} = D' \left[ \frac{\partial^2 W}{\partial r^2} + \frac{(2r + r_c)}{r^2} \frac{\partial W}{\partial r} \right] \quad (2.91)$$

where  $r_c$  is the Onsager distance. In order to solve the above diffusion equation, it is necessary to impose some boundary conditions. Assuming the reaction between the species to be diffusion controlled with an absorbing boundary at  $a$  (the encounter distance), the required boundary conditions remain the same as shown in Eqs. (2.86)–(2.88). Unfortunately, Eq. (2.91) cannot be solved in closed form with several attempts detailed in the literature which aim to provide an approximate solution [31–37]. The most rigorous of these is the solution obtained by Hong and Noolandi [38], however, the solution is exact only in the Laplace space and cannot be inverted analytically. From their formulation, the survival probability (at long times) is found to be

$$\Omega(t) = [U(r)/U(\infty)] \left( 1 + \frac{r_c}{U(\infty)\sqrt{\pi D't}} \right) \quad (2.92)$$

where  $r$  is the radical pair separation and  $U(r) = \exp(-r_c/r) + (D'r_c/va^2 - 1) \exp(-r_c/a)$  (with  $r$ ,  $a$  and  $v$  representing the distance between the ion pair, the encounter radius and reaction velocity respectively). Taking the inverse Laplace transform of Hong and Noolandi's expression (or in general the inverse Laplace transform of any expression) is notoriously numerically unstable. A much better method [39] is to use a numerical solution to the partial differential equation using a standard finite difference method, which is certain to be unconditionally stable.

For high permittivity solvents (when  $r_c$  is small), Clifford et al. [32] have obtained an approximate time dependent solution for  $W(r, t)$  as

$$W(r, t) = \left( \frac{a'_{\text{eff}}}{r_{\text{eff}}} \right) \operatorname{erfc} \left( \frac{r_{\text{eff}} - a'_{\text{eff}}}{\sqrt{4D't}} \right) \quad (2.93)$$

with the asymptotic form for the reaction probability being

$$W(r, \infty) = \frac{a'_{\text{eff}}}{r_{\text{eff}}} \quad (2.94)$$

In the above expression,  $r_{\text{eff}}$  and  $a'_{\text{eff}}$  are defined to be  $r_c/(\exp(r_c/r) - 1)$  and  $r_c/(\exp(r_c/a) - 1)$  respectively, and are referred to as the natural distance scale for the radial process.

For low permittivity solvents Green et al. [31] have developed an excellent approximation for the reaction probability as

$$W^*(x, a, \tau) \approx \frac{1}{2} \text{erfc} \left( \frac{(x - y)}{\sqrt{2} \left( s(\tau_y)^2 - s(\tau_a)^2 \frac{\tau'_a}{\tau_y} \right)^{1/2}} \right) \quad (2.95)$$

with the variables in the above equation defined to be

$$x = \frac{2r}{r_c} \quad (2.96)$$

$$y = \left[ 6((\tau + \tau_a)^{1/3} - \frac{1}{7}[6(\tau + \tau_a)]) \right]^{2/3} \quad (2.97)$$

$$\tau_x = \frac{1}{6} \left[ \frac{7}{2} (1 - \sqrt{(1 - 4x/7)}) \right]^3 \quad (2.98)$$

$$\tau'_x = \frac{\frac{1}{2} \left[ \frac{7}{2} (1 - \sqrt{(1 - 4x/7)}) \right]^2}{\sqrt{(1 - 4x/7)}} \quad (2.99)$$

$$s^2 = \frac{6\tau}{7} \quad (2.100)$$

where  $\tau = 4D't/r_c^2$ . Unfortunately, the approximation breaks down if  $\tau$  is sufficiently large because the normal distribution has a significant part of its density on the wrong side of the reflecting boundary at the origin. This situation arises at longer times because the standard deviation  $s$  increases faster than the mean (defined as  $m = (6\tau)^{1/3} - (6\tau)^{2/3}/7$ ). However, in Sect. 4.4.4.1, it will be shown how this error can be partially corrected. The corresponding unconditioned reaction probability can be found using Eq. (2.95) through the relation

$$W(x, a, \tau) = W(x, \infty, \tau) \times W^*(x, a, \tau) \quad (2.101)$$

Using the perturbation treatment [38, 40] for small  $r$  and large  $t$ , Tachiya [4] has found an approximate expression for  $\Omega(r, t)$  as

$$\Omega(r, t) = \frac{e^{-(r_c/r)} - e^{-(r_c/a)}}{1 - e^{-(r_c/a)}} \left[ 1 + \frac{1}{1 - e^{-(r_c/a)}} \times \frac{r_c}{\sqrt{\pi D't}} \right] \quad (2.102)$$

with the asymptotic expression for the survival probability found to be

$$\Omega(r, \infty) = \frac{e^{-(r_c/r)} - e^{-(r_c/a)}}{1 - e^{-(r_c/a)}} \quad (2.103)$$

which is the same as that obtained by Clifford et al. [32] [i.e. Eq. (2.94)].

## 2.4.2 Partially Diffusion Controlled Reactions

### 2.4.2.1 Neutral Species

As mentioned previously, for partially diffusion controlled reactions the reactivity of the inner boundary can be controlled using the parameter  $v$  which has units of velocity. The required inner boundary condition is of the form

$$\left. \frac{\partial \Omega}{\partial r} \right|_{r=a} = \frac{v}{D'} \Omega(a) \quad (2.104)$$

with the outer and initial conditions taking the form

$$\Omega(r \rightarrow \infty, t) = 1 \quad (2.105)$$

$$\Omega(r, 0) = 1 \quad (r > a) \quad (2.106)$$

Using the above boundary conditions, the expression for the survival probability in the absence of any interaction potential can be found to be

$$\begin{aligned} \Omega(r, t) = & 1 - \frac{a}{\left(1 + \frac{D'}{va}\right)} \left( \operatorname{erfc} \left( \frac{r-a}{\sqrt{4D't}} \right) \right. \\ & - \exp \left[ \left( \frac{va}{D'} + 1 \right) \left( \frac{r-a}{a} \right) + \left( \frac{vr}{D'} + 1 \right)^2 \left( \frac{D't}{a^2} \right) \right] \\ & \left. \times \operatorname{erfc} \left[ \frac{r-a}{\sqrt{4D't}} + \left( \frac{va}{D'} + 1 \right) \frac{\sqrt{D't}}{a} \right] \right) \end{aligned} \quad (2.107)$$

with the asymptotic form of the above to be

$$\Omega(r, \infty) = \frac{1 - (a/r) + (D'/va)}{1 + (D'/va)} \quad (2.108)$$

### 2.4.2.2 Charged Species

Using the perturbation treatment [38, 40] for small  $r$  and large  $t$ , together with the boundary conditions given in Eqs. (2.104)–(2.106), Tachiya [4] has arrived at an approximate expression for the survival probability as

$$\Omega(r, t) = \frac{e^{-(r_c/r)} + (\eta - 1) e^{-(r_c/r)}}{1 + (\eta - 1) e^{-(r_c/a)}} \times \left[ 1 + \frac{1}{1 + (\eta - 1) e^{-(r_c/a)}} \times \frac{r_c}{\sqrt{(\pi D't)}} \right] \quad (2.109)$$

where  $\eta = D'r_c/va^2$ . As expected the above equation decomposes to Eq. (2.102) in the limit  $v \rightarrow \infty$ . The asymptotic form for the survival probability is then readily found to be

$$\Omega(r, \infty) = \frac{e^{-(r_c/r)} + (\eta - 1) e^{-(r_c/a)}}{1 + (\eta - 1) e^{-(r_c/a)}} \quad (2.110)$$

which unfortunately diverges for short times. A much better approximation has been developed by Green et al. [41], which provides the same asymptotic form as Tachiya's expression, however the function is not divergent for short times. Green et al. [41] solved the backward diffusion equation subject to the inner boundary condition

$$\left. \frac{\partial W}{\partial r} \right|_{r=a} = -\frac{v}{D'} [1 - W(a)] \quad (2.111)$$

with the other boundary conditions given by Eqs. (2.87) and (2.88). The expression for the time-dependent reaction probability was found to be

$$W(r, t) \approx \frac{a'_{\text{eff}}}{r_{\text{eff}}(1 + \delta)} [\text{erfc}(\alpha) + \exp(2\alpha\beta + \beta^2) \text{erfc}(\alpha + \beta)] \quad (2.112)$$

with  $\alpha$ ,  $\beta$  and  $\delta$  defined to be

$$\alpha = \frac{r_{\text{eff}} - a'_{\text{eff}}}{\sqrt{4D't}} \quad (2.113)$$

$$\delta = \frac{D'a'_{\text{eff}}e^{r_c/a}}{va^2} \quad (2.114)$$

$$\beta = (1 + 1/\delta) \frac{\sqrt{D't}}{a'_{\text{eff}}} \quad (2.115)$$

and  $r_{\text{eff}}$  and  $a'_{\text{eff}}$  are defined to be  $(r_c/\exp(r_c/r) - 1)$  and  $(r_c/\exp(r_c/a) - 1)$  respectively. In the limit  $v \rightarrow \infty$  Eq. (2.112) reduces to Eq. (2.93) which is to be expected since the surface reactivity is now infinitely fast.

## 2.5 Bulk Recombination Rate Constant

Bulk reaction is the reaction between two particles, say A and B which are uniformly distributed in the chemical system. In this situation it becomes necessary to define the concentrations  $c_A$  and  $c_B$  of both species. In this section the bulk reaction rate is derived in terms of the pair survival probability and it is demonstrated how Smoluchowski's time dependent rate constant can be obtained by making use of the independent pairs approximation.

In general the bulk reaction rate  $k$  is proportional to both  $c_A$  and  $c_B$  as

$$-\frac{dc_A}{dt} = -\frac{dc_B}{dt} = kc_Ac_B \quad (2.116)$$

and as previously shown in this work, the usual method to calculate  $k(t)$  considers the distribution of B particles around any given A particle. The B particles are assumed to be in excess of the A particles so that the competition of an A particle to capture a B particle is not important. Also the A particles are considered to be effectively independent from one other and therefore the concentration gradients about each surviving A particle do not interfere. The rate constant  $k(t)$  is then the inward diffusive flow rate of B particles across the reaction surface at  $a$ . Shlesinger [42] has stated in the literature that this formulation for  $k(t)$  is not strictly speaking correct. Only the first B particle which diffuses towards the reaction surface will contribute to  $k(t)$ , and not the diffusive motion of all the B particles towards the reaction surface. This problem is remedied by explicitly using the pair survival probability.

### 2.5.1 Independent Pairs Approximation

The independent pairs approximation (IPA) plays an important role in describing the kinetics in microscopic nonhomogeneous systems. Rather than formulating a theory based on macroscopic systems, IPA starts with a microscopic description of the geminate pair and extends its applicability to systems of more than two particles. Consider an A particle fixed at the origin, then let the probability density of finding a B particle at distance  $r_1, r_2$  and so on from the A particle be  $u(r_1, r_2, \dots, r_N)$  (the joint probability density of  $N$  distances). The probability  $P(t)$  of the A particle surviving is then the probability of all B particles belonging to A surviving such that

$$P(t) = \int_V \int_V \dots \int_V \Omega(r_1, t) \Omega(r_2, t) \dots \Omega(r_N, t) \\ \times u(r_1, r_2, \dots, r_N) dr_1 dr_2 \dots dr_N \quad (2.117)$$

with  $V$  being the volume of the system and  $\Omega(r, t)$  the pair survival probability of species A and B.

**Uniform distribution** The bulk rate constant  $k(t)$  for a uniform distribution can now be formulated in a similar manner to Eq. (2.116) using the survival probability of the A particle as follows

$$k(t) = -\frac{1}{c_B} \frac{d \ln P}{dt} \quad (2.118)$$

Letting the B particles be distributed according to a Poisson distribution, the probability that the volume contains  $N$  particles is

$$u(N) = e^{-c_B V} \frac{(c_B V)^N}{N!} \quad (2.119)$$

Assuming for simplicity that  $V$  only contains one B particle, the survival probability of A is then simply

$$\Omega_1 = 1 - \int_a^R \frac{4\pi r^2}{V} W(r, t) dr \quad (2.120)$$

where  $W(t)$  is the reaction probability of particle A and  $R$  is the maximum distance between the A–B particle. Now making the *independent pairs approximation* such that

$$P(\text{survival}|N) = P(\text{survival}|1)^N \quad (2.121)$$

which in words states that the probability of the A particle surviving conditioned the volume contains  $N$  number of B particles, is equivalent to the probability of all B particles belonging to A surviving. The expression for  $P(t)$  can now be rewritten in the form

$$\begin{aligned} P(t) &= \sum_{N=0}^{\infty} u(N) P(\text{survival}|1)^N \\ &= \sum_{N=0}^{\infty} e^{-c_B V} \frac{(c_B V)^N}{N!} (\Omega_1)^N \\ &= [1 - c_B V][1 + c_B V \Omega_1] \\ &= e^{-c_B V(1-\Omega_1)} \\ &= \exp\left(-c_B \int_a^R 4\pi r^2 W(r, t) dr\right) \end{aligned} \quad (2.122)$$

Substituting the expression for  $P(t)$  into Eq. (2.118) then gives

$$k(t) = \frac{d}{dt} \int_a^R 4\pi r^2 W(r, t) dr \quad (2.123)$$

Making the assumption that B is in large excess over the A particles and substituting the expression for  $W(r, t)$  Eq. (2.89) into Eq. (2.123) finally gives Smoluchowski's time dependent rate constant to be

$$\begin{aligned} k(t) &= 4\pi a \int_a^\infty r \operatorname{erfc} \left( \frac{r-a}{\sqrt{4D't}} \right) dr \\ &= 4\pi a D' \left[ 1 + \frac{a}{\sqrt{\pi D't}} \right] \end{aligned} \quad (2.124)$$

The rate constant for reactions which are not fully diffusion controlled can also be readily found by substituting the complement of Eq. (2.107) into Eq. (2.123) to give

$$\begin{aligned} k(t) &= \frac{4\pi D'a}{1+\alpha} \left[ 1 + \frac{va}{D'} \exp \left( \left( \frac{va}{D'} + 1 \right)^2 \left( \frac{D't}{a^2} \right) \right) \right] \\ &\times \operatorname{erfc} \left[ \left( \frac{va}{D'} + 1 \right) \frac{\sqrt{(D't)}}{a} \right] \end{aligned} \quad (2.125)$$

where  $\alpha = D'/va$ . The above expression reduces to Eq. (2.124) for an infinitely fast boundary ( $v \rightarrow \infty$ ). This derivation has shown two important factors: (1) Smoluchowski's first assumption that the central A particle is stationary is equivalent to the independent pairs approximation and (2) Smoluchowski's second assumption that the central sink is indestructible is not necessary in this case (as shown by Steinberg and Katchalski [5] and Tachiya [4]). Other derivations of the above equation have also been presented in the literature [3]. Therefore the usual method used to calculate  $k(t)$  is correct, because in Eq. (2.116), the right hand side is multiplied by the concentration of the *surviving* A particles. The concentration of the A particle is only depleted by the inward flow of the *first* B particles and not of all the B particles. Hence only the inward flow of the first B particles contributes to the rate constant.

**Thermal distribution** From statistical mechanics the thermal distribution is known to take the form

$$u(\mathbf{r}_1, \mathbf{r}_2, \dots, \mathbf{r}_N) = \frac{e^{-\beta[\ell_1(\mathbf{r}_1)+\ell_2(\mathbf{r}_2)+\dots+\ell_N(\mathbf{r}_N)]}}{\int \int \dots \int e^{-\beta[\ell_1(\mathbf{r}_1)+\ell_2(\mathbf{r}_2)+\dots+\ell_N(\mathbf{r}_N)]} d\mathbf{r}_1 d\mathbf{r}_2 \dots d\mathbf{r}_N} \quad (2.126)$$

where  $\ell(r) = -e^2/\epsilon_r r$ , with  $\epsilon_r$  being the dielectric constant,  $e$  the electron charge and  $\beta = 1/k_B T$ , with  $k_B$  being the Boltzmann constant,  $T$  the temperature. The probability of survival of the A particle is then

$$P(t) = \left[ \frac{\int_a^V \Omega(r, t) e^{-(\beta\ell(r))} d\mathbf{r}}{\int_a^V e^{-(\beta\ell(r))} d\mathbf{r}} \right]^N \quad (2.127)$$

Under the assumption that

$$\lim_{V \rightarrow \infty} \frac{\int_a^\infty e^{-(\beta \ell(r))} d\mathbf{r}}{V} = 1 \quad (2.128)$$

and  $\ell(r)$  to drop with increasing  $r$ , the final expression for  $P(t)$  yields

$$P(t) = e^{-c_B \int [1 - \Omega(r,t)] e^{-(\beta \ell(r))} d\mathbf{r}} \quad (2.129)$$

Substituting the above expression into Eq. (2.118) then gives the bulk rate constant for a thermal distribution to be [4]

$$k(t) = - \int_a^\infty \frac{\partial \Omega(r,t)}{\partial t} e^{-(\beta \ell(r))} d\mathbf{r} \quad (2.130)$$

## 2.6 Scavenging Kinetics

### 2.6.1 Scavenger Concentration and the Inverse Laplace Transform Relationship

In radiation chemistry, experimentalists often use scavengers to intercept the radicals and ions before they recombine. The addition of scavengers often introduces an extra level of complexity into the recombination kinetics since some of the scavenged products might be capable of further reactions. It was first suggested by Monchick and Hummel [43–45] that the kinetics of recombination in a two radical spur can be extracted by observing the concentration dependence of the yields of scavenging and recombination. The yield of scavenged radicals  $G(s)$  per 100 eV of absorbed energy can be related to the recombination kinetics in hydrocarbons by the relation

$$G(s) = s \int_0^\infty \exp(-st) G(t) dt \quad (2.131)$$

where  $s$  is the pseudo-first order scavenging rate constant (equal to  $k[S]$ , with  $k$  being the steady state scavenging rate constant and  $[S]$  the concentration of scavengers) and  $G(t)$  the survival yield of radicals per 100 eV in the absence of scavengers. The unknown function  $G(t)$  can be obtained by taking the inverse Laplace transform (ILT) of  $G(s)/s$ . Hence, in order to determine  $G(t)$  a knowledge of the function  $G(s)/s$  is required from zero up to the point where all the particles are scavenged. Warman et al. [46] have studied the irradiation of hydrocarbon solutions, and have found an expression for  $G(s)$  (for low concentrations of  $[S]$ ) to be of the form

$$G(s) = [G(0) - G(\infty)] \frac{(\ell[S])^{1/2}}{1 + (\ell[S])^{1/2}} + G(\infty) \quad (2.132)$$

where  $G(0)$  is the initial yield of ions,  $G(\infty)$  is the final yield of intra-spur ions and  $\ell$  is a constant which is related to the particular scavenging reaction. The ILT of  $G(s)/s$  is then readily found to be

$$G(t) = [G(0) - G(\infty)] \exp(\lambda t) \operatorname{erfc}(t\lambda)^{1/2} + G(\infty) \quad (2.133)$$

with  $\lambda = k/\ell$ . Hummel has similarly suggested a form for the scavenging of ions to be

$$G(s) = [G(0) - G(\infty)] (1 - \exp(-(\ell[S])^{1/2})) + G(\infty) \quad (2.134)$$

with the ILT of the above expression being

$$G(t) = [G(0) - G(\infty)] \left( 1 - \operatorname{erfc} \left( \frac{1}{2(\lambda t)^{1/2}} \right) \right) + G(\infty) \quad (2.135)$$

Both Eqs. (2.132) and (2.134) are functions which can be expressed as

$$G(s) = [G(0) - G(\infty)] \frac{\sum_{i=1}^n (\ell[S])^{i/2}/i!}{\sum_{i=0}^n (\ell[S])^{i/2}/i!} + G(\infty) \quad (2.136)$$

It was found by Pimblott and La Verne [47] that an intermediate function (with  $i = 2$  in the above expression) of the form

$$G(s) = [G(0) - G(\infty)] \frac{(\ell[S])^{1/2} + \ell[S]/2}{1 + (\ell[S])^{1/2} + \ell[S]/2} + G(\infty) \quad (2.137)$$

gave a more acceptable fit to experimental data. The ILT of the above expression was found to be

$$G(t) = [G(0) - G(\infty)] \left( 2F_f \left( \frac{4\lambda t}{\pi} \right)^{1/2} \right) + G(\infty) \quad (2.138)$$

with  $F_f$  representing the auxiliary function for the Fresnel integrals.

### 2.6.2 Competition Between Scavenging and Recombination

For some of the chemical systems considered in this thesis, geminate recombination competes with scavenging. The fact that the radicals are initially close to one another means that the radicals compete for individual scavengers; this competition leads to an effect on the scavenging rate.

It has been reported in the literature [48] that Smoluchowski's rate constant overestimates the rate of scavenging for a single target that can be hit multiple times (for example DNA). In their work, the authors found that Smoluchowski's rate constant overestimated the scavenging yield in comparison to Monte Carlo random flights simulation (which makes no assumptions on the rate of scavenging as they are explicitly treated). The authors have found that a modification to Smoluchowski's rate constant is required in order to properly take the correlation of reaction times into account; however, the independent pairs approximation is still made.

In their paper [48], they show that the probability distribution for the first reaction time is given by  $P_2 = \exp(-cv_L(2t))$ , whereas assuming independence of radical-target distances this would be  $\exp(-2cv_L(t))$ , where  $c$  is the target concentration and  $v_L$  has the dimension of volume and is defined as  $v_L(t) = \frac{4}{3}\pi a^3 + 4\pi D'a(t) + 8a^2\sqrt{\pi D't}$ . Comparing the two exponents for a correlated system (Eq. 2.139) and assuming independence of radical-target distance (Eq. 2.140) they obtain the following expressions

$$v_L(2t) = \frac{4}{3}\pi a^3 + 8\pi D'at + 8a^2\sqrt{2\pi D't} \quad (2.139)$$

$$2v_L(t) = \frac{8}{3}\pi a^3 + 8\pi D'at + 16a^2\sqrt{\pi D't} \quad (2.140)$$

In the above equations, the first term representing zero time reaction is overestimated by a factor of two if independence of reaction times is assumed. This is because for a geminate pair, if the scavenger is initially far from one radical then it will also be far from the other radical. Hence there is a second possibility for the other radical to be close to the target and react. However, if the radical-target distances are correlated, and if one radical is far from the target then the other must be as well (as the radicals are close together).

The second term operates in the long time limit when steady state is achieved and any information regarding the initial radical-target correlation is lost. Therefore it is not surprising that both the exponents are the same.

The third term is the most important, as this represents the rate of reaction before a concentration profile is established. It is seen that this term is a factor of  $\sqrt{2}$  smaller than what is predicted by Smoluchowski. By slowing the transient term in Smoluchowski's time dependent rate constant, the authors report the modified expression for the correlated system to be

$$k(t) = 4\pi aD' \left( 1 + \frac{a}{\sqrt{2\pi D't}} \right) \quad (2.141)$$

The modified rate constant shows that the first radical-target reaction to be slower than what is predicted by Smoluchowski, because as mentioned earlier, if one radical is far from the target the other must be as well (with the converse also being true); whereas assuming independence of radical-target distance, there is a second possibility for the radical to be close to the target. Given that the first reaction time is slower than

what is predicted by assuming independence of distance (assuming radical decay is identical such that each radical is equidistant from the target), it is found by the authors that the second radical-target reaction time must be faster than what is predicted by Smoluchowski. This is found to be true for an indestructible sink, as the second radical is much more likely to react with the same target as the first and this will occur on a much faster timescale than what is predicted by assuming independence of reaction times. Further work conducted by the authors has shown that for a reaction scheme where scavengers are not indestructible, the second reaction is predicted to be slower than Smoluchowski's theory, since the concentration of scavengers is depleted by the first reaction.

## 2.7 Spin-Controlled Reactions

In order to model spin-dependent reactions it is necessary to introduce a spin statistical factor ( $\sigma_S$ ) into Smoluchowski's rate constant to account for the fact that only 1/4 of all interactions will be in a reactive singlet state. The modified Smoluchowski steady state rate constant for spin systems is then [3]

$$k = 4\pi D' a \sigma_S \beta \quad (2.142)$$

where  $\beta$  is  $\frac{1}{2}$  for like reactions or unity otherwise. The value of  $\sigma_S$  varies for different chemical systems and is directly related to the spin relaxation time. For radicals whose spin-relaxation time is much longer than the encounter time ( $\sim 10^{-8} - 10^{-10}$  s),  $\sigma_S = \frac{1}{4}$ , however for faster relaxing systems  $\sigma_S \rightarrow 1$ , reflecting the fact that the spin can re-orient itself whilst still inside the encounter cage. Various  $\sigma_S$  values have been tabulated in the literature [49] based on the observed rate constant for the reaction between the hydrated electron and various radicals; a spin factor of  $\frac{1}{4}$  is applicable for  $e_{\text{aq}}^- + \cdot\text{SO}_3^-, \text{CO}_3^{\cdot-}, \cdot\text{CO}_2^-, \cdot\text{C}(\text{CH}_3)_2\text{OH}, (\cdot\text{CH}_2)(\text{CH}_3)_2\text{COH}, \cdot\text{C}_6\text{H}_6\text{OH}, \text{C}_6\text{H}_5\text{O}\cdot, p\text{-(H}_3\text{C)C}_6\text{H}_4\text{O}\cdot$  and  $p\text{-OC}_6\text{H}_4\text{O}\cdot^-$ , whilst for reactions between  $e_{\text{aq}}^- + \cdot\text{OH}, \cdot\text{N}_3, \text{Br}_2^{\cdot-}$  and  $\text{I}_2^{\cdot-}$  the spin factor is found to be close to unity. For the  $e_{\text{aq}}^- + \cdot\text{OH}$  the spin factor is close to unity because of the unquenched orbital angular momentum in linear radicals, which through the spin-orbit coupling mechanism can lead to very fast spin relaxation.

Based on experimental findings by Ichino and Fessenden [49], the authors have suggested that  $\sigma_S$  is also temperature dependent. Assuming the radical pair lifetime to be inversely proportional to the mutual diffusion constant ( $D'$ ) [50], it is found that  $D'$  changes by about a factor of three between 298 and 343 K, so the radical pair lifetime should decrease by about the same factor. Therefore, with increasing temperatures, diffusive separation of triplet radical pairs may become a faster process than spin-relaxation, in which case the spin-factor would be lowered. This explanation has been found to be in agreement with experimental findings [49].

A very useful theoretical model developed by Mints and Pukhov [51] allows the relationship between the spin factor and spin relaxation to be analysed. Using the stochastic Liouville equation and a phenomenological approach to treating spin relaxation, the authors arrive at the expression for the ( $e_{aq}^- + \text{radical}$ ) reactions as

$$\sigma_S = \frac{1}{2} \frac{k\tau PQ}{k\tau(P+Q) + 2PQ} \quad (2.143)$$

where

$$\begin{aligned} \tau &= \frac{a'b'}{D'}, \quad P = 2 \left( \frac{1 + \sqrt{2x'}}{2 + \sqrt{2x'}} \right), \quad Q = 1 + \sqrt{y'} \\ x' &= \frac{1}{2T_1} \frac{b'^2}{D'}, \quad y' = \frac{1}{2T_2} \end{aligned} \quad (2.144)$$

Here,  $k$  is the rate constant for reaction,  $\tau$  is the radical pair lifetime,  $a'$  is the thickness of the reaction layer,  $b'$  is the reaction distance,  $D'$  the mutual diffusion coefficient and  $T_1$  and  $T_2$  are the longitudinal and transverse relaxation times of the counter radical. This model neglects any magnetic interactions (i.e. hyperfine and Zeeman) which could possibly influence the observed chemical kinetics.

### 2.7.1 Recovering Boundary Model

An analytical theory developed by Green et al. [9] replaces the radiation boundary condition, treating encounters and re-encounters differently and is known as *recovering boundary*. The main idea of this theory is that on an unsuccessful encounter the boundary becomes unreactive, which gradually grows back as a function of time. The nature of this recovery can take various analytical forms depending on the type of reaction. In this section only a brief review of the theory is presented which is applicable to this work. A fuller review can be found in reference [9].

The recovery boundary method finds the Laplace transform of the density of the reaction times following an unreactive encounter, which takes the form

$$\begin{aligned} f(t) &= \int_0^t w_2(t_1)w_1(t-t_1)P(t-t_1)dt_1 \\ &+ \int_0^t \int_0^{t_2} w_2(t_1)w_1(t_2-t_1)(1-P(t_2-t_1))f(t-t_2)dt_1dt_2 \end{aligned} \quad (2.145)$$

with  $w_1$  and  $w_2$  denoting the first passage density of times from  $a + \delta$  to  $a$  and  $a$  to  $a + \delta$  respectively ( $a$  being the encounter distance). The first term simply states that for a diffusion process which obtains  $a + \delta$  at  $t_1$ , the probability of reacting at time  $t$  (which denotes the time taken to diffuse from  $a$  to  $a + \delta$ ) is  $P(t - t_1)$ . The second term accounts for the diffusion process to have attained  $a$  at an earlier time  $t_2$  and was found to be unreactive with probability  $1 - P(t_2 - t_1)$ . Using the strong Markov property, the process starts anew with the probability of reaction at  $t_2$  zeroed, and eventually reacting at a later time  $t$ .

Recognising Eq. (2.145) as a convolution, the Laplace transform takes the form

$$\tilde{f}(s) = \frac{\tilde{w}(s)\tilde{v}(s)}{1 - \tilde{w}_2(s)(\tilde{w}_1(s) - \tilde{v}(s))} \quad (2.146)$$

where  $\tilde{v}(s)$  contains the recovery function and is related to  $v(t)$  by the expression  $w_1(t)P(t)$ . The authors have found that under most conditions, recovery can start as soon as the boundary is obtained; introducing any delay times (i.e. time to attain  $a + \delta$ ) is deemed unnecessary. In this case taking the limit  $\delta \rightarrow 0$  of Eq. (2.146), the authors obtain

$$\tilde{f}(s) = \frac{\tilde{v}(s)}{1 - (\tilde{w}_1(s) - \tilde{v}(s))} \quad (2.147)$$

where  $\tilde{v}(s)$  contains the recovery function and is related to  $v(t)$  by the expression  $w_1(t)P(t)$ .

In order to model spin dependent reactivity, where reaction is only possible through the singlet channel, the authors make use of the exponential model of the form  $P(t) = p(1 - e^{-\beta t})$  to calculate the probability of reaction. Here, the  $P(t)$  relaxes exponentially towards the asymptotic value of  $p$  (the probability of being in a singlet state).  $\beta$  in this expression is the inverse of the spin relaxation time. Using the shift theorem of Laplace transform, the authors derive an expression for  $\tilde{v}(s)$  to be

$$\tilde{v}(s) = p[\tilde{w}_1(s) - \tilde{w}_1(s + \beta)] \quad (2.148)$$

On substituting this definition for  $v(s)$  into Eq. (2.147), the expression for the first passage density of times is

$$\tilde{f}(s) = \frac{p[\tilde{w}_1(s) - \tilde{w}_1(s + \beta)]}{1 - [(1 - p)\tilde{w}_1(0) + p\tilde{w}_1(\beta)]} \quad (2.149)$$

The probability of ultimate reaction can then be simply calculated by using the final value theorem ( $s \rightarrow 0$ ), giving

$$F_\infty = \frac{p[\tilde{w}_1(0) - \tilde{w}_1(\beta)]}{1 - [(1 - p)\tilde{w}_1(0) + p\tilde{w}_1(\beta)]} \quad (2.150)$$

### 2.7.1.1 Homogeneous Rate Constant

The steady state rate constant can be expressed as

$$k_{\infty} = 4\pi D' a [q + (1 - q)F_{\infty}] \quad (2.151)$$

where  $q$  is the probability of reaction on first encounter. The first term of Eq. (2.151) is equivalent to Eq. (2.142) (Smoluchowski's steady state rate constant with a spin statistical factor), with the second term describing the correction for the regrowth of reactivity following each unreactive encounter. The exact solution for  $\tilde{w}_1(s)$  (assuming a spherical particle) is shown to be

$$\tilde{w}_1(s) = \frac{a}{a + \delta} \exp(-\delta\sqrt{s/D'}) \quad (2.152)$$

Using the above definition for  $\tilde{w}_1(s)$ , substituting into Eq. (2.149) and taking the limit  $s \rightarrow 0$ , the ultimate recombination probability can be expressed as

$$F_{\infty} = \frac{ap\sqrt{\beta/D'}}{1 + ap\sqrt{\beta/D'}} \quad (2.153)$$

Substituting the above expression for  $F_{\infty}$  into Eq. (2.151) gives the expression for the steady state rate constant to be

$$k_{\infty} = 4\pi D' a \left( \frac{q + ap\sqrt{\beta/D'}}{1 + ap\sqrt{\beta/D'}} \right) \quad (2.154)$$

Whether the recovering boundary or radiation boundary is applicable depends on a detailed model of the dynamics of the system and must be implemented accordingly. For the purposes of this work, the recovering boundary formalism is simply used to estimate the feasibility of certain approximations and is not implemented in any simulation.

## References

1. M.V. Smoluchowski, Z. Phys. Chem. **92**, 129 (1917)
2. M.V. Smoluchowski, Phys. Z **17**, 585 (1916)
3. S.A. Rice, *Comprehensive Chemical Kinetics* (Elsevier, Amsterdam, 1985)
4. M. Tachiya, Radiat. Phys. Chem. **21**, 167 (1983)
5. I.Z. Steinberg, E. Katchalski, J. Chem. Phys **48**, 2404 (1968)
6. U.M. Gosele, Chem. Phys. Lett. **69**, 332 (1980)
7. F.C. Collins, G.E. Kimball, J. Colloid, Sci. **4**, 425 (1949)
8. R.M. Noyes, Prog. React. Kinet. **1**, 129 (1961)
9. N.J.B. Green, R.D. Spenser-Smith, A.G. Rickerby, J. Chem. Phys. **212**, 99 (1996)

10. M. Schell, R. Kapral, J. Chem. Phys. **75**, 915 (1981)
11. G. Wilemski, M. Fixman, J. Chem. Phys. **58**, 4009 (1973)
12. E. Teramoto, N. Shigesada, J. Phys. Soc. Japan **29**, 273 (1970)
13. A.M. Kolmogorov, Math. Ann. **104**, 415 (1931)
14. L. Onsager, Phys. Rev. **54**, 554 (1938)
15. P.W. Debye, Trans. Electrochem. Soc. **82**, 265 (1942)
16. S. Karlin, H.M. Taylor, *A Second Course in Stochastic Processes* (Academic, New York, 1963)
17. P.E. Kloeden, E. Platen, *Numerical Solution of Stochastic Differential Equations* (Springer, New York, 1992)
18. J. Medhi, *Stochastic processes* (New Age International Limited, New Delhi, 2002)
19. D.R. Cox, H.D. Miller, *The Theory of Stochastic Processes* (Chapman and Hall, London, 1965)
20. B.J. Alder, T.E. Wainwright, J. Chem. Phys. **27**, 1208 (1957)
21. B.J. Alder, T.E. Wainwright, J. Chem. Phys. **31**, 459 (1959)
22. A. Rahman, Phys. Rev. A. **136**, 405 (1964)
23. F.H. Stillinger, A. Rahman, J. Chem. Phys. **60**, 1545 (1974)
24. R. Kubo, J. Phys. Soc. Japan **12**, 570 (1957)
25. M.S. Green, J. Chem. Phys. **22**, 398 (1954)
26. W.C. Swope, H.C. Anderson, P.H. Berens, K.R. Wilson, J. Chem. Phys. **76**, 637 (1982)
27. P. Langevin, C.R. Acad. Sci. (Paris) **146**, 530 (1908)
28. P. Jin-Sheng, L. Gao-Xiang, *Introduction to Modern Quantum Optics* (World Scientific Publishing Co (Pte. Ltd., Singapore, 1998)
29. N.S. Goel, N. Richter-Dyn, *Stochastic Models in Biology* (Academic, New York, 1974)
30. B.D. Ripley, Int. Statist. Rev. **51**, 301 (1983)
31. N.J.B. Green, M.J. Pilling, P. Clifford, Mol. Phys. **67**, 1085 (1989)
32. P. Clifford, N.J.B. Green, M.J. Pilling, J. Phys. Chem. **88**, 4171 (1984)
33. S. Raaen, P.C. Hemmer, J. Chem. Phys. **76**, 2569 (1982)
34. J.B. Pedersen, P.J. Sibani, J. Chem. Phys. **75**, 5368 (1981)
35. A.J. Mozumder, J. Chem. Phys. **48**, 1659 (1968)
36. M.R. Flannery, Phys. Rev. A **25**, 3403 (1982)
37. A. Szabo, K. Shulten, Z. Shulten, J. Chem. Phys. **49**, 4350 (1980)
38. K.M. Hong, J. Noolandi, J. Chem. Phys. **68**, 5163 (1978)
39. N.J.B. Green, M.J. Pilling, S.M. Pimblott, P. Clifford, J. Phys. Chem. **93**, 8025 (1989)
40. H. Sano, M. Tachiya, J. Chem. Phys. **71**, 1276 (1979)
41. N.J.B. Green, M.J. Pilling, S.M. Pimblott, P. Clifford, J. Phys. Chem. **94**, 251 (1990)
42. M.F. Shlesinger, J. Chem. Phys. **70**, 4813 (1979)
43. L. Monchick, J. Chem. Phys. **24**, 381 (1956)
44. A. Hummel, J. Chem. Phys. **48**, 3268 (1968)
45. A. Hummel, J. Chem. Phys. **49**, 4840 (1968)
46. J.M. Warman, K.D. Asmus, R.H. Schuler, J. Phys. Chem. **73**, 931 (1969)
47. S.M. Pimblott, J.A. LaVerne, J. Phys. Chem. **95**, 3196 (1991)
48. V.M. Bluett, N.J.B. Green, J. Phys. Chem. **110**, 6112 (2006)
49. T. Ichino, R.W. Fessenden, J. Phys. Chem. A **111**, 2527 (2007)
50. K.M. Salikhov, Y.N. Molin, R.Z. Sagdeev, A.L. Buchachenko, *Spin Polarisation and Magnetic Field Effects in Radical Reactions* (Elsevier, Amsterdam, 1984)
51. R.G. Mints, A.A. Pukhov, Chem. Phys. **87**, 467 (1984)

# Chapter 3

## Spin Dynamics

### 3.1 Introduction

In photochemistry absorption of a photon gives a single radical pair (known as a G-pair) whose spins are correlated. However, in radiation chemistry the situation becomes much more complicated. A spur results from a single ionisation event in which both the energy and momentum is transferred from a high energy electron (or from other types of radiation) to an electron on the absorbing medium. This process takes place very rapidly and is described by Bethe theory. The momentum transfer and relativistic speed make the theory more complicated, but the process for a high energy particle is described using a kinematic modification of the optical oscillator strength, and only optically allowed states [1, 2] can be excited (i.e. singlet states). During radiolysis the electron and cation separate very rapidly, leaving the pair in a singlet state. The subsequent slow electron processes that produce the spur may involve electron exchange, but overall the spur is formed in a singlet state. Thus the radicals in a spur are born in a spin-correlated cluster.

In principle it is not possible to develop an accurate model without an explicit treatment of spin dynamics. Because the reaction rate of a radical pair is partly dependent on its spin state, the recombination kinetics in a spur may depend strongly on the spin correlation of the radicals it contains. In photochemistry it is customary to distinguish between G-pairs (which are initially spin correlated) and F-pairs (which are not), but in a spur all the spins are entangled and this distinction is less meaningful, but nonetheless, this nomenclature will be used in this work, wherever appropriate. One important exception is the radiolysis of water, where the very fast relaxation on the hydroxyl radical destroys any spin effects, such that there is no difference in the reactivity between G-pairs and those whose spins are uncorrelated (F-Pairs).

In most models of radiation chemistry, spin dynamics are often neglected by assuming reactions to be diffusion controlled, with the microscopic parameters extracted from the experimental rate constant [3–5]. This is not completely satisfactory since the experimental rate constant consists of mostly F-pair recombinations [6], whereas in spurs the spins are correlated which means that the singlet character

will deviate from  $\frac{1}{4}$  and is subject to magnetic field effects such as quantum beats (*vide infra*). Hence, the reactivity within a spur is much more complicated and significant errors can arise if these types of reactions are generalised as F-Pairs.

### 3.2 Stochastic Liouville Theory

Most detailed studies of spin effects in the literature are based on the Stochastic Liouville equation (SLE), which treats the system as an ensemble and requires the use of the density matrix  $\rho_{ij}(r, t)$  [7–9]. The density matrix: (i) contains all the information about the ensemble physical observables of the system; (ii) describes the distribution of spin states for an ensemble of particles and (iii) is constructed from the vector representation of the spin function ( $c_n$ ) relative to some predefined basis, such that  $\rho_{ij}(r, t) = \langle c_i^* c_j \rangle$ .

The SLE for a single radical pair (with a mutual diffusion coefficient  $D'$ ) can be written as

$$\frac{\partial \rho(\mathbf{r}, t)}{\partial t} = D' \nabla^2 \rho(\mathbf{r}, t) + \frac{i}{\hbar} [\rho(\mathbf{r}, t), \hat{H}] \quad (3.1)$$

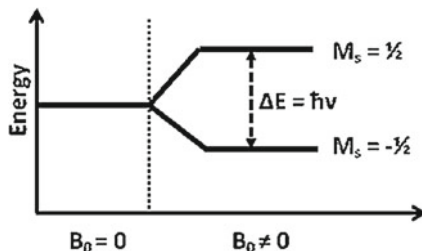
where all the necessary spin dynamics and interactions are modelled through the use of a time dependent Hamiltonian ( $\hat{H}$ ). The diffusive motion of trajectories is represented by the operator  $\nabla^2$ . Recognising the spherical symmetry of the density matrix and assuming no angular dependence of the exchange interaction, Eq. (3.1) can be simplified to

$$\frac{d\Upsilon}{dt} = D' \frac{d^2}{dr^2} \Upsilon + \frac{i}{\hbar} [\Upsilon, \hat{H}] \quad (3.2)$$

where  $\rho = \Upsilon/r$ . This equation can be readily solved using standard techniques by discretising the space and using a finite difference method.

Unfortunately, because of the dimensionality of the space required to describe diffusion, the SLE approach is limited to a single radical pair. If the SLE is numerically intractable, then it may be possible to simulate individual trajectories of the ensemble and average the required observable over the total number of realisations. For a single pair this may not be desirable, but when the diffusion space is multidimensional it may be the only possible way of modelling the system. If scavengers are also modelled, this introduces a further complication even for a single radical pair because of the random nature of the scavenging event. It is not immediately obvious how such events can be dealt with using the SLE.

**Fig. 3.1** Electron spin angular momentum dependence on the external magnetic field, showing  $\alpha$  (+1/2) and  $\beta$  (-1/2) states being raised and lowered in energy respectively. Exchange and dipolar interactions are assumed to be negligible



## 3.3 Coherent Spin Evolution

### 3.3.1 Zeeman Interaction

The interaction between the electron spin (with magnetic quantum number  $m_s = \pm \frac{1}{2}$ ) and an external magnetic field ( $B_0$ ) is termed the Zeeman interaction and is expressed as

$$\hat{H}_{EZ} = \sum_i g_i \mu_B B_0 \hat{S}_{iz} \quad (3.3)$$

where  $g$  is the electron spin  $g$ -factor, a dimensionless quantity relating the magnetic moment of a particle to its angular momentum,  $\mu_B$  the Bohr magneton and  $\hat{S}_z$  the spin angular momentum operator projected along the  $z$ -axis. In zero magnetic field and in the absence of other such magnetic interactions, the spin states  $\alpha$  ( $m_s = +1/2$ ) and  $\beta$  ( $m_s = -1/2$ ) are degenerate. However, as Fig. 3.1 and Eq. (3.3) show, this degeneracy is lifted in the presence of an applied external magnetic (static) field, with the  $\alpha$  and  $\beta$  higher and lower in energies respectively (the  $\alpha$  spin is higher in energy because it is antiparallel to the direction of the external field).

In radicals the  $g$ -factor deviates from the free electron value because the vector sum of the magnetic moments and the vector sum of the angular momenta are not colinear. Hence the orbital angular momentum ( $L$ ) is not completely quenched (i.e. does not average to zero) and contributes to the electron angular momentum via spin-orbit coupling. That is, the ground state (where  $L = 0$ ) couples with other states where  $L > 0$  via the spin-orbit coupling mechanism, which in turn introduces orbital angular momentum into the wavefunction, deviating the  $g$ -factor from the free electron value.<sup>1</sup>

In EPR experiments, the  $g$ -factor for a particular radical represents its chemical shift which greatly helps with the identification of different paramagnetic species. However, the parameter can often be difficult to calculate accurately as it depends on a number of different factors such as structure of radical and strength of spin-orbit coupling. Some typical  $g$ -factors for radicals can be found in the literature [10].

<sup>1</sup> The amount of mixing between these states can be calculated using second order perturbation theory.

In a single radical the magnetic moment of the electron precesses around  $B_0$  and the frequency of this precession is commonly termed the *Larmor* frequency ( $\omega_0$ ). The difference in the Larmor frequency for a radical pair can be found using the expression

$$\Delta\omega_0 = \frac{\Delta g\mu_B B_0}{\hbar} \quad (3.4)$$

where  $\Delta g$  is the difference in the  $g$ -factors of the two radicals. It can be seen from Eq. (3.4) that if the radicals have different  $g$ -factors or experience different or fluctuating local magnetic field at the radical centre, then their spins precess at different rates causing the  $S$  and  $T_0$  spin states to mix.

The oscillation of the  $S - T_0$  can be shown more formally by starting with the time-dependent Schrödinger equation

$$\frac{\partial\psi}{\partial t} = -\frac{i}{\hbar}\hat{H}\psi \quad (3.5)$$

where  $\psi$  is the wavefunction of the system and  $\hat{H}$  the system Hamiltonian containing only the Zeeman interaction (with the external magnetic field oriented along the  $z$ -axis). Expanding in the singlet-triplet basis (with the basis restricted to the  $\alpha\beta$  and  $\beta\alpha$  states) gives

$$\frac{d}{dt} \begin{pmatrix} C_S \\ C_T \end{pmatrix} = -i\ell \begin{pmatrix} 0 & 1 \\ 1 & 0 \end{pmatrix} \begin{pmatrix} C_S \\ C_T \end{pmatrix} \quad (3.6)$$

where  $\ell = B_0\mu_B(g_1 - g_2)/2\hbar$ .  $C_S$  and  $C_T$  are the coefficients of the singlet and triplet states which can be expressed as a linear combination of the Zeeman states as

$$C_S = \frac{1}{\sqrt{2}} (|\alpha\beta\rangle - |\beta\alpha\rangle) \quad (3.7)$$

$$C_T = \frac{1}{\sqrt{2}} (|\alpha\beta\rangle + |\beta\alpha\rangle) \quad (3.8)$$

Differentiating the expression for  $dC_S/dt$  again and substituting into the expression for  $dC_T/dt$  gives the second-order differential equation of the form

$$\frac{d^2}{dt^2} C_S = -\ell^2 C_S \quad (3.9)$$

which has the general solution

$$C_S = \varphi_1 \cos(\ell t) + \varphi_2 \sin(\ell t) \quad (3.10)$$

$$C_T = -\varphi_1 i \sin(\ell t) + \varphi_2 i \cos(\ell t) \quad (3.11)$$

Assuming the radical pair is singlet correlated at zero time, the initial conditions then require  $C_S = 1$  and  $C_T = 0$ , which gives  $\varphi_1 = 1$  and  $\varphi_2 = 0$ . The solution for

the coefficients is then simply  $C_S = \cos(\ell t)$  and  $C_T = -i \sin(\ell t)$ , showing that the wavefunction oscillates between the singlet and triplet states under the influence of the Zeeman interaction.

The  $\Delta g$ -mechanism can affect the course of reactions within a spur by modifying the singlet character in the wavefunction. For example, for a single radical pair initially singlet correlated, Eq. (3.4) shows that increasing either  $\Delta g$  or  $B_0$  has the effect of increasing  $S - T_0$  mixing. Assuming reaction to proceed only via the singlet channel, subsequent encounters are likely to be in a triplet state and therefore less likely to react, leading to more escape. The situation is obviously reversed if the initial precursor state was a triplet.

### 3.3.2 Hyperfine Interaction

The hyperfine interaction provides the fine structure of the EPR spectrum. It is the interaction between the electron and nuclear magnetic moment, described by the Hamiltonian<sup>2</sup>

$$\hat{H}_{HF} = a_H \hat{\mathbf{I}} \cdot \hat{\mathbf{S}} \quad (3.12)$$

where  $a_H$  is the hyperfine coupling constant,  $\hat{\mathbf{I}}$  and  $\hat{\mathbf{S}}$  being the nuclear and electron spin operators respectively. This interaction splits the energy levels of the electron and is composed of two components. The first is called the dipole-dipole interaction where the nucleus and electron are treated as magnetic dipoles, occurring in radicals when the electron is far from the nucleus. The second component is called the Fermi contact interaction, where there is a magnetic interaction between the nucleus (acting as a point dipole) with the electron density (acting like a dipole), which is in close proximity to the nucleus. The precession rate of the electron is therefore directly coupled to the nuclear spin and influences the rate of  $S - T_0$  mixing at high fields ( $S - T_{\pm 1}$  mixing is inhibited due to the Zeeman interaction), and additionally  $S - T_{\pm 1}$ , at low fields as shown in Fig. 3.2.

The  $S - T_0$  mixing mechanism can be shown more formally by considering a radical pair with only one magnetic nucleus (only the effect of the hyperfine interaction is considered). The energy levels of the hyperfine states can be calculated as

$$\hat{H} | +_1 \alpha_1 \beta_2 \rangle = \frac{a_1}{4} | +_1 \alpha_1 \beta_2 \rangle \quad (3.13)$$

$$\hat{H} | +_1 \beta_1 \alpha_2 \rangle = -\frac{a_1}{4} | +_1 \beta_1 \alpha_2 \rangle + \frac{a_1}{2} | -_1 \alpha_1 \alpha_2 \rangle \quad (3.14)$$

$$\hat{H} | -_1 \alpha_1 \beta_2 \rangle = -\frac{a_1}{4} | -_1 \alpha_1 \beta_2 \rangle + \frac{a_1}{2} | +_1 \beta_1 \beta_2 \rangle \quad (3.15)$$

$$\hat{H} | -_1 \beta_1 \beta_2 \rangle = \frac{a_1}{4} | -_1 \beta_1 \beta_2 \rangle \quad (3.16)$$

<sup>2</sup> Valid for this chemical system because anisotropic contributions are averaged by the rapid molecular tumbling.

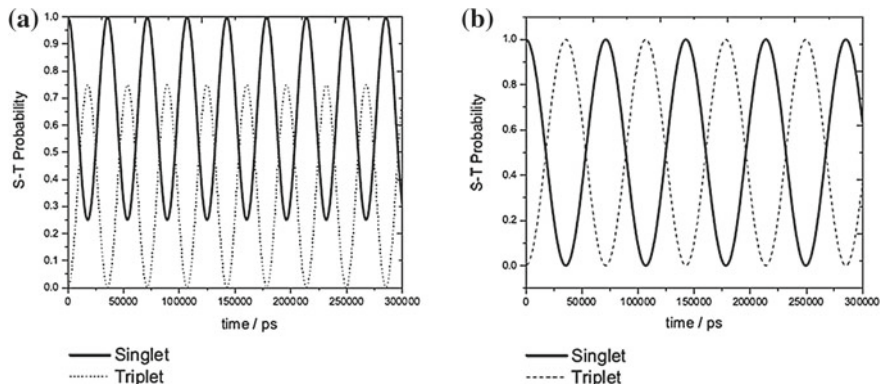


**Fig. 3.2** Singlet (*solid black*) and triplet (*dots*) probability for a radical pair with one magnetic nucleus using a  $g$ -factor of 2.0025 for both radicals and a hyperfine coupling constant 0.001 T. External static field amounted to **a** 0 T and **b** 1 T. Starting nuclear configuration was chosen at random

with  $+$ ,  $-$  and  $\alpha$ ,  $\beta$  referring to the nuclear and electron spin states respectively,  $a_1$  is the hyperfine coupling constant on radical one and the subscripts refer to the radical. The effect of the hyperfine Hamiltonian on the singlet state is given by<sup>3</sup>

$$\begin{aligned}\hat{H}|S\rangle &= \frac{1}{\sqrt{2}} \left[ \frac{a_1}{4} (|+1 \alpha_1 \beta_2\rangle + |+1 \beta_1 \alpha_2\rangle) - \frac{a_1}{2} |-1 \alpha_1 \alpha_2\rangle \right] \\ &= \frac{a_1}{4} |+1 T_0\rangle - \frac{a_1}{2\sqrt{2}} |-1 T_{+1}\rangle\end{aligned}\quad (3.17)$$

and similarly the effect on the  $T_0$  state is

$$\begin{aligned}\hat{H}|T_0\rangle &= \frac{1}{\sqrt{2}} \left[ \frac{a_1}{4} (|+1 \alpha_1 \beta_2\rangle - |+1 \beta_1 \alpha_2\rangle) + \frac{a_1}{2} |-1 \alpha_1 \alpha_2\rangle \right] \\ &= \frac{a_1}{4} |+1 S\rangle + \frac{a_1}{2\sqrt{2}} |-1 T_{+1}\rangle\end{aligned}\quad (3.18)$$

which clearly shows the singlet-triplet mixing mechanism under the influence of the hyperfine interaction. For one radical containing  $n_1$  equivalent nuclei and another radical containing  $n_2$  equivalent nuclei (with the unpaired electron on radicals 1 and 2 having Larmor frequencies  $\omega_{01}$  and  $\omega_{02}$  and hyperfine coupling constants  $a_1$  and  $a_2$  respectively), the analytical expression [11, 12] for the time-dependent singlet probability (valid at high fields) is known to be

$$\rho_{ss}^B(t) = \frac{1}{2} + \frac{1}{2} \cos[(\omega_{01} - \omega_{02})t] \left( \cos \frac{a_1 t}{2} \right)^{n_1} \left( \cos \frac{a_2 t}{2} \right)^{n_2}\quad (3.19)$$

<sup>3</sup> The nuclear configuration has been restricted to the  $|+\rangle$  spin state for simplicity.

### 3.3.3 Exchange Interaction

The exchange interaction is a purely quantum mechanical phenomenon, which causes the expectation energy of the spin states to either increase or decrease when the wavefunction for identical particles overlap. The Hamiltonian describing this interaction, between two electrons on radicals  $i$  and  $j$  can be expressed as

$$H_{EX} = - \sum_{ij} 2J_{ij} \hat{S}_i \cdot \hat{S}_j \quad (3.20)$$

In solutions, whenever the orbitals of electrons overlap, there is an ‘interchange’ of electrons, such that the linear combination of the  $S - T_0$  state directly affects the spin wavefunction, with the singlet and triplet states being either raised and lowered in energy depending on the sign of the exchange interaction  $J(r)$ . Assuming  $J(r) < 0$  for a single radical pair ( $R_1$  and  $R_2$ ), where  $R_1$  contains  $n$  magnetic nuclei with hyperfine coupling constant  $a_H$ , the expectation energies of the singlet and triplet states can be written as [13]

$$E(S) = \langle S, \chi_N | \hat{H} | S, \chi_N \rangle = J(r) \quad (3.21)$$

$$E(T_x) = \langle T_x, \chi_N | \hat{H} | T_x, \chi_N \rangle = -J(r) + xg\mu_B B_0 + \frac{n}{2} \sum_k^n a_{Hk} m_{Ik} \quad (3.22)$$

where  $\chi_N$  represents the nuclear spin state with spin quantum number  $m_I$  and  $x = -1, 0$  or  $+1$  and  $g = (g_1 + g_2)/2$ . All other terms have their customary meanings. Formally  $J_{ij}(r)$  can be defined as

$$J_{ij}(r) = \int \int C \phi_i(r_i) \phi_i^*(r_j) \phi_j(r_j) \phi_j^*(r_i) dV_i dV_j \quad (3.23)$$

where  $C$  is the Coulombic repulsion between the electrons and  $\phi_i(r_i)$ , the orbital wave functions. The orbital overlap necessary for exchange of electrons depends critically on the distance between the radicals and consequently the number of intervening orbitals. For liquids the exchange interaction is smaller than that for solids and is approximated to decay exponentially with increasing distance between the spin radical pair. Making this approximation is not totally unreasonable, since the radial dependence of the orbital wavefunction can be modelled as an exponential function at large distances. In liquids it is reasonable to assume that the exchange interaction decays completely at a distance greater than  $10 \text{ \AA}$ .

The approximation that the exchange interaction is dependent only on the interparticle separation and unaffected by the relative molecular orientation is employed in all simulations as part of this work [i.e. the Hamiltonian in Eq. (3.20) is used]. With this simplification,  $J_{ij}(r)$  can be modelled by Eq. (3.24) [14, 15], with  $J_0$  being the exchange strength at the encounter radius ( $a$ ),  $\beta$  the range parameter and  $r_{ij}$  the interparticle separation.

$$J_{ij}(r) = J_0 e^{-\beta(r_{ij}-a)} \quad (3.24)$$

For radical pairs, if  $J_0 < 0$ , the singlet state is lower in energy, which is thought to be the case for neutral radicals; if the converse is true such that  $J_0 > 0$ , the  $|S\rangle$  lies above the  $|T_0\rangle$  state. The exchange interaction is a coherent process only if the distance between the radicals is fixed. However, in a realistic chemical environment the exchange interaction becomes an incoherent process due to molecular diffusion, whereby the radical pair distance is constantly changing for the radical pair. In this case, the only viable method of modelling this effect is either by numerical simulation or the SLE.

### 3.4 Incoherent Spin Evolution

Relaxation can be formally described as a perturbed system returning to its equilibrium state. A radical pair with an unequal population of energy levels or known phase relationships will approach thermal equilibrium in a magnetic field implying: (1) all coherences are destroyed (phases are randomised) and (2) the populations of the spin states are in a Boltzmann distribution at the temperature of the molecular environment. Spin relaxation can be divided into two types: (i) spin-lattice (longitudinal) relaxation is responsible for restoring the population back to thermal equilibrium (with time constant  $T_1$ ) and involves an exchange of energy, and (ii) spin-spin relaxation (transverse) is concerned with the decay of coherences (with time constant  $T_2$ ) involving no energy exchange and occurs at a rate comparable to or faster than  $T_1$  in solutions.

#### 3.4.1 Bloch Equations

In 1946, Bloch [16] presented a theory for nuclear spin relaxation in which he derived a set of equations of motion to predict the behaviour of an ensemble of isolated spins interacting weakly with the lattice. In brief, the Bloch equations describe the evolution of the longitudinal (diagonal elements of the density matrix) and transverse (off-diagonal elements of the density matrix) spin magnetisation to their respective equilibrium values phenomenologically, with the first order rate of both processes being  $T_1^{-1}$  and  $T_2^{-1}$  respectively. The evolution of the magnetisation is described by the well known equations

$$\frac{dM_x(t)}{dt} = \gamma(\mathbf{M}(t) \times \mathbf{B}(t))_x - \frac{M_x(t)}{T_2} \quad (3.25)$$

$$\frac{dM_y(t)}{dt} = \gamma(\mathbf{M}(t) \times \mathbf{B}(t))_y - \frac{M_y(t)}{T_2} \quad (3.26)$$

$$\frac{dM_z(t)}{dt} = \gamma(\mathbf{M}(t) \times \mathbf{B}(t))_z - \frac{M_z(t) - M_z^0}{T_1} \quad (3.27)$$

where  $\gamma$  is the gyromagnetic ratio,  $\mathbf{M}(t)$  the time-dependent magnetisation,  $M_z^0$  is the equilibrium magnetisation (in the  $+z$  direction) and  $\mathbf{B}(t)$  the time-dependent fluctuating field. The Bloch equations describe the net magnetisation of all the nuclei/electrons in the ensemble and cannot describe the magnetisation loss of an individual nucleus or electron. In addition, the Bloch equations cannot be used to identify the origin and magnitude of  $T_1$  and  $T_2$  and nor can it be extended to coupled spin systems, making its use quite limited.

### 3.4.2 Solomon Equations

Spin relaxation for coupled systems was later studied by Solomon [17] who considered the rate of transitions between the different energy states. To illustrate the mechanism, consider a single radical pair which has a single magnetic nucleus and electron spin; the energy states of which are represented as  $|m_I m_S\rangle$ . The first order rate constants  $W_0$ ,  $W_I$ ,  $W_S$  and  $W_2$  are defined to be as follows:  $W_0$  represents a transition in which both spins (nuclear + electron) are flipped in the opposite sense (i.e.  $\alpha\beta \rightarrow \beta\alpha$ );  $W_I$  is the transition involving the nuclear spin to flip;  $W_S$  denotes the spin flip of the electron and  $W_2$  representing a spin-flip in which both spins (nuclear + electron) are flipped in the same sense (i.e.  $\alpha\alpha \rightarrow \beta\beta$ ). The spin magnetisation can be expressed in terms of the population differences as

$$I_z(t) = P_{\alpha\alpha} + P_{\alpha\beta} - P_{\beta\alpha} - P_{\beta\beta} \quad (3.28)$$

$$S_z(t) = P_{\alpha\alpha} - P_{\alpha\beta} + P_{\beta\alpha} - P_{\beta\beta} \quad (3.29)$$

$$2I_z(t)S_z(t) = P_{\alpha\alpha} - P_{\alpha\beta} - P_{\beta\alpha} + P_{\beta\beta} \quad (3.30)$$

with the rate of change of the spin magnetisation in the  $z$ -direction given by the expressions

$$\frac{d\Delta I_z(t)}{dt} = -\rho_I \Delta I_z(t) - \sigma_{IS} \Delta S_z(t) - \Delta_I 2I_z(t)S_z(t) \quad (3.31)$$

$$\frac{d\Delta S_z(t)}{dt} = -\rho_S \Delta S_z(t) - \sigma_{IS} \Delta I_z(t) - \Delta_S 2I_z(t)S_z(t) \quad (3.32)$$

$$\frac{d2\Delta I_z(t)\Delta S_z(t)}{dt} = -\Delta_I I_z(t) - \Delta_S S_z(t) - R_{IS} 2I_z(t)S_z(t) \quad (3.33)$$

where  $\Delta I_z(t) = \langle I_z \rangle(t) - \langle I_z^0 \rangle$  with  $\langle I_z^0 \rangle$  being the equilibrium magnetisation of the  $I$  spin. A similar expression is also obtained for  $\Delta S_z(t)$ . In the above expression  $\rho_I = (W_0 + 2W_I + W_2)$ ,  $\rho_S = (W_0 + 2W_S + W_2)$ ,  $\sigma_{IS} = (W_2 - W_0)$ ,  $\Delta_I = (2W_I)$ ,  $\Delta_S = (2W_S)$  and  $R_{IS} = (2W_I + 2W_S)$ . The term  $\rho_{I/S}$  is known as the auto-relaxation rate constant (sometimes referred to as *self relaxation* rate constant) which describes the  $I$  and  $S$  spin lattice relaxation.  $\sigma_{IS}$  is known as the cross-relaxation rate constant and describes the rate at which magnetisation is transferred between the two spins.  $\Delta_{I/S}$  describes the transfer of the  $I_z(t)S_z(t)$  magnetisation to  $I$  and  $S$  spin magnetisation respectively. The term  $R_{IS}$  is the self relaxation rate constant of  $2I_zS_z$ . Unfortunately, like the Bloch equations, the first-order rate constants are treated as parameters without taking into account the explicit nature of the relaxation mechanism.

### 3.4.3 Redfield Theory

Redfield theory [18–20] is a microscopic semi-classical theory of spin relaxation in which the spin system is treated quantum mechanically whilst the coupling of the spins with the lattice is treated classically. In this classical approximation, the spin states are in equilibrium and a correction factor is needed to ensure the spin ensemble relaxes to the correct limits. This problem can be overcome by treating the lattice quantum mechanically, however, the details and nature of the computational details are beyond the scope of this thesis. In this section a brief introduction to Redfield theory for spin relaxation is provided, a more detailed analysis of the theory can be found elsewhere [21].

The time evolution of the density matrix is known to be described by the well known Liouville–von Neumann equation [21]

$$\frac{d}{dt}\rho(t) = -i[\hat{H}_0 + \hat{H}_1(t), \rho(t)] \quad (3.34)$$

where  $\rho(t)$  is the density matrix,  $\hat{H}_0$  is the static Hamiltonian and  $\hat{H}_1(t)$  is the time-dependent stochastic Hamiltonian which couples the spin system to the lattice. In general,  $\hat{H}_1$  can be expanded into a sum of product time-invariant spin ( $\hat{A}^q$ ) and spatial operators ( $\hat{F}^{(-q)}$ ) as

$$\hat{H}_1(t) = \sum_q (-1)^q \hat{A}^q \hat{F}^{(-q)}(t) \quad (3.35)$$

with  $q$  representing the rank of the tensor. Equation (3.34) can be solved by firstly removing the time dependence of  $\hat{H}_1(t)$  by converting to the interaction representation<sup>4</sup> [using the transformation operator  $U = \exp(iH_0t)$ ] and then using second-order perturbation theory to give

---

<sup>4</sup> In the interaction representation the operator  $\hat{A}_I$  can be expressed in terms of the Schrödinger representation ( $\hat{A}$ ) as  $\hat{A}_I(t) = U\hat{A}(t)U^{-1}$ .

$$\begin{aligned} \rho^*(t) \simeq & \rho^*(0) - i \int_0^t [\hat{H}_1^*(t'), \rho^*(0)] dt' \\ & - \int_0^t dt' \int_0^{t'} dt'' [\hat{H}_1^*(t'), [\hat{H}_1^*(t''), \rho^*(0)]] \end{aligned} \quad (3.36)$$

where the asterisk in the operator is used to signify transformation of the operator to the interaction representation. Taking the time derivative of Eq. (3.36) and making certain approximations such that  $\hat{H}_1^*(t)$  and  $\rho^*(0)$  are not correlated and that  $\overline{\hat{H}_1^*(t)} = 0$ , where the bar is used to signify the ensemble average, one obtains a set of linear differential equations of the form [21]

$$\frac{d\rho_{\alpha\alpha'}^*(t)}{dt} = \sum_{\beta\beta'} \exp[i(\omega_{\alpha\alpha'} - \omega_{\beta\beta'})t] R_{\alpha\alpha\beta\beta'} [\rho^*(t) - \rho(0)]_{\beta\beta'} \quad (3.37)$$

where  $\omega_{\alpha\alpha'} = \omega_\alpha - \omega_{\alpha'}$  represents the frequency of transition  $|\alpha\rangle \rightarrow |\alpha'\rangle$ . The relaxation superoperator  $R_{\alpha\alpha\beta\beta'}$  elements are given by

$$\begin{aligned} R_{\alpha\alpha'\beta\beta'} = & J_{\alpha\beta\alpha'\beta'}(\omega_{\alpha\beta}) + J_{\alpha\beta\alpha'\beta'}(\omega_{\beta'\alpha'}) - \delta_{\alpha'\beta'} \sum_{\gamma} J_{\gamma\beta\gamma\alpha}(\omega_{\gamma\beta}) \\ & - \delta_{\alpha\beta} \sum_{\gamma} J_{\gamma\alpha'\gamma\beta'}(\omega_{\gamma\beta'}) \end{aligned} \quad (3.38)$$

where the spectral densities, which are the Fourier transform of the correlation function are defined as

$$J_{\alpha\beta\alpha'\beta'}(\omega) = \int_0^{\infty} G_{\alpha\beta\alpha'\beta'}(\tau) \exp(-i\omega\tau) d\tau \quad (3.39)$$

where  $G_{\alpha\beta\alpha'\beta'}(\tau)$  is the correlation function which contains the information regarding the molecular motion of the system. It can be formally stated as

$$G_{\alpha\beta\alpha'\beta'}(\tau) = \overline{\langle \alpha | \hat{H}_1(t) | \beta \rangle \langle \alpha' | \hat{H}_1(t - \tau) | \beta' \rangle^*} \quad (3.40)$$

with the bar representing an ensemble average. If the stochastic Hamiltonian  $\hat{H}_1$  contains several auto and cross correlation terms (such that  $\hat{H}_1(t) = \sum_n \hat{H}_n^1$ ), then the expression for  $G_{\alpha\beta\alpha'\beta'}(\tau)$  is given by

$$\begin{aligned}
G_{\alpha\beta\alpha'\beta'}(\tau) &= \sum_n \overline{\langle\alpha|\hat{H}_n^1(t)|\beta\rangle\langle\alpha'|\hat{H}_n^1(t-\tau)|\beta'\rangle^*} \\
&+ \sum_{n<n', n\neq n'} \overline{\langle\alpha|\hat{H}_n^1(t)|\beta\rangle\langle\alpha'|\hat{H}_{n'}^1(t-\tau)|\beta'\rangle^*} \quad (3.41)
\end{aligned}$$

with the first term and second terms on the RHS representing the auto-correlation and cross-correlation terms respectively. If the oscillatory terms in Eq. (3.37) are small such that their contributions can be neglected (*secular approximation* [22]), then the evolution of the density matrix simplifies to

$$\frac{d\rho_{\alpha\alpha'}^*(t)}{dt} = \sum_{\beta\beta'}' R_{\alpha\alpha'\beta\beta'}[\rho^*(t) - \rho(0)]_{\beta\beta'} \quad (3.42)$$

The prime in the summation indicates only the terms where  $\omega_{\alpha\alpha'}$  and  $\omega_{\beta\beta'}$  are retained. Transforming Eq. (3.42) to the laboratory frame gives the solution for the evolution of the density matrix to be

$$\frac{d\rho_{\alpha\alpha'}(t)}{dt} = -i\omega_{\alpha\alpha'}\rho_{\alpha\alpha'}(t) + \sum_{\beta\beta'} R_{\alpha\alpha'\beta\beta'}[\rho(t) - \rho(0)]_{\beta\beta'} \quad (3.43)$$

The first term in the above equation provides the frequency of the transition ( $\alpha \neq \alpha'$ ), whilst the second term gives its relaxation.

### 3.4.4 Measuring Spin Relaxation

**$T_1$  relaxation** Measuring  $T_1$  spin relaxation can be done using the inversion recovery method, which initially applies a  $\pi$  pulse switching the magnetisation from the  $+z$  to the  $-z$  axis (assuming the static external field is along the  $+z$  axis). Then following a delay time  $t$ , a  $\frac{\pi}{2}$  pulse is applied causing the magnetisation to precess along the  $x$ - $y$  plane and the Fourier transformed spectrum of the free induction decay is recorded. This procedure is repeated for different delay times and a fit of a decaying exponential to the recorded spectrum allows  $T_1$  to be calculated using the relation  $M_z(t) = M_z^0(1 - 2\exp(-t/T_1))$ , where  $M_z(t)$  and  $M_z^0$  are the time-dependent and equilibrium magnetisations respectively along the  $z$ -axis.

**$T_2$  relaxation** Measuring  $T_2$  relaxation experimentally is more challenging and can be measured using the spin-echo method as originally proposed by Hahn [23], which essentially relies on using a basic two pulse sequence. Applying an initial  $\pi/2$  pulse (commonly called the *excitation pulse*) rotates the longitudinal magnetisation into the  $x$ - $y$  plane. The transverse magnetisation starts to dephase due to local magnetic field inhomogeneities, causing the spins to precess at different Larmor frequencies. This dephasing takes place for a time  $t$  after which a  $\pi$  pulse is applied (commonly called the *refocusing pulse*), which rotates the transverse magnetisation in the axis

of the initial alignment, reversing the direction of the dephasing, so that after a further time  $t$ , the phase coherence is re-established and a spin echo forms. The time constant  $T_2$  can then be determined by repeating the experiment for multiple values of  $t$  and measuring the decay in the amplitude of the spin echo using the relation  $M_{xy}(t) = M_{xy}^0 \exp(-t/T_2)$ , with  $M_{xy}(t)$  and  $M_{xy}^0$  being the time-dependent and equilibrium magnetisations along the  $x$ - $y$  plane respectively. Further in-depth details on the process of measuring spin relaxation can be found in the literature [24].

**CPMG sequence** In 1954, it was shown by Carr and Purcell (Cpmg) that performing a simple modification of Hahn's spin-echo method can reduce the influence of diffusion on  $T_2$ . In the CPMG sequence the general sequences of pulses can be described as  $[90^\circ, \tau, 180^\circ, 2\tau, 180^\circ, 2\tau, \dots]$ , so for example, if a  $\pi$  pulse is applied at  $3\tau$ , then a spin-echo will develop at  $4\tau$  (obviously with a reduced intensity due to spin-spin relaxation). This method is much faster and more efficient than the one described earlier, which allows for repeated refocusing of the spin echo.

### 3.4.5 Spin-Locking

Spin-locking is a technique for creating transverse magnetisation after the application of a  $\pi/2$  pulse which subsequently becomes 'spin-locked'. As it has been demonstrated above, transverse magnetisation will decay to zero because of  $T_2$  relaxation after the  $90^\circ$  pulse. However, if a rotating field  $B_{SL}$  is applied after this pulse, the transverse magnetisation will instead oscillate with a Larmor frequency of  $\omega_{SL} = \gamma B_{SL}$  [25]. Hence in the rotating frame  $B_{SL}$  is a static field which is analogous to a static field  $B_0$  in the laboratory frame. In the rotating frame therefore, loss in the transverse magnetisation (with time constant  $T_{1\rho}$ ) can be measured as

$$M_{xy} = M_{xy}^0 \exp(-\tau_{SL}/T_{1\rho}) \quad (3.44)$$

where  $\tau_{SL}$  is the time span of the spin-lock pulse. Hence spin-locking is often referred to as the limiting case of the CPMG sequence, as a continuous  $B_{SL}$  pulse is equivalent to a series of short pulses in the CPMG method. This method does have the advantage of studying relaxation processes (and extracting the parameter  $T_{1\rho}$ ) at lower frequencies where much better signal-to-noise ratio can be obtained.

## 3.5 Radical Pair Mechanism

### 3.5.1 Introduction

The Radical Pair Mechanism (RPM), first presented in 1969 [26–29] has undergone intense investigation to help explain experimental observations. According to the RPM, a radical pair is created in a non-stationary electronic spin state which in the

absence of any static magnetic field can undergo oscillations between the  $|S\rangle$  and  $|T_{0,\pm 1}\rangle$  states. In the RPM framework, spin polarisations (non-Boltzmann distribution of spin states) can develop as a result of the mixing of these non-stationary states via spin-exchange interactions during the stochastic motion of the radical pair together with spin-dependent reactivity. A brief review of the RPM is now presented in the subsequent sections.

### 3.5.2 Radical-Triplet Pair Mechanism

Electron polarisation obtained by the Radical-Triplet Pair Mechanism (RTPM) [30] is related to the RPM in that diffusive encounters are still required, but differs in that it involves the interaction of a photoexcited triplet state ( $S = 1$ ) with a doublet state ( $S = 1/2$ ) radical. At high concentrations, the production of a photoexcited triplet state interacts with the doublet to form quartet and doublet states, which in the Zeeman basis can be expressed as:

$$\begin{aligned}
 |Q_{+3/2}\rangle &= \alpha_1\alpha_2\alpha_R \\
 |Q_{+1/2}\rangle &= \frac{1}{\sqrt{3}}(\alpha_1\alpha_2\beta_R + \alpha_1\beta_2\alpha_R + \beta_1\alpha_2\alpha_R) \\
 |Q_{-1/2}\rangle &= \frac{1}{\sqrt{3}}(\beta_1\beta_2\alpha_R + \beta_1\alpha_2\beta_R + \alpha_1\beta_2\beta_R) \\
 |Q_{-3/2}\rangle &= \beta_1\beta_2\beta_R \\
 |D_{+1/2}\rangle &= \frac{1}{\sqrt{6}}[2(\alpha_1\alpha_2\beta_R) - \alpha_1\beta_2\alpha_R - \beta_1\alpha_2\alpha_R] \\
 |D_{-1/2}\rangle &= \frac{1}{\sqrt{6}}[2(\beta_1\beta_2\alpha_R) - \beta_1\alpha_2\beta_R - \alpha_1\beta_2\beta_R] \quad (3.45)
 \end{aligned}$$

where the subscript  $R$  represents the radical;  $\alpha$  and  $\beta$  represent a spin of  $(+1/2)$  and  $(-1/2)$  respectively. As the radicals diffuse and enter the exchange region, the states  $|Q_{-1/2}\rangle \leftrightarrow |D_{+1/2}\rangle$  and  $|Q_{-3/2}\rangle \leftrightarrow |D_{-1/2}\rangle$  start to mix<sup>5</sup>; further diffusion towards the encounter radius allows the mixing of the spin state  $|Q_{-3/2}\rangle \leftrightarrow |D_{+1/2}\rangle$  as well. This mixing of the spin states causes a redistribution of spin populations and if operating concurrently with the other magnetic interactions can lead to an unequal population of the spin-states to produce spin-polarisation.

---

<sup>5</sup> Assuming  $J < 0$  where the doublet states are lower in energy than the quartet states.

### 3.5.3 Zero Field Splitting

In the triplet molecule, the three triplet states ( $T_0, T_{\pm 1}$ ) are not degenerate, but are decoupled because of the dipolar interaction (i.e. the  $2S + 1$  degeneracy is removed). This is known as *zero field splitting*. The expression for the dipolar Hamiltonian between two electrons can be written as

$$\hat{H} = (g^2 \mu_B^2) \left[ \frac{\hat{\mathbf{S}}_1 \cdot \hat{\mathbf{S}}_2}{r^3} - 3 \frac{(\hat{\mathbf{S}}_1 \cdot \mathbf{r})(\hat{\mathbf{S}}_2 \cdot \mathbf{r})}{r^5} \right] \quad (3.46)$$

where  $\hat{\mathbf{S}}_1$  and  $\hat{\mathbf{S}}_2$  are the electron spin operators for electrons 1 and 2 respectively,  $\mathbf{r}$  is the vector joining the two spins and  $r$  is the separation distance of the two spins. Equation (3.46) can be rewritten in matrix form as  $\hat{H} = \hat{\mathbf{S}} \cdot \mathbf{D}^z \cdot \hat{\mathbf{S}}$ , with the elements of  $\mathbf{D}^z$  being

$$D_{ij}^z = \frac{1}{2} g^2 \mu_B^2 \left\langle \frac{r^2 \delta_{ij} - 3ij}{r^5} \right\rangle \quad (3.47)$$

with  $i, j = x, y, z$  (the components of the interparticle spin vector). The dipolar Hamiltonian in the principal axis system (which diagonalises the matrix  $\mathbf{D}^z$ ) can be shown to be

$$\begin{aligned} \hat{H} &= D_{XX}^z \hat{S}_X^2 + D_{YY}^z \hat{S}_Y^2 + D_{ZZ}^z \hat{S}_Z^2 \\ &= D^0 (S_z^2 - S(S+1)/3) + E^0 (S_X^2 - S_Y^2) \end{aligned} \quad (3.48)$$

where the zero field parameters are defined as  $D^0 = (3/2)D_{ZZ}^z$ ,  $E^0 = (1/2)|D_{XX}^z - D_{YY}^z|$  and  $\hat{S}_i$  being the electron spin operator along each of the molecular axes  $i = x, y, z$ . The Hamiltonian in Eq. (3.46) can now be rewritten in terms of the ladder operators as

$$\hat{H} = D^0 \left( S_z^2 - \frac{1}{3} S(S+1) \right) + \frac{E^0}{2} (S_+^2 + S_-^2) \quad (3.49)$$

### 3.5.4 Chemically Induced Dynamic Nuclear Polarisation

Radical pair theory states that the rate of  $S-T_0$  mixing is directly related to the nuclear spin configuration through the hyperfine interaction, which in turn determines the recombination yield. The nuclear spin polarisation generated in both the recombined and escaped products is known as *chemically induced dynamic nuclear polarisation* [6, 31–33].

Two types of CIDNP effects can be observed experimentally:

1. **Net effect**, one radical is observed in emission (E) and the other radical in enhanced absorption (A) (requiring  $\Delta g \neq 0$  and  $\Delta g B_0$  being much greater than the hyperfine interaction).
2. **Multiplet effect**, each radical has half its spectrum in enhanced absorption and the other in emission (requiring  $\Delta g = 0$ ) because of the difference in the rate of  $S - T_0$  mixing.  $S - T_{\pm 1}$  mixing can also occur concurrently with  $S - T_0$  mixing in two ways although it operates less frequently: (1) at low fields where the splitting of the energy levels by the Zeeman interaction is negligible or comparable to the hyperfine term, making the  $T_{\pm 1}$  states accessible and (2) when  $J(r) < 0$ ,  $S - T_{-1}$  states mix due to the exchange interaction which becomes more important with increasing solvent viscosity. Depending on the sequence of transitions arising from low fields (corresponding to higher chemical shifts) and high field (corresponding to lower chemical shifts) the patterns are defined as A/E (enhanced absorption in low field and emission at high field) or E/A (emission in low field and enhanced absorption at high field).

To illustrate how nuclear spin polarisation arises, consider a radical pair initially triplet correlated with one only magnetic nucleus (with hyperfine constant  $a_1$ ). The rates of  $S - T_0$  mixing for the two nuclear spin orientations is then given by the expression (assuming  $\Delta g > 0$  and  $a_1 > 0$ )

$$\Delta\omega^+ = \frac{1}{2} \left[ \frac{B_0 \Delta g \mu_B}{\hbar} + \frac{1}{2} a_1 \right] \quad (3.50)$$

$$\Delta\omega^- = \frac{1}{2} \left[ \frac{B_0 \Delta g \mu_B}{\hbar} - \frac{1}{2} a_1 \right] \quad (3.51)$$

with  $\Delta\omega^+$  and  $\Delta\omega^-$  being the rates of  $S - T_0$  mixing for the  $\alpha$  and  $\beta$  nuclear spin configuration respectively. It can be seen from the above expressions (and the plotted singlet probabilities in Fig. 3.3) that for a nucleus spinning in the  $\alpha$  configuration, faster  $S - T_0$  mixing is induced as opposed to the  $\beta$  nuclear spin.

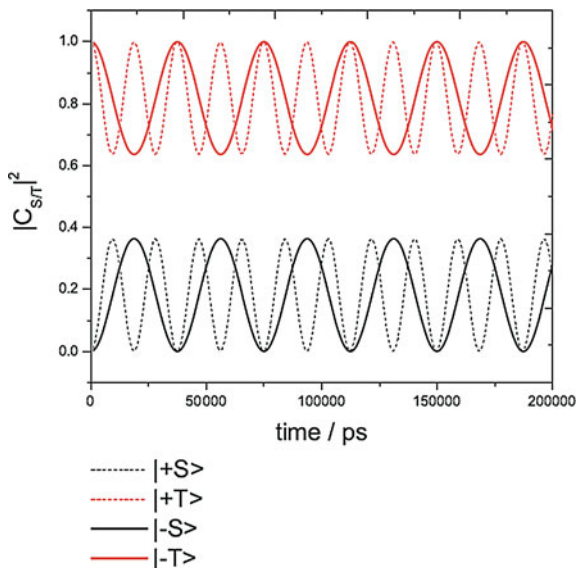
This difference in the Larmor frequency of the electron spin gives the recombination product an excess of  $\alpha$  nuclear spin which will be observed as emission in the CIDNP spectrum. The converse is true for escaped products, which will have an excess of  $\beta$  nuclear spins and will be observed as enhanced absorption in the CIDNP spectrum.<sup>6</sup> Obviously, for a singlet correlated radical pair the opposite is true with an excess of  $\beta$  and  $\alpha$  nuclear spins observed on the recombination and escaped products respectively.

**Theoretical treatment** Assuming that the wavefunction of the radical pair can be described as  $\psi(t) = C_{S_n}(t)|S, \chi_n\rangle + C_{T_n}(t)|T_0, \chi_n\rangle$  (where  $\chi_n$  is the nuclear spin wavefunction with magnetic quantum number  $m_I = \pm 1/2$ ), then using the time dependent Schrödinger equation (with boundary conditions that  $C_{S_n}(0) = 1$  and

---

<sup>6</sup> It is assumed that the nuclear gyromagnetic ratio  $\gamma_p < 0$ .

**Fig. 3.3**  $|S\rangle$  and  $|T\rangle$  probability as a function of the nuclear spin. A hyperfine coupling constant of 0.001 T together with a  $\Delta g$  of 0.001 was used. A static external field of 1 T was used. (+) and (-) represents (+1/2) and (-1/2) nuclear spin respectively



$C_{Tn}(0) = 0$ ) one obtains an expression for the singlet probability [13] of the radical pair to be

$$|C_{S_n}|^2 = 1 - \left( \frac{\Delta\omega_{0n}}{(J^2(r) + \Delta\omega_{0n}^2)^{1/2}} \right)^2 \sin^2(J^2(r) + \Delta\omega_{0n}^2)^{1/2} t \quad (3.52)$$

where  $\Delta\omega_{0n}$  is the difference in the Larmor frequencies for the different nuclear spin configurations and  $J(r)$  is the exchange interaction. It can be seen that polarisations only develop outside the exchange region (i.e. when  $J(r)$  is small), where the mechanism of  $S - T_0$  mixing is most efficient. Within the exchange region the spin dynamics correlate the phases of the  $|S\rangle$  and  $|T_0\rangle$  states, which can later manifest as population difference if the pair once again separates outside the exchange region. This form of generating CIDNP polarisation is considered negligible in comparison to the  $S - T_0$  mixing that occurs when  $J(r) \approx 0$ . The CIDNP intensity ( $I_c$ ) [13] for the transition due to nucleus  $i$  from the state  $|\chi_n\rangle = |m_{Li}, m_{Ik}\rangle$  to  $|\chi_n\rangle = |m_{Li} - 1, m_{Ik}\rangle$  (where radicals  $R_1$  and  $R_2$  contain  $a$  and  $b$  magnetic nuclei respectively) is<sup>7</sup>

$$I_c = \frac{\mu_I \varepsilon}{2\hbar^2} a_i \left[ \Delta g \mu_B B_0 + \sum_{p \neq i}^a a_p m_{Ip} - \sum_k^b a_i m_{Ik} + a_k (m_{Li} - 1/2) \right] \quad (3.53)$$

where  $\mu_I$  is negative (positive) for a singlet (triplet) precursor,  $\varepsilon$  is negative (positive) for escaped (recombined) radicals. The first term in Eq. (3.53) gives rise to the net

<sup>7</sup> Nucleus  $p$  and  $i$  are located on the same radical, but nucleus  $k$  is on the other radical.

effect with the phase of the polarisation determined by the sign of  $\Delta g a_i$ ; the second and third terms give rise to the multiplet effect.

### 3.5.4.1 Kaptein's Sign Rule

To help with the analysis of the polarisation phases for radical pairs, a set of quantitative rules have been devised by Kaptein [6, 34] for both the net and multiplet effects. For the net effect, the phase of the polarisation is given by

$$\Gamma_i^n = \mu' \varepsilon \Delta g A_i \quad (3.54)$$

and similarly the expression for the multiplet effect is given as

$$\Gamma_{ij}^m = \mu' \varepsilon A_i A_j J'_{ij} \sigma_{ij} \quad (3.55)$$

where  $i$  and  $j$  are used to represent the nuclei. The signs in the above expression take the following values:

$\mu'$	+	triplet precursor
	-	singlet precursor
$\varepsilon$	+	recombination product
	-	escaped product
$\Delta g$		sign of the difference in $g$ -factor ( $g_i - g_j$ )
$A_i$		sign of the hyperfine coupling constant on nucleus $i$
$A_j$		sign of the hyperfine coupling constant on nucleus $j$
$J'_{ij}$		sign of the nuclear coupling constant between nuclei $i$ and $j$
$\sigma_{ij}$	+	when nuclei $i$ and $j$ are on the same radical
	-	when nuclei $i$ and $j$ are different radicals
$\Gamma^n$	+	absorption (A)
	-	emission (E)
$\Gamma^m$	+	emission/absorption (E/A)
	-	absorption/emission (A/E).

### 3.5.5 Chemically Induced Dynamic Electron Polarisation

Chemically induced dynamic electron polarisation (CIDEP) [6, 32], a related phenomenon to CIDNP is the non-Boltzmann distribution of *electron* spin states. This section will examine how electron polarisation arises from the  $S - T_0$  and  $S - T_{-1}$  mixing mechanisms (assuming  $J(r) < 0$ ) and show how these polarisations can be readily understood within the framework of quantum mechanics.

### 3.5.6 $S - T_0$ Mixing

Electron polarisations arise in a similar manner to CIDNP, namely by diffusive separation (allowing  $S - T_0$  mixing to occur) followed by an *unreactive* encounter. To understand how  $S - T_0$  mixing together with  $J(r)$  operates, consider a hypothetical radical pair  $R^\cdot + H^\cdot$  (with electron spins of  $\alpha$  or  $\beta$ ), where it is assumed only the  $H^\cdot$  has a magnetic nucleus (nuclear spin of  $\alpha_N$  or  $\beta_N$ ) with a hyperfine coupling constant  $a_H$ . The unreacted radical pair separates to the distance  $r_{ST_0}$  where  $S - T_0$  mixing is now possible. The  $T_0(\alpha_N)$  and  $S(\alpha_N)$  states separate adiabatically to  $|\alpha\alpha_N\beta_R\rangle$ <sup>8</sup> and  $|\beta\alpha_N\alpha_R\rangle$  respectively, and similarly the  $T_0(\beta_N)$  and  $S(\beta_N)$  states separate adiabatically to  $|\beta\beta_N\alpha_R\rangle$  and  $|\alpha\beta_N\beta_R\rangle$  respectively. If the radical pair was in a triplet correlated state, then the states  $|\alpha\alpha_N\beta_R\rangle$  and  $|\beta\beta_N\alpha_R\rangle$  would become preferentially populated, leading to an E/A polarisation phase. The opposite is expected for a singlet correlated radical pair. Similarly, CIDEP effects can also arise from F-pairs whose uncorrelated electron spins become correlated by the exchange parameter  $J(r)$ . Depletion of the more reactive singlet radical pairs via reaction leaves a preponderance of triplet radical pairs, which show the same polarisation characteristics as a triplet correlated radical pair (i.e. E/A polarisation phase). This is known as *F-pair polarisation*.

**Electron polarisation arising from the  $S - T_0$  mixing** Consider a radical pair ( $R_1$  and  $R_2$ ) in which  $R_1$  has  $n$  magnetic nuclei with hyperfine coupling constants  $\sum_i^n a_i$ . Let the spin state of the radical pair be described by the wavefunction

$$\psi(t) = C_{S_n}(t)|S, \chi_n\rangle + C_{T_n}(t)|T_0, \chi_n\rangle \quad (3.56)$$

where  $\chi_n$  represents the nuclear spin states with a magnetic quantum number  $m_I$ . When the energy separation between the  $S$  and  $T_0$  states is zero, then the  $S - T_0$  mixing arises from the matrix element

$$\langle T_0, \chi_N | \hat{H} | S, \chi_N \rangle = \frac{1}{2} \left[ \frac{\Delta g \mu_B B_0}{\hbar} + \left( \sum_k^n a_k m_{Ik} \right) \right] \quad (3.57)$$

Using the time dependent Schrödinger equation gives

$$\frac{d}{dt} \begin{pmatrix} C_{S_n}(t) \\ C_{T_n}(t) \end{pmatrix} = -i \begin{pmatrix} J(r) & \ell \\ \ell & -J(r) \end{pmatrix} \begin{pmatrix} C_{S_n}(t) \\ C_{T_n}(t) \end{pmatrix} \quad (3.58)$$

where

$$\ell = \frac{1}{2} \left[ \frac{\Delta g \mu_B B_0}{\hbar} + \sum_k a_k m_{Ik} \right] \quad (3.59)$$

---

<sup>8</sup> Subscript R is used to denote the spin on  $R^\cdot$ .

Assuming  $J(r)$  to be constant for simplicity (with an exchange strength  $J_0$ ), the solution can be readily obtained by differentiating the expression for  $\frac{dC_{Sn}(t)}{dt}$  again and substituting into this expression the value for  $\frac{dC_{Tn}}{dt}$  to give

$$\frac{d^2}{dt^2} C_{Sn} = -(J_0^2 + \ell^2) C_{Sn} \quad (3.60)$$

Defining  $\omega_n = \sqrt{J_0^2 + \ell^2}$ , the general solution is then found to be

$$C_{Sn}(t) = \varphi_1 \cos(\omega_n t) + \varphi_2 \sin(\omega_n t) \quad (3.61)$$

$$C_{Tn}(t) = \frac{\varphi_2 i \omega_n - \varphi_1 J_0}{\ell} \cos(\omega_n t) - \frac{\varphi_1 i \omega_n + \varphi_2 J_0}{Z} \sin(\omega_n t) \quad (3.62)$$

Assuming the initial radical pair starts in a pure singlet state such that  $C_{Sn}(t) = 1$  and  $C_{Tn}(t) = 0$ , then  $\varphi_1 = 1$  and  $\varphi_2 = -\frac{iJ_0}{\omega_n}$ . The solution for the coefficients is then

$$C_{Sn}(t) = \cos(\omega_n t) - \frac{iJ_0}{\omega_n} \sin(\omega_n t) \quad (3.63)$$

$$C_{Tn}(t) = -\frac{i\ell}{\omega_n} \sin(\omega_n t) \quad (3.64)$$

The polarisation on radical one can now be readily calculated as

$$\begin{aligned} P_1 &= (C_{Sn}(t)C_{Tn}^*(t) + C_{Tn}(t)C_{Sn}^*(t)) \\ &= -\frac{2J_0\ell}{\omega_n^2} \sin^2(\omega_n t) \end{aligned} \quad (3.65)$$

Hence the sign of the polarisation is determined by the sign of the product  $J_0\ell$ . Both must be nonzero to obtain any polarisation.

### 3.5.6.1 Kaptein's Sign Rule

As with CIDNP, a set of quantitative rules have been devised [6, 34] to help predict the phases of the electron polarisation. For the net effect (with hyperfine coupling constants  $a_i$  and  $a_j$  on nucleus  $i$  and  $j$  respectively being zero) the phase is given as

$$\Gamma^n = \mu' J_0 \Delta g \quad (3.66)$$

Similarly the expression for the multiplet effect (with  $\Delta g = 0$ ) is given by the expression

$$\Gamma^m = \mu' J_0 \quad (3.67)$$

where the signs take the following values:

$\mu'$	+	triplet precursor and F-pairs
	-	singlet precursor
$\Delta g$		sign of the difference in $g$ -factor ( $g_i - g_j$ )
$J_0$		sign of the exchange coupling constant
$\Gamma^n$	+	absorption (A)
$\Gamma^n$	-	emission (E)
$\Gamma^m$	+	low field absorption/high field emission (A/E)
$\Gamma^m$	-	low field emission/high field absorption (E/A).

### 3.5.7 $S - T_{-1}$ Mixing

If the exchange interaction  $J(r)$  is negative then  $S - T_{-1}$  also becomes possible, however, it is considered less important than the  $S - T_0$  mixing because the radical pair distance required is relatively small in comparison to that required in the  $S - T_0$  mechanism. Nonetheless, the  $S - T_{-1}$  mechanism can become important in chemical systems in which the radical pairs have a high hyperfine coupling constant or diffusion is hindered by the solvent viscosity, allowing the radical pair to spend more time near the cross-over region.

To illustrate how  $S - T_{-1}$  mixing can give rise to CIDEP consider the same radical pair as discussed previously ( $R \cdot + H \cdot$ ) where the  $H \cdot$  has a magnetic nucleus ( $m_I = \pm 1/2$ ) with a large hyperfine constant. The  $S - T_{-1}$  mixing mechanism must obey the selection rules  $\Delta M_S = \pm 1$  and  $\Delta M_I = \mp 1$ , with  $M_S$  and  $M_I$  being the magnetic quantum numbers of the electron and nuclear spins respectively. Assuming the radical pair to start with a triplet precursor, the  $T_{-1}$  state  $|\alpha_N \beta \beta_R\rangle$  will populate the singlet state  $\frac{1}{\sqrt{2}}(|\beta_N \alpha \beta_R\rangle - |\beta_N \beta \alpha_R\rangle)$ , creating excess population in the states  $|\beta_N \alpha\rangle$ ,  $|\beta_N \beta\rangle$  and  $|\alpha_R\rangle$ . The mixing of the state  $|\beta_N \beta \beta_R\rangle$  to the corresponding singlet state does not occur because the condition  $\Delta M_I = -1$  is not fulfilled. For the  $H \cdot$  atom, the  $S - T_{-1}$  mixing will give an emissive signal, with no polarisation observed for the high field signal. If the radical pair had been in a singlet correlated state, then a reverse polarisation phase will be obtained (i.e. low-field absorptive signal). If  $J(r)$  is positive, a similar polarisation phase is expected to arise via the  $S - T_{+1}$  mixing. Therefore, for the  $S - T_{\pm 1}$  mixing, the sign rule for the polarisation is  $\Gamma_{S-T_{\pm 1}} = \mu' J_0$ , with the values for  $\mu'$  and  $J_0$  defined as:

$\mu'$	+	triplet precursor and F-pairs
	-	singlet precursor
$J_0$		sign of the exchange coupling constant
$\Gamma_{S-T_{\pm 1}}$	+	absorption (A)
$\Gamma_{S-T_{\pm 1}}$	-	emission (E)

**Electron polarisation arising from the  $S - T_{-1}$  mixing** When the energy between the states  $|T_{-1}\rangle$  and  $|S\rangle$  states becomes close to zero, then spin mixing occurs through the off-diagonal matrix elements

$$\langle T_{-1}, \chi'_N | \hat{H} | S, \chi_N \rangle = \frac{\mp a_k}{2\sqrt{2}} [I_k(I_k + 1) - m_{Ik}(m_{Ik} \mp 1)]^{1/2} \quad (3.68)$$

where as before  $\chi_N$  is the nuclear spin wavefunction with spin  $I_k$ , and magnetic spin quantum number ( $m_I$ ). The  $k$  nucleus spin interacts with the electron spin with hyperfine coupling constant  $a_k$ . For a single radical pair with one magnetic nucleus (with hyperfine coupling constant  $a_1$ ) the eigenvalues under the action of the hyperfine Hamiltonian for the  $|S, -\rangle$  ( $m_I = -1/2$ ) and  $|T_{-1}, +\rangle$  ( $m_I = +1/2$ ) are given as

$$\hat{H}|S, -\rangle = -\frac{a_1}{4}|T_0, -\rangle + \frac{a_1}{2\sqrt{2}}|T_{-1}, +\rangle \quad (3.69)$$

$$\hat{H}|T_0, -\rangle = -\frac{a_1}{4}|S, -\rangle + \frac{a_1}{2\sqrt{2}}|T_{-1}, +\rangle \quad (3.70)$$

$$\hat{H}|T_{-1}, +\rangle = -\frac{a_1}{4}|T_{-1}, +\rangle + \frac{a_1}{2\sqrt{2}}(|S, -\rangle + |T_0, -\rangle) \quad (3.71)$$

Letting the wavefunction which describes the spin state of the radicals be

$$\psi(t) = C_S(t)|S, -\rangle + C_{T_0}(t)|T_0, -\rangle + C_{T_{-1}}(t)|T_{-1}, +\rangle \quad (3.72)$$

Then the probability of each state in the absence of the Zeeman and exchange is found to be

$$P_S = \frac{5}{8} + \frac{3}{8} \cos(a_1 t) \quad (3.73)$$

$$P_{T_0} = \frac{1}{8} - \frac{1}{8} \cos(a_1 t) \quad (3.74)$$

$$P_{T_{-1}} = \frac{2}{8} - \frac{2}{8} \cos(a_1 t) \quad (3.75)$$

The polarisation on radical one and two is then given by the expressions  $P_1 = \frac{1}{2} \cos(a_1 t) - \frac{1}{2}$  and  $P_2 = -\frac{1}{2} \cos(a_1 t) + \frac{1}{2}$  respectively. In the presence of a static field  $B_0$  (and with  $g$ -factors  $g_1 = g_2$ ), the singlet probability is given by the expression  $P_S = \frac{1}{2}[1 + \cos(\frac{1}{2}a_1 t)]$  [35].

### 3.6 Triplet Mechanism

The Triplet Mechanism (TM) [36, 37], unlike the RPM is much more restrictive with the origin of the polarisation arising from the excited states of the parent molecule. In the TM the polarisation arises from the intersystem crossing from the excited singlet

state to the three triplet states, with the rate determined by the strength of spin-orbit coupling. If spin-orbit coupling is anisotropic, the rate of intersystem crossing from the excited singlet state to the three triplet states occurs at different rates resulting in spin polarisation. Unlike the RPM, the magnitude and phase of the polarisation are the same for both radicals (i.e. both in emission or absorption) with no hyperfine dependence since the polarisation has already been generated on dissociation of the parent molecule.

The triplet state eigenfunctions at zero field are not the same as the non-zero field Zeeman eigenfunctions, but are rather a linear combination which can be expressed as [38]

$$T_z = T_0 \quad T_x = \frac{1}{\sqrt{2}}(T_{-1} - T_{+1}) \quad T_y = \frac{i}{\sqrt{2}}(T_{-1} + T_{+1}) \quad (3.76)$$

These zero field triplet eigenfunctions are not degenerate but are split by the internal geometry of the molecule arising from the dipolar interaction of the electrons [given by the Hamiltonian in Eq. (3.46)]. In general the eigenvalues ( $X, Y, Z$ ) for the eigenfunctions  $|T_x\rangle$ ,  $|T_y\rangle$  and  $|T_z\rangle$  have the ordering  $X > Y > Z$  [39]. As the magnetic field increases, the major cause of the splitting shifts from the dipolar interaction to the Zeeman effect.

To retain the polarisation generated by the TM mechanism the parent molecule must dissociate to yield radicals (with rate  $k_d$ ), which retains the spin multiplicity of the precursor. If  $k_d$  can compete with the spin-relaxation time  $T_{1s}$ , then the time-dependence of the polarisation generated by the TM can generally be described as [40]

$$P_{\text{TM}} = \frac{k_d P_T}{k_d + T_{1s}^{-1}} [1 - \exp(-(k_d + T_{1s}^{-1})t)] \quad (3.77)$$

where  $P_T$  is the population difference of the  $T_{-1}$  and  $T_{+1}$  states. The TM is only applicable to chemical systems where the dissociation rate constant is of the order  $10^8 - 10^9 \text{ s}^{-1}$  as typical values for  $T_{1s}$  range in the order of nanoseconds. If  $P_{\text{TM}} > 0$  an enhanced absorption signal is observed since the  $T_{-1}$  sublevel is preferentially populated; the converse is true when  $P_{\text{TM}} < 0$  [40].

The magnitude of TM polarisation depends on many factors, but is maximised when the Zeeman interaction is comparable in strength to the dipolar interaction (to retain the population in the  $T_{\pm 1}$  states) and when molecular tumbling is slow (preventing spin relaxation from redistributing the spin states). Other factors which minimise the TM polarisations include rapid rotation of the triplet states due to tumbling, spin-lattice relaxation time and the rate of intersystem crossing from the excited singlet state  $S_1$  to the three triplet sub-levels. Since both the RPM and the TM depend on the viscosity and the diffusion coefficient, there can often be a competition between the two mechanisms, which makes the origin of spin polarisation difficult to isolate. Nonetheless, electron polarisation arising from the TM does have the advantage of providing the spin-relaxation time of a triplet precursor, a parameter which is not easily obtainable.

### 3.7 Magnetic Field Effect

In the literature, there are a number of reviews highlighting the correlation between Magnetic Field Effects (MFE) and radical reactions [35, 41]. As it has been demonstrated, MFEs arise because the applied static field can interfere with the mixing of the singlet-triplet states of the radical pair, leading to a change in the recombination yield through the singlet channel (assuming the triplet channel to be unreactive) [11, 42–51]. At zero field, the three triplet states ( $T_{\pm 1}, T_0$ ) are degenerate, and the singlet state can mix freely through magnetic interactions. Assuming no exchange interaction takes place and the radical pair is singlet correlated, increasing the magnetic field suppresses  $S - T_{\pm 1}$  mixing due to the Zeeman interaction, making the probability of the radical pair being in the singlet state greater at high fields than at zero fields. Hence, increasing the field would increase the recombination product assuming reaction is only possible through the singlet channel. With the same assumptions,  $S - T_0$  mixing via the  $\Delta g$  mechanism would tend to decrease the singlet population with increasing field due to a difference in precession rates of the electron spins, which leads to a larger escape for neutral radical pairs.

Assuming reaction can only proceed via the singlet channel (to form a stable product) and for the radical pair to be in a singlet state, the magnetic field dependence on product yield can be summarised as follows:

1.  $\Delta g$  mechanism (assuming  $J = 0$  T,  $\Delta g \neq 0$  and  $a_i = a_j = 0$  T). At zero field there is no  $S - T_{0,\pm 1}$  mixing, however, as the field increases  $S - T_0$  mixing can occur. Hence with increasing field the rate of  $S - T_0$  also increases which *reduces* the product yield.
2. Hyperfine coupling mechanism (HFCM) (assuming  $J = 0$  T,  $\Delta g = 0$  and  $a_i$  and/or  $a_j \neq 0$  T). At zero field the  $|S\rangle$  mixes with  $|T_{0,\pm 1}\rangle$  states, but as the field is increased  $S - T_{\pm 1}$  mixing is suppressed due to the Zeeman interaction. This leads to a decrease in the rate of  $S - T_{\pm 1}$  mixing with increasing field, which *increases* the product yield.
3. HFCM and  $\Delta g$  mechanism (assuming  $J = 0$  T,  $\Delta g \neq 0$  and  $a_i$  and/or  $a_j \neq 0$  T). This is the effect on the product yield when both the  $\Delta g$  and hyperfine mechanisms operate simultaneously. At low fields, the MFE is dominated by the hyperfine mechanism, but as the field strength increases the  $\Delta g$  mechanism starts to dominate. This has the effect of first *increasing* the product yield at lower fields and then *reducing* the yield with increasing  $B_0$ .
4. Level crossing mechanism (assuming  $J \neq 0$  T and  $a_i$  and/or  $a_j \neq 0$  T). This is the level-crossing between the  $|S\rangle$  and  $|T_{\pm 1}\rangle$  states occurring at a field strength of  $B_{LC} = 2|J(r)|/g\mu_B$ . This crossing of the states ( $S - T_{\pm 1}$  mixing) depletes the singlet state and populates the  $T_{\pm 1}$  state (depending on the sign of  $J$ ), leading to a *decrease* in the product yield and an *increase* in the escape products.

MFE can be observed experimentally through measuring reaction yields, isotopic substitution or through the phenomena known as quantum beats [52, 53], with most observations being successfully explained through the radical pair mechanism.

### 3.7.1 Low Field Effect

An interesting phenomenon at low fields ( $<1$  mT) occurs whereby as the field is increased from zero field, the rate of  $S - T_0$  mixing also increases. This effect is known as the *Low Field Effect* (LFE) [54, 55] and has been extensively discussed in the literature [11, 47–51, 54, 56–58]. The origin of the LFE can be understood by considering a radical pair  $R^\cdot + RH^\cdot$ , where one radical has a proton of spin  $1/2$  [54]. Assuming the radical pair is formed in a singlet-correlated state, the total spin angular momentum is consequently  $\pm 1/2$  (total electron spin angular momentum for the singlet state is zero). Similarly for the three triplet states,  $T_0$  and  $T_{\pm 1}$ , the components of total electron spin angular momentum are 0 and  $\pm 1$  respectively, with a total spin angular momentum of  $\pm 1/2$  or  $\pm 3/2$ . The physical reason responsible for LFE is due to the breakdown of the zero field selection rules with increasing field strengths. At zero field both the (i) total angular momentum and (ii) the component of the total angular momentum along a given direction must be conserved at all times [54]; this allows for only  $S - T_0$  mixing since (i) is violated if  $S - T_{\pm 1}$  mixing is allowed. As the field gradually increases, the zero field selection rules start to breakdown and there is a gradual change to the high field selection rules, which only requires the component of the total angular momentum in the direction of the static field to be conserved. This removes the constraint induced by (i) allowing the possibility of  $S - T_0$  and  $S - T_{\pm 1}$  mixing. With increasing strength of the magnetic fields, the Zeeman interaction starts to dominate, which again decouples the  $S$  and  $T_{\pm 1}$  states and prevents any mixing from occurring.

### 3.7.2 Quantum Beats

For a radical pair formed in a nonstationary state, the singlet probability will exhibit a characteristic time dependence at the frequency corresponding to the energy difference between the  $|S\rangle \leftrightarrow |T_0\rangle$  states.<sup>9</sup> The modulating pattern occurring at this frequency is termed *quantum beats*. As the  $|S\rangle$  is time-dependent and subject to magnetic field effects, quantum beats can be commonly observed in recombination fluorescence [53, 59, 60].

Quantum beats can arise in a chemical system via the  $\Delta g$  or hyperfine mechanism which induce  $S - T_0$  mixing. For the  $\Delta g$ -mechanism the frequency of oscillation between the  $S - T_0$  states is given by the Larmor frequency (Eq. 3.4). In the case of an isotropic hyperfine interaction occurring on each radical as well, the frequency of oscillation is

$$\omega = |\Delta g \mu_B \hbar^{-1} B_0 + \sum_{j1} a_{j1} m_{j1} - \sum_{j2} a_{j2} m_{j2}| \quad (3.78)$$

<sup>9</sup> Assuming the  $T_{\pm 1}$  states to be inaccessible.

with  $a_{jx}$  being the hyperfine coupling constant with the  $j$ th nucleus on radical  $x$  and  $m_{jx}$  is the projection of the spin of the  $j$ th nucleus on radical  $x$  in the direction of the external field. Experimentally observing quantum beats arising from the  $\Delta g$  is much more challenging because there must be a large difference in the  $g$ -factors of the radicals for the effect to be noticeable.

Molin [61] have shown that the parameters of quantum beats can usually be decomposed into (1) the frequency of the oscillation; (2) the time taken for the oscillation to decay; (3) the phase shift of oscillations and (4) the amplitude of the oscillation. The authors show that all these parameters can provide invaluable information of the spin-correlated radical pair. For example (1) gives information about the splitting in the ESR spectrum; (2) contains information about the spin relaxation times; (3) contains information about the time delay in forming the radical pair, and (4) can show the presence of spin-uncorrelated radical pairs (by comparing with theory).

### 3.7.3 Magnetic Effect on Reaction Yield

Magnetic effect on Reaction Yield (MARY) [62] as the name suggests, is primarily concerned with the effect of the static magnetic field on the geminate recombination yield. As discussed earlier in this chapter (Sect. 3.3.1), increasing the static magnetic field removes the degeneracy of the  $T_{\pm 1}$  states because of the Zeeman effect, preventing any spin-mixing between the  $S - T_{\pm 1}$  states from occurring. In this case, the field effect reaches a plateau whose half value is typically denoted as  $B_{1/2}$  and can be theoretically calculated (within the semiclassical approximation<sup>10</sup> [63, 64]) as [65]

$$B_{1/2} = \frac{2(\langle a_1^2 \rangle + \langle a_2^2 \rangle)}{\langle a_1 \rangle + \langle a_2 \rangle} \quad (3.79)$$

where  $\langle a_r \rangle = [\sum_i I_i(I_i + 1)(a_i^2)]^{1/2}$ , with  $I_i$  being the nuclear spin on radical  $i$ . MARY spectroscopy uses fluorescence from the exciplex to detect the variation in the singlet-triplet spin dynamics of a radical ion pair as a function of the magnetic field.

In radiation chemistry, X-ray tubes are the most commonly used source of radiation for MARY experiments to study the hole lifetime and reactivity in non-polar solvents (details can be found in Ref. [66]). In particular, MARY can be very useful to study short-lived transient species that are otherwise much more difficult to study using standard ESR techniques.

---

<sup>10</sup> In the semiclassical approximation the electron spin on each radical is treated quantum mechanically, whilst the nuclear spins are treated classically. The unpaired electron precesses about the static field and the resultant of the nuclear spins.

### 3.7.4 *Optically Detected Magnetic Resonance*

In optically detected magnetic resonance (ODMR) experiments [67, 68] a resonance microwave field is applied which causes a redistribution of the spin population. For a radical pair in a strong magnetic field, the triplet manifold is decoupled with only the  $S$  and  $T_0$  degenerate. In an ODMR experiment either the microwave frequency or the magnetic field is swept to allow transitions from the  $T_0$  to the  $T_{\pm 1}$  states. As  $S - T_0$  mixing can still occur, the singlet population is gradually lost to the  $T_{\pm 1}$  states via the  $T_0$  state, which leads to less recombination (and less luminescence) and more escape yield (assuming reaction is only possible via the singlet channel) at short times. However, at long times the  $T_{\pm 1} - T_0$  mixing would repopulate the depleted  $T_0$  state, which (through the  $S - T_0$  mixing) would lead to an increase in the singlet luminescence [69].

If the applied resonant field is larger than the hyperfine splitting, then the microwaves strongly couple  $T_0$  to the  $T_{\pm 1}$  states, which isolates the singlet state and prevents any  $S - T_0$  mixing from occurring. This mechanism is commonly referred to as *state locking*, which increases the recombination probability and fluorescence intensity. A typical ODMR spectrum in general plots the optical transition versus the swept microwave or magnetic field.

### 3.7.5 *Reaction Yield Detected Magnetic Resonance*

The reaction yield detected magnetic resonance (RYDMR) technique [62, 70] has been applied to a wide variety of spin systems (such as crystals, micelles, biological systems and scintillator solutions) and involves the use of a resonant microwave field as well as a static magnetic field to control the chemical reactivity by inducing magnetic resonance transitions in the spin-correlated radical pair. Due to rapid intersystem crossing between the  $T_0 - S$  states, the radical pairs converted to the  $T_0$  state recombine much faster than those in the  $T_{\pm 1}$  states (assuming reaction only possible via the singlet channel), which enhances the yield of recombination product. Consequently, one can observe the electron spin resonance spectrum of radical pairs by observing the product yields. The signal obtained from RYDMR is proportional to the concentration of the radical pair, which allows for the observation of the main radical reaction of interest (unlike time-resolved EPR, where minor products produce a signal intensity making the spin-dynamics difficult to understand).

## 3.8 Summary

This chapter has highlighted the main concepts of spin dynamics for a single radical pair and has illustrated how their reactivity can be controlled through the application of a magnetic field. It seems evident that spin dynamics must be treated

explicitly in simulations to properly model the chemistry of spurs. The next chapter will implement the underlying theory of spin dynamics into simulation programs and demonstrate how the theory can be extended for a full radiation track. Simulation techniques will then be used to investigate effects such as quantum beats, spin entanglement and spin-relaxation to better understand the chemistry of radiolytic and photolytic radical pairs.

## References

1. B. Brocklehurst, *Int. Rev. Phys. Chem.* **4**, 279 (1985)
2. J.L. Magee, M. Burton, J.S. Kirby-Smith, *Comparative Effects in Radiation* (Wiley, New York, 1960)
3. H.A. Schwarz, *J. Phys. Chem.* **73**, 1928 (1969)
4. W.G. Burns, H.E. Sims, J.A. Goodall, *Radiat. Phys. Chem.* **23**, 143 (1984)
5. C.N. Trumbore, D.R. Short, J.E. Fanning, H. Olsen, *J. Phys. Chem.* **82**, 1539 (1990)
6. L.T. Muus, P.W. Atkins, K.A. McLauchlan, J.B. Pedersen, *Chemically Induced Magnetic Polarisation* (Reidel, Dordrecht, 1977)
7. J.B. Pedersen, J.H. Freed, *J. Chem. Phys.* **58**, 2746 (1973)
8. J.B. Pedersen, J.H. Freed, *Chem. Phys. Lett.* **59**, 2869 (1973)
9. G.T. Evans, P.D. Fleming, R.G. Lawler, *J. Chem. Phys.* **58**, 2071 (1973)
10. R.G. Saifutdinov, L.I. Larina, T.I. Vakul'skaya, M.G. Voronkov, *Electron Paramagnetic Resonance in Biochemistry and Medicine* (Springer, New York, 2001)
11. B. Brocklehurst, *J. Chem. Soc. Faraday Trans. II* **72**, 1869 (1976)
12. V.A. Bagryansky, V.I. Borokov, Y.N. Molin, *Chem. Phys.* **255**, 237 (2000)
13. H. Hayashi, *Introduction to Dynamic Spin Chemistry* (World Scientific Publishing Co Pte Ltd, Singapore, 2004)
14. F.J.J.D. Kanter, R. Kaptein, R.A.V. Santen, *Chem. Phys. Lett.* **45**, 575 (1977)
15. F.J.J.D. Kanter, T.A. Hollander, A.H. Huizer, R. Kaptein, *Mol. Phys.* **34**, 857 (1977)
16. F. Bloch, *Phys. Rev.* **70**, 460 (1946)
17. I. Solomon, *Phys. Rev.* **99**, 559 (1955)
18. F. Bloch, *Phys. Rev.* **102**, 135 (1956)
19. R.K. Wangsness, F. Bloch, *Phys. Rev.* **89**, 728 (1953)
20. A.G. Redfield, *Relaxation Theory, Density Matrix Formalism. Encyclopedia of Nuclear Magnetic Resonance* (Wiley, Chichester, 1996)
21. A. Abragam, *Principles of Nuclear Magnetism* (Oxford University Press, Oxford, 1961)
22. A.G. Redfield, *Advan. Magn. Reson.* **1**, 1 (1966)
23. E. Hahn, *Phys. Rev.* **80**, 580 (1950)
24. T.D.W. Claridge, *High Resolution NMR Techniques in Organic Chemistry* (Elsevier, Oxford, 2004)
25. K.D. Sattlet, *Nanomedicine and Nanorobotics* (CRC Press, Boca Raton, 2010)
26. R. Kaptein, L.J. Oosterhoff, *Chem. Phys. Lett.* **4**, 195 (1969)
27. G.L. Closs, *J. Amer. Chem. Soc.* **91**, 4552 (1969)
28. H.J. Werner, K. Schulten, A. Weller, *Biochim. Biophys. Acta* **502**, 255 (1978)
29. R. Haberkorn, M.E. Michel-Beyerle, *J. Biophys.* **26**, 489 (1979)
30. C. Blattler, F. Jent, H. Paul, *Chem. Phys. Lett.* **166**, 375 (1990)
31. K.M. Salikhov, Y.N. Molin, R.Z. Sagdeev, A.L. Buchachenko, *Spin Polarisation and Magnetic Field Effects in Radical Reactions* (Elsevier, Amsterdam, 1984)
32. A.P. Lopley, G.L. Closs, *Chemically Induced Dynamic Nuclear Polarisation* (Wiley-Interscience, New York, 1973)
33. R. Kaptein, *J. Amer. Chem. Soc.* **94**, 6251 (1972)

34. R. Kaptein, *Chem. Commun.* **432**, 732 (1971)
35. B. Brocklehurst, *Int. Rev. Phys. Chem.* **4**, 279 (1985)
36. P.W. Atkins, G.T. Evans, *Chem. Phys. Lett.* **25**, 108 (1974)
37. S.K. Wong, D.A. Hutchinson, J.K.S. Wan, *J. Chem. Phys.* **58**, 985 (1973)
38. H.F. Hameks, N.J. Oosterhoof, *Mol. Phys.* **1**, 358 (1958)
39. J.H. van der Waals, W.G. van Dorp, T.J. Schaafsma, *Electron Spin Resonance of Porphyrin Excited States* (Academic Press, New York, 1979)
40. A. Schweiger, G. Jeschke, *Principles of Pulse Electron Paramagnetic Resonance* (Oxford University Press, Oxford, 2001)
41. U.E. Steiner, T. Ulrich, *Chem. Rev.* **89**, 51 (1989)
42. H. Staerk, R. Treichel, A. Weller, *Chem. Phys. Lett.* **96**, 28 (1983)
43. D.N. Nath, M. Chowdhury, *Chem. Phys. Lett.* **109**, 13 (1984)
44. K. Schulten, H. Staerk, A. Weller, H.J. Werner, B. Nickel, *Z. Phys. Chem.* **101**, 371 (1976)
45. A. Weller, H. Staerk, R. Treichel, *Faraday Discuss. Chem. Soc.* **78**, 271 (1984)
46. S.N. Batchelor, C.W.M. Kay, K.A. McLauchlan, I.A. Shkrob, *J. Phys. Chem.* **97**, 13250 (1993)
47. H. Fischer, *Chem. Phys. Lett.* **100**, 255 (1983)
48. C.A. Hamilton, J.P. Hewitt, K.A. McLauchlan, U.E. Steiner, *Mol. Phys.* **65**, 423 (1988)
49. A. Shkrob, V.F. Tarasov, A.L. Buchachenko, *Chem. Phys.* **153**, 443 (1991)
50. D.V. Stass, N.N. Lukzen, B.M. Tadjikov, Y.N. Molin, *Chem. Phys. Lett.* **233**, 444 (1995)
51. V.O. Saik, A.E. Ostafin, S. Lipsky, *J. Chem. Phys.* **103**, 7347 (1995)
52. O.A. Anisimov, V.L. Bizyaev, N.N. Lukzen, V.M. Grigoryantz, Y.N. Molin, *Chem. Phys. Lett.* **101**, 131 (1983)
53. A.V. Veselov, V.I. Melekhov, O.A. Anisimov, Y.N. Molin, *Chem. Phys. Lett.* **136**, 263 (1987)
54. B. Brocklehurst, K.A. McLauchlan, *Int. J. Radiat. Biol.* **69**, 3 (1996)
55. D.V. Stass, B.M. Tadjikov, Y.N. Molin, *Chem. Phys. Letts.* **235**, 511 (1995)
56. M. Sacher, G. Grampp, B. Bunsenges, *Phys. Chem.* **101**, 971 (1997)
57. C. Timmel, U. Till, B. Brocklehurst, K.A. McLauchlan, P.J. Hore, *Mol. Phys.* **95**, 71 (1998)
58. M. Justinek, G. Grampp, S. Landgraf, P.J. Hore, N.N. Lukzen, *J. Am. Chem. Soc.* **126**, 5635 (2004)
59. B. Brocklehurst, *J. Chem. Soc. Faraday Trans.* **93**, 1079 (1997)
60. V.A. Bagryansky, O.M. Usov, V.I. Borokov, *Chem. Phys.* **255**, 237 (2000)
61. Y.N. Molin, *Bull. Korean Chem. Soc.* **20**, 7 (1999)
62. K.A. McLauchlan, S.R. Natrass, *Mol. Phys.* **65**, 1483 (1988)
63. K. Schulten, P.G. Wolynes, *J. Chem. Phys.* **68**, 3292 (1978)
64. E.W. Knapp, K. Schulten, *J. Chem. Phys.* **71**, 1878 (1979)
65. A. Weller, F. Nolting, H. Staerk, *Chem. Phys. Lett.* **96**, 24 (1983)
66. D.V. Stass, F.B. Sviridenko, Y.N. Molin, *Radiat. Phys. Chem.* **67**, 207 (2003)
67. O.A. Anisimov, V.M. Grigoryants, V.K. Molchanov, Y.N. Molin, *Chem. Phys. Lett.* **66**, 265 (1979)
68. O.A. Anisimov, V.M. Grigoryants, Y.N. Molin, *J. Phys. Chem.* **84**, 1853 (1980)
69. I.A. Shkrob, A.D. Trifunac, *Radiat. Phys. Chem.* **50**, 227 (1997)
70. S.N. Batchelor, K.A. McLauchlan, I.A. Shkrob, *Z. Phys. Chem.* **180**, 9 (1993)

# Chapter 4

## Simulation Techniques and Development

### 4.1 Introduction

In this chapter a detailed analysis is presented of the two main simulation packages commonly used to model the fast radiation chemistry in spurs, namely the independent reaction times model (IRT) and Monte Carlo random flights simulation. Although the random flights simulation is commonly used to model radiation tracks, it unfortunately requires significant computation resources, making its applicability limited to spurs containing a small number of radical pairs. This situation is further compounded if an accurate description of spin dynamics is required. In the latter part of this chapter a detailed review of two newly designed programs called *Hybrid* and *Slice* is presented, which are both computationally much more efficient than the random flights technique. In particular, *Slice* which is completely based on the IRT framework, is capable of simulating a full radiation track with the option to explicitly treat spin-dynamics (including any spatial interactions), without compromising on the computational resources. In addition *Slice* allows simulation to much longer timescales than what is currently achievable with random flights simulations.

### 4.2 Random Number Generation

Random numbers are defined as a sequence of numbers which lack any pattern, unlike pseudorandom numbers which starting from an arbitrary seed state, will tend to repeat after a certain period. In simulations, random numbers are constantly generated to model stochastic processes and other events; any correlation between random numbers will have the effect of biasing the results with an unphysical correlation. In the Appendices (Sect. B.1) statistical tests were first carried out to ensure that no bias was detected in the algorithm adopted for this work. The analysis of the statistical tests showed that the random number generator was capable of producing the required level of randomness required for this work.

## 4.3 Monte Carlo Random Flights Simulation

### 4.3.1 Introduction

The random flights simulation of spur kinetics involves starting from a given spatial distribution of radicals in an isolated spur [1, 2]. The initial spatial configuration can be generated by sampling from an appropriate probability distribution or using a predefined set of coordinates (i.e. those obtained from a simulated track structure). The simulation proceeds by checking for zero time reactions from this spatial configuration, making the necessary changes to chemical properties of the reacted pair and incrementing the reaction counter. All surviving particles are then allowed to diffuse for a given time step, with the new set of coordinates recorded. At the end of each time step, a bridging process [3, 4] is used to test whether the particles may have encountered during the diffusive jump. A single realisation is completed once all possible reactions have either taken place or a pre-defined cut-off time is reached. To obtain acceptable statistics the simulation must be repeated (typically  $10^5$ – $10^6$  times) with identical simulation parameters but a different random number sequence. A flow diagram is presented in the Appendix (Fig. C.1 in Sect. C.1), highlighting the key stages of a random flights simulation.

The diffusive motion of each particle is a random process which can be described by the stochastic differential equation [5, 6] as

$$d\mathbf{X} = -\frac{D}{k_B T} \nabla U dt + (2D)^{1/2} d\mathbf{W}_t \quad (4.1)$$

where  $k_B$  is the Boltzmann constant,  $T$  the temperature,  $D$  the diffusion coefficient,  $d\mathbf{W}_t$  represents the increment of a three-dimensional Wiener process and  $U$  represents the potential energy of the pair. If only Coulombic interactions between ions are included,  $U$  takes the form (ignoring any screening potential)

$$U_i = \sum_{j \neq i} \frac{k_B T z_i z_j r_c}{r_{ij}} \quad (4.2)$$

with  $z_i$  and  $z_j$  representing the charges on ion  $i$  and  $j$  respectively,  $r_{ij}$  the interparticle vector and  $r_c$  the Onsager distance [defined in Eq. (2.37)]. Although other more detailed models of diffusion are available, such as Brownian dynamic methods based on the Langevin equation, the timescales of kinetics required in the simulations are sufficiently long (typically  $> 10$  ps), that more elaborate methods add nothing more than computational expense. The formulation chosen is mathematically equivalent to the multi-body diffusion equation, which is the basis of the most widely accepted theories of diffusion kinetics.

Unfortunately, Eq. (4.1) is only exact when  $dt$  is infinitesimal, however it can be approximated by using the Itô interpretation of a Wiener process [7], such that the increment  $W_t - W_s$  is shown to have the property of a normally distributed random

number ( $\mathbf{N}(0, \sqrt{(t-s)})$ ) with zero mean and standard deviation  $\sqrt{(t-s)}$ . Using the Itô interpretation of the Wiener process and discretising Eq. (4.1), the position increment of a particle in a given time step ( $\delta t$ ) can be expressed as

$$\delta \mathbf{X}_i = - \sum_{j \neq i} \frac{z_i z_j r_c}{r_{ij}^3} \mathbf{r}_{ij} D_i \delta t + \sqrt{(2D_i)\delta t} \mathbf{N}_3(0, 1) \quad (4.3)$$

The first term in Eq. (4.3) known as the *drift* represents the mean non-random displacement of the particle due to electrostatic forces. For particles which are electrically neutral, this term is zero. The second term of Eq. (4.3) known as the *dispersion* represents the random motion of the particle caused by the repeated collision with the solvent particles. The exact value used for  $\delta t$  depends upon the simulation parameters and number of particles being modelled; in any case this parameter must be carefully chosen as this will greatly affect the observables of the chemical system. In any simulation  $\delta t$  must be sufficiently small to (i) ensure that the drift does not change significantly during jumps; (ii) minimise the probability of reaction occurring during the diffusive jump and (iii) minimise the probability of one particle undergoing multiple reactions. In the literature, simulations have been reported which make use of a fixed time step for  $\delta t$  [8], which is computationally inefficient, since larger steps for  $\delta t$  can be taken if the particles are far apart and there is minimal probability of reaction. A more efficient method is to use a variable time step [9] which decides the value of  $\delta t$  to use based on the separation of the particles, the probability of reaction and the change in the interparticle drift. The implementation of a variable time step in a random flights simulation is discussed in detail later in this chapter (Sect. 4.3.4).

For reactions which are diffusion controlled, reaction occurs with certainty on encounter with the time of the reaction noted. If the product of recombination is unreactive then it is removed from further consideration, otherwise the newly formed product replaces the reactants in the simulation and the simulation resumes as normal. For reactions which are partially diffusion controlled, the probability of reaction on encounter is calculated depending on the reactivity of the boundary. If the encounter is found to be unreactive, the particle positions are modified to account for reflection and the simulation would proceed as normal. A more thorough analysis will be presented later in this chapter (Sect. 4.3.3).

### 4.3.2 Brownian Bridge Probability

To deal with reactions occurring during the diffusive jump of the particles properly, a Brownian bridge [3, 4] is implemented, which calculates the survival probability ( $\Omega(t)$ ) for every pair at every time step  $\delta t$  taken in the simulation, conditioned on the separation of the pair before ( $x$ ) and after ( $y$ ) the time increment  $\delta t$ . This can be readily calculated using Bayes' theorem as

$$\Omega(\text{not hit } a|(x, y, \delta t)) = \frac{p_{\text{abs}}(x, y, \delta t)}{p(x, y, \delta t)} \quad (4.4)$$

where  $p(x, y, \delta t)$  is the transition density for a freely diffusing pair to pass from  $x$  to  $y$  in the time  $\delta t$ , and  $p_{\text{abs}}(x, y, \delta t)$  is the same but with an absorbing inner boundary at  $a$  (where  $a < \min(x, y)$ ). Provided that the time step  $\delta t$  remains sufficiently small, the separation of the pair can be approximated by a one-dimensional Wiener process with constant drift. The Green's functions of the one-dimensional diffusion equation are well known [4] (see Sect. 2.3.2), which when substituted into Eq. (4.4) give

$$\Omega(x, y, \delta t) = 1 - \exp[-(x - a)(y - a)/D'\delta t] \quad (4.5)$$

with  $D'$  being the mutual diffusion coefficient of the pair. Alternatively, for a three-dimensional Bessel process (which uses only the radial part of diffusion process) the survival probability can be similarly obtained as

$$\Omega(x, y, \delta t) = \frac{1 - \exp[-(x - a)(y - a)/D'\delta t]}{1 - \exp[-(yx)/D'\delta t]} \quad (4.6)$$

No such result is available in general for an ion pair, but since  $\delta t$  is chosen such that the particle's drift does not change significantly, Eq. (4.5) can be used for the ionic case as well.

In the simulation program, the survival probability is calculated after every  $\delta t$  and compared against a uniformly distributed random number between (0,1] [10]. If the survival probability is less than this random number, the particles have reacted and the relevant changes are made. The validity of this technique relies on the fact that the time step is relatively small such that the drift term remains constant. For fixed time step calculations, this method provides a reliable way of testing whether convergence is achieved with respect to  $\delta t$ .

### 4.3.3 Reflection

Reflection of two particles can occur if for example the boundary is unreactive or the particles are in the wrong spin states for reaction to occur. In all cases, it is important that the reflected particles have the correct spatial configuration as otherwise this could possibly lead to biased kinetics. In this section, the algorithm developed by Green [4, 11] is discussed which has been extensively tested against other simulation methods and is known to provide an accurate description for reflected particles. If the position of two particles are denoted  $\mathbf{X}_1$  and  $\mathbf{X}_2$  with diffusion coefficients  $D_1$  and  $D_2$  respectively, the interparticle vectors of  $\mathbf{R}$  and  $\mathbf{S}$  can be formed as a linear combination of  $\mathbf{X}_1$  and  $\mathbf{X}_2$  as

$$\mathbf{R} = \mathbf{X}_2 - \mathbf{X}_1 \quad (4.7)$$

and

$$\mathbf{S} = D_2 \mathbf{X}_2 + D_1 \mathbf{X}_1 \quad (4.8)$$

These vectors evolve independently of each other [12] with the reflection of two particles affecting only  $\mathbf{R}$  and not  $\mathbf{S}$ . Before executing the diffusive jump in the simulation, these two vectors are calculated for every possible reaction. After executing the jump, the new position of the particles are used to calculate the vector increment  $\delta\mathbf{R}$  to the interparticle vector. If it is found that the particles encountered during the time step, then the vector  $\mathbf{R} + \delta\mathbf{R}$  needs to be resolved into two components; one parallel to  $\mathbf{R}$  and one perpendicular to  $\mathbf{R}$ . Assuming a planar boundary, which is a reasonable assumption as long  $\delta t$  is sufficiently small, the perpendicular component remains unaffected and need not be altered. However, the component parallel to the boundary needs to be modified. Describing the parallel component as a one dimensional Wiener process with a constant drift, the recipe to generate the reflected position can be expressed as<sup>1</sup>

$$X_{\text{ref}}(t) = \begin{cases} X(\delta t) & M(\delta t) > a \\ X(\delta t) + a - M(\delta t) & M(\delta t) \leq a \end{cases} \quad (4.9)$$

with  $X(\delta t)$  being the separation of the particles at time  $\delta t$  without any reflecting boundary,  $M(\delta t)$  the shortest distance possible for the pair during this time step and  $a$  the encounter radius. Therefore, if the separation of the particles before and after the time step is  $x$  and  $y$  respectively and the minimum distance between them is  $m$ , then if  $m < a$ , the separation of the particles is increased from  $y$  to  $y + a - m$ , simulating reflection. In order to calculate a value for  $m$ , it is necessary to sample from the probability distribution of  $M(\delta t)$  conditioned on  $x$  and  $y$ . Equation (4.5) gives the probability of passing from  $x$  to  $y$  via  $a$ ; hence the probability of passing from  $x$  to  $y$  via  $m$  obeys the same probability distribution, which is simply  $M(\delta t) = \exp[-(y - m)(x - m)/D't]$ . Using the standard inversion method [13] a value for  $M$  can be generated as

$$M = \frac{1}{2} \left\{ x + y - [(x - y)^2 - 4D't \ln U(0, 1)]^{1/2} \right\} \quad (4.10)$$

with  $U(0,1]$  representing a uniformly distributed random number between  $(0,1]$ . Once a minimum separation value has been calculated the final separation distance of the pair is increased by the factor  $f = (y + a - m)/y$ , which completes the modification of the vector  $\mathbf{R} + \delta\mathbf{R}$  parallel to  $\mathbf{R}$ . Letting  $\mathbf{R}'$  denote the new interparticle vector with necessary adjustments made to the parallel component, and recalling that the

---

<sup>1</sup> This recipe is exact for a Brownian motion with drift (proof is shown in the Appendix Sect. A.11).

vector  $\mathbf{S}$  diffuses independently of  $\mathbf{R}$  and is therefore unaffected by the reflection, the modified position vectors  $\mathbf{X}'_1$  and  $\mathbf{X}'_2$  can be determined from the equations

$$\mathbf{S} = D_2\mathbf{X}'_1 + D_1\mathbf{X}'_2 \quad (4.11)$$

$$\mathbf{R}' = \mathbf{X}'_2 - \mathbf{X}'_1 \quad (4.12)$$

Hence,

$$\mathbf{X}'_1 = \frac{\mathbf{S} - D_1\mathbf{R}'}{D_1 + D_2} \quad (4.13)$$

$$\mathbf{X}'_2 = \frac{\mathbf{S} + D_2\mathbf{R}'}{D_1 + D_2} \quad (4.14)$$

#### 4.3.4 New Variable Time Step Algorithm

In random flights simulations the single most important parameter is the time step  $\delta t$ , which if not properly converged leads to incorrect results. If the drift remains effectively constant throughout the time step, then the separation between the pair behaves as a one dimensional Wiener process with constant drift. The relative drift or drift in the interparticle distance for a pair of particles separated by a distance  $x$  can be written as

$$\mu = \frac{2D'}{x} + \frac{D'r_c}{x^2} \quad (4.15)$$

with the first term representing *geometric* drift (applies for both neutral and charged species i.e. the tendency of diffusing particles to drift apart in 3D), and the second term representing the *electrostatic* interaction between charged species.

In order to select a time step, consider the relationship between the stochastic differential equation for  $df(X)$  and  $dX$ , where  $f(X)$  is the same function of  $X$ , given by the Itô transformation formula<sup>2</sup>

$$df(X) = \left[ f'(X)\mu(X) + \frac{1}{2}f''\sigma^2(X) \right] dt + [f'(X)\sigma(X)]dW_t \quad (4.16)$$

with the discretised version taking the form

$$\delta f(X) = \left[ f'(X)\mu(X) + \frac{1}{2}f''\sigma^2(X) \right] \delta t + [f'(X)\sigma(X)]N(\mu, \sigma)\sqrt{\delta t} \quad (4.17)$$

---

<sup>2</sup> This is the standard method for transforming a stochastic differential equation.

with  $N(\mu, \sigma)$  being a normally distributed random variable within the range  $\pm C$ . In the simulation the time step is generated such that at a certain level of confidence (say 95 %) the relative drift does not change by proportion greater than  $\epsilon_D$  i.e.

$$-\epsilon_D \leq \frac{\delta f(X)}{f(X)} \leq \epsilon_D \quad (4.18)$$

On substituting the definition of  $\delta f(X)$  into Eq. (4.18) and letting

$$A = \left[ \frac{f'(X)}{f(X)} \mu(X) + \frac{1}{2} \frac{f''(X)}{f(X)} \sigma^2(X) \right] \quad (4.19)$$

$$B = \left[ \frac{f'(X)}{f(X)} \sigma(X) \right] \quad (4.20)$$

and replacing  $\tau^2 = \delta t$ , the general solution to the quadratic is found to be

$$0 \leq \tau \leq \frac{-|B|C + \sqrt{B^2 C^2 + 4|A|\epsilon_D}}{2|A|} \quad (4.21)$$

There is a complication in applying this formula to the function  $f(X) = \mu$  because when the ions are oppositely charged, there is always a distance where  $\mu = 0$  and so  $d\mu/\mu$  cannot be controlled in this region. However, both terms contributing to  $\mu$  are of the form  $ax^p$ , and so if both these terms are controlled separately, then the absolute variation in their sum will be acceptable.  $A$  and  $B$  can then defined as

$$A = \left[ \frac{p}{X} \mu(X) + \frac{p(p-1)}{X^2} \frac{\sigma^2(X)}{2} \right] \quad B = \frac{p}{X} \sigma(X) \quad (4.22)$$

Using the definition of the drift term presented earlier (Eq. 4.15) and recognising  $\sigma = \sqrt{2D}$  (with  $D$  being the diffusion coefficient), Eq. (4.22) can then be expressed as

$$0 \leq \tau \leq \frac{X|p|C \left[ -1 + \sqrt{1 + \left| \frac{2\epsilon_D}{pC^2} \left[ \frac{r_c}{X} + (p+1) \right] \right|} \right]}{\sqrt{2D} |p| \left[ \frac{r_c}{X} + (p+1) \right]} \quad (4.23)$$

Considering the first limiting case when  $\epsilon_D \ll 1$ , Eq. (4.23) reduces to

$$0 \leq \tau \leq \frac{\epsilon_D X}{C|p|\sqrt{2D'}} \quad (4.24)$$

which can be used to simulate the time steps for neutral particles. The second limiting case is when the ratio  $|r_c/X| \gg |(p+1)|$  giving the required time step for charged particles as

$$0 \leq \tau \leq \frac{X^2 C}{|r_c| \sqrt{2D'}} \left( -1 + \sqrt{1 + \frac{2\epsilon_D |r_c|}{pC^2 X}} \right) \quad (4.25)$$

which can be used irrespective of whether the force is attractive or repulsive. In the simulation program, a value for  $\delta t$  is calculated for all possible pairs and the minimum of these values is used as the time increment.

### 4.3.5 Partially Diffusion Controlled Reactions

The recipe to simulate partially diffusion controlled reactions involves calculating the probability of survival on diffusing from  $x$  to  $y$  via the encounter radius  $a$  in the time step  $\delta t$  as

$$\Omega(\text{survival}|x, y, \delta t \text{ via } a) = \frac{p_{\text{rad}}(x, y, \delta t \text{ via } a \text{ and survive})}{p_{\text{ref}}(x, y, \delta t \text{ via } a)} \quad (4.26)$$

with  $p_{\text{rad}}(x, y, \delta t)$  being the one dimensional transition density on going from  $x$  to  $y$  subject to radiation boundary conditions at  $a$ , and  $p_{\text{ref}}(x, y, \delta t)$  the same but with a reflective boundary at  $a$ . There are two types of diffusion processes which constitute the numerator of Eq. (4.26); those trajectories which never hit  $a$  [given by the transition density  $p_a(x, y, \delta t)$ ] and those trajectories which have hit  $a$  and survived. As the numerator in Eq. (4.26) is only interested in the trajectories which go via  $a$ , it can be simplified to the form

$$p_{\text{rad}}(x, y, \delta t) - p_a(x, y, \delta t) \quad (4.27)$$

Similarly, the denominator of Eq. (4.26) can be decomposed into trajectories which do not strike the boundary  $a$  and those that do hit  $a$  but are reflected. Hence the denominator of Eq. (4.26) can be rewritten as

$$p_{\text{ref}}(x, y, \delta t) - p_a(x, y, \delta t) \quad (4.28)$$

As long as  $\delta t$  remains sufficiently small, the transition densities for the one dimensional diffusion process with constant drift can be used to calculate the survival probability at every time step  $\delta t$  using the equation

$$\Omega(x, y, \delta t) = \frac{p_{\text{rad}}(x, y, \delta t) - p_a(x, y, \delta t)}{p_{\text{ref}}(x, y, \delta t) - p_a(x, y, \delta t)} \quad (4.29)$$

The explicit expression for the numerator and denominator respectively are given as

$$p_{\text{rad}}(x, y, \delta t) - p_a(x, y, \delta t) = \frac{1}{\sqrt{\pi D' \delta t}} \exp \left[ -\frac{(x-a)(y-a)}{D't} - \frac{(x-y+\mu t)^2}{4D't} \right]$$

$$\begin{aligned}
& - \frac{2v + \mu}{2D'} \exp[v(x + y - 2a + \mu\delta t + v\delta t) + \mu(y - a)/D'] \\
& \times \operatorname{erfc} \left( \frac{(x + y - 2a + (2v + \mu)\delta t)}{\sqrt{4D'\delta t}} \right) \quad (4.30)
\end{aligned}$$

$$\begin{aligned}
p_{\text{ref}}(x, y, \delta t) - p_a(x, y, \delta t) &= \frac{1}{\sqrt{\pi D'\delta t}} \exp \left[ - \frac{(x - a)(y - a)}{D'\delta t} - \frac{(x - y + \mu t)^2}{4D'\delta t} \right] \\
& - \frac{\mu}{2D'} \exp[\mu(y - a)/D'] \times \operatorname{erfc} \left( \frac{(x + y - 2a + \mu\delta t)}{\sqrt{4D'\delta t}} \right) \quad (4.31)
\end{aligned}$$

To decipher whether reaction has taken place, a uniformly distributed random number is generated between (0,1]. If this random number is greater than  $\Omega(x, y, \delta t)$  then reaction has taken place and the relevant changes are made in the simulation (i.e. update reaction counters and change chemical properties).

### 4.3.6 Exact Simulation of Sample Paths

Recently in the mathematical literature [14] an exact algorithm for the simulation of a class of Itô's diffusion is presented, which allows the stochastic differential equation to be simulated without the need for Euler discretisation. If adaptable into the random flights framework, the efficiency at which simulations of chemical systems can be performed would be greatly increased, allowing much better statistics to be obtained through the use of many more realisations. The general recipe for the exact algorithm proceeds as follows:

Starting with the stochastic differential equation of the form

$$dX_t = \alpha(X_t)dt + dW_t \quad (4.32)$$

where  $\alpha$  is the drift function. In order to generate exact sample paths, the drift function must obey the three conditions:

1.  $\alpha$  is differentiable
2. The function  $h = \exp[A(u) - (u - x)^2/2\mathfrak{S}]$  can be integrated. Here  $A(u) = \int_0^u \alpha(y)dy$  and  $\mathfrak{S}$  the stopping time of the Brownian process.
3. The function  $\frac{\alpha^2 + \alpha'}{2}$  is bounded from below.

The basic idea is to propose sample paths from the biased Brownian motion  $\hat{W}$  conditioned that the end point  $W_{\mathfrak{S}} = h$ , to allow rejection sampling to be performed. By performing some complex analysis the authors have shown that it is possible to define the Radon-Nikodym derivative as

$$\frac{d\mathbb{Q}}{d\mathbb{Z}} \propto \exp \left[ - \int_0^{\mathfrak{S}} \phi(X_t) dt \right] \quad (4.33)$$

where  $\mathbb{Q}$  is the probability measure of the stochastic process and  $\mathbb{Z}$  is the probability measure of the biased Brownian motion.  $\phi(u)$  can then be shown to be

$$\phi(u) = \frac{\alpha^2(u) + \alpha'(u)}{2} - k \quad (4.34)$$

with  $k \leq \inf(\alpha^2 + \alpha')(u)/2$ . The general algorithm to sample exact paths then proceeds as follows:

1. Generate an end value for  $y$  from the distribution  $\exp[A(u) - (u - x)^2/2\mathfrak{S}]$
2. Produce a realisation  $x_1, x_2 \dots x_r$  of a Poisson process on  $[0, \mathfrak{S}] \times [0, M]$ .  $\mathfrak{S}$  is the end time of the diffusion process and  $M = \sup(\alpha^2 + \alpha')(u)/2 - \inf(\alpha^2 + \alpha')(u)/2$ .
3. Simulate a realisation  $X \sim \mathbb{Z}$
4. Construct a Brownian bridge for the process started at  $x$  at time zero and ends on  $y$  at  $\mathfrak{S}$ .
5. Calculate the indicator function  $I = \prod_{i=1}^k \mathbf{1}_{\phi(y_i) \leq v_i}$
6. If  $I = 1$ , the trajectory is accepted, otherwise the process is repeated.

The authors report two further variations of the algorithm described above which relax the restriction of  $\phi$ . Unfortunately, the adaption of this algorithm to simulate the stochastic differential equation for charged species is not possible since  $\phi(u) = r_c^2/8u^4$ ; clearly this function is not bounded from below. Further complications also arise, since the function  $A(u)$  is not defined at  $y = 0$ , making it impossible to simulate a biased diffusion path  $\hat{W}$ . The authors have not yet generalised their procedure to the problem where  $\phi(u)$  is bounded purely because of an inner boundary. Such a generalisation will obviously be very useful.

## 4.4 Independent Reaction Times

### 4.4.1 Introduction

The IRT model [1, 2, 12, 15] is essentially a Monte Carlo algorithm which assumes the independence of reaction times (i.e. each reaction is independent of other such reactions and that the covariance of these reaction times is zero). Unlike the random flights simulation, the diffusive trajectories are not tracked but instead encounter times are generated by sampling from an appropriate probability density function conditioned on the initial separation of the pair. The first encounter takes place at the minimum of the key times generated  $\min(t_1; t_2; t_3 \dots)$  and all subsequent reactions occur based on the minimum of surviving reaction times. Unlike random flights

simulations, the IRT can efficiently simulate to much longer timescales and does not suffer from discretisation errors. A flow diagram is presented in the Appendix (Fig. C.2 in Sect. C.2), highlighting the key stages involved in the simulation program.

## 4.4.2 Diffusion Controlled Reactions: Neutral Species

### 4.4.2.1 Recombination Times

From Sect. 2.4.1 the time dependent survival probability for a neutral pair is known to be

$$\Omega(t) = 1 - \frac{a}{r} \operatorname{erfc} \left[ \frac{r-a}{\sqrt{4D't}} \right] \quad (4.35)$$

with  $a$  representing the encounter radius,  $r$  the separation of the radical pair,  $D'$  the mutual diffusion coefficient and  $\operatorname{erfc}$  being the complementary error function. Reaction times can be generated from this distribution by generating a uniformly distributed random number  $U(0, 1]$  between  $(0,1]$  and then transforming this to the correct distribution using the inversion method to give an expression for the geminate time ( $T_g$ ) as

$$T_g = \frac{(r-a)^2}{4D' \left[ \operatorname{erfc}^{-1} \left( \frac{rU(0,1]}{a} \right) \right]^2} \quad (4.36)$$

In the simulation if  $U(0, 1] > a/r$ , the particles have escaped and will never recombine. In this situation, the recombination time  $T_g = t_{\max}$ . Otherwise a separate  $T_g$  is generated from Eq. (4.36) for all possible encountering pairs.

### 4.4.2.2 Scavenging Reaction Times

To treat scavenging within the IRT simulation there are two possibilities: (i) treat the scavengers explicitly or (ii) assume the scavenging process is a pseudo-first order process. In the former case, it is necessary to generate reaction times from Eq. (4.36) conditioned on the separation between the radical and the scavenger; in the latter case, it is necessary to sample from the correct probability distribution for scavenging times using the inversion technique.<sup>3</sup> Clearly the latter method is computationally much more efficient, since in the former case a large array is required to store all possible reaction times which needs to be constantly traversed to extract the minimum event time.

---

<sup>3</sup> Although other methods of sampling from a probability distribution are available, the inversion method is the simplest.

The probability distribution of scavenging with a given rate is known to be  $\exp(-c \int_0^t k(t) dt)$ , with  $c$  being the concentration of scavengers and  $k(t)$  the time dependent scavenging rate constant. As it has been previously shown (Sect. 2.2.1.1), the analytical expression for the scavenging rate constant is  $k(t) = 4\pi D'a \left[ 1 + a/\sqrt{\pi D't} \right]$ , giving the probability distribution for scavenging to be

$$\Pr(T_s < t) = 1 - \exp(-kc(T_s + 2\alpha\sqrt{T_s})) \quad (4.37)$$

where  $\alpha = a/\pi D'$ , with  $a$  being the encounter distance and  $k$  being Smoluchowski's steady state rate constant ( $4\pi D'a$ ). Using the standard inversion technique, the scavenging times can be generated as

$$T_s = -\alpha + \sqrt{\alpha^2 - \frac{\ln U(0, 1]}{kc}} \quad (4.38)$$

#### 4.4.2.3 New Reflected Distance Algorithm

In the simulation not all encounters will result in reaction due to some constraint. The two most common reasons for the encountering pairs to not react are: (i) the reactions are partially diffusion controlled and the boundary is not reactive, or (ii) the radical pair is in the wrong spin state to react. In either case a careful treatment for the reflection is required to correctly model the subsequent kinetics, something which is not easily attainable in the IRT framework as the diffusive trajectories are not tracked. This section now presents a new analytical method of finding the distance of the radical pair following an unsuccessful encounter.

To generate a reflected distance it is necessary to know the probability distribution function for a pair started at contact subject to the boundary being reflective. Using the renewal theorem, the transition density of reflecting at  $a$  and separating to a distance  $r$  is

$$\tilde{p}_{\text{ref}}(a, r, s) = \tilde{p}(a, r, s) - \tilde{p}(a, a, s) \frac{\tilde{p}_x(a, r, s)}{\tilde{p}_x(a^+, a, s)} \quad (4.39)$$

where  $\tilde{p}(a, r, s)$  and  $\tilde{p}(a, a, s)$  are the transition densities for an unbounded diffusion process;  $\tilde{p}_x(a, y, s)$  and  $\tilde{p}_x(a^+, a, s)$  are the first derivatives of an unbounded transition density of the form  $\tilde{p}(x, y, s) = (y/x\sqrt{4D's}) (e^{-|y-x|\gamma} - e^{-(y+x)\gamma})$  with respect to  $x$ , with the process starting at  $x = a$ . Each term in Eq. (4.39) can now be explicitly stated as

$$\tilde{p}(a, r, s) = \frac{r}{a} \frac{1}{\sqrt{4D's}} \left( e^{-|r-a|\gamma} - e^{-(r+a)\gamma} \right) \quad (4.40)$$

$$\tilde{p}(a, a, s) = \frac{1}{\sqrt{4D's}} \left( 1 - e^{-(2a)\gamma} \right) \quad (4.41)$$

$$\tilde{p}_x(a, r, s) = -\frac{1}{2} \frac{ye^{-y\gamma} \sinh(a\gamma)}{D'sa^2} + \frac{1}{2} \frac{ye^{-y\gamma} \cosh(a\gamma)\gamma}{D'sa} \quad (4.42)$$

$$\tilde{p}_x(a^+, a, s) = -\frac{1}{2D'sa} e^{-a\gamma} \sinh(a\gamma)(1 + a\gamma) \quad (4.43)$$

where  $\gamma = \sqrt{s/D'}$ ,  $a$  the encounter radius,  $D'$  the mutual diffusion coefficient and  $s$  the Laplace variable. Substituting the above expressions into Eq. (4.39) gives the Laplace transform of  $\tilde{p}_{\text{ref}}(a, r, s)$  to be

$$\tilde{p}_{\text{ref}}(a, r, s) = \frac{r \exp\left[-(r-a)\sqrt{\frac{s}{D'}}\right]}{D'(1 + a\sqrt{\frac{s}{D'}})} \quad (4.44)$$

This equation can be inverted to give the probability distribution in the time domain to be

$$p(r, t) = \frac{r}{a} \left[ \frac{\exp\left[-\frac{(r-a)^2}{4D't}\right]}{\sqrt{\pi D't}} - \frac{1}{a} \exp\left[\frac{(r-a)}{a} + \frac{D't}{a^2}\right] \right. \\ \left. \times \operatorname{erfc}\left(\frac{r-a}{\sqrt{4D't}} + \frac{\sqrt{D't}}{a}\right) \right] \quad (4.45)$$

Converting to a dimensionless coordinate system by letting  $y = [(r-a)/a]$  and  $\tau = 4D't/a^2$ , Eq. (4.45) can be rewritten as

$$p(y, \tau) = (y+1) \left[ \frac{2 \exp\left[-\frac{y^2}{\tau}\right]}{\sqrt{\pi\tau}} - \exp\left[(y-1) + \frac{\tau}{4}\right] \operatorname{erfc}\left(\frac{y}{\sqrt{\tau}} + \frac{\sqrt{\tau}}{2}\right) \right] \quad (4.46)$$

The function  $p(y, \tau)$  is of the form  $g(y) - h(y)$ , and can be sampled using the rejection method. Hence, sample from  $g(y)$  and accept the value of  $y$  with probability  $(g(y) - h(y))/g(y)$ . The normalised form of  $g(y)$  can be shown to be

$$g(y) = \frac{\sqrt{\frac{\tau}{\pi}}}{1 + \sqrt{\frac{\tau}{\pi}}} \frac{2y \exp\left(-\frac{y^2}{\tau}\right)}{\tau} + \frac{1}{1 + \sqrt{\frac{\tau}{\pi}}} \frac{2 \exp\left(-\frac{y^2}{\tau}\right)}{\sqrt{\pi\tau}} \quad (4.47)$$

which is of the form  $pg_1(y) + (1-p)g_2(y)$ , whereby  $g_1$  and  $g_2$  are normalised themselves. Hence,  $g(y)$  is a mixture of  $g_1$ , the probability density function of a two dimensional Bessel process with standard deviation  $\sqrt{\tau/2}$  and,  $g_2$  the probability density function of the absolute value of a normal distribution with standard deviation  $\sqrt{\tau/2}$ . The reflected distance of a pair can now be readily calculated by following

**Table 4.1** Acceptance probability ( $P_A$ ) and number of cycles required to calculate a reflected distance using the rejection algorithm as a function of  $\delta t$

$\delta t$ (ps)	$P_A$	No. of cycles
10	0.56	1.76
100	0.296	3.37
1,000	0.116	8.57
10,000	0.04	25.04

the algorithm as shown in the Appendix (C.3 in Sect. C.3). Typical values for the acceptance probability are shown in Table 4.1 as a function of  $\delta t$ .

To prevent the overflow in the  $\text{erfc}(x)$  function (defined as  $e^{x^2} \int_x^\infty e^{-t^2} dt$ ) in Eq. (4.45) as  $t$  becomes large, it is possible to approximate the exponential error function to second order such that

$$\text{erfc}\left(\frac{r-a}{\sqrt{4D't}} + \frac{\sqrt{D't}}{a}\right) \approx \frac{a}{\sqrt{\pi D't}} \left(1 - \frac{r-a}{\sqrt{4D't}} \frac{a}{\sqrt{D't}} + \dots\right) \quad (4.48)$$

to give the density of the reflected distance as

$$p(r) = \frac{r(r-a) \exp[-(r-a)^2/4D't]}{\sqrt{4\pi(D't)^3}} \quad (4.49)$$

Hence, the pseudo-algorithm to sample from this density proceeds as follows (under the constraint that  $\sqrt{D't}/a \gg 1$ ): (i) generate three normally distributed random numbers  $N(\mu, \sigma)$  with  $\mu = 0$  and  $\sigma = 1/\sqrt{2}$ ; (ii) calculate the distance from the origin as  $X = \sqrt{N_1^2 + N_2^2 + N_3^2}$ ; (iii) the reflected distance is then calculable as  $r = X\sqrt{4D't} + a$ .

#### 4.4.2.4 Reactive Products

Accurate treatment of products which are capable of further reactions is another challenging problem in the IRT algorithm, since again the diffusive trajectories are not traced. The necessity to generate the correct spatial distribution of reactive products is of paramount importance, as this ultimately affects the subsequent kinetics that follow. In the literature, three approximations have been discussed by Clifford et al. [12] which aim to calculate either the new interparticle separation or a new reaction time directly. A brief discussion is now presented.

**Position approach** The first of these is known as the *position approach* which calculates the position of the reactive particles explicitly at the reaction time  $t$ . All non-reactive particles are assumed to diffuse freely, whilst the reactive particles are conditioned on having a separation distance equal to the encounter distance at  $t$ .

The recipe of the algorithm proceeds as follows: at time  $t$  the separation of the radical pair must be the encounter radius  $a$  such that

$$|\mathbf{R}_1 - \mathbf{R}_2| = a \quad (4.50)$$

where  $\mathbf{R}_i$  is the position vector of the  $i$ th particle. To generate the position, the authors consider two position vectors of the form

$$\mathbf{S}_1 = \mathbf{R}_1 - \mathbf{R}_2 \quad (4.51)$$

$$\mathbf{S}_2 = D_2\mathbf{R}_1 + D_1\mathbf{R}_2 \quad (4.52)$$

where  $D_i$  is the diffusion coefficient of particle  $i$ . The vector  $\mathbf{S}_2$  diffuses independently of vector  $\mathbf{S}_1$  [12]. The authors show that  $\mathbf{S}_2$  is given by

$$\mathbf{S}_2 = [D_2\mathbf{R}_1 + D_1\mathbf{R}_2] + N_3[0, (\sigma_1^2 + \sigma_1^4/\sigma_2^2)\mathbf{1}] \quad (4.53)$$

where  $\sigma_i^2 = 2D_i\delta t$  is the variance of the diffusion process and  $\mathbf{1}$  is a unit matrix. Hence the vector  $\mathbf{S}_2$  can be generated by sampling from a Gaussian distribution with the appropriate variance. The angular density function for distribution of the reactive product conditioned on the separation being  $a$  is

$$p(\theta, \phi; t|a, t) = p(a, \theta, \phi; t)/p(a, t) \quad (4.54)$$

The evolution of the initial interparticle vector  $\mathbf{r}^i$  to  $\mathbf{r}^f$  at time  $t$  is known to have the form

$$p(\mathbf{r}^f, t|\mathbf{r}^i) = (4\pi D't)^{-3/2} \exp[-(\mathbf{r}^f - \mathbf{r}^i)^2/4D't] \quad (4.55)$$

By choosing a suitable coordinate system in which  $\mathbf{r}^i$  is along the  $z$  axis, the marginal radial density function can be extracted as

$$p(a, t) = \int \int p(a, \theta, \phi) d\theta d\phi \quad (4.56)$$

which when multiplied by Eq. (4.55) gives the joint density for the random angles  $\varphi$  and  $\phi$  at time  $t$  to be

$$p(\theta, \phi; t|a, t) = [ar^i \sin \theta \exp(ar^i \cos \theta/2D't)]/[8\pi D't \sinh(ar^i/2D't)] \quad (4.57)$$

The angle  $\phi$  has a uniform density of  $1/2\pi$  and random values for  $\phi$  can be generated as  $\sigma = 2\pi U_1(0, 1]$ , where  $U_1(0, 1]$  is a uniformly distributed random number between 0 and 1. Integrating Eq. (4.57) with respect to  $\phi$  gives the density function for the random angle  $\varphi$  to be

$$p(\theta; t) = [ar^i \sin \theta \exp(ar^i \cos \theta a/2D't)]/[4D't \sinh(ar^i/2D't)] \quad (4.58)$$

Hence the probability distribution  $\Pr(\varphi < \theta)$  is then simply

$$\Pr(\varphi < \theta) = [ar^i/4D't \sinh(ar^i/2D't)] \int \sin \theta \exp(ar^i \cos \theta/2D't) d\theta \quad (4.59)$$

$$= [\exp(ar^i/2D't) - \exp(ar^i \cos \theta/2D't)] / [\exp(ar^i/2D't) - \exp(-ar^i/2D't)] \quad (4.60)$$

The random angle  $\varphi$  can now be generated from the above probability distribution function (using the inversion method) as

$$\varphi = \cos^{-1}[1 + (1/\alpha) \ln\{1 - U_2(0, 1)[1 - \exp(-2\alpha)]\}] \quad (4.61)$$

with  $\alpha = ar^i/2D't$  and  $U_2(0, 1)$  a uniform random number between 0 and 1. Now that the direction of  $\mathbf{S}_1$  can be calculated, the explicit positions can now be generated from the vectors  $\mathbf{S}_1$  and  $\mathbf{S}_2$  (under the assumption that the angular distribution to be unaffected by reaction) as

$$\mathbf{R}_1 = (D_1\mathbf{S}_1 + D_2\mathbf{S}_2)/(D_1 + D_2) \quad (4.62)$$

$$\mathbf{R}_2 = D_2(\mathbf{S}_2 - \mathbf{S}_1)/(D_1 + D_2) \quad (4.63)$$

**Time approach** The *time approach* depends entirely on the reaction times of the particles without consideration of the distance between them at the time of encounter. On reaction, the product inherits the time sequence of one of its parents which is chosen at random; with the reaction time of the product scaled correctly to account for the difference in the mutual diffusion coefficients. Relevant corrections are also made if the encounter distance is different between the reactive product and remaining species.

Consider particles  $i, j, k$  which can all react with each other at geminate times  $t_{ij}, t_{ik}$  and  $t_{jk}$ . If particles  $i$  and  $j$  react to produce  $l$  (which replaces  $i$ ), then the diffusive trajectory for  $lk$  will be the same as  $ik$  had reaction not occurred but it will be followed with the new relative diffusion coefficient. Hence, the new species  $l$  follows the same trajectory path as species  $i$  would have, with a new relative diffusion coefficient up to the encounter distance point  $a_{ik}$ . The new scaled reaction time for the geminate recombination time  $lk$  is then given by

$$t(a_{ik}) = t_{ij} + (t_{ik} - t_{ij}) \frac{D'_{ik}}{D'_{kl}} \quad (4.64)$$

Equation (4.64) is only applicable if the encounter distances  $a_{ij}$  and  $a_{kl}$  are the same. If  $a_{kl} < a_{ik}$  then species  $k$  would still need to diffuse through the shell  $a_{ik}$  before reaction can take place. In this case, Eq. (4.64) must be modified to the form

$$t_{kl} = t_{ij} + (t_{ik}^* - t_{ij}) \frac{D'_{ik}}{D'_{kl}} \quad (4.65)$$

where  $t_{ik}^*$  is the random reaction time for the pair  $ik$  if their encounter distance had been  $a_{ik}$ . In the situation when  $a_{kl} > a_{ik}$ ,  $t_{ik}^*$  might possibly be less than  $t_{ij}$ . The authors assume that whenever  $t_{ij} > t_{ik}^*$  instantaneous reaction takes place, which helps to simplify the model. Hence, reaction times are generated as follows:

$$t_{kl} = t_{ij} + (t_{ik}^* - t_{ij}) \frac{D'_{ik}}{D'_{kl}} \quad t_{ik}^* > t_{ij} \quad (4.66)$$

$$t_{kl} = t_{ij} \quad t_{ik}^* < t_{ij} \quad (4.67)$$

**Diffusion approach** The last approximation known as the *diffusion approach* is the simplest of all three. The interparticle separation evolves by diffusion independently of other such distances. Thus, if at time  $t$  the interparticle separation is  $\mathbf{r}$ , then at  $t'$  the new interparticle separation is  $\mathbf{r}' = \mathbf{r} + \mathbf{N}_3(0,1)$ , with  $\mathbf{N}_3(0,1)$  being a three dimensional normally distributed random number with mean zero and variance  $2D't$ , with  $D'$  being the mutual diffusion coefficient.

**First passage approach** In this section a new analytical treatment to deal with reactive products (known as the *first passage approach* from hereon) is presented, which calculates the distance of the newly formed product to the remaining reactants by conditioning on the independent reaction time that exists for that pair. This method is developed for a single radical pair where the chemical nature of one radical changes randomly such as a scavenging event. A thorough derivation is now presented.

Let the probability density function  $p^\dagger(r_0, r_1, t_1)$  be a diffusion process started at  $r_0$  and separating to a distance  $r_1$  at time  $t_1$ , conditioned that the encounter radius  $a$  is hit for the first time at  $t$ . From Bayes' theorem of probability theory together with the time homogeneity of diffusion paths, the expression for  $p^\dagger(r_0, r_1, t)$  can be expressed as

$$p^\dagger = \frac{p(r_0 \rightarrow r_1, t_1 \cap \text{without hitting } a) \times w(r_1 \rightarrow a(t - t_1))}{w(r_0 \rightarrow a \text{ at } t)} \quad (4.68)$$

with the first and second terms in the numerator representing the probability density of diffusing from  $r_0$  to  $r_1$  at time  $t_1$  without hitting  $a$ , and subsequently hitting  $a$  for the first time at  $t$  respectively. The term in the denominator represents the first passage time density of going from  $r_0$  to  $a$  at time  $t$ . The expressions for  $w(r_1 \rightarrow a \text{ at } (t - t_1))$  and  $w(r_0 \rightarrow a \text{ at } t)$  are simply the derivative of the probability distribution function

$$W(t) = \frac{a}{r_0} \operatorname{erfc} \left( \frac{r_0 - a}{\sqrt{4D't}} \right) \quad (4.69)$$

with respect to  $(t - t_1)$  and  $t$  respectively, giving

$$w(r_1 \rightarrow a \text{ at } (t - t_1)) = \frac{a(r_1 - a)}{r_1 \sqrt{4D'\pi(t - t_1)^3}} \exp\left(-\frac{(r_1 - a)^2}{4D'(t - t_1)}\right) \quad (4.70)$$

$$w(r_0 \rightarrow a \text{ at } t) = \frac{a(r_0 - a)}{r_0 \sqrt{4D'\pi t^3}} \exp\left(-\frac{(r_0 - a)^2}{4D't}\right) \quad (4.71)$$

Taking the ratios of the first passage time densities, and letting  $p^*(r_0, r_1, t_1) = p(r_0 \rightarrow r_1, t_1 \cap \text{ without hitting } a)$  Eq. (4.68) simplifies to

$$p^\dagger = p^*(r_0, r_1, t_1) \times \frac{r_0(r_1 - a)}{r_1(r_0 - a)} \left[ \exp\left(-\frac{(r_1 - a)^2}{4D'(t - t_1)}\right) \exp\left(-\frac{(r_0 - a)^2}{4D'(t)}\right) \right] \quad (4.72)$$

The expression for  $p^*(r_0, r_1, t_1)$  can be found by making use of the renewal theorem of a diffusion process as follows

$$p^*(r_0, r_1, t_1) = p(r_0, r_1, t_1) - \int_0^{t_1} w(r_0, a, t') p(a, r_1, t_1 - t') dt' \quad (4.73)$$

The first term on the right hand side represents the probability density for a diffusion process started at  $r_0$  and finishing at  $r_1$ , which contains all trajectories that go through the boundary  $a$  during the time interval  $t_1$ . The solution for  $p(r_0, r_1, t_1)$  is well known<sup>4</sup> to be exactly

$$p(r_0, r_1, t_1) = \frac{r_1}{r_0} \frac{1}{\sqrt{4\pi D't_1}} \left[ \exp\left(-\frac{(r_1 - r_0)^2}{4D't_1}\right) - \exp\left(-\frac{(r_1 + r_0)^2}{4D't_1}\right) \right] \quad (4.74)$$

Similarly, the solution for  $p(a, r_1, t_1 - t')$  is found to be

$$p(a, r_1, t_1 - t') = \frac{r_1}{a} \frac{1}{\sqrt{4\pi D'(t_1 - t')}} \left[ \exp\left(-\frac{(r_1 - a)^2}{4D'(t_1 - t')}\right) - \exp\left(-\frac{(r_1 + a)^2}{4D'(t_1 - t')}\right) \right] \quad (4.75)$$

Using the Laplace convolution theorem to evaluate the integral in Eq. (4.73), the solution for  $p^*$  is the transition density for a three dimensional Bessel process (subject to an inner absorptive boundary) and is also well known to be<sup>5</sup>

<sup>4</sup> Solution for the transition density for an unrestricted process is derived in the Appendix (Sect. A.9).

<sup>5</sup> Solution for the transition density for an absorbing inner boundary is derived in the Appendix (Sect. A.10).

$$p^*(r_0, r_1, t) = \frac{r_1}{r_0} \frac{1}{\sqrt{4\pi D't_1}} \left( \exp\left(\frac{-(r_1 - r_0)^2}{4D't_1}\right) - \exp\left(\frac{-(r_1 + r_0 - 2a)^2}{4D't_1}\right) \right) \quad (4.76)$$

Substituting the solution for  $p^*$  into Eq. (4.72) gives the solution for  $p^\dagger$

$$p^\dagger = \frac{r_1}{r_0} \frac{1}{\sqrt{4\pi D't_1}} \left[ \exp\left(-\frac{(r_1 - r_0)^2}{4D't_1}\right) - \exp\left(-\frac{(r_1 - r_0 - 2a)^2}{4D't_1}\right) \right] \\ \times \frac{r_0 (r_1 - a)}{r_1 (r_0 - a)} \exp\left(-\frac{(r_1 - a)^2}{4D'(t - t_1)}\right) \exp\left(\frac{(r_0 - a)^2}{4D't}\right) \frac{\sqrt{t^3}}{\sqrt{(t - t_1)^3}}$$

Defining  $r_1^* = (r_1 - a)$ ,  $r_0^* = (r_0 - a)$ ,  $q = r_0^*(t - t_1)/t$  and  $\tau = (t - t_1)t_1/t$ , the expression for  $p^\dagger$  can be simplified to

$$p^\dagger = \frac{1}{\sqrt{4\pi D'\tau}} \frac{r_1^*}{q} \left[ \exp\left(-\frac{(r_1^* - q)^2}{4D'\tau}\right) - \exp\left(-\frac{(r_1^* + q)^2}{4D'\tau}\right) \right] \quad (4.77)$$

which is the probability density function for a three dimensional Bessel process started at  $q$  and run for a time  $\tau$ . Hence the new distance ( $r'_{ik}$ ) from the newly formed reactive product  $i$  (formed via the reaction of  $l$  and  $m$  with an encounter distance  $a_{lm}$ ) to the remaining reactant  $k$  involves sampling from the probability distribution (Eq. 4.77) by generating three Gaussian distributed random numbers; two with mean ( $\mu$ ) zero and standard deviation  $\sigma = \sqrt{2D'\tau} (N_{1/2}(0, \sigma))$  and one with  $\mu = q$  and  $\sigma = \sqrt{2D'\tau} (N_3(q, \sigma))$ . The new distance for the pair  $ik$  is then  $r'_{ik} = a_{lm} + \sqrt{N_1^2 + N_2^2 + N_3^2}$ . This new value for  $r'_{ik}$  is subsequently used to generate a new reaction time for the pair  $ik$  using Eq. (4.36).<sup>6</sup>

### 4.4.3 Partially Diffusion Controlled Reactions: Neutral Species

#### 4.4.3.1 Recombination Times

The IRT algorithm has been extended to model partially diffusion controlled reactions by Green and Pimblott [16] and a brief resume is presented in this section. Using the radiation boundary condition such that

$$\left(\frac{\partial\Omega}{\partial r}\right)_{r=a} = \frac{v}{D'}\Omega(t) \quad (4.78)$$

<sup>6</sup> In this situation the initial distance ( $r_0$ ) for the pair  $ik$  should be replaced by  $r'_{ik}$ .

where  $\Omega$  is the survival probability,  $v$  is a parameter to measure the reactivity of the surface with units of velocity and  $D'$  is the mutual diffusion coefficient. Using this boundary condition to solve the backward diffusion equation gives the well known solution [17] for the reaction probability ( $W(r, t)$ ), for a pair separated initially by a distance  $r$  to be

$$W(r, t) = \frac{va^2}{r(va + D')} \left[ \operatorname{erfc} \left( \frac{r - a}{\sqrt{4D't}} \right) - \exp \left( \frac{(va + D')^2 t}{a^2 D'} + \frac{(va + D')(r - a)}{aD'} \right) \right. \\ \left. \times \operatorname{erfc} \left( \frac{r - a}{\sqrt{4D't}} + \frac{va + D'}{aD'} (D't)^{1/2} \right) \right] \quad (4.79)$$

In order to apply the IRT method, Eq. (4.79) needs to be inverted for  $t$ , in order to extract a reaction time, which is not straightforward. The authors have devised two methods to make sampling from this distribution function possible. The first method involves fitting this probability distribution to an incomplete  $\gamma$ -function for a range of  $r$ . A random uniform number is then generated from the appropriate  $\gamma$ -distribution [16]. The second method generates a random number  $U(0,1)$  uniform in the interval (0,1] and solves the equation

$$U(0,1) = W(r, T_g) \quad (4.80)$$

for  $T_g$  (geminate reaction time) numerically, using for example Newton's method. The authors have carried out calculations using both methods, and essentially identical kinetics are obtained.

#### 4.4.3.2 Reactive Products

Unfortunately, the first passage algorithm cannot be used for partially diffusion controlled reactions because of the complex nature of the transition density, making it difficult to use the inversion method to sample from the cumulative distribution function. It is however shown in Chap. 6 (Sect. 6.3.4), that a new model called the *centre of diffusion vector approach* can accurately model the spatial distribution of reactive products originating from partially diffusion controlled reactions. Like the first passage approach, the implementation is relatively straightforward and does not compromise on the computational resources.

### 4.4.4 Ionic Species

#### 4.4.4.1 Recombination Times

The foundations of the IRT relies on generating a reaction time from the correct marginal distribution. For the uncharged case, the exact time dependent recombination probability is known and reaction times can be directly simulated. However,

when the species are charged the time-dependent diffusion equation cannot be solved analytically in closed form [18]. For the purpose of this work the backward diffusion equation with drift is numerically solved for an initial separation distance  $r_0$  with reaction times generated by interpolating from a look-up table [2]. This approach is considered to be both faster and more stable than having to numerically invert the solution as obtained by Hong and Noolandi [18] on every realisation.

**Solution to the conditioned backward diffusion equation** Starting with the time dependent geminate recombination probability for ions and converting to a dimensionless coordinate system such that

$$x = 2r_0/r_c \quad \tau = 4D't/r_c^2 \quad (4.81)$$

the dimensionless backward diffusion equation takes the form

$$\frac{\partial W}{\partial \tau} = \frac{\partial^2 W}{\partial x^2} + \frac{2(x+1)}{x^2} \frac{\partial W}{\partial x} \quad (4.82)$$

In order to obtain a proper probability distribution, it is necessary to project out the asymptotic reaction probability  $W_\infty(r_0)$  which takes the form

$$W_\infty(r_0) = \frac{1 - \exp(r_c/r_0)}{1 - \exp(r_c/a)} \quad (4.83)$$

from  $W(r_0, t)$  via the relation  $W(r_0, t) = W_\infty(r_0)W^*(r_0, t)$ , to give the required reaction probability distribution for  $W^*(r_0, t)$  conditioned on ultimate reaction as

$$\frac{\partial W^*}{\partial \tau} = \frac{\partial^2 W^*}{\partial x^2} + \frac{2}{x^2}(x - \coth(1/x)) \frac{\partial W^*}{\partial x} \quad (4.84)$$

Equation (4.84), can now be solved using the Crank-Nicolson [19, 20] method<sup>7</sup> by transforming to a logarithm time and space coordinate system, with  $\ln x = U_x$  and  $\ln \tau = V_\tau$  to make the solution tractable. Rewriting Eq. (4.84) in the logarithmic scale then gives

$$\frac{\partial W^*}{\partial V_\tau} = \exp(-2U_x + V_\tau) \left[ \frac{\partial^2 W^*}{\partial U_x^2} + (1 - 2 \exp(-U_x) \coth(\exp(-U_x))) \frac{\partial W^*}{\partial U_x} \right] \quad (4.85)$$

Letting  $\gamma = \exp(-2U_x + V_\tau)$  and  $\beta = \exp(-2U_x + V_\tau)[(1 - 2 \exp(-U_x) \coth(\exp(-U_x)))]$ , Eq. (4.85) can be simplified to

---

<sup>7</sup> Crank-Nicolson method has been chosen for this work because it is unconditionally stable.

$$\frac{\partial W^*}{\partial V_\tau} = \gamma \frac{\partial^2 W^*}{\partial U_x^2} + \beta \frac{\partial W^*}{\partial U_x} \quad (4.86)$$

Discretising the time and space domain, the following is obtained

$$\begin{aligned} \frac{W_i^{t+1} - W_i^t}{\Delta V_\tau} &= \frac{\gamma}{2(\Delta U_x)^2} \left[ (W_{i+1}^{t+1} - 2W_i^{t+1} + W_{i-1}^{t+1}) + (W_{i+1}^t - 2W_i^t + W_{i-1}^t) \right] \\ &+ \frac{\beta}{4\Delta U_x} \left[ (W_{i+1}^{t+1} - W_{i-1}^{t+1}) + (W_{i+1}^t - W_{i-1}^t) \right] \end{aligned} \quad (4.87)$$

Equation (4.87) can be rearranged to

$$\begin{aligned} W_{i+1}^{t+1} \left[ -\frac{\gamma \Delta V_\tau}{2(\Delta U_x)^2} - \frac{\beta \Delta V_\tau}{4\Delta U_x} \right] + W_i^{t+1} \left[ 1 + \frac{\gamma \Delta V_\tau}{2(\Delta U_x)^2} \right] + W_{i-1}^{t+1} \left[ -\frac{\gamma \Delta V_\tau}{2(\Delta U_x)^2} + \frac{\beta \Delta V_\tau}{4\Delta U_x} \right] \\ = W_{i+1}^t \left[ \frac{\gamma \Delta V_\tau}{2(\Delta U_x)^2} + \frac{\beta \Delta V_\tau}{4\Delta U_x} \right] + W_i^t \left[ 1 - \frac{\gamma \Delta V_\tau}{2(\Delta U_x)^2} \right] + W_{i-1}^t \left[ \frac{\gamma \Delta V_\tau}{2(\Delta U_x)^2} - \frac{\beta \Delta V_\tau}{4\Delta U_x} \right] \end{aligned} \quad (4.88)$$

with the unknown coefficients ( $W^{t+1}$ ) on the left hand side and the known coefficients ( $W^t$ ) on the right. Equation (4.88) may now be written in a more compact notation as

$$\sum_k T_{ik} W_k = R_i \quad (4.89)$$

where  $T_{ik}$  represents the coefficients of  $W_i^{t+1}$  [left hand side of Eq. (4.88)] and  $R_i$  represents the right hand side of Eq. (4.88). This method is stable for all step sizes and requires solution of a tridiagonal system of simultaneous equations. This may be achieved efficiently by inversion of the tridiagonal matrix by upper and lower triangular decomposition and subsequent forward and backward substitution. The boundary conditions required to solve Eq. (4.88) are as follows

$$W(U_x, -\infty) = 0 \quad (4.90)$$

$$W(U_{x0}, V_\tau) = 1 \quad (4.91)$$

$$W(U_{x\max}, V_\tau) = 0 \quad (4.92)$$

where  $U_{x0}$  is the limit  $V \rightarrow -\infty$  and  $U_{x\max}$  is sufficiently large in order to allow for sufficient convergence. With the above boundary conditions, the reaction probability at the inner (with  $i = 1$  and  $i - 1 = 0$ ) and outer boundary (with  $i = n$  and  $i + 1 = n + 1$ ) can be written using Eq. (4.89) as

$$T_{12}W_{12} + T_{11}W_{11} = R_1 - T_{10}W_{10} \quad (4.93)$$

$$T_{nn}W_{nn} + T_{nn-1}W_{nn-1} = R_n - T_{nn+1}W_{nn+1} \quad (4.94)$$

The solution to Eq. (4.85) was found over a large range of  $x$  and  $X$  (dimensionless encounter distance) to allow a large variety of chemical systems to be modelled. The area spanned by  $x - X$  was  $-5 \leq \ln X \leq 4.5$  and  $-4.5 \leq \ln x \leq 5$ , with intervals between successive solution of  $\delta(\ln x)$  and  $\delta(\ln X) = 0.05$ . A much smaller interval of 0.005 was used for  $\delta\tau$ . Each solution was integrated until  $W^* = 0.99$ , so that for each value of  $x$  and  $X$ , a dimensionless time at which  $W^*$  attains a certain value can be extracted. Although this method has previously been reported [2], the grid was not sufficiently fine to use for this work.

**Interpolation of the three-dimensional grid** On having obtained a three dimensional grid, generating a reaction time is straightforward and proceeds as follows: firstly, the parameters  $x$ ,  $X$  are calculated based on the simulation parameters and the three closest lattice points bracketing the point are calculated in the logarithmic  $x$ ,  $X$  space. Next a random number is generated uniformly on  $(0,1]$  representing the value of  $W$  to be inverted for the reaction time. If this number is greater than the asymptotic value  $W_\infty$  for the pair then the particles escape, otherwise the random number is divided by  $W_\infty$  to provide a value for  $W^*$ . Next the percentiles bracketing  $W^*$  are found and by performing a linear interpolation in the  $(\ln x) - (\ln X)$  plane, giving the dimensionless reaction time for the appropriate values of  $x$ ,  $X$  and the two bracketing percentiles. In the  $W^*$  dimension,  $\tau$  varies approximately as  $W^{*1/2}$ , however when  $W^*$  is close to 0 or 1, other optimum powers for  $W^*$  are instead used in the interpolation process, to allow  $\tau$  be interpolated as precisely as possible. As the  $x - X$  array is logarithmic, the interpolation for reaction time  $\tau$  of the form

$$\tau = a \ln x + b \ln X + c \quad (4.95)$$

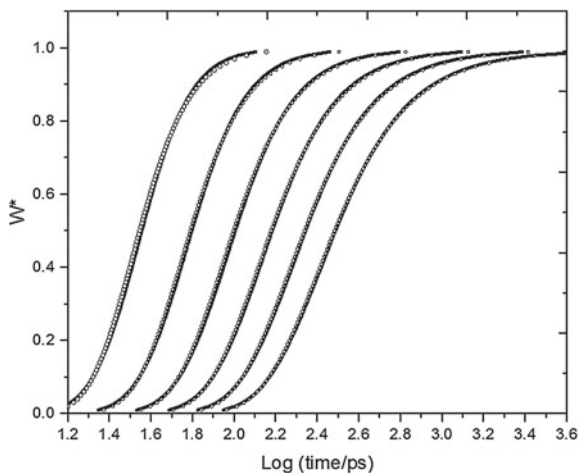
is acceptable. In the simulation the three reaction times bracketing the point of interest form a triangle, which in matrix notation can be written as

$$\begin{bmatrix} \tau_1 \\ \tau_2 \\ \tau_3 \end{bmatrix} = \begin{bmatrix} \ln x_1 & \ln X_1 & 1 \\ \ln x_2 & \ln X_2 & 1 \\ \ln x_3 & \ln X_3 & 1 \end{bmatrix} \times \begin{bmatrix} a \\ b \\ c \end{bmatrix} \quad (4.96)$$

Hence the unknown coefficients can be determined as  $\mathbf{v} = \mathbf{M}^{-1}\mathbf{T}$ , where  $\mathbf{T}$  is the vector of reaction times and  $\mathbf{v}$  the vector of coefficients. As the change in  $x$  and  $X$  is fixed (given by the parameter  $h$ ), the solution for  $\mathbf{M}^{-1}$  if the point lies in the lower triangular area simplifies to

$$\mathbf{M}^{-1} = \begin{bmatrix} h & 0 & -h \\ 0 & -h & h \\ -h(x_1 + h) & hy_1 & h(x_1 - y_1) \end{bmatrix} \quad (4.97)$$

**Fig. 4.1** Reaction probability for a single ion-pair obtained using a grid in which every  $\delta x$  and  $\delta X$  of 0.1 was printed (dashed lines) and compared with a grid in which every 0.05 elements were printed (circle). Starting  $r_0 = 20 \text{ \AA}$  (+4  $\text{\AA}$  from left to right),  $r_c = 290 \text{ \AA}$ ,  $D' = 0.28 \text{ \AA}^2 \text{ ps}^{-1}$  and  $a = 5 \text{ \AA}$



Similarly, if the point lies in the upper triangular area,  $M^{-1}$  simplifies to

$$M^{-1} = \begin{bmatrix} 0 & h & h \\ -h & 0 & h \\ h(x_1 + h) & -hy_1 & h(x_1 + y_1) \end{bmatrix} \quad (4.98)$$

where  $x_1 = \ln x_1$  and  $y_1 = \ln X_1$ . As the size of the grid grows considerably with decreasing values of  $\delta x$  and  $\delta X$ , producing a grid which is converged with respect to the reaction times and at the same time computationally manageable poses additional problems. To thoroughly test for convergence, a set of grids were developed in which  $\delta x$  and  $\delta X$  were varied and the reaction times directly interpolated for the geminate recombination of  $R^-$  and  $P^+$  (Fig. 4.1). It is seen that the reaction times are sufficiently converged when  $\delta x$  and  $\delta X = 0.05$  (writing only every 0.1 value) in comparison with a much finer grid mesh (in which every 0.05 value for  $\delta x$  and  $\delta X$  was written).

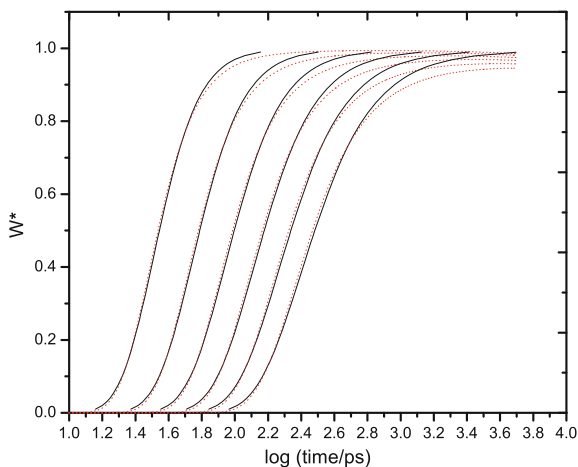
Figure 4.2 shows the comparison of the ultimate recombination probability obtained using the interpolation technique and that obtained using the normal approximation for  $W_0^*(x, \tau)$  developed by Green et al. [21] for low permittivity solvents. For a Brownian motion with a given mean ( $\mu$ ) and standard deviation ( $\sigma$ ), the reaction probability can be approximated as [22]

$$W_0^*(x, \tau) \approx \frac{1}{2} \operatorname{erfc} \left( (x - \mu) / \sqrt{2\sigma} \right) \quad (4.99)$$

with the mean and variance found to be  $\mu = (6\tau)^{1/3} - [(6\tau)^{2/3}]/7$ ,  $\sigma^2 = 6\tau/7$  respectively. The deconvoluted expression for the conditioned reaction probability for any arbitrary inner boundary is given in Eq. (2.95) [21], which can be obtained from  $W_0^*$  through the Laplace relation

$$\tilde{W}_a^*(x, s) = \tilde{W}_0^*(x, s) / s \tilde{W}_0^*(a, s) \quad (4.100)$$

**Fig. 4.2** Reaction probability for a single ion-pair obtained using the interpolation from a grid (*dashed lines*) in which every  $\delta x$  and  $\delta X$  of 0.1 was used and compared with the approximation developed by Green et al. [21] (Eq. 2.95) for low permittivity solvents (*red dots*). Starting  $r_0 = 20 \text{ \AA}$  (+4  $\text{\AA}$  from *left* to *right*),  $r_c = 290 \text{ \AA}$ ,  $D' = 0.28 \text{ \AA}^2 \text{ ps}^{-1}$  and  $a = 5 \text{ \AA}$



where  $s$  is the Laplace variable. As explained in Sect. 2.4.1.2, this approximation breaks down for larger  $\tau$  values because the standard deviation  $s$  increases much more rapidly than the mean  $m$  for large  $\tau$ . The normal approximation used by the authors to model the transition density of the reverse process (i.e. for a diffusion process started at the inner boundary which is reflective), introduces an unphysical effect by placing part of the density on the wrong side of the reflecting boundary at the origin. Although the asymptotic yield is not correctly predicted, the approximation nonetheless, gives excellent agreement for  $W_0^*(x, \tau) < 0.8$  and provides a reliable way to check (i) that the grid is sufficiently converged and (ii) the accuracy of the interpolation technique.

#### 4.4.4.2 New Approximate Solution for Geminate Ion Recombination in Low Permittivity Solvents

In Fig. 4.3a it is seen that the approximation developed by Green et al. [21] fails to describe the reaction probability for large distances (and at longer times) due to the standard deviation ( $\sigma$ ) increasing faster than the mean ( $\mu$ ), which causes a significant part of the transition density to be placed on the wrong side of the reflecting boundary. During the course of this work, it was found that this error can be partially corrected by damping  $\sigma$ , preventing the transition density from being in artificial regions. The corrected expression for the variance was found to be  $\sigma^2 = (6\tau/7) \exp(-x\sqrt{\tau})$ , with  $x = \left(\frac{1}{\sqrt{7}}\right) r_c/r_0$  and  $\tau = 4D't/r_c^2$ . As seen from Fig. 4.3b, excellent agreement can be obtained using this new analytical formulation for initial separation distances of  $r_0 \leq 80 \text{ \AA}$ . The theory will still fail for larger distances because the initial moments were calculated assuming  $r_0/r_c < 0.35$  [21]. Hence, although at an initial separation of  $100 \text{ \AA}$  the recombination yield up to  $\sim 5 \text{ ns}$  is well approximated, the theory fails to adequately describe the yield for times greater than this.

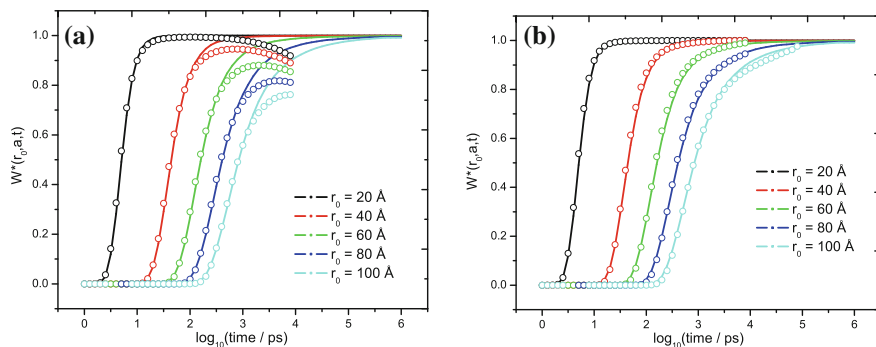


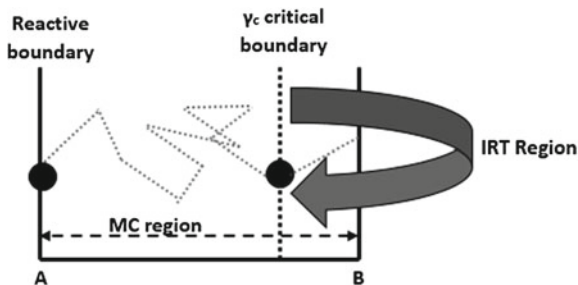
**Fig. 4.3** Recombination yield for a single ion pair using an encounter radius of  $5 \text{ \AA}$ ,  $D' = 2 \text{ \AA}^2 \text{ ps}^{-1}$  and  $r_c = 290 \text{ \AA}$ . **a**  $\sigma^2 = (6\tau/7)$  and **b**  $\sigma^2 = (6\tau/7) \exp(-x\sqrt{\tau})$ , with  $x = \left(\frac{1}{\sqrt{7}}\right) r_c/r_0$ . (Line) and (open circle) correspond to random flights simulation and analytical expression respectively

**Ionic reaction time** In order to generate a random time from the distribution given in Eq. (2.95) a numerical method such as rejection sampling must be employed. However, the choice of the envelope distribution function must be known at the start of the simulation for a given set of parameters. In addition, the envelope function must be sufficiently efficient such that most points will fall within the ‘acceptance’ subspace. Through a series of IRT simulations, it was found that using the rejection sampling algorithm was not a feasible method to utilise. Instead, a much better approach is to construct a look-up table for  $W^*(x, a, \tau)$  at the start of the simulation and interpolate for the required random variable. Whilst this method is similar to the numerical technique used in Sect. 4.4.4.1, there are two important differences: (i) the analytical method does not discretise the backward diffusion equation; (ii) the analytical method is computationally much simpler to implement in the IRT framework instead of solving the numerical grid using the Crank-Nicolson method. Unfortunately, whilst this analytical formulation is correct for initial separation distances up to  $80 \text{ \AA}$ , it still must be used in conjunction with the numerical grid to describe the recombination kinetics outside this parameter space.

## 4.5 Hybrid Simulation Package

Whilst the simulation of spur kinetics can be entirely modelled using the IRT algorithm, it nonetheless lacks the ability to model spatially dependent interactions such as the spin exchange interaction. In the modelling of spur kinetics, spin dynamics is often neglected due to the complexity introduced, and this is found to be acceptable in cases where spin-relaxation is very fast (such as chemical systems involving the hydroxyl radical). However, where the spin-relaxation time is comparable to other

**Fig. 4.4** Hybrid algorithm showing the switching between the IRT and random flights algorithm for a Bessel process. In the IRT region first passage times are generated, whereas in the random flights region a full history of the trajectory is traced



coherent magnetic interactions, spin-dynamics can play an important part in the spurkinetics, and a proper treatment of spin-dynamics must be taken into consideration.

In an attempt to incorporate a realistic description of spin dynamics (in particular the exchange interaction) into the simulation packages, and allow the simulation of spin polarisation, a new Hybrid algorithm was written which utilises both the strengths of the random flights and IRT algorithms. When spatial dependent interactions can be neglected, simulation proceeds via the IRT; when spatial dependent interactions are necessary to be taken into account the simulation would proceed via the random flights part (as shown in Fig. 4.4). In this scenario, all events which can possibly occur outside the spatially dependent interaction boundary are ‘fast tracked’ allowing a significant saving in computational resources.

The general recipe for the Hybrid algorithm proceeds as follows: if the separation of the neutral radical pair lies outside the boundary of interest (identified as B in Fig. 4.4), then generate a first passage time ( $\tau$ ) back to the second outer boundary ( $\gamma_c$ ) by sampling from the probability distribution function

$$\Omega(\tau) = 1 - \frac{\gamma_c}{r} \operatorname{erfc} \left[ \frac{r - \gamma_c}{\sqrt{4D'\tau}} \right] \quad (4.101)$$

where  $r$  is the separation distance of the radical pair. If  $\tau$  is the minimum of all possible event times, then the separation of the neutral pair is changed to lie at the outer boundary  $\gamma_c$ . At this point, the random flights algorithm would control the simulation and evolve the trajectories in the normal manner by solving the stochastic differential equation. If the radical pair once again diffuses outside the outer boundary, then another first passage time is generated by sampling from Eq. (4.101). This process is repeated for all particles until (i) all possible reactions are complete or (ii) a predefined  $t_{\max}$  (maximum simulation time) is reached. The positions of all other radical pairs are evolved in a similar manner using either the random flights algorithm, in which the remaining radical pairs diffuse up to the minimum IRT event time (assuming the distance lies inside  $\gamma_c$ ). It becomes evident that for larger systems, there will be some particles lying within the boundary whilst others outside. In this case, a careful management of event times is required as this ultimately dictates the observables of the chemical system.

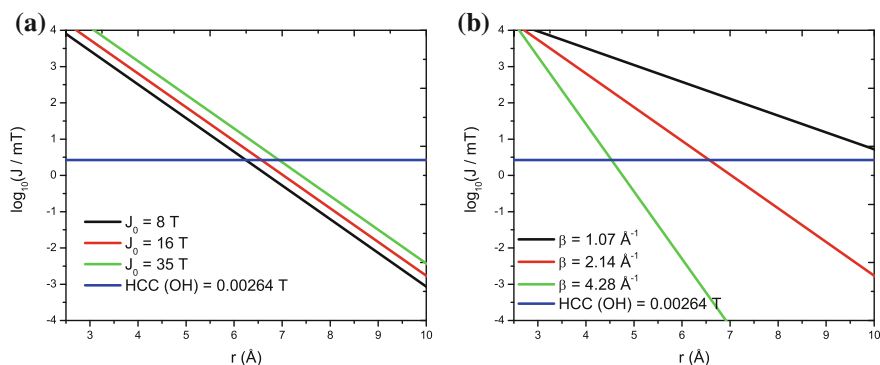


**Fig. 4.5** **a** Exchange interaction  $J(r)$  calculated using an exchange range ( $\beta$ ) of  $2.14 \text{ \AA}^{-1}$ . **b** Exchange interaction  $J(r)$  calculated using an exchange strength ( $J_0$ ) of 16 T. An encounter distance of  $2.52 \text{ \AA}$  was used. Abbreviation HCC represents the hyperfine coupling constant on the hydroxyl radical

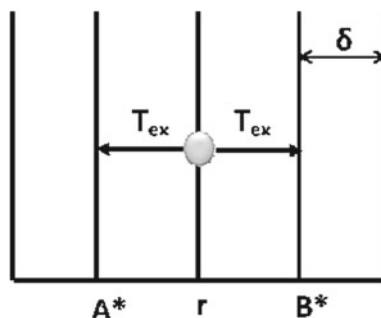
### 4.5.1 Choice of the Critical Boundary

In the Hybrid algorithm it is important to choose the position of the critical boundary carefully, such that the exchange interaction is much smaller than other magnetic interactions such as the hyperfine interaction. Using the hyperfine coupling constants of  $2.64 \text{ mT}$  for the  $\cdot\text{OH} + \cdot\text{OH}$  reaction, it can be seen from Fig. 4.5 that at a radical pair distance of  $\sim 10 \text{ \AA}$ , the exchange interaction becomes inappreciable in comparison to the hyperfine interaction in the parameter space investigated. Figure 4.5 also shows that using an exchange strength ( $J_0$ ) of 16 T and an exchange range of  $1.07 \text{ \AA}^{-1}$ , the exchange interaction becomes comparable to the hyperfine coupling constant at  $10 \text{ \AA}$ . Hence at this parameter space a larger outer exchange boundary is required ( $\sim 20 \text{ \AA}$ ). Therefore, in the parameter space investigated for the  $\cdot\text{OH} + \cdot\text{OH}$  reaction, the position of the critical boundary  $\gamma_c$  should not be more than  $2 \text{ \AA}$  from the outer exchange boundary (B) if an exchange range of  $2.14 \text{ \AA}^{-1}$  is used.

## 4.6 Slice Simulation Package

The Hybrid simulation package was written to make the simulation of spatially dependent interactions possible, in the belief that it was not possible to do this within the IRT framework. However, it was realised that inside the spatial dependent boundary, the separation between the particles can be generalised as a one dimensional random walk between slices, where the separation distance is known at all times. This is the origin of the *Slice* program. *Slice* has the added advantage of not having to switch between two different algorithms, making its implementation quite straightforward and computer efficient.

**Fig. 4.6** Separation of the radical pair within the exchange region.  $T_{\text{ex}}$  signifies the first passage exit times to  $A^*$  (with probability  $P_{\text{up}}$ ) and  $B^*$  (with probability  $P_{\text{down}}$ )



The Slice program divides the spatial region of interest into  $x$  segments, which is a variable parameter set at the start of the simulation. Letting the inner boundary of this segment be  $A^*$  and the outer boundary be  $B^*$  (i.e. distance at which spatial dependent interactions can be neglected). If the radical pair distance lies within the  $A^*B^*$  region, exit times are generated to allow movement between the slices, otherwise an exit time to hit the boundary  $B^*$  is calculated. Figures 4.6, 4.7 and 4.8 show the three possible situations which can occur within the simulation: (1) radical pair within the  $A^*B^*$  region with the option to diffuse to either slice (Fig. 4.6); (2) unsuccessful encounter with the radical pair being reflected to the  $B^*$  slice (Fig. 4.7); (3) radical pair diffusing back to the  $A^*B^*$  region (Fig. 4.8).<sup>8</sup>

In situation (1), it is assumed that the separation of the radical pair is always on one of the slices. However, in a realistic chemical environment the radical pair separation could reside anywhere between these slices. In this situation, a first passage time is required for the separation of the radical pair to hit either of the slices together with its respective probability of either moving closer together or further apart. This scenario is diagrammatically shown in Fig. 4.9.

#### **Situation 1**

See Fig. 4.6.

#### **Situation 2**

See Fig. 4.7.

#### **Situation 3**

See Fig. 4.8.

#### **Situation 4**

See Fig. 4.9.

<sup>8</sup> Figure C.4 (Sect. C.4) in the Appendix shows the general flow diagram for the Slice algorithm.

**Fig. 4.7** Separation of the radical pair at the encounter distance. On an unsuccessful encounter the probability of moving to the previous slice is one with an exit time  $T_{ex}$

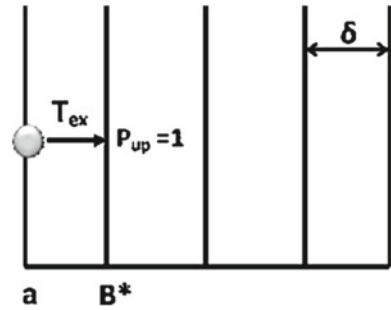


**Fig. 4.8** Separation of the radical pair outside the exchange region. A first passage time is generated to calculate when the separation of the radical pair will approach  $(B^* - \delta)$

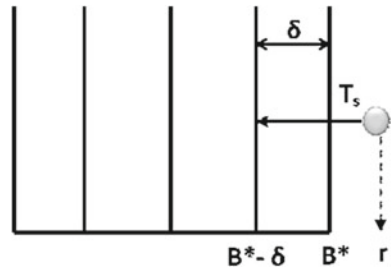
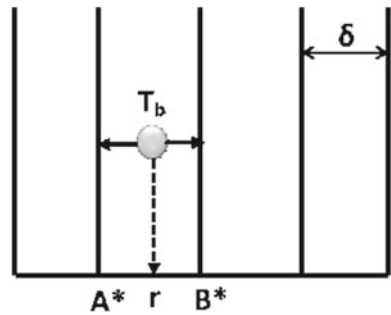


**Fig. 4.9** Separation of the radical pair not on one of the slices. Probability of reaching either slice ( $P_1$  and  $P_2$ ) is calculated conditioned on the current separation. A first passage time  $T_b$  is calculated to either slice



### 4.6.1 Situation 1: Mean Exit Time Between Slices for Neutral Species

To generate the required exit times on diffusing from one slice to the next (Fig. 4.6), the backward diffusion equation must be solved for the survival probability  $\Omega(r, t)$  subject to an absorbing inner and outer boundary. The complete derivation is presented in the Sect. A.2 of the Appendix, with the final expression for  $\tilde{\Omega}(r, s)$  found to be

$$\tilde{\Omega}(r, s) = -\frac{A^* \sinh(B^* - r)\gamma}{sr \sinh(B^* - A^*)\gamma} - \frac{B^* \sinh(r - A^*)\gamma}{sr \sinh(B^* - A^*)\gamma} + \frac{1}{s} \quad (4.102)$$

where  $\gamma = \sqrt{s/D'}$ , with  $s$  being the Laplace variable and  $D'$  the mutual diffusion coefficient. The expression for the density of reaction times can then be readily obtained using the relation  $\tilde{w}(r, s) = s\tilde{W}(r, s)$  to give

$$\tilde{w}(r, s) = \frac{A^* \sinh(B^* - r)\gamma}{r \sinh(B^* - A^*)\gamma} + \frac{B^* \sinh(r - A^*)\gamma}{r \sinh(B^* - A^*)\gamma} \quad (4.103)$$

where  $\tilde{W}(r, s) = 1/s - \tilde{\Omega}(r, s)$ . Analytically inverting the above equation gives the probability density function to be

$$w(r, t) = \frac{A^*}{r} \sum_{k=-\infty}^{\infty} \frac{(\ell - u + 2k\ell)^2}{\sqrt{2\pi t^{3/2}}} \exp\left(-\frac{(\ell - u + 2k\ell)^2}{2t}\right) + \frac{B^*}{r} \sum_{k=-\infty}^{\infty} \frac{(\ell - n + 2k\ell)^2}{\sqrt{2\pi t^{3/2}}} \exp\left(-\frac{(\ell - n + 2k\ell)^2}{2t}\right) \quad (4.104)$$

with the corresponding expression for the cumulative distribution function for the reaction probability found to be

$$W(r, t) = \frac{A^*}{r} \sum_{k=-\infty}^{\infty} \operatorname{erfc}\left(\frac{|\ell - u + 2k\ell|}{\sqrt{2t}}\right) + \frac{B^*}{r} \sum_{k=-\infty}^{\infty} \operatorname{erfc}\left(\frac{|\ell - n + 2k\ell|}{\sqrt{2t}}\right) \quad (4.105)$$

where

$$u = \frac{(r - A^*)}{\sqrt{2D'}}, \quad \ell = \frac{(B^* - A^*)}{\sqrt{2D'}}, \quad n = \frac{(B^* - r)}{\sqrt{2D'}} \quad (4.106)$$

Unfortunately analytically inverting Eq. (4.105) in order to generate a reaction time is not possible. However, by letting  $r$  reside halfway between the boundary  $A^*$  and  $B^*$  which is always the case if the slices are separated by a constant  $\delta$  the expression for the density of first passage times (Eq. 4.103) can be simplified to<sup>9</sup>

$$\begin{aligned} \tilde{w}(r, s) &= \frac{2 \sinh(B^* - A^*) \frac{\gamma}{2}}{\sinh(B^* - A^*)\gamma} \\ &= \frac{1}{\cosh(B^* - A^*) \frac{\gamma}{2}} \end{aligned} \quad (4.107)$$

The cumulative distribution function of the survival probability in the Laplace domain then takes the form

<sup>9</sup> The last term in Eq. (4.107) arising from the identity  $\sinh(2x) = 2\sinh(x) \cosh(x)$ .

$$\begin{aligned}
\tilde{W}(r, s) &= \frac{1}{s} \frac{1}{\cosh \tau \sqrt{s}} \\
&= \frac{2}{s} \frac{1}{e^{\tau \sqrt{s}} + e^{-\tau \sqrt{s}}} \\
&= \frac{2}{s} \frac{e^{-\tau \sqrt{s}}}{1 + e^{-2\tau \sqrt{s}}} \\
&= \frac{2}{s} \sum_{k=0}^{\infty} (-1)^k e^{-(2k+1)\tau \sqrt{s}} \tag{4.108}
\end{aligned}$$

where  $\tau = (B^* - A^*)/2\sqrt{D'}$ . On inverting the last expression, the reaction probability is

$$W(r, t) = 2 \sum_{k=0}^{\infty} (-1)^k \operatorname{erfc} \left( \frac{(2k+1)\tau}{\sqrt{4t}} \right) \tag{4.109}$$

The mean time of Eq. (4.107) can be calculated as  $\lim_{s \rightarrow 0} \left( -\frac{d\tilde{w}}{ds} \right)$ , which gives  $(b-a)^2/8D'$ . Unfortunately, one cannot sample from a mixture which alternates in sign, making Eq. (4.109) unusable. However, it is possible to sample from an exponential density distribution with the same mean exit time as Eq. (4.109). Assuming  $s$  to be small, the cosh term can be approximated by expanding as a power series to give the solution

$$\begin{aligned}
\tilde{w}(r, s) &= \frac{1}{\cosh \left( \frac{(B^* - A^*)}{2} \sqrt{\frac{s}{D'}} \right)} \\
&= \frac{1}{1 + \frac{1}{2} \frac{(B^* - A^*)^2}{4} \frac{s}{D'}} \\
&= \frac{8D'}{(B^* - A^*)^2} \frac{1}{s + \frac{8D'}{(B^* - A^*)^2}} \tag{4.110}
\end{aligned}$$

The inverse Laplace transform of the above equation is then readily found to be

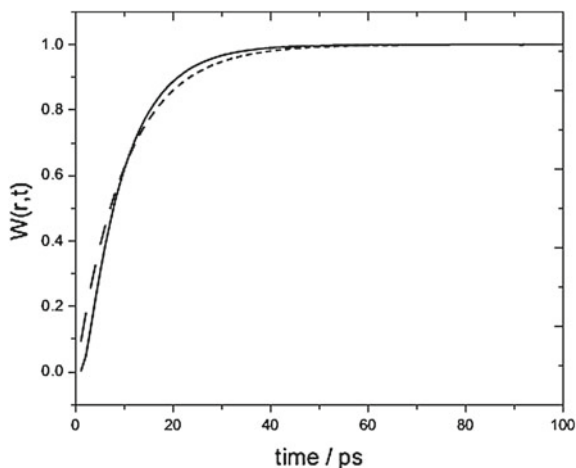
$$w(r, t) = \frac{8D'}{(B^* - A^*)^2} \exp \left( -\frac{8D't}{(B^* - A^*)^2} \right) \tag{4.111}$$

which has the cumulative distribution

$$W(r, t) = 1 - \exp \left( -\frac{8D't}{(B^* - A^*)^2} \right) \tag{4.112}$$

Figure 4.10 shows the reaction probability calculated using the exact function (Eq. 4.109) and compared against the exponential function (Eq. 4.112) from which

**Fig. 4.10** Comparison of Eq. (4.109) (line) and Eq. (4.112) (dashed lines) from which exit times between slices are generated. Increasing the number of slices has no overall effect on the fit of the exponential in Eq. (4.112). On computing the  $\text{erfc}(x)$  the summation was taken from  $k = 0$  to 1,000. A slice spacing of  $1 \text{ \AA}$  was used; outer boundary =  $10 \text{ \AA}$ , reaction radius =  $1 \text{ \AA}$  and  $D' = 1 \text{ \AA}^2 \text{ ps}^{-1}$



the exit times are generated using a separation distance between the slices to be  $1 \text{ \AA}$ . It is not surprising that the exponential function deviates at short times, since the limit  $s \rightarrow 0$  was taken to derive the long term behaviour of Eq. (4.107). However, after many such steps the deviations will be negligible because the central limit theorem ensures that any model with the correct mean and finite standard deviation will converge to the exact solution.

The algorithm for generating an exponential time with the mean of Eq. (4.107) is then

$$\bar{T}_{ex} = -\ln(U(0, 1)) \frac{(B^* - A^*)^2}{8D'} \quad (4.113)$$

with  $U(0, 1]$  being a uniformly distributed random number in the interval  $(0,1]$ .

### 4.6.2 Situation 3: Time to Hit the Boundary

In this situation a first passage time can be generated for the radical pair to be at a distance  $(B^* - \delta)$  as

$$T_s = \frac{(r - (B^* - \delta))^2}{4D'[\text{erfc}^{-1}(rU(0, 1]/(B^* - \delta))]^2} \quad (4.114)$$

where  $D'$  is the mutual diffusion coefficient,  $r$  the current separation of the radical pair,  $U(0,1]$  is a uniformly distributed random number in the interval  $(0,1]$  and  $\delta$  the spacing between slices.

### 4.6.3 Situation 4: Mean Exit Time to One of the Slices

If the separation of the particle is not on one of the slices (as in Fig. 4.9), then the required time to reach one of the slices is obtained by solving Eq. (4.103), without the assumption that  $r = (A^* + B^*)/2$ . One such method is to approximate the sinh term to second order to give the general solution

$$\tilde{w}(r, s) = \frac{1}{1 + \frac{s}{6D'} \left( B^{2*} + A^*B^* + A^{2*} - \frac{A^*B^*(B^*+A^*)}{r} - r^2 \right)} \quad (4.115)$$

Alternatively the mean time is  $\lim_{s \rightarrow 0} \left( -\frac{d\tilde{w}}{ds} \right)$  which gives

$$\mu = \frac{\left( B^{2*} + A^*B^* + A^{2*} - \frac{A^*B^*(B^*+A^*)}{r} - r^2 \right)}{6D'}$$

The algorithm to generate an exponential time with the above mean using a uniformly distributed random number  $U(0,1]$  is then simply

$$\bar{T}_b = -\mu \ln(U(0,1)) \quad (4.116)$$

### 4.6.4 Probability of Exit Boundary: Neutral Species

To calculate the probability of moving up or down a slice for a diffusion process one needs to solve the backward diffusion equation subject to the boundary conditions  $p(B^*) = 1$  and  $p(A^*) = 0$  (i.e. the distance of the radical pair moves one slice further apart). The complete derivation is presented in Sect. A.3 of the Appendix, with the final exit probability found to be

$$P_2 = \frac{B^*(B^* - A^*)}{r(r - A^*)} \quad (4.117)$$

Similarly, using the boundary condition  $p(A^*) = 1$  and  $p(B^*) = 0$  (the probability of moving down one slice) is given as

$$P_1 = \frac{A^*(B^* - r)}{r(B^* - a)} \quad (4.118)$$

From Eqs. (4.117) and (4.118), the probability of moving up or down one slice subject to  $r = x$  and letting  $A^* = (x - \delta)$  and  $B^* = (x + \delta)$ , where  $\delta$  is a change in the separation of the radical pair (or in this case the slice spacing), the probability of moving up one slice is

$$p_{\text{up}}(x \rightarrow x + \delta) = \frac{1}{2} \left( 1 + \frac{\delta}{x} \right) \quad (4.119)$$

Following a similar procedure as above, with the boundary condition  $p(A^*) = 1$  and  $p(B^*) = 0$  (i.e. the distance of the radical pair moves one slice closer), the probability of moving down a slice is given by the expression

$$p_{\text{down}}(x \rightarrow x - \delta) = \frac{1}{2} \left( 1 - \frac{\delta}{x} \right) \quad (4.120)$$

### 4.6.5 Slice: Partially Diffusion Controlled Reactions

Unlike diffusion controlled reactions, where reaction takes place as soon as the interparticle separation hits the boundary  $a$ ; partially diffusion controlled reactions involve an extra complexity, such that the probability of reaction must be calculated based on the surface reactivity. This probability can be calculated by solving the backward diffusion equation to find the survival probability  $\Omega(a, B^*)$  on going from boundary  $a$  to  $B^*$  (defined as  $a + \delta$ ) subject to a radiation boundary condition at surface  $a$  (situation 2 as shown in Fig. 4.7). Using the boundary condition  $\Omega'(a) = (v/D')p(a)$  and  $\Omega(B^*) = 1$ , the survival probability  $\Omega(a, B^*)$  is found to be

$$\Omega(a, B^*) = \frac{(r(1 + (D'/va)) - a)B^*}{(B^*(1 + D'/va) - a)r} \quad (4.121)$$

Defining  $a'_{\text{eff}}$  to be  $a/(1 + (D'/va))$  and evaluating the expression at  $r = a$  gives the survival probability  $\Omega(a, b)$  of exiting at  $b$  starting at  $a$  to take the form

$$\Omega(a, B^*) = \frac{(a - a'_{\text{eff}})B^*}{(B^* - a'_{\text{eff}})a} \quad (4.122)$$

#### 4.6.5.1 Probability of Reaction on Diffusion from the Interval [a,b]

Although Eq. (4.122) allows the implementation of partially diffusion controlled reactions, another possibility needs to be considered: on reaction at the inner boundary  $a$  the radical pair separates to  $x$  which is less than  $B^*$  (with  $B^*$  defined to be  $a + \delta$ ) and survive reaction. The pair then undergo spin relaxation at the point  $x$  and re-approach the boundary  $a$  without ever hitting the boundary  $B^*$ . The likelihood of this situation can be tested using the recovering boundary formalism. A thorough derivation is now presented.<sup>10</sup>

---

<sup>10</sup> To avoid complicating the notation the boundary  $B^*$  is represented as  $b$ .

The expression for the probability of going from  $a$  to  $b$  without reaction is given by

$$B_{\text{rec}}(a) = \int_0^{\infty} w_b(a, b, t) e^{-\alpha t} dt + \int_0^{\infty} \int_a^b f(t) p_{ab}(a, x, t') [B_a(x) + (1 - B_a(x))(1 - p) B_{\text{rec}}(a)] dx dt' \quad (4.123)$$

where  $f(t) = \alpha \exp(-\alpha t)$  is the probability density function of the spin relaxation times. In Eq. (4.123)

1.  $\int_0^{\infty} w_b(a, b, t) e^{-\alpha t} dt$  is the probability of hitting  $b$  for the first time at  $t$ , starting from  $a$  which is reflecting ( $w_b(a, b, t)$ ) multiplied by the probability that relaxation has not occurred by  $t$  ( $e^{-\alpha t}$ ).
2.  $\int_0^{\infty} \int_a^b f(t) p_{ab}(a, x, t') dx dt'$  represents the fact that relaxation occurs before reaching  $b$  at time  $t'$  ( $f(t)$ ), multiplied by the probability of diffusing to  $x$  without hitting  $b$  at  $t'$  ( $p_{ab}(a, x, t')$ ), multiplied by the probability that diffusion subsequently goes to  $b$  from  $x$  with a reaction. This final probability can be decomposed further as: (i) probability that  $b$  is hit starting from  $x$  without hitting  $a$  first ( $B_a$ ) combined with the probability that  $a$  is hit first ( $1 - B_a$ ), multiplied by the probability of no reaction occurring ( $1 - p$ ). (ii)  $(1 - B_a(x))(1 - p)$  is then multiplied by the probability of no reaction at  $a$  and exiting to  $b$ . This is a recurrence relation for  $B_{\text{rec}}$ .

The first and second term in Eq. (4.123) can be written in terms of Laplace transform (with the Laplace variable  $\alpha$ ) as

$$B_{\text{rec}}(a) = \tilde{w}_b(a, b, \alpha) + \int_a^b \alpha \tilde{p}_{ab}(a, x, \alpha) [B_a(x) + (1 - B_a(x))(1 - p) B_{\text{rec}}(a)] dx \quad (4.124)$$

The expression for  $B_a(x)$  can be calculated from Eq. (4.117). Defining

$$\tilde{Q}_{ab}(a, \alpha) = \int_a^b \tilde{p}_{ab}(a, x, \alpha) B_a(x) dx \quad (4.125)$$

$$\tilde{\Omega}(a, \alpha) = \int_a^b \tilde{p}_{ab}(a, x, \alpha) dx \quad (4.126)$$

and substituting into Eq. (4.124) gives an expression for  $B_{\text{rec}}(a)$  to be

$$B_{\text{rec}}(a) = \frac{\alpha \tilde{Q}_{ab}(a, \alpha) + \tilde{w}_b(a, \alpha)}{1 - (1-p)\alpha(\tilde{\Omega}_{ab}(a, \alpha) - \tilde{Q}_{ab}(a, \alpha))} \quad (4.127)$$

The transition density for a diffusion process subject to an inner reflective boundary and outer absorptive boundary can be found using the renewal theorem as

$$\tilde{p}_{ab}(a, y, \alpha) = \tilde{p}_{\text{ref}}(a, y, \alpha) - \frac{\tilde{p}_{\text{ref}}(a, b, \alpha)\tilde{p}_{\text{ref}}(b, y, \alpha)}{\tilde{p}_{\text{ref}}(b, b, \alpha)} \quad (4.128)$$

The first term counts all the trajectories from  $a$  to  $y$  with reflection at  $a$ , whilst the second term removes all those trajectories that pass through  $b$ . The transition density for a Bessel process started at  $b$  and diffusing to  $y$  subject to an inner reflecting boundary is

$$\tilde{p}_{\text{ref}}(b, y, \alpha) = p(b, y, \alpha) - p(b, a, \alpha) \frac{p_x(a, y, \alpha)}{p_x(a^+, a, \alpha)} \quad (4.129)$$

The terms  $\tilde{p}_x(a, y, s)$  and  $\tilde{p}_x(a^+, a, s)$  are the first derivative of an unbounded transition density of the form  $\tilde{p}(x, y, s) = (y/x\sqrt{4D's}) (e^{-|y-x|\gamma} - e^{-(y+x)\gamma})$  with respect to  $x$ , with the process starting at  $x = a$ . The transition density for each term in the above equation can be readily calculated to be

$$\tilde{p}(b, y, \alpha) = \frac{y}{b} \frac{1}{\sqrt{4D's}} \left( e^{-|y-b|\gamma} - e^{-(y+b)\gamma} \right) \quad (4.130)$$

$$\tilde{p}(b, a, \alpha) = \frac{a}{\sqrt{D'\alpha b}} e^{-b\gamma} \sinh(a\gamma) \quad (4.131)$$

$$\tilde{p}_x(a, y, \alpha) = -\frac{1}{2} \frac{ye^{-y\gamma} \sinh(a\gamma)}{D'\alpha a^2} + \frac{1}{2} \frac{ye^{-y\gamma} \cosh(a\gamma)\gamma}{D'\alpha a} \quad (4.132)$$

$$\tilde{p}_x(a^+, a, \alpha) = -\frac{1}{2D'\alpha a} e^{-a\gamma} \sinh(a\gamma)(1 + a\gamma) \quad (4.133)$$

with  $\gamma = \sqrt{\frac{\alpha}{D'}}$ . Substituting the above into Eq. (4.129) gives the solution for  $\tilde{p}_{\text{ref}}(b, y, \alpha)$  to be

$$\tilde{p}_{\text{ref}}(b, y, \alpha) = \frac{y}{b} \frac{1}{2\gamma D'} \left( e^{-\gamma(b-y)} + \frac{(\gamma a - 1)}{(\gamma a + 1)} e^{-2\gamma(b-2a+y)} \right) \quad (4.134)$$

The terms  $\tilde{p}_{\text{ref}}(a, y, \alpha)$  and  $\tilde{p}_{\text{ref}}(a, b, \alpha)$  have already been formulated in Eq. (4.44), which are

$$\tilde{p}_{\text{ref}}(a, y, \alpha) = \frac{ye^{-\gamma(y-a)}}{D'(\gamma a + 1)} \quad (4.135)$$

$$\tilde{p}_{\text{ref}}(a, b, \alpha) = \frac{b}{D'} \frac{e^{-\gamma(b-a)}}{(\gamma a + 1)} \quad (4.136)$$

The term  $\tilde{p}_{\text{ref}}(b, b, \alpha)$  can also be formulated in a similar manner as Eq. (4.134) with  $y = b$  to give

$$\tilde{p}_{\text{ref}}(b, b, \alpha) = \frac{1}{2\gamma D'} \left( 1 + \frac{(\gamma a - 1)}{(\gamma a + 1)} e^{-2\gamma(b-a)} \right) \quad (4.137)$$

On substituting the expressions for  $\tilde{p}_{\text{ref}}(a, y, \alpha)$ ,  $\tilde{p}_{\text{ref}}(a, b, \alpha)$ ,  $\tilde{p}_{\text{ref}}(b, y, \alpha)$  and  $\tilde{p}_{\text{ref}}(b, b, \alpha)$  into Eq. (4.128),  $\tilde{p}_{ab}(a, y, \alpha)$  is found to be

$$\begin{aligned} \tilde{p}_{ab}(a, y, \alpha) &= \frac{y}{D'(\gamma a + 1)} \\ &\times \left[ e^{-\gamma(y-a)} - \frac{e^{-\gamma(b-a)} \left( e^{-\gamma(b-y)} + \left( \frac{\gamma a - 1}{\gamma a + 1} \right) e^{-\gamma(b+y-2a)} \right)}{1 + \frac{(\gamma a - 1)}{(\gamma a + 1)} e^{-2\gamma(b-a)}} \right] \end{aligned} \quad (4.138)$$

The expression for the first passage time density from  $a$  to  $b$

$\tilde{w}_b(a, b, \alpha) = \tilde{p}_{\text{ref}}(a, b, \alpha) / \tilde{p}_{\text{ref}}(b, b, \alpha)$  is then

$$\tilde{w}_b(a, b, \alpha) = \frac{b \frac{e^{-\gamma(b-a)}}{\gamma a + 1}}{\frac{1}{2\gamma} \left( 1 + \left( \frac{\gamma a - 1}{\gamma a + 1} \right) e^{-2\gamma(b-a)} \right)} \quad (4.139)$$

The required integral for  $\tilde{Q}_{ab}(a, \alpha)$  can now be evaluated as follows

$$\begin{aligned} \tilde{Q}_{ab}(a, \alpha) &= \int_a^b p_{ab}(a, y, \alpha) \frac{(y-a)b}{(b-a)y} dy \\ &= \int_a^b \frac{y}{D'(\gamma a + 1)} \left[ e^{-\gamma(y-a)} - \frac{e^{-\gamma(b-a)} \left( e^{-\gamma(b-y)} + \left( \frac{\gamma a - 1}{\gamma a + 1} \right) e^{-\gamma(b+y-2a)} \right)}{1 + \frac{(\gamma a - 1)}{(\gamma a + 1)} e^{-2\gamma(b-a)}} \right] \\ &\quad \times \frac{(y-a)b}{(b-a)y} dy \end{aligned} \quad (4.140)$$

Defining  $L = D'(\gamma a + 1)$ ;  $Z = 1 + \frac{(\gamma a - 1)}{(\gamma a + 1)} e^{-2\gamma(b-a)}$ ;  $Y = \frac{(\gamma a - 1)}{(\gamma a + 1)}$  and  $b^* = (a - b)$  the expression for  $\tilde{Q}_{ab}(a, \alpha)$  evaluates to

$$\begin{aligned} \tilde{Q}_{ab}(a, \alpha) &= -\frac{b}{Lb^*Z\gamma^2} \left[ e^{3\gamma(b^*)} Y - e^{\gamma(b^*)} Z \gamma b - e^{\gamma(b^*)} Z + e^{\gamma(b^*)} a Z \gamma \right. \\ &\quad \left. + e^{3\gamma(b^*)} Y \gamma b - e^{\gamma(b^*)} \gamma b + e^{3\gamma(b^*)} Y a \gamma + e^{\gamma(b^*)} a \gamma + Z \right. \\ &\quad \left. - e^{2\gamma(b^*)} Y - e^{2\gamma(b^*)} \right] \end{aligned} \quad (4.141)$$

In a similar manner the survival probability  $\tilde{\Omega}(a, \alpha)$  is found to be

$$\begin{aligned} \tilde{\Omega}(a, \alpha) &= \int_a^b \frac{y}{D'(\gamma a + 1)} \\ &\quad \times \left[ e^{-\gamma(y-a)} - \frac{e^{-\gamma(b-a)} \left( e^{-\gamma(b-y)} + \left( \frac{\gamma a - 1}{\gamma a + 1} \right) e^{-\gamma(b+y-2a)} \right)}{1 + \frac{(\gamma a - 1)}{(\gamma a + 1)} e^{-2\gamma(b-a)}} \right] dy \\ &= -\frac{1}{LZ\gamma^2} \left[ e^{\gamma(b^*)}\gamma b + e^{\gamma(b^*)}Z\gamma b + e^{\gamma(b^*)}Z - e^{3\gamma(b^*)}Y\gamma b - e^{\gamma(b^*)} - e^{3\gamma(b^*)}Y \right. \\ &\quad \left. - e^{2\gamma(b^*)}\gamma a - aZ\gamma - Z + e^{2\gamma(b^*)}Y a\gamma + e^{2\gamma(b^*)} + e^{2\gamma(b^*)}Y \right] \end{aligned} \quad (4.142)$$

All terms required to calculate  $B_{\text{rec}}(a)$  (probability on going from  $a$  to  $b$ , undergoing spin relaxation at an earlier instance, reaching the boundary  $b$  without reaction) are now calculated, and the complete expression is shown in Eq. (4.143). Whilst the solution to  $B_{\text{rec}}(a)$  assumes diffusion controlled reactivity at the surface  $a$ , it can be argued that if  $B_{\text{rec}}(a)$  is negligible for diffusion controlled reactions, then it must also be negligible for partially diffusion controlled reactions as well.

$$\begin{aligned} B_{\text{rec}}(a) &= \frac{\alpha b}{LZb^*\gamma^2} \left[ e^{3\gamma(b^*)}Y - e^{\gamma(b^*)}Z\gamma b - e^{\gamma(b^*)}Z + e^{\gamma(b^*)}aZ\gamma \right. \\ &\quad \left. + e^{3\gamma(b^*)}Y\gamma b - e^{\gamma(b^*)}\gamma b - e^{3\gamma(b^*)}Y a\gamma + e^{\gamma(b^*)} + e^{\gamma(b^*)}a\gamma + Z - e^{2\gamma(b^*)}Y - e^{2\gamma(b^*)} \right] \\ &\quad + \frac{2be^{\gamma(b^*)}\gamma}{(\gamma a + 1) \left( \frac{1 + (\gamma a - 1)e^{2\gamma b^*}}{\gamma a + 1} \right)} \\ &\quad \div \frac{b}{LZb^*\gamma^2} \left[ e^{3\gamma(b^*)}Y - e^{\gamma(b^*)}Z\gamma b - e^{\gamma(b^*)}Z + e^{\gamma(b^*)}aZ\gamma + e^{\gamma(b^*)}Y\gamma b \right. \\ &\quad \left. - e^{\gamma(b^*)}\gamma b - e^{3\gamma(b^*)}Y a\gamma + e^{\gamma(b^*)} + e^{\gamma(b^*)}a\gamma + Z - e^{2\gamma(b^*)}Y - e^{2\gamma(b^*)} \right] \end{aligned} \quad (4.143)$$

Investigating this situation for a chemical system containing two hydroxyl radicals (which is later investigated in this work) using the parameters:  $a = 2.52 \text{ \AA}$ ,  $D' = 0.44 \text{ \AA}^2 \text{ ps}^{-1}$ ,  $p = 0.25$ ,  $B_{\text{rec}}(a) \sim 1$  for a spacing of  $4 \text{ \AA}$  using a value of  $\alpha = 0.01 \text{ ps}^{-1}$ . This value decreases to  $\sim 0.9$  when  $\alpha = 0.1 \text{ ps}^{-1}$  and further decreases to  $0.67$  when  $\alpha = 1 \text{ ps}^{-1}$ , suggesting a spacing of  $4 \text{ \AA}$  to be much too wide. With a spacing of  $1 \text{ \AA}$  and  $\alpha = 1 \text{ ps}^{-1}$ , one obtains a value for  $B_{\text{rec}}(a)$  to be  $0.88$ , which suggests the spacing between the boundary at  $a$  and the next slice at  $a + 1 \text{ \AA}$  to be sufficiently converged in order to describe the recombination kinetics involving the hydroxyl radical for relatively fast spin relaxation times.

If the exchange interaction is also included in the model, (which is assumed to be negligible at distance beyond  $10 \text{ \AA}$ ), then a minimum of ten slices is required. In Sect. 5.7, it will be investigated whether acceptable statistics when computing the spin polarisation can also be obtained using ten slices.

### 4.6.6 Situation 2: Mean Exit Time After Reflection for Neutral Species

Equation (4.143) now allows the analytical computation of the probability of going from the boundary  $a$  to  $b$  and provides an analytical approach in determining whether the spacing between the slices are too large, such that reaction occurs at an interval  $y < b$  without ever reaching  $b$ .

The last step to implementing partially diffusion controlled reactions into the Slice program involves finding the exponential time  $\bar{T}_{ex}$  using the mean of  $-\frac{\partial \tilde{w}_{B^*}(a, B^*, \alpha)}{\partial \alpha}$  in the limit  $\alpha \rightarrow 0$ , which gives  $\mu = \{-3B^*a^2 + 2a^3 + B^{3*}\}/(6B^*D')$ . The algorithm for generating a random time with the correct  $\mu$  is then simply

$$\bar{T}_{ex} = -\mu(\ln U(0,1]) \quad (4.144)$$

The algorithm for treating partially diffusion controlled reactions within the Slice program therefore proceeds as follows: on reaching the first slice (such that  $r = a$ ), the particles are reflected to the first nearest slice  $B^*$  which is defined as  $a + \delta$ , with  $\delta$  being the spacing between the slices. A mean first passage time is calculated on going from  $a$  to  $B^*$  from Eq. (4.144) and the time is accumulated ( $t = t + \bar{T}$ ). A uniform random number  $U(0,1]$  is generated and the survival probability of the radical pair is calculated from Eq. (4.122). If  $U(0,1] > \Omega(a, B^*, t)$  the pair react, otherwise they separate to  $B^*$  and the algorithm would continue as normal.

### 4.6.7 Situation 1: Mean Exit Time for Charged Species

The Slice simulation package relies on generating exit times from the centre of each overlapping slice and the respective probability of exit at either the upper or lower ends of the slice. In this section the generation of the mean exit time is presented which extends the functionality of Slice for ionic systems. The time dependent diffusion equation for charged species is known to be

$$\frac{\partial \Omega}{\partial t} = D' \left[ \frac{\partial^2 \Omega}{\partial r^2} + \left( \frac{2}{r} + \frac{r_c}{r^2} \right) \frac{\partial \Omega}{\partial r} \right] \quad (4.145)$$

with  $\Omega$  representing the survival probability,  $r_c$  the Onsager distance,  $r$  the separation distance of the pair and  $D'$  the mutual diffusion coefficient. The Laplace transform of the Eq. (4.145) can be written in the form

$$s\tilde{\Omega} - 1 = \hat{L}\tilde{\Omega} \quad (4.146)$$

where  $\hat{L}$  is the diffusion operator. The mean exit time can be obtained as  $\lim_{s \rightarrow 0} \tilde{\Omega}$ ; hence the above equation simplifies to

$$-1 = \hat{L}\bar{T} \quad (4.147)$$

Substituting  $u = \partial\bar{T}/\partial r$  into the above equation gives

$$\frac{\partial u}{\partial r} + \left(\frac{2}{r} + \frac{r_c}{r^2}\right)u = -\frac{1}{D'} \quad (4.148)$$

Equation (4.148) can be directly integrated using the integrating factor  $\exp\left[\int\left(\frac{2}{r} + \frac{r_c}{r^2}\right)dr\right]$  to give

$$ur^2 \exp[-r_c/r] = -\frac{\mathfrak{Z}(r)}{D'} \quad (4.149)$$

where

$$\mathfrak{Z}(r) = \frac{r^3}{6} \left(2 - \frac{r_c}{r} + \frac{r_c^2}{r^2}\right) \exp[-r_c/r] + \frac{r_c^3}{6} \text{Ei}(-r_c/r) \quad (4.150)$$

In Eq. (4.150),  $\text{Ei}(-r_c/r)$  is the exponential integral defined as

$$\text{Ei}(x) = \int_{-\infty}^x \frac{e^t}{t} dt \quad (4.151)$$

Integrating Eq. (4.149) using the required boundary conditions finally yields an expression for the mean exit time as

$$\begin{aligned} \bar{T} = & \frac{\exp[r_c/r]}{(\exp[r_c/B^*] - \exp[r_c/A^*])r_c D'} \\ & \times \left( \exp[r_c/A^*](\mathfrak{Z}(r) - \mathfrak{Z}(A^*)) - \exp[r_c/B^*](\mathfrak{Z}(B^*) - \mathfrak{Z}(r)) + \left(\frac{B^{3*} - A^{3*}}{3}\right) \right) \\ & + \frac{(\mathfrak{Z}(A^*) - \mathfrak{Z}(B^*)) + \exp[-r_c/B^*] \left(\frac{B^{3*} - r^3}{3}\right) + \exp[-r_c/A^*] \left(\frac{r^3 - A^{3*}}{3}\right)}{(\exp[-r_c/A^*] - \exp[-r_c/B^*])r_c D'} \end{aligned} \quad (4.152)$$

### 4.6.8 Probability of Exit Boundary: Charged Species

To generate the exit probability between slices, the steady state backward diffusion equation of the form

$$\left[ \frac{\partial^2 p}{\partial r^2} + \left( \frac{2}{r} + \frac{r_c}{r^2} \right) \frac{\partial p}{\partial r} \right] = 0 \quad (4.153)$$

needs to be solved subject to certain boundary conditions. Substituting  $u = \partial p / \partial r$  into the above equation, the probability  $p$  is given by the expression

$$p = \frac{Ae^{-r_c/r}}{r_c} + B \quad (4.154)$$

where  $A$  and  $B$  are the constants to be determined. Using the first boundary condition such that  $p(B^*) = 0$  gives  $B = -A \exp(-r_c/B^*)/r_c$ . Applying the second boundary condition  $p(A^*) = 1$  (i.e. the probability of exiting to the lower slice) gives

$$A = \frac{r_c}{\exp(-r_c/A^*) - \exp(-r_c/B^*)} \quad (4.155)$$

and when substituted back into the expression for  $B$  gives

$$B = -\frac{\exp(-r_c/B^*)}{\exp(-r_c/A^*) - \exp(-r_c/B^*)} \quad (4.156)$$

Therefore, the probability for the pair to exit at the lower boundary is

$$P_{\text{down}} = \frac{e^{-r_c/r} - e^{-r_c/B^*}}{e^{-r_c/A^*} - e^{-r_c/B^*}} \quad (4.157)$$

where the boundaries  $A^*$  and  $B^*$  correspond to  $(r - \delta)$  and  $(r + \delta)$  respectively, with  $\delta$  being the spacing between the slices. Using a similar procedure as above, the probability for the pair to exit at the upper  $B^*$  can be obtained using the boundary conditions  $p(A^*) = 0$  and  $p(B^*) = 1$ , to give

$$P_{\text{up}} = \frac{e^{-r_c/r} - e^{-r_c/A^*}}{e^{-r_c/B^*} - e^{-r_c/A^*}} \quad (4.158)$$

## 4.7 Summary

This chapter has presented the foundations of the IRT and random flights simulation techniques and how they have been extended to widen their application in the field of radiation chemistry. In Chap. 8 it will be shown how the IRT can be further extended

to model a full radiation track with explicit treatment of spin dynamics, allowing the simulation of complex chemical systems, which was previously intractable using the much slower random flights algorithm due to computational demands. The next chapter will now implement and utilise the strength of Slice together with a new algorithm for treating spin relaxation to study the photodissociation of  $\text{H}_2\text{O}_2$  and the generation of CIDEP effects.

## References

1. P. Clifford, N.J.B. Green, M.J. Pilling, S.M. Pimblott, *J. Phys. Chem.* **91**, 4417 (1987)
2. N.J.B. Green, M.J. Pilling, S.M. Pimblott, P. Clifford, *J. Phys. Chem.* **93**, 8025 (1989)
3. P. Clifford, N.J.B. Green, *Mol. Phys.* **57**, 123 (1986)
4. N.J.B. Green, *Mol. Phys.* **65**, 1399 (1988)
5. L. Arnold, *Stochastic Differential Equations* (Wiley, New York, 1972)
6. I.I. Gikhman, A.V. Skorokhod, *Stochastic Differential Equations* (Springer, Berlin, 1971)
7. W.J. Rumelin, *J. Numer. Anal.* **19**, 604 (1982)
8. W.M. Bartczak, A. Hummel, *J. Phys. Chem.* **87**, 5222 (1987)
9. N.J.B. Green (unpublished)
10. N.J.B. Green, S.M. Pimblott, B. Brocklehurst, *J. Chem. Soc. Faraday Trans.* **91**, 223 (1995)
11. S.M. Pimblott, N.J.B. Green, *J. Phys. Chem.* **96**, 9338 (1992)
12. N.J.B. Green, M.J. Pilling, S.M. Pimblott, P. Clifford, M.J. Oldfield, *J. Chem. Soc. Faraday Trans. I* **82**, 2673 (1986)
13. L. Devroye, *Non-uniform Random Variate Generation* (Springer, New York, 1986)
14. A. Beskos, G.O. Roberts, *Ann. App. Prob.* **15**, 2422 (2005)
15. N.J.B. Green, M.J. Pilling, P. Clifford, *J. Phys. Chem.* **86**, 1322 (1982)
16. N.J.B. Green, S.M. Pimblott, *J. Phys. Chem.* **96**, 9338 (1992)
17. S.A. Rice, *Comprehensive Chemical Kinetics* (Elsevier, Amsterdam, 1985)
18. K.M. Hong, J. Noolandi, *J. Chem. Phys.* **68**, 5163 (1978)
19. J. Crank, P. Nicolson, *Proc. Cambridge Philos. Soc.* **43**, 50 (1947)
20. J. Crank, *The Mathematics of Diffusion* (Oxford University Press, Oxford, 1975)
21. N.J.B. Green, M.J. Pilling, P. Clifford, *Mol. Phys.* **67**, 1085 (1989)
22. D.R. Cox, H.D. Miller, *The Theory of Stochastic Processes* (Chapman and Hall, London, 1965)

# Chapter 5

## Photodissociation of Hydrogen Peroxide

### Solution: Singlet or Triplet Precursor?

#### 5.1 Introduction

Recent evidence for a possible triplet precursor in the photolytic dissociation of  $\text{H}_2\text{O}_2$  has been presented by Bhattacharjee et al. [1]. Until now this dissociation has generally been thought to go through a repulsive singlet state, noting the ground state  $\text{H}_2\text{O}_2$  to be singlet  $\tilde{X}^1\text{A}$  and photoexcitation to any other spin state is forbidden, since the spin-orbit coupling mechanism responsible for excitation to a triplet state is weak. The authors back up their proposal of a triplet precursor from the observation that in the gas phase, the  $\Lambda$ -type preference of the  $\cdot\text{OH}$  radical, in which there is a small preferential population of the  $\Pi^- \Lambda$  doublet of  $\cdot\text{OH}$  with increasing rotational angular momentum [2–4]. An excited triplet potential energy surface is required to account for this observation. As the dissociation of  $\text{H}_2\text{O}_2$  takes place in less than 60 fs [5] in the gas phase, direct detection of the dissociating state is impossible. Furthermore, the products of the dissociation ( $2\cdot\text{OH}$ ) have extremely fast spin relaxation times, thought to be the result of ineffective quenching of the orbital angular momentum in solution, making them undetectable by EPR techniques [6]. To overcome this problem, the authors have conducted their experiment in 2-propanol solution, where the radicals are rapidly scavenged by 2-propanol. If the scavenging timescale is faster than spin relaxation the spins are trapped in 2-propanolyl radicals, which then relax much more slowly (2.7  $\mu\text{s}$ ) [7]. Hence, by indirectly measuring the spin polarisation of geminate 2-propanolyl radical pairs, one can infer the nature of dissociating state of the precursor, so long as the time required for hydrogen abstraction can effectively compete with spin relaxation.

The complete reaction scheme is shown in Fig. 5.1 for the photolytic dissociation, highlighting how the initial spin state of the hydroxyl radical is trapped in the 2-propanolyl radicals. Hydrogen abstraction of the 2-propanol mainly occurs at the  $\alpha$ -position, however, the reaction is non-selective and multiple secondary radicals are produced [8] with the yields of the products indicated in Fig. 5.2.

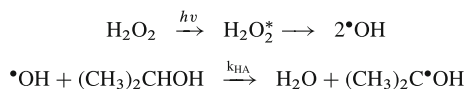
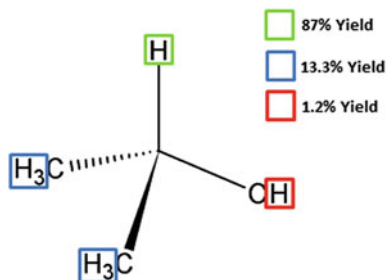


**Fig. 5.1** Reaction scheme for the photolytic dissociation of hydrogen peroxide.  $k_{\text{HA}}$  is the hydrogen abstraction rate constant

**Fig. 5.2** Relative yield of the multiple secondary radicals formed on hydrogen abstraction [8]



By conducting a time resolved EPR study ( $\lambda = 248$  nm in the photolysis of  $\text{H}_2\text{O}_2$ ), with the EPR spectrometer operating at 0.33 T (X-band region), the observed chemically induced dynamic electron polarisation (CIDEP) effects, are interpreted by Bhattacharjee et al. as evidence for a triplet precursor [1], by noting the similarities in the spectrum of  $(\text{CH}_3)_2\text{C}\cdot\text{OH}$  at 298 K between the  $\text{H}_2\text{O}_2$  in 2-propanol and the well studied system, acetone-2-propanol [9–16], known to have a triplet precursor. The spectrum of  $(\text{CH}_3)_2\text{C}\cdot\text{OH}$  obtained by the group [1] at 241 K shows that the polarisation generated as early as 0.6  $\mu\text{s}$  is due to spin-correlated geminate radical pairs  $(\text{CH}_3)_2\text{C}\cdot\text{OH}$  and not randomly encountering F-pairs because of the antiphase signal observed in the spectrum. The intensity of the EPR lines reduces with time due to the separation of the geminate radical pair by diffusive motion. Distinguishing between encountering geminate pairs and F-pairs is important, as the latter would provide the same polarisation pattern (E/A), (low field emissive and high field absorptive) as observed by the authors, with the crucial difference being that all knowledge regarding the dissociating state of the precursor has been lost. To allow hydrogen abstraction to effectively compete with spin relaxation, the experiment has been conducted in a 12 M solvent of 2-propanol giving an estimated lifetime of the hydroxyl radicals to be  $\leq 40$  ps; considered to be much less than the currently accepted value for the spin relaxation time of the hydroxyl radical ( $\sim 100$  ps) [17].

On conducting the experiment at 241 K, the authors report seeing some weak EPR lines because of the formation of  $\cdot\text{CH}_2\text{CH}(\text{OH})\text{CH}_3$ . For the purpose of this study, it is assumed that scavenging always produces the main product  $(\text{CH}_3)_2\text{C}\cdot\text{OH}$  and all by-products are ignored. Scavenging by the 2-propanol is nearly diffusion controlled with the rate constant at room temperature found to be  $\approx 2 \times 10^9 \text{ M}^{-1} \text{ s}^{-1}$  in aqueous solution [18]. Hence in aqueous solution, a hydroxyl radical has to diffuse to a 2-propanol molecule for the reaction to take place. However, in the experiment the

solvent itself is 2-propanol and a hydroxyl radical would find a 2-propanol molecule in its immediate vicinity for reaction, giving a pseudo first order rate constant of  $\approx 2.4 \times 10^{10} \text{ s}^{-1}$  in 12 M concentration. In this situation, the authors state that the rate of scavenging should be  $\geq 2 \times 10^9 \text{ M}^{-1} \text{ s}^{-1}$  and diffusion should not be the rate determining step, allowing scavenging to effectively compete with the spin relaxation time on the hydroxyl radical.

Dissociation or reaction of a molecule occurs with conservation of spin multiplicity since the parent molecule exists in a pure spin state which leads to the formation of geminate radical pairs with the same overall spin state as the parent molecule. Simulating the evolution of radical pairs is a challenging problem as it depends on a number of different parameters, namely the initial spin state of the precursor state, strength of the external magnetic field, relative diffusion coefficient of the radicals, type of interaction occurring between them, and their individual magnetic properties. Radical pairs may be created in either singlet or triplet spin states depending on which state is lower in energy, with recombination only possible through the singlet channel. The diffusive motion of the radical pair together with the spin evolution of the wavefunction therefore directly dictates whether the pair recombine or escape, and this indirectly affects the polarisation phase. Modelling of this system is further complicated by the necessity to design computationally efficient algorithms which incorporate spin dynamics, together with exploration of the parameter space, which itself contains many adjustable parameters, making the results difficult to analyse. At present, analytical treatments for the recombination probability are calculable for only simple one-step reaction schemes, and in the case of the current system which involves reactive products, one must model by numerical methods.

Through computational modelling of the geminate recombination of the  $\cdot\text{OH}$  radicals, their scavenging by 2-propanol and the subsequent behaviour of the 2-propanolyl radicals, this work aims to:

1. Investigate the feasibility of an alternative mechanism in which the triplet nature of the radical pair is generated by fast relaxation of the  $\cdot\text{OH}$  radicals before they can be scavenged.
2. Decipher whether it is possible that the non-equilibrium Boltzmann population of electron spin states is formed by the radical pair mechanism rather than the triplet mechanism as postulated by Das and co-workers [1].
3. Determine how fast spin relaxation on the hydroxyl radical needs to be to reproduce the observed polarisation phase, assuming the dissociative route of  $\text{H}_2\text{O}_2$  to proceed via the singlet state.

Although the IRT algorithm is sufficiently developed to completely simulate the system under study, the results are nevertheless compared with full Monte Carlo random flights simulation to make sure the correct kinetics and spin dynamics are obtained with no source of bias introduced by the IRT approximation.

## 5.2 Spin Relaxation of $\cdot\text{OH}$

The EPR spectrum of hydroxyl radicals cannot be observed in liquids,<sup>1</sup> which is believed to result from very rapid relaxation due to inefficient quenching<sup>2</sup> of the orbital angular momentum (which gives rise to anisotropy in the  $g$ -tensor). In the gas phase the ground state is known to be  $^2\Pi_{3/2}$ , which is further split due to interaction of the orbital motion of the electron and the rotation of the nuclei ( $\Lambda$ -doubling).

Spin lattice relaxation ( $T_1$ ) occurs when an applied or local magnetic field interacts with an electron spin at the Larmor precession frequency  $\omega_0$ .  $T_2$  relaxation involves randomisation of the phases of the spin precession, which arises due to fluctuations in the local magnetic fields. One such mechanism which can give rise to both  $T_1$  and  $T_2$  relaxation is the rapid tumbling of the molecule in the solvent, where constant perturbations in the local magnetic fields interact with the magnetic moment of the spin and give rise to  $T_2$  relaxation. If tumbling occurs with a rate  $\omega_0$  then  $T_1$  can take place as well.

The time taken for a molecule to rotate by one radian is usually referred to as the rotational correlation time ( $\tau_c$ ). This parameter typically depends on the properties of the molecule, solvent viscosity ( $\eta$ ) and temperature ( $T$ ) [19]. A value for  $\tau_c$  of 2.5 ps has been reported for water at 298 K [20, 21]. In the literature, Brocklehurst has investigated the relationship between the spin relaxation time and  $\tau_c$  [19] making use of the parameters for  $\cdot\text{OH}$  in ice [22]. He found that the contribution from the Zeeman and hyperfine terms to spin relaxation can be calculated as [19]

$$\frac{1}{T_2} = \mu_B^2 B_0^2 (g:g) [(2/15)j_0 + (1/10)j_1] + (A^\circ:A^\circ)(7/120)j_0 + (1/12)j_1 \quad (5.1)$$

$$\frac{1}{T_1} = \mu_B^2 B_0^2 (g:g)(1/5)j_1 + (A^\circ:A^\circ)(1/20)j_1 \quad (5.2)$$

where  $B_0$  is the external field,  $\mu_B$  the Bohr magneton,  $j_0 = \tau_c$ ,  $j_1 = \tau_c(1 + \omega_0^2 \tau_c^2)^{-1}$ ,  $\omega_0 = g\mu_B B_0/\hbar$  (Larmor frequency),  $(g:g)$  and  $(A^\circ:A^\circ)$  are the inner products of the tensors of  $g$  and  $A^\circ$  (which represent deviations from the mean value of the  $g$ -factor and the hyperfine terms respectively). At high fields the first terms dominates in Eqs. (5.1) and (5.2), whilst at zero field only the second terms in Eqs. (5.1) and (5.2) are applicable with  $j_1 = j_0$ .<sup>3</sup>

Spin rotation interaction can also provide another mechanism by which the hydroxyl radical can undergo spin relaxation due to the anisotropy of the  $g$ -tensor, in which relaxation could occur via the Zeeman interaction. The rate of spin relaxation via this mechanism has been found to be [19]

<sup>1</sup> The EPR spectrum of  $\cdot\text{OH}$  can only be observed when trapped in solids or ice-crystals.

<sup>2</sup> In the hydroxyl radical, the orbital motion of the electron is mostly quenched by interactions such as hydrogen bonding.

<sup>3</sup> It should be cautioned that Eqs. (5.1) and (5.2) are applicable only for high field and it is not strictly correct to apply these to the zero field case.

$$\frac{1}{T_1} = \frac{1}{T_2} = (1/9)(\Delta g:\Delta g)\tau_c^{-1} \quad (5.3)$$

where  $\Delta g$  measures the difference in the  $g$ -value from the free electron value. Equation (5.3) shows that in the spin-rotation relaxation mechanism, the parameters  $T_1$  are equal  $T_2$  and independent of the external static field, so long as  $\tau_c$  occurs at a rate much faster than the Larmor frequency. Clearly this condition will not be true at large values of the external static field.

Equation (5.3) is not valid when  $\Delta g$  is large [23, 24] and it has been shown in the literature how Eq.(5.3) can be understood in terms of the ‘adiabatic rotation of effective spin orientations’ (ARES) [23, 24]. The authors show that the term  $(\Delta g:\Delta g)$  in Eq. (5.3) should be replaced by the  $\gamma$  tensor (which relates  $\mathbf{L} + \mathbf{S}$  to  $\mathbf{S}^{\text{eff}}$ , with  $\mathbf{S}^{\text{eff}}$  representing the effective spin angular momentum,  $\mathbf{L}$  and  $\mathbf{S}$  are the vector operators of the orbital and spin angular momentum respectively). The  $\gamma$  tensor therefore is a measure of how effectively  $\mathbf{S}^{\text{eff}}$  follows the molecular axis. Only in the weak spin-orbit coupling case (i.e. where the effective spin follows the rotation of the molecular axis weakly) does the traditional spin-rotation Hamiltonian follow the ARES Hamiltonian.<sup>4</sup> (i.e. Eq. (5.3) is obtained.)

Brocklehurst [19] found that  $T_1$  and  $T_2$  should be proportional to  $\tau_c$ , which will increase with the solvent viscosity ( $\eta$ ). Both  $T_1$  and  $T_2$  are independent of the field until  $\eta \sim 1 \text{ kg m}^{-1} \text{ s}^{-1}$  and it is predicted that at higher viscosities  $T_2$  tends to decrease whilst  $T_1$  will increase with the applied field, relative to zero field. In ice, the observed line-width for  $\cdot\text{OH}$  is found to provide a lower limit for  $T_2$  of 50 ns [22] but unfortunately no value for  $T_1$  is known. It can however be approximated as  $T_1 \sim 1,000 \times T_2$  [25] as generally found for radicals trapped in solids. In mobile liquids however (where  $\omega_0\tau_c < 1$ ),  $T_1 \approx T_2$ . This will be reflected in the computational model developed for the chemical system under study in the next section.

## 5.3 Computational Model of the Kinetics

### 5.3.1 Diffusion Controlled

The complete reaction scheme for the proposed system is shown below, which highlights the different kinetic events that can occur. Within the IRT framework, the geminate recombination times ( $T_{g1}$ ,  $T_{g2}$  and  $T_{g3}$ ) can be generated according to Eq. (4.36) and scavenging times ( $S_1$  and  $S_2$ ) according to Eq.(4.38).  $T_{g1}$  is the  $\cdot\text{OH} + \cdot\text{OH}$  recombination time, whilst  $S_1$  and  $S_2$  are the first and second scavenging times respectively. If scavenging happens first, it is necessary to generate  $T_{g2}$  to model the possible recombination of  $\text{R}\cdot + \cdot\text{OH}$ . However, if  $S_2$  happens before the  $T_{g2}$  event, it becomes necessary to generate a further time  $T_{g3}$  for the  $\text{R}\cdot + \text{R}\cdot$  recombination. For the purpose of this work, the chemical species  $\text{R}\cdot$  is given the characteristic properties

<sup>4</sup> The ARES Hamiltonian is valid for any arbitrary strength of spin-orbit coupling.

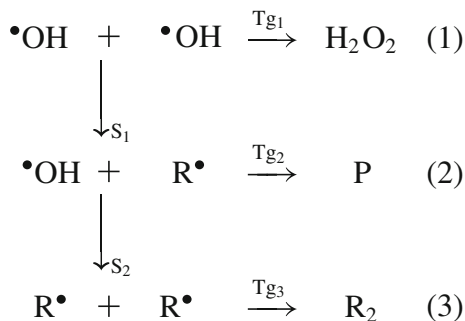


**Fig. 5.3** Reaction scheme employed in this work to model the spin polarisation on the escaped  $\text{R}\bullet$  radicals. In this scheme,  $S_1$  and  $S_2$  are the first and second scavenging times respectively;  $T_{g1}$ ,  $T_{g2}$  and  $T_{g3}$  are the recombination times to form the products  $\text{H}_2\text{O}_2$ ,  $\text{P}$  and  $\text{R}_2$  respectively. In this reaction scheme  $\text{R}\bullet$  is given the characteristic properties of 2-propanolyl radicals

of  $(\text{CH}_3)_2\text{C}\bullet\text{OH}$ . No kinetic or spin parameters are assigned to  $\text{P}$  or  $\text{R}_2$  as these are the final products. The flow diagram for the IRT algorithm used to simulate the chemical system is shown in the Appendix (Fig. C.5 in Sect. C.5), which highlights the key events involved.

Although analytical computation of the system under study is not possible (due to the random scavenging events), it is however, possible to analytically calculate the average formation of  $\text{H}_2\text{O}_2$ . This allows the IRT algorithm to be tested for the recombination kinetics and ensure that no bias has been introduced by making the independent pairs approximation. The derivation now proceeds as follows: letting  $P_2 = 2[\bullet\text{OH}]$ , the survival probability subject to scavenging and recombination is then

$$\begin{aligned}
 \frac{dP_2}{dt} &= -wP_2 - 2kcP_2 \\
 P_2 &= e^{-\int_0^t w dt} e^{-2kct} \\
 P_2 &= \Omega e^{-2kct}
 \end{aligned} \quad (5.4)$$

where  $w$  is the first passage time density for the hydroxyl radicals to recombine,  $k$  is the steady state rate constant for scavenging of the hydroxyl radical,  $c$  the concentration of scavengers and  $\Omega(t)$  is the survival probability expressed as  $\Omega(t) = \exp(-\int_0^t w dt)$ . Hence, the rate of formation of  $[\text{H}_2\text{O}_2]$  is then simply

$$\begin{aligned}
 \frac{d[\text{H}_2\text{O}_2]}{dt} &= wP_2 \\
 &= w\Omega e^{-2kct} \\
 [\text{H}_2\text{O}_2] &= \int_0^t w e^{-\int_0^{t'} w dt''} e^{-2kct'} dt'
 \end{aligned} \quad (5.5)$$

The above integral can be evaluated by parts to give

$$[\text{H}_2\text{O}_2] = [1 - e^{-2kct} \Omega]_0^t - 2kc \int_0^t \Omega e^{-2kct'} dt' \quad (5.6)$$

$$= e^{-2kct} (1 - \Omega) + 2kc \frac{a}{r} \int_0^t e^{-2kct} \operatorname{erfc} \left( \frac{r-a}{\sqrt{4D't}} \right) dt \quad (5.7)$$

where  $r$ ,  $a$  and  $D'$  are the initial separation distance, encounter radius and mutual diffusion coefficient respectively. Letting  $\alpha = 2kc$  and  $\beta = (r-a)/\sqrt{4D'}$ , the above integral can be evaluated by parts to give

$$\begin{aligned} \int e^{-\alpha t} \operatorname{erfc} \left( \frac{\beta}{\sqrt{t}} \right) dt &= -\frac{1}{\alpha} e^{-\alpha t} \operatorname{erfc} \left( \frac{\beta}{\sqrt{t}} \right) \\ &+ \frac{1}{2\alpha} \left[ e^{2\beta\sqrt{\alpha}} \operatorname{erfc} \left( \frac{\beta}{\sqrt{t}} + \sqrt{\alpha t} \right) + e^{-2\beta\sqrt{\alpha}} \operatorname{erfc} \left( \frac{\beta}{\sqrt{t}} - \sqrt{\alpha t} \right) \right] \end{aligned} \quad (5.8)$$

Substituting the above integral into Eq.(5.7) gives the analytical solution for the  $[\text{H}_2\text{O}_2]$  to be

$$\begin{aligned} [\text{H}_2\text{O}_2] &= \frac{a}{2r} e^{-(r-a)\sqrt{\frac{2kc}{D'}}} \operatorname{erfc} \left( \frac{r-a}{\sqrt{4D't}} + \sqrt{2kct} \right) \\ &+ \frac{a}{2r} e^{-(r-a)\sqrt{\frac{2kc}{D'}}} \operatorname{erfc} \left( \frac{r-a}{\sqrt{4D't}} - \sqrt{2kct} \right) \end{aligned} \quad (5.9)$$

### 5.3.2 Partially Diffusion Controlled

The Arrhenius plot for the self-recombination of hydroxyl radicals as calculated by Buxton and Elliot [26] shows the deviation of  $k_{\text{diff}}$  (diffusion controlled rate constant) from  $k_{\text{obs}}$  with increasing temperature, suggesting that the self-recombination of the hydroxyl is indeed partially diffusion controlled for a wide temperature range. The Arrhenius plot for the self-recombination of 2-propanol radicals as a function of temperature highlight that  $2k_{\text{obs}} \neq 2k_{\text{diff}}$  at the temperature range investigated by the authors [27]. As shown in Table 5.1, if the  $\text{R}^\cdot + \text{R}^\cdot$  reaction is assumed to be diffusion controlled with a spin factor of  $\sigma_{\text{S}} = 1/4$ , then  $2k_{\text{diff}}$  is still much larger than  $2k_{\text{obs}}$ , which suggests partially diffusion controlled conditions. The activation energy calculated experimentally for this reaction was found to be  $18.8 \pm 1.2 \text{ kJ mol}^{-1}$ . Although  $2k_{\text{diff}}$  also has a similar magnitude for the activation energy, the reaction cannot be diffusion controlled since  $2k_{\text{obs}} \neq 2k_{\text{diff}}$ . Hence Mezyk and Madden [27]

**Table 5.1** Experimental rate constants for the self-recombination of 2-propanol in aqueous solution [27]

Temperature (K)	$10^{-9} 2k_{\text{obs}} (\text{M}^{-1} \text{s}^{-1})$	$10^{-9} 2k_{\text{diff}} (\text{M}^{-1} \text{s}^{-1})$	$10^{-9} 2k_{\text{react}} (\text{M}^{-1} \text{s}^{-1})$
278	$0.89 \pm 0.24$	2.49	$1.38 \pm 0.58$
288	$1.15 \pm 0.10$	3.34	$1.75 \pm 0.23$
299	$1.56 \pm 0.10$	4.41	$2.41 \pm 0.24$
308	$1.75 \pm 0.18$	5.54	$2.56 \pm 0.38$
315	$1.98 \pm 0.28$	6.50	$2.85 \pm 0.58$
324	$3.02 \pm 0.45$	7.91	$4.88 \pm 1.18$
344	$4.18 \pm 0.64$	12.0	$6.41 \pm 1.51$

concludes that reactivity ( $k_{\text{react}}$ ) and not diffusion ( $k_{\text{diff}}$ ) is the main process for the self-recombination of 2-propanol radicals in water.

In both the  $\cdot\text{OH} + \cdot\text{OH}$  and  $\text{R}\cdot + \text{R}\cdot$  cases, a realistic description of the chemical kinetics entails treating these reactions as partially diffusion controlled which employs the radiation boundary conditions. For comparative purposes, all reactions will be treated as both diffusion controlled and partially diffusion controlled in this work to investigate what effect this has on the observed polarisation phases.

## 5.4 Computational Model for the Spin Dynamics

The Hamiltonian used for the evolution of the spin wavefunction is given by

$$\hat{H} = \sum_i g_i \mu_B B_0 \hat{S}_{iz} + \sum_i a_{1i} \hat{S}_1 \cdot \hat{I}_{1i} + \sum_j a_{2j} \hat{S}_2 \cdot \hat{I}_{2j} + \sum_{i>j} -J_{ij}(r_{ij}) \left( 2\hat{S}_i \cdot \hat{S}_j + \frac{1}{2} \right) \quad (5.10)$$

where  $g$  is the electron  $g$ -factor,  $\mu_B$  the Bohr magneton,  $B_0$  the external magnetic field,  $\hat{S}$  and  $\hat{I}$  representing the electron and nuclear spin operator respectively. The first term accounts for the interaction of the unpaired electron spin to interact with the external magnetic field (Zeeman interaction); the second and third terms account for the interaction of the magnetic nuclei and the electron spins (hyperfine interaction); the fourth term accounts for the spin-exchange interaction between the electrons and is one of the predominant mechanisms responsible for producing spin polarisation. In the system under study, the size of the basis set is  $2^4$  which incorporates one nuclear and electron spin on each of the two radicals, and is set up as  $|n_1 n_2 e_1 e_2\rangle$  unless otherwise stated.

The form of the exchange interaction implemented into the Hamiltonian assumes it is independent of the molecular orientation and is only affected by the interparticle separation. It is usual practice to parameterise  $J_{ij}$  as an exponential of the form

$$J_{ij}(r_{ij}) = J_0 e^{-\alpha(r_{ij}-a)} \quad (5.11)$$

where  $J_0$  is the exchange strength (typically ranging from  $-0.15$  to  $-3.37$  ps $^{-1}$  [28]),  $\alpha$  the range parameter (typically ranging from  $1.06$  to  $1.9$  Å $^{-1}$  [28]),  $r_{ij}$  the interparticle separation and  $a$  the encounter distance. The sign of  $J_0$  determines whether the singlet or triplet state is higher in energy, with  $E_{\text{triplet}} > E_{\text{singlet}}$  for negative  $J_0$  and the contrary being true for a positive  $J_0$ .

Modelling the hyperfine interaction of every individual proton with the unpaired electron is not feasible as the size of the basis set would grow considerably (i.e. with seven nuclear spins and one electron spin the basis set would be  $2^8$ ). Instead, for the purpose of this study an effective hyperfine interaction [29, 30] is employed, which models the *average* hyperfine interaction felt by the unpaired electron in the presence of six protons using the relation

$$a_{\text{eff}} = \sqrt{\sum_i a_i^2 I_i(I_i + 1)} \quad (5.12)$$

where  $a_{\text{eff}}$  is the effective hyperfine constant,  $a_i$  the hyperfine coupling constant and  $I_i$  the nuclear spin on radical  $i$ . Hence, in the simulated EPR spectrum a doublet is produced which is separated by the hyperfine frequency instead of the septet as seen by the experimentalists. The high field signal will be observed at the frequency  $f = (B_0 g \mu_B / \hbar - a_{\text{eff}} / 2\hbar)$  and similarly the low field signal will be observed at  $f = (B_0 g \mu_B / \hbar + a_{\text{eff}} / 2\hbar)$ . Using the spin parameters listed in Table 5.3,  $a_{\text{eff}}$  was calculated to be  $4.18$  mT for the R' radical. This gives the high and low field hyperfine transitions on the escaped R' (where  $J(r) = 0$ ) to be  $f = 5.79 \times 10^{10}$  rad s $^{-1}$  (9.23 GHz) and  $f = 5.83 \times 10^{10}$  rad s $^{-1}$  (9.28 GHz) respectively.

### 5.4.1 Singlet–Triplet Probabilities

In the simulation it is necessary to extract the singlet character of the wavefunction to determine whether reaction can take place (for the purpose of this work the triplet state is unreactive). This can readily be achieved by converting from the Zeeman basis to the ST-basis using the transformation matrix ( $P$ ),<sup>5</sup> which for a fixed nuclear spin state is

$$\begin{pmatrix} c_{n_1 n_2 T_{+1}} \\ c_{n_1 n_2 T_0} \\ c_{n_1 n_2 S} \\ c_{n_1 n_2 T_{-1}} \end{pmatrix} = \begin{pmatrix} 1 & 0 & 0 & 0 \\ 0 & \frac{1}{\sqrt{2}} & \frac{1}{\sqrt{2}} & 0 \\ 0 & \frac{1}{\sqrt{2}} & -\frac{1}{\sqrt{2}} & 0 \\ 0 & 0 & 0 & 1 \end{pmatrix} \begin{pmatrix} c_{n_1 n_2 \alpha\alpha} \\ c_{n_1 n_2 \alpha\beta} \\ c_{n_1 n_2 \beta\alpha} \\ c_{n_1 n_2 \beta\beta} \end{pmatrix} \quad (5.13)$$

<sup>5</sup> For convenience the matrix  $P$  shown in Eq. (5.13) has been restricted to a  $4 \times 4$  size to allow the change of basis method to be demonstrated. In the simulation, matrix  $P$  is  $16 \times 16$  allowing all of the coefficients in the Zeeman basis to be converted in one passing.

where the left hand side represent the coefficients in the new ST-basis, with  $n_i$  denoting the nuclear spin on radical  $i$ . The singlet probability for a reacting pair is then calculable as follows

$$\text{Pr}(\text{singlet}) = \sum_{i=1}^n |c_{iS}|^2 \quad (5.14)$$

where the summation is over all possible nuclear spin configurations. A similar procedure can be applied to convert the density matrix  $\rho(t)$  (Zeeman basis) to  $\rho_{ST}$  (ST-basis) as

$$\rho^{ST}(t) = P\rho(t)P \quad (5.15)$$

with the singlet component given as (summing over all possible nuclear spin configurations)

$$\text{Pr}(\text{singlet}) = \sum_{i=1}^n \rho_{iS,iS}^{ST}(t) \quad (5.16)$$

### 5.4.2 Spin Evolution and Relaxation: The Wavefunction Approach

To evolve the wavefunction with a certain Hamiltonian (which is time-independent), it is necessary to solve the time dependent Schrödinger equation of the form

$$i\hbar \frac{\partial \psi}{\partial t} = \hat{H} \psi \quad (5.17)$$

which gives the general solution in the Zeeman basis as

$$\psi(t) = e^{-i\hat{H}t/\hbar} \psi(0) \quad (5.18)$$

where  $\psi(t)$  and  $\psi(0)$  are a vector of coefficients at  $t > 0$  and  $t = 0$  respectively in the Zeeman basis.

As the Hamiltonian for the system is not diagonal, taking its exponential is not straightforward and may be approximated by expanding the term  $\exp(-i\hat{H}t/\hbar)$  as an exponential series and truncating at an acceptable level of accuracy. An analytical treatment would involve diagonalising the Hamiltonian and evolving the wavefunction within this basis for every time step. The basic recipe is as follows: find the set of eigenvectors which diagonalises the Hamiltonian to calculate the diagonal matrix  $E$  as

$$E = U^T H U \quad (5.19)$$

where  $U$ ,  $U^T$  are the eigenvectors and transpose of the eigenvectors of the Hamiltonian ( $H$ ) respectively. As the Hamiltonian is symmetric,  $U^T U = I$ , where  $I$  is the identity

matrix. Then the Hamiltonian can be rewritten in the diagonal basis as

$$H = U E U^T \quad (5.20)$$

Using this expression for  $H$ , the time dependent Schrödinger equation becomes

$$i \hbar \frac{\partial \psi}{\partial t} = U E U^T \psi \quad (5.21)$$

multiplying both sides by  $U^T$  gives

$$i \hbar \frac{\partial (U^T \psi)}{\partial t} = E (U^T \psi) \quad (5.22)$$

Letting  $\bar{y} = U^T \psi$ , the Schrödinger equation can be rewritten as

$$i \hbar \frac{\partial \bar{y}}{\partial t} = E \bar{y} \quad (5.23)$$

The solution for  $\bar{y}$  in this basis is then simply

$$\bar{y}(t) = e^{-iEt/\hbar} \bar{y}(0) \quad (5.24)$$

Hence, the vector  $\bar{y}(t)$  is propagated with the diagonal matrix  $E$  with respect to the vector of coefficients,  $\bar{y}(0)$ . The two basis vectors can be converted from the Zeeman basis ( $\psi$ ) to the diagonal basis ( $\bar{y}$ ) and vice versa using the relation  $\psi = U \bar{y}$  and  $\bar{y} = U^T \psi$  respectively. The above analysis is based under the assumption that the Hamiltonian is time-independent. However, the exchange interaction parameter  $J(r)$  varies with the particle position making the Hamiltonian time-dependent. In the simulation to counteract this problem, it becomes necessary to take small time steps to ensure  $J(r)$  does not change substantially. Under this constraint the above methodology becomes valid.

#### 5.4.2.1 Spin Relaxation to a Uniform Distribution

The chemical system under study requires a description of spin-relaxation on the hydroxyl radicals, as it is this parameter which is hypothesised to produce the observed polarisation phase. For the purpose of this work a new algorithm has been developed to model this effect using the wavefunction of the system (as first suggested by B. Brocklehurst, unpublished), which requires far fewer computational resources than a traditional density matrix calculation would typically utilise, allowing many more realisations to be computed (required to obtain acceptable statistics in the spin polarisation). This has not been previously attempted with a random flights or IRT simulation.

In the algorithm, a  $T_1$  relaxation event involves a permutation of the coefficients of the spin states and a  $T_2$  involves using a dephasing factor between these spin states. Spin relaxation is therefore treated by selecting a random event time (for the IRT case) or else allowing relaxation with a given probability at each time step (for the random flights case). In the simulation packages, spin relaxation is modelled as a single event which occurs concurrently with other processes such as scavenging and recombination.

To illustrate the algorithm, consider a wavefunction set up as  $|n_1 n_2 e_1 e_2\rangle$ , (with  $n_1, n_2, e_1, e_2$  representing the nuclear and electron spins on radicals 1 and 2 respectively)

$$\psi(t) = c_1 |n_1 n_2 \alpha \alpha\rangle + c_2 |n_1 n_2 \alpha \beta\rangle + c_3 |n_1 n_2 \beta \alpha\rangle + c_4 |n_1 n_2 \beta \beta\rangle \quad (5.25)$$

In the random flights simulation, at time  $(t + \delta t)$  a random number  $U(0, 1]$  is generated from a uniform distribution<sup>6</sup> and is compared to  $(1 - e^{-\delta t / T_{Ri}})$ , where  $T_{Ri}$  is the relaxation time of the radical  $i$ . If  $U(0, 1] < (1 - e^{-\delta t / T_{Ri}})$ , then spin relaxation takes place via a simple permutation of the coefficients of the wavefunction. For example if spin relaxation occurred on radical 1 then the wavefunction in Eq. (5.25) becomes

$$\psi(t + \delta t) = c_3 |n_1 n_2 \alpha \alpha\rangle + c_4 |n_1 n_2 \alpha \beta\rangle + c_1 |n_1 n_2 \beta \alpha\rangle + c_2 |n_1 n_2 \beta \beta\rangle \quad (5.26)$$

Similarly, spin relaxation on radical 2 gives

$$\psi(t + \delta t) = c_2 |n_1 n_2 \alpha \alpha\rangle + c_1 |n_1 n_2 \alpha \beta\rangle + c_4 |n_1 n_2 \beta \alpha\rangle + c_3 |n_1 n_2 \beta \beta\rangle \quad (5.27)$$

For the IRT simulation, an event time ( $\tau_i$ ) is generated for spin relaxation such that  $\tau = \ln U(0, 1] T_{Ri}$  for each radical  $i$ . If  $\tau_i$  is found to be the minimum event time, then relaxation occurs on radical  $i$  and another  $\tau_i$  is generated by sampling from the same probability distribution function. Hence, the effect of  $T_1$  spin relaxation for radical 1 and 2 can be written in matrix notation respectively as

$$\psi(t + \delta t) = \begin{pmatrix} 0 & 0 & 1 & 0 \\ 0 & 0 & 0 & 1 \\ 1 & 0 & 0 & 0 \\ 0 & 1 & 0 & 0 \end{pmatrix} \psi(t) \quad \psi(t + \delta t) = \begin{pmatrix} 0 & 1 & 0 & 0 \\ 1 & 0 & 0 & 0 \\ 0 & 0 & 0 & 1 \\ 0 & 0 & 1 & 0 \end{pmatrix} \psi(t) \quad (5.28)$$

$T_2$  relaxation is the randomisation of the phase of the wavefunction due to fluctuating local fields. It is assumed that the phase of an  $\alpha$  spin is altered by  $\exp(i\phi)$  where  $\phi$  is a random angle between 0 and  $2\pi$ , with a  $\beta$  spin altered by phase factor  $\exp(-i\phi)$ . The computational set up for modelling  $T_2$  relaxation is analogous to that shown for  $T_1$  relaxation, except the spin wavefunction is now modified according to Eqs. (5.29) or (5.30) for relaxation on radicals 1 and 2 respectively.<sup>7</sup>

<sup>6</sup> A uniformly distributed random number is required for each radical.

<sup>7</sup> In Eqs. (5.29) and (5.30)  $U_1 - U_4$  are four uniformly distributed random numbers in the range (0,1].

For the system under study, both  $T_1$  and  $T_2$  events are modelled to occur simultaneously, such that the spin wavefunction is modified by both a permutation of the coefficients ( $T_1$ ) [as described by Eq. (5.28)], and by the random dephasing of the spins ( $T_2$ ) [as described by Eqs. (5.29), (5.30)].

$$\psi(t + \delta t) = \begin{pmatrix} e^{iU_1(0,1]2\pi} & 0 & 0 & 0 \\ 0 & e^{iU_2(0,1]2\pi} & 0 & 0 \\ 0 & 0 & e^{-iU_3(0,1]2\pi} & 0 \\ 0 & 0 & 0 & e^{-iU_4(0,1]2\pi} \end{pmatrix} \psi(t) \quad (5.29)$$

$$\psi(t + \delta t) = \begin{pmatrix} e^{iU_1(0,1]2\pi} & 0 & 0 & 0 \\ 0 & e^{-iU_2(0,1]2\pi} & 0 & 0 \\ 0 & 0 & e^{iU_3(0,1]2\pi} & 0 \\ 0 & 0 & 0 & e^{-iU_4(0,1]2\pi} \end{pmatrix} \psi(t) \quad (5.30)$$

#### 5.4.2.2 Stochastic Treatment of a Spin- $\frac{1}{2}$ Particle in a Fluctuating Transverse Field

In this section, Redfield's theory of spin relaxation in the presence of a fluctuating transverse field is formulated in such a way that it can be included in a simulation using stochastic theory which utilises the wavefunction of the chemical system. Although the method of simulating relaxation as a discrete event on  $\psi$  is plausible (as described in the previous section), it is nevertheless important to compare this method with more usual methods to ensure no errors have been introduced.

The Hamiltonian for a spin- $\frac{1}{2}$  particle in a static field along the  $z$ -direction (with a Larmor frequency  $\omega_0$ ) with fluctuating transverse fields ( $\omega_x(t)$  and  $\omega_y(t)$ ) can be described by the Hamiltonian

$$\hat{H}(t) = -\omega_0 \hat{S}_z - \omega_x(t) \hat{S}_x - \omega_y(t) \hat{S}_y \quad (5.31)$$

which can be rewritten in terms of the ladder operators as

$$\hat{H}(t) = -\hat{S}^+ \left[ \frac{1}{2} \omega_x(t) - \frac{1}{2} i \omega_y(t) \right] - \hat{S}^- \left[ \frac{1}{2} \omega_x(t) + \frac{1}{2} i \omega_y(t) \right] - \omega_0 \hat{S}_z \quad (5.32)$$

where  $S^+$  and  $S^-$  are the spin raising and lower operators respectively. Assuming an exponential model for the correlation time, the fluctuating fields are taken to be uncorrelated Gaussian random variables such that

$$\langle \omega_x(t) \omega_x(0) \rangle = \langle \omega_y(t) \omega_y(0) \rangle = B \lambda \exp^{-\lambda|t|} \quad (5.33)$$

where  $1/\lambda$  is the correlation time of the fluctuations and  $B$  is proportional to the strength of the mean-square fluctuations (with units of frequency). The fluctuating

random fields (along the  $x$ ,  $y$  directions) can then be generated by sampling from the probability density of the conditioned bivariate normal distribution

$$f(\omega_q(t)|\omega_q(t - \delta t)) = \frac{\exp\left[-\frac{(\omega_q(t) - \Phi\kappa y)^2}{2\sigma_{\omega_q(t)}^2}\right]}{\sqrt{2\pi}\sqrt{(1 - \Phi^2)\sigma_{\omega_q(t)}}} \quad (5.34)$$

where  $\kappa = \left(\frac{\sigma_{\omega_q(t)}}{\sigma_{\omega_q(t - \delta t)}}\right)$ ,  $q = x$  or  $y$ ,  $\sigma_{\omega_q}$  is the standard deviation of the random variable  $\omega_q$ , and  $\Phi$  is the correlation coefficient. In a typical Monte Carlo random flights simulation, for every time step ( $\delta t$ ) taken, two conditioned normally distributed random variables  $N(\mu, \sigma)$  need to be generated to represent the fluctuating fields along the  $x$  and  $y$  directions. For a conditioned bivariate distribution, the conditioned mean ( $\mu$ ) and standard deviation ( $\sigma$ ) take the form

$$\mu = \Phi\omega_q(t - \delta t) \quad (5.35)$$

$$\sigma = \sqrt{(1 - \Phi^2)\sigma_{\omega_q(t)}} \quad (5.36)$$

In the example considered  $\sigma_{\omega_q(t)}^2 = B\lambda$  and the correlation coefficient ( $\Phi$ ) during each time step is simply  $\exp(-\lambda|\delta t|)$ . For all results presented  $\omega_0 = 1$  and all frequencies are reported in units of  $\omega_0$  and all times in units of  $1/\omega_0$ . Letting the initial wavefunction have the coefficients for the ground and excited state of  $[(2 + \sqrt{2})/4]^{1/2}$  and  $[(2 - \sqrt{2})/4]^{1/2}$  respectively, it can be seen that this model gives non-exponential relaxation under some parameter regimes (Fig. 5.4). Comparing this simulation model for a single spin with that developed by Aihara et al. [31] which uses the density matrix method, it can be seen from Fig. 5.4 that essentially spin relaxation can be accurately modelled using the wavefunction of the system. All characteristics of the oscillations of  $W(t)$  (population difference between the ground and excited states) are reproduced as well as the non-Markovian (non-exponential) relaxation using different correlation times and strengths of the coupling constants. The oscillations seen in Fig. 5.4 arise because when  $t$  is less than the correlation time, the Hamiltonian appears static and since it is not diagonal in the Zeeman basis, the population difference oscillates at roughly the Rabi frequency  $\bar{\Omega} = (\omega_0^2 + 2B\lambda)^{1/2}$ . Hence, transverse random fields not only damp the oscillations of the spin-system but also mix the two spin states in a partially coherent manner.

### 5.4.3 Spin Evolution and Relaxation: The Density Matrix Approach

In this section spin relaxation is investigated using the density matrix formalism to ensure no significant errors have been introduced by treating relaxation as a discrete event as described in Sect. 5.4.2.1.

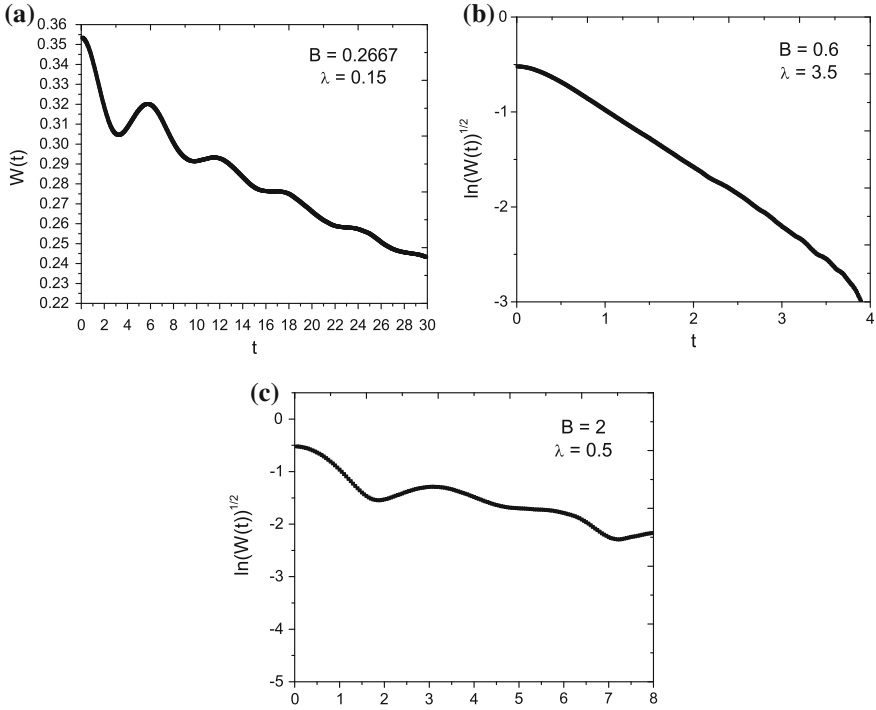


**Fig. 5.4** Non-Markovian spin relaxation obtained using the stochastic approach. A value for the Larmor frequency  $\omega_0 = 1$  was used, with  $B$  and  $\lambda$  having units of  $\omega_0$

Treating  $T_1$  spin relaxation using the density matrix involves setting up a rate equation for the diagonal elements and then solving the required coupled partial differential equations for the time evolution [32]. Assuming no nuclear spins for simplicity and the basis set to comprise of the eigenstates  $|\alpha\alpha\rangle$ ,  $|\alpha\beta\rangle$ ,  $|\beta\alpha\rangle$ ,  $|\beta\beta\rangle$ , the rate equations used to model  $T_1$  spin relaxation can be expressed as

$$\begin{aligned}
 \frac{\partial \rho_{11}}{\partial t} &= \frac{(\rho_{22} - \rho_{11}) - (\rho_{22}(T) - \rho_{11}(T))}{\tau_1(2)} + \frac{(\rho_{33} - \rho_{11}) - (\rho_{33}(T) - \rho_{11}(T))}{\tau_1(1)} \\
 \frac{\partial \rho_{22}}{\partial t} &= \frac{(\rho_{11} - \rho_{22}) - (\rho_{11}(T) - \rho_{22}(T))}{\tau_1(2)} + \frac{(\rho_{44} - \rho_{22}) - (\rho_{44}(T) - \rho_{22}(T))}{\tau_1(1)} \\
 \frac{\partial \rho_{33}}{\partial t} &= \frac{(\rho_{44} - \rho_{33}) - (\rho_{44}(T) - \rho_{33}(T))}{\tau_1(2)} + \frac{(\rho_{11} - \rho_{33}) - (\rho_{11}(T) - \rho_{33}(T))}{\tau_1(1)} \\
 \frac{\partial \rho_{44}}{\partial t} &= \frac{(\rho_{33} - \rho_{44}) - (\rho_{33}(T) - \rho_{44}(T))}{\tau_1(2)} + \frac{(\rho_{22} - \rho_{44}) - (\rho_{22}(T) - \rho_{44}(T))}{\tau_1(1)}
 \end{aligned} \tag{5.37}$$

where  $\rho(T)$  is the thermal equilibrium matrix, which for the system under study has diagonal elements equal to  $(1/16)$  with zero off-diagonal elements;  $\tau_1(1)$  and  $\tau_1(2)$  denote the spin relaxation times on radical one and two respectively. The loss in coherence ( $T_2$  relaxation) can be treated in a similar manner as

$$\frac{\partial \rho_{jk}}{\partial t} = -\frac{\rho_{jk}}{\tau_2(k)} \quad (5.38)$$

for decoherence in which only one electron spin changes (i.e.  $\alpha\alpha \rightarrow \beta\alpha$ ). For decoherence between two spins (such as  $\alpha\alpha \rightarrow \beta\beta$ ), the above equation can be extended as

$$\frac{\partial \rho_{jk}}{\partial t} = -\left(\frac{\rho_{jk}}{\tau_2(j)} + \frac{\rho_{jk}}{\tau_2(k)}\right) \quad (5.39)$$

Extending this scheme for the system under study, the complete coupled partial differential equation can be written as

$$\frac{\partial \rho}{\partial t} = -\frac{i}{\hbar}[\hat{H}, \rho] + M(\rho - \rho(T)) \quad (5.40)$$

where the first term is known as the Liouville operator which evolves the density matrix with a given Hamiltonian and  $M$  is the relaxation matrix. Equation (5.40) is known as the *stochastic Liouville equation*. Finding a solution to Eq. (5.40) is complicated for two reasons: (i) the Hamiltonian is not diagonal for the system under study and (ii) Eq. (5.40) cannot be decoupled by finding a set of orthogonal eigenvectors because of the spin relaxation matrix  $M$ , which may not necessarily be diagonal in this basis. One approach for a full analytical solution is to stretch the density matrix into a vector and rewrite Eq. (5.40) in terms of the Liouville operator as

$$\frac{\partial \bar{\rho}}{\partial t} = \frac{i}{\hbar}L\bar{\rho} + M^*(\bar{\rho} - \bar{\rho}(T)) \quad (5.41)$$

where the overbar indicates the vectorisation of the density matrix and  $M^*$  is the modified spin relaxation matrix. Matrices  $L$  and  $M^*$ , both being of the same dimension can be combined for  $\bar{\rho}$  to give a new matrix  $\Lambda$  (noting that matrix  $\Lambda$  is a complex symmetric matrix with orthogonal complex eigenvectors). Equation (5.41) then becomes

$$\frac{\partial \bar{\rho}}{\partial t} = \Lambda\bar{\rho} - M^*\bar{\rho}(T) \quad (5.42)$$

Taking the integrating factor  $\exp(-\Lambda t)$ , Eq. (5.42) can now be solved by elementary means as follows

$$\begin{aligned}
\frac{\partial \bar{\rho}}{\partial t} - \Lambda \bar{\rho} &= -M^* \bar{\rho}(T) \\
\frac{\partial}{\partial t} (e^{-\Lambda t}) \bar{\rho} &= -e^{-\Lambda t} M^* \bar{\rho}(T) \\
e^{-\Lambda t} \bar{\rho} - \bar{\rho}(0) &= -M^* \bar{\rho}(T) \int_0^t e^{-\Lambda t} dt \\
&= \left[ \Lambda^{-1} e^{-\Lambda t} \right]_0^t M^* \bar{\rho}(T) \\
&= -\Lambda^{-1} (I - e^{-\Lambda t}) M^* \bar{\rho}(T) \\
\bar{\rho}(t) &= e^{\Lambda t} \bar{\rho}(0) - \Lambda^{-1} (e^{\Lambda t} - I) M^* \bar{\rho}(T) \tag{5.43}
\end{aligned}$$

where  $I$  is the identity matrix. Finding the set of orthogonal eigenvectors ( $\varphi$ ), its transpose ( $\varphi^T$ ) and eigenvalues ( $\lambda$ ) which diagonalises  $\Lambda$ , the formal solution to Eq. (5.43) is found to be

$$\bar{\rho}(t) = \varphi e^{\lambda t} \varphi^T \bar{\rho}(0) - \varphi \lambda^{-1} \varphi^T (\varphi e^{\lambda t} \varphi^T - I) M^* \bar{\rho}(T) \tag{5.44}$$

Alternatively, the exponential in Eq. (5.43) can be approximated by expanding the exponent using the exponential series such that  $e^{\Lambda \delta t} = 1 + \frac{\Lambda \delta t}{1!} + \frac{\Lambda^2 \delta t^2}{2!} + \dots$ . Terminating after the first two terms, and recognising that  $\delta t$  must be sufficiently small so as to preserve the normalisation, the approximated version of Eq. (5.43) takes the form

$$\bar{\rho}(t + \delta t) = \bar{\rho}(0) + \Lambda \delta t \bar{\rho}(0) - M^* \delta t \bar{\rho}(T) \tag{5.45}$$

In order to test the validity of using the wavefunction to simulation spin relaxation (as outlined in Sect. 5.4.2.1), the hydroxyl radicals (in Fig. 5.3) were given a variable spin relaxation time and the recombination yield of all singlet  $\text{H}_2\text{O}_2$ , P and  $\text{R}_2$  was recorded. The results were then compared directly with the density matrix formalism outlined above. The results are not reported here, but within the limits of the error, good agreement was obtained between the two methods with no bias detected across a wide parameter space.

#### 5.4.4 Spin Dependent Reactivity

For the chemical system under study, it is important to deal with unreactive encounters accurately from a spin dynamics point of view. As previously stated, upon encounter of any two radical pairs, the wavefunction is converted to the ST-basis and the singlet probability  $P_s$  is calculated. To determine the nature of the encounter a uniformly distributed random number  $U(0, 1]$  is generated and compared to the probability of being singlet. If  $P_s > U(0, 1]$  then reaction takes place and the spin state of the pair

remains constant for the rest of the realisation. If, however, the converse is true then the radical pair is reflected according to the prescription given in Chap. 4 (Sects. 4.3.3, 4.4.2.3) or Sect. 4.6.6 (within Slice). In this situation, the singlet component in the ST-basis is zeroed, the triplet coefficients are normalised and transformed back to the Zeeman basis. Hence, the radical pairs escape in a purely triplet state and any subsequent fast re-encounters are likely to be unreactive until the wavefunction has had time to evolve both coherently and incoherently. In this prescription any coherence between the three triplet states is preserved in the encounter.

#### 5.4.4.1 Partially Diffusion Controlled

For partially diffusion controlled reactions there are two situations possible following an encounter: (1) the boundary is unreactive and the particles reflect or (2) the boundary is reactive but the encountering pair is in a repulsive triplet state and consequently unreactive. To handle the above situation, two models have been developed which are described below:

##### Method 1

(a) Simulate reflection according to the algorithm as outlined in Sect. 4.6.6; (b) calculate  $P_s$  (the singlet probability from the wavefunction); (c) collapse the wavefunction on encounter to either a singlet or triplet state and renormalise  $\psi$ ; (d) if the radical pair is in a singlet state then it reacts with a probability of  $P_{\text{rad}}$ . An expression for the survival probability  $\Omega(a, r, t)$  on going from  $a$  to  $r$  at time  $t$  subject to radiation boundary conditions at  $a$  was calculated in Sect. 4.6.5 and found to be

$$\Omega(a, r, t) = \frac{(a - a'_{\text{eff}})r}{(r - a'_{\text{eff}})a} \quad (5.46)$$

where  $a$  is the encounter radius,  $r$  is the interparticle distance and  $a'_{\text{eff}}$  is the effective encounter radius, which is given as

$$a'_{\text{eff}} = \frac{a}{1 + (D'/va)} \quad (5.47)$$

In the above expression,  $v$  is the boundary reactivity and  $D'$  the mutual diffusion coefficient. Hence  $P_{\text{rad}} = 1 - \Omega(a, r, t)$ . The simulation would then proceed as normal using the collapsed form of the wavefunction.

##### Method 2

(a) Simulate reflection according to the algorithm as outlined in Sect. 4.6.6; (b) calculate  $P_s$  and  $P_{\text{rad}}$ ; (c) the probability of the radical pair being in a singlet state and reactive is then simply  $P_s \times P_{\text{rad}}$ ; (d) if the pair is found to be unreactive, then the singlet component of  $\psi$  is reduced by  $\sqrt{P_s(1 - P_{\text{rad}})}$ , which retains all the coherences between the eigenstates.  $\psi$  is then renormalised and the simulation would proceed as normal using this wavefunction.

**Table 5.2** Diffusion controlled kinetic parameters in aqueous solution

Parameter	$\cdot\text{OH} + \cdot\text{OH}$	$\cdot\text{OH} + \text{R}\cdot$	$\text{R}\cdot + \text{R}\cdot$
Relative diffusion coefficient <sup>1</sup> ( $\text{\AA}^2 \text{ps}^{-1}$ )	0.44 <sup>a</sup>	0.326 <sup>a,c</sup>	0.212 <sup>c</sup>
Experimental rate constant $k_{\text{obs}}$ ( $10^9 \text{M}^{-1} \text{s}^{-1}$ )	8.4 <sup>b</sup>	1.9 <sup>b</sup>	1.56 <sup>c</sup>
Encounter distance $a$ ( $\text{\AA}$ )	2.52 <sup>a</sup>	0.77 <sup>d</sup>	3.89 <sup>c,e</sup>
Initial separation $r_0$ ( $\text{\AA}$ )	4.63 <sup>f</sup>		

<sup>a</sup>Reference [33]<sup>b</sup>Reference [34]<sup>c</sup>Reference [7]<sup>d</sup>Calculated value (using  $k_{\text{diff}} = 4\pi D'a\sigma_S\beta$ )<sup>e</sup>Reference [27] and <sup>f</sup>calculated using  $\Omega(\infty) = 1 - (a/r_0)$ . For a reaction between like species, the value of  $2k_{\text{obs}}$  is given. All values for  $k_{\text{obs}}$  are reported at 298 K

In method 1, if the radical pair is in a triplet state then all fast re-encounters are most likely be unreactive, since the wavefunction has not had the opportunity to evolve. This is not the case in method 2, where fast re-encounters can result in reaction following an initial unsuccessful encounter.

## 5.5 Simulation Parameters

### 5.5.1 Kinetic Parameters: Diffusion Controlled Conditions

In aqueous solution, the only well known experimental kinetic parameters are the rate coefficients (and in some cases their temperature dependence). To model this system as accurately as possible, the simulation also requires the microscopic parameters that describe diffusion and reaction. For diffusion controlled reactions, it was assumed the experimental rate constant  $k_{\text{obs}} = k_{\text{diff}}$  where  $k_{\text{diff}}$  is Smoluchowski's steady state rate constant. From experimental findings [7], it is found that the spin statistical factor  $\sigma_S$  is  $\sim 1$  for reactions involving the hydroxyl radical. Therefore, for the  $\cdot\text{OH} + \cdot\text{OH}$  and  $\cdot\text{OH} + \text{R}\cdot$  reactions, the microscopic parameters were calculated from the expression  $k_{\text{diff}} = 4\pi D'a\sigma_S\beta$ , with  $\sigma_S = 1$  (based on the analysis done by Buxton and Elliot [26]) and  $\beta$  being  $\frac{1}{2}$  for identical reactants, but unity otherwise. From preliminary simulations it was found that both the phases and magnitude of the spin polarisation remained relatively the same using  $\sigma_S = 0.25$  for the  $\cdot\text{OH} + \cdot\text{OH}$  and  $\cdot\text{OH} + \text{R}\cdot$  reactions. Hence, the  $\sigma_S$  parameter was found to be unimportant in explaining the observed E/A spin polarisation on the escaped 2-propanolyl radicals.

For the  $\text{R}\cdot + \text{R}\cdot$  reaction it is necessary to use a value of  $\sigma_S = 0.25$  (since (i) only 25% will be singlet and reactive and (ii) spin relaxation is slow in  $\text{R}\cdot$ ), with the microscopic parameters calculated from the expression  $k_{\text{diff}} = 2\pi D'a\sigma_S$ . For all simulations, to help simplify the model and allow acceptable statistics to be obtained, the scavengers were assumed stationary.

**Table 5.3** Spin parameters (in aqueous solution) used in computing the phases of the polarisation in the simulation program

Parameter	$\cdot\text{OH}$	$\text{R}\cdot$
$g$ -factor	2.025 <sup>a</sup>	2.00317 <sup>b</sup>
Hyperfine constant <sup>b,c,d,e</sup>	2.64 mT (−2.61 mT)	1.97 mT

<sup>a</sup>Reference [36]<sup>b</sup>Reference [37]<sup>c</sup>Reference [38]<sup>d</sup>Reference [39]<sup>e</sup>From experimental data it is known that  $\cdot\text{OH}$  has a negative hyperfine coupling

## 5.5.2 Photochemistry

The quantum yield ( $\Omega$ ) for the decomposition of  $\text{H}_2\text{O}_2$  and subsequent escape of the hydroxyl radicals in aqueous solution using a 248 nm laser pulse (experimental condition) is found to be 0.44 [35]. From this known survival probability, the initial distance  $r_0$  can be calculated using the relation  $\Omega(\infty) = 1 - (a/r_0)$ , giving a theoretical value of  $\sim 5 \text{ \AA}$ . It must be stressed that this value is only used to verify the feasibility of the different algorithms developed to model the system. When computing the polarisation on the escaped 2-propanolyl radicals, the effect of the initial distance ( $r_0$ ) parameter on the polarisation phase is also investigated.

## 5.5.3 Spin Parameters

The spin parameters for the hydroxyl radical were obtained from the EPR spectrum in ice conducted at a temperature of 77 K. Spin parameters for the 2-propanolyl radical can be obtained in a straightforward manner and all information has been extracted from the EPR spectrum. For the hydroxyl radical, the spin relaxation time was varied over the range 20–100 ps, and it was assumed that the spin-lattice relaxation time was equal to the spin-spin relaxation time (i.e.  $T_1 = T_2$ ). Upon scavenging of the hydroxyl radical the spin relaxation of 2-propanol was not simulated as its relaxation time is known to be  $\sim 2.7 \times 10^{-6} \text{ s}$  [7], which is longer than the timescale of the simulation (1  $\mu\text{s}$ ). For all results presented an external static magnetic field of 0.33 T was used to reproduce experimental conditions.

### 5.5.3.1 Exchange Interaction

Reasonable values for the exchange range and strength parameters were taken from the literature [40] (values of  $2.14 \text{ \AA}^{-1}$  and 16 T respectively) for the  $\cdot\text{OH} + \cdot\text{OH}$ ,  $\cdot\text{OH} + \text{R}\cdot$  and  $\text{R}\cdot + \text{R}\cdot$  reactions. However these parameters are varied (in Sect. 5.8.1.3) to analyse their importance on the observed polarisation phase. An

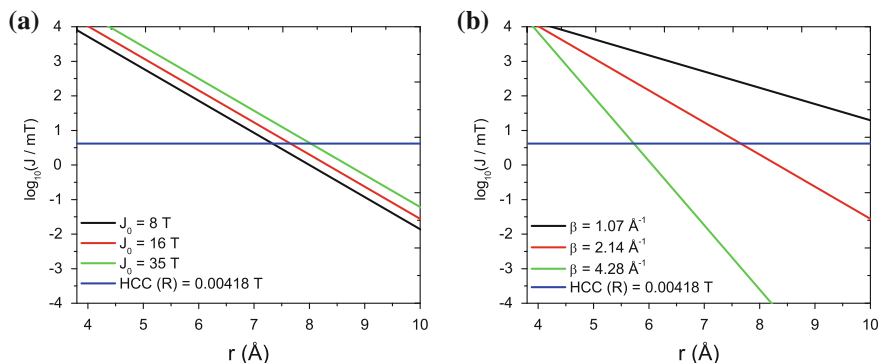
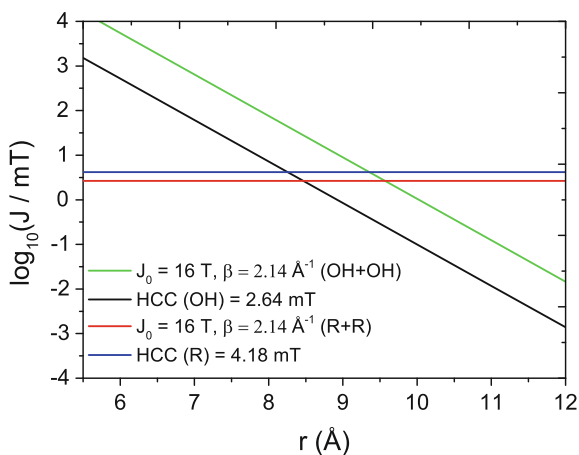


**Fig. 5.5** Exchange interaction  $J(r)$  calculated for the  $R^\cdot + R^\cdot$  reaction assuming diffusion controlled conditions ( $a = 3.89 \text{ \AA}$ ). **a** An exchange range ( $\beta$ ) of  $2.14 \text{ \AA}^{-1}$  was used. **b** An exchange strength ( $J_0$ ) of 16 T was used. Abbreviation HCC represents the hyperfine coupling constant on the 2-propanol radical

**Fig. 5.6** Exchange interaction  $J(r)$  calculated for the  $\cdot\text{OH} + \cdot\text{OH}$  ( $a = 4.4 \text{ \AA}$ ) and  $R^\cdot + R^\cdot$  ( $a = 5.5 \text{ \AA}$ ) reactions assuming partially diffusion controlled conditions. An exchange range ( $\beta$ ) of  $2.14 \text{ \AA}^{-1}$  and exchange strength ( $J_0$ ) of 16 T was used. Abbreviation HCC represents the hyperfine coupling constant



exchange interaction cutoff of  $10 \text{ \AA}$  was used based on the analysis done in Sect. 4.5.1 for the  $\cdot\text{OH} + \cdot\text{OH}$  reaction. From Figs. 5.5 and 5.6 it can be seen that using an exchange range and strength of  $2.14 \text{ \AA}^{-1}$  and 16 T respectively, a  $10 \text{ \AA}$  exchange interaction cutoff is also acceptable for the  $R^\cdot + R^\cdot$  reaction as well.

#### 5.5.4 Scaled 2-Propanol Parameters: Diffusion Controlled

For the purpose of computing the polarisation, the values of the mutual diffusion coefficients for all species were scaled down by 2.040 (Sigma-Aldrich, unpublished) (since the viscosity of 2-propanol is  $2.040 \times$  the viscosity of water) to model the

**Table 5.4** Scaled parameters for simulation in 2-propanol solution

Parameter	$\cdot\text{OH} + \cdot\text{OH}$	$\cdot\text{OH} + \text{R}\cdot$	$\text{R}\cdot + \text{R}\cdot$
Relative diffusion coefficient ( $\text{\AA}^2 \text{ps}^{-1}$ )	0.216 <sup>a</sup>	0.16 <sup>a,c</sup>	0.104 <sup>c</sup>
Rate constant $k_{\text{obs}}$ ( $10^9 \text{M}^{-1} \text{s}^{-1}$ )	4.12 <sup>b</sup>	0.93 <sup>b</sup>	0.77 <sup>c</sup>
Encounter distance $a$ ( $\text{\AA}$ )	2.52 <sup>a</sup>	0.77 <sup>d</sup>	3.89 <sup>c,e</sup>

<sup>a</sup>Reference [33] ( $D'$  scaled)<sup>b</sup>Reference [34] ( $D'$  scaled)<sup>c</sup>Reference [7] ( $D'$  scaled)<sup>d</sup>Calculated value (using  $k_{\text{diff}} = 4\pi D' a \sigma_S \beta$ )<sup>e</sup>Reference [27]. For reaction between like species, the value of  $2k_{\text{obs}}$  is reported. All values for  $k_{\text{obs}}$  are reported at 298 K

experimental conditions (i.e. simulating the entire system with 2-propanol as the solvent). Hence the scaling  $D'_i(\text{aqueous})/2.040$  was applied to all species  $i$ , with the encounter distances being kept the same as there is no physical reason for their change. The scaled kinetic parameters are shown in Table 5.4. As previously mentioned, a value for the spin statistical factor of  $\sigma_S = 1$  was used for the  $\cdot\text{OH} + \cdot\text{OH}$  and  $\cdot\text{OH} + \text{R}\cdot$  reactions, whilst  $\sigma_S = 0.25$  was used for the  $\text{R}\cdot + \text{R}\cdot$  reaction. In this parameter space the scavengers were assumed stationary to simplify the model.

### 5.5.5 Scaled 2-Propanol Parameters: Partially Diffusion Controlled Conditions

The reaction scheme under study was also modelled by employing the radiation boundary condition, using the parameter  $v$  to control the surface reactivity. The observed rate constant  $k_{\text{obs}}$  using this boundary condition can be written as

$$k_{\text{obs}} = \beta \sigma_S \frac{4\pi D' a^2 v}{av + D'} \quad (5.48)$$

with  $\beta$  being  $\frac{1}{2}$  for like species or unity otherwise and  $\sigma_S$  the spin statistical factor. The above equation is equivalent to

$$\frac{1}{k_{\text{obs}}} = \frac{1}{\beta \sigma_S k_{\text{diff}}} + \frac{1}{\beta \sigma_S k_{\text{react}}} \quad (5.49)$$

with  $k_{\text{react}} = 4\pi a^2 v$  (intrinsic reaction rate constant) and  $k_{\text{diff}}$  being the diffusion controlled rate constant. Again for the reaction scheme involving  $\cdot\text{OH} + \cdot\text{OH}$  and  $\cdot\text{OH} + \text{R}\cdot$  a spin-factor of unity was used, whilst a value of  $\frac{1}{4}$  was used for the  $\text{R}\cdot + \text{R}\cdot$  reaction. The complete set of parameters used in the simulation program are shown in Table 5.5. Finally, in the simulation all scavenging events were treated as fully diffusion controlled using the effective encounter radius as given in Table 5.4.

**Table 5.5** Scaled parameters for simulation in 2-propanol solution

Parameter	$\cdot\text{OH} + \cdot\text{OH}$	$\cdot\text{OH} + \text{R}'$	$\text{R}' + \text{R}'$
Relative diffusion coefficient ( $\text{\AA}^2 \text{ps}^{-1}$ )	0.216 <sup>a</sup>	0.16 <sup>a,c</sup>	0.104 <sup>c</sup>
Scaled rate constant $k_{\text{obs}}$ ( $10^9 \text{M}^{-1} \text{s}^{-1}$ )	4.12 <sup>b</sup>	0.93 <sup>b</sup>	0.77 <sup>c</sup>
Encounter distance $a$ ( $\text{\AA}$ )	4.4 <sup>e,f</sup>	4.95 <sup>e,c</sup>	5.5 <sup>c</sup>
Surface reactivity $v$ ( $\text{\AA} \text{ps}^{-1}$ )	0.0657 <sup>d</sup>	0.006 <sup>d</sup>	0.045 <sup>d</sup>

<sup>a</sup>Reference [33] ( $D'$  scaled)<sup>b</sup>Reference [34] ( $D'$  scaled)<sup>c</sup>Reference [7] ( $D'$  scaled)<sup>d</sup>Calculated using  $k_{\text{react}} = 4\pi a^2 v \sigma_S \beta$ <sup>e</sup>Reference [41]<sup>f</sup>Reference [26]. For reaction between like species, the value of  $2k_{\text{obs}}$  is reported. All values for  $k_{\text{obs}}$  are reported at 298 K. In this table a larger encounter radius is used to give the correct  $k_{\text{obs}}$  due to the limited surface reactivity (in comparison with Table 5.4)

### 5.5.6 Variable Parameters

A maximum simulation time  $t_{\text{max}} = 1 \mu\text{s}$  was used for all simulations to reproduce the experimental conditions, where the E/A polarisation phase (low field emissive and high field absorptive) was detected as early as  $0.6 \mu\text{s}$  by Das and co-workers [1]. Therefore, for the escaped  $\text{R}'$  radicals (i.e. 2-propanolyl radicals), the spin wavefunction evolves until  $1 \mu\text{s}$  in the simulation before the phases of the polarisation are calculated. For computing the polarisations,  $5 \times 10^6$  number of realisations were used to obtain acceptable statistics within the Slice program.

## 5.6 Kinetics

### 5.6.1 Kinetics with No Spin Dynamics Incorporated

Figure 5.7 shows the recombination yield of hydroxyl radicals in the presence of scavengers using the parameters listed in Table 5.2 (i.e. aqueous solution). At this stage no spin dynamics were incorporated into the simulation. To allow direct comparison with the analytical formulation [Eq. (5.9)] the time dependence of the scavenging rate constant was not taken into consideration. It can be seen that at a wide range of concentration strengths for the scavengers, the IRT algorithm is essentially in exact agreement with the analytical formula with no source of bias introduced by the IRT approximation. This test verified that the IRT algorithm for generating reaction times was working correctly.

As Das and co-workers [1] conduct their study using 12M concentration of 2-propanol, from hereon all the results presented use the same scavenger concentration. Using the time dependent scavenging rate constant in the IRT simulation,

**Fig. 5.7** Yield of  $\text{H}_2\text{O}_2$  obtained using the IRT method and compared with analytical result [Eq. (5.9)] at six different concentrations of scavengers. Number of realisations used:  $1 \times 10^6$ . A time independent scavenging rate constant was used in both cases

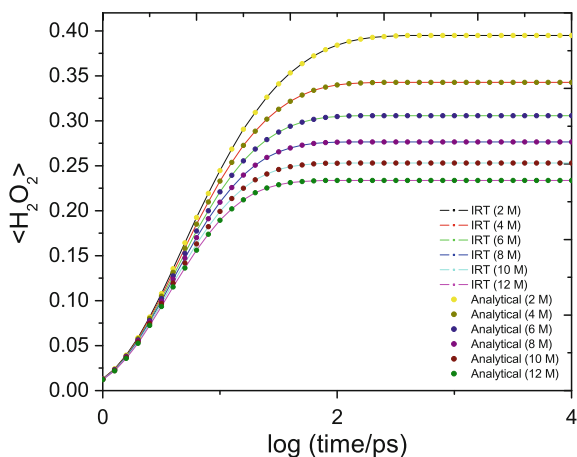


**Fig. 5.8** Yield of P and  $\text{R}_2$  obtained using the IRT method and compared with Monte Carlo random flights using a 12 M scavenger concentration. Number of realisations used:  $1 \times 10^6$  (IRT) and  $5 \times 10^4$  (random flights simulation)

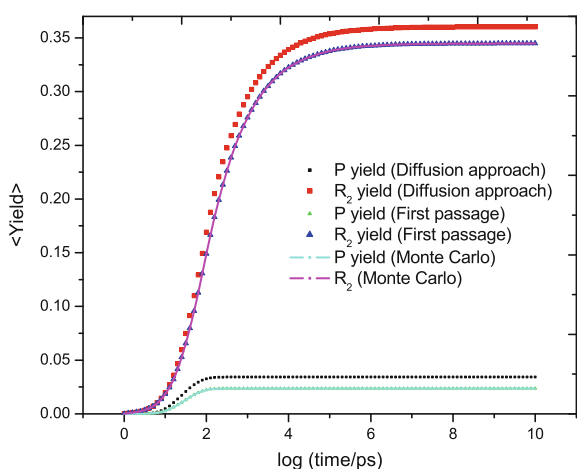


Fig. 5.8 presents a comparison between the diffusion approach and first passage approach for treating reactive products within the IRT framework. Reactions were assumed to be diffusion controlled and no spin-dynamics was taken into consideration. It is clear that the diffusion approach does not describe the scavenging yield correctly under the conditions investigated, and that the first passage approach is far superior. All results therefore, presented from hereon employ the *first passage* algorithm for treating reactive products.

The standard errors of the kinetics in Fig. 5.8 were computed by using the properties of a binomial distribution, such that  $\sigma = \sqrt{np(1-p)}$ , where  $n$  is the number of realisations ( $1 \times 10^6$  (IRT) and  $5 \times 10^4$  (random flights)) and  $p$  is the probability of success. For the final yield of P, the standard error (to  $2\sigma$ ) was calculated to be:  $0.034 \pm 1.8 \times 10^{-4}$  (diffusion approach);  $0.0235 \pm 1.5 \times 10^{-4}$

(first passage approach) and  $0.0233 \pm 6.75 \times 10^{-4}$  (random flights). Similarly for  $R_2$  the standard error (to  $2\sigma$ ) was calculated to be:  $0.36 \pm 4.8 \times 10^{-4}$  (diffusion approach);  $0.345 \pm 4.75 \times 10^{-4}$  (first passage approach) and  $0.342 \pm 2.1 \times 10^{-3}$  (random flights). Within the limits of the error, the first passage algorithm is in excellent agreement with random flights results.

### 5.6.2 Kinetics with Spin Dynamics Incorporated

In this section the kinetics are presented for the recombination yields of  $H_2O_2$ , P and  $R_2$ , utilising the full spin Hamiltonian using the parameters detailed in Tables 5.3 and 5.4 (scaled values for isopropanol), and using a spin relaxation time for  $\cdot OH$  of 100 ps. Figure 5.9 shows the results obtained by using the Hybrid and Slice simulation package (using 10 slices) and compared against the density matrix formalism within the random flights framework. It can be seen that the wavefunction approach used to model spin relaxation provides the same kinetics as that predicted by the density matrix, however requiring substantially fewer computational resources. A typical simulation using the parameters in Tables 5.3 and 5.4 for the random flights algorithm (with  $5 \times 10^4$  realisations) can take  $>24$  h; the Hybrid algorithm reduces the computational time to  $\sim 1$  h, with Slice providing the best computational time of  $<20$  min.<sup>8</sup> These timings are only rough values with the actual time of the simulation depending on many factors, such as the microscopic parameters and the time step for random flights. As obtaining electron polarisations requires substantially more realisations ( $>1 \times 10^6$  realisations) than those needed for the kinetics, the solution becomes tractable only if the Slice algorithm is used.

In the kinetics shown in Fig. 5.9, the standard error (to 95% confidence limits) for  $H_2O_2$ , P and  $R_2$  was calculated to be:  $0.15 \pm 3.8 \times 10^{-3}$ ,  $0.027 \pm 1.4 \times 10^{-3}$  and  $0.17 \pm 3.3 \times 10^{-3}$  respectively (using  $5 \times 10^4$  realisations). Within the limits of the error, all three algorithms predict the correct recombination yield, allowing Slice to be used with reasonable confidence. Although for the recombination kinetics ten slices were found to be sufficient, this may not be sufficient to model the exchange interaction, which is responsible for creating electron polarisation. An analysis of this is now presented in the next section.

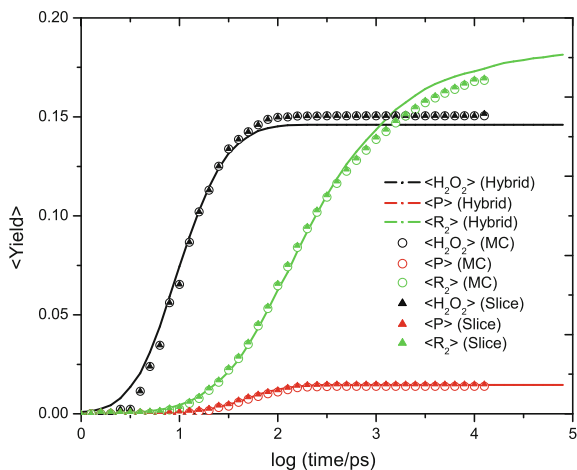
## 5.7 Electron Polarisation Using Slice and Hybrid

For the purpose of testing the Slice algorithm the electron polarisation was calculated from the wavefunction (in the Zeeman basis) at predefined times as

---

<sup>8</sup> The exact computation time required for Slice depends on the number of slices used. As the number of slices increases, the computation time also increases as essentially the simulation is performing a Monte Carlo random flights simulation on a lattice.

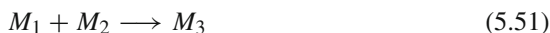
**Fig. 5.9** Yield of  $\text{H}_2\text{O}_2$ , P and  $\text{R}_2$  obtained using the Hybrid and Slice simulation packages and compared with random flights simulation using a spin relaxation time of 100 ps on the hydroxyl radical. 12M scavenger concentration was used in all cases. Number of realisations used:  $5 \times 10^4$ . Full simulation parameters are detailed in Tables 5.3 and 5.4. Here MC refers to random flights simulation



$$P = \sum_{j=1}^{2^n} m_{sj} |c_j|^2 \quad (5.50)$$

where  $n$  is the number of electron spins,  $m_{sj}$  is the magnetic spin quantum number of spin  $j$  and  $c_j$  is the element of the wavefunction vector corresponding to electron spin  $j$ . Hence, Eq. (5.50) effectively calculates the difference in the population of the spin states, with a positive (negative) value for  $P_i$  representing  $\alpha$  ( $\beta$ ) polarisation on radical  $i$ .

In this section the Slice simulation package was verified against full Monte Carlo random flights simulation to: (1) determine the number of slices required in the exchange region for a general two radical system, and (2) ensure that the correct magnitude and sign (and any characteristics such as oscillations) of electron polarisations are reproduced for this two radical system. The reaction scheme considered is of the form



where the two radicals,  $M_1$  and  $M_2$  separated by an initial distance 10 Å and are given the characteristic properties of the hydroxyl radical in terms of their kinetics (as described by the parameters given in Table 5.4). No scavenging of either radical was allowed to take place, and the simulation finished after the formation of  $M_3$ . In addition, to help simplify the model, the reaction between  $M_1$  and  $M_2$  was assumed to be diffusion controlled. At the start of every realisation the nuclear spins were chosen at random and the electron spins were correlated in a singlet state. For all simulations the number of realisations used in the IRT and Hybrid simulation was  $5 \times 10^4$ .

As the purpose of these simulations was to analyse the magnitude and phase of the electron polarisation, no spin relaxation was allowed to take place. The results of

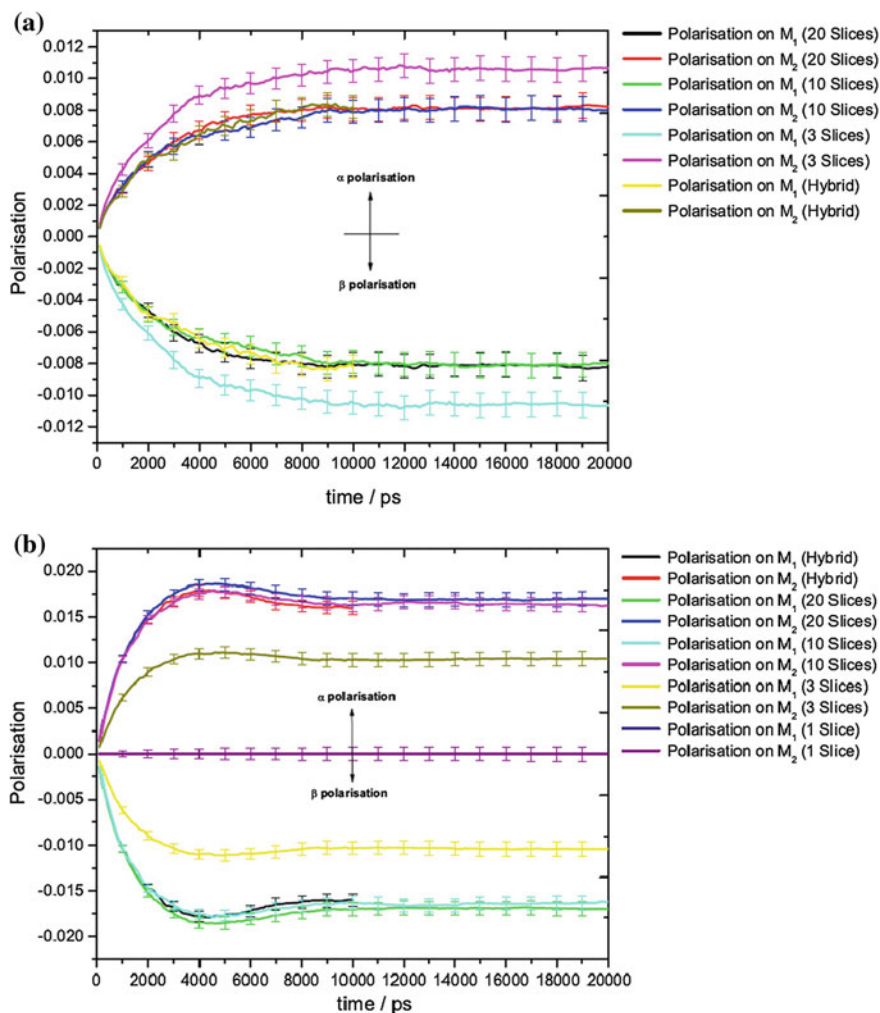


**Fig. 5.10** Spin polarisation ( $P_\alpha - P_\beta$ ) on radicals  $M_1$  and  $M_2$  as a function of the number of slices and compared against full random flights simulations. The  $g$ -factors and the hyperfine constant on  $M_1$  and  $M_2$  were  $2.025$ ,  $2.02$  and  $2.64 \times 10^{-3}$  T respectively. **a** An exchange range and strength respectively of  $1.07 \text{ \AA}^{-1}$  and  $16$  T were used. **b** An exchange range and strength of  $2.14 \text{ \AA}^{-1}$  and  $8$  T respectively were used. Polarisation is per remaining radical

the simulation are presented in Fig. 5.10, with error bars shown to 84 % confidence levels. Within the limits of the error, it is seen that ten slices are sufficient to reproduce the results (i.e. the magnitude and sign of the polarisation) as obtained by Hybrid simulations for reasonable values of  $J(r)$ . Extensive testing with other spin parameters (results not reported here) also showed ten slices to be sufficient to model a general chemical system with exchange interaction incorporated. Hence, for the

purpose of this work, ten slices were used in all simulations to calculate the CIDEP spectrum for the escaped 2-propanolyl radicals.

## 5.8 CIDEP Spectrum: Escaped 2-Propanolyl Radicals

For the purpose of this work, no attempt to model the lineshape is made but rather to simply calculate the phase and magnitude of the polarisation. The EPR spectrum is calculated from the accumulated populations of the spin states on the escaped 2-propanolyl radicals during the simulation and averaged over a large number of realisations. The relative intensity of each peak can be calculated as

$$I \propto | \langle i | \hat{S}_+ | j \rangle |^2 (p_i - p_j) \quad (5.52)$$

In this expression,  $i$  and  $j$  are the eigenstates,  $p_i$  and  $p_j$  represent the population of the spin states and  $\hat{S}_+$  is the raising spin operator. To compute the standard deviation in the intensity, the population of the spin states of the escaped 2-propanolyl radicals, together with the square of the populations were accumulated after every realisation and averaged over the total number of realisations. The variance in the intensity can be calculated to be

$$\begin{aligned} \sigma^2(I) &= | \langle i | \hat{S}_+ | j \rangle |^4 \times \sigma_i^2(2p_i) \\ &= | \langle i | \hat{S}_+ | j \rangle |^4 \times 4(\mathbb{E}(p_i^2) - \mathbb{E}(p_i)^2) \end{aligned} \quad (5.53)$$

where  $\mathbb{E}(p_i)$  and  $\mathbb{E}(p_j)$  are the expectation values of the population for states  $i$  and  $j$  respectively and  $p_{ij} = |c_{ij}^2|$  and  $p_{ij}^2 = |c_{ij}^4|$ . The standard error of the intensity is then

$$\sigma_E(I) = \frac{\sigma(I)}{\sqrt{n}} \quad (5.54)$$

with  $n$  being the number of realisations and  $\sigma(I)$  the standard deviation of the intensity. The expectation value of the intensity is

$$\mathbb{E}(I) = | \langle i | \hat{S}_+ | j \rangle |^2 (\mathbb{E}(p_i) - \mathbb{E}(p_j)) \quad (5.55)$$

All the results presented for  $\mathbb{E}(I)$  are reported to 84% confidence, with the sign of the polarisation identified within reasonable confidence limits.

As previously mentioned, all simulations were done using the Slice package and wherever possible repeated with the Hybrid program as a way of verifying the results. Unless otherwise mentioned, the spin parameters used in the simulation are those detailed in Table 5.3 and the kinetic parameters are those detailed in Table 5.4 (diffusion controlled conditions) or Table 5.5 (partially diffusion controlled conditions). The initial nuclear spin configuration was selected randomly at the start of every

realisation and the results averaged over the total number of realisations. In all cases (unless otherwise stated), the initial electronic wavefunction was always set up to be in a pure singlet state. The results, where presented in tabular format for the intensity, are given in the format (+) and (−) which signify an absorptive and emissive signal respectively.

### 5.8.1 Diffusion Controlled Reactivity

#### 5.8.1.1 Effect of the Initial Separation and Treatment of $\cdot\text{OH} + \cdot\text{OH}$ and $\cdot\text{OH} + \text{R}\cdot$ Reactions

This section presents the results for the observed polarisation phases by investigating the effect of:

1. The initial separation of the hydroxyl radicals (using the kinetic parameters listed in Table 5.4), with the results presented in Tables 5.6, 5.7, 5.8, 5.9, 5.10, 5.11.
2. The treatment for the reactivity of the  $\cdot\text{OH} + \cdot\text{OH}$  and  $\cdot\text{OH} + \text{R}\cdot$  reaction. For the purpose of this work the  $\cdot\text{OH} + \cdot\text{OH}$  and  $\cdot\text{OH} + \text{R}\cdot$  reaction were treated in two different ways: (1) the first method assumes diffusion controlled conditions i.e. reaction takes place instantly on encounter (Fig. 5.11), irrespective of the singlet character of the wavefunction. (2) The second method involves projecting the singlet component of the wavefunction ( $P_s$ ) and comparing with a uniformly distributed random number  $U(0, 1]$ . Reaction takes place only if  $P_s > U(0, 1]$  (Fig. 5.12). The main difference between the two models is that in the latter, if reaction has not taken place then the singlet component is zeroed and the radical pair escapes in a purely triplet state. Any fast re-encounters are unlikely to be reactive which leads to a greater escape yield which in turn leads to more scavenging product. Method (2) was used for the  $\text{R}\cdot + \text{R}\cdot$  reaction in both cases.

From the polarisation intensities obtained (Figs. 5.11a, 5.12a) no major difference is seen using either model to treat the  $\cdot\text{OH} + \cdot\text{OH}$  and  $\cdot\text{OH} + \text{R}\cdot$  reactions. The same magnitude of the relative intensity on the surviving  $\text{R}\cdot + \text{R}\cdot$  pairs is observed, and the cross-over point is also seen to occur at similar positions in both methods (within the limits of the standard error). The effect of the initial distance on the overall polarisation phase seems to make little difference as well, with only a reduction in the magnitude of the intensity is observed. This is thought to arise because with decreasing initial hydroxyl distances, there are fewer escaped  $\text{R}\cdot$  radicals which can contribute to the relative intensity. The polarisations calculated in Figs. 5.11 and 5.12 demonstrate that at the steady state scavenging lifetime of the hydroxyl radical ( $\sim 85$  ps), the main source of spin polarisation arises via the surviving  $\text{R}\cdot + \text{R}\cdot$  radicals, with little contribution from the  $\text{R}\cdot + \cdot\text{OH}$  and  $\cdot\text{OH} + \cdot\text{OH}$  reactions.

From the results, there appears to be a cross-over period at a spin-relaxation time of  $< 40$  ps on the  $\cdot\text{OH}$  radical for all hydroxyl radical separations investigated. Although the experimentally observed polarisation phases can be obtained, it should

**Table 5.6** Polarisation phase obtained using an initial particle separation distance  $r_0 = 5.0 \text{ \AA}$ 

Spin relaxation time (ps)	Intensity ( $\nu = 5.83 \times 10^{10} \text{ rad/s}$ )	Intensity ( $\nu = 5.79 \times 10^{10} \text{ rad/s}$ )	Polarisation phase
100	$2.43 \times 10^{-3} (\pm 6 \times 10^{-4})$	$-3.322 \times 10^{-3} (\pm 6 \times 10^{-4})$	A/E
80	$1.126 \times 10^{-3} (\pm 6 \times 10^{-4})$	$-2.04 \times 10^{-3} (\pm 6 \times 10^{-4})$	A/E
60	$5.5 \times 10^{-4} (\pm 6 \times 10^{-4})$	$-9.6 \times 10^{-4} (\pm 6 \times 10^{-4})$	A/E
40	$-3.3 \times 10^{-4} (\pm 6 \times 10^{-4})$	$1.3 \times 10^{-4} (\pm 6 \times 10^{-4})$	(E/A) <sup>a</sup>
20	$-1.161 \times 10^{-3} (\pm 6 \times 10^{-4})$	$1.45 \times 10^{-3} (\pm 6 \times 10^{-4})$	E/A

Numbers in bracket indicate the standard error in the intensity

<sup>a</sup>Signifies polarisation phases could not be determined within the error limits

**Table 5.7** Polarisation phase obtained using an initial particle separation distance  $r_0 = 6.0 \text{ \AA}$ 

Spin relaxation time (ps)	Intensity ( $\nu = 5.83 \times 10^{10} \text{ rad/s}$ )	Intensity ( $\nu = 5.79 \times 10^{10} \text{ rad/s}$ )	Polarisation phase
100	$2.21 \times 10^{-3} (\pm 6 \times 10^{-4})$	$-2.85 \times 10^{-3} (\pm 6 \times 10^{-4})$	A/E
80	$1.64 \times 10^{-3} (\pm 6 \times 10^{-4})$	$-2.28 \times 10^{-3} (\pm 6 \times 10^{-4})$	A/E
60	$8.7 \times 10^{-4} (\pm 6 \times 10^{-4})$	$-1.23 \times 10^{-3} (\pm 6 \times 10^{-4})$	A/E
40	$-1.4 \times 10^{-4} (\pm 6 \times 10^{-4})$	$-3.0 \times 10^{-4} (\pm 6 \times 10^{-4})$	(E/A) <sup>a</sup>
20	$-1.41 \times 10^{-3} (\pm 6 \times 10^{-4})$	$1.2 \times 10^{-3} (\pm 6 \times 10^{-4})$	E/A

Numbers in bracket indicate the standard error in the intensity

<sup>a</sup>Signifies polarisation phases could not be determined within the error limits

**Table 5.8** Polarisation phase obtained using an initial particle separation distance  $r_0 = 7.0 \text{ \AA}$ 

Spin relaxation time (ps)	Intensity ( $\nu = 5.83 \times 10^{10} \text{ rad/s}$ )	Intensity ( $\nu = 5.79 \times 10^{10} \text{ rad/s}$ )	Polarisation phase
100	$2.52 \times 10^{-3} (\pm 6 \times 10^{-4})$	$-2.9 \times 10^{-3} (\pm 6 \times 10^{-4})$	A/E
80	$1.85 \times 10^{-3} (\pm 6 \times 10^{-4})$	$-2.26 \times 10^{-3} (\pm 6 \times 10^{-4})$	A/E
60	$1.04 \times 10^{-3} (\pm 6 \times 10^{-4})$	$-1.16 \times 10^{-3} (\pm 6 \times 10^{-4})$	A/E
40	$-8.0 \times 10^{-5} (\pm 6 \times 10^{-4})$	$-3.4 \times 10^{-4} (\pm 6 \times 10^{-4})$	(E/A) <sup>a</sup>
20	$-1.42 \times 10^{-3} (\pm 6 \times 10^{-4})$	$1.36 \times 10^{-3} (\pm 6 \times 10^{-4})$	E/A

Numbers in bracket indicate the standard error in the intensity

<sup>a</sup>Signifies polarisation phases could not be determined within the error limits

be stressed that this relaxation time is largely dependent on the scavenging time, which for this parameter range is  $\sim 90$  ps (for steady state scavenging conditions). The results therefore indicate that the rate of spin relaxation on the hydroxyl radical has to be at least  $\times 4$  faster than the scavenging lifetime of the hydroxyl radical to reproduce the E/A polarisation phase. However, this value does not take into account the time-dependence of scavenging, which in this parameter space (where a high concentration of scavengers are used) will accelerate scavenging before steady state conditions can be achieved. A discussion for this effect is now presented.

**Table 5.9** Polarisation phase obtained using an initial particle separation distance  $r_0 = 8.0 \text{ \AA}$ 

Spin relaxation time (ps)	Intensity ( $\nu = 5.83 \times 10^{10} \text{ rad/s}$ )	Intensity ( $\nu = 5.79 \times 10^{10} \text{ rad/s}$ )	Polarisation phase
100	$2.55 \times 10^{-3} (\pm 6 \times 10^{-4})$	$-3 \times 10^{-3} (\pm 6 \times 10^{-4})$	A/E
80	$1.83 \times 10^{-3} (\pm 6 \times 10^{-4})$	$-2.04 \times 10^{-3} (\pm 6 \times 10^{-4})$	A/E
60	$9.8 \times 10^{-4} (\pm 6 \times 10^{-4})$	$-1.24 \times 10^{-3} (\pm 6 \times 10^{-4})$	A/E
40	$2.0 \times 10^{-4} (\pm 6 \times 10^{-4})$	$-3.1 \times 10^{-4} (\pm 6 \times 10^{-4})$	(E/A) <sup>a</sup>
20	$-9.4 \times 10^{-4} (\pm 6 \times 10^{-4})$	$9.7 \times 10^{-4} (\pm 6 \times 10^{-4})$	E/A

Numbers in bracket indicate the standard error in the intensity

<sup>a</sup>Signifies polarisation phases could not be determined within the error limits

**Table 5.10** Polarisation phase obtained using an initial particle separation distance  $r_0 = 9.0 \text{ \AA}$ 

Spin relaxation time (ps)	Intensity ( $\nu = 5.83 \times 10^{10} \text{ rad/s}$ )	Intensity ( $\nu = 5.79 \times 10^{10} \text{ rad/s}$ )	Polarisation phase
100	$2.79 \times 10^{-3} (\pm 6 \times 10^{-4})$	$-2.95 \times 10^{-3} (\pm 6 \times 10^{-4})$	A/E
80	$1.9 \times 10^{-3} (\pm 6 \times 10^{-4})$	$-2.03 \times 10^{-3} (\pm 6 \times 10^{-4})$	A/E
60	$1.02 \times 10^{-3} (\pm 6 \times 10^{-4})$	$-1.32 \times 10^{-3} (\pm 6 \times 10^{-4})$	A/E
40	$2.0 \times 10^{-4} (\pm 6 \times 10^{-4})$	$-2.0 \times 10^{-4} (\pm 6 \times 10^{-4})$	(E/A) <sup>a</sup>
20	$-1.09 \times 10^{-3} (\pm 6 \times 10^{-4})$	$7.7 \times 10^{-4} (\pm 6 \times 10^{-4})$	E/A

Numbers in bracket indicate the standard error in the intensity

<sup>a</sup>Signifies polarisation phases could not be determined within the error limits

**Table 5.11** Polarisation phase obtained using an initial particle separation distance  $r_0 = 10.0 \text{ \AA}$ 

Spin relaxation time (ps)	Intensity ( $\nu = 5.83 \times 10^{10} \text{ rad/s}$ )	Intensity ( $\nu = 5.79 \times 10^{10} \text{ rad/s}$ )	Polarisation phase
100	$2.66 \times 10^{-3} (\pm 6 \times 10^{-4})$	$-2.87 \times 10^{-3} (\pm 6 \times 10^{-4})$	A/E
80	$1.97 \times 10^{-3} (\pm 6 \times 10^{-4})$	$-2.22 \times 10^{-3} (\pm 6 \times 10^{-4})$	A/E
60	$1.17 \times 10^{-3} (\pm 6 \times 10^{-4})$	$-1.24 \times 10^{-3} (\pm 6 \times 10^{-4})$	A/E
40	$2.4 \times 10^{-4} (\pm 6 \times 10^{-4})$	$-3.2 \times 10^{-4} (\pm 6 \times 10^{-4})$	(E/A) <sup>a</sup>
20	$-8.8 \times 10^{-4} (\pm 6 \times 10^{-4})$	$8.3 \times 10^{-4} (\pm 6 \times 10^{-4})$	E/A

Numbers in bracket indicate the standard error in the intensity

<sup>a</sup>Signifies polarisation phases could not be determined within the error limits

**Time dependent scavenging** In order to understand why spin relaxation has to be at most 20 ps on the hydroxyl radical, it is important to first calculate the mean scavenging time. This can be calculated as

$$\langle T_s \rangle = s \int_0^{\infty} (t + \alpha \sqrt{t}) e^{-s(t + 2\alpha \sqrt{t})} dt \quad (5.56)$$

where  $\alpha = a/\sqrt{\pi D'}$  and  $s = 4\pi D'ac$ , with  $c$  being the concentration of scavengers. Evaluating the integral in the above equation gives an expression for  $\langle T_s \rangle$  to be

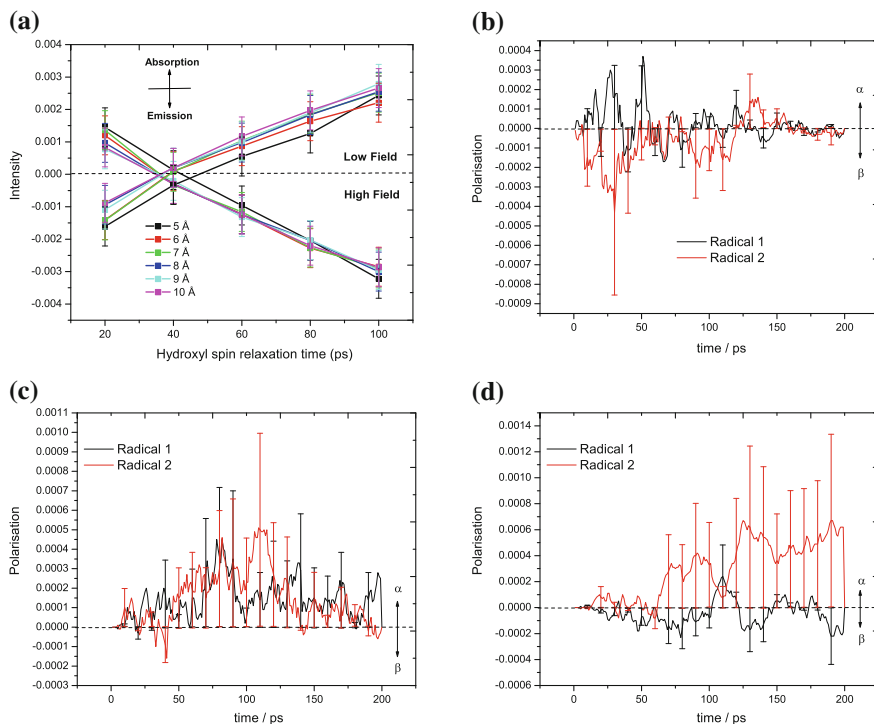


**Fig. 5.11** **a** Intensity of the observed polarisation at various initial hydroxyl radical separations  $r_0$ . For all encounters involving the hydroxyl radical, reaction was assumed to take place instantaneously. Error bars have been omitted for clarity purposes. Polarisation on the surviving radical pairs: **b** 'OH + 'OH; **c** 'OH + R' and **d** R' + R' using a spin relaxation time of 20 ps and an initial separation of 5 Å. Standard errors on the polarisation are quoted to one standard deviation

$$\langle T_s \rangle = \frac{1}{s} - \sqrt{\frac{\pi}{s}} \exp(\alpha^2/s) \operatorname{erfc}\left(\frac{\alpha}{\sqrt{s}}\right) \quad (5.57)$$

In the parameter space considered for this section, it was found that  $\langle T_s \rangle \cong 20$  ps. Therefore, in order for spin relaxation to effectively compete with the *transient scavenging process*, spin relaxation on the hydroxyl radical must occur with the same rate as scavenging to make the chemical system statistically triplet. As scavenging is fastest at zero time, there will be a probability of forming an R' + R' pair which has never undergone spin relaxation at all, which would lessen the triplet character of the chemical system. The probability of forming unrelaxed R' + R' (including those scavenged at zero time) are shown in Table 5.12 at various spin relaxation times. The results highlight that even with a spin relaxation time of 20 ps,  $\sim 6\%$  of the R' + R' escape in a pure singlet state and would produce the A/E polarisation phase. This is, however, destroyed by the bulk of escaped R' + R' which have undergone spin relaxation and are statistically triplet in character, producing an overall

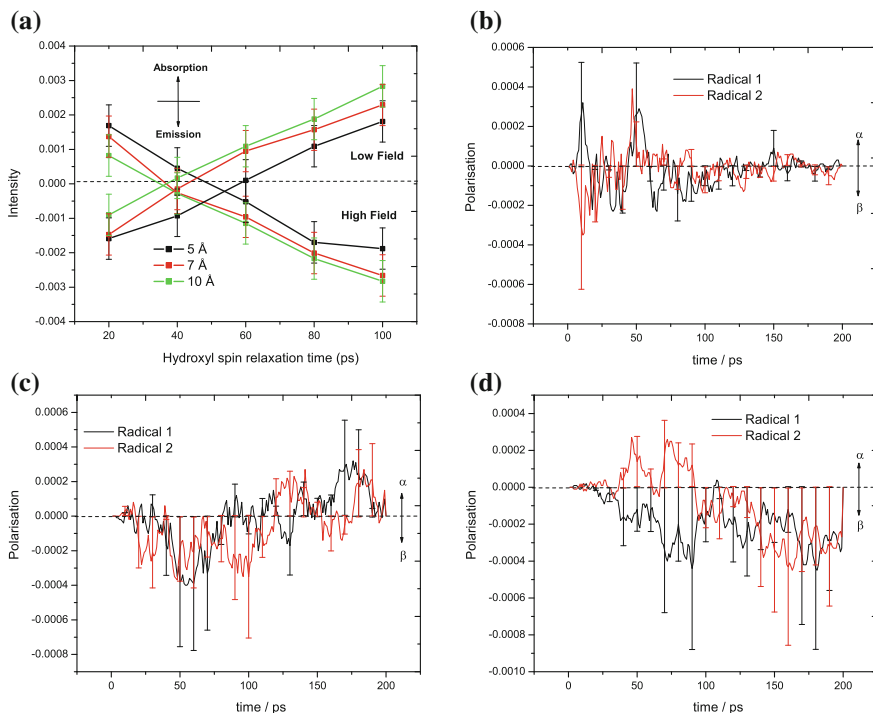


**Fig. 5.12** **a** Intensity of the observed polarisation at various initial hydroxyl radical separations  $r_0$ . For all encounters involving the hydroxyl radical, the probability of reaction was obtained by projecting out the singlet component of the wavefunction. Polarisation on the surviving radical pairs: **b**  $\cdot\text{OH} + \cdot\text{OH}$ ; **c**  $\cdot\text{OH} + \text{R}\cdot$  and **d**  $\text{R}\cdot + \text{R}\cdot$  using a spin relaxation time of 20 ps and an initial separation of 5 Å. Standard errors on the polarisation are quoted to one standard deviation

**Table 5.12** Probability of forming an unrelaxed  $\text{R}\cdot + \text{R}\cdot$  pair using an initial separation distance of 5 Å

Spin relaxation time (ps)	Probability
100	0.302
80	0.253
60	0.203
40	0.138
20	0.059

E/A polarisation phase. An analytical method was developed to compute the probability of forming unrelaxed  $\text{R}\cdot + \text{R}\cdot$  pairs, however, it made use of the steady state scavenging rate constant which significantly underestimated the probability. A solution using the time-dependent rate was not thought to be possible.

**Negative hyperfine coupling constant** In a separate set of simulations a negative hyperfine coupling constant for the hydroxyl radical was used to compute the polarisation phases. It was found that within the range of the standard error, no significant deviations in the results were observed (in comparison to using a positive hyperfine coupling constant). This is in agreement with the CIDEP sign rule. All simulations results presented in this work have made use of a positive hyperfine constant.

As the electron spin on the hydroxyl can rapidly re-orient itself within the encounter ‘cage’ (resulting in reaction), it is acceptable to treat reactions involving the hydroxyl radical using the first method (i.e. reaction takes place upon encounter). Hence, for all calculations presented from hereon (except in Sect. 5.8.2), diffusion controlled reactivity was assumed for reactions  $\cdot\text{OH} + \cdot\text{OH}$  and  $\cdot\text{OH} + \text{R}\cdot$  (i.e. singlet probability at the point of recombination is one); for the  $\text{R}\cdot + \text{R}\cdot$  reaction the singlet component of the wavefunction was interrogated.

### 5.8.1.2 Scavenging Model for the $\cdot\text{OH}$ Radical

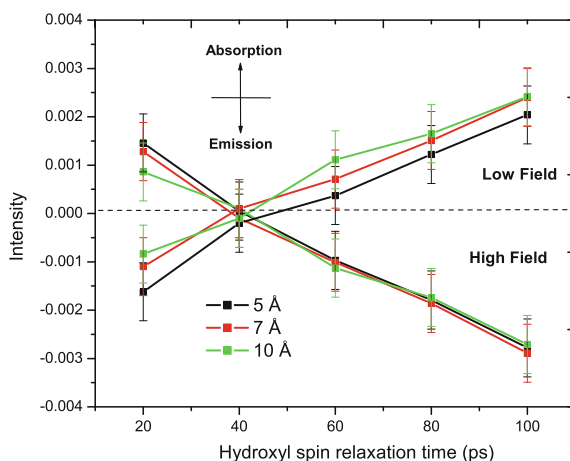
In this section the effect of using  $\alpha = a/\sqrt{2\pi D'}$  in the time dependent rate constant was used to account for the correlation that exists between the scavenging times (as discussed in Sect. 4.4.2.2). If the radicals are close to one another, the distances to a given scavenger (S) from each radical are highly correlated (i.e. if one of the distances is large so is the other). Taking this effect into account reduces the time-dependent rate constant, so that  $\alpha$  is reduced by  $\sqrt{2}$ . This however, is only applicable if the  $\cdot\text{OH}-\cdot\text{OH}$  distance is small relative to the  $\cdot\text{OH}-\text{S}$  distance, which is not thought to be the case at this high concentration of scavengers. Provisional random flights simulations with explicit treatment for scavengers showed that this correlation was indeed not required, since the recombination kinetics for  $\text{H}_2\text{O}_2$  and P was accurately described by Smoluchowski’s  $\alpha = a/\pi D'$ . Nonetheless, the effect of this correlation on the intensity spectrum was investigated to analyse the relationship between the scavenging time and the observed polarisation phase.

From the intensity spectrum (Fig. 5.13), it can be seen that at all initial hydroxyl separation distances considered, the scavenging model does not directly affect the phases of the polarisation in comparison to that obtained using Smoluchowski’s time dependent rate constant (Fig. 5.11a). On this basis it is acceptable to assume that any correlation between  $\cdot\text{OH} + \cdot\text{OH}$  and  $\cdot\text{OH} + \text{R}\cdot$  is negligible, and that the scavenging process can be accurately described with Smoluchowski’s time dependent rate constant.

### 5.8.1.3 Exchange Interaction

In order to extract the relationship between the spin exchange parameters and the observed polarisation phase, both the exchange strength and range are altered in this section. Figure 5.14a shows the polarisation phase using an exchange strength of 8 T and exchange range of  $2.14 \text{ \AA}^{-1}$  with the kinetics parameters listed in Table 5.4.

**Fig. 5.13** Intensity of the observed polarisation at various initial hydroxyl radical separations  $r_0$  using a  $\sqrt{2}$  reduced transient term in Smoluchowski's time dependent rate constant. Kinetics parameters used are those listed in Table 5.4



It is seen that with these exchange parameters, the phases of the polarisation remains relatively unchanged, with an E/A polarisation phase observed at 20 ps spin relaxation time on the hydroxyl radical. Changing either the exchange strength ( $J_0$ ) or the exchange range ( $\beta$ ) was also found to minimally contribute to the overall polarisation phases (Fig. 5.14b, c). The results presented so far imply that the chemical system is sensitive to two main factors: (i) the hydroxyl spin relaxation time and (ii) the scavenging rate. All other parameters are found to affect the magnitude of the polarisation to some extent, but do not directly affect the phases of the polarisation. The next section will now examine the importance of (i) and (ii) in more detail, and investigate whether similar polarisation phases can be obtained at  $T_1 = 20$  ps when the steady state scavenging lifetime of the  $\cdot\text{OH}$  is reduced.

#### 5.8.1.4 Scavenging Dependence on the CIDEP Spectrum

In this section the properties of the solvent are changed to better understand the relationship between the scavenging rate and the observed polarisation phase. The two changes made to the simulation program are as follows:

1. Changing the microscopic parameters to model scavenging and diffusion in aqueous solution using the kinetic parameters listed in Table 5.2 and spin parameters in Table 5.3.
2. Using a scavenging rate of  $1.9 \times 10^9 \text{ M}^{-1} \text{ s}^{-1}$  for the hydroxyl radicals in isopropanol solvent (using a concentration of 12 M of scavengers).

The difference between the previous set of simulations and the ones reported in this section are as follows: in the previous set of simulations the kinetics parameters were scaled to account for the difference in the solvent viscosity between water

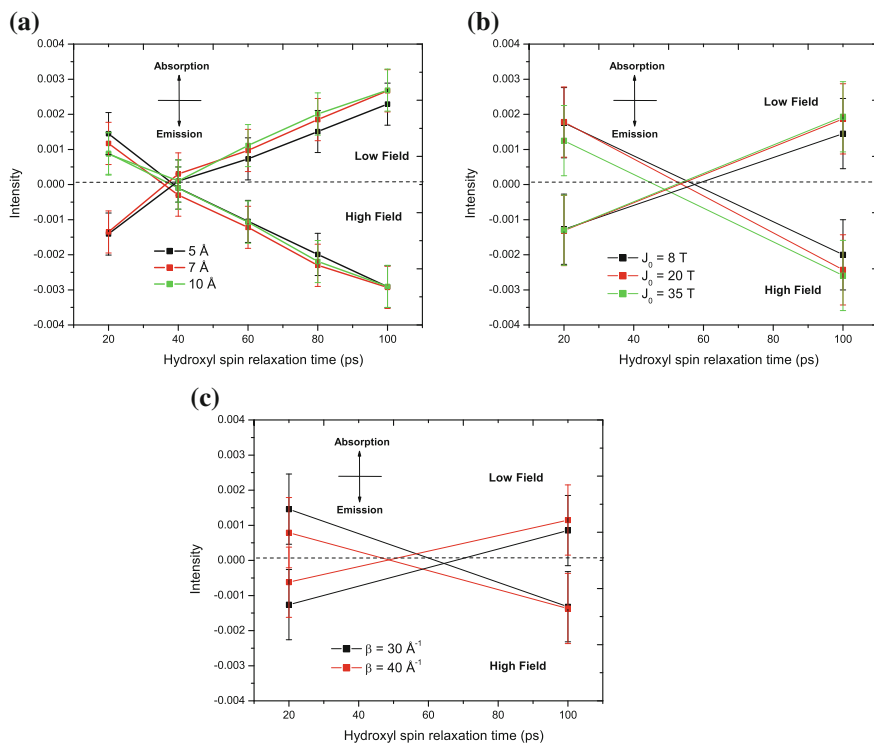


**Fig. 5.14** **a** Intensity of the observed polarisation at various initial hydroxyl radical separations  $r_0$  using an exchange strength of 8 T and exchange range of  $2.14 \text{ \AA}^{-1}$ . Intensity of the observed polarisation at a spin relaxation time of 100 ps and 20 ps on the hydroxyl radical using: **b** different values for the exchange strength ( $J_0$ ) with an exchange range of  $2.14 \text{ \AA}^{-1}$ ; **c** different values of the exchange range ( $\beta$ ) with an exchange strength of 16 T. An initial ion pair distance of  $5 \text{ \AA}$  was used

and isopropanol (as most of the microscopic parameters are only known in aqueous solution). However, in this section, the first set of simulation uses the unscaled kinetic parameters to model the reaction scheme in aqueous solution (i.e. those parameters in Table 5.2 are used); the aim of this model was to observe what effect the microscopic parameters (in particular the scavenging parameters) had on the observed polarisations.

The second set of simulations in this section uses the scaled isopropanol microscopic parameters (with the kinetic parameters listed in Table 5.4), however, to account for the fact that the solvent itself is the scavenger (as in the experiment), the rate of scavenging is increased from  $0.93 \times 10^9 \text{ M}^{-1}$  to  $1.9 \times 10^9 \text{ M}^{-1} \text{ s}^{-1}$  (which is the scavenging rate constant for  $\cdot\text{OH}$  in aqueous solution). This models the fact that an  $\cdot\text{OH}$  radical rapidly finds a 2-propanol molecule in the near vicinity and reacts, with diffusion no longer being the rate determining step.

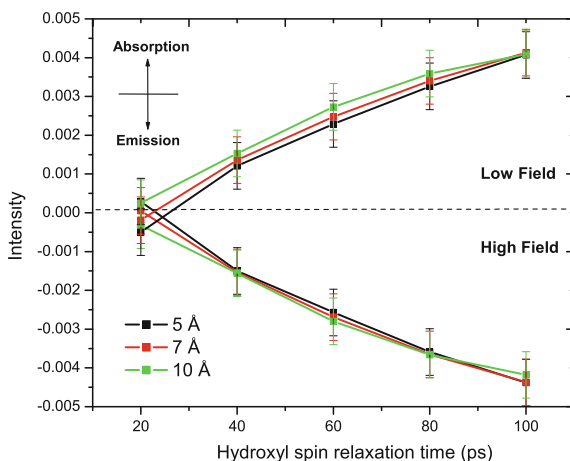
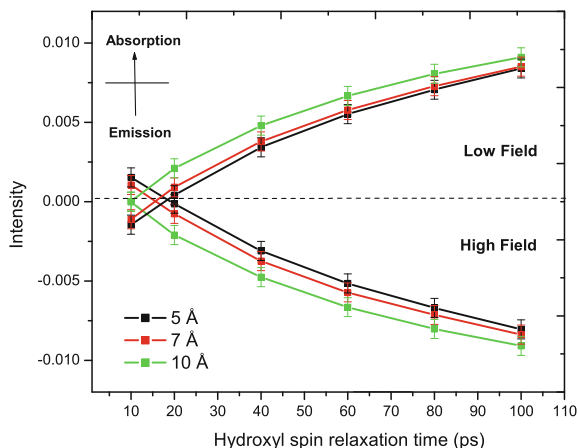


**Fig. 5.15** Intensity of the observed polarisation at various initial hydroxyl radical separation  $r_0$  in aqueous solution

**Aqueous solution** In aqueous solution (containing a concentration of 12 M of scavengers), scavenging occurs with a pseudo-first order rate constant of  $2.3 \times 10^{10} \text{ s}^{-1}$  (with a steady state scavenging time of  $\sim 44$  ps) in comparison with that in 2-propanol which is  $1.12 \times 10^{10} \text{ s}^{-1}$ . Hence, in aqueous solution although a spin relaxation time of 20 ps can effectively compete with scavenging, the probability of making the chemical system statistically triplet is lower, since the  $\cdot\text{OH}$  lifetime has been reduced from  $\sim 85$  ps (2-propanol solvent) to  $\sim 44$  ps (aqueous solution). Using the time dependent scavenging rate constant, the mean transient scavenging time was found to 9.46 ps, which suggests scavenging can now more effectively compete with the rate of spin relaxation in this parameter space. As expected, Fig. 5.15 shows that now  $\sim 10$  ps is required to produce the observed E/A polarisation phases, such that spin relaxation on the hydroxyl radical must be of the same rate as the transient scavenging process in order for the chemical system to be statistically triplet.

**Isopropanol solvent** In this model scavenging occurs with a rate  $1.9 \times 10^9 \text{ M}^{-1} \text{ s}^{-1}$ , with the mean transient scavenging time calculated to be  $\sim 20$  ps. The steady state scavenging lifetime of the  $\cdot\text{OH}$  in this scenario has been reduced from  $\sim 85$  ps to  $\sim 44$  ps. As seen from Fig. 5.16, at a spin relaxation time of 20 ps the observed polarisation phases can indeed be obtained, although with a reduced intensity in comparison with the simulation presented in Fig. 5.11 due to the shorter hydroxyl lifetime. Both of the simulations presented have shown that the main parameters which govern the polarisation phases are: (i) the spin relaxation time, and (ii) the mean transient scavenging time. To allow enough triplet character in the chemical system to arise and reproduce the observed polarisation phase, spin relaxation on the hydroxyl radical must be of the same magnitude as the mean transient scavenging time.

**Fig. 5.16** Intensity of the observed polarisation at various hydroxyl radical separation  $r_0$  in 2-propanol solvent. In the simulation the encounter radius for the  $R' + \cdot OH$  reaction was changed to 1.64 Å to correctly model the observed rate constant



### 5.8.1.5 Discussion for Diffusion Controlled Reactivity

From the obtained results, the following observations can be drawn if the  $\cdot OH$  pair is initially singlet:

1. A spin relaxation time of 100 ps produces the A/E polarisation phase in all cases as predicted by the sign rule. This is because the hydroxyl radicals are rapidly scavenged before the spins can relax, thus creating a majority of singlet 2-propanolyl radical pairs. As the 2-propanolyl radicals diffuse further apart the exchange interactions becomes negligible and only the hyperfine interaction operates on them ( $\Delta g = 0$ ). Hence the wavefunction on the escaped 2-propanolyl radicals remains predominately singlet character.
2. If the spin relaxation time is faster than the scavenging lifetime of the hydroxyl radical, the initial singlet wavefunction of the hydroxyl radical pair is transformed into one which is predominately triplet in character (i.e. with ratio 75 % triplet and 25 % singlet). Rapid scavenging together with spin-selective reaction for the  $R' + R'$  reaction further depletes the singlet state. The 2-propanolyl radicals will have randomised spin states and will be indistinguishable from F-pairs, but will still be subject to magnetic field effects. The escaped 2-propanolyl radicals now have <25 % singlet character with an overwhelming triplet character; this provides an explanation for the spin polarisation to once again get stronger once spin relaxation can effectively compete with scavenging. In order to observe this effect, it is seen that spin relaxation on the hydroxyl radical needs to be of the same magnitude as the mean transient scavenging time.

### 5.8.2 Partially Diffusion Controlled Reaction

This section presents the results by treating all reactions as partially diffusion controlled, using the spin parameters listed in Table 5.3 and kinetic parameters in Table 5.5. As previously mentioned, most chemical reactions are not fully diffusion controlled and one must employ the use of the radiation boundary condition to control the surface reactivity (i.e. use the microscopic parameters that reproduce the observed rate constant and its time dependence). The aim of this section is to test the validity of the *diffusion controlled conditions* employed in the previous section to verify whether similar polarisation phases can be obtained within the parameter space explored.

Treating spin dependent reactivity poses a special problem in the current model as there are two possibilities which can arise: (i) radical pairs encounter and the surface is unreactive or (ii) the radical pairs encounter but are in an unreactive spin-configuration. The two algorithms designed to treat partially diffusion controlled reactions have already been discussed in Sect. 5.4.4. In brief, method 1 collapses the wavefunction ( $\psi$ ) upon encounter and reaction occurs with a probability  $P_{\text{rad}}$  (Fig. 5.17); method 2 calculates the probability of reaction ( $P_s \times P_{\text{rad}}$ ) and reduces the singlet component of  $\psi$  by  $\sqrt{P_s(1 - P_{\text{rad}})}$  if no reaction had occurred (Fig. 5.18). To simplify the model, it was assumed the scavenging process was diffusion controlled, which was modelled using a pseudo-first order rate constant.

On modelling the system as partially diffusion controlled, the same polarisation phases are obtained as that predicted using Smoluchowski's diffusion controlled conditions. Therefore, no bias has been introduced into the simulations in which diffusion controlled conditions are considered. Both diffusion controlled and partially diffusion controlled reactions have verified that  $<20$  ps is indeed sufficient on the hydroxyl radical to obtain the observable polarisation (in this parameter range the mean transient scavenging time is also  $\sim 20$  ps). It can therefore be concluded that: (i) spin-selective reactions on the  $\cdot\text{OH} + \cdot\text{OH}$  and  $\cdot\text{OH} + \text{R}$  contribute minimally to the overall triplet character of the chemical system, as essentially the magnitude of the polarisations phases are similar to those presented in Fig. 5.11; (ii) from the polarisations in Figs. 5.17 and 5.18 most of the spin polarisations are generated via the  $\text{R} + \text{R}$  encounters with little contribution arising from the  $\cdot\text{OH} + \cdot\text{OH}$  radical pairs due to the rapid scavenging.

### 5.8.3 Symmetrical and Non-symmetrical Encounters

Recently in the literature, Forbes et al. [42] have proposed an alternative mechanism for the observed polarisation phase. They note that in the EPR spectrum there is a small net absorptive peak ( $E/A^*$ ) which can arise when the two radicals have different  $g$ -factors. In the reaction scheme investigated by Das and co-workers [1], no net absorptive peak is seen since the hydroxyl radicals are rapidly scavenged to

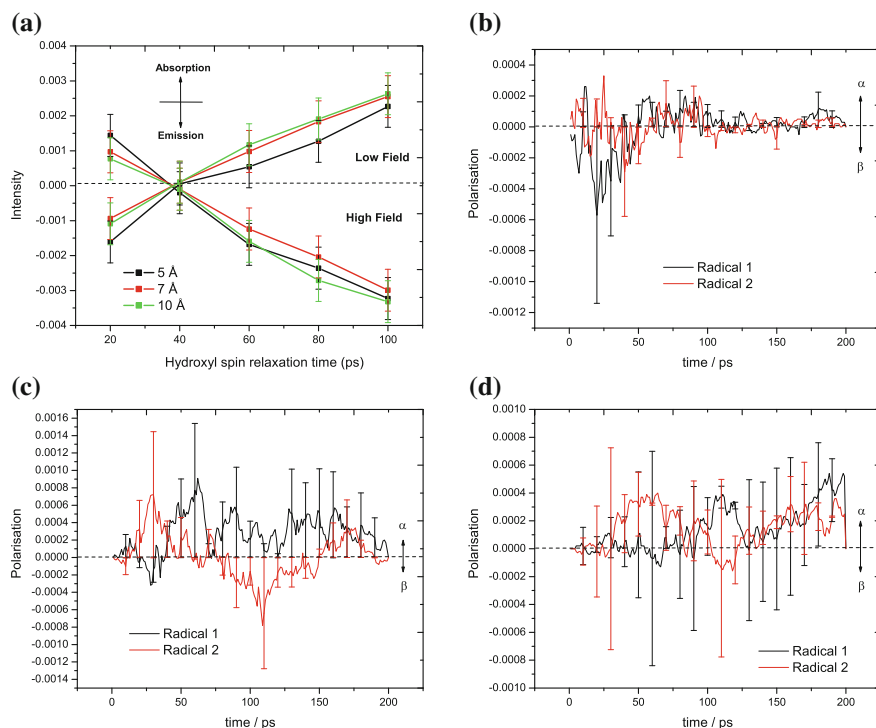


**Fig. 5.17** a Intensity of the observed polarisation at various initial separation  $r_0$  using method 1. An exchange strength of 16 T and exchange range of  $2.14 \text{ \AA}^{-1}$  were used. Polarisation on the surviving radical pairs: b  $\cdot\text{OH} + \cdot\text{OH}$ ; c  $\cdot\text{OH} + \text{R}^\cdot$  and d  $\text{R}^\cdot + \text{R}^\cdot$  using a spin relaxation time of 20 ps and an initial separation of  $5 \text{ \AA}$ . Standard errors on the polarisation are quoted to one standard deviation

produce two symmetrical 2-propanolyl radicals with equal  $g$ -factors, giving an equal E/A polarisation phase. Forbes has shown that the E/A\* polarisation can arise if two different types of F-pairs, one symmetric (2-propanolyl radicals reacting) and one non-symmetric (2-propanolyl radical and an  $\text{HO}^\cdot$  radical) encounter in the solution. If the polarisation produced from each of the two types of encounter is calculated and added together, the observed polarisation pattern<sup>9</sup> can be reproduced.

Forbes further argues that because such a large polarisation can be created on the escaped  $^3(\text{R}^\cdot + \cdot\text{OH})$ , even very fast spin relaxation may not completely quench the polarisation. In this mechanism, the nature of the precursor is irrelevant as well as the hydroxyl spin relaxation time. However the concentration of scavengers and the lifetime of both the symmetrical and non-symmetrical radical pairs will influence the magnitude of the E/A\* phase as well as spin-dependent reactivity. Whilst this mechanism offers the simplest explanation for the observed polarisation phase, it

<sup>9</sup> In this scenario the polarisation produced arises from the Radical Pair Mechanism and spin-dependent reactivity.

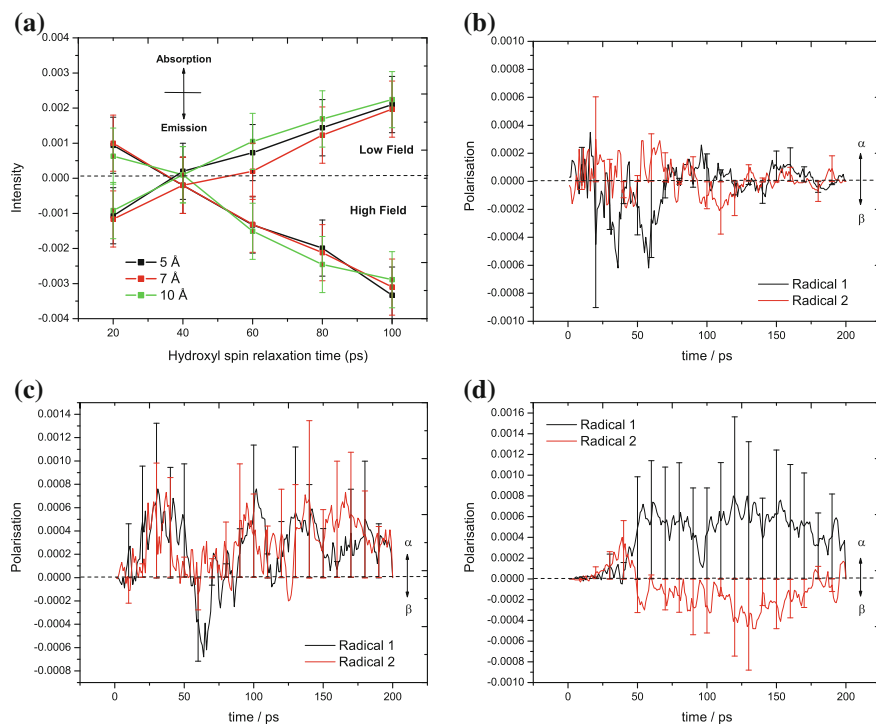


**Fig. 5.18** **a** Intensity of the observed polarisation at various initial separation  $r_0$  using method 2. An exchange strength of 16 T and exchange range of  $2.14 \text{ \AA}^{-1}$  were used. Upon reflection the singlet elements are set to  $\sqrt{P_s(1 - P_{\text{rad}})}$ . Polarisation on the surviving radical pairs: **b**  $\cdot\text{OH} + \cdot\text{OH}$ ; **c**  $\cdot\text{OH} + \text{R}^\cdot$  and **d**  $\text{R}^\cdot + \text{R}^\cdot$  using a spin relaxation time of 20 ps and an initial separation of  $5 \text{ \AA}$ . Standard errors on the polarisation are quoted to one standard deviation

does rely on F-pair encounters; the E/A polarisation phase obtained at  $\sim 0.6 \mu\text{s}$  by Das et al. suggests that G-pairs and not F-pairs are responsible for the generation of spin polarisation.

This work has shown that using a spin relaxation time of  $\sim 20$  ps, the observed E/A polarisation phase can indeed be obtained within the parameter space investigated. If this value is used in Forbes' reaction scheme, then essentially the  $\text{R}^\cdot + \cdot\text{OH}$  and  $\text{R}^\cdot + \text{R}^\cdot$  are statistically triplet in character, owing to the large lifetime of the hydroxyl radical in his reaction scheme (since a low concentration of scavengers is used). In this case surviving geminate  $\cdot\text{OH}$  radicals will resemble the kinetics of F-pairs but will behave like G-pairs from the view point of their spin dynamics. Hence the same E/A\* spectrum can be obtained, but without the need to invoke the relaxation induced F-pair polarisation mechanism. Therefore, in Forbes' reaction scheme it becomes necessary to distinguish between those 'F-pairs' created via fast relaxation of the hydroxyl radical and F-pairs which arise via uncorrelated radical pairs.

## 5.9 Discussion

The original aim of this work was to investigate (1) whether fast spin relaxation on the hydroxyl radical can produce the E/A polarisation phase as observed by Bhattacharjee and Das [1] and (2) estimate a value for the spin relaxation time required to produce this polarisation phase. From the results of this work, it has been shown that the E/A polarisation phase can be obtained with a singlet precursor, as long as spin relaxation can compete with the scavenging process. It has been shown that even in the presence of fast scavenging of the hydroxyl radical, a theoretical value of  $<20$  ps spin relaxation can produce the observable polarisation phase. This revised value is very much in agreement with that claimed by Buxton and Elliot [26], who have argued that the spin relaxation time of  $\cdot\text{OH}$  has to be less than the total encounter time for the  $\cdot\text{OH} + \cdot\text{OH}$  reaction ( $2r^2/D' = 44$  ps), suggesting a value for the relaxation time to be  $\sim 40$  ps.

Our simulation results further reinforce experimental findings by Fessenden [7], who suggested the spin relaxation time to be  $\sim 1$  ps on the hydroxyl radical. Using the property of the second order rate constant for the reaction between  $e_{\text{aq}}^- + \cdot\text{OH}$ , Fessenden notes: (1) the high rate constant ( $k_{\text{obs}} = 3.2 \times 10^{10} \text{ M}^{-1} \text{ s}^{-1}$  at 298 K) suggests a spin statistical factor larger than 1/4; (2) As the  $e_{\text{aq}}^-$  diffusion is much faster than that of  $\cdot\text{OH}$  at room temperature, the mutual diffusion coefficient in Smoluchowski's rate constant should be dominated by the diffusion of the  $e_{\text{aq}}^-$  towards the  $\cdot\text{OH}$  radical. The apparent activation energy for  $e_{\text{aq}}^-$  diffusion is found to be  $20.25 \text{ kJ mol}^{-1}$  [43, 44] in the temperature range of 288–348 K. As the apparent activation energy for the  $e_{\text{aq}}^- + \cdot\text{OH}$  reaction is measured to be  $16.3 \text{ kJ mol}^{-1}$  [7], this seems to imply partially diffusion controlled conditions, although the large rate constant observed seems to indicate otherwise. Fessenden suggests that both the reaction distance and the spin statistical factor are temperature dependent (that is for the change in competition between rates of spin relaxation and diffusive separation) to account for the experimental observations. If the radical pair lifetime is inversely proportional to the mutual diffusion ( $D'$ ) coefficient [45] (the temperature dependence of  $D'$  is found to change by a factor of three between 298 and 343 K, with the lifetime of the radical decreasing by the same factor [7]), then at higher temperatures diffusive separation of triplet radical pairs can effectively compete with spin-relaxation, which has the effect of lowering the spin-factor and the effective activation energy. This competition between  $S$ - $T$  mixing and diffusive separation is put forward as a possible explanation by the authors for the lower activation energy observed for the  $e_{\text{aq}}^- + \cdot\text{OH}$  reaction.

Recently in the literature, Karogodina et al. [46] have explored the spin relaxation on the  $\text{NO}\cdot$  radical based on the spin-rotation relaxation mechanism. The rotational correlation time in Eq. (5.3) can be calculated by the relation

$$\tau_c = \frac{4\pi R^3 \eta}{3k_B T} f \quad (5.58)$$

where  $R$  representing the van der Waals radius,  $\eta$  the solvent viscosity and the parameter  $f$  determining whether ‘stick’ ( $f = 1$ ) or ‘slip’ ( $f \ll 1$ ) conditions are applicable. In the paper by Spiess et al. [47]  $\tau_c$  has been calculated for  $\text{CS}_2$  (in  $\text{CS}_2$ ) to be 1.4 ps at 293 K with  $\eta = 0.36\text{cP}$ . This value has shown to be applicable to the slip condition, with a value of  $\sim 7.2$  ps applicable for the stick condition. Karogodina et al. [46] have shown that for  $\text{NO}^\cdot$  in aqueous solution, although perfect slip conditions may not be achievable, a  $\tau_c$  value of 1.4 ps might still be applicable for this chemical system. If this value for  $\tau_c$  is also assumed to be applicable for the  $\cdot\text{OH}$  radical, then from the analysis done by Brocklehurst [19] (which uses the spin parameters for  $\cdot\text{OH}$  in ice) a relaxation time of  $\sim 3$  ns is obtained. Whilst this spin relaxation time is larger than 20 ps (obtained in this work), it must be stressed that anisotropy of the  $g$ -tensor in the liquid phase will be much larger than in ice (due to weaker hydrogen bonding), which will have the effect of reducing the spin-relaxation time quite considerably. In the literature Karogodina et al. [46] have calculated the  $g$ -tensors for  $\text{NO}^\cdot$  in aqueous solution at room temperature as ( $g_e$  is the free electron  $g$ -factor)

$$g_{zz} = g_e - 2 \frac{\lambda}{\sqrt{\lambda^2 + \Delta^2}} \quad (5.59)$$

$$g_{xx} = g_{yy} = g_e \frac{\Delta}{\sqrt{\lambda^2 + \Delta^2}} \quad (5.60)$$

for two cases: (i) when  $\lambda = \Delta$  and (ii) when  $\lambda \ll \Delta$ , with  $\lambda$  and  $\Delta$  being the spin-orbit coupling and ligand field splitting parameters respectively. The obtained parameters are shown in Table 5.13. If these  $g$ -tensors are also used to describe  $\cdot\text{OH}$  in aqueous solution, a spin relaxation time of 5 ps is obtained (under slip conditions) and 24 ps (under stick conditions) when  $\lambda/\Delta = 1$ , which are both sufficient to produce the observed E/A polarisation phase in water. Additionally, if  $\tau_c$  scales linearly with the solvent viscosity then a theoretical value of  $\sim 10$  ps (under slip condition) is obtained for the spin relaxation time of the hydroxyl radical in 2-propanol, which is again sufficient to produce the experimental E/A polarisation phase. If stick conditions are assumed then a theoretical spin relaxation time of  $\sim 50$  ps is obtained for  $\cdot\text{OH}$  in 2-propanol; this value is not sufficient to produce the E/A polarisation.

Based on the analysis by Karogodina et al. [46], it can be seen that for the spin-rotation relaxation to contribute appreciably a  $\overline{\delta g^2}$  (defined as  $(g_{\parallel} - g_e)^2 + 2(g_{\perp} - g_e)^2$ )  $> 0.8$  is required when  $\tau_c = 1.4$  ps (slip condition) or  $\overline{\delta g^2} > 1.8$  at  $\tau_c = 7.2$  ps (stick condition) in order to produce the observed E/A polarisation phase.

From all available information in the literature and the results from this work, it is highly suggestive that the hydroxyl radical has a spin relaxation time of at least 20 ps. An attempt to model spin-orbit coupling explicitly was made based on Redfield theory using this value for  $\tau_c$ , but unfortunately a proper treatment requires a basis set of  $2^6 \times 2^6$  (two nuclear spins, two electron spins and two orbital angular momentum states). This together with the necessity to use random flights simulations to treat spin-relaxation using small time-steps makes the calculation intractable, since a very

**Table 5.13**  $g$ -tensors ( $g_{\parallel} = g_{zz}$  and  $g_{\perp} = g_{xx} = g_{yy}$ ) calculated by Karogodina et al. [46] for two values of  $x$  (defined as  $x = \lambda/\Delta$  with  $\lambda$  and  $\Delta$  being the spin-orbit coupling and ligand field splitting parameters respectively)

$x$	$g_{\parallel}$	$g_{\perp}$	$\langle g \rangle$	$T_1 = T_2$ (ps)
1	0.59	1.41	1.14	5 (slip), 24 (stick)
0.1	1.80	1.99	1.92	305 (slip), 1,571 (stick)

$\langle g \rangle$  represents the isotropic  $g$ -value of the radical. A  $\tau_c$  value of 1.4 ps (slip) 7.2 ps (stick) was used

large number of realisations are required to converge the magnitude of the intensities to their expectation value.

Although Das et al. have presented evidence for the possibility of a triplet precursor in the photodissociation of hydrogen peroxide[1], the results from this work suggest an alternative possibility for the observed polarisation phase. After photodissociation of singlet hydrogen peroxide the two hydroxyl radicals, which carry the signature of the precursor undergo rapid spin relaxation before any scavenging can occur. This effectively destroys any spin correlation between the hydroxyl radicals and all information regarding the state of the precursor is now lost. These hydroxyl radicals which now have randomised electron spins behave like F-pairs and independently undergo hydrogen abstraction to create a pair of 2-propanolyl radicals. In this scenario, 25% of these radicals are in a singlet state and are rapidly depleted by reaction leaving a preponderance (75%) of triplet 2-propanolyl radicals which are unreactive. The spin state of the system is now predominately triplet in character and resembles what would have been produced, had the dissociation occurred via the triplet mechanism. The origin of the polarisation in this proposed scenario however, occurs via the magnetic interactions occurring during the diffusive motion of the radical pair, and not during the intersystem crossing on photodissociation of hydrogen peroxide. It can be concluded that by conducting the experiment  $\text{H}_2\text{O}_2$ -2-propanol in 12 M, (1) scavenging *cannot* effectively compete with the rate of spin relaxation on the hydroxyl radical and (2) although the triplet mechanism can explain the observed results, the radical pair mechanism can also do, so long as the  $\cdot\text{OH}$  spin relaxation in 2-propanol is  $\sim 20$  ps or less.

## References

1. B. Bhattacharjee, R. Das, Mol. Phys. **105**, 1053 (2007)
2. K.H. Gericke, S. Klee, F.J. Comes, R.N. Dixon, J. Chem. Phys. **85**, 4463 (1986)
3. H. Golzenleuchter, K.H. Gericke, F.J. Comes, J. Chem. Phys. **89**, 93 (1984)
4. A. Morita, S. Kato, J. Phys. Chem. **96**, 1067 (1992)
5. S. Klee, K.H. Gericke, F.J. Comes, J. Chem. Phys. **85**, 40 (1986)
6. S. Siegel, L.J. Baum, S. Skolnik, J.M. Flourno, J. Chem. Phys. **32**, 1249 (1960)
7. T. Ichino, R.W. Fessenden, J. Phys. Chem. A **111**, 2527 (2007)
8. K.D. Asmus, H. Moeckel, A.J. Henglein, J. Phys. Chem. **77**, 1218 (1973)
9. S.K. Wong, T.M. Chiu, J.R. Bolton, J. Phys. Chem. **85**, 12 (1981)
10. K.Y. Choo, J.K.S. Wan, J. Am. Chem. Soc. **97**, 7127 (1975)

11. I. Carmichael, H. Paul, J. Chem. Phys. Lett. **67**, 519 (1979)
12. S. Yamauchi, K. Tominaga, N. Hirota, J. Phys. Chem. **90**, 2367 (1986)
13. H. Paul, J. Chem. Phys. **40**, 265 (1979)
14. S. Basu, A.I. Grant, K.A. McLauchlan, J. Chem. Phys. Lett. **94**, 517 (1983)
15. K.A. McLauchlan, *Modern Pulsed and Continuous Wave Electron Spin Resonance* (Wiley, New York, 1990)
16. P.R. Levstein, H. van Willigen, J. Chem. Phys. **95**, 900 (1991)
17. N.C. Verma, R.W. Fessenden, J. Chem. Phys. **65**, 2139 (1976)
18. L.M. Dorfman, D.E. Adams, *Reactivity of the Hydroxyl Radical in Aqueous Solution* (National Bureau of Standards, Washington, 1972)
19. B. Brocklehurst, J. Chem. Soc. Faraday Trans. **2**(75), 123 (1979)
20. D. Eisenberg, W. Kauzmann, *The Structure and Properties of Water* (Oxford University Press, Oxford, 1969)
21. F. Franks, *Water: A Comprehensive Treatise* (Plenum Press, New York, London, 1972)
22. H. Box, E.E. Budzinski, K.T. Lilga, H.C. Freund, J. Chem. Phys. **53**, 1059 (1970)
23. U.E. Steiner, Y.A. Serebrennikov, J. Chem. Phys. **100**, 7503 (1994)
24. U.E. Steiner, Y.A. Serebrennikov, J. Chem. Phys. **100**, 7508 (1994)
25. B. Brocklehurst, Nature **221**, 921 (1969)
26. G.V. Buxton, A.J. Elliot, J. Chem. Soc. Faraday Trans. **89**, 485 (1993)
27. S.P. Mezyk, K.P. Madden, J. Phys. Chem. **103**, 235 (1998)
28. F.J.J.D. Kanter, T.A. Hollander, A.H. Huizer, R. Kaptein, Mol. Phys. **34**, 857 (1977)
29. K. Schulten, P.G. Wolynes, J. Chem. Phys. **68**, 3292 (1978)
30. E.W. Knapp, K. Schulten, J. Chem. Phys. **71**, 1878 (1979)
31. M. Aihara, H.M. Seviran, J.L. Skinner, Phys. Rev. A **41**, 6596 (1990)
32. C.P. Slichter, *Principle of Magnetic Resonance* (Springer, Berlin, 1979)
33. H.A. Schwarz, J. Phys. Chem. **73**, 1928 (1969)
34. G.V. Buxton, C.L. Greenstock, W.P. Helman, A.B. Ross, J. Phys. Chem. Ref. Data **17**, 513 (1988)
35. R.A. Crowell, R. Lian, M.C. Sauer, D.A. Oulianov, I.A. Shkrob, Chem. Phys. Lett. **383**, 481 (2004)
36. B. Kalyanaraman, R.P. Manson, B. Tainer, T.E. Eling, J. Biol. Chem. **257**, 4764 (1982)
37. R. Livingston, H. Zeldes, J. Chem. Phys. **44**, 1245 (1965)
38. J.A. Brivati, M.C.R. Symons, D.J.A. Tingling, J. Chem. Soc. **77**, 6504 (1965)
39. K.R. Leopold, K.M. Evensons, E.R. Comben, J.M. Brown, J. Mol. Spectro. **122**, 440 (1987)
40. A.R. O'Dea, A.F. Curtis, N.J.B. Green, C. Timmel, P.J. Hore, J. Phys. Chem. **103**, 4446 (1999)
41. A.J. Elliot, D.R. McCracken, G.V. Buxton, N.D. Wood, J. Chem. Soc. Faraday. Trans. **86**, 1539 (1990)
42. M.D.E. Forbes, N.V. Lebedeva, R.C. White, T.K. Chen, R. Macarthur, P. Caregnato, T.E. Hill, Mol. Phys. **105**, 2127 (2007)
43. K.H. Schmidt, P. Hans, D.M. Bartels, J. Phys. Chem. **96**, 199 (1992)
44. K.H. Schmidt, P. Hans, D.M. Bartels, J. Phys. Chem. **99**, 10530 (1995)
45. K.M. Salikhov, Y.N. Molin, R.Z. Sagdeev, A.L. Buchachenko, *Spin Polarisation and Magnetic Field Effects in Radical Reactions* (Elsevier, Amsterdam, 1984)
46. T.Y. Karogodina, I.G. Dranov, S.V. Sergeeva, D.V. Stass, U.E. Steiner, J. Phys. Chem. A **12**, 1714 (2011)
47. H.W. Spiess, D. Schweitzer, U. Haeberlen, K.H. Hausser, J. Magn. Reson. **5**, 101 (1971)

# Chapter 6

## Reactive Products: New IRT Algorithm

### 6.1 Introduction

Reactive products play an important part in radiation chemistry and pose a challenging problem in their theoretical modelling within the IRT framework. This is because in IRT the diffusive trajectories are not tracked and as result the distance of the newly formed product to the remaining reactants is not known. This information is needed in the IRT in order to generate a new reaction time from a suitable marginal distribution function. In an attempt to deal with this problem, new methods have been developed which have been applied and tested for two chemical systems: (1) photodissociation of  $\text{H}_2\text{O}_2$  and (2) reactive products following the radiolysis of water. Chapter 5 showed that the first passage algorithm was excellent in describing reactive products originating from a scavenging event, however the parameter space that was explored was quite restricted due to the chemical system being investigated. Therefore, the first part of this chapter checks the accuracy of the first passage algorithm across a much wider parameter range and the results are compared with the diffusion approach and random flights simulations.

The second part of this chapter looks at reactive products for high-permittivity solvents (i.e. water) where a careful scaling of both the initial separation distance and encounter radius is required. Such three body chemical systems are difficult to treat in the IRT due to subtle correlations in distances and reaction times, and it will be checked whether the first passage algorithm is still applicable. As this chapter only investigates the recombination kinetics (which in turn is controlled by the placement of reactive products), no spin effects are required in the model.

## 6.2 Photodissociation of H<sub>2</sub>O<sub>2</sub>

In the photodissociation of H<sub>2</sub>O<sub>2</sub>, scavengers are used to intercept the self-recombination of hydroxyl radicals to allow reactive products R (which are given the characteristic properties of 2-propanolyl radicals) to be formed according to the reaction scheme (Fig. 6.1).

In this reaction scheme,  $S_1$  and  $S_2$  are the scavenging times of the hydroxyl radicals which are obtained from Smoluchowski's time dependent rate constant using the inversion method [1] to give

$$S_{1/2} = -\alpha + \sqrt{\alpha^2 - \frac{\ln U(0, 1]}{kc}} \quad (6.1)$$

where  $k = 4\pi D' a$ ,  $\alpha = a/\pi D'$ , with  $a$  being the encounter radius and  $D'$  the mutual diffusion coefficient.  $T_{g1}$ ,  $T_{g2}$  and  $T_{g3}$  are the geminate recombination times which can be generated from the probability distribution

$$T_g = \frac{(r - a)^2}{4D' \left[ \operatorname{erfc}^{-1} \left( \frac{rU(0,1]}{a} \right) \right]^2} \quad (6.2)$$

where  $r$  is the radical pair separation and  $U(0, 1]$  is a uniformly distributed random number in the interval (0, 1]. In the above reaction scheme, the product of scavenging of the hydroxyl radical by the solvent (which produces R') occurs with a rate constant of  $1.9 \times 10^9 \text{ M}^{-1} \text{ s}^{-1}$  [2]. The placement of reactive products has already been discussed extensively in Sect. 4.4.2.4 and only a brief resumé will be given.

### 6.2.1 Reactive Products Algorithm

**Diffusion approach** The diffusion approach being the simplest algorithm for treating reactive products evolves the interparticle separation by diffusion independently of other such distances. Thus, if at time  $t$  the interparticle separation is  $\mathbf{r}$ , then at  $t'$  the new interparticle separation is  $\mathbf{r}' = \mathbf{r} + \mathbf{N}_3(0,1)$ , with  $\mathbf{N}_3(0,1)$  being a three dimensional normally distributed random number with mean zero and variance  $2D't$ , with  $D'$  being the mutual diffusion coefficient.

**First passage approach** The first passage approach calculates the distance of the newly formed product to the remaining reactants by conditioning on the independent reaction time that exists for that pair. An interparticle distance is generated by sampling from the probability density function

$$p^\dagger = \frac{1}{\sqrt{4\pi D'\tau}} \frac{r_1^*}{q} \left[ \exp\left(-\frac{(r_1^* - q)^2}{4D'\tau}\right) - \exp\left(-\frac{(r_1^* + q)^2}{4D'\tau}\right) \right] \quad (6.3)$$

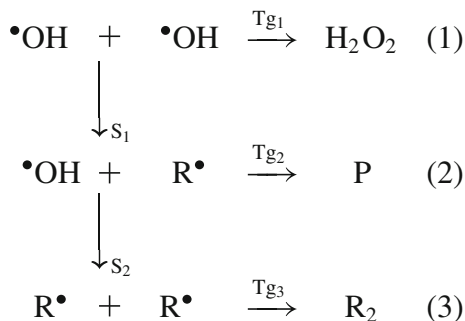


**Fig. 6.1** Reaction scheme employed in this work to model the kinetics of reactive products R<sup>•</sup> formed at steps (2) and (3). In this scheme,  $S_1$  and  $S_2$  are the first and second scavenging times respectively;  $T_{g1}$ ,  $T_{g2}$  and  $T_{g3}$  are the recombination times to form the products H<sub>2</sub>O<sub>2</sub>, P and R<sub>2</sub> respectively. In this reaction scheme R<sup>•</sup> is given the characteristic properties of 2-propanolyl radicals

which is the density for a three dimensional Bessel process started at  $q$  and run for a time  $\tau$ . In the above expression  $r_1^* = (r_1 - a)$ ,  $r_0^* = (r_0 - a)$ ,  $q = r_0^*(t - S_1)/t$  and  $\tau = (t - S_1)S_1/t$ . The new distance ( $r'_{ik}$ ) from the newly formed reactive product  $i$  (formed via the reaction of  $l$  and  $m$  at an encounter distance  $a_{lm}$ ) to the remaining reactant  $k$  involves sampling from the probability distribution (Eq. 4.77) by generating three Gaussian distributed random numbers; two with mean ( $\mu$ ) zero and standard deviation  $\sigma = \sqrt{2D'\tau} (N_{1/2}(0, \sigma))$  and one with  $\mu = q$  and  $\sigma = \sqrt{2D'\tau} (N_3(q, \sigma))$ . The new distance for the pair  $ik$  is then  $r'_{ik} = a_{lm} + \sqrt{N_1^2 + N_2^2 + N_3^2}$ . This new value for  $r'_{ik}$  is subsequently used to generate a new reaction time for the pair  $ik$  using Eq. (6.2).

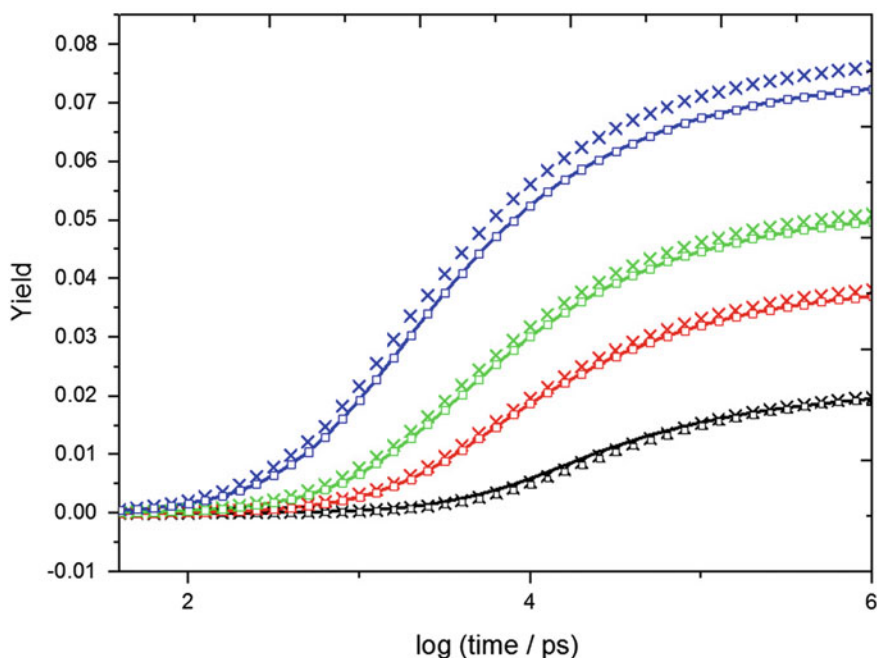
## 6.2.2 Simulation Results

For the purpose of this work, the initial hydroxyl radical separation distances investigated are 5, 7 and 10 Å, using four different concentrations of scavengers (0.1, 0.3, 0.5 and 1.0 M). These parameters are thought to be the most important which influence the placement of reactive products and it is believed that this parameter space is sufficiently wide to test the both the diffusion approach and first passage approach algorithms. The kinetic parameters used in both the IRT and random flights simulations are listed in Table 6.1, with  $5 \times 10^4$  realisations used in all simulations. The simulation results obtained for the recombination yield of R<sub>2</sub> are shown in Figs. 6.2, 6.3 and 6.4

As the placement of the reactive products directly determines the yield of recombination, an inaccurate treatment would obviously lead to an incorrect yield. For example, placing the reactive products too close would lead to more recombination

**Table 6.1** Parameters used in testing all the algorithms in aqueous solution

Parameter	'OH + 'OH	'OH + R'	R' + R'
Relative diffusion coefficient $D'$ ( $\text{\AA}^2 \text{ps}^{-1}$ )	0.44 <sup>a</sup>	0.315 <sup>a,b</sup>	0.19 <sup>b</sup>
Encounter distance $a$ ( $\text{\AA}$ )	2.2 <sup>a</sup>	0.797 <sup>c</sup>	2.76 <sup>c,d</sup>

<sup>a</sup>Reference [3]<sup>b</sup>Reference [4]<sup>c</sup>Calculated as  $k = 4\pi D' a \beta$  ( $\beta$  is  $\frac{1}{2}$  for like species or unity otherwise)<sup>d</sup>Reference [5]**Fig. 6.2** Yield of  $R_2$  obtained at four different concentrations of the scavenger: **a** 0.1 M (*black*) **b** 0.3 M (*red*), **c** 0.5 M (*green*) and **d** 1.0 M (*blue*) using an initial hydroxyl separation of  $5 \text{\AA}$ . Random flights *solid line*, first passage *open square* and diffusion approach *multiplication symbol*

with the converse also true. Hence by indirectly measuring the recombination kinetics one can obtain information about the probability distribution of the spatial distance of the reactive products.

From the analysis of the recombination yield, it is seen that at the parameter space investigated, the first passage approach accurately describes the spatial distribution of reactive products which results in the correct recombination yield. In the case of the diffusion approach, a greater recombination yield of both  $R_2$  and  $P^1$  is predicted in all cases, especially for the case when the hydroxyl radicals are close together

<sup>1</sup> Results are not reported here for the P recombination yield.

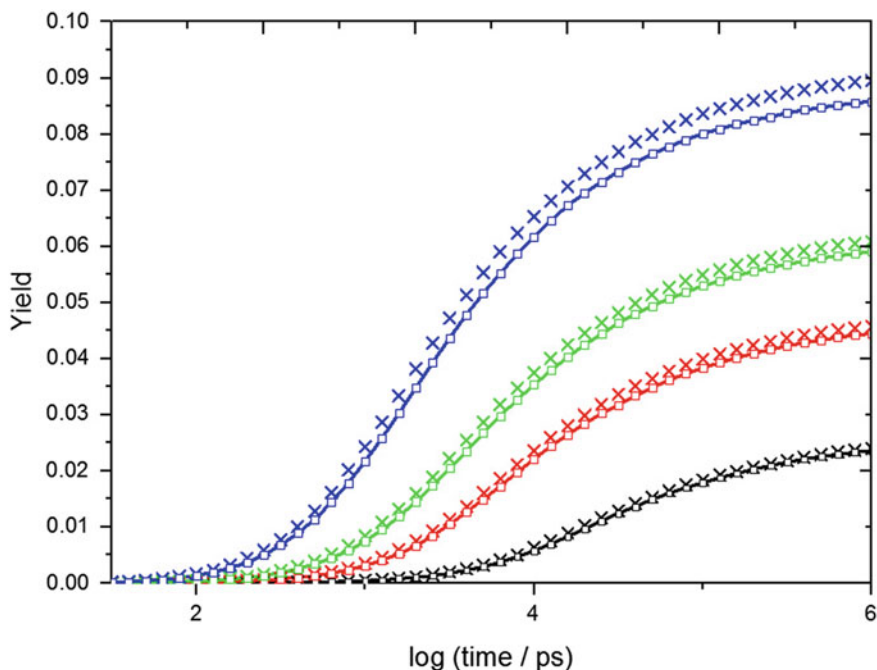


**Fig. 6.3** Yield of R<sub>2</sub> obtained at four different concentrations of the scavenger: **a** 0.1 M (black) **b** 0.3 M (red), **c** 0.5 M (green) and **d** 1.0 M (blue) using an initial hydroxyl separation of 7 Å. Random flights *solid line*, first passage *open square* and diffusion approach *multiplication symbol*

and a relatively high concentration of scavengers is used. The final yield plots in Fig. 6.5 show that the diffusion approach places the reactive product much closer to the encounter radius, leading to an overall increase in the reaction probability. As the scavenger concentration increases this problem is made much worse. However, for a small concentration of scavengers (<0.5 M) the diffusion approach can be reliably used to model reactive products, as essentially good agreement has been obtained with the analytical formulation.

The problem of the reactive product being placed too close to the remaining reactant does not arise in the first passage approach, because the algorithm conditions on when the original encounter radius (i.e. ·OH + ·OH reaction) would be first obtained. Hence, all trajectories which were close to the encounter radius of the ·OH + ·OH pair would have been depleted by reaction, leaving a smaller probability of the reactive product to be anywhere near the encounter cage of the remaining reactant. Clearly, the diffusion approach is unsuitable in accurately modelling the treatment of reactive products in situations where either the initial radicals are close together or a relatively high concentration of scavengers are used.

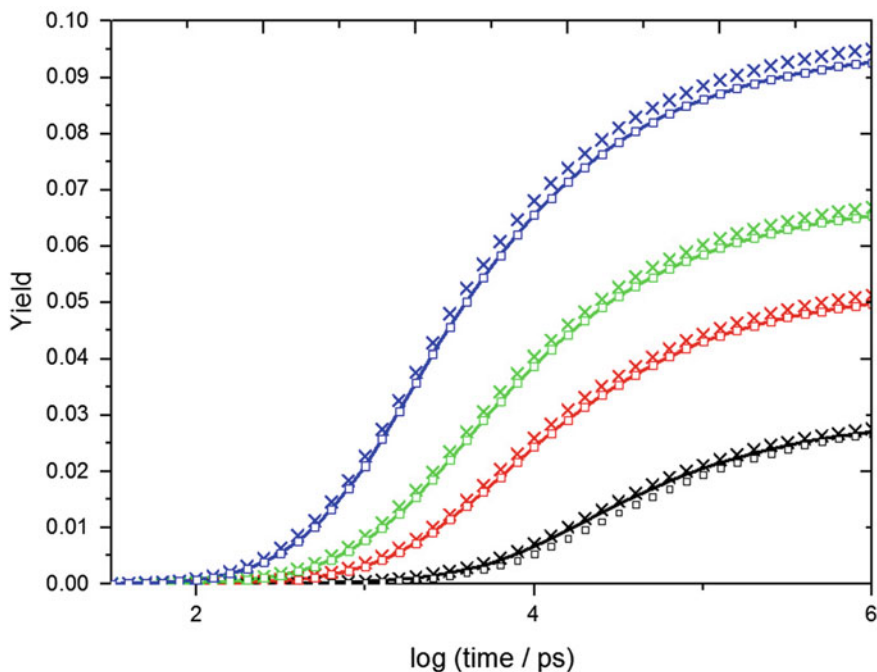


**Fig. 6.4** Yield of  $R_2$  obtained at four different concentrations of the scavenger: **a** 0.1 M (black) **b** 0.3 M (red), **c** 0.5 M (green) and **d** 1.0 M (blue) using an initial hydroxyl separation of  $10\text{\AA}$ . Random flights *solid line*, first passage *open square* and diffusion approach *multiplication symbol*

## 6.3 Radiolysis of Water

The second reaction scheme investigated in this work is shown in Table 6.2, with the respective diffusion coefficients for all the species involved shown in Table 6.3. In this reaction scheme, reactive products are generated at steps (1) and (2) of the reaction scheme. For  $H^+ + e_{aq}^-$ , the reaction is not fully diffusion controlled because  $a'_{\text{eff}} < -r_c$  and it becomes necessary to impose a boundary velocity. A reaction distance of  $5\text{\AA}$  has been used by Pimblott et al. [6] based on the work done by Hart and Anbar [7], using a reaction boundary velocity of  $4.2\text{ m s}^{-1}$ .

### 6.3.1 Diffusion Controlled Reactions

As the reaction scheme contains charged species with a Coulomb potential, generating an analytical recombination time is not possible since the backward diffusion equation for ions cannot be solved in closed form (as discussed in Chap. 4 of this work). However, for high-permittivity solvents such as water, an excellent approximation has been developed [6] which scales the encounter radius and initial separation

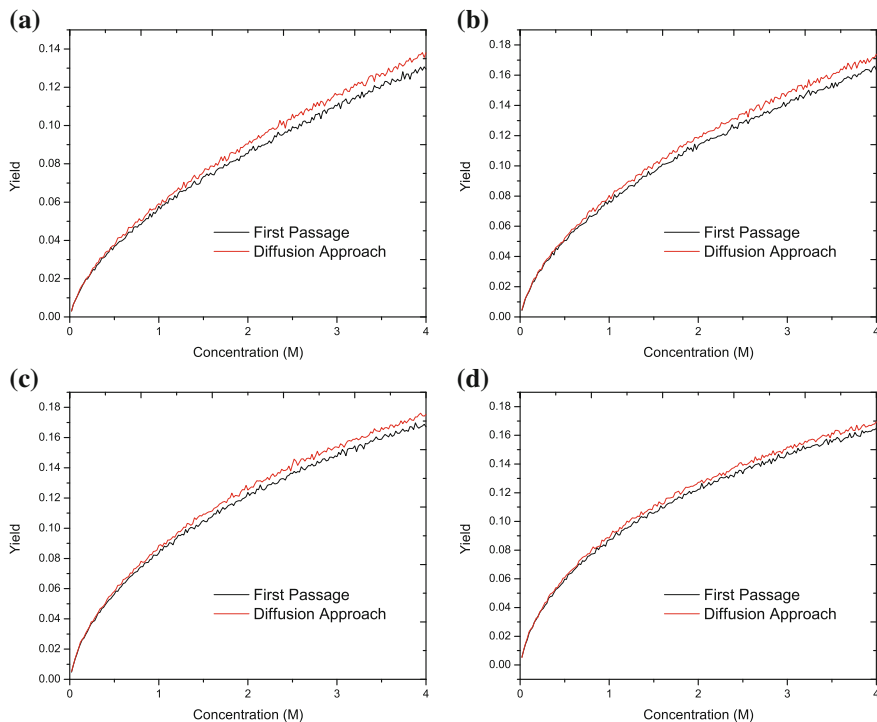


**Fig. 6.5** Plot of the final  $R_2$  yield as a function of the scavenger concentration using an initial radical separation of **a** 4 Å; **b** 6 Å; **c** 8 Å and **d** 10 Å

distance to reduce the system analogous to the neutral case. The expression for the asymptotic yield analogous to the neutral case is known to be exactly

$$W_\infty = a'_{\text{eff}}/r_{\text{eff}} \quad (6.4)$$

with the expression for the time dependent ultimate recombination probability to be

$$W^*(t) = \text{erfc} \left( \frac{r_{\text{eff}} - a'_{\text{eff}}}{\sqrt{2D't}} \right) \quad (6.5)$$

where  $a'_{\text{eff}}$  and  $r_{\text{eff}}$  are defined by the natural scale for diffusion controlled reactions as

$$x_{\text{eff}} = -r_c/[1 - \exp(r_c/x)] \quad (6.6)$$

with  $x = a$  (unscaled encounter radius) and  $r$  (unscaled initial distance) respectively. Reaction times can now be generated for diffusion controlled reactions between ions by sampling from Eq. (6.5) using the standard inversion technique [8].

**Table 6.2** Partial reaction scheme used to model the reactive products of water [6]

Number	Reaction	$k/10^{10} \text{ M}^{-1} \text{ s}^{-1}$	$a/\text{\AA}$	$v/\text{\AA} \text{ ps}^{-1}$
1	$\text{H}^+ + \text{e}_{\text{aq}}^- \rightarrow \text{H}$	2.4	5.0	0.0419
2	$\cdot\text{OH} + \text{e}_{\text{aq}}^- \rightarrow \text{OH}^-$	3.0	5.4	
3	$\text{H} + \cdot\text{OH} \rightarrow \text{H}_2\text{O}$	2.0	2.7	
4	$\text{OH}^- + \text{H}^+ \rightarrow \text{H}_2\text{O}$	14.3	12.3	

**Table 6.3** Diffusion coefficient of the species involved following the radiolysis of water [6]

Species	$D/\text{\AA}^2 \text{ ps}^{-1}$
$\text{e}_{\text{aq}}^-$	0.45
H	0.7
$\text{H}^+$	0.9
$\cdot\text{OH}$	0.28
$\text{OH}^-$	0.5

Pimblott et al. [9] have demonstrated the importance of using the transformed distance scale for both the encounter distance and interparticle separation. If only  $a'_{\text{eff}}$  is used, significant errors are shown to occur for reactants at short separation distances, greatly biasing the spur kinetics.

### 6.3.2 Partially Diffusion Controlled Reactions

For partially diffusion controlled reactions the reactivity of the surface must be taken into consideration, which can be readily achieved by using the radiation boundary conditions of the form

$$p(a) = \left. \frac{D'}{v} \frac{\partial p}{\partial r} \right|_a \quad (6.7)$$

with  $p(a)$  being the probability density for the pair to be at the encounter radius  $a$ ,  $v$  is the reactivity of the surface,  $D'$  is the mutual diffusion coefficient and  $r$  the initial radical pair separation. The expression for the asymptotic yield is

$$W_\infty = a'_{\text{eff}}/r \quad (6.8)$$

and the recombination probability conditioned on ultimate reaction is

$$W^* = \text{erfc}(b) - \exp(q^2 + 2qb)\text{erfc}(q + b) \quad (6.9)$$

with

$$a'_{\text{eff}} = \frac{vr^2}{(rv + D')} \quad (6.10)$$

$$q = \frac{rv + D'}{R} \left( \frac{t}{D'} \right)^{1/2} \quad (6.11)$$

$$b = \frac{r - a}{2(D't)^{1/2}} \quad (6.12)$$

The effective reaction distance  $a'_{\text{eff}}$  can be used to link  $v$  to the bimolecular rate constant  $k_2$  as

$$k_2 = 4\pi D' a'_{\text{eff}} = \frac{4\pi D' a^2 v}{(rv + D')} \quad (6.13)$$

Green [10] has shown that Eq. (6.9) can also be applied for partially diffusion controlled reactions between ions by using the definition of  $q$  and  $b$  to be

$$q = \frac{4r^2\alpha}{r_c^2} \left( \frac{t}{D'} \right) \sinh^2 \left( \frac{r_c}{2R} \right) \quad (6.14)$$

$$b = r_c [\coth(r_c/2r) - \coth(r_c/2a)] / 4(D't)^{1/2} \quad (6.15)$$

with

$$\alpha = v + r_c D' / [a^2(1 - \exp(-r_c/a))] \quad (6.16)$$

The asymptotic yield  $W_\infty$  is now equal to  $a'_{\text{eff}}/r_{\text{eff}}$ , with  $r_{\text{eff}}$  given by Eq. (6.6) and  $a'_{\text{eff}}$  defined as

$$a'_{\text{eff}} = -r_c / [1 - \exp(r_c/a)(1 + D'r_c/va^2)] \quad (6.17)$$

### 6.3.3 Simulation Results

The reaction scheme under consideration is complicated by the necessity to know the distance of the newly formed product to the remaining reactants. For example if  $\text{H}^+$  and  $\text{e}_{\text{aq}}^-$  react to form H, then the position of the reactive product H is generated conditioned on either the  $\text{H}^+$  or  $\text{e}_{\text{aq}}^-$  position. This is clearly not a feasible method since choosing either position will introduce a source of bias. The first passage algorithm does not suffer from this problem as the algorithm calculates the conditioned distance and time for the  $\text{H}^+ \cdot \text{OH}$  reaction, from the distribution of when the  $\text{e}_{\text{aq}}^- + \cdot \text{OH}$  would first have hit the encounter boundary.

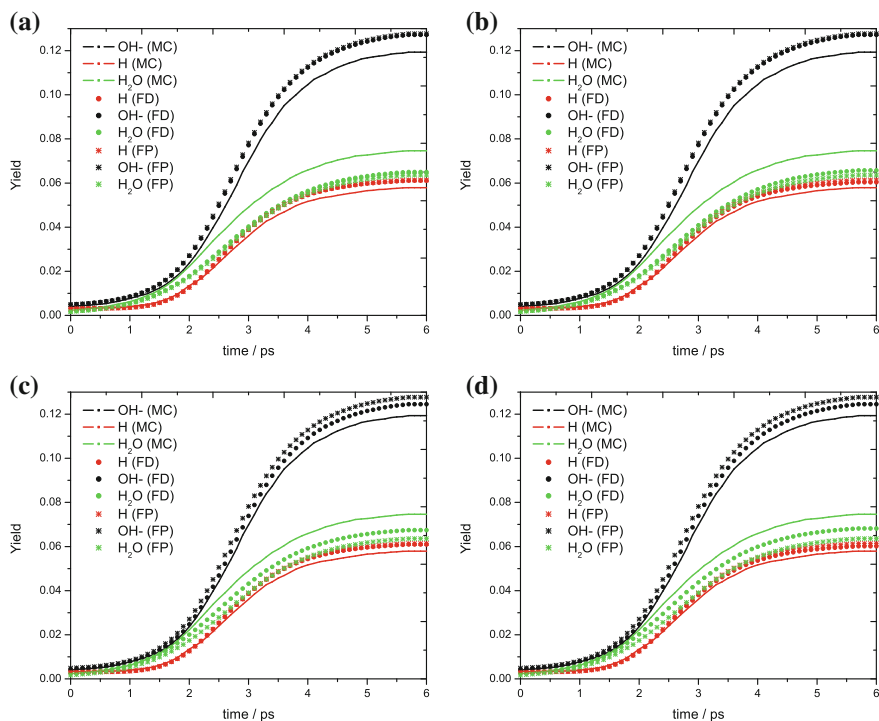


**Fig. 6.6** Reactive product H/OH<sup>-</sup> placed at: **a** e<sub>aq</sub><sup>-</sup> position; **b** H<sup>+</sup>/e<sub>aq</sub><sup>-</sup> position; **c** e<sub>aq</sub><sup>-</sup>/OH position; **d** H<sup>+</sup>/OH position. Abbreviation used: free diffusion (FD) and first passage (FP). A spur width of  $\sigma(7.5 \text{ \AA})$  was used for <sup>•</sup>OH, H<sup>+</sup> and  $\sigma(20 \text{ \AA})$  for e<sub>aq</sub><sup>-</sup>. Here MC refers to random flights simulation. *x*-axis are on a logarithmic scale

In this section, the effect of placing the reactive products H and OH<sup>-</sup> conditioned on the position of the reactants is investigated within the diffusion approach and compared with random flights simulations and the first passage algorithm. This will allow the magnitude of the bias introduced by the diffusion approach to be analysed in detail. For all simulations presented, the initial configuration chosen for the <sup>•</sup>OH, e<sub>aq</sub><sup>-</sup> and H<sup>+</sup> is similar to the configuration chosen by Pimlott [11] such that the <sup>•</sup>OH and H<sup>+</sup> are distributed according to a Gaussian distribution with a spur width of  $\sigma(7.5 \text{ \AA})$  and the e<sub>aq</sub><sup>-</sup> is Gaussian distributed with a variable spur width of  $\sigma(20 \text{ \AA})$ ,  $\sigma(30 \text{ \AA})$  and  $\sigma(40 \text{ \AA})$  (Figs. 6.6, 6.7 and 6.8 respectively). Three different spur widths were chosen for the e<sub>aq</sub><sup>-</sup> to allow the parameter space to be explored as fully as possible. Furthermore, to thoroughly test the effect of the spatial configuration of H<sup>+</sup>, OH<sup>-</sup> and e<sub>aq</sub><sup>-</sup> on the placement of reactive products, another spatial configuration was considered in Sect. 6.3.4, in which the H<sup>+</sup> and OH<sup>-</sup> was separated by  $3 \text{ \AA}$  and e<sub>aq</sub><sup>-</sup> was Gaussian distributed from the midpoint of (H<sup>+</sup>, OH<sup>-</sup>) pair.<sup>2</sup> The number of

<sup>2</sup> This spatial configuration is more realistic for H<sup>+</sup>, OH<sup>-</sup> and e<sub>aq</sub><sup>-</sup> following the photolysis of water.

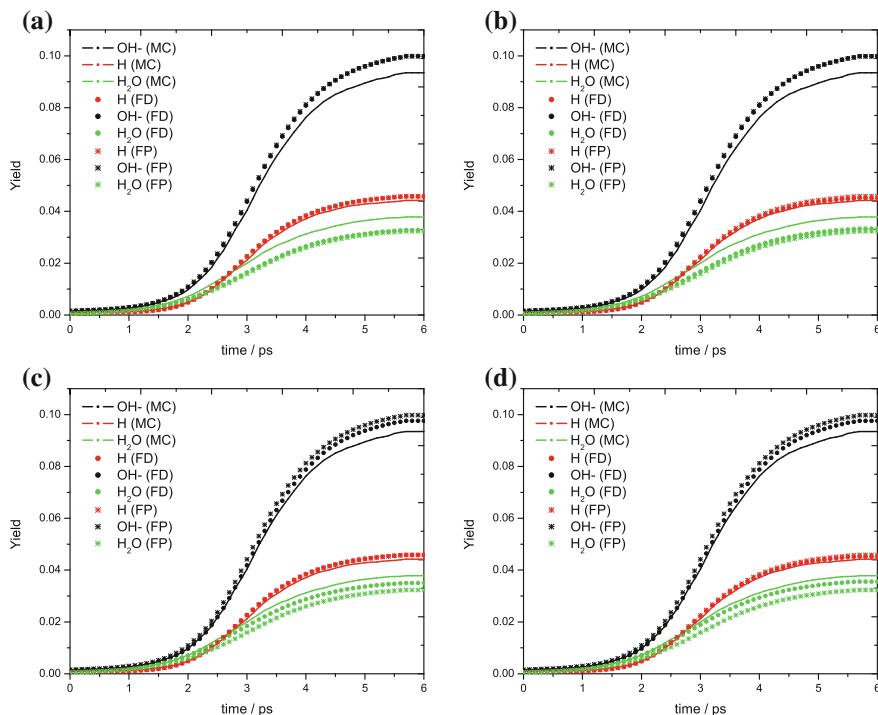


**Fig. 6.7** Reactive product H/OH<sup>-</sup> placed at: **a**  $e_{aq}^-$  position; **b**  $H^+/e_{aq}^-$  position; **c**  $e_{aq}^-/OH$  position; **d**  $H^+/OH$  position. Abbreviation used: free diffusion (FD) and first passage (FP). A spur width of  $\sigma(7.5 \text{ \AA})$  was used for  $\cdot OH$ ,  $H^+$  and  $\sigma(30 \text{ \AA})$  for  $e_{aq}^-$ . Here MC refers to random flights simulation.  $x$ -axis are on a logarithmic scale

realisations used in all simulations which were found to provide acceptable statistics were  $5 \times 10^4$  (random flights) and  $1 \times 10^6$  (IRT).

**Experimentally observable yield** Although in this section the yields of all possible reactions are presented (i.e. H, OH<sup>-</sup> and H<sub>2</sub>O), it is important to note that the only experimentally detectable yield is the decay of  $e_{aq}^-$  owing to its large molar extinction coefficient ( $2.27 \times 10^{-3} \text{ M}^{-1} \text{ \AA}^{-1}$  [12]). However, as the aim of this chapter is to analyse the spatial distribution of reactive products, simply modelling the decay of the  $e_{aq}^-$  will not provide sufficient information.

### 6.3.3.1 Analysis

It can be seen from the simulations (Figs. 6.6, 6.7 and 6.8) that in the parameter space investigated, the effect of having to choose where to place the reactive product becomes more significant as the spur density increases. For example, with a spur

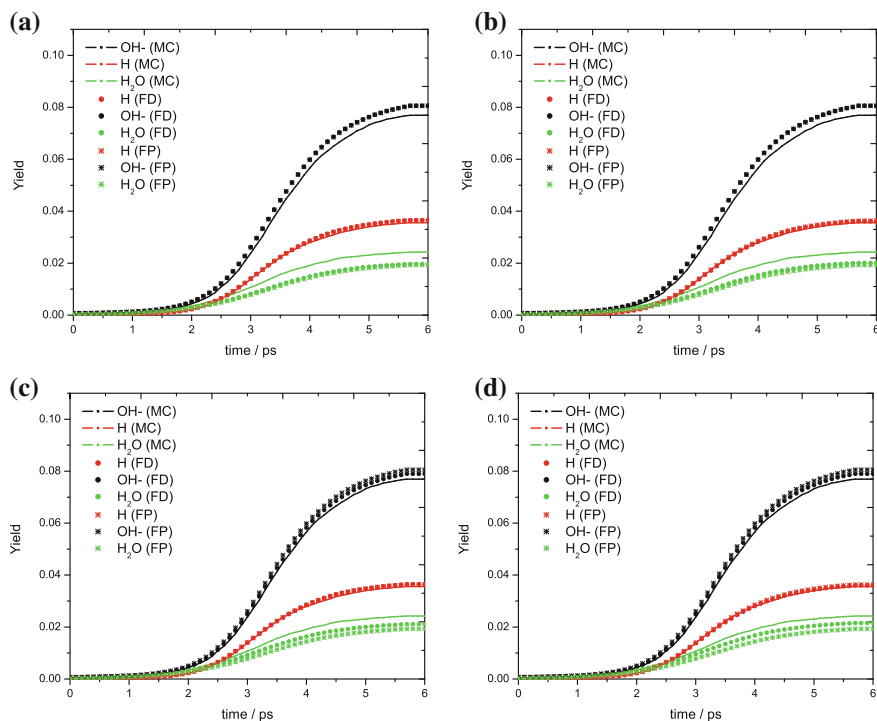


**Fig. 6.8** Reactive product H/OH<sup>-</sup> placed at: **a** e<sub>aq</sub><sup>-</sup> position; **b** H<sup>+</sup>/e<sub>aq</sub><sup>-</sup> position; **c** e<sub>aq</sub><sup>-</sup>/OH position; **d** H<sup>+</sup>/OH position. Abbreviation used: free diffusion (FD) and first passage (FP). A spur width of  $\sigma(7.5 \text{ \AA})$  was used for  $\cdot\text{OH}$ , H<sup>+</sup> and  $\sigma(40 \text{ \AA})$  for e<sub>aq</sub><sup>-</sup>. Here MC refers to random flights simulation.  $x$ -axis are on a logarithmic scale

width of  $\sigma(40 \text{ \AA})$  and  $\sigma(7.5 \text{ \AA})$  for e<sub>aq</sub><sup>-</sup> and H<sup>+</sup>,  $\cdot\text{OH}$  respectively, the kinetics are in good agreement with random flights simulations. However, upon decreasing the spur width to  $\sigma(20 \text{ \AA})$  for e<sub>aq</sub><sup>-</sup> the yield of H<sub>2</sub>O is significantly underestimated. This problem becomes worse if the initial species are placed closer together. It can be inferred from the results that essentially both the first passage and diffusion approach place the reactive products too far from the remaining reactant, which leads to more OH<sup>-</sup> and H escaping. The reason for the analytical first passage algorithm to fail in reproducing the kinetics can be attributed to subtle three-body spatial correlations in the distance and reaction times (i.e. both models neglect the fact that if the  $\cdot\text{OH}$  was close to e<sub>aq</sub><sup>-</sup> then the H<sup>+</sup> should be as well (with the converse also true) because the distribution of the H<sup>+</sup> and  $\cdot\text{OH}$  is narrow and both species are initially close together). Hence at the point of recombination the first passage algorithm places the reactive product too far from the remaining reactant leading to more escape as seen from Figs. 6.6, 6.7 and 6.8. A discussion of this correlation is now presented in the next section.

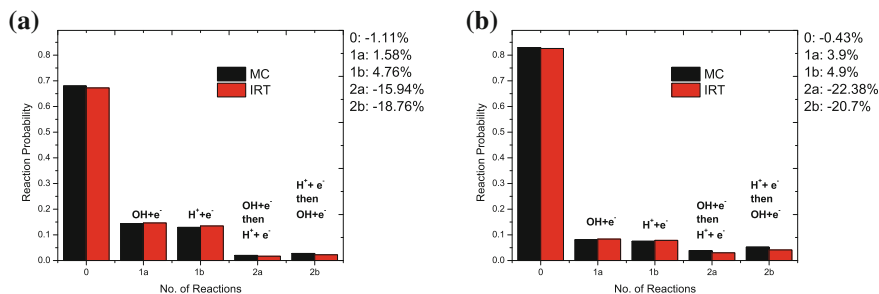


**Fig. 6.9** Recombination yield for H, OH<sup>-</sup> and H<sub>2</sub>O with % error, highlighting the spatial correlation. A spur width of  $\sigma(7.5 \text{ \AA})$  was used for  $\cdot\text{OH}$ , H<sup>+</sup> and **a**  $\sigma(20 \text{ \AA})$ ; **b**  $\sigma(40 \text{ \AA})$  for  $e_{\text{aq}}^-$ . In (b) the 2 reactions have been increased by a factor of 6 for clarity. All reactions were assumed diffusion controlled and all particles were made neutral. Here MC refers to random flights simulation

### 6.3.3.2 Three-Body Correlations

In order to extract the correlation between the  $e_{\text{aq}}^-$ , H<sup>+</sup> and  $\cdot\text{OH}$  distances, a set of random flights simulations were done in which at the point of the first reaction, the simulation carried on as normal as if the first reaction had not occurred (the type of the first reaction was however recorded). At the end of the simulation, a series of histograms were obtained which showed the probability of undergoing 0, 1 or 2 reactions and the type of reactions that had occurred. The results presented in Figs. 6.9 and 6.10 highlight the following:

- 0 reactions: IRT underestimates this because if  $\cdot\text{OH} + e_{\text{aq}}^-$  fails,  $e_{\text{aq}}^-$  has also diffused away from H<sup>+</sup> making the reaction  $e_{\text{aq}}^- + \text{H}^+$  less likely as well. IRT neglects this correlation and makes the distances ( $\cdot\text{OH}$ ,  $e_{\text{aq}}^-$ ) and ( $e_{\text{aq}}^-$ , H<sup>+</sup>) independent.
- 2 reactions: IRT underestimates because if  $\cdot\text{OH} + e_{\text{aq}}^-$  happens,  $e_{\text{aq}}^-$  has diffused towards  $\cdot\text{OH}$  and therefore towards H<sup>+</sup> as well, increasing the likelihood of  $e_{\text{aq}}^- + \text{H}^+$  reaction. Again IRT makes the two reactions possible independent.
- 1 reaction: IRT overestimates because by treating the  $e_{\text{aq}}^-$ , H<sup>+</sup> and  $\cdot\text{OH}$  distances as independent, this effectively gives too much chance for 1 reaction irrespective of other. Also the probabilities have to add up to one.

It is also seen from Figs. 6.9b, 6.10b and 6.11b that as the spur density decreases (i.e. as the spur width increases), the spatial correlation becomes less important due to the large escape yield, which explains the convergence in the recombination kinetics between the IRT and random flights at larger spur widths. From further simulations it was found that changing either the encounter radius or mutual diffusion coefficient for the  $e_{\text{aq}}^- + \cdot\text{OH}$  or  $e_{\text{aq}}^- + \text{H}^+$  reactions by 10% did not significantly affect the correlation in the recombination kinetics.

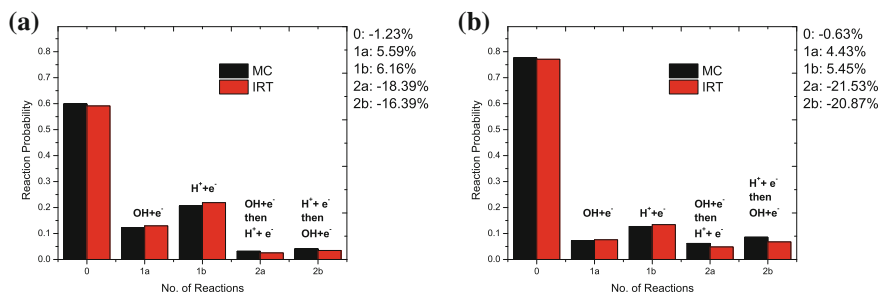


**Fig. 6.10** Recombination yield for H, OH<sup>-</sup> and H<sub>2</sub>O with % error, highlighting the spatial correlation. A spur width of  $\sigma(7.5 \text{ \AA})$  was used for  $\cdot\text{OH}$ , H<sup>+</sup> and **a**  $\sigma(20 \text{ \AA})$ ; **b**  $\sigma(40 \text{ \AA})$  for  $e_{\text{aq}}^-$ . In **(b)** the 2 reactions have been increased by a factor of 6 for clarity. All reactions were assumed diffusion controlled with H<sup>+</sup> and  $e_{\text{aq}}^-$  now charged. Here MC refers to random flights simulation

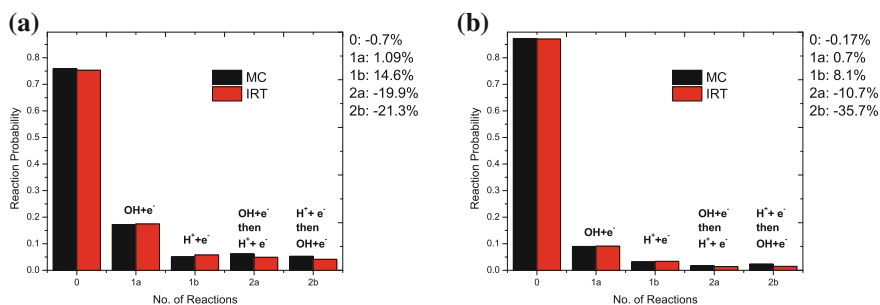


**Fig. 6.11** Recombination yield for H, OH<sup>-</sup> and H<sub>2</sub>O with % error, highlighting the spatial correlation. A spur width of  $\sigma(7.5 \text{ \AA})$  was used for  $\cdot\text{OH}$ , H<sup>+</sup> and **a**  $\sigma(20 \text{ \AA})$ ; **b**  $\sigma(40 \text{ \AA})$  for  $e_{\text{aq}}^-$ . In **b** the 2 reactions have been increased by a factor of 6 for clarity. Reaction H<sup>+</sup> +  $e_{\text{aq}}^-$  was made partially diffusion controlled (and charged). Here MC refers to random flights simulation

### 6.3.4 Centre of Diffusion Vector Method

In the previous section it was shown that both the first passage and free diffusion approach place the reactive products with an incorrect probability distribution function, leading to a bias in the recombination products. In this section, the bias within the free diffusion approach is removed by calculating the centre of diffusion vector of the encountering diffusion pair<sup>3</sup> and generating a new reaction time, assuming the reactive product is placed at the centre of mass of the reacting pair. All other reactants diffuse independently of the centre of mass. To illustrate the algorithm, if the reaction H<sup>+</sup> +  $e_{\text{aq}}^-$  had occurred first, then the centre of diffusion vector ( $C_{H^+e^-}$ ) is calculated as

<sup>3</sup> Derivation shown in Sect. A.1 of the Appendix.

$$\mathbf{C}_{H^+e^-} = \frac{D_{e^-}\mathbf{R}_{H^+} + D_{H^+}\mathbf{R}_{e^-}}{D_{e^-} + D_{H^+}} \quad (6.18)$$

with  $D_x$  and  $\mathbf{R}_x$  being the diffusion coefficient and position vector of particle  $x$  respectively. At the moment of geminate recombination between  $H^+ + e_{\text{aq}}^-$ , the distance between  $\mathbf{C}_{H^+e^-}$  and  $\cdot\text{OH}$  (the remaining reactant) is generated from the initial  $\mathbf{C}_{H^+e^-}$  and  $\cdot\text{OH}$  distance, assuming  $\mathbf{C}_{H^+e^-}$  and  $\cdot\text{OH}$  diffuse independently<sup>4</sup> with mutual diffusion coefficient  $D'$  equalling to  $D_{\mathbf{C}_{H^+e^-}} + D_{\text{OH}}$ , where

$$D_{\mathbf{C}_{H^+e^-}} = \frac{D_{e^-}D_{H^+}}{D_{e^-} + D_{H^+}} \quad (6.19)$$

In this method the bias is removed, since the distance between the  $\cdot\text{OH}$  to the newly formed H is calculated based on the centre of diffusion vector of  $H^+$  and  $e_{\text{aq}}^-$ , and is not biased towards the positions of either the  $H^+$  or  $e_{\text{aq}}^-$ . This procedure can obviously be repeated should the reaction between the  $\cdot\text{OH}$  and  $e_{\text{aq}}^-$  had occurred first, with the centre of diffusion vector given instead as

$$\mathbf{C}_{e^- \text{OH}} = \frac{D_{e^-}\mathbf{R}_{\text{OH}} + D_{\text{OH}}\mathbf{R}_{e^-}}{D_{e^-} + D_{\text{OH}}} \quad (6.20)$$

Using the same initial configuration of the  $H^+$ ,  $e_{\text{aq}}^-$  and  $\cdot\text{OH}$  as previously reported, the centre of diffusion vector method significantly corrects for the recombination kinetics with good agreement obtained for a spur width of  $\sigma(40 \text{ \AA})$  for the  $e_{\text{aq}}^-$  (Fig. 6.12). The small discrepancy seen in the recombination yields for a spur width of  $\sigma(20 \text{ \AA})$  for the  $e_{\text{aq}}^-$  arises again due to three-body spatial and time correlations which the algorithm has not taken into consideration (i.e. the independent reaction times approximation is still made). The centre of diffusion vector approach was tested for even smaller spur widths of  $\cdot\text{OH}$ ,  $H^+$  and  $e_{\text{aq}}^-$  where the correlations strongly influence the recombination kinetics. From Fig. 6.12d, it can be seen that using a spur width of  $\sigma = 7.5 \text{ \AA}$  for all three species (which would enhance the effect of spatial correlations in the distances), excellent agreement can still be obtained even though no explicit consideration of the correlations has been taken into account.

To thoroughly test the centre of diffusion vector approach, the spatial configuration of  $e_{\text{aq}}^-$ ,  $H^+$  and  $\text{OH}^-$  was further varied, in which  $H^+$  and  $\text{OH}^-$  were separated by one water molecule ( $3 \text{ \AA}$ ) and the  $e_{\text{aq}}^-$  was Gaussian distributed with a variable spur width from the midpoint of  $H^+$  and  $\cdot\text{OH}$ . Within this spatial configuration, excellent agreement is again obtained (Fig. 6.13), suggesting the centre of diffusion vector approach to be applicable for handling reactive products following the photolysis of water.

---

<sup>4</sup> Using the free diffusion approach.

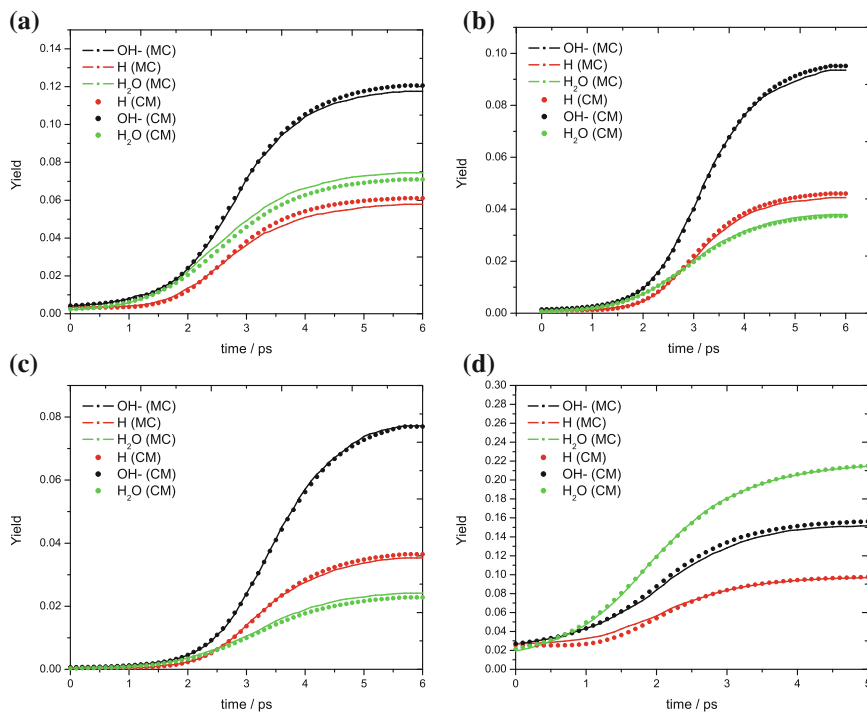


**Fig. 6.12** Recombination yield for H, OH<sup>-</sup> and H<sub>2</sub>O using a spur width of  $\sigma(7.5 \text{ \AA})$  for  $\cdot\text{OH}$ , H<sup>+</sup> and **a**  $\sigma(20 \text{ \AA})$ ; **b**  $\sigma(30 \text{ \AA})$ ; **c**  $\sigma(40 \text{ \AA})$  and **d**  $\sigma(7.5 \text{ \AA})$  for  $e_{\text{aq}}^-$ . x-axis are on a logarithmic scale. Abbreviations used: Monte Carlo random flights (MC) and centre of diffusion vector approach (CM)

### 6.3.4.1 Correcting the Centre of Diffusion Vector Approach for Electrostatic Interaction

In the centre of diffusion vector approach, it was assumed that the centre of mass of the reacting pair and the remaining reactant diffuse independently. In this chemical system however, the relative motion of the centre of diffusion vector for  $e_{\text{aq}}^- + \cdot\text{OH}$  and the H<sup>+</sup> will be influenced by the electrostatic interaction, and treating these as independent is not strictly correct. In an attempt to take this into account, the following method was employed: if the reaction of  $e_{\text{aq}}^- + \cdot\text{OH}$  occurs first, the centre of mass vector  $\mathbf{C}_{H+e^-}$  is calculated from Eq. (6.18). At the point of recombination of  $e_{\text{aq}}^- + \cdot\text{OH}$  the position vector of  $\mathbf{R}_{e^-}$  is substituted by  $\mathbf{R}_{\text{OH}}$  into Eq. (6.18) (making use of the fact that  $\mathbf{R}_{\text{OH}} = \mathbf{R}_{e^-}$ ), and by rearranging this equation the explicit position of  $\mathbf{R}_{H^+}$  can be found. From Fig. 6.14 it can be seen that although good agreement for the H yield can be obtained, the kinetics for the formation of OH<sup>-</sup> and H<sup>+</sup> (for all distributions of the  $e_{\text{aq}}^-$  investigated) is too slow, which suggests the OH<sup>-</sup> and H<sup>+</sup> are formed too far apart leading to more escape. This method is clearly not an improvement and was investigated no further.

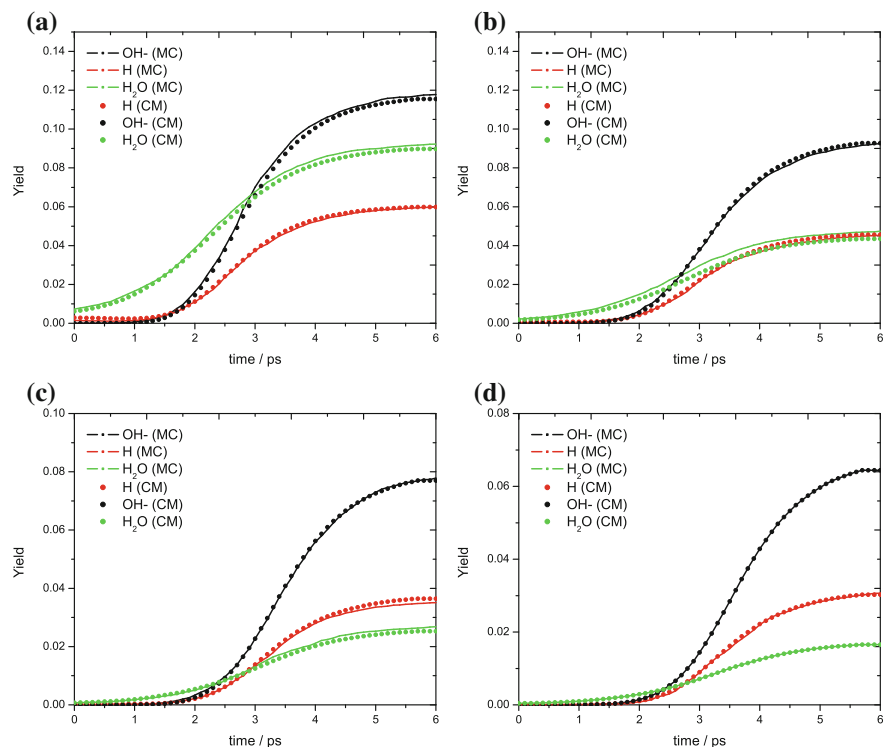


**Fig. 6.13** Recombination yield for H, OH<sup>-</sup> and H<sub>2</sub>O with the H<sup>+</sup> and ·OH separated by 3 Å; e<sub>aq</sub><sup>-</sup> was Gaussian distributed from the midpoint of H<sup>+</sup> and ·OH with a spur width of **a** 20 Å, **b** 30 Å, **c** 40 Å and **d** 50 Å. *x*-axis are on a logarithmic scale. Abbreviations used: Monte Carlo random flights (MC) and centre of diffusion vector approach (CM)

### 6.3.5 Discussion and Further Work

From the analysis of the results presented in this chapter, it appears that for a complex chemical system like the radiolysis of water, the centre of diffusion vector algorithm is a substantial improvement on all previous algorithms for placing reactive products. For chemical systems with greater than two particles, the diffusion approach is not a feasible method, since the reactive product needs to be placed conditioned on the initial position of one of the encountering particles. As to which position will give a more accurate description of the kinetics can only be obtained by trial and error, making it unfeasible to use for large chemical systems or for track structure modelling. In the case of the radiolysis of water, the first passage approach has also been shown to place the reactive products further apart, leading to more escape yield. This is because independence of reaction times is assumed, but for a three-body system there are subtle spatial correlations which need to be taken into account.

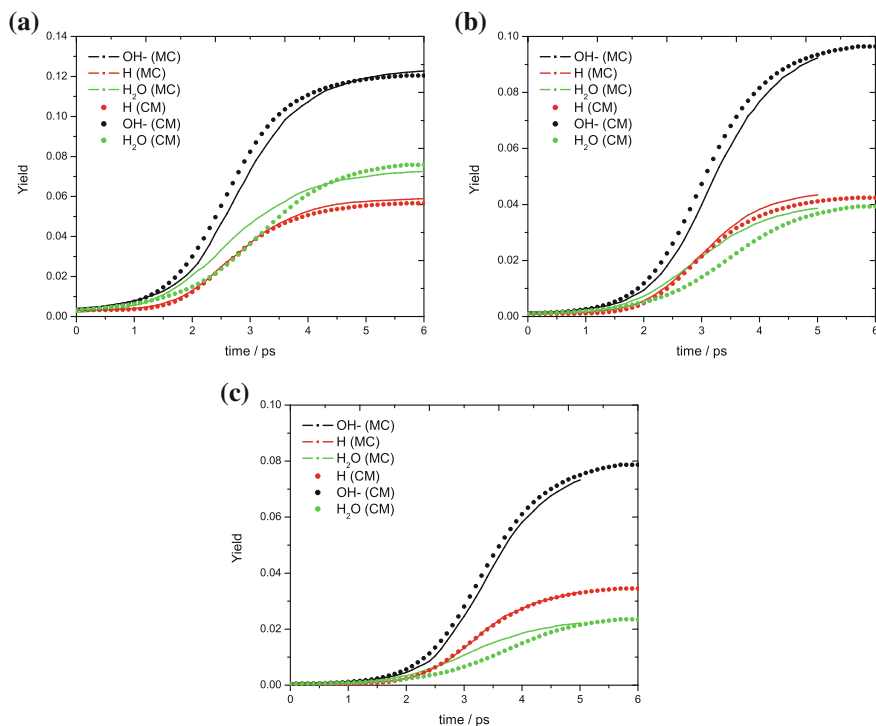


**Fig. 6.14** Recombination yield for H, OH<sup>-</sup> and H<sub>2</sub>O using a spur width of  $\sigma(7.5 \text{ \AA})$  for  $\cdot\text{OH}$ , H<sup>+</sup> and **a**  $\sigma(20 \text{ \AA})$ ; **b**  $\sigma(30 \text{ \AA})$  and **c**  $\sigma(40 \text{ \AA})$  for  $e_{\text{aq}}^-$ . x-axis are on a logarithmic scale. Abbreviations used: Monte Carlo random flights (MC) and centre of diffusion vector approach (CM)

In conclusion, for an accurate treatment of reactive products in the IRT framework the first passage algorithm should be utilised to treat all *scavenging events*, whilst for three body systems, the centre of diffusion vector method should be utilised to treat all *geminate recombinations*. Further work in this area includes investigating whether spatial correlations for spurs containing more than three particles still exist, and under what parameter range the first passage algorithm can be utilised to treat both geminate recombination and scavenging.

## References

1. L. Devroye, *Non-uniform Random Variate Generation* (Springer, New York, 1986)
2. L.M. Dorfman, D.E. Adams, *Reactivity of the Hydroxyl Radical in Aqueous Solution* (National Bureau of Standards, Washington, 1972)
3. A.J. Elliot, D.R. McCracken, G.V. Buxton, N.D. Wood, *J. Chem. Soc. Faraday. Trans* **86**, 1539 (1990)
4. T. Ichino, R.W. Fessenden, *J. Phys. Chem. A* **111**, 2527 (2007)

5. S.P. Mezyk, K.P. Madden, *J. Phys. Chem.* **103**, 235 (1998)
6. N.J.B. Green, M.J. Pilling, S.M. Pimblott, P. Clifford, *J. Phys. Chem.* **94**, 251 (1990)
7. E.J. Anbar, *The Hydrated Electron* (Wiley, New York, 1970)
8. B.D. Ripley, *Int. Statist. Rev.* **51**, 301 (1983)
9. P. Clifford, N.J.B. Green, M.J. Pilling, S.M. Pimblott, *J. Phys. Chem.* **91**, 4417 (1987)
10. N.J.B. Green, *Chem. Phys. Lett.* **107**, 485 (1984)
11. S.M. Pimblott, J.A. LaVerne, *J. Phys. Chem.* **101**, 5828 (1997)
12. P.M. Hare, E.A. Price, D.M. Bartels, *J. Phys. Chem. A.* **112**, 6800 (2008)

# Chapter 7

## Correlation Between Scavenging and Recombination Times for Ions in Low Permittivity Solvents

### 7.1 Introduction

The competition between scavenging and geminate ion recombination is complicated by the Coulombic interaction between the particles. The complexity arises for two reasons: (i) the difficulty of describing the ion recombination and (ii) the possible effect on the scavenging rate of the drift caused by the Coulomb potential. The first can be described using the analytic solution of Hong and Noolandi [1], which gives the scavenging probability under the assumptions:

1. Scavenging is unaffected by the Coulombic drift
2. The scavenging rate constant is time independent

The scavenging probability can also be taken into consideration using the numerical grid generated for recombination (see Sect. 4.4.4.1) using either a time-dependent pseudo first order scavenging rate constant, or an explicit treatment of the scavengers. Unfortunately, this method does not help with (1); it is known that ion recombination is dominated by drift, and it is an acceptable approximation to use the approximation by Williams [2] for the recombination time. It is also known that the steady state scavenging rate constant in an electric field depends on drift [3], and it is an obvious question to ask whether the drift in ion recombination has an effect on the competing scavenging rate. This chapter aims to provide a detailed study to investigate this effect.

### 7.2 One Scavengeable Species

The simplest reaction scheme used to test Smoluchowski's time dependent rate constant takes the form



**Table 7.1** Kinetic parameters used in both the random flights and IRT simulation programs to test Smoluchowski's time dependent scavenging rate constant for ions

Parameter	Value
Geminate reaction distance (Å)	5
Scavenging reaction distance (Å)	4
Onsager distance $r_c$ (Å)	290 ( <i>n</i> -hexane)
No. of realisations (yields)	$5 \times 10^4$ (random flights and IRT)
No. of realisation (rate constant)	$1 \times 10^5$ (random flights and IRT)

where geminate recombination and scavenging effectively compete with each other. In this particular reaction scheme only the electron is scavengable by a scavenger S. Although the  $eS^-$  can further react with  $h^+$ , this reaction is unimportant as only the scavenging rate is of interest. To simplify the model, scavengers were assumed to be stationary. The initial parameters used to simulate the reaction scheme are detailed in Table 7.1.

In the random flights simulation, scavengers were treated explicitly, such that the  $e^-$  has to diffuse towards a stationary S to react. The IRT algorithm made use of Smoluchowski's time dependent rate constant, in which reaction times were generated from the probability distribution

$$T_s = -\alpha + \sqrt{\alpha^2 - \frac{\ln U(0, 1]}{kc}} \quad (7.3)$$

where  $\alpha = \sqrt{\pi D' t}$ ,  $c$  is the concentration of scavengers,  $k$  is the scavenging rate constant,  $D'$  the relative diffusion coefficient and  $U(0, 1]$  is a uniformly distributed random number. Reaction times between the  $e^-$  and  $h^+$  were generated according to the algorithm outlined in Sect. 4.4.4.1.

Figure 7.1 shows an interesting discrepancy in the  $eS^-$  yield obtained using both the random flights and IRT methods. When the  $e^- + h^+$  are placed at a distance of 20 Å apart, random flights simulations show that scavenging intercepts recombination more effectively leading to more scavenging yield and less recombination yield. This effect is neglected in the IRT because the effect of the relative drift of the ions on the scavenger subspace is not explicitly taken into consideration. The results clearly show that for ions close together (where the relative drift vector is appreciable), simply using Smoluchowski's time dependent rate constant is not correct, since it significantly underestimates the yield of scavenging.

It was hypothesised that the extra scavenging effect should diminish with increasing separation of the radical ion-pair. This is because as the ion-pair separation increases the initial drift velocity decreases (as shown in Eq. 7.10). If the drift velocity remains small whilst the  $e^-$  is scavenged then the kinetics should be accurately described using Smoluchowski's time dependent rate constant. As seen from the results presented in Fig. 7.2, this hypothesis is indeed found to be true.

To explain the discrepancy in the scavenging yield, it was hypothesised that the failure for the IRT algorithm to reproduce the scavenging kinetics arose because of

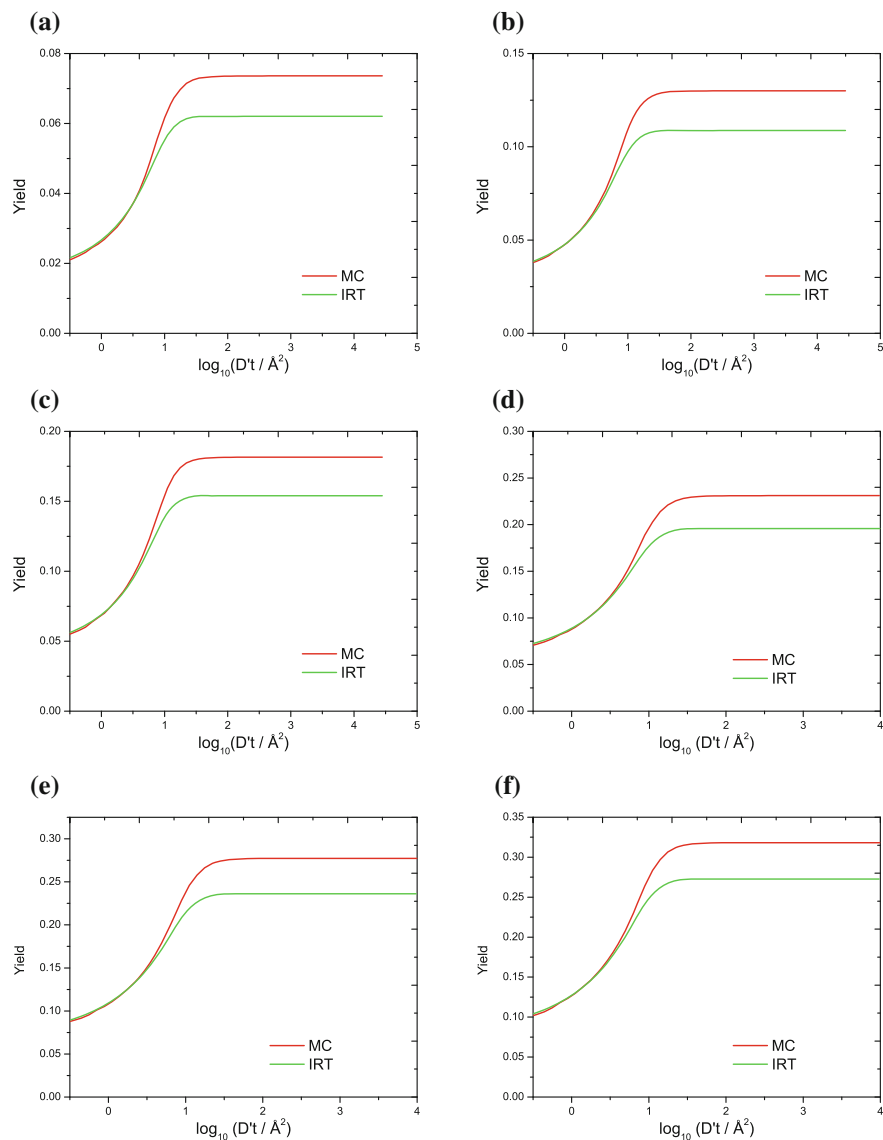


**Fig. 7.1** Yield of  $eS^-$  obtained as a function of six different concentrations **a** 0.1M, **b** 0.18M, **c** 0.26M, **d** 0.34M, **e** 0.42M, **f** 0.5M. An initial separation of  $20\text{\AA}$  was used for  $e^-$  and  $h^+$ . Standard error on the final yield to one standard deviation is: **a**  $\pm 0.0011$  (IRT) and  $\pm 0.00106$ ; **b**  $\pm 0.0015$  (IRT) and  $\pm 0.0013$  (MC); **c**  $\pm 0.0017$  (IRT) and  $\pm 0.0015$  (MC); **d**  $\pm 0.0018$  (IRT) and  $\pm 0.0017$  (MC); **e**  $\pm 0.0019$  (IRT) and  $\pm 0.0018$  (MC) and **f**  $\pm 0.002$  (IRT) and  $\pm 0.0019$  (MC). Here MC refers to random flights simulation

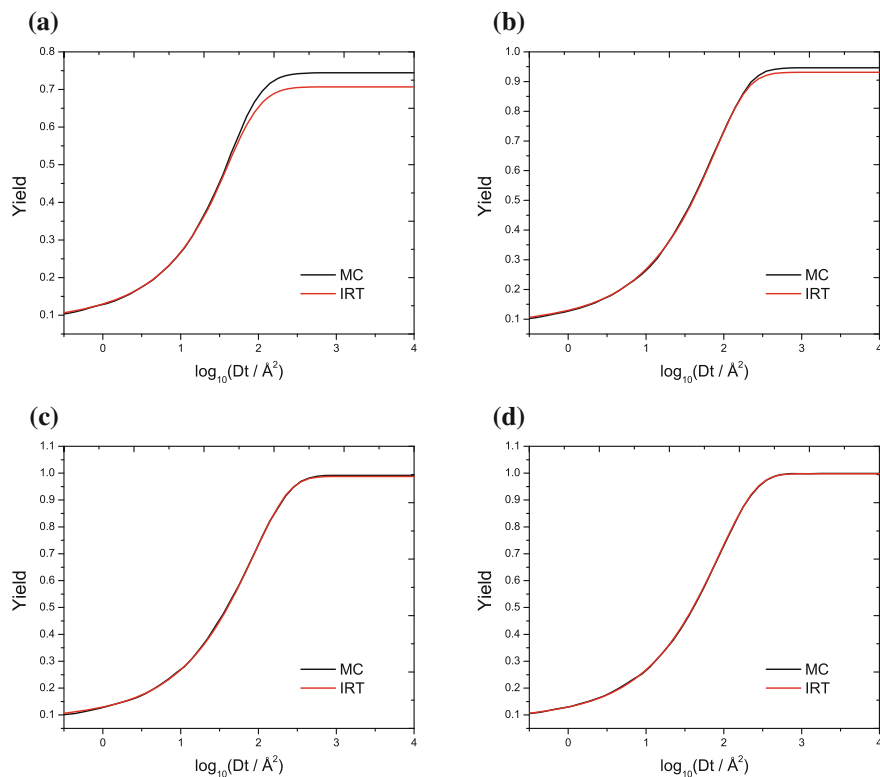


**Fig. 7.2** Scavenging yield of  $eS^-$  using an initial ion-pair separation of **a** 40 Å; **b** 60 Å; **c** 80 Å and **d** 100 Å. A Scavenger concentration of 0.5 M was used in both simulations. Here MC refers to random flights simulation

the strong Coulombic drift between the ions. If the ions are close together then the strong Coulombic drift causes them to diffuse across a greater ‘scavenger space’ before geminate recombination can eventually take place. This effectively gives an extra probability of scavenging before geminate recombination can take place. A detailed discussion investigating this hypothesis is now presented in the subsequent sections.

### 7.2.1 Understanding the Nature of the Fast Scavenging Kinetics

To physically understand the scavenging model consider a reaction scheme of the form



where  $e_s^-$  represents a scavenged electron, but still possesses the characteristics of  $e^-$ . In this reaction scheme the time dependent yield of  $e_s^-$  is recorded as function of the constant drift velocity ( $v_c$ ) between the ions. The results presented in Fig. 7.3 show two important effects: (1) When  $v_c \rightarrow 0$  (Smoluchowski condition) the  $e_s^-$  yield is higher than that obtained when  $v_c = 0.203 \text{ \AA ps}^{-1}$  (this is the velocity of the ions at  $20 \text{ \AA}$  separation calculated using Eq. (7.7) using a mutual diffusion coefficient of  $0.28 \text{ \AA}^2 \text{ ps}^{-1}$ ). Let the time period ( $\mathfrak{S}$ ) be defined as  $T_{\text{he}} - S_e$ , with  $T_{\text{he}}$  and  $S_e$  being the geminate recombination time of  $e^- + h^+$  and scavenging time for  $e^-$  respectively. When  $v_c = 0$ ,  $\mathfrak{S}$  is estimated to be  $3,200 \text{ ps}$  and similarly when  $v_c = 0.203 \text{ \AA ps}^{-1}$ ,  $\mathfrak{S} \sim 100 \text{ ps}$ . Therefore, when  $v_c = 0$  the  $e^-$  is allowed to sample more of the scavenger space since geminate recombination competes on a much longer timescale (i.e. the scavenging probability is proportional to  $T_{\text{he}}$ ). (2) When  $v_c = 0.203 \text{ \AA ps}^{-1}$  there is a much higher probability of forming  $e_s^-$  in the period  $0-100 \text{ ps}$  than what is predicted by Smoluchowski. This is because at this velocity, the  $e^-$  can effectively sample more of the scavenger space in a shorter time giving it a higher probability of forming  $e_s^-$ . Therefore, two important points need to be highlighted:

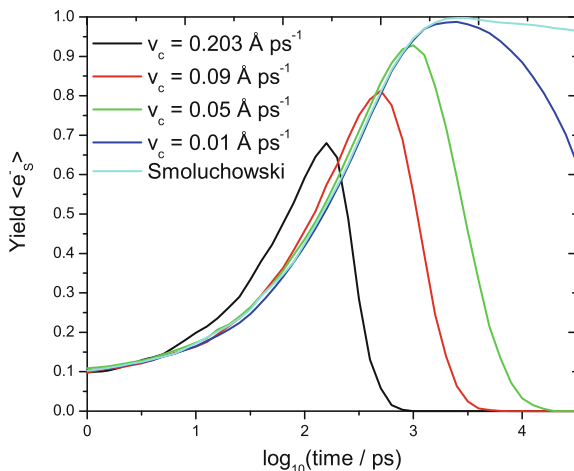
1. The *total* scavenging yield is governed by  $\mathfrak{S}$  (the period between  $e^- + S$  and  $e^- + h^+$ ). As  $\mathfrak{S}$  becomes smaller the scavenging yield will also be reduced, due to geminate recombination. Hence, it can be inferred that the kinetic parameters for the reaction  $e^- + h^+$  will actually determine the yield of  $e_s^-$ .
2. The *rate* of scavenging is faster when  $v_c \rightarrow \infty$ , because the  $e^-$  can sample a greater scavenger space in a shorter period of time. As  $v_c$  is determined by the distance ( $r$ ) between  $e^- + h^+$ , it can be inferred that  $r$  actually determines the rate of scavenging.

Therefore, in both cases it seems that the parameters of  $e^- + h^+$  can actually determine the scavenging yield of  $e_s^-$ , which seems to imply some degree of correlation between the scavenging and recombination times. The results presented in Fig. 7.1 imply that Smoluchowski's time dependent rate constant underestimates the scavenging yield because of the distance between  $e^-$  and  $h^+$ . Using Smoluchowski's time dependent rate constant, the  $e^-$  sweeps a smaller scavenger space because: (i) the  $e^-$  is treated as undergoing only diffusion motion and (ii) the fast recombination with  $h^+$  reduces the lifetime of  $e^-$  (and hence its scavenging probability). The validity of a possible correlation existing will now be thoroughly investigated in the remainder of this chapter.

### 7.2.2 Steady State Scavenging Rate for Charged Species

In order to understand the difference in the recombination yield at small ion pair distances, the steady state scavenging rate constant for charged species was calculated by making the deterministic approximation [2] (i.e treat the Coulombic drift as a simple relative velocity), such that the Coulombic contribution to the relative drift is  $D' r_c / r^2$  (with  $D'$  being the mutual diffusion coefficient  $r_c$  the Onsager distance

**Fig. 7.3**  $e_s^-$  yield at constant drift velocities for the ion pair. An initial ion pair separation of  $80 \text{ \AA}$  was used. Smoluchowski corresponds to  $v_c = 0$ . Constant velocity of  $v_c$  0.203, 0.09, 0.05 and  $0.01 \text{ \AA ps}^{-1}$  corresponds to an ion pair separation of 20, 30, 40 and  $90 \text{ \AA}$  respectively using a mutual diffusion coefficient of  $0.28 \text{ \AA}^2 \text{ ps}^{-1}$



and  $r$  the ion-pair separation), which is true only if  $2/r \ll |r_c|/r^2$ . As hydrocarbons have an Onsager distance in the region of  $290 \text{ \AA}$ , making this approximation may be reasonable. Hence, the relative velocity of a diffusing ion pair can be expressed as

$$\frac{dr}{dt} = D' \frac{r_c}{r^2} \quad (7.7)$$

which can be solved by separation of variables to give the geminate recombination time ( $T_D$ ) as [2]

$$T_D = \frac{r_0^3 - a^3}{3|r_c|D'} \quad (7.8)$$

with  $r_0$  and  $a$  representing the initial cation-anion separation distance and encounter distance respectively. Equation (7.8) has been previously used by Freeman [4] to predict the initial distribution of particles, however, it was shown by Ludwig [5] to lead to an overestimate of the reaction rate due to a neglect of the random dispersive term at long distances. Another drawback of using this approximation is its failure to account for the probability that the two ions may never react in an infinite three-dimensional space. Nonetheless, making this approximation provides the necessary first step for understanding the competition between scavenging and recombination.

For times smaller than  $T_D$ , the distance between the ion pair at any given time ( $t$ ) is given by the expression

$$r = (r_0^3 - 3|r_c|D't)^{1/3} \quad (7.9)$$

Substituting the above expression into Eq. (7.7) then gives the relative drift velocity of the approaching particle with a given diffusion coefficient  $D$  to be

$$v_c = \frac{Dr_c}{(r_0^3 - 3|r_c|D't)^{2/3}} \quad (7.10)$$

**Steady state scavenging rate constant for ions** The full time dependent scavenging rate constant for a constant  $v_c$  in the Laplace space is analytically known to be [3]

$$\begin{aligned} \tilde{k}(s) = & \frac{(2\pi)^2 D'^2}{s v_c} \sum_l (-1)^l (2l+1) \frac{I_{l+\frac{1}{2}}(q)}{K_{l+\frac{1}{2}}(\lambda a)} \\ & \times \left[ q K_{l+\frac{1}{2}}(\lambda a) I_{l-\frac{1}{2}}(q) + \lambda a K_{l-\frac{1}{2}}(\lambda a) I_{l+\frac{1}{2}}(q) \right] \end{aligned} \quad (7.11)$$

where  $I_{1/2}$  and  $K_{1/2}$  are the modified Bessel functions of the first and second kind respectively;  $q = v_c a / 2D'$ ;  $a$  is the encounter radius,  $\lambda = \sqrt{v_c^2 / 4D'^2 + s/D'}$ ,  $D'$  is the mutual diffusion coefficient and  $s$  is the Laplace variable. Unfortunately, the inverse Laplace transform for the full time dependent solution of the scavenging rate constant for a charged species is not known. Instead one must rely on the steady state limit  $\left( \lim_{s \rightarrow 0} s \tilde{k}(s) \right)$  which gives

$$k_{ss} = \frac{4\pi^2 D'^2}{v_c} \sum_{l=0}^{\infty} (-1)^l (2l+1) \frac{I_{l+1/2}(q)}{K_{l+1/2}(q)} \quad (7.12)$$

In order to calculate the summation involved in Eq. (7.12), two methods were utilised. The first method involved directly calculating the summation, however the series converges very slowly when  $v_c a / D'$  is large, making the method quite restrictive. The second method improves the convergence of Eq. (7.12) using the Euler transform, which takes a series of the form

$$\sum_{k=0}^{\infty} (-1)^k \ell_k = \ell_0 - \ell_1 + \ell_2 + \dots \quad (7.13)$$

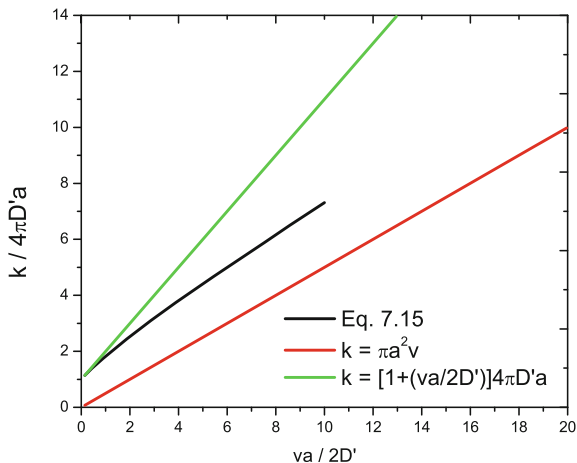
and transforms it into a more rapidly converging series as

$$k_{ss} = \sum_{k=0}^{\infty} \frac{(-1)^k \Delta^k \ell_0}{2^{k+1}} \quad (7.14)$$

with  $\Delta^k \ell_0 = \sum_{m=0}^k (-1)^m \binom{k}{m} \ell_{k-m}$ . For the series under consideration,  $\ell_k = (2k+1) \frac{I_{k+1/2}(q)}{K_{k+1/2}(q)}$  with Eq. (7.14) taking the form

$$k_{ss} = \frac{\pi}{2q} \sum_{k=0}^{\infty} \frac{(-1)^k}{2^{k+1}} \sum_{m=0}^k (-1)^m \binom{k}{m} (2(k-m)+1) \frac{I_{(k-m)+1/2}(q)}{K_{(k-m)+1/2}(q)} \quad (7.15)$$

**Fig. 7.4** Linear dependence of  $k_{ss}$  (black), high velocity rate constant (red) and the rate constant at low electric fields (green) as a function of  $v_c a / 2D'$



This series converges much more rapidly but still suffers from slow convergence with increasing values for  $v_c a / D'$ . In the limit of high velocity, the rate constant is analytically known to be  $k_{high} = \pi a^2 v_c$  [3]. A plot of the dependence of  $k_{ss}$ ,  $k_{high}$  and the rate constant at low electric fields is shown in Fig. 7.4 as a function of  $v_c a / 2D'$ .

It was hypothesised that ionic motion is dominated by the Coulombic attraction and that this causes an increase in the scavenging rate by dragging the ions through the field of scavengers at an increased rate. There are some analyses available of the dependence of the rate constant on the velocity, but there are several problems:

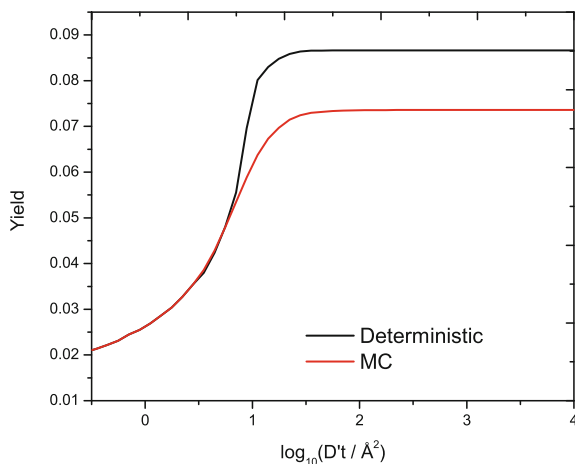
1. Only  $k_{ss}$  can be computed (which uses a fixed  $v_c$ ) and in the system under study  $v_c$  is changing at every timestep.
2. The series in Eq. (7.15) converges very slowly when  $v_c a / 2D'$  is large, making it difficult to calculate when  $v_c$  becomes large (i.e. when the ion pair is close together).

The first step in trying to correct the IRT simulation was to use either the maximum of Smoluchowski's time dependent rate constant or  $k_{ss}$  (as given in Eq. 7.12). In order to generate a reaction time for scavenging, the rate constant was numerically integrated for a given concentration and the reaction probability was calculated as a function of time. This allowed the generation of a look-up table. Within the simulation a random uniform number  $U(0, 1)$  was generated in the interval  $(0, 1]$  to represent the reaction probability, and the corresponding time was interpolated from the look-up table as:

$$T_{scav} = \frac{(U(0, 1) - W_{min})}{W_{max} - W_{min}} \times (t_{max} - t_{min}) + t_{min} \quad (7.16)$$

where  $t_{min}$  and  $t_{max}$  are the lower and upper scavenging times respectively bounding the value of  $U(0, 1)$  and similarly,  $W_{min}$  and  $W_{max}$  are respectively the lower and upper reaction probability values bounding  $U(0, 1)$ . Figure 7.5 shows that the

**Fig. 7.5** Yield of  $eS^-$  using a scavenger concentration of 0.1 M. An initial ion-pair separation of 20 Å was used. Standard error calculated on the final yield to one standard deviation is:  $\pm 0.0012$  (IRT) and  $\pm 0.00114$  (MC). Here MC refers to random flights simulation



deterministic rate constant tends to overestimate the yield of scavenging with a similar trend found for other concentration strengths of scavengers. A higher scavenging yield is obtained because the simulation neglects the asymptotic limit of  $k_{ss}$  and as a result  $k_{ss}$  increases much too rapidly.

### 7.2.3 Rate Constant Extracted from Simulations

As using the deterministic rate constant did not reproduce the correct kinetics, the next stage of the analysis involved extracting the rate constant from random flights simulations to explain the extra scavenging effect. The rate constant  $k_{scav}$  from random flights simulation was extracted using the expression

$$k_{scav} = \frac{k_{MC}}{\Omega(e^-) \times c_{scav}} \quad (7.17)$$

where  $\Omega(e^-)$  is the survival probability of the  $e^-$  and  $c_{scav}$  is the concentration of scavengers. The numerical rate constant  $k_{MC}$  was obtained from the random flights simulation in a discrete way, by counting the number of scavenging reactions in each histogram box, and dividing by the time interval.

The extracted rate constant from random flights simulations is presented in Fig. 7.6, along with (i) Smoluchowski's time dependent rate constant, (ii)  $k_{ss}$  (along the deterministic trajectory) and (iii) a simulation in which scavengers were treated explicitly in the IRT simulation. In (iii), no assumption regarding the scavenging rate was made, but rather a reaction time of  $e^-$  to each of the scavengers was generated as described in Sect. 4.4.4.1. It is seen from the random flights simulation, that a peculiar 'bump' arises in the rate constant, showing the scavenging kinetics to deviate

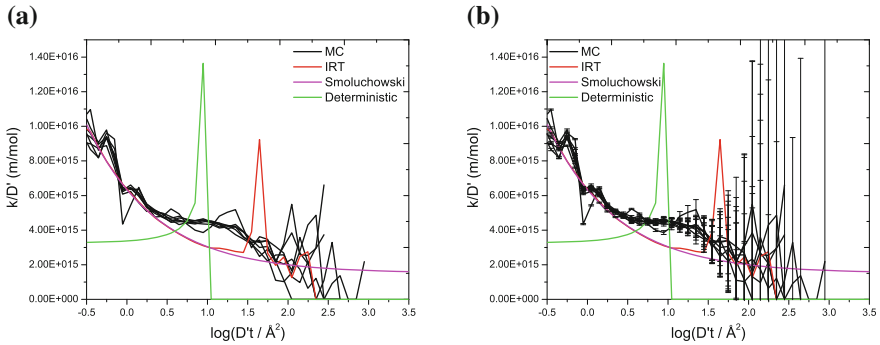


**Fig. 7.6** Rate constant extracted for  $eS^-$  from random flights and IRT simulation and compared with that obtained using the time dependent Smoluchowski's rate constant with an initial separation of  $20 \text{ \AA}$ . Scavenger concentration ranged from 0.02 to 0.5 M. **a** Without error bars and **b** standard error shown to one standard deviation. Here MC refers to random flights simulation

from Smoluchowski's time dependent rate constant in the interval  $\sim 10 - 100 \text{ ps}$ . The physical origin for this bump was thought to arise because as the  $e^-$  and  $h^+$  diffuse towards each other, the relative drift velocity rapidly increases with the electron dragged across a greater volume of scavengers, which in turn leads to more scavenging.

The IRT with explicit treatment of scavengers just simply gives Smoluchowski's rate constant, which neglects the effect of drift. The deterministic rate  $k_{ss}$  along the deterministic trajectory shows a large increase at the end of the trajectory (i.e. at the deterministic recombination time). Beyond this region there is no possibility of scavenging, but in reality there is a dispersion of reaction times and the random flights simulation shows a bump hypothesised to be an average of  $k_{ss}(r)$  over the real trajectories. It was thought that if the bump could be reproduced as closely as possible, this should accurately describe the scavenging kinetics in the IRT framework. This is now discussed in the next section.

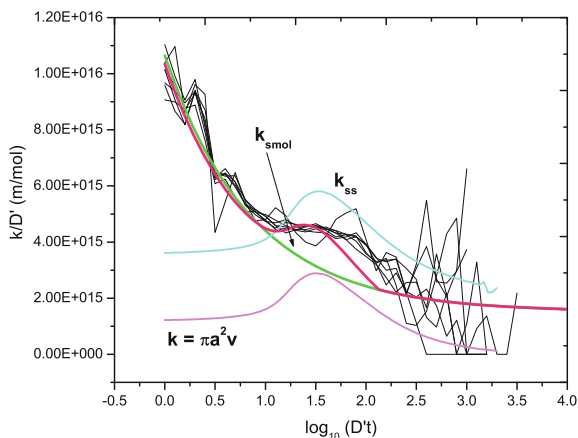
### 7.2.4 Kac Functional

In an attempt to model the scavenging kinetics, another approach was formulated in which a 'killing' term was introduced into the backward diffusion equation as

$$\frac{\partial \Omega}{\partial t} = D' \left[ \frac{\partial^2 \Omega}{\partial r_0^2} + \left( \frac{2}{r_0} + \frac{r_c}{r_0^2} \right) \frac{\partial \Omega}{\partial r_0} \right] - ck_{\text{drift}}(r_0)\Omega \quad (7.18)$$

$$\frac{\partial S}{\partial t} = D' \left[ \frac{\partial^2 S}{\partial r_0^2} + \left( \frac{2}{r_0} + \frac{r_c}{r_0^2} \right) \frac{\partial S}{\partial r_0} \right] - ck_{\text{drift}}(r_0)S \quad (7.19)$$

**Fig. 7.7** Simulated scavenging rate constant obtained for  $e^- + S$  at 0.5 M of scavengers using an Onsager distance of 290 Å. An initial distance of 20 Å was used between the radical ion pair. The red line is the maximum of either Smoluchowski's time dependent rate constant ( $k_{smol}$ ) or  $k_{smol} + \pi a^2 v_c$ ; green line corresponds to Smoluchowski's time dependent rate constant. Error bars have been omitted for clarity purposes. Units of  $x$ -axis are in Å<sup>2</sup>



with  $k_{drift}(r_0)$  being the scavenging rate constant for a drifting particle separated by distance  $r_0$ , and  $\Omega$  and  $S$  representing the survival and scavenging probabilities respectively. Using suitable boundary conditions of the form  $\Omega(0) = 0$ ,  $\Omega(\infty) = 0$ ,  $\Omega(t = 0) = 1$ ;  $S(0) = 0$ ,  $S(\infty) = \exp(-ck_{smol}t)ck_{smol}$ ,  $S(t = 0) = ck_{drift}(r_0)$  (with  $k_{smol} = 4\pi D'a$ , Eqs. (7.18) and (7.19) were solved using the Crank Nicolson method. The time dependent solutions for  $\Omega(t)$  and  $S(t)$  were then used to calculate the scavenging rate constant as  $k_{num}(t) = S(t)/\Omega(t)$ . The obtained scavenging rate constant is shown in Fig. 7.7 with  $k_{drift}$  being either the rate constant from Eq. (7.12) or the high velocity rate constant ( $k_{high} = \pi a^2 v_c$ ).

As the ‘bump’ arises in the correct place, it was thought that using the maximum of either Smoluchowski's time dependent rate constant ( $k_{smol}$ ) and  $k_{smol} + \pi a^2 v_c$ , one should reproduce the correct scavenging rate constant (red line in Fig. 7.7). Unfortunately, the scavenging of  $eS^-$  was still found to be overestimated, even though the random flights rate constant was modelled as closely as possible. Hence, it was thought that an IRT simulation which uses the numerical rate constant extracted directly from the random flights simulation should be able to reproduce the scavenging kinetics exactly. The validity of this second hypothesis is discussed in the next section.

### 7.2.4.1 Numerical Rate Constant

As modelling the ‘bump’ in the last section failed to reproduce the scavenging kinetics, simulating with the rate constant extracted from the random flights simulation was further attempted within the IRT framework. The results using a concentration of 0.1 and 0.5 M are shown in Fig. 7.8a and b respectively. It is seen that modelling the random flights numerical rate constant still overestimates the scavenging kinetics, even though the actual scavenging rate constant has been used.

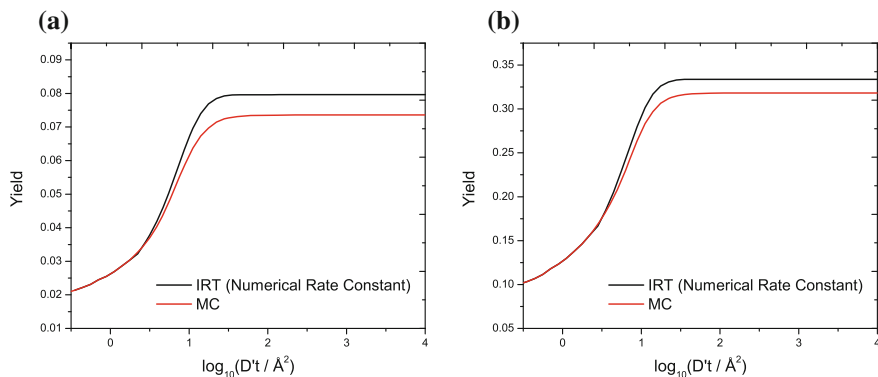


**Fig. 7.8** Yield of  $eS^-$  using a scavenger concentration of **a** 0.1 M and **b** 0.5 M. An initial ion-pair separation of  $20 \text{\AA}$  was used in both cases. Standard error calculated on the final yield to one standard deviation is: **a**  $\pm 0.0011$  (IRT and MC); **b**  $\pm 0.0021$  (MC and IRT). Here MC refers to random flights simulation

The inability for the IRT to reproduce the scavenging kinetics led to the conclusion that a correlation must exist between the recombination and scavenging processes. This possibility is explored in some detail in Sect. 7.2.6.

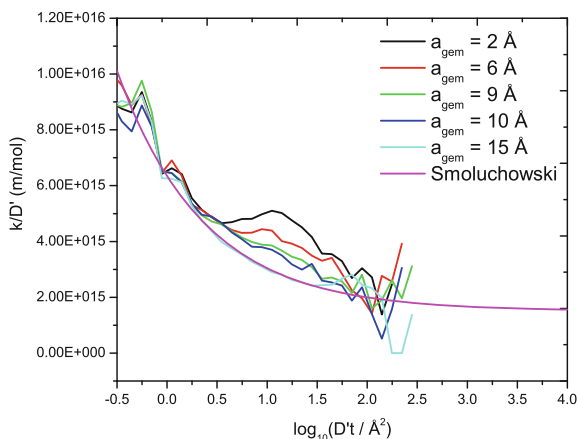
Before trying to understand the nature of the correlation between the scavenging and recombination times, it is important to first analyse how the extra scavenging effect depends on both the Onsager distance and the encounter radius for the reactions  $e^- + S$  and  $e^- + h^+$ . This is now explored in the next section.

### 7.2.5 Effect of Encounter Radius and Onsager Distance

**Geminate encounter radius** The geminate encounter radius is thought to affect the kinetics of scavenging due to the strong interparticle drift velocity. This is because as the encounter radius increases: (i) the number of scavengers which can intercept geminate recombination becomes smaller (as some scavengers will now reside inside the region spanned by the ion-pair encounter radius and as a result cannot intercept ion recombination); (ii) the interparticle drift of the ion pair is not sufficiently large to allow the sampling of the extra scavenging space. As Fig. 7.9 shows, with a sufficiently large encounter radius, ionic systems can indeed be accurately described using Smoluchowski's time dependent rate constant, even for low permittivity solvents.

**Scavenging encounter radius** The effect of the scavenger encounter radius on the scavenging kinetics is further shown in Fig. 7.10, with no major differences seen between the two cases. Two important limiting cases however, should be noticed: (i) when the scavenging encounter radius gets smaller, there is less probability of the ion pair to be intercepted by a scavenger and consequently the 'extra' scavenging

**Fig. 7.9** Simulated scavenging rate constant obtained for  $e^- + S$  at 0.5 M of scavengers using an Onsager distance of 290 Å and an initial distance of 20 Å between the radical ion pair. A scavenging encounter radius of 4 Å was used in all cases. In this simulation  $a_{\text{gem}}$  refers to the geminate encounter distance for the reaction  $e^- + h^+$ . Error bars have been omitted for clarity purposes



effect should decay with decreasing scavenger radius; (ii) when the scavenging encounter radius becomes increasingly large, scavenging intercepts geminate recombination before any appreciable drift between the ion pair can develop. In both cases, the scavenging rate constant would effectively follow Smoluchowski's time dependent rate constant.

Figure 7.11 shows the scavenging rate at Onsager distances of 190 and 9 Å as a function of the geminate pair encounter radius. It is not surprising to see that decreasing the Onsager distance causes the scavenging rate to follow Smoluchowski's time dependent rate constant due to the decrease in the interparticle drift velocity (i.e. the ion-pair is pulled less slowly towards each other with decreasing  $r_c$ , which causes them to sweep less of the scavenger space).

Up to now, no method has been successful in reproducing the extra scavenging effect seen in the random flights simulations. The hypothesis of a correlation between the recombination and scavenging times provides a possible explanation as to why using the numerically extracted rate constant in the IRT algorithm still failed to reproduce the observed kinetics. The validity of this hypothesis is now investigated fully in the next section.

### 7.2.6 Conditioned Diffusion Process

In order to test the hypothesis of a correlation existing between the rates of scavenging and recombination, a conditioned Brownian process was modelled which conditions on the recombination time of the  $e^-$  and  $h^+$ . The reason for doing this was to sample only the important area of the diffusive space to allow better statistics to be obtained. In the language of applied probability, this is known as *importance sampling*.

The probability of diffusing from  $x$  to  $y$  at time  $s$ , conditioned on the particles hitting  $a$  for the first time at time  $t$  can be expressed as

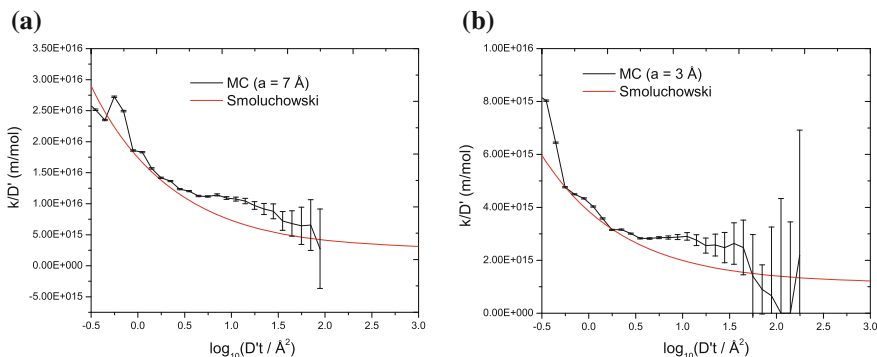


**Fig. 7.10** Simulated scavenging rate constant obtained for  $e^- + S$  using a scavenging encounter radius of **a** 7 Å and **b** 3 Å. A scavenger concentration of 0.5 M was used, with the ion-pair initially separated by 20 Å. Geminate encounter radius of 5 Å together with an Onsager distance of 290 Å was used in both cases. Here MC refers to random flights simulation

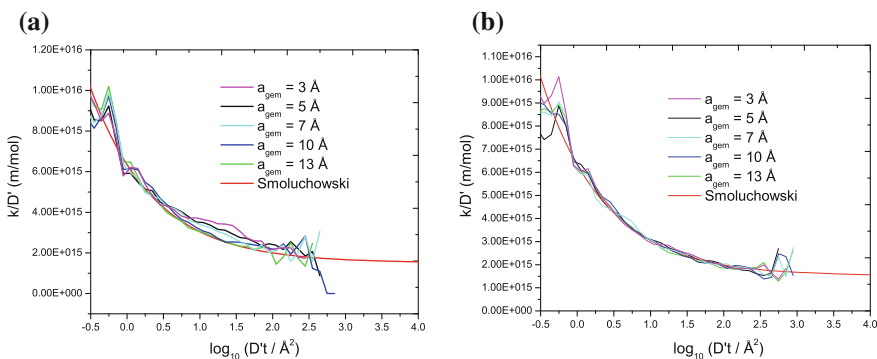


**Fig. 7.11** Simulated scavenging rate constant obtained for  $e^- + S$  at 0.5 M of scavengers using an Onsager distance of **a** 190 Å and **b** 9 Å with an initial distance of 20 Å between the radical ion pair. A scavenging encounter radius of 4 Å was used in all cases. In this simulation  $a_{\text{gem}}$  refers to the geminate encounter distance for the reaction  $e^- + h^+$ . Error bars have been omitted for clarity purposes

$$\Pr(x, y, s | a, t > s) = p^*(x, y, s) \frac{w(y, a, t - s)}{w(x, a, t)} \quad (7.20)$$

where  $p^*(x, y, s)$  is the transition density for all trajectories of the diffusion going from  $x$  to  $y$  without hitting  $a$  at time  $s$ ,  $w(y, a, t - s)$  is the first passage time density from  $y$  to  $a$  at time  $(t - s)$ , and  $w(x, a, t)$  is the first passage time density from  $x$  to  $a$  at time  $t$ . Letting  $X(s)$  represent a diffusion process subject to the condition that it equals  $x$  at time  $s$ , Eq. (7.20) can be defined as

$$p^*(x, y, \zeta) \frac{w(y, a, t - s - \zeta)}{w(x, a, t - s)} \quad (7.21)$$

Taylor expanding the above function about  $x$  (recognising that  $y$  is close to  $x$  at time  $\zeta$ ) yields

$$p^*(x, y, \zeta) \left[ \frac{w(x, a, t-s) + (y-x)w'(x, a, t-s) + \dots}{w(x, a, t-s)} \right] \quad (7.22)$$

The above expansion is terminated after the second term as all higher moments for a diffusion process are zero. The mean and variance of  $(y-x)$  is then calculated as

$$\begin{aligned} \frac{1}{h} \int_0^h p^*(x, y, h) \left[ (y-x) + (y-x)^2 \frac{w'(x, a, t-s)}{w(x, a, t-s)} \right] \\ = \mu(x) + \frac{w'(x, a, t-s)}{w(x, a, t-s)} \sigma^2(x) \end{aligned} \quad (7.23)$$

with conditioned mean ( $\mu^*$ ) and variance ( $\sigma^*$ ) for the diffusion process found to be

$$\mu^* = \mu(x) + \frac{w'(x, a, t-s)}{w(x, a, t-s)} \sigma^2(x) \quad (7.24)$$

$$\sigma^{2*} = 2D' \quad (7.25)$$

For the uncharged case, all the terms required for the conditioned mean can be analytically calculated by recalling that the reaction probability for two neutral species is

$$W(x, t) = \frac{a}{x} \operatorname{erfc} \left( \frac{x-a}{\sqrt{4D't}} \right) \quad (7.26)$$

The first passage time density  $w(x, t-s) = dW/dt$  is then

$$w(x, t-s) = \frac{1}{2} \frac{a(x-a)}{x\sqrt{\pi D'(t-s)^3}} e^{-(x-a)^2/4D'(t-s)} \quad (7.27)$$

and similarly  $w'(x, t-s) = dw/dx$  is

$$w'(x, t-s) = \frac{e^{-(x-a)^2/4D'(t-s)}}{\sqrt{\pi D'(t-s)^3}} \left[ \frac{a(x-a)^2}{4D'} + \frac{a}{2x} - \frac{a(x-a)}{2x^2} \right] \quad (7.28)$$

Substituting the above expressions into Eq. (7.24) gives the conditioned mean for the 3D case to be

$$\mu^* = \left[ \frac{2D'a}{x(x-a)} - \frac{D(x-a)}{D'(t-s)} \right] \frac{\mathbf{r}_n}{|r|} \quad (7.29)$$

The first term represents the species diffusing further apart (which dominates at shorter times); the second term dominates as  $s$  approaches  $t$ , representing the species diffusing towards each other and ultimately recombining at  $t$ . In Eq. (7.29),  $\mathbf{r}_n$  represents the interparticle vector and  $r$  is the interparticle separation.

### 7.2.6.1 Crank-Nicolson Method

Although the backward diffusion can be analytically solved for neutral species, it unfortunately cannot be solved in closed form for charged species. In order to numerically extract  $w(x, t - s)$  and  $w'(t - s)$  for charged species, the backward diffusion equation must be numerically solved. The first step in the process involves solving the backward diffusion equation for charged species using the Crank-Nicolson method [6, 7]. The strategy used to solve the diffusion equation was demonstrated in Chap. 4 of this work (Sect. 4.4.4.1), however it was conditioned on ultimate reaction, which cannot be applied in this case due to scavenging.

The reaction probability ( $W(x, s)$ ) for  $e^- + h^+$  is known to obey the backward diffusion equation of the form

$$\frac{\partial W}{\partial s} = \frac{1}{2}\sigma^2 \frac{\partial^2 W}{\partial x^2} + \mu \frac{\partial W}{\partial x} \quad (7.30)$$

where  $\mu$  and  $\sigma^2$  are the mean and variance of the diffusion process. Converting to a logarithmic scale (to allow the calculation to be tractable) such that  $\ln x = u$  and  $\ln s = \tau$ , gives the transformed diffusion equation to be of the form

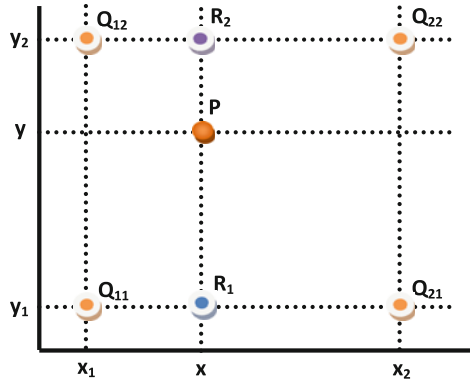
$$\frac{\partial W}{\partial \tau} = \frac{1}{2}\sigma^2 e^{-2u+\tau} \frac{\partial^2 W}{\partial u^2} + (\mu e^{-u+\tau} - \frac{1}{2}\sigma^2 e^{-2u+\tau}) \frac{\partial W}{\partial u} \quad (7.31)$$

After using the Crank-Nicolson discretisation method, the above equation becomes

$$\begin{aligned} W_{i+1,j+1} & \left[ -\bar{\sigma}^2 \frac{\delta\tau}{4\delta u^2} - \frac{\bar{\mu}\delta\tau}{4\delta u} \right] + W_{i,j+1} \left[ 1 + \bar{\sigma}^2 \frac{\delta\tau}{2\delta u^2} \right] \\ & + W_{i-1,j+1} \left[ -\bar{\sigma}^2 \frac{\delta\tau}{4\delta u^2} + \frac{\bar{\mu}\delta\tau}{4\delta u} \right] \\ & = W_{i+1,j} \left[ \bar{\sigma}^2 \frac{\delta\tau}{4\delta u^2} + \frac{\bar{\mu}\delta\tau}{4\delta u} \right] + W_{i,j} \left[ 1 - \bar{\sigma}^2 \frac{\delta\tau}{2\delta u^2} \right] \\ & + W_{i-1,j} \left[ -\bar{\sigma}^2 \frac{\delta\tau}{4\delta u^2} - \frac{\bar{\mu}\delta\tau}{4\delta u} \right] \end{aligned} \quad (7.32)$$

with  $\bar{\sigma}^2 = \sigma^2 e^{-2u+\tau}$  and  $\bar{\mu} = \mu e^{-u+\tau} - \frac{1}{2}\sigma^2 e^{-2u+\tau}$ . In Eq. (7.32) the unknown coefficients are on the left hand side and the known coefficients are on the right. As in Chap. 4 of this work (Sect. 4.4.4.1), Eq. (7.32) can be readily solved by inversion of the tridiagonal matrix by upper and lower triangular decomposition

**Fig. 7.12** Diagram to show the interpolation of the value  $f(x, y)$  at point P, with known values of the function at  $Q_{11}$ ,  $Q_{12}$ ,  $Q_{21}$  and  $Q_{22}$



and subsequent forward and backward substitution using the boundary conditions  $W(x = a, s = 0) = 1$  and  $W(x = \infty, s = 0) = 0$ , with the initial condition  $W(x > a, s = 0) = 0$ . The step size of 0.001 and 0.1 was chosen for  $u$  and  $\tau$  respectively.

Having obtained a sufficiently converged grid for the  $W(x, s)$  ( $G^1$ ), the data was numerically differentiated to allow the generation of a new grid for  $w(x, s)$  ( $G^2$ ). The data in  $G^2$  was again numerically differentiated with respect to  $x$ , producing a new grid ( $G^3$ ) for  $w'(x, s)$ . In the random flights simulation the diffusive ‘jump’ of the particles then proceeded by extracting the correct values for  $w(x, s)$  and  $w'(x, s)$  at every time step. The algorithm to do this is now presented in the next section.

### 7.2.6.2 Bilinear Interpolation of the 3D Grid

To extract the required value for  $w$  and  $w'$  for a given  $x$  and  $s$ , the four points boxing the required value were found using Eq. (7.33) at every time step in the random flights simulation program. The variables used in Eq. (7.33) are defined in Fig. 7.12, which aims to show the interpolation of the function  $f(x, y)$  at a point  $P$ .

$$\begin{aligned}
 f(x, y) = & \frac{f(Q_{11})}{(x_2 - x_1)(y_2 - y_1)}(x_2 - x)(y_2 - y) \\
 & + \frac{f(Q_{21})}{(x_2 - x_1)(y_2 - y_1)}(x - x_1)(y_2 - y) \\
 & + \frac{f(Q_{12})}{(x_2 - x_1)(y_2 - y_1)}(x_2 - x)(y - y_1) \\
 & + \frac{f(Q_{22})}{(x_2 - x_1)(y_2 - y_1)}(x - x_1)(y - y_1) \tag{7.33}
 \end{aligned}$$

For the uncharged case, Fig. 7.13a shows that a very good agreement between the analytical and interpolated values for the ratio  $w'/w$  is obtained at different conditioned

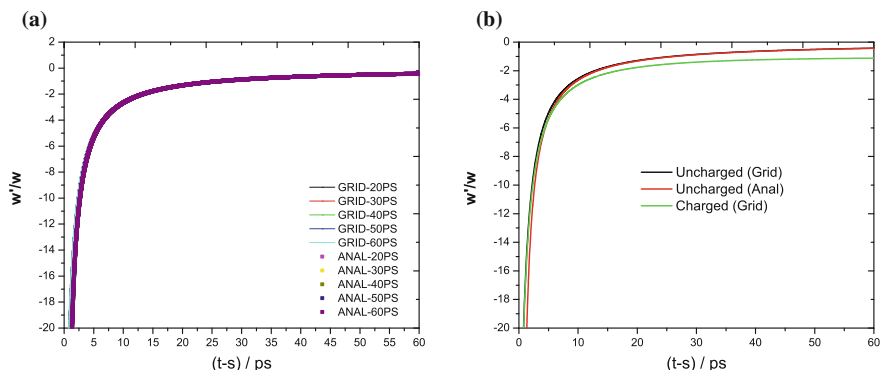


**Fig. 7.13** Comparison of the ratio  $w'/w$  **a** obtained analytically and using the lookup table for different conditioned recombination times for the uncharged case; **b** obtained for the charged case and compared with the uncharged case. A conditioned recombination time of 60 ps was set in the simulation. An initial radical separation of 20 Å was used

recombination times. This provides the necessary assurance that (i) the grid was sufficiently converged with respect to the time step and (ii) the interpolation procedure correctly extracted the values from the grid. The procedure as described above was repeated for the charged case, which has an unconditional  $\mu$  and  $\sigma^2$  of  $D'(r_c/x^2 + 2/x)$  and  $2D'$  respectively. Figure 7.13b shows the results obtained using the interpolation method for the charged case (using grids  $G^2$  and  $G^3$  in the simulation) and compared with the uncharged case (using both the interpolated technique and analytical formalism) for a conditioned diffusion process set to recombine at 60 ps. In this figure it is seen that as  $(t-s)$  tends to zero, the ratio  $w'/w$  for the charged case approaches the uncharged case; this allows for the uncharged analytical expression to be used without the need for constant interpolation in this region.

### 7.2.6.3 Extraction of Scavenging Rate Constant

Having established an accurate method for calculating the values for  $w'$  and  $w$ , the simulation was first done for the uncharged case using the conditioned  $\mu^*$  (Eq. 7.29) and  $\sigma^*$  (Eq. 7.25), to allow direct comparison with Smoluchowski's time dependent rate constant. The simulated rate constant in the random flights simulation was then extracted using Eq. (7.17). Figure 7.14a and b show the results of the simulated rate constant for  $e^- + S$  (with all species neutral) and  $e^- + S$  (with  $e^-$  and  $h^+$  now charged) respectively, conditioned that  $e^-$  and  $h^+$  recombine at a predefined time.

Figure 7.14a shows the scavenging kinetics to follow Smoluchowski's time dependent rate constant irrespective of when the pair recombine, which is to be expected for neutral species. Figure 7.14b highlights the existence of a correlation between the scavenging and recombination times for ion recombination. Those species which tend to recombine faster are scavenged much more rapidly. Hence, scavenging is

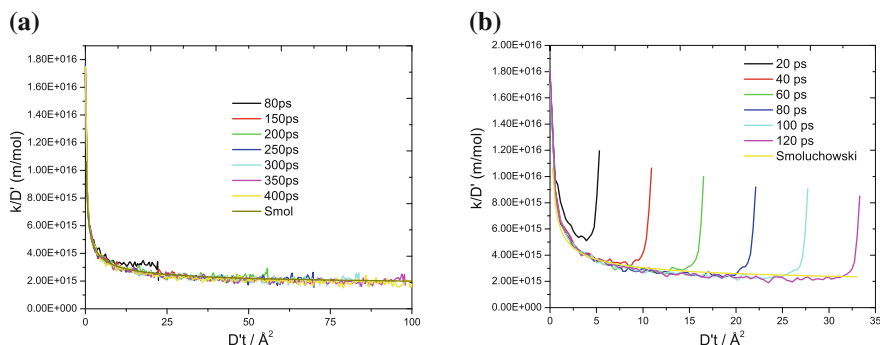


**Fig. 7.14** Simulated rate constant obtained for  $e^- + S$  with **a** no charge for any species and **b**  $e^-$  and  $h^+$  are now charged set to recombine at different conditioned recombination times. Number of realisations used in the simulation was set to  $1 \times 10^5$  using a scavenger concentration of 0.5 M. An Onsager radius of 290 Å was used

more effective in competing with recombination than expected, particularly at short times. This finding supports the original hypothesis that the deviations arise from the drift velocity, which is greatest just before recombination.

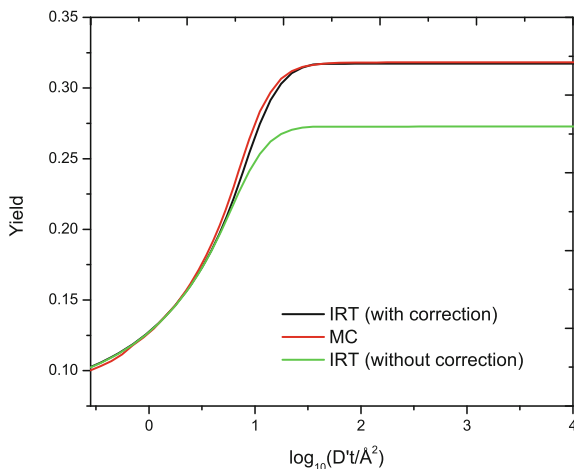
### 7.2.7 Correcting the IRT Algorithm Using a Predefined Deterministic Time

The discovery of an important correlation between scavenging and recombination at first seems to be fatal for the IRT method, which assumes independence of reaction times. However, in this case there is a simple modification that generalises the IRT method to take account of this correlation [i.e. simulate recombination first (with time  $T_g$ ) and then generate a scavenging time ( $T_{scav}$ ) conditioned on the generated recombination, taking into account of the final acceleration of scavenging as recombination is approached].

The pseudo-algorithm described below (which is only to be followed if  $T_{scav} > T_g$ ) allows for the correct scavenging rate to be generated by using a parameter ( $\delta$ ) to represent the deterministic period just prior to ion recombination in which scavenging is found to be accelerated. The algorithm proceeds as follows:

1. From the geminate recombination time, determine the initial distance required from Eq. (7.8) and determine the value of  $\delta$ , the period preceding recombination ( $T_g$ ), in which the deterministic trajectory is to be assumed.
2. Calculate the velocity of the drifting particle from Eq. (7.10) for the period  $(T_g - \delta) - T_g$ .
3. Calculate  $k_{ss}(\delta)$ , which is the steady state rate of scavenging for a drifting particle (Eq. 7.12).

**Fig. 7.15** Scavenged  $eS^-$  yield obtained using an initial ion pair separation of  $20 \text{ \AA}$ , with a deterministic time period of  $5.4 \text{ ps}$ . A scavenger concentration of  $0.1 \text{ M}$  was used. Standard error calculated on the final yield to one standard deviation is:  $\pm 0.0011$  [IRT (corrected) and MC] and  $\pm 0.001$  [IRT(uncorrected)]. Here MC refers to random flights simulation



4. Calculate the scavenging survival probability in this deterministic period by numerically integrating  $k_{ss}(\delta)$  as:  $\Omega_{\text{extra}}(\delta) = \exp\left(-c \int_{T_{g-\delta}}^{T_g} k_{ss} dt\right)$ .
5. Calculate the probability of scavenging in this deterministic period as:  $P_{\text{add}} = 1 - \Omega_{\text{extra}}(\delta)$ .
6. Generate a uniformly distributed random number  $U(0, 1]$ . If  $U(0, 1] \leq P_{\text{add}}$  then there is an additional scavenging reaction. The scavenging time  $T_{\text{scav}}$  is then randomly set between  $T_{(g-\delta)}$  and  $T_g$ .

Using the above algorithm to take into account the correlation between reaction times, the yield of  $eS^-$  was recalculated with the result presented in Fig. 7.15 (using an initial ion-pair separation of  $20 \text{ \AA}$  and  $\delta = 5.4 \text{ ps}$ ). It is seen that good agreement can now be obtained for the scavenging of a charged species.<sup>1</sup>

### 7.2.8 Deterministic Region

As it was shown in Fig. 7.9, the size of the deterministic region required to model the extra scavenging effect decays with increasing geminate encounter radius. With a sufficiently large encounter radius the deterministic region lies near or on the boundary of the encounter radius, for which no extra scavenging occurs. By performing several Monte Carlo random flights simulations and comparing with the IRT corrected algorithm, the region of the deterministic space was found to be approximated as<sup>2</sup>

<sup>1</sup> Results are only shown for a concentration of  $0.5 \text{ M}$ . Excellent agreement for other scavenger concentrations was obtained as well.

<sup>2</sup> This equation assumes an ion-pair separation of  $20 \text{ \AA}$ . For mutual diffusion coefficients much larger than  $D_{\text{ref}}$  this equation will tend to overestimate the deterministic time.

$$\frac{D\delta}{D_{\text{ref}}} = (-3.217 \times 10^5 \pm 2.308 \times 10^4)x^3 + (2.7332 \times 10^4 \pm 1.92 \times 10^3)x^2 - (7.96 \times 10^2 \pm 47.25)x + 12.757 \pm 0.323 \quad (7.34)$$

where  $x = a_{\text{gem}}/r_c$ , with  $a_{\text{gem}}$  representing the geminate encounter radius (for the reaction  $e^- + h^+$ ),  $\delta$  is time required within the deterministic region,  $D$  is the diffusion coefficient of the ion, and  $D_{\text{ref}}$  is the reference mutual diffusion coefficient ( $0.14 \text{ \AA}^2 \text{ ps}^{-1}$ ) which was used in the simulation to extract the relationship between  $\delta$  and  $x$ . As shown in Fig. 7.16, this correction provides good agreement with Monte Carlo random flights simulation for the scavenging kinetics using an Onsager distance of  $190 \text{ \AA}$  as well.

The deterministic region ( $R_{\text{critical}}$ ) (i.e. the critical region at which a deterministic trajectory is followed by the ion pair) can be extracted from  $\delta$  by the relation

$$R_{\text{critical}} = (3|r_c|D'\delta + a_{\text{gem}}^3)^{1/3} \quad (7.35)$$

where  $D'$  is the mutual diffusion coefficient of the ion-pair. Typical values for  $\gamma_{\text{critical}}$  which is the difference between the deterministic region and the geminate encounter radius (i.e.  $R_{\text{critical}} - a_{\text{gem}}$ ) are shown in Table 7.2 at three different Onsager distances. It can be seen that essentially as the encounter radius increases, the deterministic space required to model the extra scavenging effect is reduced. As mentioned earlier, this can be attributed to the fact that with increasing encounter radius: (i) the number of scavengers which can intercept geminate recombination becomes less, since some scavengers will be positioned inside the encounter radius of the ion-pair, and will be unable to intercept recombination; (ii) the interparticle drift of the ion pair is not sufficiently large to allow the sampling of the extra scavenging space.

For commonly used non-polar solvents such as diethyl ether (with dielectric constant  $\epsilon_r = 4.3$ ) and toluene ( $\epsilon_r = 2.3$ ), the extra scavenging effect is quite noticeable as seen in Fig. 7.17 (using a geminate ion-pair encounter radius of  $5 \text{ \AA}$  with an initial distance of  $20 \text{ \AA}$ ). This suggests that the scavenging effect should be noticeable for most non-polar solvents and subject to initial conditions (such as the deterministic region, encounter radius, scavenger concentrations and initial ion pair separation) the effect should be mildly seen in solvents such as dichloroethane ( $\epsilon_r = 9.1$ ). The effect is not expected to be seen at all in polar solvents such as water ( $\epsilon_r = 79$ ), dimethyl sulfoxide ( $\epsilon_r = 48.9$ ), acetonitrile ( $\epsilon_r = 37.5$ ) and N,N-dimethylformamide ( $\epsilon_r = 36.7$ ) because of the reduction of the interparticle drift. Hence, in the latter solvents Smoluchowski's time dependent rate constant can be used without the need for modification. However, in moderately polar solvents, whether Smoluchowski's scavenging rate constant can be used depends on the initial experimental conditions and the type of chemical system being investigated. For non-polar solvents, a deterministic region must be included in the scavenging rate to properly account for the relationship between the interparticle drift and scavenging.

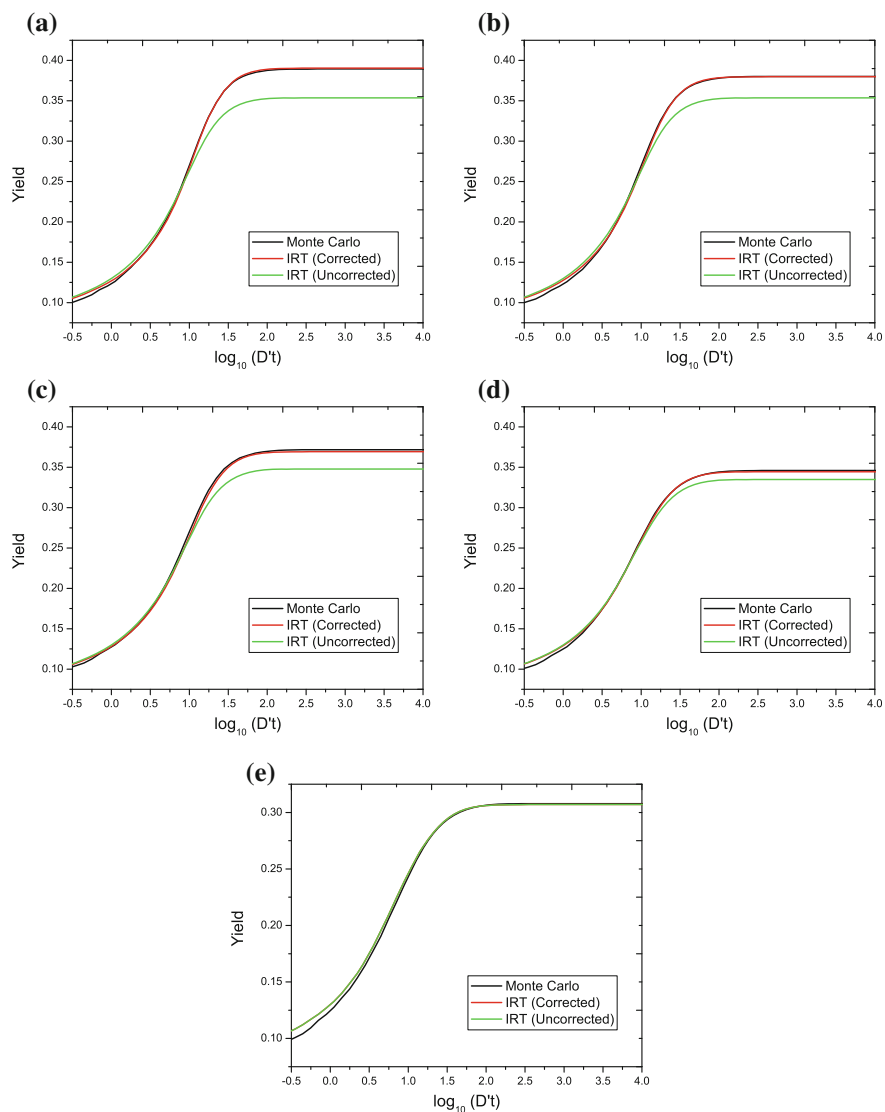


**Fig. 7.16** Yield of  $eS^-$  at five different ion pair encounter distances: **a** 3 Å, **b** 5 Å, **c** 7 Å, **d** 10 Å and **e** 13 Å, using a scavenger concentration of 0.5 M and an Onsager distance of 190 Å. An initial distance of 20 Å between the radical ion pair was used, together with a scavenging encounter radius of 4 Å. Standard error calculated on the final yield to one standard deviation is: **a**  $\pm 0.00216$  (MC and IRT) and  $\pm 0.00213$  [IRT (uncorrected)]; **b**  $\pm 0.00216$  (MC and IRT) and  $\pm 0.00211$  [IRT (uncorrected)]; **c**  $\pm 0.00213$  (MC and IRT) and  $\pm 0.0021$  [IRT (uncorrected)]; **d**  $\pm 0.002$  (MC and IRT); **e**  $\pm 0.002$  (MC and IRT). Here Monte Carlo (MC) refers to random flights simulation. Units of  $x$ -axis are in Å<sup>2</sup>

**Table 7.2**  $\gamma_{\text{critical}}$  values for three different Onsager distances

$a_{\text{gem}}$ (Å)	$\gamma_{\text{critical}}$ (Å) (290 Å)	$\gamma_{\text{critical}}$ (Å) (190 Å)	$\gamma_{\text{critical}}$ (Å) (90 Å)
2	10.76	9.97	9.04
4	7.51	6.92	5.34
6	5.40	5.09	4.94
8	3.94	3.18	2.53
10	2.79	1.83	—
12	1.84	—	—
14	0.71	—	—

Where (—) is shown, this signifies no deterministic boundary is required and Smoluchowski's time dependent rate constant should be applicable

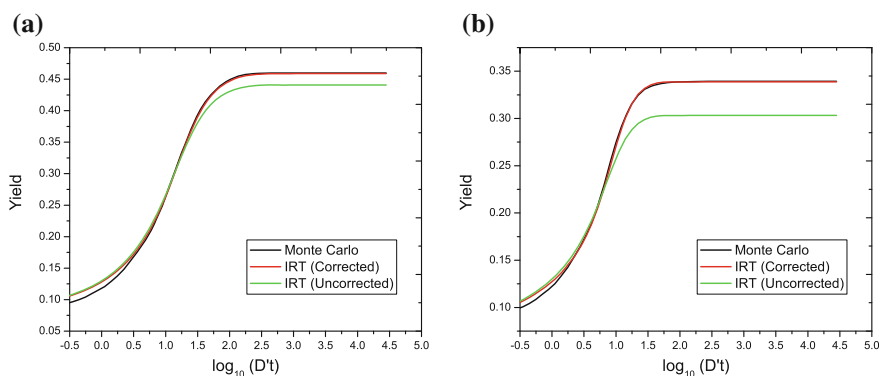


**Fig. 7.17** Yield of  $eS^-$  in **a** diethyl ether and **b** toluene using an ion encounter radius of  $5 \text{ \AA}$  and scavenging radius of  $4 \text{ \AA}$ . An initial distance of  $20 \text{ \AA}$  between the ion pair was used. For both simulations a concentration of  $0.5 \text{ M}$  for scavengers was used. Standard error calculated on the final yield to one standard deviation is: **a**  $\pm 0.0022$  (MC and IRT); **b**  $\pm 0.0021$  (MC and IRT) and  $\pm 0.002$  [IRT (uncorrected)]. Here Monte Carlo (MC) refers to random flights simulation. Units of  $x$ -axis are in  $\text{\AA}^2$

### 7.2.9 Correcting the IRT Algorithm for Any Given Parameter Space

Up to now the analysis has been concerned with a fixed initial separation distance of  $20 \text{ \AA}$  between the radical pair, however in a realistic chemical simulation the ions can be distributed at any arbitrary distance, and it may not be computationally efficient to run a series of simulations to decipher which  $\delta$  (period in which a deterministic trajectory is assumed) is required to produce the correct scavenging kinetics. In this section, the IRT algorithm is generalised to remove the necessity to know  $\delta$ , by directly simulating from a mixture of Smoluchowski's time dependent rate constant and the high velocity scavenging rate constant ( $k_{\text{high}}$ ). The pseudo-algorithm (which is only to be used if the geminate recombination time is larger than the scavenging time) proceeds as follows:

1. From the geminate recombination time ( $T_g$ ), determine the initial distance required from Eq. (7.8).
2. Calculate at which time interval ( $\tau$ ) where  $k_{ss} > k_{smol}$  (i.e. when the rate constant in Eq. (7.12) is greater than Smoluchowski's time dependent rate constant).
3. Calculate the velocity of the drifting particle from the asymptotic rate constant,  $k_{high} = \pi a^2 v_c$  in the period  $(T_g - \tau) - T_g$ .
4. Calculate the scavenging survival probability in this deterministic period by numerically integrating  $k_{high}(\tau)$  using the expression:

$$\Omega_{extra}(\delta) = \exp\left(-c \int_{T_{g-\tau}}^{T_g} k_{high} dt\right).$$

5. Calculate the probability of scavenging in this deterministic period as:  $P_{add} = 1 - \Omega_{extra}(\tau)$
6. Generate a uniformly distributed random number  $U(0, 1]$  in the range  $(0, 1]$ . If  $U(0, 1] \leq P_{add}$  then there is an additional scavenging reaction. The scavenging time  $T_{scav}$  is then randomly set between  $T_{(g-\tau)}$  and  $T_g$ .

Although only a brief set of results are presented in Fig. 7.18, further simulations performed across a wide parameter range showed the above pseudo-algorithm to accurately describe the scavenging process in comparison with random flights simulations.

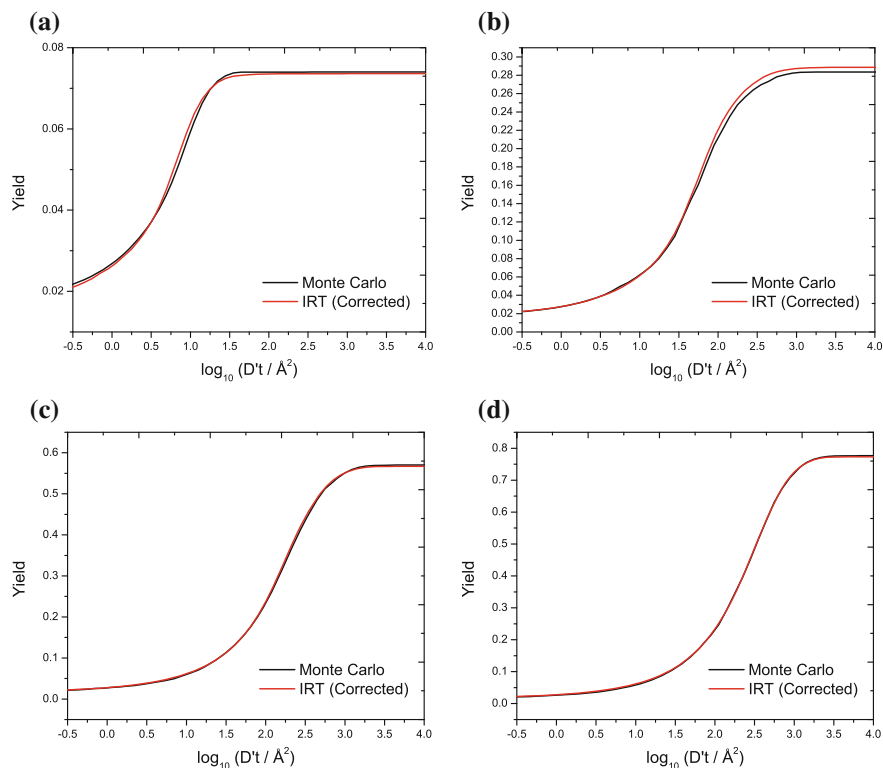
### 7.2.9.1 Mobile Scavengers

As expected, when the scavengers are made mobile the same 'bump' is seen in the rate constant; however, with increasing diffusion coefficients of the scavengers the bump becomes confined to a smaller time region due the narrower dispersion of geminate reaction times. As expected, using Smoluchowski's time dependent rate constant to describe the scavenging kinetics was found to still underestimate the scavenging yield in the IRT framework. Even for such a complex system, the scavenging yield can be correctly simulated within the IRT algorithm by performing the path decomposition of the diffusive trajectory as shown in Fig. 7.19 using the algorithm outlined above.

## 7.3 Two Scavengeable Species

In this section, the correction to Smoluchowski's time dependent rate constant is investigated for two scavengeable species using the reaction scheme

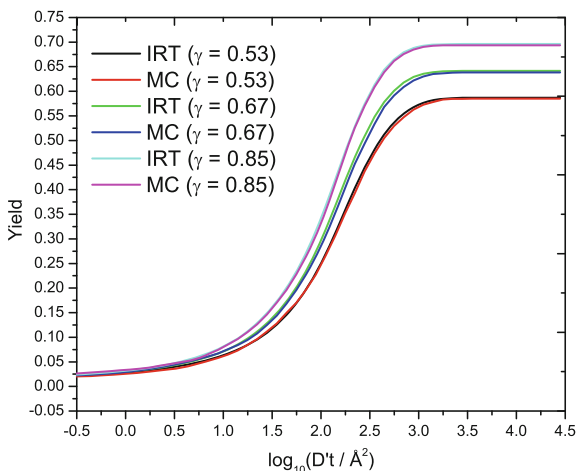




**Fig. 7.18** Yield of  $eS^-$  obtained at **a** 20 Å; **b** 40 Å; **c** 60 Å and **d** 80 Å. A scavenger concentration of 0.1 M was used, together with a geminate and scavenging radius of 5 and 4 Å respectively. Standard error on the final yield to one standard deviation is: **a**  $\pm 0.0011$  (MC and IRT); **b**  $\pm 0.002$  (MC and IRT); **c**  $\pm 0.0022$  (MC and IRT) and **d**  $\pm 0.0019$  (MC and IRT). Here Monte Carlo (MC) refers to random flights simulation

where the products of scavenging are  $eS^-$  and  $hT^+$  and the geminate product being neutral  $eh$ . The scavengers  $S$  and  $T'$  are assumed stationary to allow simplification of the model and allow bigger time steps to be taken in the random flights algorithm (in turn allowing more realisations to be performed). The rest of the simulation parameters remain the same as given in Table 7.1.

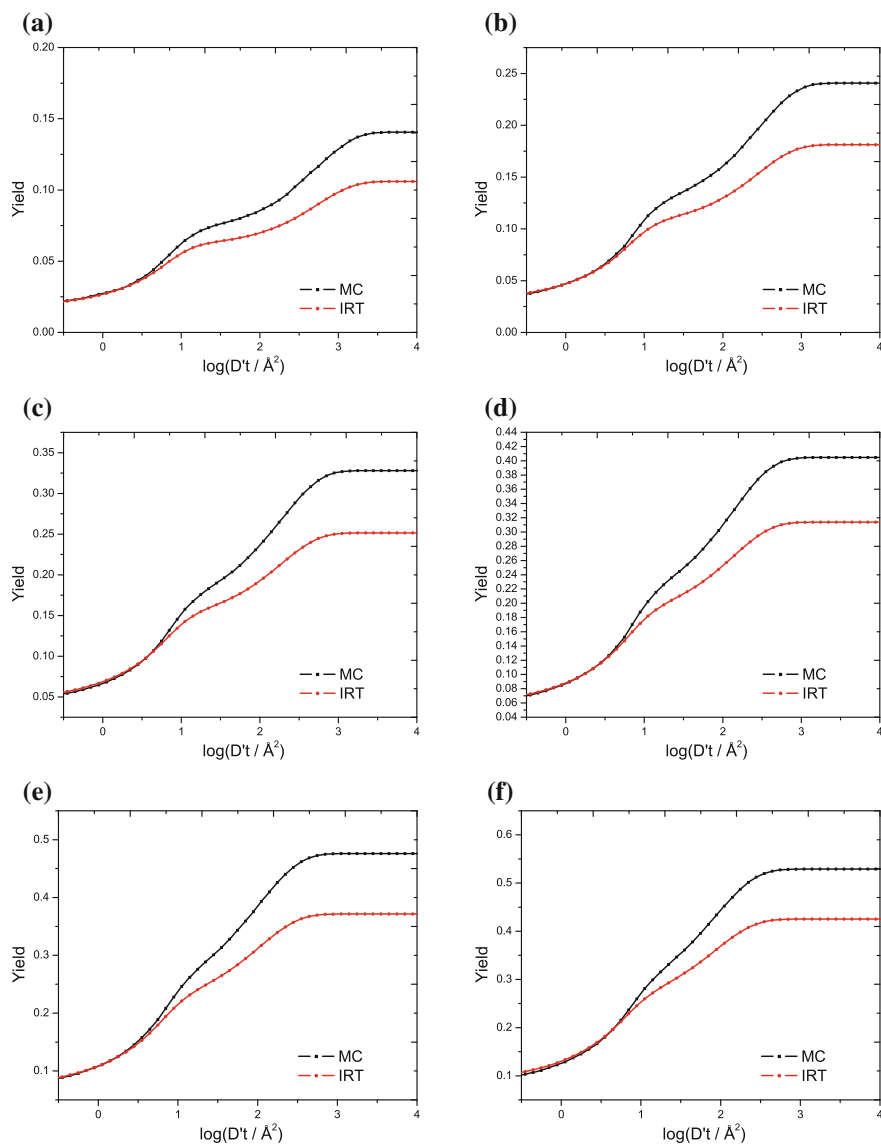
The result for the scavenging kinetics at an initial ion-pair separation of 20 Å is presented in Fig. 7.20 ( $hT^+$  yield is not presented since the kinetics are identical to that of  $eS^-$  due to symmetry). It is again seen that the IRT algorithm is unable to reproduce the scavenging kinetics when the interparticle force between the ion-pair is strong, with a greater probability of scavenging predicted by the random flights algorithm for an ion-pair separation distance in the range 20–60 Å. However, from the analysis done in the previous section, the nature of this discrepancy is now known to arise from the correlation between the scavenging and recombination times.



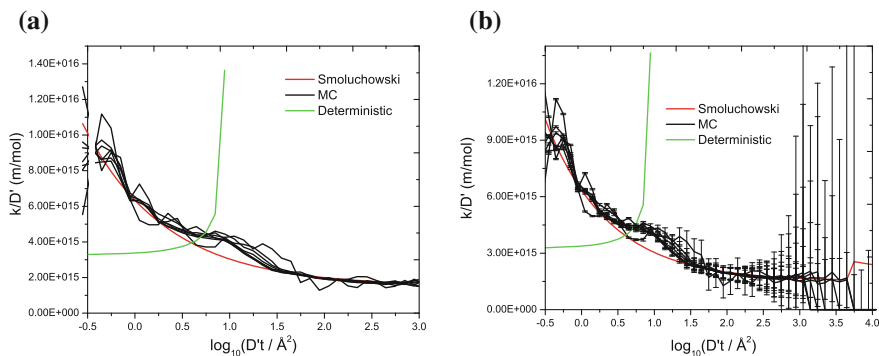
**Fig. 7.19** Scavenging yield for  $eS^-$  obtained using mobile scavengers, with  $\gamma$  being the ratio of mutual diffusion coefficient of the scavenger + ion and ion + ion; (a)  $\gamma = 0.53$  (diffusion coefficient of ion and scavenger was 0.14 and  $0.01 \text{ Å}^2 \text{ ps}^{-1}$  respectively); (b)  $\gamma = 0.67$  (diffusion coefficient of ion and scavenger was 0.14 and  $0.05 \text{ Å}^2 \text{ ps}^{-1}$  respectively) and (c)  $\gamma = 0.85$  (diffusion coefficient of ion and scavenger was 0.14 and  $0.1 \text{ Å}^2 \text{ ps}^{-1}$  respectively). An encounter radius for ion recombination of  $5 \text{ Å}$  and scavenging radius of  $4 \text{ Å}$  was used. Initial distance between the ion pair was set to  $60 \text{ Å}$ . For all simulations a concentration of  $0.1 \text{ M}$  for scavengers was used. Here MC refers to random flights simulation

Figure 7.21 shows the extracted rate constant from random flights simulations (using Eq. 7.17) and is compared with the steady state rate constant for a particle following a deterministic trajectory. A similar ‘bump’ is found at the instance of geminate recombination suggesting a competition between scavenging and recombination. The size of the ‘bump’ however, is found to be smaller than that obtained for the one scavengeable species. A possible explanation is that the ions are scavenged more rapidly outside the deterministic period in the two scavenger case, which rapidly collapses the ionic system to the neutral case. Therefore, fewer surviving ion-pairs can now reach the deterministic region which results in fewer ions becoming scavenged inside this region, which in turn results in a smaller ‘bump’ than in the one scavengeable case.

Figure 7.22 shows a plot of the final yield as a function of the scavengers concentration for  $eS^-$  ( $hT^+$  has been omitted as it will be identical to  $eS^-$  due to symmetry). It is seen that even at typical electron thermalisation distances of  $80 \text{ Å}$ , the scavenging effect manifests itself at low concentration of scavenger concentrations. As the concentration is increased to  $0.5 \text{ M}$ , the effect vanishes due to rapid scavenging of the ions before they can enter the deterministic region  $R_{\text{critical}}$ . The scavenger concentration therefore affects the scavenging rate in a subtle way since this parameter controls how quickly the scavengers are intercepted. For example, if the concentration of scavengers is very high, then the ion pair become scavenged before any



**Fig. 7.20** Yield of  $eS^-$  obtained as a function of six different concentrations **a** 0.1 M, **b** 0.18 M, **c** 0.26 M, **d** 0.34 M, **e** 0.42 M, **f** 0.5 M. Initial separation distance of  $20 \text{\AA}$  was used. Standard error on the final yield to one standard deviation is: **a**  $\pm 0.0013$  (IRT) and  $\pm 0.00105$  (MC); **b**  $\pm 0.0017$  (IRT) and  $\pm 0.0019$  (MC); **c**  $\pm 0.0019$  (IRT) and  $\pm 0.0021$  (MC); **d**  $\pm 0.0021$  (IRT) and  $\pm 0.0022$  (MC); **e**  $\pm 0.0022$  (IRT) and  $\pm 0.0022$  (MC) and **f**  $\pm 0.0022$  (IRT) and  $\pm 0.00223$  (MC). Here MC refers to random flights simulation

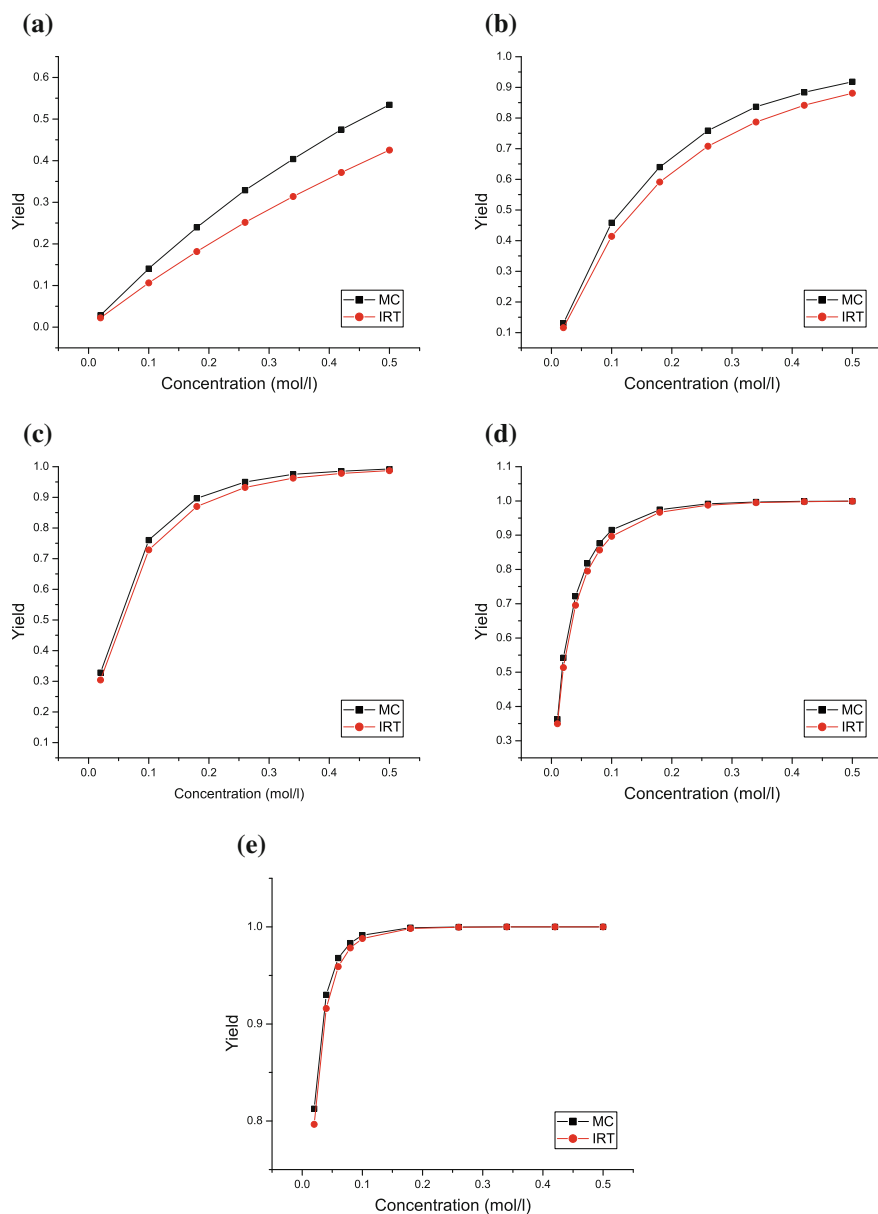


**Fig. 7.21** Simulated scavenging rate constant obtained for  $e^- + S$  using a concentration strength in the range 0.02–0.5 M. An initial ion-pair spacing of 20 Å was used with an Onsager distance of 290 Å. **a** Without error bars and **b** standard error shown to one standard deviation. Here MC refers to random flights simulation

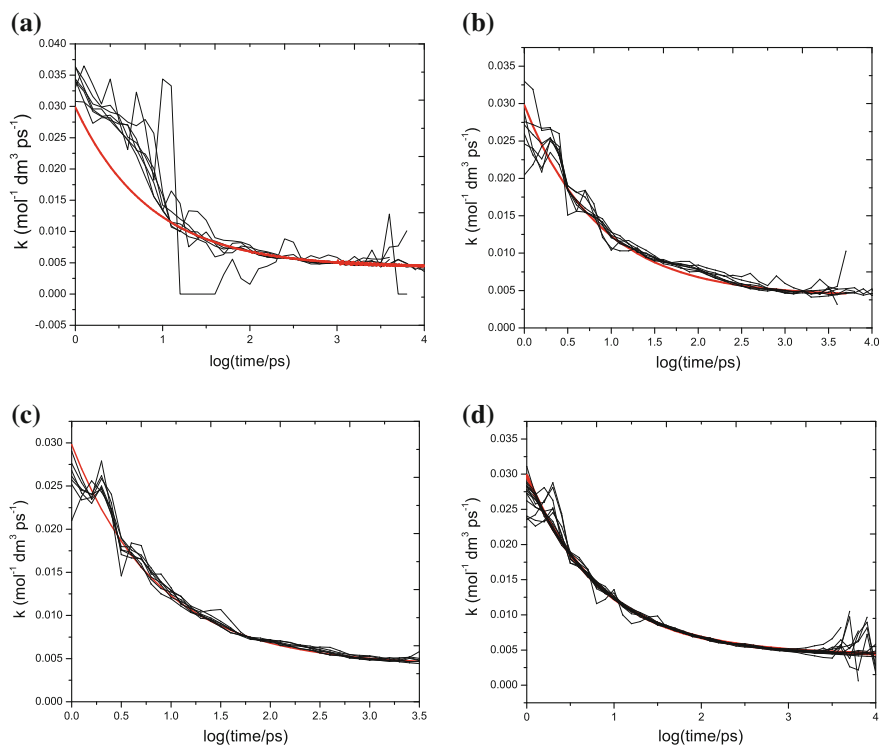
drift between the pair can build up as seen in the case with an initial ion-pair of 80 Å using 0.5 M of scavengers. In this case the rate of scavenging can be accurately described by Smoluchowski's time dependent rate constant for neutral species. If the concentration of scavengers is small, then scavenging occurs on a longer timescale which causes the build up of drift between the ion-pair, causing them to be scavenged with an increased rate. This effect can be seen using an initial ion-pair separation of 80 Å using a scavenger concentration of 0.02 M. Hence, even at typical electron thermalisation distances, the extra scavenging effect is still noticeable.

Figure 7.23 further shows the numerically extracted scavenging rate constants for the  $e^- + S$  reaction from random flights simulations (using Eq. 7.17). As expected a similar 'bump' is found which can now be attributed to the strong correlation between scavenging and recombination. It is seen that at initial separation of 10 Å, the strong electrostatic interaction causes the relative drift of the ion-pair to rapidly increase and become scavenged just prior to geminate recombination. The 'bump' in the rate constant is found to shift towards a smaller timescale (in comparison with the 20 Å case), because the distribution of geminate recombination times is now much narrower. As the distance between the ion-pair increases, the scavenging rate constant for ions resembles that of Smoluchowski's time dependent rate constant for neutral species. This is because with increasing ion-pair distances, there is a greater probability for scavenging to intercept geminate recombination before the drift velocity can become appreciable. However, from Fig. 7.22 and previous discussion, even with large ion-pair distances, the extra scavenging effect might be noticeable at low concentration of scavengers.

The final set of simulations involved calculating the scavenging yield of both  $eS^-$  and  $hT^+$  using: (i) the same diffusion coefficient for both  $e^-$  and  $h^+$ , and (ii) making the  $e^-$  diffuse slightly faster than the  $h^+$ . Using the corrected pseudo-algorithm (as described in Sect. 7.2.9), the results (presented in Fig. 7.24) show the IRT algorithm to



**Fig. 7.22** Final yield of  $eS^-$  obtained as a function of six different separation distances **a** 20 Å, **b** 40 Å, **c** 60 Å, **d** 80 Å, **e** 120 Å. An Onsager radius of 290 Å was used in all cases. A mutual diffusion coefficient of  $0.28 \text{ \AA}^2 \text{ ps}^{-1}$  was used. Here MC refers to random flights simulation



**Fig. 7.23** Simulated scavenging rate constant obtained for  $e^- + S$  using Monte Carlo random flights simulation (*black*) and compared with Smoluchowski's time dependent rate constant (*red*). Ion-pair separation distances used: **a** 10 Å, **b** 30 Å, **c** 40 Å and **d** 80 Å using a scavenger concentration in the range 0.02–0.5 M and an Onsager distance of 290 Å. Error bars have been omitted for clarity purposes. A mutual diffusion coefficient of  $0.28 \text{ \AA}^2 \text{ ps}^{-1}$  was used

accurately describe the scavenging kinetics in both cases. Further extensive testing of the IRT algorithm across a wide parameter space showed the IRT algorithm to provide the correct scavenging kinetics, so long as the path decomposition trajectory was performed correctly, and the correlation between the scavenging and recombination times was taken into consideration.

## 7.4 Discussion

The conclusion of this chapter is that the rate of scavenging is strongly influenced by the separation of the ion-pair and there is a significant correlation between scavenging and recombination times. In the literature, Smoluchowski's time dependent rate constant is often used to model the scavenging of charged species inside a spur without

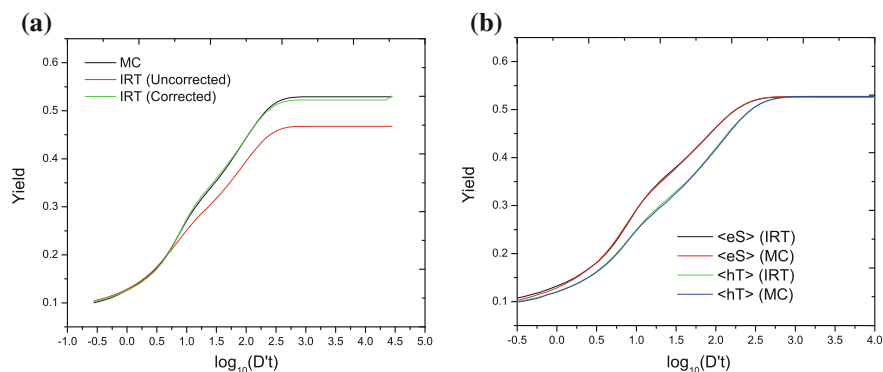


**Fig. 7.24** Yield of  $eS^-$  obtained at 0.5 M of scavengers using an Onsager radius of 290 Å. **a** Both scavengable species are given the same diffusion coefficient ( $0.14 \text{ \AA}^2 \text{ ps}^{-1}$ ). Standard error on the final yield to one standard deviation is  $\pm 0.0022$  (MC and IRT). **b**  $e^-$  and  $h^+$  diffusion coefficient are 0.14 and  $0.1 \text{ \AA}^2 \text{ ps}^{-1}$  respectively. Standard error on the final yield to one standard deviation is  $\pm 0.0022$  (random flights and IRT) on both products. Here MC refers to random flights simulation. Units of  $x$ -axis are in  $\text{\AA}^2$

conditioning on the interparticle separation. It has been shown in this chapter that the scavenging of charged particles is complicated and a careful consideration needs to be paid to the following parameters: (i) correlation between the scavenging and recombination times, (ii) encounter radius of both scavenging and geminate recombination, (iii) ion-pair separation and scavenger concentration, (iv) time period ( $\delta$ ) at which a deterministic trajectory is to be followed and (v) the diffusion coefficient of the ions. A neglect of any one of these factors can result in scavenging being significantly underestimated and consequently biased kinetics will be obtained. Even with the dependence of scavenging kinetics on a number of different parameters, the corrected algorithm outlined in Sect. 7.2.9, has been shown to provide good agreement with random flights simulations. This algorithm does not require any prior knowledge of  $\delta$  (the deterministic period) and can be applied to any chemical system, including the modelling of a full radiation track.

**Validity of the scavenging model** Whilst in this section an initial ion-pair separation of 20 Å has shown to provide an increased scavenging yield (due to the strong ion-pair drift), it is important to note that typical thermalisation distances of the  $e^-$  are normally  $>60 \text{ \AA}$  where the effect of the ‘extra’ scavenging is shown to be small. In highly dense radiation tracks however, ion-pair distances can be within the 20 Å range (or possibly smaller) making the correlation between the scavenging and recombination times very important for these chemical systems.

This chapter has shown that a careful handling of both the scavenging and recombination kinetics is required within the IRT framework due to the correlation that exists between them. This dependence of scavenging rate on recombination time is a fundamental breakdown of the assumptions underlying both the theory of diffusion kinetics and the IRT method. Although the effect is mainly noticeable for

solvents which are non-polar in nature, the complex relationship between the  $a_{\text{gem}}$  (ion-pair encounter distance),  $D'$  (mutual diffusion of the ion-pair) and  $r_c$  together with other variable parameters, could make the extra scavenging effect noticeable for even moderately polar solvents such as tetrahydrofuran (where  $r_c \sim 70 \text{ \AA}$ ).

## References

1. K.M. Hong, J. Noolandi, J. Chem. Phys. **68**, 5163 (1978)
2. F. Willams, J. Am. Chem. Soc. **86**, 3964 (1964)
3. M. Tachiya, J. Chem. Phys. **87**, 4622 (1987)
4. G.R. Freeman, Ann. Rev. Phys. Chem. **34**, 463 (1983)
5. P.K. Ludwig, J. Chem. Phys. **50**, 1787 (1969)
6. J. Crank, P. Nicolson, Proc. Cambridge Philos. Soc. **43**, 50 (1947)
7. J. Crank, *The Mathematics of Diffusion* (Oxford University Press, Oxford, 1975)

# Chapter 8

## Correlation Between Spin Entanglement and the Spin Relaxation Time

### 8.1 Introduction

The track structure created by radiolysis depends on many factors such as the type of ionising radiation used and the initial kinetic energy of this radiation. As such radiolysis gives rise to a complicated spatial arrangement. During the passage of the radiation several radical ion pairs are born in the same spatial region, which can either undergo geminate or cross-recombination. It is considered that all geminate pairs are initially singlet-correlated (*optical approximation*), although the production of triplet ion-pairs is also possible through low-energy electron ionisation.

It is generally thought that the intensity of luminescence arising from cross recombination of ions within a spur is not affected by magnetic field effects, since the spins are uncorrelated and their spin evolution is unaffected by the application of an external static field (i.e. the weight of the singlet state remains 1/4 at all times). This finding seems to be supported by experiments on magnetic field effects [1]. Interestingly, some doubt has been cast on the absence of magnetic field effects for cross-recombination by investigating the track structure of alkane solutions irradiated with helium ions of 20 MeV [2]. The track structure generated is spatially very dense, which means that the vast majority of recombination occurs via cross-recombination. Even with these experimental conditions a small magnetic effect is still observed. It is hypothesised as first discussed by Brocklehurst [3], that any magnetic field effect in cross-recombination is likely to be caused by the quantum phenomenon known as the Einstein-Podolsky-Rosen (ERP)<sup>1</sup> effect [4]. This chapter investigates the ERP contribution to the unusually fast paramagnetic relaxation times observed following the radiolysis of highly symmetrical cyclic hydrocarbon systems, and investigates the rates of relaxation for a photolytic and radiolytic chemical system.

---

<sup>1</sup> The acronym ERP is used in this chapter to avoid any confusion with the acronym EPR (electron paramagnetic resonance).

**Table 8.1** Simple reaction scheme used to illustrate the detection of luminescence [7]

No.	Reaction
1	$\text{Solv} \longrightarrow \text{Solv}^+ + \text{e}^-$
2	$\text{Solv}^+ + \text{S}_h \longrightarrow \text{Solv} + \text{S}_h^+$
3	$\text{e}^- + \text{S}_e \longrightarrow \text{S}_e^-$
4	$\text{S}_h^+ + \text{S}_e^- \longrightarrow \text{S}_h + \text{S}_e^*$
5	$\text{S}_e^* \longrightarrow \text{S}_e$

## 8.2 Theory of Quantum Beats in Recombination Luminescence of Spin-Correlated Radical Ion Pairs

As discussed in Sect. 3.7.2, the oscillation between the singlet-triplet transitions in spin-correlated radical pairs gives rise to a phenomenon known as quantum beats, which was first detected experimentally by Klein and Voltz in 1976 [5] and then independently by Brocklehurst [6]. They arise because the singlet and triplet states are a superposition of several stationary states. Strong spin-orbit coupling, hyperfine coupling or a difference in  $g$ -factors can induce oscillations between the  $S - T_0$  states, with a frequency given by the expression [7]

$$\omega = \left| \frac{\mu_B}{\hbar} B_0 (g_1 - g_2) + \sum_{j1} a_{j1} m_{Ij1} - \sum_{j2} a_{j2} m_{Ij2} \right| \quad (8.1)$$

In the above expression  $\mu_B$  is the Bohr magneton,  $B_0$  the external field strength,  $g$  is the  $g$ -factor,  $a_{jx}$  is the hyperfine coupling constant of the  $j$ th nucleus on radical  $x$ , and  $m_{Ijx}$  is the projected spin of the  $j$ th nucleus of radical  $x$  in the direction of the external field.

Quantum oscillations in a radical pair can be monitored by observing the luminescence arising from the singlet products. To illustrate how this arises, consider the reaction scheme as given in Table 8.1. In this reaction scheme the electron scavenger ( $\text{S}_e$ ) is used as the luminophore which has the property of a short fluorescence time; the hole scavenger ( $\text{S}_h$ ) is used to intercept reaction (1) of the scheme. Irradiation of the solvent molecule (assuming a singlet state) produces ( $\text{Solv}^+ / \text{e}^-$ ) with the same spin multiplicity as its precursor. If the rate of scavenging of the  $\text{Solv}^+$  and  $\text{e}^-$  [reactions (2) and (3)] is faster than the singlet-triplet transition, the secondary pair ( $\text{S}_h^+ + \text{S}_e^-$ ) will also be in a singlet state. Upon recombination of this secondary pair, the excited  $\text{S}_e^*$  rapidly fluoresces to produce a stable ground state species. Therefore, the  $S - T_0$  mixing in the secondary radical pair will induce modulation in the kinetics of recombination fluorescence.

The most optimal conditions for monitoring quantum beats are in non-polar solvents for the following reasons [7]: (1) the separation of the radical pair is usually much less than the Onsager radius and the radical ion pairs recombine geminately; (2) a strong luminescence signal can be observed due to the small solvation energy;

(3) the radical ion pair recombines on first encounter regardless of its spin state due to the strong Coulombic attraction.

### 8.2.1 Time Resolved Magnetic Field Effect

Since singlet-triplet mixing can be induced by the application of a static field, the spin dynamics can be investigated using the time-resolved magnetic field effect (TR MFE) on fluorescence. This method has been exploited to give measurements of spin-lattice relaxation times [8, 9]. It has been well documented in the literature that the experimentally observed fluorescence intensity  $I(t)$  can be expressed by the relation<sup>2</sup>

$$I(t) \propto F(t) \left[ \theta \rho_{ss}(t) + \frac{1}{4}(1 - \theta) \right] \quad (8.2)$$

Here  $F(t)$  is the recombination rate of the ion pair,  $\theta$  is the fraction of spin-correlated pairs, which is assumed to be constant but can vary for different chemical systems and  $\rho_{ss}(t)$  is the time dependence of the singlet state population of the spin-correlated pair. The second term in Eq. (8.2) includes the contribution of the singlet component of the spin-uncorrelated pairs to the fluorescence intensity. Typically, the results of the TR MFE decay are presented as a ratio of the fluorescence intensity at an applied field ( $I_B$ ) and at zero field ( $I_0$ ), which becomes independent of the unknown function  $F(t)$ .

$$\frac{I_B(t)}{I_0(t)} = \frac{\theta \rho_{ss}^B + \frac{1}{4}(1 - \theta)}{\theta \rho_{ss}^0 + \frac{1}{4}(1 - \theta)} \quad (8.3)$$

Molin and co-workers [9] have presented an analytical formulation for  $\rho_{ss}(t)$  under the influence of spin relaxation, hyperfine modulation and  $\Delta g$  mechanism at both high and zero field. The general form for the singlet probability in the presence ( $\rho^B$ ) and absence ( $\rho^0$ ) of an applied magnetic field take the form

$$\rho_{ss}^B(t) = \frac{1}{4} + \frac{1}{4}e^{-t/T_1} + \frac{1}{2}e^{-t/T_2}G_c^B(t)G_a^B(t) \quad (8.4)$$

$$\rho_{ss}^0(t) = \frac{1}{4} + \frac{3}{4}e^{-t/T_0}G_c^0(t)G_a^0(t) \quad (8.5)$$

with  $T_1$  and  $T_2$  representing the spin-lattice and spin-spin relaxation times, with  $1/T_1 = 1/T_{1a} + 1/T_{1c}$ ,  $1/T_2 = 1/T_{2a} + 1/T_{2c}$  and  $1/T_0 = 1/T_{0a} + 1/T_{0c}$ , with the indices  $a$  and  $c$  signifying the radical anion and cation respectively.  $T_0$  is the effective phase relaxation time at zero field and  $G(t)$  are functions which are directly

<sup>2</sup> This formula assumes that fluorescence occurs almost instantaneously and can therefore only be used in the tail of the recombination probability distribution.

determined by the hyperfine coupling constants and  $g$ -values of the radical. Within the semiclassical approximation<sup>3</sup> [10, 11], the authors have derived an expression for the function  $G(t)$  at zero and high field to be respectively [9]

$$G^0(t) = \frac{1}{3} \left[ 1 + 2(1 - \gamma_e^2 \sigma_R^2 t^2) \exp(-\gamma_e^2 \sigma_R^2 t^2 / 2) \right] \quad (8.6)$$

$$G^B(t) = e^{-\gamma_e^2 \sigma_R^2 t^2 / 2} \quad (8.7)$$

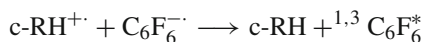
with  $\gamma_e$  being the gyromagnetic ratio and  $\sigma_R^2$  is the second moment of the EPR spectrum of the radical, which takes the form

$$\sigma_R^2 = \frac{1}{3} \sum_n a_n^2 I_n (I_n + 1) \quad (8.8)$$

with  $a_n$  and  $I_n$  being the hyperfine coupling constant and nuclear spin on the  $n$ th nucleus respectively. It can be seen from Eqs. (8.4) and (8.5) that at long times (when  $t \gg T_2$  and  $T'_0$ ) the ratio  $I_B(t)/I_0(t)$  will decay monoexponentially as  $1 + \theta \exp(-t/T_1)$  [12] allowing the longitudinal relaxation time to be extracted irrespective of the relaxation mechanism.

The TR MFE technique has been extensively used to measure the spin-lattice relaxation rates of radical ions in solutions, with a number of aromatic radical ions found to have a relaxation time in the order of 1  $\mu$ s [13]. However, for cyclohexane and adamantane radical cations and their alkyl-substituted analogues [14–16] there is a surprising discrepancy in the relaxation times as shown in Table 8.2. The experimental values presented in Table 8.2 have been obtained by preparing a solution of the cycloalkane (c-RH) and hexafluorobenzene in  $n$ -hexane with typical concentrations of 0.01–0.1 and 0.01 M respectively. Upon irradiation of  $n$ -hexane with X-rays, the primary singlet correlated pairs are rapidly scavenged (within sub-nanoseconds) to produce the secondary c-RH<sup>+</sup> and C<sub>6</sub>F<sub>6</sub><sup>-</sup> radical ion pair.

These secondary radical ion pairs recombine according to the reaction



and the fluorescence arising from <sup>1</sup>C<sub>6</sub>F<sub>6</sub>\* excited state is detected. Hence, the spin dynamics of the secondary radical pair (c-RH<sup>+</sup>) / (C<sub>6</sub>F<sub>6</sub><sup>-</sup>) directly determines the fluorescence intensity. It is assumed that due to the rapid scavenging of the primary radical ions, their contribution to the spin dynamics is negligible.<sup>4</sup> The experimentalists have shown that normal relaxation mechanisms, such as modulation of hyperfine

<sup>3</sup> In the semiclassical approximation the electron spin on each radical is treated quantum mechanically, whilst the nuclear spins are treated classically. The unpaired electron precesses about the static field and the resultant of the nuclear spins.

<sup>4</sup> This assumption will be utilised to simplify the computational model.

**Table 8.2** Spin lattice relaxation times of radical ions in nonpolar solvents [15]

Compound	$T_1/\text{ns}$	$T_2/\text{ns}$
Hexafluorobenzene <sup>-•</sup>	350 ± 15	15 ± 5
cis-Decalin <sup>+•</sup>	390 ± 15	10 ± 5
Cyclohexane <sup>+•</sup>	9 ± 2	9 ± 2
Methylcyclohexane <sup>+•</sup>	57 ± 10	5 ± 2
Ethylcyclohexane <sup>+•</sup>	21 ± 3	10 ± 5
Propylcyclohexane <sup>+•</sup>	38 ± 4	7 ± 3
Isopropylcyclohexane <sup>+•</sup>	280 ± 20	20 ± 5
cis-1,2-Dimethylcyclohexane <sup>+•</sup>	280 ± 20	20 ± 5
Adamantane <sup>+•</sup>	6.5 ± 1	5 ± 3
1,3-Dimethyladamantane <sup>+•</sup>	8.2 ± 1	5 ± 3

Experimental luminescence was detected by single photon counting technique using an X-ray fluorimeter

coupling constant,  $g$ -tensor anisotropy, degenerate electron exchange or spin-rotation interaction are unable to reproduce the observed relaxation times [17–20].

From Redfield theory in the limit of fast spectral exchange ( $(\gamma \Delta \tau_c)^2 \ll 1$ ), the spin lattice relaxation time can be evaluated as

$$\frac{1}{T_1} = \frac{2(\gamma \Delta)^2 \tau_c}{1 + (\gamma B_0)^2 \tau_c^2} \quad (8.9)$$

with  $\Delta$  being the mean-square value of the perturbation causing relaxation,  $\tau_c$  is the correlation time of the perturbation,  $\gamma$  is the gyromagnetic ratio and  $B_0$  is the strength of the external field. In a field of 1 T, assuming  $\gamma B_0 \tau_c = 1$  (which provides the maximum relaxation rate) and using typical values of  $\Delta$  and  $\tau_c$  of 6.5 mT and 6 ps respectively for the cyclohexane radical, Molin and co-workers have calculated the shortest expected value of the spin-relaxation time to be  $T_1 = 130$  ns [15]. As the measured  $T_1$  is an order of magnitude shorter, they concluded that the modulation of the hyperfine coupling constant can indeed not be responsible for the observed relaxation.

One intriguing explanation considers the degeneracy of the molecular orbital where the unpaired electron lies [12, 21]. Upon dissociation, the radical possesses a lower symmetry than that of its parent (neutral) species due to deformation of molecular bonds. The degeneracy of the singly occupied molecular orbital however, can be restored by the rapid fluctuations between different Jahn-Teller structures [22, 23], which together with strong spin-orbit coupling results in paramagnetic relaxation.

### 8.3 Electron Exchange in Spurs

In order to understand the origin of the ERP effect, consider a simple two-pair spur in the absence of other coherent and incoherent effect, which can exhibit two types of correlation: the first type considers two singlet correlated radical pairs (type 1) and the second considers two triplet correlated radical pairs (type 2).

**Two singlet correlated radical pairs** Considering the type (1) first, the wavefunction  $\psi$  for the two ion-pair spur can be written as

$$\begin{aligned}\psi &= \frac{1}{\sqrt{2}}(\alpha^1\beta^2 - \beta^1\alpha^2) \times \frac{1}{\sqrt{2}}(\alpha^3\beta^4 - \beta^3\alpha^4) \\ &= \frac{1}{2}(\alpha^1\beta^2\alpha^3\beta^4 - \alpha^1\beta^2\beta^3\alpha^4 - \beta^1\alpha^2\alpha^3\beta^4 + \beta^1\alpha^2\beta^3\alpha^4)\end{aligned}\quad (8.10)$$

where the superscripts in Eq. (8.10) denote the spins on radicals (1–4). If radical pairs {1, 2} and {3, 4} are singlet correlated then any cross-reaction between {1, 3} and {2, 4} is likely to have a singlet-triplet ratio of 1:3. This can be demonstrated by rewriting Eq. (8.10) for the cross-reaction {2, 3} as

$$\psi = \frac{1}{2}(\beta^2\alpha^3\alpha^1\beta^4 - \beta^2\beta^3\alpha^1\alpha^4 - \alpha^2\alpha^3\beta^1\beta^4 + \alpha^2\beta^3\beta^1\alpha^4)\quad (8.11)$$

which can be rewritten in the singlet-triplet basis as

$$\psi = \frac{1}{2}(T_0^{14}T_0^{23} - T_{+1}^{14}T_{-1}^{23} - T_{-1}^{14}T_{+1}^{23} - S^{14}S^{23})\quad (8.12)$$

Equation (8.12) has two important features: (i) The wavefunction is still overall singlet but has an overall probability of 75% triplet and 25% singlet for pairs {1, 4} and {2, 3}. (ii) If radical pair {2, 3} reacts and is found to be triplet, then pair {1, 4} must also be triplet as there is no component in the wavefunction in Eq. (8.12), where one pair is singlet and the other triplet. This incoherent change in the spin state of the disjoint radical pair is hypothesised to act as an extra source of relaxation. It can be seen that this non-local effect is independent of the distance between radical pairs and any magnetic interactions.

**Two triplet correlated radical pairs** The second type of ‘action at a distance’ concerns type (2) spurs where a triplet encounter between {1, 4} (which occurs in 75% of the cases in spurs) causes the disjoint pair {2, 3} to adopt the same spin multiplicity. The normalised wavefunction after removing the singlet terms becomes

$$\psi = \frac{1}{\sqrt{3}}(T_0^{14}T_0^{23} - T_{+1}^{14}T_{-1}^{23} - T_{-1}^{14}T_{+1}^{23})\quad (8.13)$$

which when rearranged gives

$$\begin{aligned}
\psi &= \frac{1}{4}(\alpha^1\alpha^2\beta^3\beta^4 + \alpha^1\beta^2\alpha^3\beta^4 + \beta^1\alpha^2\beta^3\alpha^4 + \beta^1\beta^2\alpha^3\alpha^4) \\
&\quad - \frac{1}{2}(\alpha^1\beta^2\beta^3\alpha^4 + \beta^1\alpha^2\alpha^3\beta^4) \\
&= \frac{1}{2\sqrt{3}} \left[ (T_+^{12}T_-^{34} + T_-^{12}T_+^{34} - T_0^{12}T_0^{34} + 3S^{12}S^{34}) \right] \quad (8.14)
\end{aligned}$$

with the probability for pairs {1, 2}, {3, 4} being in the triplet and singlet states given as  $\frac{1}{4}$  and  $\frac{3}{4}$  respectively, thereby giving a higher probability of reaction on subsequent reactions for pairs {1, 2} and {3, 4} should reaction only be possible through the singlet channel. This effect has been studied by Brocklehurst [3] and is explained as follows: on an unsuccessful encounter between pair {1, 4}, the exchange in the pair {1, 4} redistributes the singlet and triplet character to the pairs {1, 2}, {3, 4} and {1, 3}, {2, 4}. Again, this is a non-local effect and can arise irrespective of the radical pair separation distance or the magnetic field strength. These exchange processes do not directly produce any magnetic field effects and there is also no direct evidence of their occurrence in spurs. However, these effects may be difficult to detect because of the complexity of spur dynamics and inadequate information about the spatial distributions. A first attempt to incorporate spin effects was made by Brocklehurst [24], however it lacked the ability to model a full radiation track structure.

### 8.3.1 Singlet and Triplet Frequency

Recently in the literature Il'ichov et al. [25] have studied the effect of the spin entanglement in radical ion pairs and the effect this has on the frequency of singlet and triplet recombinations. They have shown that in the absence of spin evolution, the non-local swapping of the spin multiplicity does not in fact manifest itself in the singlet and triplet recombination frequencies. The authors have shown that the average spin state operator can be written in the form

$$\langle \hat{\rho}(\mathbf{r}_1, \mathbf{r}_2) \rangle = \frac{1}{4} [\hat{\sigma}_0 \otimes \hat{\sigma}_0 - \xi(\mathbf{r}_1, \mathbf{r}_2) \hat{\sigma}_k \otimes \hat{\sigma}_k] \quad (8.15)$$

with  $\hat{\sigma}_0$  being a unit  $2 \times 2$  matrix,  $\hat{\sigma}_k$  the Pauli spin matrices with  $k$  signifying the spatial index ( $x, y, z$ ; summation over repeated indices is assumed). Without going into the derivation of  $\xi(\mathbf{r}_1, \mathbf{r}_2)$  which requires an explicit form of the kinetic equation, the authors have found that the value for the rate of change of  $\xi(r)$  averaged over the volume of the system is [26]

$$\frac{\partial \xi(r)}{\partial t} = -2\kappa g_D \xi(r) + (D_+ + D_-) \nabla_{\mathbf{r}}^2 \xi(r) + \frac{\gamma^{(0)} - \gamma^{(1)}/3}{g_D^2} \varphi(r) \quad (8.16)$$

where  $\kappa$  is the recombination rate of the radical pairs,  $D_+$  and  $D_-$  are the diffusion coefficients of the cation and anion respectively,  $\gamma^0$  and  $\gamma^1$  are the generation rates of a radical pair in the singlet and triplet states respectively by ionisation;  $g_D$  is the spatial density of the cation and anion (which are assumed to be identical) and  $\varphi(r)$  is the distribution of the relative positions of the created radicals via ionisation. The main point in Eq. (8.16) is that the swapping of the spin multiplicity makes no contribution to the evolution of the average spin operator  $\langle \hat{Q}(r) \rangle$  and hence the frequency of the singlet-triplet recombination yields. The evolution simply depends on the recombination rate of the ion pair (either by cross or geminate recombination), the diffusion of the ion pair and the creation of new ion pairs by ionisation. Therefore, for a chemical system containing radical pairs with equal  $g$ -factors with no hyperfine interaction (in the absence of spin-relaxation), the hypothesis of the ERP effect acting as an extra source of relaxation does not appear to be valid.

## 8.4 Computational Model

The preceding sections have illustrated the main concepts behind the TR MFE technique and how electron exchange in spurs can influence the spin dynamics of radical pairs. This section will now present in detail the computational model used to investigate the ERP effect on the spin-lattice relaxation time within the IRT framework, using the algorithm as discussed in Sect. 4.4 of this work.

### 8.4.1 Projection Operator

Unlike neutral species, reaction of ionic species is possible through both the singlet and triplet channels due to the strong Coulombic electrostatic interaction. In the simulation program, at the point of geminate recombination it is necessary to project out the singlet component of the wavefunction to decipher the nature of the encounter. For each radical pair in the chemical system there exists a separate singlet projection operator, which makes it important to record which species are recombining. The projection operator may be constructed using the general expression

$$\hat{P}_S^n = \sum_{i=1}^k |S^n \phi_i\rangle \langle S^n \phi_i| \quad (8.17)$$

where  $S^n$  is the singlet wavefunction for the radical pair  $n$ ,  $\phi$  represents the configuration for the disjoint spins, and the summation running across all different permutations of disjoint spins. To construct the elements of the projection matrix, it is necessary to represent each state  $|S^n \phi\rangle$  by its respective column and row vector and then compute Eq. (8.17) for all elements in the basis set.

### 8.4.2 Spin-Correlation Following Cross Recombination

Supposing radical pairs {1, 2} and {3, 4} are spin correlated, then the spin-dynamics of correlated pair {1, 2} can be described by wavefunction  $\psi_{12}$  and correlated pair {3, 4} by wavefunction  $\psi_{34}$ . Each individual one-pair spin wavefunction evolves independently according to its Hamiltonian. Following a cross recombination, it is necessary to construct the total wavefunction  $\psi_{\text{tot}} = \psi_{12}\psi_{34}$  and collapse the wavefunction  $\psi_{\text{tot}}$  onto either a singlet or triplet state depending on the spin-dynamics of the encountering pair. It is then necessary to extract the coefficients for the surviving radical pair and reconstruct the one pair wavefunction. From hereon, this is referred to as the *decomposition method*.

Although a simple two pair spur can be simulated entirely using  $\psi_{\text{tot}}$ , it becomes necessary to use the decomposition method for a large number of radical pairs because of the increasing size of the basis set.

**Singlet encounter** Assuming the encounter of the disjoint radical pair {1, 3} is found to be in a singlet state, the algorithm constructs the one pair wavefunction for the radical pair {2, 4} by first collapsing  $\psi_{\text{tot}}$  in which the radical pair {1, 3} is in a pure singlet state.  $\psi_{\text{tot}}$  can be expressed more formally as

$$\begin{aligned}\psi_{\text{tot}} &= \left[ \frac{1}{\sqrt{2}}(\alpha_1\beta_3 - \beta_1\alpha_3) \right] \times \psi_{24} \\ &= |S^{13}\rangle\psi_{24}\end{aligned}\tag{8.18}$$

The second step involves constructing  $\psi_{24}$ , by extracting all the coefficients from  $\psi_{\text{tot}}$  that contain the state  $|\alpha_1\beta_3\rangle$  (with subscripts representing the spin on the radical) and populating back the one pair basis set. Obviously the state  $|\beta_1\alpha_3\rangle$  could also be chosen, in which case the coefficients would be equal but opposite.

**Triplet encounter** For a triplet encounter, the process of extracting the coefficients is similar to that described above. At the moment of encounter the wavefunction collapses onto a triplet state and the probability of each triplet substate is calculated from the coefficients of the wavefunction. A uniformly distributed random number is generated between (0,1] which is used to decide in which triplet substate the encountering pair is formed.<sup>5</sup> Next, the coefficients belonging to the encountering pair from  $\psi_{\text{tot}}$  are used to repopulate the coefficients of the disjoint pair.

#### 8.4.2.1 Spin-Wavefunction Analysis

Following a cross recombination, it is important to verify that the wavefunction for the newly correlated pair has the correct singlet-triplet probability. For this reason, a separate simulation in which  $\psi_{\text{tot}}$  is simulated at all times was also adopted to

---

<sup>5</sup> This method does have the disadvantage that the coherences between the triplet spin states are not retained.

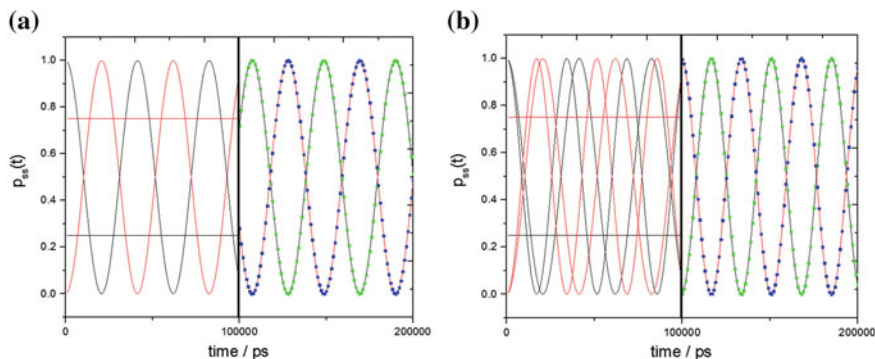


**Fig. 8.1** Spin wavefunction in an external field of 0.33 T, which at the moment of cross-recombination collapses onto a **singlet state** for pairs (1,4). **a** Nuclear configuration  $|+1 +2 +3 +4\rangle$  and **b**  $|+1 -2 +3 +4\rangle$ . Number in subscript represents the radical where the magnetic nucleus resides. *Black and red line* represents (respectively) the singlet and triplet probability simulated using  $\psi_{\text{tot}}$  throughout; *green and blue dots* represent the same using the decomposition method. After 0.1  $\mu\text{s}$ , the spin wavefunction for pair {2, 3} is shown

allow comparison with the decomposition method. When simulating  $\psi_{\text{tot}}$ , following a recombination event, the spin parameters belonging to the encountering pair are zeroed and the remaining pair evolves under its respective Hamiltonian. Figures 8.1 and 8.2 show the simulated wavefunction following a recombination event for pairs {1, 4} using both approaches at an external field strength of 0.33 T with a predefined nuclear spin configuration. In all cases, two  $\text{hT}^+$  and  $\text{eS}^-$  radicals were simulated, each with one magnetic nucleus (with hyperfine coupling constant 2 mT). The  $g$ -factors used for  $\text{hT}^+$  and  $\text{eS}^-$  were 2.0069 and 2.0014 respectively (typical values for  $\text{C}_6\text{H}_6^+$  and  $\text{C}_6\text{F}_6^-$ ). Since only the spin wavefunction is simulated, set to collapse at a predefined time (0.1  $\mu\text{s}$ ), all diffusive parameters are unimportant.

Figure 8.3 shows the simulated wavefunction using the same parameters as mentioned above, but with the field strength changed to 0 T. In all cases examined, the decomposition of  $\psi_{\text{tot}}$  does not introduce any significant bias into the system wavefunction and correctly describes the spin dynamics (i.e. singlet and triplet probabilities) following a cross-recombination. This allows any number of spin particles to be modelled within a spur, since the maximum size of the basis set is  $2^8$  for  $\psi_{\text{tot}}$  at all times following a cross-recombination, or  $2^4$  following a geminate recombination for  $\psi_{\text{gem}}$ . If however,  $\psi_{\text{tot}}$  is simulated then the basis set grows exponentially with the number of radicals. A basis set of  $2^{16}$  is needed just to simulate eight particles, each with a single magnetic nucleus. This is clearly not a feasible method.

### 8.4.3 Spin Relaxation: Boltzmann Distribution

The process of spin relaxation using the wavefunction has already been discussed in Sect. 5.4.2.1. In this section the algorithm is extended to allow the spins to relax

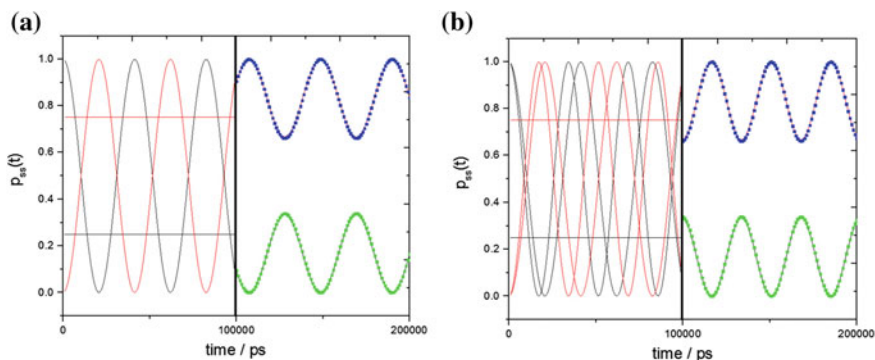


**Fig. 8.2** Spin wavefunction in an external field of 0.33 T, which at the moment of cross-recombination collapses onto a **triplet state** for pairs (1,4). **a** Nuclear configuration  $|+1 +2 +3 +4\rangle$  and **b**  $|+1 -2 +3 +4\rangle$ . Number in subscript represents the radical where the magnetic nucleus resides. *Black and red line* represents (respectively) the singlet and triplet probability simulated using  $\psi_{\text{tot}}$  throughout; *green and blue dots* represent the same using the decomposition method. After 0.1  $\mu\text{s}$ , the spin wavefunction for pair {2, 3} is shown

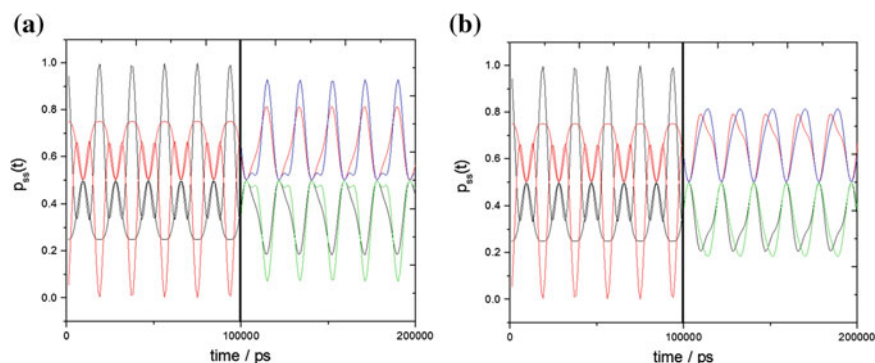


**Fig. 8.3** Spin wavefunction in an external field of 0 T, which at the moment of cross-recombination collapses onto a **a** singlet state and **b** triplet state for pairs (1,4). A nuclear configuration  $|+1 +2 -3 -4\rangle$  was used for both cases. Number in subscript represents the radical where the magnetic nucleus resides. *Black and red line* represents (respectively) the singlet and triplet probability simulated using  $\psi_{\text{tot}}$  throughout; *green and blue lines* represent the same using the decomposition method. After 0.1  $\mu\text{s}$ , the spin wavefunction for pair {2, 3} is shown

to a Boltzmann distribution rather than a uniform distribution. For the sake of completeness, the algorithm is illustrated for a two radical pair system each with a single nuclear spin.

The first step in the algorithm is to calculate the relaxation probability for each nuclear spin configuration  $k$  as

$$\mathfrak{S}_k = \sum_{n=1}^j c_n c_n^* \quad (8.19)$$

where the summation runs across all the electron states belonging to that particular nuclear configuration,  $c_n$  is the coefficient of the state  $n$  and  $c_n^*$  being its complex conjugate. For each nuclear spin state  $k$ , the Boltzmann population can be calculated as  $b_{kj} = e^{-E_{kj}/k_B T}$ , where  $E_{kj}$  is the energy of the electron state  $j$  belonging to a nuclear configuration  $k$ ,  $k_B$  the Boltzmann constant and  $T$  is the temperature. For a spin state with more than one eigenvalue, it was found acceptable to take the average of all possible energy states. The partition function  $Q_k$  for each nuclear spin configuration can be written as

$$Q_k = \sum_j b_{kj} \quad (8.20)$$

with the summation running across all electron states  $j$  belonging to that nuclear spin configuration  $k$ . For each  $k$ , a random number  $U(0, 1]$  is generated and compared with the Boltzmann probability

$$B_k = \sum_j \frac{b_{kj}}{Q_k} \quad (8.21)$$

If the probability of  $B_k > U(0, 1]$ , then the coefficient for the state  $j$  with a nuclear spin configuration  $k$  collapses as  $\sqrt{\mathfrak{S}_k} \times e^{(2\pi U(0,1]i)}$ , with the exponential term modelling phase relaxation ( $T_2$ ). This process is repeated until all the permutations of the nuclear spins in the basis set have been considered. Obviously, this mechanism can be extended to model relaxation to a uniform distribution by setting the probability of  $B_k = \frac{1}{\eta}$ , where  $\eta$  is equal to the total number of  $j$  states for the nuclear configuration  $k$ .

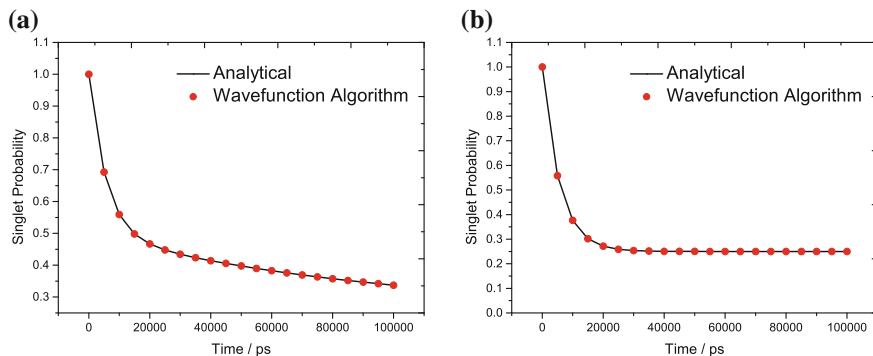
#### 8.4.3.1 Testing the Wavefunction Algorithm

Figure 8.4 shows the singlet probability obtained using the spin-relaxation algorithm<sup>6</sup> and compared with Eqs. (8.4) and (8.5) at both zero and high fields, ignoring any hyperfine and  $\Delta g$  mechanisms (i.e.  $G_a$  and  $G_c$  are set to 1). In the calculation it was assumed that the spin relaxation parameter at zero field  $T_0'$  was equal to  $T_2$  since there is no preferred axis. It can be seen that essentially good agreement is obtained between the wavefunction formalism and that obtained using analytical formulation.

Although analytical formulations are available to calculate the intensity of fluorescence, they lack the ability to predict the effect of electron exchange in spurs and their contribution to the spin relaxation times. Currently the only viable method to take these into account is to use numerical simulations such as IRT or Monte Carlo

---

<sup>6</sup> In this simulation spin relaxation was modelled to a uniform distribution.



**Fig. 8.4** Evolution of the singlet probability at **a** high field and **b** zero field using the wavefunction algorithm and compared with analytical formulation (Eqs. 8.4, 8.5). **a**  $T_{1c} = 130$  ns,  $T_{2c} = 9$  ns,  $T_{1a} = 350$  ns and  $T_{2a} = 15$  ns. **b**  $1/T_0 = 1/T_{2c} + 1/T_{2a}$ ;  $T_{1c} = T_{2c} = 9$  ns;  $T_{1a} = T_{2a} = 15$  ns. Subscripts *c* and *a* refer to the cation and anion respectively

random flights and explicitly treat the wavefunction for each ion-pair. Unfortunately, this does have the drawback of requiring a very large number of realisations in order to obtain acceptable statistics. However, with the recent developments made in the IRT algorithm [as highlighted in Sect. 4.4] the computation is nevertheless tractable.

#### 8.4.4 Spin-Dependent Reactivity

As per previous simulation methods, on encounter the spin state of the pair is interrogated by projecting out the singlet component of the wavefunction. The nature of the encounter is determined by generating a random number  $U(0, 1]$ . If the probability of the singlet state ( $P_s$ ) is greater than  $U(0, 1]$ , then the pair react through the singlet channel, otherwise reaction proceeds through the triplet channel. In either case, the wavefunction is collapsed onto the relevant state and re-normalised. For neutral species, reaction is only possible via the singlet channel; if the encountering pair is found to be in a triplet state then the particles are simply reflected.

#### 8.4.5 Simulation Flow Diagrams

All simulations were carried out using the IRT algorithm, but have been repeated (wherever possible) using the Monte Carlo random flights method. The general flow diagram for both algorithms are shown in the Appendix (Fig. C.6 in Sects. C.6 and C.7 in Sect. C.7), which highlights the main computational details used to model the ERP effect in low-permittivity solvents within the IRT and random flights framework. The next section now implements these algorithms to model the radiolysis of *n*-hexane

**Table 8.3** Reaction scheme detailing the possible encounters following the radiolysis of *n*-hexane, containing a solution of hexafluorobenzene and cyclohexane with their rate constants *k* or the reaction probabilities  $P_c$  (with dimensionless units) [7]

No.	Reaction	<i>k</i> or $P_c$
1	$e^- + \text{Solv}^+ \longrightarrow \text{Solv}$	1
2	$e^- + S_e \longrightarrow S_e^-$	$1 \times 10^{10} \text{ M}^{-1} \text{ s}^{-1}$
3	$S_e^- + \text{Solv}^+ \longrightarrow \text{Solv} + S_e$	1
4	$\text{Solv}^+ + \text{c-RH} \longrightarrow \text{c-RH}^+ + \text{Solv}$	$1 \times 10^{10} \text{ M}^{-1} \text{ s}^{-1}$
5	$e^- + \text{c-RH}^+ \longrightarrow \text{c-RH}$	1
6	$S_e^- + \text{c-RH}^+ \longrightarrow \text{c-RH} + {}^1,3S_e^*$	1
7	${}^1S_e^* \longrightarrow S_e$	$1 \text{ ns}^{-1}$

Here  $S_e^-$ ,  $\text{c-RH}^+$  and  $\text{Solv}^+$  represents hexafluorobenzene anion, cyclo-hexane cation and solvent cation respectively

containing a solution of hexafluorobenzene and cyclohexane, and investigate the contribution of the ERP effect based on the experimentally observed magnetic field effect.

## 8.5 Radiolysis of *n*-Hexane Containing a Solution of Hexafluorobenzene and Cyclohexane

The reaction scheme considered in this section takes the form as shown in Table 8.3, which is based on the reaction scheme shown in Table 8.1. In this work, the  $\Delta g$  mechanism and hyperfine interactions are not treated explicitly, but rather are taken into account phenomenologically based on the experimentally determined rate of relaxation. This helps to simplify the model and increase the computational efficiency of the IRT algorithm.

In the above reaction scheme  $\text{Solv}^+$ ,  $\text{c-RH}^+$ ,  $S_e^-$  represent the solvent cation, cyclohexane cation and hexafluorobenzene (HFB) anion respectively. The spin-dynamics of  $S_e^-$  and  $\text{c-RH}^+$  determine the magnetic field effect, since the spin wavefunction for the ion pair ( $S_e^- / \text{c-RH}^+$ ) evolves differently at the different magnetic field strengths. The intensity of recombination fluorescence of the solution is determined by the rate of radiative deactivation of  ${}^1S_e^*$  [reaction (7)], which is accumulated within the simulation program. Although this model is not a complete description of the radiolysis of *n*-hexane which contains a solution of HFB and cyclohexane, it does however, take into account the most important aspect of the proposed relaxation mechanism, namely cross recombination. A more detailed reaction scheme for the radiolysis of *n*-dodecane is considered later in this chapter (in Sect. 8.6), which takes into account the excited state chemistry as well as spin-exchange reactions.

### 8.5.1 Scavenging Kinetics and Diffusion Parameters

For the scavenging reactions (2) and (4), a quasi-unimolecular time-dependent rate constant was used (Eq. 8.22) using a concentration of 1 M for HFB and cyclohexane. This gives a scavenging lifetime for  $e^-$  and  $\text{Solv}^+$  of 100 ps, which is much faster than any other spin dynamic processes, making the spin dynamics of the primary ion-pair unimportant.

$$k(t) = 4\pi D'a \left[ 1 + \frac{a}{\sqrt{\pi D't}} \right] \quad (8.22)$$

In the above expression  $D'$  is the mutual diffusion coefficient and  $a$  the encounter radius. As the diffusion coefficient influences the statistics of the TR MFE decay curves, this parameter is varied (reported alongside each simulation) to allow optimum convergence to be obtained without the need to perform an exceedingly large number of realisations. In addition, a high concentration of scavengers (in comparison to experimental values which use 0.001–0.3 M) is purposely used to reduce the noise in the recombination fluorescence and allow better statistics to be obtained. This form of *importance sampling* allows more of reaction (7) to occur at both zero and high fields without affecting the chemical kinetics or spin-dynamics.

In the simulation, the scavengers were assumed stationary to help simplify the IRT model. For all geminate encounters an encounter radius of 10 Å was found acceptable to model the chemistry [27], although the size of this parameter is unimportant for low-permittivity solvents due to the strong Coulombic force. All the simulations have been done using  $1 \times 10^6$  realisations, which was found to provide acceptable statistics.

### 8.5.2 Recombination Kinetics and Spin Dynamics

The kinetics obtained using the IRT simulation were first directly compared with random flights simulations and essentially excellent agreement was obtained. The correlation that exists between the scavenging and recombination times (as discussed in Sect. 7.2.6) can therefore be neglected for this chemical system, so long as the radicals are: (1) separated at a distance greater than 20 Å and (2) they are rapidly scavenged before any appreciable drift can arise. Reactive products produced in the chemical system are treated using the *time approach* as described in Sect. 4.4.2.4 (within the IRT framework), which provided the most accurate description of the recombination kinetics in comparison with random flights simulations.

For the purpose of this work, the rates of longitudinal and transverse  $T_2$  relaxation were assumed the same at zero field, such that  $T'_0 = T_2$ , where  $T'_0$  is the zero field relaxation time. In order to reproduce experimental conditions, a  $T'_0$  value of 9 and 15 ns was used for cyclohexane and HFB respectively at zero field as determined by Molin and co-workers [15]. To simplify the model, no spin relaxation was allowed

to take place on either  $e^-$  or  $\text{Solv}^+$  as these species are rapidly scavenged and this occurs on a much faster timescale than other spin dynamic processes. Hence, in the model developed, zero field refers to calculations with  $T_0' = T_2$ , and high field refers to calculations with either (a)  $T_1$  and  $T_2$  set to  $T_{\text{max}}$ , such that no relaxation can take place; or (b)  $T_1$  and  $T_2$  take the experimental values extracted at 1 T field (detected by single photon counting technique using an X-ray fluorimeter).

The spatial configuration of the cations was assumed linear using a variable spacing. The anions were distributed from their respective cations with a standard deviation of 80 Å. This is a typical spatial distribution adopted in the literature for treating primary events in non-polar solvents [28].

### 8.5.3 Quantum Beats in the Singlet Probability

The quantum entanglement of spins and the collapse of the wavefunction on reaction can affect the singlet character of radical pairs through the ERP effect. As demonstrated in Sect. 8.3 a single cross-recombination collapses the spin-state for the remaining disjoint pair onto either a singlet or triplet state (assuming no other coherent and incoherent processes operate) due to the conservation of spin multiplicity. In a single realisation these disjoint pairs are correlated and subject to magnetic field effects. Over many realisations, the encounter of disjoint radical pairs occurs at random times, which in turn collapses the wavefunction randomly as well. This has the effect of (1) destroying any phase correlation of the remaining disjoint pair and (2) make the disjoint pair behave like F-pairs.

Unfortunately, explicitly treating all the hyperfine interactions is not possible due to the increasing dimensionality of the basis set. Instead within the semiclassical approximation [10, 11] an ‘effective’ hyperfine constant was calculated (Eq. 8.23) which allows the modelling of the chemical system to be tractable.

$$a_{\text{eff}} = \sqrt{\sum_i a_i^2 I_i (I_i + 1)} \quad (8.23)$$

In the above equation the summation runs over the identical number of magnetic nuclei with spin  $I_i$  and hyperfine coupling constant  $a_i$ . It can be seen from Fig. 8.5 (using the spin parameters [15, 29] as shown in Table 8.4), that the magnitude of the singlet oscillation is much larger for a single ion pair; as the number of pairs increases the magnitude of the quantum beats starts to decrease. This is because in the track structure generated by radiolysis, cross-recombination rapidly destroys the spin-correlation of the radical pairs and makes the surviving radical pairs exhibit the characteristics typical of an F-pair. Hence the claim the ERP mechanism acting as an extra source of relaxation seems justified.

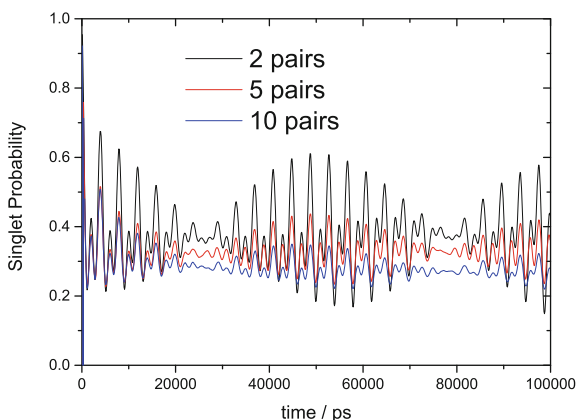


**Fig. 8.5** Singlet probability of the surviving radical pairs as a function of the number of pairs ( $e^- + \text{Solv}^+$ ) using an external field of 0.33 T. A mutual diffusion coefficient ( $D'$ ) of  $0.5 \text{ \AA}^2 \text{ ps}^{-1}$  was used for  $S_e^- / c\text{-RH}^+$ . Cations were arranged on a line  $20 \text{ \AA}$  apart, with anions Gaussian distributed from their respective cations with a standard deviation of  $80 \text{ \AA}$ . Hyperfine coupling constant was averaged using Eq. (8.23)

**Table 8.4** Spin parameters used for modelling the singlet probability [15, 29]

Species	<i>g</i> -factor	HFC (mT)
$S_e^-$	2.0014	13.4
$c\text{-RH}^+$	2.0069	4.3

Here,  $S_e^-$  is given the characteristic properties of HFB. It is assumed the unpaired electron in cyclohexane radical cation couples to the six equivalent equatorial protons with the six axial protons not interacting to any significant extent. Abbreviation used: HFC (hyperfine coupling constant)

## 8.5.4 TR MFE Decay Curves

### 8.5.4.1 No High Field Relaxation

Figure 8.6 shows the rate of relaxation calculated as a function of the number of particles in the spur. In this simulation, no spin-relaxation was assumed at high fields, and as such, any decay seen in the TR MFE decay curve should arise solely due cross-recombination. From the analysis of the data given in Table 8.5, it can be seen that for extremely dense spurs, spin relaxation ( $T_1$ ) can be as fast as 45 ns which suggests that this type of relaxation mechanism operates quite considerably for any chemical system which promotes cross-recombination. The noise present in the TR MFE curves at times greater than 30 ns arises because of a loss in radical pairs which exhibit magnetic field effects at high fields (i.e. most surviving radical pairs resemble the characteristics of an F-pair due to the cross-recombination mechanism).

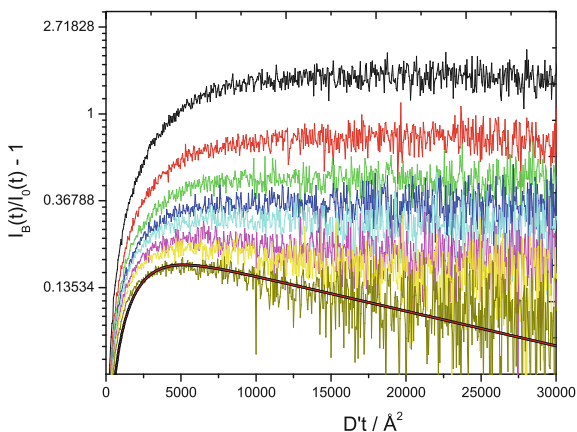


**Fig. 8.6** Semilogarithmic plot of the ratio of fluorescence intensity using: 2 pairs (*black*); 4 pairs (*red*); 6 pairs (*green*); 8 pairs (*blue*); 10 pairs (*cyan*); 15 pairs (*magenta*); 20 pairs (*yellow*) and 40 pairs (*dark yellow*) of  $[e^- + \text{Solv}^+]$ . A mutual diffusion coefficient ( $D'$ ) of  $0.5 \text{ \AA}^2 \text{ ps}^{-1}$  was used for  $S_e^- / c\text{-RH}^+$ . Cations were arranged on a line  $20 \text{ \AA}$  apart, with anions Gaussian distributed from their respective cations with a standard deviation of  $80 \text{ \AA}$ . Shortest  $T_1$  was calculated to be  $\sim 50 \text{ ns}$  (*dark yellow*). Smooth line corresponds to Eq. (8.3) with  $T_2 = 3 \text{ ns}$  and  $T_1 = 50 \text{ ns}$  ( $\theta = 0.22$ )

**Table 8.5** Spin relaxation time as a function of  $\zeta$  (fraction of pairs that recombine via cross-recombination) and  $\theta$  (fraction of original spin-correlated pairs that recombined)

No. of pairs	$\zeta$	$\theta$	Spin relaxation time (ns)
10	0.624	0.20	$234 \pm 55$
15	0.663	0.181	$140 \pm 15$
20	0.682	0.173	$107 \pm 12$
25	0.692	0.166	$85 \pm 10$
30	0.701	0.162	$63 \pm 7$
35	0.704	0.159	$57 \pm 6$
40	0.711	0.156	$45 \pm 4$

Zero field spin relaxation time ( $T'_0$ ) was set to  $9 \text{ ns}$ . Cations were arranged on a line  $20 \text{ \AA}$  apart, with anions Gaussian distributed from its respective cation with a standard deviation of  $80 \text{ \AA}$

#### 8.5.4.2 Phenomenological Treatment of High Field Relaxation

In this section the effect of: (i) treating spin relaxation phenomenologically and (ii) the spatial distribution of the cations is explored to analyse how the TR MFE curve changes. All high field simulations were done using a relaxation time of  $T_1 = 350$  and  $130 \text{ ns}$  and  $T_2 = 15$  and  $9 \text{ ns}$  for  $S_e^-$  and  $c\text{-RH}^+$  respectively. These parameters are the experimentally determined spin relaxation time for  $S_e^-$  and  $c\text{-RH}^+$  as shown in Table 8.2, apart from the  $T_1$  value for  $c\text{-RH}^+$ , which was calculated from Eq. (8.9). For all zero field simulations it was assumed  $T'_0 = T_2$ . In the TR MFE decay curves where *line* is indicated, the cations were distributed on a straight line  $20 \text{ \AA}$  apart and where *sphere* is indicated, the cations were distributed on a sphere of radius  $20 \text{ \AA}$ .

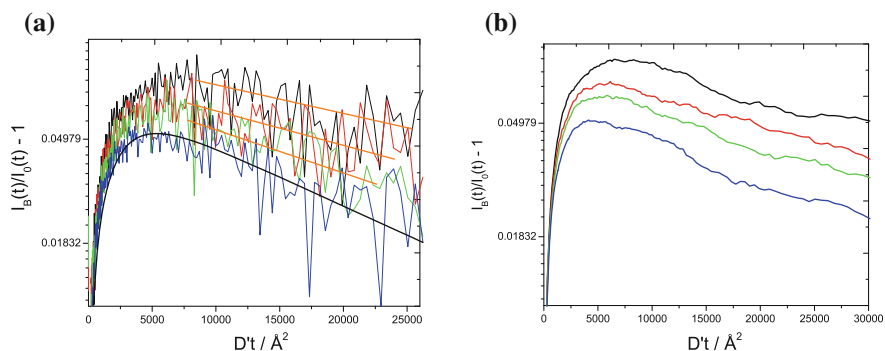


**Fig. 8.7** **a** Semilogarithmic plot of the ratio of fluorescence intensity obtained in the simulation and **b** adjacent average smoothing using: (1) 10 pairs (*black*); (2) 15 pairs with cations on a line (*red*); (3) 20 pairs (*green*); (4) 40 pairs (*blue*). In all cases the cations were distributed on a line 20 Å apart. A mutual diffusion coefficient ( $D'$ ) of  $0.5 \text{ \AA}^2 \text{ ps}^{-1}$  was used for  $S_e^- / c\text{-RH}^+$ . *Solid black line* fitted to (4) corresponds to Eq. (8.3) with  $T_2 = 4.5 \text{ ns}$  and  $T_1 = 36 \text{ ns}$

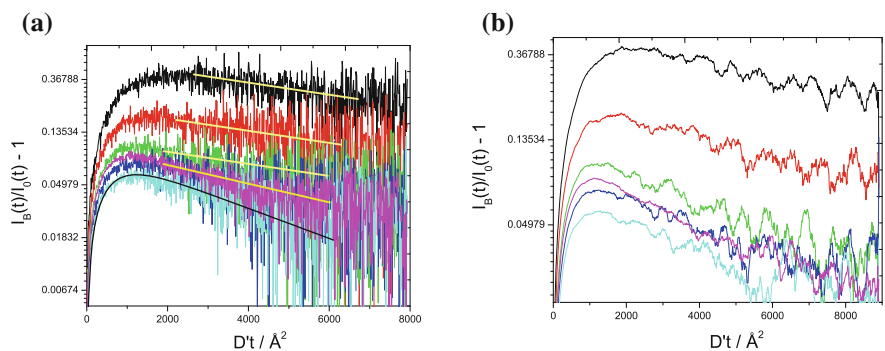


**Fig. 8.8** **a** Semilogarithmic plot of the ratio of fluorescence intensity obtained in the simulation and **b** adjacent average smoothing using: (1) 2 pairs with cations on a line (*black*); (2) 5 pairs with cations on a line (*red*); (3) 20 pairs with cations on a line (*green*); (4) 20 pairs with half the cations on a line and half distributed on a sphere (*blue*); (5) 40 pairs with half cations on a line and half distributed on a sphere (*cyan*); (6) 50 pairs with cations on a line (*magenta*). A mutual diffusion coefficient ( $D'$ ) of  $0.1 \text{ \AA}^2 \text{ ps}^{-1}$  was used for  $S_e^- / c\text{-RH}^+$ . *Solid black line* fitted to (5) corresponds to Eq. (8.3) with  $T_2 = 5 \text{ ns}$  and  $T_1 = 36 \text{ ns}$

In all cases, the anion was normally distributed from its respective cation with mean zero and standard deviation of 80 Å.

Analysing Figs. 8.7 and 8.8 together with the values in Tables 8.6 and 8.7, it is seen that the rate of relaxation increases as the spur becomes increasingly dense. For example, simulating half the cations on a line and half on a sphere (which promotes more cross-recombination), the relaxation time can be as short as 46 ns. This is three times smaller than the initial  $T_1$  parameter of 130 ns, and can only arise as a result of cross-recombination. The effect of cross-recombination can also be readily seen

**Table 8.6** Calculated spin relaxation times using the data from the simulation and that obtained using adjacent average smoothing (AAS)

No. of pairs	$T_1$ (ns) (simulated data)	$T_1$ (ns) (AAS)
10	$75 \pm 19$	$74 \pm 2$
15	$60 \pm 16$	$68 \pm 2$
20	$70 \pm 20$	$66 \pm 2$
40	$45 \pm 12$	$34 \pm 2$

The spatial configuration of the cation and anion is detailed in Fig. 8.7

**Table 8.7** Calculated spin relaxation times using the data from the simulation and that obtained using adjacent average smoothing (AAS)

No. of pairs	$T_1$ (ns) (simulated data)	$T_1$ (ns) (AAS)
2	$135 \pm 19$	$102 \pm 4$
5	$70 \pm 16$	$86 \pm 4$
20	$50 \pm 7$	$55 \pm 3$
40	$43 \pm 6$	$38 \pm 3$
50	$40 \pm 3$	$36 \pm 2$

The spatial configuration of the cation and anion is detailed in Fig. 8.8

from Fig. 8.8 by comparing the decay in the TR MFE curves using 2 pairs and 50 pairs of ( $e^- + \text{Solv}^+$ ). When only 2 pairs are used, the relaxation rate is slower because there is no possibility of undergoing multiple cross-recombinations. This has the effect of mildly reducing the spin relaxation time from 130 to 102 ns. In a separate simulation, the effect of the Lorentz force on the track structure was also investigated which would promote more cross-recombination at high-fields. It was found that within the parameter space investigated, this effect was deemed negligible and did not contribute to the overall spin-relaxation mechanism.

### 8.5.5 Explicit Treatment of the Hyperfine Coupling

In this section, the TR MFE curves obtained using an explicit treatment of the hyperfine coupling constants for  $S_e^-$  and c-RH<sup>+</sup> [as given in Table 8.4 and averaged using Eq. (8.23)] are presented. The  $g$ -factors were kept the same for all radicals and were given a value of 2.002. The purpose of these simulations was to analyse how coherent spin evolution together with incoherent effects contribute to the observed spin relaxation time. For zero field calculations it was again assumed  $T'_0 = T_2$ . All high field calculations made use of a static external field of 1 T to model experimental conditions. For all simulations presented, a  $T_1 = 350$  and 130 ns and  $T_2 = 15$  and 9 ns were used for  $S_e^-$  and c-RH<sup>+</sup> respectively.

From Figure 8.9 together with the tabulated values in Table 8.8, it can be seen that the contribution of the hyperfine coupling makes no significant contribution to the overall relaxation mechanism, since the experimentally determined value for the paramagnetic relaxation time of 9 ns cannot be obtained. The results do however,

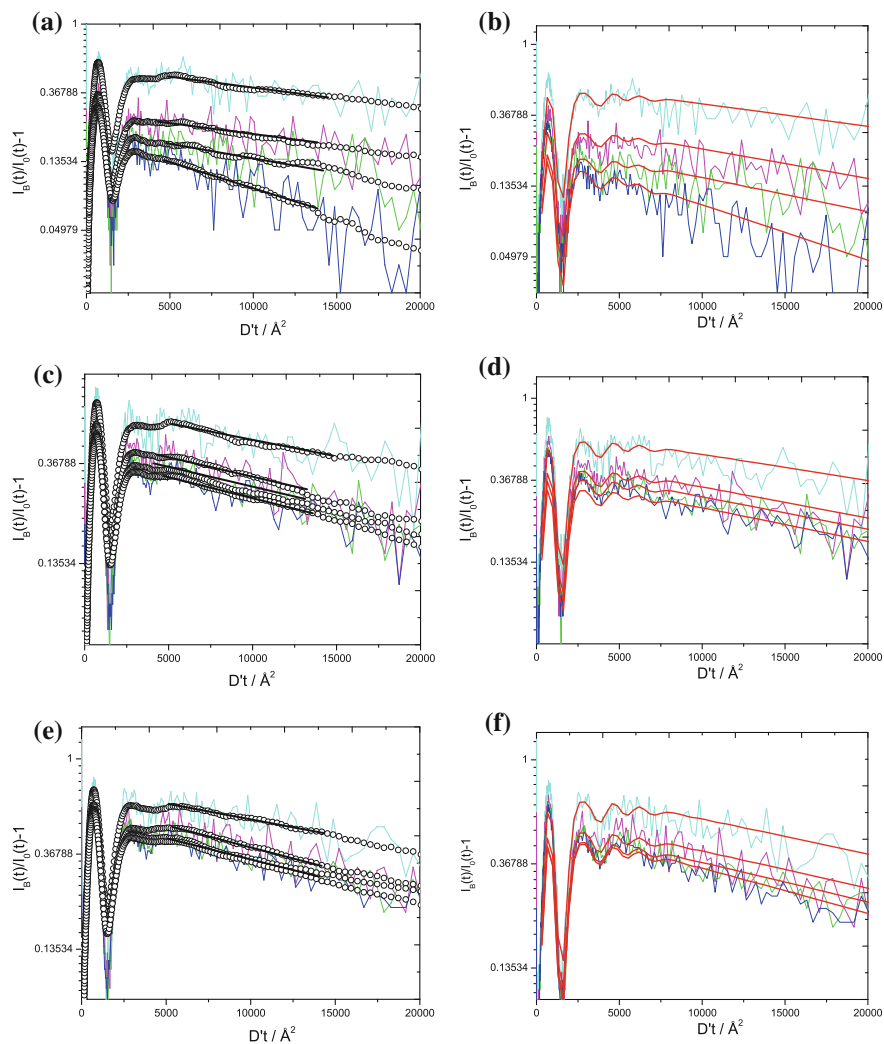


**Fig. 8.9** Semilogarithmic plot of the ratio of fluorescence intensity obtained in the simulation (*line*) and adjacent average smoothing (*circle*) using: 2 pairs (*cyan*); 5 pairs (*magenta*); 10 pairs (*green*) and 15 pairs (*blue*). Cations were linearly distributed with a mean spacing of **a** 40 Å **c** 100 Å and **e** 150 Å. In **b**, **d** and **f** the *solid red line* is the analytically calculated magnetic field effect using the  $T_1$  values in Table 8.8, with  $T_2 \sim 5$  ns. Anions were distributed using a Gaussian distribution with mean zero and standard deviation of 80 Å. A mutual diffusion coefficient ( $D'$ ) of  $0.325 \text{ \AA}^2 \text{ ps}^{-1}$  was used for  $S_e^- / c\text{-RH}^+$

show quite clearly two important factors arising from the cross-recombination mechanism: (1) the spacing between cations affects the magnitude of the TR MFE decay curves. For cations which are more closely distributed, there is a greater probability

**Table 8.8** Calculated spin relaxation times obtained using adjacent average smoothing (AAS) for the linear configuration of the cations with a mean spacing: <sup>a</sup>40 Å, <sup>b</sup>100 Å and <sup>c</sup>150 Å

No. of pairs	$T_1$ (ns) (AAS)
2	95 <sup>a</sup> , 95 <sup>b</sup> , 95 <sup>c</sup>
5	73 <sup>a</sup> , 84 <sup>b</sup> , 90 <sup>c</sup>
10	63 <sup>a</sup> , 77 <sup>b</sup> , 86 <sup>c</sup>
15	41 <sup>a</sup> , 74 <sup>b</sup> , 78 <sup>c</sup>

The spatial configuration of the cations and anions is detailed in Fig. 8.9. Standard error in the gradient was found to be  $\pm 3$  ns

of cross-recombination to occur and hence the cross-recombination mechanism acts as an extra source of relaxation; (2) the magnitude of the cross-recombination relaxation mechanism depends on the number of pairs and how many of these recombine in an uncorrelated manner.

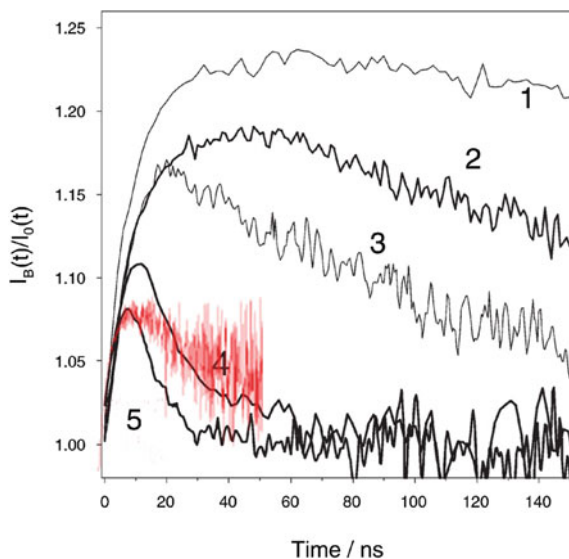
### 8.5.6 Discussion

From the experimentally observed TR MFE decay curves for c-RH<sup>+</sup> [15] as shown in Fig. 8.10, it can be seen that using the shortest possible  $T_1$  value from Redfield theory (Eq. 8.9) for c-RH<sup>+</sup> together with remaining  $T_1$  and  $T_2$  values for S<sub>e</sub><sup>-</sup> and c-RH<sup>+</sup> (Table 8.2), the magnitude of the magnetic field effect together with the decay can be reasonably approximated using 50 ion pairs distributed along a line. Although the experimentally observed TR MFE decay curve is much faster than what has been obtained by simulation, it is important to remember that in these highly symmetrical cations, the Jahn-Teller distortion together with strong spin-orbit coupling is also thought to contribute significantly to the overall spin-lattice relaxation time. Hence, it is not expected for the simulation to exactly reproduce the decay experimentally seen in the TR MFE curve, since the model does not take this relaxation mechanism into consideration. The exact nature of the relaxation mechanism causing the fast relaxation in cyclic alkanes still remains unknown, however from the results it is seen that cross-recombination relaxation plays a considerable role for highly dense spurs, and could considerably contribute to the overall spin relaxation mechanism in these cyclic systems as well.

#### 8.5.6.1 Hypothesis for Radiolytic and Photolytic Radical Pairs

The results of this section have highlighted that because cross-recombination contributes to the overall spin-lattice relaxation rate, this should lead to a difference in the spin relaxation times (and other observables such as the recombination yield) for a photolytic and radiolytic chemical system.

**Fig. 8.10** Experimental TR MFE curves [15] obtained for *n*-hexane solution of:  $10^{-3}$  M *p*-TP-d<sub>14</sub> (curve 1); 0.01 M C<sub>6</sub>F<sub>6</sub> +  $10^{-3}$  *p*-TP-d<sub>14</sub> (curve 2); 0.01 M C<sub>6</sub>F<sub>6</sub> + 0.1 M *cis*-decalin (curve 3); 0.01 M C<sub>6</sub>F<sub>6</sub> + 0.1 M *trans*-decalin (curve 4); 0.01 M C<sub>6</sub>F<sub>6</sub> + 0.1 M cyclohexane (curve 5). Red solid line represents the simulated TR MFE curve (this work) using 50 ion pairs, with cations distributed along a line



## 8.6 Radiolysis of *n*-Dodecane Containing a Solution of Tetramethyl-*p*-Phenylenediamine

The second reaction scheme investigated (shown in Tables 8.10 and 8.11) as part of this work is much more exhaustive and takes into account the excited state and neutral radical chemistry, which can both influence the fluorescence rate. The model includes radical cations of the solvent ( $S^+$ ) and of the electron donor ( $D^+$ ), electrons ( $e^-$ ) and excited states of the solvent ( $^{1,3}S^*$ ) and the solute ( $^{1,3}D^*$ ). The diffusion coefficient of all the species involved in the reaction scheme are shown in Table 8.9. These parameters are typical for the well studied chemical system tetramethyl-*p*-phenylenediamine solutions in *n*-dodecane [30–33].

### 8.6.1 Spur Structure

The modelling of this chemical system by Borovkov demonstrated that a track produced by 20-keV X-ray quanta in *n*-dodecane in the studied time range could be described by a set of isolated spherical spurs containing 4–5 ion pairs (under the premise that 4–5 ion pairs were produced per 100 eV) [34, 35]. The radius of such ‘effective’ spurs were found to be about 50 Å for four pairs or 90–100 Å for five pairs [34, 35]. For the purpose of this work two different spatial distributions of the spur were adopted: (i) a spherical spur of radius 50 Å with the cations randomly placed within the sphere, and the electrons distributed around their respective cations

**Table 8.9** Diffusion coefficient  $D$ , mobility ( $\mu_m$ ) and radius ( $R$ ) of particles used to model the reactions (1)–(25) [35, 36] in Tables 8.10 and 8.11

Particle	$D, \text{\AA}^2 \text{ ps}^{-1}$	$\mu_m, \text{\AA}^2 \text{ V}^{-1} \text{ ps}^{-1}$	$R, \text{\AA}$
$\text{S}^+$	0.05	2	5
$\text{e}^-$	2.5	10	5
$\text{D}^+$	0.05	2	5
$^1,^3\text{S}^*$	0.1	–	5
$^1,^3\text{D}^*$	0.1	–	5
$\text{R}^{\cdot}$	0.05	–	5
$\text{D}$	0.01	–	5

according to the probability distribution function  $f(r) = \exp(-r/b)$ , with  $b = 60 \text{ \AA}$ . This spatial distribution of the cations comes from the analysis as done by Borovkov [34, 35], who also found that changing the electron thermalisation distance by 20–30 % did not significantly affect the TR MFE curves; (ii) a linear spur with cations placed along a line (with a mean separation of 20 and 60  $\text{\AA}$ ) and the electrons placed around their respective geminate cation using a Gaussian distribution, with mean ( $\mu$ ) zero and standard deviation ( $\sigma$ ) of 80  $\text{\AA}$  [28].

## 8.6.2 Reaction Scheme

As in the previous reaction scheme, reactions with a neutral TMPD molecule (D) were described as a quasi-monomolecular reaction with a rate constant  $k$  using a predefined concentration of D. An electron scavenger is not included in this reaction scheme because of the extra complexity it introduces. If a scintillator solute, scavenging of radicals and both negative and positive charges are included, then 108 possible reactions in the scheme are possible [37]; a task quite difficult to model even within the IRT framework. If only reaction and diffusion are incorporated, then modelling such a large reaction scheme is not an issue using the random flights simulations. However because of the necessity to explicitly treat spin dynamics together with the requirement of using small time steps, the random flights simulation method is not practical to use for this chemical system.

For the purpose of this work, only scavenging of the cation is considered. In addition no attempt to treat hyperfine interaction or  $\Delta g$  mechanisms explicitly is made. Instead a phenomenological approach is used, which indirectly takes into account all possible relaxation mechanisms by using the experimentally determined rate of relaxation.

In Table 8.10, reaction (1) describes the solvent ionisation event, producing  $\text{S}^+ / \text{e}^-$  pairs, whose spin multiplicity is determined by the geminate pair wavefunction. The intensity of delayed fluorescence of the solution is determined by the rate of radiative deactivation of  $^1\text{D}^*$  (reaction 10). For this reaction scheme,  $^1\text{D}^*$  states are produced via reaction (4) (recombination of  $\text{D}^+ / \text{e}^-$  pairs [32, 37, 38]), from  $^1\text{S}^*$  to luminophore molecules as given in reaction (6) and via triplet-triplet annihilation of

**Table 8.10** Reactions of reactive particles involved in the model and the rate constants  $k$  or the reaction probabilities upon contact  $P_c$  [36] (with dimensionless units)

No.	Reaction	$k$ or $P_c$
1	$S \longrightarrow S^{+\cdot} + e^{-}$	–
2	$S^{+\cdot} + e^{-} \longrightarrow {}^1,3S^*$	1
3	$S^{+\cdot} + (D, {}^1,3D^*) \longrightarrow S + D^{+\cdot}$	$1 \times 10^{10} \text{ M}^{-1} \text{ s}^{-1}$ (D), 1/3 ( ${}^3D^*$ ), 1 ( ${}^1D^*$ )
4	$D^{+\cdot} + e^{-} \longrightarrow {}^1,3D^*$	1
5	${}^1S^* \longrightarrow {}^3S^*$	$2.5 \times 10^8 \text{ s}^{-1}$
6	${}^1S^* + D \longrightarrow S + {}^1D^*$	1
7	${}^1D^* \longrightarrow {}^3D^*$	$1.8 \times 10^8 \text{ s}^{-1}$
8	${}^3D^* + {}^3D^* \longrightarrow D + {}^1D^*$	1/9
9	${}^3D^* + {}^3D^* \longrightarrow D + {}^3D^*$	1/3
10	${}^1D^* \longrightarrow D + h\nu$	$2 \times 10^7 \text{ s}^{-1}$
11	${}^1D^* + {}^3D^* \longrightarrow {}^3D^* + {}^3D^*$	1/3
12	${}^1D^* + {}^1D^* \longrightarrow {}^3D^* + {}^3D^*$	1/9
13	${}^1S^* + {}^3D^* \longrightarrow {}^3S^* + {}^3D^*$	1/3
14	${}^1S^* + {}^1S^* \longrightarrow {}^3S^* + {}^3S^*$	1/9
15	$(S^{+\cdot}, e^{-})\uparrow + {}^1S^* \longrightarrow (S^{+\cdot}, e^{-})\downarrow + {}^3S^*$	1/3
16	$(D^{+\cdot}, e^{-})\uparrow + {}^1D^* \longrightarrow (D^{+\cdot}, e^{-})\downarrow + {}^3D^*$	1/3
17	$(D^{+\cdot}, e^{-})\uparrow + {}^3D^* \longrightarrow (D^{+\cdot}, e^{-})\downarrow + {}^3D^*$	2/3

**Table 8.11** Reactions of reactive particles involved in the model together with their respective reaction probabilities upon contact  $P_c$  [35] (with dimensionless units)

No.	Reaction	$P_c$
18	${}^3S^* \longrightarrow R^{\cdot}\uparrow + R^{\cdot}\uparrow$	Instantaneous
19	$R^{\cdot} + R^{\cdot} \longrightarrow \text{Products}$	1/4
20	$S^{+\cdot}\uparrow + R^{\cdot}\downarrow \longrightarrow S + R^+$	1/4
21	$e^{-}\uparrow + R^{\cdot}\downarrow \longrightarrow R^{-}$	1/4
22	$D^{+\cdot}\uparrow + R^{\cdot}\downarrow \longrightarrow D^{+\cdot}\downarrow + R^{\cdot}\uparrow$	1/2
23	$R^{\cdot}\uparrow + ({}^1D^*, {}^1S^*) \longrightarrow R^{\cdot}\downarrow + ({}^3D^*, {}^3S^*)$	2/3
24	$R^+ + e^{-} \longrightarrow R^{\cdot}$	1
25	$(S^{+\cdot}, D^{+\cdot}) + R^{-} \longrightarrow (S, D) + R^{\cdot}$	1

The value of  $P_c$  is calculated assuming the encountering pair is an F-Pair

${}^3D^*$  [reaction (8)]. It is known that  ${}^3S^*$  dissociates rapidly to give neutral species [39, 40] according to the reaction scheme shown in Table 8.11. Although these reactions are taken into account in the simulation model, it was found by Borovkov [36] that such decomposition has no effect on the mobility of charge carriers and does not change significantly the rate of TMPD radical cation formation.

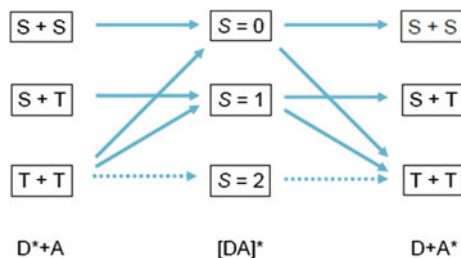


**Fig. 8.11** Wigner spin conservation rules used to calculate the probability of all contact interactions

### 8.6.3 Spin Exchange Reactions

All contact reactions involving spin species occur with a probability determined by the necessity for the conservation of spin multiplicity, [37, 38]. For example, reaction (8) which shows a triplet-triplet annihilation occurs with a probability of  $1/9$ , whilst the recombination of all ionic species in reactions (2), (4) and (6) occurs with a probability of unity. These rules (known as *Wigner's spin conservation rules*) are shown more formally in Fig. 8.11. For reactions involving spin-exchange [i.e. reactions (15), (16) and (17)] Wigner's sign rule for a doublet + singlet or doublet + triplet are used to calculate the probability of reaction.

In the simulation, following an encounter a uniformly distributed random number  $U(0, 1]$  is generated and compared with the probability of reaction. If  $U(0, 1] < P_c$  then reaction is assumed to take place, otherwise the particles are reflected according to the algorithm as outlined in Sect. 4.4.2.3. In the model, following an initial unsuccessful encounter between neutral species, allowance is made for subsequent reactions to take place, irrespective of the elapsed time. To simplify the model and to allow the reaction scheme to be modelled in the IRT framework, dipole-dipole interactions were not included.

The arrows in reactions (15)–(17) are used to illustrate that upon the change in the multiplicity of the excited molecules, the spin wavefunction for the radical ion that interacted with the neutral species also changed [36]. Unlike Borokov's analysis [36], it is not assumed in the model that the spin correlated radical pair completely loses its spin correlation upon reaction. Instead for reactions (15), (16) and (17) the wavefunction belonging to the ion-pair is multiplied by the appropriate wavefunction of the excited species (i.e. the collapsed  $\psi$  of the ion-pair forming the excited neutral species). For example, in reaction (15) the total wavefunction for the  $(S^{+}, e^{-})\uparrow + {}^1S^*$  is

$$\psi_{\text{tot}} = \psi_{\text{ion}} \times \psi_S \quad (8.24)$$

where the wavefunction  $\psi_S$  for  ${}^1S^*$  is constructed when the singlet encounter  $S^{+} + e^{-}$  took place via reaction (2). If a reaction between  $e^{-}$  and  ${}^1S^*$  occurs, the spins on the  $e^{-}$  and  ${}^1S^*$  are flipped (i.e.  $\alpha \leftrightarrow \beta$ ) in the wavefunction  $\psi_{\text{tot}}$ . Next  $\psi_{\text{tot}}$  is collapsed to form  ${}^3S^*$  and a random number  $U(0, 1]$  is generated to decide in which

triplet substate the  $^3S^*$  is formed in. Then using the decomposition method, the basis for  $\psi_{ion}$  and  $\psi_S$  are repopulated by finding all the coefficients in which  $^3S^*$  is a triplet. Upon reaction, the particles are reflected as they are no longer in the correct spin state to react. However, subsequent re-encounters are allowed to take place due to the incoherent spin-evolution via the spin relaxation mechanism. A similar strategy is also used for reaction (22) (in Table 8.11), with the spins on  $D^{+\cdot}$  and  $R\cdot$  both exchanged if a uniformly distributed random number  $U(0, 1] > 1/2$ . If the encounter is through a cross-recombination, then the  $D^{+\cdot} / R\cdot$  pair and their disjoint partners subsequently become spin correlated. This technique attempts to follow the spin correlations properly as the spur evolves.

To help simplify the model, all spin evolution on the excited species is neglected. Instead the probability of reaction involving all excited species is determined by a predefined parameter, which takes into account that only a certain fraction of encountering pair will have the correct spin multiplicity to react.

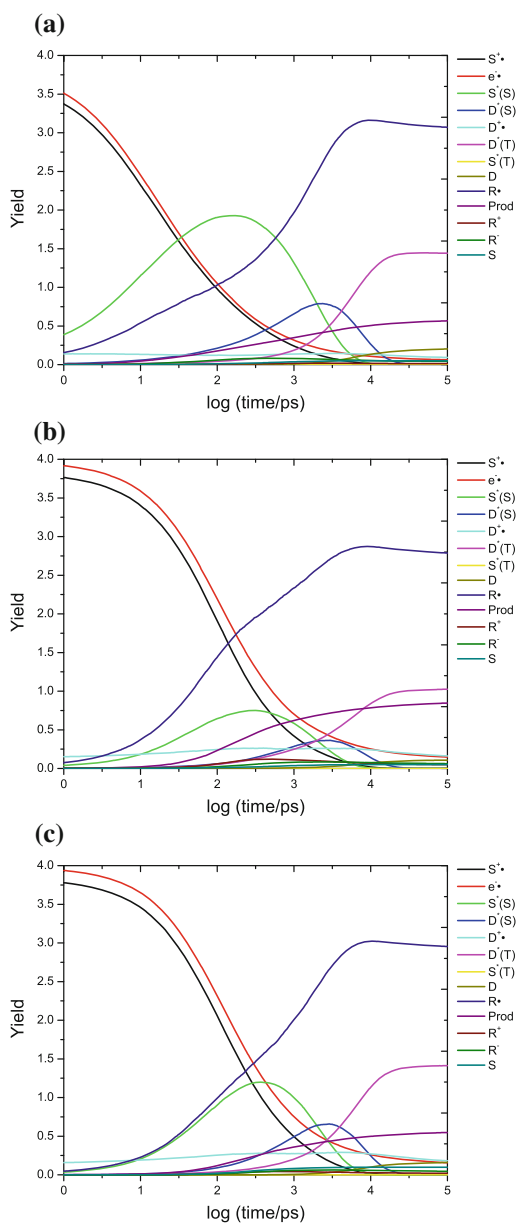
### 8.6.4 Kinetics

Figure 8.12 shows the yields of all the species in the spur with  $[D] = 0.02$  M, using a spherical and linear distribution for the solvent cations. When the solvent cations are placed on a line (20 Å apart) the following differences are seen in comparison to a spherical distribution of the cations<sup>7</sup>:

1. There is a greater cross-recombination probability in the linear spur structure. This in turn leads to less correlated ( $S^{+\cdot} / e^-$ ) recombining in the singlet state which in turn produces less intersystem crossing from  $^1S^* \rightarrow ^3S^*$  yield.
2. Due to cross-recombination of the ( $S^{+\cdot} / e^-$ ) pair, the rate of reaction (6) is greatly reduced for a linear spur, producing less  $^1D^*$ , which in turn leads to less fluorescence. In addition, because of more cross-recombination of the ( $D^{+\cdot} / e^-$ ) pair in the linear structure there is less  $^1D^*$  produced via reaction (4), which in turn has the effect of further depleting the recombination fluorescence via reaction (10).
3. Reactions (8) and (9) have a higher frequency in the spherical structure, because there is less probability of escape unlike the linear structure. Hence more D is formed in the spherical structure.
4. There is more escape of the  $D^{+\cdot}$  in the linear structure, which leads to a greater survival probability of the  $e^-$  at longer times. The loss of the  $D^{+\cdot}$  ion further depletes reactions and yields involving the excited state chemistry of  $^1D^*$  and  $^3D^*$ .
5. The yield of neutral products [reaction (19)] is slightly higher in the linear structure because of the higher rate of cross recombination involving the ( $S^{+\cdot} / e^-$ ) pair.

<sup>7</sup> It is important to note that the IRT algorithm does overestimate cross-recombination when the spur structure is in a linear arrangement.

**Fig. 8.12** Yields of all species using  $[D] = 0.02$  M. 4 pairs of  $S^{+} / e^{-}$  were simulated using the configuration **a** placed inside a sphere radius of 50 Å; **b** cations distributed along a line with a spacing of 20 Å; **c** cations distributed along a line with a spacing of 60 Å. (S) and (T) signify the singlet and triplet respectively



This in turn produces more neutral  $R^{\cdot}$  which recombine via reaction (19) to give neutral products.

On increasing the spacing between the cations it is found that more  $(S^{+} / e^{-})$  and  $(D^{+} / e^{-})$  pair geminately recombine to give a slightly higher recombination

fluorescence. From the results it seems that the linear structure is more susceptible to cross-recombination using four ion pairs due to the complex trajectories followed by the ions. For example, as the  $e^-$  approaches its geminate cation, strong Coulombic interaction of a nearby cation can modify the trajectory of the  $e^-$  which can result in cross recombination. In the spherical case this will not happen because the cations are sparsely separated and the trajectory of the  $e^-$  is rarely modified by other nearby Coulombic interactions. A brief discussion of this effect is discussed in Sect. 8.7.

It is seen from the kinetics (Figs. 8.13–8.16) that the main channel of formation of  $^1D^*$  in both configurations is via the ionic recombination [reaction (4)]. At this chosen parameter range, triplet-triplet annihilation does not contribute significantly to the decay of the magnetic field effect except at long times ( $>80$  ns); however, upon increasing either  $[D]$  or the number of pairs inside the spur, reaction (8) becomes more important at much smaller times. In this case, the decay of the TR MFE curves will be controlled by the rate of triplet-triplet annihilation and will have the effect of destroying any magnetic field effect generated by the ion-pair recombination via reaction (4) as shown in Fig. 8.17. It was found by Borovkov [34, 35] that the formation of neutral radicals in a spur via the decay of triplet excited solvent molecules does not affect significantly the time-resolved magnetic field effect curve in the parameter space considered. However, for completeness these reactions will be taken into consideration when calculating the TR MFE curve in Sect. 8.6.5.

It was found that contact interactions of the intermediates [reactions (11)–(17)] (i) acted as an extra source of spin relaxation for spin-correlated  $D^{+\cdot} / e^-$  pairs and (ii) decreased the frequency of annihilation for  $^3D^*$ . The former is due to spin exchange in reactions (3) and (15)–(17), as these reactions have the effect of incoherently changing the spin states of the correlated pairs; the latter is due to the enhancement of the singlet-triplet intersystem crossing of  $^1S^*$  in reactions (13)–(15), which depletes  $^1S^*$  and the frequency of reaction (6). Hence this results in a subsequent decrease in the yields of  $^1D^*$  and  $^3D^*$  as well. This analysis was also found to be true by Borovkov [36]. It can also be seen from Fig. 8.13 that the contribution of the annihilation of triplet solutes to the recombination fluorescence intensity becomes comparable with reaction (4) at  $\sim 30$  ns time range at the luminophor concentration of about 20 mM.

From Fig. 8.13, it is seen that at the model parameters chosen, the recombination fluorescence intensity at times to about 40 ns resembles an exponential process, which was also reported by Borovkov [34, 35]. This recombination fluorescence is created mostly via energy transfer from  $^1S^*$  [reaction (6)] at very short times. Although the lifetimes of both  $^1S^*$  and  $^1D^*$  is relatively short, this effect manifests itself because of the high rate of reaction of (6), which dominates for times of up to 20 ns (as seen in Fig. 8.13). The recombination of  $D^{+\cdot} + e^-$  pairs contributes to a minor extent.

### 8.6.5 Time-Resolved Magnetic Field Effect

In order to calculate the time-resolved magnetic field effect, the simulation commenced by placing the cations and anions according to a particular distribution.

**Fig. 8.13** Rate of reaction leading to the formation of  $^1D^*$  and its depletion. *Solid line* and *circle* represents the cations distributed on a line (mean spacing of 20 Å) and within a sphere of radius 50 Å respectively

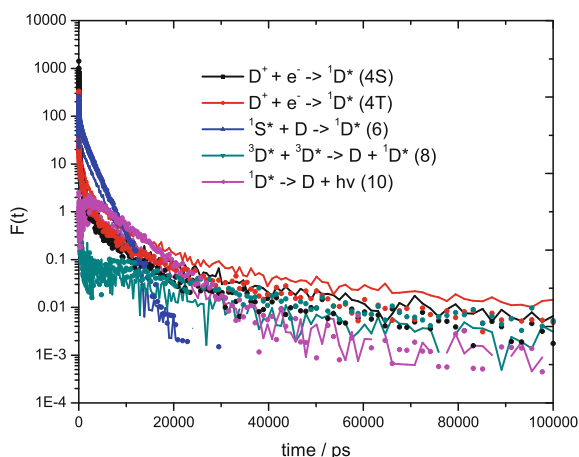
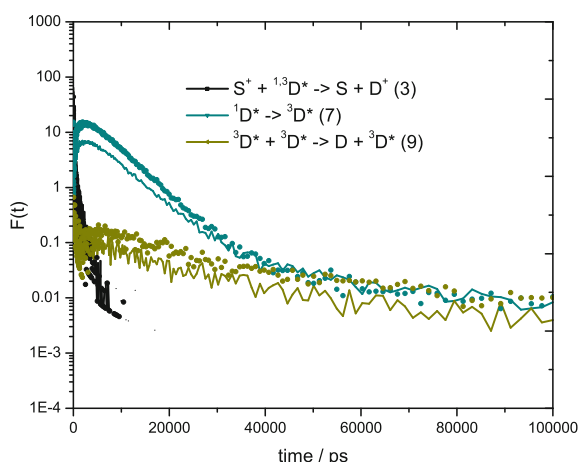


**Fig. 8.14** Rate of reaction for the excited state species. *Solid line* and *circle* represents the cations distributed on a line (mean spacing of 20 Å) and within a sphere of radius 50 Å respectively



Reactions which have occurred at ‘zero time’ are replaced by their reactive products (if applicable). For all surviving species reaction times are generated from a model distribution conditioned on the radical pair separation distance. The fluorescence intensity  $I(t)$  (which is the experimentally observable quantity) is detected as  $^1D^* \rightarrow D$  [reaction (10)] and  $^1D^* \rightarrow ^3D^*$  [reaction (7)] to allow better statistics to be obtained. The simulation is therefore run twice, one with zero field parameters and one using high field parameters; the ratio of  $I_B(t)/I_0(t)$  is then obtained to observe the magnetic field effect. In the simulation, no  $T_1$  or  $T_2$  relaxation mechanism was assumed to take place at high fields (unless otherwise stated). For zero field calculations  $T'_0$  was assumed to be equal to  $T_2$  with the spin-spin relaxation time set to a value of 30 and 9 ns for  $S^{+\cdot}$  and  $D^{+\cdot}$  respectively. These values are based on the analysis by Borovkov on the rate of electron self-exchange [34, 41, 42] for  $S^{+\cdot}$  and  $D^{+\cdot}$ , with

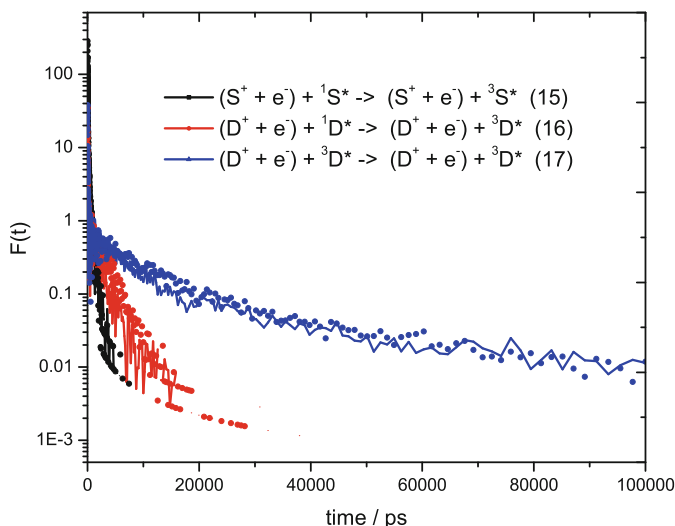


**Fig. 8.15** Rate of reaction for the spin exchange involving a geminate pair and an excited species. *Solid line* and *circle* represents the cations distributed on a line (mean spacing of 20 Å) and within a sphere of radius 50 Å respectively

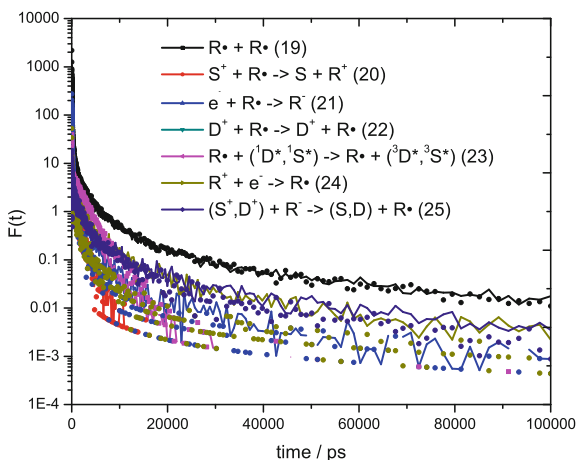


**Fig. 8.16** Rate of reaction involving the  $R^\bullet$  species. *Solid line* and *circle* represents the cations distributed on a line (mean spacing of 20 Å) and within a sphere of radius 50 Å respectively

the  $T_2$  value found to be dependent on the TMPD concentration. The mechanism for the electron exchange for both primary and secondary cations can be described as that given in Table 8.12 where the transfer of the electron causes the spin state of the magnetic nucleus coupled to the unpaired electron via the hyperfine interaction to randomly change.

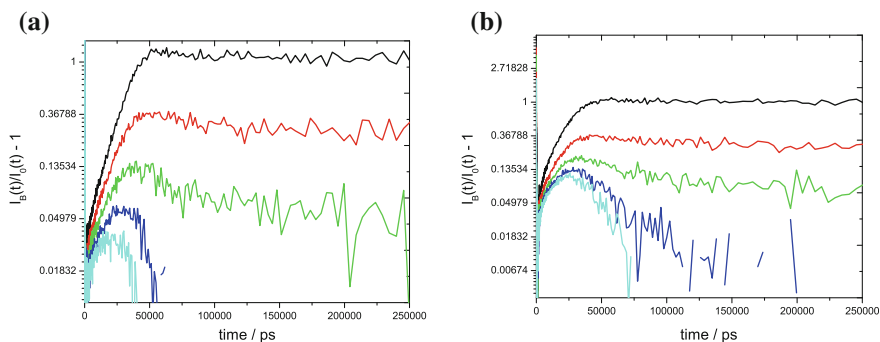


**Fig. 8.17** Semilogarithmic plot for the ratio of the fluorescence intensity using: 2 pairs (*black*); 4 pairs (*red*); 6 pairs (*green*); 8 pairs (*blue*) and 10 pairs (*cyan*). Reactions (18)–(25) were not taken into consideration. **a** Cations were placed inside a sphere of radius 50 Å and **b** cations were placed along a line with a mean spacing of 20 Å. Shortest  $T_1$  was calculated to be  $\sim 20 \pm 5$  ns (*cyan*) for both cases

**Table 8.12** Reaction of reactive particles involved in the model with their respective reaction probabilities upon contact  $P_c$  [34]

No.	Reaction
26	$S^{+\cdot} + S' \rightarrow S + (S')^{+\cdot}$
27	$D^{+\cdot} + D' \rightarrow D + (D')^{+\cdot}$

The value of  $P_c$  is calculated assuming the encountering pair is an F-Pair

In the first simulation (Fig. 8.18a), the effects of spin-exchange reactions (15), (16) and (17) were taken into consideration indirectly by using the experimentally determined  $T_1$  and  $T_2$  values. The purpose of this simulation was to isolate the effect of cross-recombination without complicating the decay of the TR MFE curve by other random processes which can cause relaxation as well.

The second simulation (Fig. 8.18b) treated spin-exchange reactions (15), (16) and (17) as well as cross-recombination, but did not assume any high field spin-lattice relaxation rate (i.e.  $T_1 = \infty$ ). The purpose of this simulation was to isolate the effect of cross-recombination and spin-exchange reactions on the overall spin relaxation rate. In both simulations, in order to simplify the computation model and make the solution tractable, no  $\Delta g$  mechanism or hyperfine interaction was taken into account. It is found by the experimentalists that direct manifestation of the hyperfine interactions in  $\text{TMPD}^{+\cdot}$  is unobservable due to (i) the delay in the formation of  $\text{TMPD}^{+\cdot}$ , (ii) the self-exchange reaction [reaction (27)] and (iii) the long fluorescence lifetime [34, 35].

From the analysis of the TR MFE curves,<sup>8</sup> a number of distinctive conclusions can be made. First of all, when a high field relaxation rate is phenomenologically treated using a value of  $T_1 = 220$  ns, the decay in the TR MFE curve is not accelerated by

<sup>8</sup> Experimental and simulated TR MFE curve shown were extracted from reference [34].

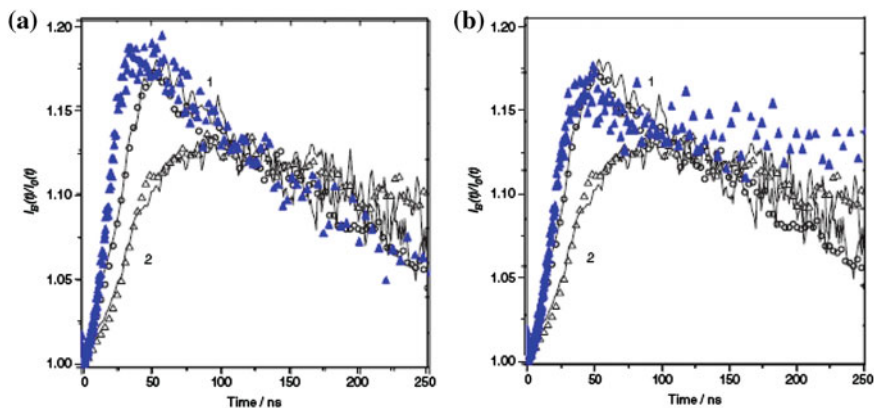


**Fig. 8.18** TR MFE curves obtained using 4 pairs of  $S^{+}/e^{-}$ , with cations distributed inside a sphere of radius of 50 Å.  $[D] = 0.02$  M. Blue triangle, circular symbol and solid line represents the TR MFE curves calculated in this work, by Borovkov and experiment respectively. Second curve with a lower magnetic field effect corresponds to  $[D] = 1$  mM. **a** Spin relaxation treated phenomenologically at high field without allowance for reactions (15), (16) and (17). **b** No paramagnetic spin relaxation was assumed at high field but included reactions (15), (16) and (17)

cross-recombination (or alternatively cross-recombination does not manifest itself in this parameter range). The finding that  $\theta = 0.32$  for secondary ion pairs agrees well with the results of Borovkov [34, 35]. For the cross-recombination relaxation mechanism to contribute, it was shown in the radiolysis of *n*-hexane that a significant proportion of the ion-pairs must recombine in an uncorrelated manner and that there must be a large number of ion-pairs formed within the spur. As expected, this relaxation mechanism does not manifest itself considerably for this chemical system in which 4 ion-pairs are modelled. From the results in Fig. 8.18b, the shortest  $T_1$  was calculated to be  $\sim 800$  ns, which is much bigger than the observed relaxation time of 220 ns. Hence, spin-exchange reactions and cross-recombination both do not substantially contribute to the spin-lattice relaxation times in this parameter range.

In agreement with the findings of Borovkov [34, 35], the source of the spin-lattice relaxation in  $\text{TMPD}^{+}$  remains unclear as typical relaxation mechanisms cannot provide the observed relaxation time. From the kinetics, it is also clear that the decay of the TR MFE curve cannot be explained by an increase in the fraction of magnetic-field-insensitive emission due to reaction (8), since its frequency decreases after several nanoseconds after the formation of the secondary ion pairs. Borovkov [34, 35] has also highlighted that long-range spin-spin dipole interactions cannot resolve the problem either.

**Linear spur structure** To investigate the effect of the spatial distribution of the cations on the overall decay of the TR MFE curves, a second simulation was done in which the cations were placed along a line (with a mean spacing of 60 Å found to produce the correct magnitude of the magnetic field effect). No high field spin relaxation mechanism was assumed to take place but reactions (15), (16) and (17)

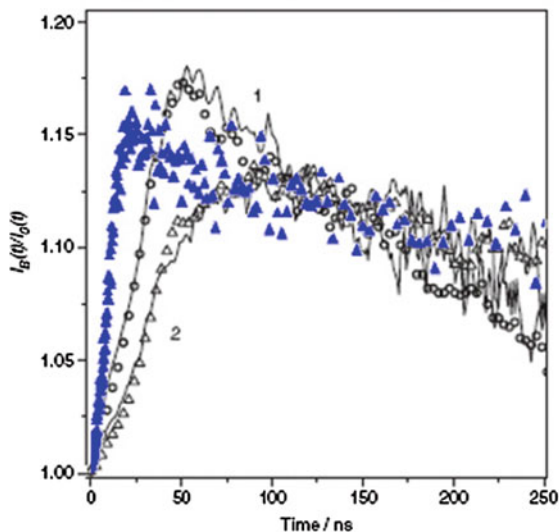


**Fig. 8.19** TR MFE curves obtained using 4 pairs of  $S^{+}/e^{-}$ , with cations distributed along a line, with a separation of 60 Å. The electrons were placed around each geminate cation from a Gaussian distribution with mean zero and standard deviation of 80 Å. In this simulation  $[D] = 0.02$  M. *Blue triangle, circular symbol and solid line* represents the TR MFE curves calculated in this work, by Borovkov and experiment respectively. Second curve with a lower magnetic field effect corresponds to  $[D] = 1$  mM. No high field paramagnetic spin relaxation was assumed to take place, but reactions (15), (16) and (17) were allowed to take place

were included in the reaction scheme. It can be seen from Fig. 8.19 that the decay TR MFE curve does not agree well with the experimental curve, with a larger magnetic field arising at times up to 25 ns. Additionally the TR MFE curve does not decay with the same rate as observed experimentally.<sup>9</sup> Hence, regardless of the spatial distribution of the  $S^{+}/e^{-}$  pairs, the contribution from the cross-recombination relaxation seems negligible for this chemical system.

### 8.7 IRT Algorithm: *Stealing Reactivity*

During the course of this work, it was found that although the IRT algorithm can accurately simulate the overall kinetics of ion-pair recombination, it cannot accurately calculate the yields of geminate or cross-recombination products. For example, if the cation  $h_1^{+}$  has a geminate  $e_1^{-}$  partner, and there is also another  $h_2^{+}$  near the vicinity, the IRT algorithm tends to overestimate the  $h_2^{+} + e_1^{-}$  reaction (cross-recombination) over the  $h_1^{+} + e_1^{-}$  reaction (geminate recombination) as shown in Fig. 8.20. This effect

<sup>9</sup> Experimental and simulated TR MFE curve shown were extracted from reference [34].

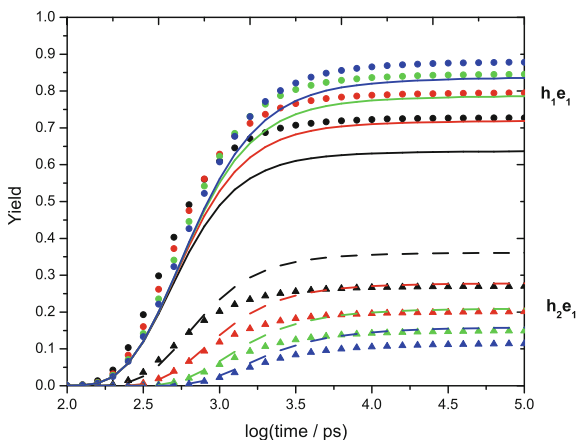


**Fig. 8.20** Geminate ( $h_1e_1$ ) and cross recombination ( $h_2e_1$ ) products obtained using the IRT (solid and dashed lines) and compared with random flights simulations (circle and triangle) for a system containing one of each  $h_1^+$ ,  $h_2^+$  and  $e_1^-$ . The cation-cation distance was varied as: 50 Å (black), 70 Å (red), 90 Å (green) and 110 Å (blue). The  $e_1^-$  was placed 80 Å away along the z-axis from its geminate partner  $h_1^+$ . Cations were made stationary and  $e_1^-$  had a diffusion coefficient of  $1 \text{ \AA}^2 \text{ ps}^{-1}$ . An encounter radius of 5 Å was used for all reactions

known as *stealing reactivity* or *shadow effect* [43] has an important application in the chemical system under study, since cross-recombination itself directly determines the spin-lattice relaxation time.

This error arises because the IRT algorithm neglects the fact that some  $e_1^-$  trajectories which are destined to react with  $h_2^+$  pass through the reactive boundary  $h_1^+$  first and consequently react. This is clearly shown in the contour plots in Fig. 8.21, where the probability of geminate reaction occurs with a lower probability in the IRT algorithm, even though the  $e_1^-$  is near its vicinity. On the other hand, the error is somewhat partially cancelled in the IRT, which allows for a greater probability (in comparison with random flights simulation) of geminate recombination when the  $e_1^-$  is situated behind  $h_2^+$ .

A simple correction to the IRT algorithm has been developed in this work, which allows the correct recombination kinetics to be obtained irrespective of the distribution of the  $e_1^-$  from its geminate partner. The pseudo-algorithm proceeds as follows:

1. Generate the normal reaction times conditioned on the initial distance.
2. If the geminate reaction time  $T_1$  is greater than the cross reaction time  $T_2$ , then it is necessary to check whether the geminate distance  $r_{\text{gem}}$  was less than the cross distance  $r_{\text{cross}}$ .
3. If the above conditions are true, then it is necessary to calculate a value for the parameter  $x$ , which scales  $r_{\text{cross}}$  to decide whether  $r_{\text{gem}} < xr_{\text{cross}}$ . This parameter indirectly takes into account that the trajectory originally destined to react with  $h_2^+$ , had to go through the reactive  $h_1^+$  boundary. The relationship between  $x$  and

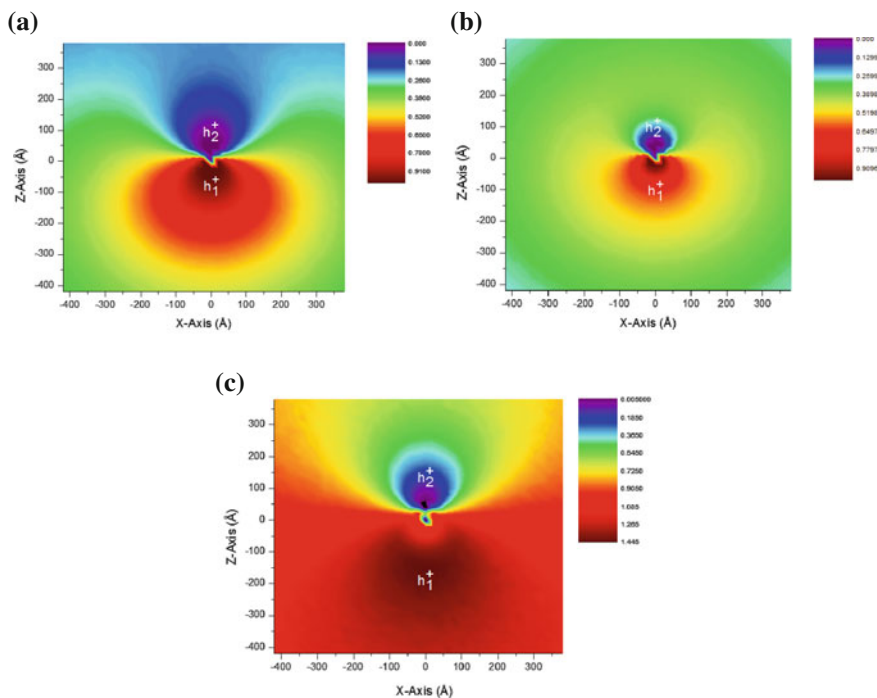


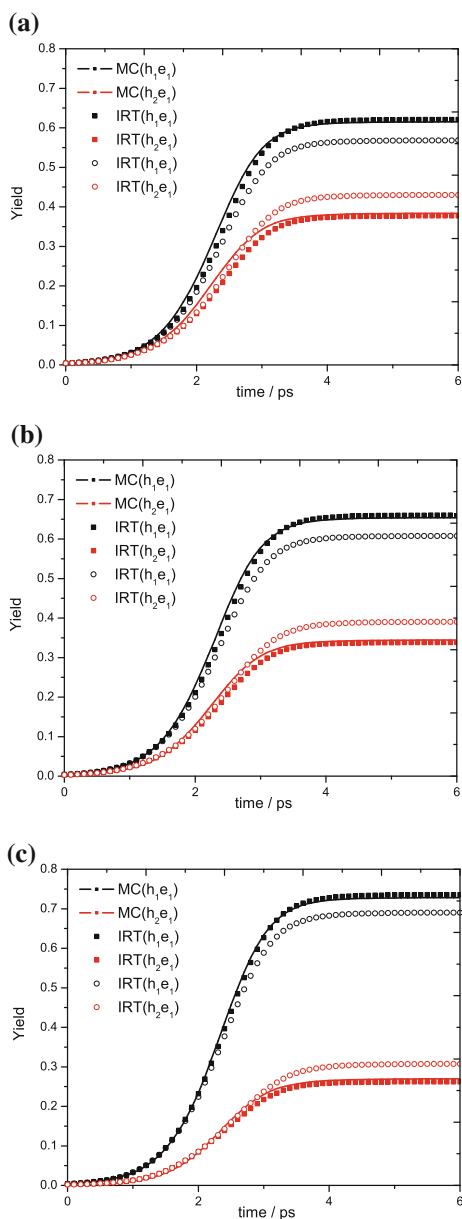
**Fig. 8.21** Contour plots showing the probability of reaction for  $e_1^-$  with its geminate partner  $h_1^+$ . **a** Random flights simulation; **b** IRT simulation and **c** ratio plot (random flights/IRT). Cations were made stationary ( $30 \text{ \AA}$  apart along the  $z$ -axis) and  $e_1^-$  had a diffusion coefficient of  $1 \text{ \AA}^2 \text{ ps}^{-1}$ . An encounter radius of  $5 \text{ \AA}$  was used for all reactions

the  $h_1^+ - h_2^+$  distance ( $\zeta_{hh}$ ) was calculated from numerical simulations and found to obey the approximation:  $x = 0.91314 - 0.00206 \times \zeta_{hh}$ .

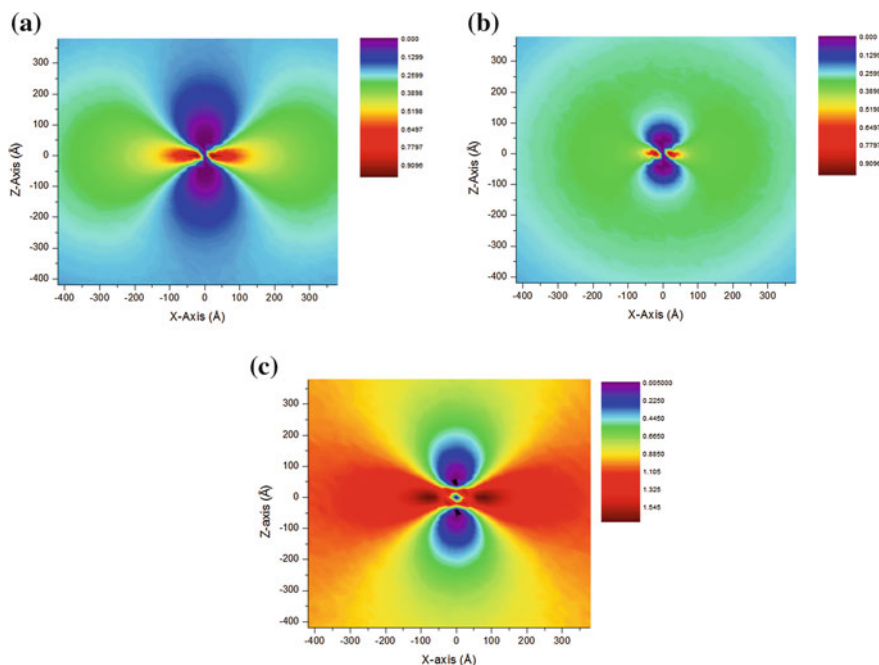
4. If the  $r_{\text{gem}} < x r_{\text{cross}}$  condition is true, then another  $T_1$  is generated and used in the simulation.

Figure 8.22 shows the recombination yields obtained using the above pseudoalgorithm. Although only a limited amount of results are presented here, an investigation of the full parameters space showed the IRT to be in excellent agreement with random flights simulations. Obviously, this algorithm can be extended for a spur containing any number of anions by treating each geminate and cross reaction independently and conditioning on the respective  $h_1^+ - h_2^+$  distance. Unfortunately, this correction does not apply to a situation where three cations are placed on a line with one anion distributed randomly from its respective geminate partner. The failure of the correction is because the  $e_1^-$  trajectory becomes much more complex and it is no longer sufficient to condition on the  $h_1^+ - h_2^+$  distance. The contour plots calculated for three cations separated by  $30 \text{ \AA}$  are shown in Fig. 8.23, with the geminate cation

**Fig. 8.22** Recombination yield of geminate ( $h_1e_1$ ) and cross product ( $h_2e_1$ ) using a  $h_1^+ - h_2^+$  distance of **a** 30 Å; **b** 40 Å and **c** 60 Å. In all cases the  $e_1^-$  was normally distributed from  $h_1^+$  with a mean zero and standard deviation 40 Å along each direction. The cations were made stationary whilst the  $e_1^-$  diffused with a coefficient  $1 \text{ \AA}^2 \text{ ps}^{-1}$ . Red and black (open square) and (open circle) correspond to the corrected and uncorrected IRT algorithm respectively. Solid black and red line corresponds to random flights simulation. An encounter radius of 10 Å was used for all reactions. Here MC refers to random flights simulation



situated at the origin in the middle. Again in the IRT simulation, cross-recombination is overestimated which is not surprising since the contours show a higher probability of reacting with either cross  $h^+$  than what is obtained from random flights simulations.



**Fig. 8.23** Contour plots showing the probability of reaction for  $e_1^-$  with its geminate partner  $h_1^+$ . **a** Random flights simulation and **b** IRT simulation and **c** ratio plot (random flights/IRT). Cations were made stationary ( $30 \text{ \AA}$  apart along the  $z$ -axis) and  $e_1^-$  had a diffusion coefficient of  $1 \text{ \AA}^2 \text{ ps}^{-1}$ . An encounter radius of  $5 \text{ \AA}$  was used for all reactions

## 8.8 Discussion and Further Work

In this work, simulation results have shown that quantum spin entanglement acts as an extra source of spin relaxation in spurs. For example, in a 4 radical spur, if  $\{1, 3\}$  and  $\{2, 4\}$  are spin-correlated, a single cross-recombination between  $\{1, 4\}$  decides the spin multiplicity of the disjoint pair  $\{2, 3\}$  because of the conservation of overall spin, causing the collapse of the wavefunction. Although the disjoint pair  $\{2, 3\}$  is subject to magnetic field effects, over many realisations these effects are destroyed due to the random nature of the encounters. Hence, a single cross-recombination has the effect of (1) incoherently changing the spin state of  $\{2, 3\}$  and (2) destroying any spin correlations for the disjoint pair  $\{2, 3\}$ .

By modelling the TR MFE fluorescence decay curves in low-permittivity solvents using new simulation techniques, it has been shown that the spin-lattice relaxation time can be significantly decreased by this cross-combination effect, depending on the number of radical pairs in the spur. It is hypothesised that this effect acts as an extra source of spin relaxation in hydrocarbons where the recombination fluorescence is slowed down by an electron scavenger, such as hexafluorobenzene. It has also been hypothesised that different spin-lattice relaxation times are to be expected for photolytic and radiolytic pairs.

The complexity of simulating an entire track structure from the IRT framework has been highlighted in this chapter. Although in the TR MFE decay curves the contribution of cross-recombination may have been overestimated, the results nonetheless highlight a distinctive correlation between cross-recombination and the spin-lattice relaxation time. Further work is now required to: (1) incorporate a more realistic description of the magnetic interactions (in particular the exchange and dipole interactions); (2) use a realistic description for the track structure to describe the radiolysis of hydrocarbons, where the ERP effect can be properly understood in terms of the spatial distribution of the primary and secondary ion-pairs.

## References

1. B. Brocklehurst, *Radiat. Phys. Chem.* **50**, 213 (1997)
2. J.A. LaVerne, B. Brocklehurst, *Radiat. Phys. Chem.* **47**, 71 (1996)
3. B. Brocklehurst, *Int. Rev. Phys. Chem.* **4**, 279 (1985)
4. D. Bohm, *Quantum Theory* (Prentice-Hall, New Jersey, 1951)
5. J. Klein, R. Voltz, *Phys. Rev. Lett.* **36**, 1214 (1976)
6. B. Brocklehurst, *Radiat. Phys. Chem.* **21**, 577 (1983)
7. V.A. Bagryansky, V.I. Borovkov, Y.N. Molin, *Russ. Chem. Rev.* **76**, 493 (2007)
8. D.V. Stass, B.M. Tadjikov, Y.N. Molin, *Chem. Phys. Letts.* **235**, 511 (1995)
9. V.A. Bagryansky, O.M. Usov, V.I. Borokov, *Chem. Phys.* **255**, 237 (2000)
10. K. Schulten, P.G. Wolynes, *J. Chem. Phys.* **68**, 3292 (1978)
11. E.W. Knapp, K. Schulten, *J. Chem. Phys.* **71**, 1878 (1979)
12. V.I. Borovkov, Y.N. Molin, *Phys. Chem.* **396**, 123 (2004)
13. D.M. Bartels, R.G. Lawler, A.D. Trifunac, *J. Chem. Phys.* **83**, 2686 (1985)
14. B.M. Tadjikov, D.V. Stass, Y.N. Molin, *J. Phys. Chem. A.* **101**, 377 (1997)
15. V.I. Borovkov, Y.N. Molin, *Phys. Chem. Chem. Phys.* **6**, 2119 (2004)
16. V.I. Borovkov, Y.N. Molin, *Chem. Phys. Lett.* **398**, 422 (2004)
17. M.R. Das, S.B. Wagner, J.H. Freed, *J. Chem. Phys.* **52**, 5404 (1970)
18. J.H. Freed, R.G. Kooser, *J. Chem. Phys.* **49**, 4715 (1968)
19. H.M. McConnell, *J. Chem. Phys.* **34**, 13 (1961)
20. D. Kivelson, *J. Chem. Phys.* **34**, 13 (1966)
21. P.V. Schastnev, L.N. Shchegoleva, *Molecular Distortions in Ionic and Excited States* (CRC, Boca Raton, 1995)
22. A. Lund, M. Lindgren, S. Lunell, J. Maruani, *Molecules in Physics, Chemistry and Biology* (Kluwer, Dordrecht, 1989)
23. V.I. Melekhov, O.A. Anisimov, L. Sjoqvist, A. Lund, *Chem. Phys. Lett.* **174**, 95 (1990)
24. B. Brocklehurst, *Faraday Discuss. Chem. Soc.* **78**, 303 (1984)
25. L.V. Il'ichov, S.V. Anishchik, *J. Phys. B. Mol. Opt. Phys.* **42**, 1 (2009)
26. A. Mozumder, *Fundamentals of Radiation Chemistry* (Academic Press, London, 1999)
27. M. Wojcik, W.M. Bartczak, J. Kroh, *Radiat. Phys. Chem.* **39**, 65 (1992)
28. W.M. Bartczak, A. Hummel, *Radiat. Phys. Chem.* **27**, 71 (1996)
29. O.A. Anisimov, V.M. Grigoryants, Y.N. Molin, *Chem. Phys. Lett.* **74**, 15 (1980)
30. A. Saeki, T. Kozawa, Y. Yoshida, S. Tagawa, *Radiat. Phys. Chem.* **60**, 319 (2001)
31. V.I. Borovkov, S.V. Anishchik, O.A. Anisimov, *Radiat. Phys. Chem.* **67**, 639 (2003)
32. R. Mehnert, O. Brede, W. Naumann, R. Herman, *Radiat. Phys. Chem.* **32**, 325 (1988)
33. V.I. Borovkov, S.V. Anishchik, O.A. Anisimov, *Chem. Phys. Lett.* **270**, 327 (1997)
34. V.I. Borovkov, K.A. Velizhanin, *Radiat. Phys. Chem.* **76**, 998 (2007)
35. V.I. Borovkov, K.A. Velizhanin, *Radiat. Phys. Chem.* **76**, 988 (2007)

36. V.I. Borovkov, *High Energy Chem.* **42**, 113 (2008)
37. B. Brocklehurst, *J. Chem. Soc. Faraday Trans.* **88**, 167 (1992)
38. B. Brocklehurst, *J. Chem. Soc. Faraday Trans.* **88**, 2823 (1992)
39. A.K. Pikaev, *Modern Radiation Chemistry: Radiolysis of Gases and Liquids* (Nauka, Moscow, 1986)
40. F.P. Schwarz, D. Smith, S.G. Lias, P.J. Ausloos, *Chem. Phys.* **75**, 3800 (1981)
41. G. Grampp, S. Landgraf, J. Rasmussen, *J. Chem. Soc. Perkin Trans.* **2**, 1897 (1999)
42. J. Telo, G. Grampp, M.C.B.L. Shohoji, *Phys. Chem. Chem. Phys.* **1**, 99 (1999)
43. S.D. Traytak, M. Tachiya, *J. Chem. Phys.* **107**, 9907 (1997)

## Chapter 9

# Extending the IRT for Micelles

The diffusive behaviour of particles inside a micelle and other confined systems has been extensively studied, both experimentally and theoretically [1–9]. Most simulation methods to date use Monte Carlo random flights simulation to model the diffusive motion of radicals and their subsequent recombination kinetics in confined systems. In this chapter, the possibility of using the IRT simulation to model the complete recombination kinetics and scavenging is explored (i) inside the micelle (ii) on the surface of the micelle and (iii) reversible reactions involving the micelle (i.e. adsorption and escape of solvent particles from the surface of the micelle).

The approximation of one particle fixed at the origin whilst the other partner moves with the mutual diffusion coefficient is not valid to model the situation in which both particles diffuse. Therefore modelling such system poses a challenging problem within the IRT framework. The motivation for this work comes from the fact that (i) simulations involving the IRT are much faster than random flights and provide much better statistics by the use of more realisations, and (ii) IRT simulations have never previously been reported for confined systems. In this chapter the IRT algorithm is developed in stages to allow comparison with random flights simulations and help analyse any correlation which may arise between reaction times.

**First stage** The first model considers two particles inside a micelle with an outer reflecting boundary, with only geminate recombination possible (Sect. 9.2). The second model then simulates the breakage of the micelle in the event one particle hits the surface of the micelle and escapes into the bulk solution (Sect. 9.3). In this model no recombination is possible. This model is then further developed to allow recombination to take place inside the micelle (Sect. 9.4). These three models are then used to generalise the IRT algorithm to simulate recombination and scavenging inside the micelle for any number of particles which can all be randomly distributed (Sect. 9.5).

**Second stage** The second stage involves developing the IRT algorithm to model the diffusive behaviour on the surface of a micelle, which has important applications in

astrophysics and astrochemistry. Again, the IRT is generalised to allow (i) scavenging of a particle to be modelled and (ii) the recombination of  $n$  particles (Sect. 9.6).

**Third stage** The third stage considers reversible reactions within the IRT framework, in which a single solvent particle can undergo association/dissociation from the micellar surface to the bulk solution. Through the use of an exponential time with the correct mean within the IRT framework, it will be shown in this chapter that essentially excellent agreement between random flights simulation and IRT can be obtained for neutral species (Sect. 9.7).

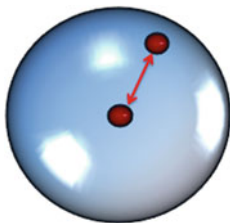
## 9.1 Parameter Space

As the kinetics simply scale with the diffusion coefficient the choice of this parameter is unimportant. Hence, all reaction/survival yields are presented in the form  $D't$ , which factors out the effect of the diffusion coefficient. The choice of the encounter radius used to model reactions inside the micelle (reported alongside each result) is based on the data given in Ref. [10]. The radius of the micelle (reported alongside each result) was chosen based on the work by Bruce and co-workers [11]. For a spherical micelle the maximum radius  $R$  must be the same as the maximum extended length of the hydrophobic chain  $l_c$ . Hence, for a micelle to form a spherical structure the following condition must be satisfied

$$R = \frac{3V}{a_0} \leq l_c \quad (9.1)$$

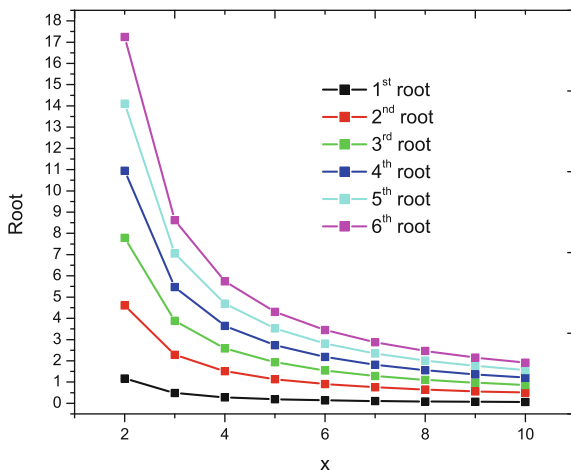
where  $a_0$  is the headgroup area and  $V$  is the volume. Typically a spherical micelle has a radius of 20 Å and contains  $\sim 100$  molecules.

## 9.2 Reflective Outer Boundary with Geminate Recombination



In this section two particles are distributed inside a spherical micelle with one fixed at the origin and the other randomly distributed, which is mobile. This is the simplest model to test the IRT algorithm against random flights simulations. The outer boundary is reflective, hence reaction completes once the two particles recombine.

**Fig. 9.1** First six roots of the equation  $\tan(\alpha(x - 1)) = \alpha x$ , as a function of  $x$ . In this transcendental equation  $x = R/a$  and  $\alpha = \beta a$



The backward diffusion equation for the survival probability ( $\Omega(t)$ ) to describe this problem can be written as

$$\frac{\partial \Omega}{\partial t} = D \left[ \frac{\partial^2 \Omega}{\partial r^2} + \frac{2}{r} \frac{\partial \Omega}{\partial r} \right] = \frac{D}{r} \frac{\partial^2 (\Omega r)}{\partial r^2} \tag{9.2}$$

which assumes spherical symmetry inside the micelle [i.e. the diffusion of the particles is only dependent on  $r$  (the separation distance of the radical pair) and is independent of the angles  $\phi$  and  $\theta$ ]. In the expression  $D$  is the diffusion coefficient of the mobile particle. The initial condition is of the form  $\Omega(t = 0) = 1$ , with the inner boundary condition being  $\Omega(r = a) = 0$ , and outer boundary condition being  $\frac{\partial \Omega}{\partial r} \Big|_{r=R} = 0$ . Using the method of separation of variables, the survival probability is found to be

$$\Omega(t) = \sum_n \frac{A_n}{r} \sin(\beta_n(r - a)) \exp(-\beta_n^2 D t) \tag{9.3}$$

with  $r$  being the interparticle separation,  $a$  the encounter radius and  $D$  the diffusion coefficient of the particle. The coefficient  $\beta_n = \sqrt{\lambda/D}$  are the solutions of the equation

$$\tan(\beta(R - a)) = \beta R \tag{9.4}$$

with  $R$  being the radius of the micelle and  $\lambda$  an arbitrary constant. The above equation is equivalent to the dimensionless form  $\tan(\alpha(x - 1)) = \alpha x$ , where  $x = R/a$  and  $\alpha = \beta a$ . A plot of the first six solutions for this equation are shown in Fig. 9.1 as a function of  $x$ . It can be seen that for small  $x$  the first root is sufficient to describe the kinetics.

The coefficient  $A_n$  can be found from the initial condition such that  $\sum_n A_n \sin(\beta_n(r - a)) = r$ , which gives

$$A_n = \frac{2a}{\beta_n [R - a - R \cos^2(\beta_n(R - a))]} \quad (9.5)$$

In order to find the survival probability for a randomly placed particle relative to the fixed particle, Eq. (9.3) must be integrated over all possible values of  $r$ . The corresponding expression is

$$\Omega(t) = \frac{3a}{(R^3 - a^3)} \sum_n \frac{A_n}{\beta_n} \exp(-\beta_n^2 D t) \quad (9.6)$$

The mean reaction time  $\bar{T}$  can be readily found using the steady state backward equation of the form

$$\frac{D}{r} \frac{\partial^2(\bar{T}r)}{\partial r^2} = -1 \quad (9.7)$$

which has the general solution

$$\bar{T}(r) = A + \frac{B}{r} - \frac{r^2}{6D} \quad (9.8)$$

with coefficients  $A$  and  $B$  to be determined by the boundary conditions. In this section, we employ an outer reflecting boundary

$$D \frac{\partial \Omega(r)}{\partial r} \Big|_{r=R} = 0 \quad (9.9)$$

and an inner absorptive boundary such that  $\Omega(a) = 0$ , which gives the expression for the mean reaction time to be

$$\bar{T} = \frac{2rR^3 - 2aR^3 + ra^3 - ar^3}{6Dar} \quad (9.10)$$

with  $r$  being the separation of the pair,  $a$  the encounter radius,  $R$  the radius of the sphere and  $D$  the diffusion coefficient of the mobile particle. Figure 9.2a shows the survival probability calculated using Eq. (9.6) and compared against a Monte Carlo random flights simulation of the same system. In the analytical expression, only the first nontrivial root of Eq. (9.4) was taken (i.e. only  $\beta_1$  was used). Essentially, exact agreement is obtained between both methods. Figure 9.2b shows the survival probability for a pair of neutral species calculated using an exponential time with the same mean as Eq. (9.10) within the IRT algorithm and compared against full random flights simulations. In this simulation, one particle is fixed at the origin whilst the

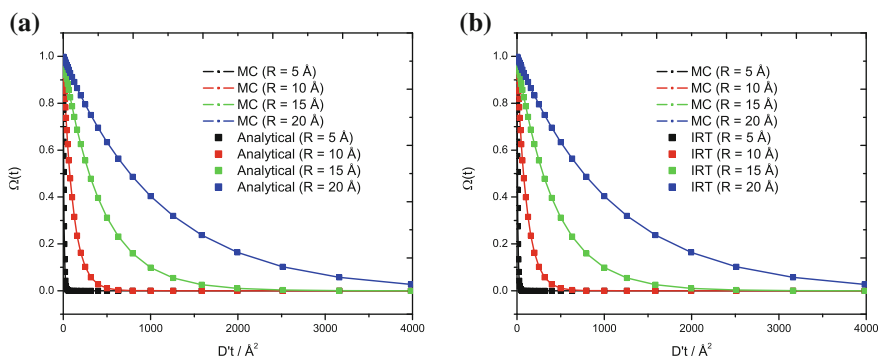
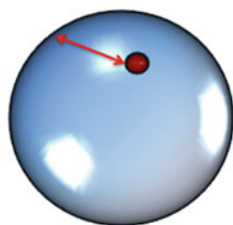


**Fig. 9.2** Survival probability calculated **a** using the analytical expression and compared with random flights simulations; **b** using random flights simulations and compared with the exponential time with the mean given in Eq. (9.10) in the IRT. All simulations were done as a function of the radius of the micelle ( $R$ ). The encounter radius was set to 2 Å. Here MC refers to random flights simulation

other particle is randomly placed inside the sphere and is allowed to diffuse with a given diffusion coefficient. The mean reaction time is found to accurately predict the survival probability for a micelle radius in the range 5–20 Å, showing that no substantial errors are introduced by assuming that the kinetics are exponential and ignoring the initial separation.

### 9.3 Partially Absorbing Outer Boundary with No Geminate Recombination



In this section, the analytical expressions are presented for a micelle which can partially break leading to the escape of the particle. Hence, the outer boundary is subject to radiation boundary conditions. For simplicity, no geminate reaction is allowed to take place within the micelle at this stage (i.e. there is no fixed particle at the origin). This model is later used to allow the simulation of  $n$  particles randomly distributed inside a sphere in which both recombination and escape are possible.

To model the breakage of the micelle (and consequently leading to the escape of the particle from the micelle), the outer radiation elastic boundary condition of the form

$$D \left. \frac{\partial \Omega}{\partial r} \right|_{r=R} = -v\Omega(r=R) \quad (9.11)$$

is used. In this expression, the rate of the particle leaving from the micelle is controlled through the parameter  $v$  which is related to the rate constant for reactivity via the relation  $k_{\text{act}} = 4\pi a^2 v$ ;  $D$  is the diffusion coefficient,  $\Omega(r)$  is the survival probability,  $r$  the distance from the centre of the sphere and  $R$  being the radius of the sphere.

### 9.3.1 Monte Carlo Random Flights Algorithm

As the outer surface is now reactive, it is necessary to modify the random flights algorithm to take this reactivity into account using the radiation boundary condition. As discussed in Sect. 4.3.5, the simulation proceeds by assuming the outer boundary is reflective. If this outer boundary is hit during the diffusive motion of the particle, then the probability of escape is calculated based on the parameter  $v$  which controls the surface reactivity. This section presents the algorithm to (i) handle the reflection of a particle subject to an upper reflective boundary and (ii) calculating the probability of reaction.

#### 9.3.1.1 Reflection Algorithm

The algorithm as described in Sect. 4.3.3 needs to be modified to account for the fact that the upper boundary is now reflecting. If  $Y_t$  is a Brownian motion started at  $x$  with  $R$  defined as the upper boundary, and  $M$  is the supremum of the path  $Y_t$ , then the reflected trajectory takes the form

$$Z_{\text{ref}}(t) = \begin{cases} Y_t & M(\delta t) < R \\ Y_t + R - M(\delta t) & M(\delta t) \geq R \end{cases} \quad (9.12)$$

which is an exact sample of a Brownian motion with drift reflected at  $R$ . In the above expression, the value for  $M$  can be calculated as

$$M = \frac{1}{2} \left[ (x + y) + [(x - y)^2 - 4Dt \ln U(0, 1)]^{1/2} \right] \quad (9.13)$$

where  $U(0, 1]$  is a random number uniformly distributed between (0,1].

### 9.3.1.2 Brownian Bridge

The transition density of passing through  $R$  and reaching  $y$  in a step  $\delta t$  subject to an upper elastic boundary is given in Eq. (9.14),<sup>1</sup> where  $\beta = v/D'$ , with  $v$  being the reactivity of the surface with units of velocity,  $\mu$  is the drift term and  $D'$  is the mutual diffusion coefficient. The equivalent transition density for the reflected probability is

$$\begin{aligned}
 p_{\text{rad}}(x, y, \delta t \text{ via } R) &= \frac{1}{\sqrt{4\pi D' \delta t}} \exp(-y - x - \mu \delta t)^2 / 4D' \delta t \\
 &+ \exp(-\mu(R - y)/D') \left[ \frac{1}{\sqrt{4\pi D' \delta t}} \exp(-(2R - y - x - \mu \delta t)^2 / 4D' \delta t) \right. \\
 &\times \left( \beta - \frac{\mu}{2D'} \right) - \exp(\beta(2R - y - x - \mu \delta t + \beta D' \delta t)) \\
 &\times \left. \operatorname{erfc} \left( \frac{2R - y - x - \mu \delta t + 2\beta D' \delta t}{\sqrt{4D' \delta t}} \right) \right] \quad (9.14)
 \end{aligned}$$

$$\begin{aligned}
 p_{\text{ref}}(x, y, \delta t \text{ via } R) &= \frac{1}{\sqrt{4\pi D' \delta t}} \exp[(-y - x - \mu \delta t)^2 / 4D' \delta t] \\
 &+ \exp(-\mu(R - y)/D') \left[ \frac{1}{\sqrt{4\pi D' \delta t}} \exp(-(2R - y - x - \mu \delta t)^2 / 4D' \delta t) \right. \\
 &- \left. \left( \frac{\mu}{2D'} \right) \operatorname{erfc} \left( \frac{2R - y - x - \mu \delta t + 2\beta D' \delta t}{\sqrt{4D' \delta t}} \right) \right] \quad (9.15)
 \end{aligned}$$

The probability of survival on a bridge from  $x$  to  $y$  subject to an upper elastic boundary is then simply the ratio of the form

$$\Omega(\text{via } R|x, y, t) = \frac{p_{\text{rad}}(x, y, \delta t \text{ via } R)}{p_{\text{ref}}(x, y, \delta t \text{ via } R)} \quad (9.16)$$

As before, if the particle's position after a time step  $\delta t$  is greater than  $R$ , the particle is reflected so that  $r < R$  and  $\Omega(\text{via } R|x, y, t)$  is calculated. A uniformly distributed random number  $U(0,1]$  is next generated. If  $U(0,1] > \Omega(\text{via } R|x, y, t)$  the micelle surface has broken and the particle has escaped, otherwise the particle is reflected back into the micelle.

---

<sup>1</sup> Transition density for a 1D diffusion process with an outer elastic/reflective boundary is derived in the Appendix (Sect. A.8).

### 9.3.2 Analytical Formula and Mean Reaction Time

Using the method of separation of variables, the solution to the backward diffusion equation employing the boundary condition as given in Eq. (9.11) is found to be

$$\Omega(t) = \sum_n \frac{A_n}{r} \sin(\beta_n r) \exp(-\beta_n^2 D t) \quad (9.17)$$

which when integrated over all possible values of  $r$  gives

$$\Omega(t) = \frac{3}{R^3} \sum_n \frac{A_n (\sin(\beta_n R) - \beta_n R \cos(\beta_n R))}{\beta_n^2} \exp(-\beta_n^2 D t) \quad (9.18)$$

The coefficient  $\beta_n = \sqrt{\lambda/D}$  (where  $\lambda$  being an arbitrary constant) are the solutions of the equation

$$\tan(\beta R) = \frac{D\beta R}{D - vR} \quad (9.19)$$

and the coefficient  $A_n$  can be found from the initial condition such that at  $t = 0$ ,  $\Omega(0) = 1$ , to give

$$A_n = -2 \left[ \frac{-\sin(\beta_n R) + \beta_n R \cos(\beta_n R)}{\beta_n (-\cos(\beta_n R) \sin(\beta_n R) + \beta_n R)} \right] \quad (9.20)$$

The mean reaction time  $\bar{T}$  is subsequently given as

$$\bar{T} = \frac{2RD + vR^2 - vr^2}{6Dv} \quad (9.21)$$

where  $v$  is the reactivity of the surface and directly controls the breakage of the micelle. Figure 9.3a shows the survival probability obtained with random flights simulations and compared against the analytical formulation (using only the first root  $\beta_1$ ), whilst Fig. 9.3b shows the comparison in the kinetics using the mean reaction time and the analytical expression. Within the parameter space investigated, the IRT simulation is shown to accurately describe the survival probability with no noticeable deviations seen within the transient period.

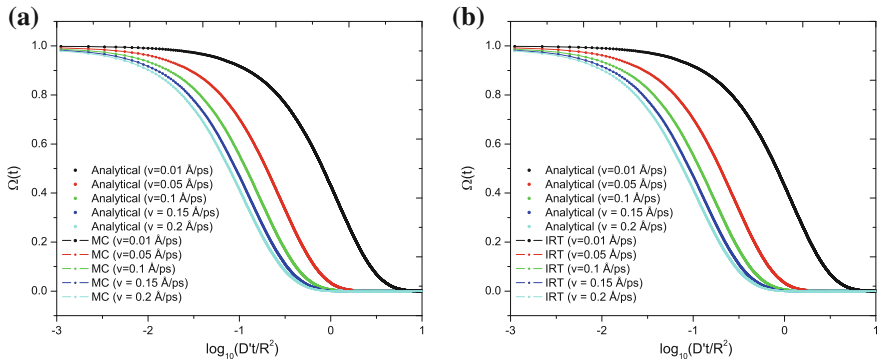
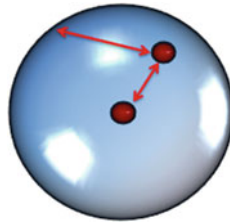


**Fig. 9.3** Survival probability calculated **a** using random flights simulation; **b** using the mean time shown in Eq. (9.21). All simulations were done at various values for the reactivity of the outer boundary and compared with analytical formulation. An encounter radius of 5 Å was used in all cases together with a micelle radius of 30 Å. Here MC refers to random flights simulation

## 9.4 Partially Absorbing Outer Boundary with Geminate Recombination



This section extends the outer radiation boundary condition in the previous model to include geminate reaction within the micelle. In this model a single particle diffuses with a sink at the centre and an outer radiation boundary. The required initial condition is  $\Omega(t = 0) = 1$ , inner boundary  $\Omega(r = a) = 0$  and outer boundary condition  $D \frac{\partial \Omega}{\partial r} \Big|_{r=R} = -v\Omega(r = R)$ . Solving the backward diffusion equation with these boundary conditions gives the analytical expression for the survival probability to be

$$\Omega(t) = \sum_n \frac{A_n}{r} \sin(\beta_n(r - a)) \exp(-\beta_n^2 Dt) \quad (9.22)$$

which when integrated over all possible values of  $r$ , with one particle fixed at the origin gives

$$\Omega(t) = \frac{3}{(R^3 - a^3)} \sum_n \frac{A_n(-\sin(\beta_n(-R + a)) - \beta_n R \cos(\beta_n(-R + a))) + \beta_n a}{\beta_n^2} \times \exp(-\beta_n^2 Dt) \quad (9.23)$$

The coefficient  $\beta_n = \sqrt{\lambda/D}$  (where  $\lambda$  being an arbitrary constant) are the solutions of the equation

$$\tan(\beta(R-a)) = \frac{D\beta R}{D-vR} \quad (9.24)$$

with the coefficient  $A_n$  (determined from the initial condition) found to be

$$A_n = -2 \left[ \frac{-\sin(\beta_n(a-R)) + \beta_n R \cos(\beta_n(a-R)) + \beta_n a}{\beta_n(-\cos(\beta_n(a-R)) \sin(\beta_n(a-R)) + \beta_n(R-a))} \right] \quad (9.25)$$

The analytical form of the first passage time densities in the Laplace space is given by the expression

$$\tilde{w}(r, s) = \frac{\sinh(\gamma(-r+R))[avb-aD] - vR^2 \sinh(\gamma(a-r)) + aRD\gamma \cosh(\gamma(-r+R))}{r(\sinh(\gamma(-R+a))[D-vR] + \gamma RD \cosh(\gamma(-R+a)))} \quad (9.26)$$

with  $\gamma = \sqrt{s/D}$ . Unfortunately, analytically inverting Eq. (9.26) is not possible and one must resort to numerical techniques. If Eq. (9.26) is inverted to the time domain, the corresponding cumulative distribution function (given as  $\tilde{W}(r, s) = (1/s)\tilde{w}(r, s)$ ) must also be numerically inverted in order to generate a reaction time within the IRT framework. A much better approach is to use the mean reaction time which eliminates any numerical instability encountered when transforming from the Laplace space to the time domain. The expression for the mean time  $\bar{T}$  is

$$\bar{T} = -\frac{(r-a)(R^4v + 2R^3D) + R^2v(r^3 - a^3) + (Rv + D)(ra^3 - r^3a)}{6Dr(-Da - vR^2 + vRa)} \quad (9.27)$$

In order to decipher whether the mean reaction time corresponds to a reaction with the surface or geminate recombination, it is necessary to calculate the probabilities of each event. Using a similar strategy as before, the steady state backward diffusion equation must be solved subject to the boundary conditions:

$$\begin{aligned} p(a) &= 1 \\ p'(R) &= -\frac{v}{D}p(R) \end{aligned} \quad (9.28)$$

The probability of hitting the inner boundary first is then

$$P_{\text{in}} = \frac{a(vR^2 + rD - rvR)}{r(vR^2 + aD - avR)} \quad (9.29)$$

with the probability of hitting the outer surface first simply being  $P_{\text{out}} = 1 - P_{\text{in}}$ . In order to decide which boundary is hit, it is necessary to generate a uniformly

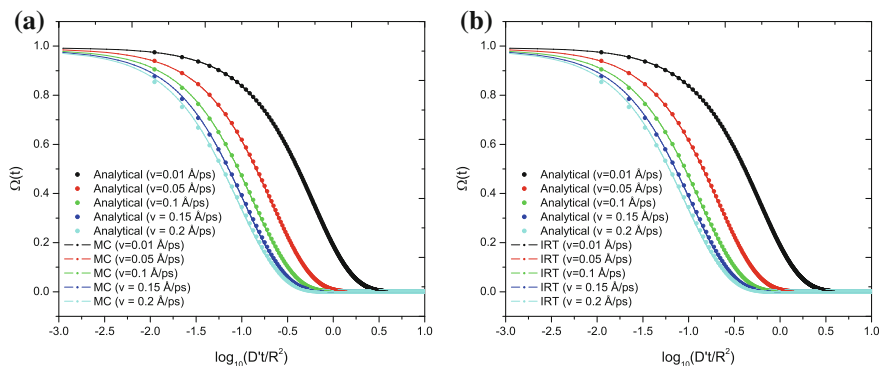
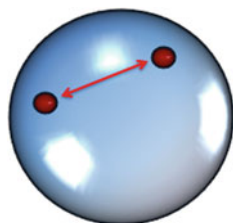


**Fig. 9.4** Survival probability calculated **a** using random flights simulation and compared with analytical formulation; **b** using the mean time shown in Eq. (9.21) and compared with analytical formulation. All simulations were done as a function of the reactivity of the outer boundary of the micelle ( $v$ ). An encounter radius of 5 Å was used together with a micelle radius of 30 Å. Here MC refers to random flights simulation

distributed random number  $U(0, 1]$ . If  $P_{in} > U(0, 1]$  then the inner boundary is hit, otherwise the particle has escaped from the micelle. From the results presented in Fig. 9.4a, b the mean reaction time appears to nicely describe the kinetics for a particle which can either escape the micelle or geminately recombine. In addition, Fig. 9.5 shows that excellent agreement can be obtained for the kinetics with a micelle radius ranging from 20–70 Å by making use of the mean reaction time. In the next section this model will be further developed to include two randomly distributed particles within the micelle which are both mobile and compete between recombination and escape.

## 9.5 Randomly Distributed Radical Pairs Inside a Micelle

### 9.5.1 Reflecting Outer Boundary



In the last section, the diffusion equation was used to model the recombination kinetics inside the micelle which assumed one of the particles to be fixed at the origin. However, in a realistic environment the particles could be randomly

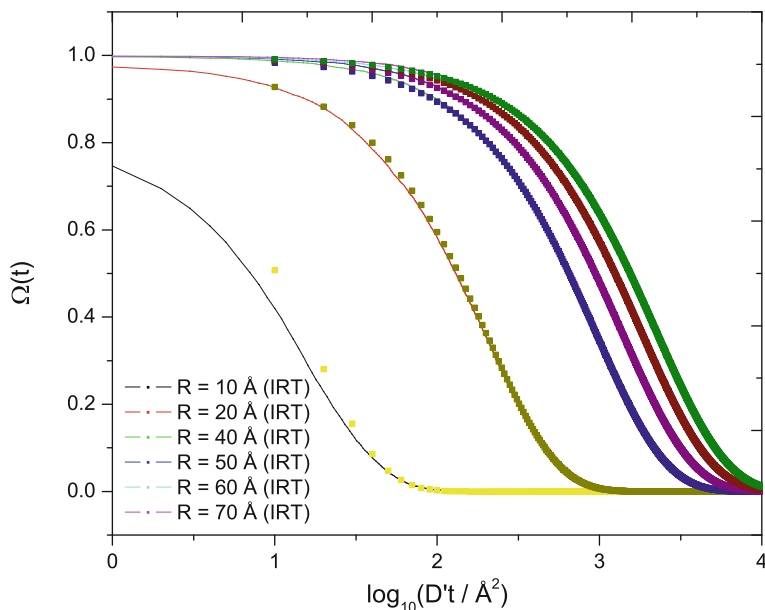


**Fig. 9.5** Survival probability calculated using Eq. (9.23) (square) and compared with Eq. (9.27) (solid line). An encounter radius of 5 Å was used together with a surface reactivity of  $0.01 \text{ \AA ps}^{-1}$

distributed anywhere inside the micelle and all the particles can move. The problem now is that there is no exact solution. The mean distance between two particles (with one fixed at the origin) in a sphere of unit radius is 0.75; however, when both particles are randomly distributed inside a sphere the mean distance is found to 1.028 [calculated from Eq. (9.48)]. Therefore, if the mean reaction time belonging to the case in which one particle is fixed at the origin (with the other moving with the relative diffusion coefficient) is used to describe the recombination kinetics of two randomly distributed particles (which diffuse with their individual diffusion coefficients), the kinetics will be too fast. This is indeed found to be the case as shown in Fig. 9.6a.

In order to correct for the survival probability within the IRT framework, a series of random flights simulations were done in which the survival probability was calculated as a function of the  $(a/R)$  ratio, with  $a$  being the encounter distance and  $R$  the spherical radius. Within the IRT algorithm a correction factor  $\zeta$  was applied to the mutual diffusion ( $D'$ ) coefficient and optimised until convergence was obtained for the survival probability across the  $(a/R)$  parameter space. The value of  $\zeta$  was then plotted as a function of the  $(a/R)$  ratio and was found to obey the approximation of the form

$$\zeta = 0.934 - 2.036 \left( \frac{a}{R} \right) \quad (9.30)$$

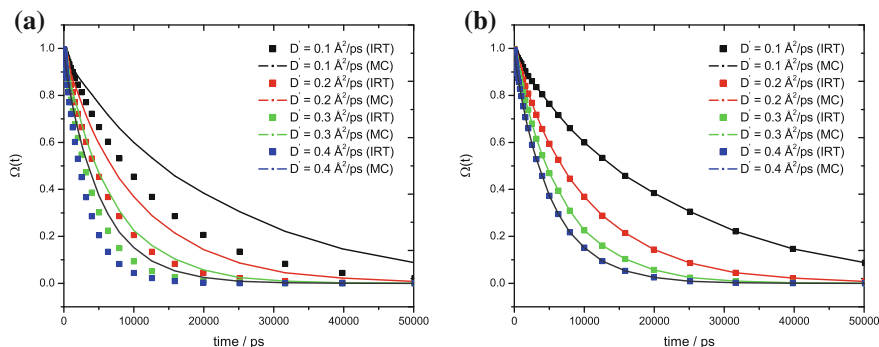
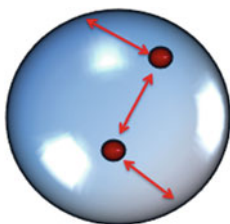


**Fig. 9.6** Survival probability calculated using the mean reaction time and compared with random flights simulations using an outer reflective boundary. The micelle radius was 30 Å and the encounter radius was set to 4 Å for all reactions. **a** Using the actual mutual diffusion equation without scaling and **b** using Eq. (9.30) to correct for the mutual diffusion. Here MC refers to random flights simulation

The expression for the effective mutual diffusion coefficient can therefore be calculated as  $D'_{\text{eff}} = D' \times \zeta$ . Figure 9.6b shows the survival probability for a single pair of neutral species distributed randomly inside a sphere of radius 30 Å with different values for  $D'$ . An outer reflective boundary was used in all cases. It can be seen that very good agreement is now obtained in the recombination yield across a wide parameter range for the mutual diffusion coefficient. It should be noticed that treating reactive products in this model is also relatively easy, since only the appropriate mean reaction time is required; at no stage of the simulation is the position of any particle required.

### 9.5.2 Elastic Outer Boundary



In this section, two randomly distributed particles inside the micelle are considered which can either escape from the micelle or undergo geminate recombination. To generate a time for the recombination, it is necessary to sample from Eq. (9.10) subject to the correction in the mutual diffusion equation as given in Eq. (9.30). For reaction with the outer boundary, Eq. (9.21) is used to generate the two possible event

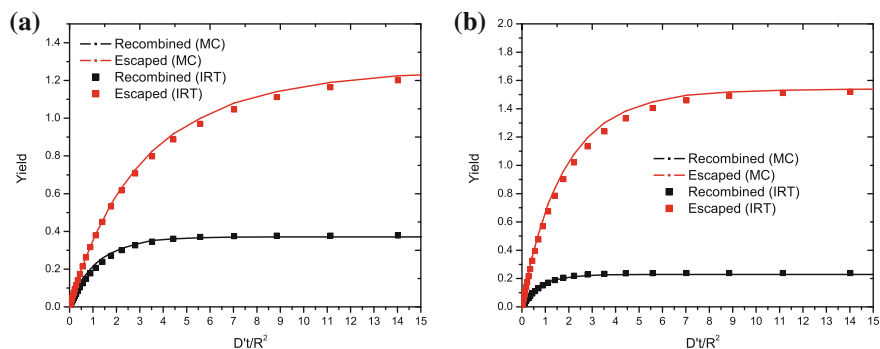


**Fig. 9.7** Reaction probability calculated using the mean reaction time and compared with random flights simulations using an outer elastic boundary and inner absorptive boundary with an encounter radius of 3 Å. **a**  $v = 0.0005 \text{ \AA ps}^{-1}$  and **b**  $v = 0.001 \text{ \AA ps}^{-1}$ . Here MC refers to random flights simulation

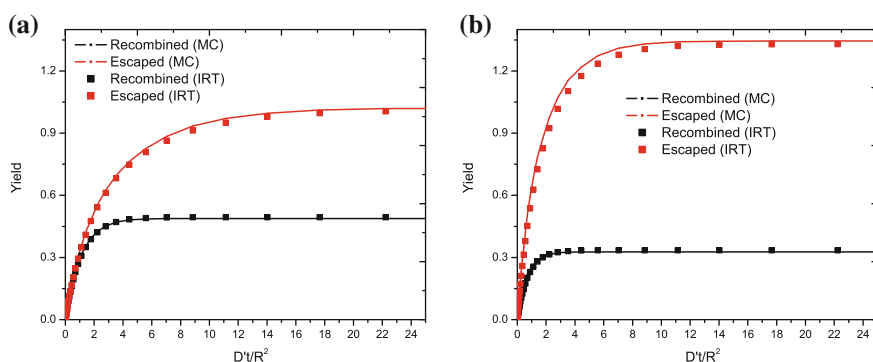


**Fig. 9.8** Reaction probability calculated using the mean reaction time and compared with random flights simulations using an outer elastic boundary and inner absorptive boundary with an encounter radius of 5 Å. **a**  $v = 0.0005 \text{ \AA ps}^{-1}$  and **b**  $v = 0.001 \text{ \AA ps}^{-1}$ . Here MC refers to random flights simulation

times using the individual diffusion coefficients of the particles. It should be noticed that in this case no correction to the diffusion coefficient is needed for reaction with the outer surface. As previously done, the minimum of the event times is selected and the event is executed.<sup>2</sup> As seen from Figs. 9.7, 9.8, 9.9, using an encounter radius of 3, 5 and 7 Å, both the recombination and escape yield are well described in the IRT, even though there is a correlation between the escape and recombination times.

<sup>2</sup> If one particle reacts with the outer boundary, no geminate recombination can occur and consequently the second particle must also react with the outer boundary.

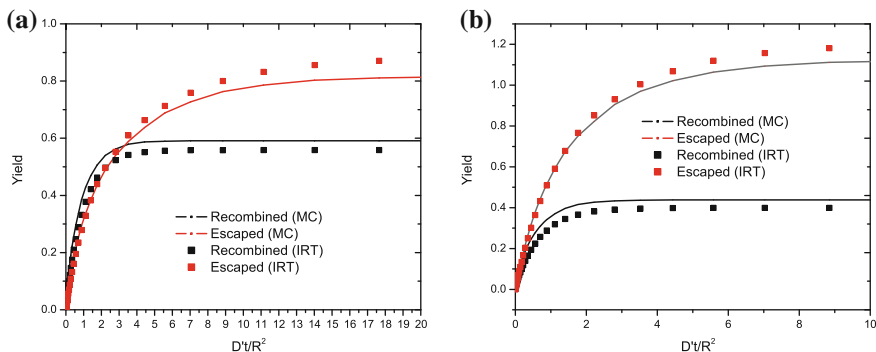


**Fig. 9.9** Reaction probability calculated using the mean reaction time and compared with random flights simulations using an outer elastic boundary and inner absorptive boundary with an encounter radius of 7 Å. **a**  $v = 0.0005 \text{ \AA ps}^{-1}$  and **b**  $v = 0.001 \text{ \AA ps}^{-1}$ . Here MC refers to random flights simulation

### 9.5.3 Scavenging of Neutral Species: Reflecting Outer Boundary

Experiments usually employ quenchers or scavengers to intercept geminate recombination in order to gain a better understanding of the chemistry (i.e. magnetic field effects, rate constants and spin dynamics) by slowing down the recombination kinetics. Analytically for a micelle containing  $m$  mobile quenchers (with the static particle at the origin), the kinetics can be described by the rate constant [12]

$$k_q = mD' \alpha_1^2 \quad (9.31)$$

with  $D'$  being the mutual diffusion coefficient and  $\alpha_1$  being the first non-trivial root of the equation  $\tan[(R - a)\alpha] = R\alpha$  (where  $a$  is the encounter radius and  $R$  the sphere radius). However, in a realistic chemical scheme the particles can be distributed anywhere inside the micelle (which can be mobile) and can contain any number of scavengers (which can also be mobile). In order to model scavenging as realistically as possible within the IRT framework, the reaction scheme of the form



was considered, where  $P_3$  and  $SP$  are the final products of recombination and scavenging respectively, and  $S$  is the scavenger. In this reaction scheme only  $P_2$  is scavengeable. In the simulation,  $P_1$  and  $P_2$  are mobile whose initial distribution is chosen to reside randomly inside the sphere. Unless otherwise stated, scavengers were made stationary with a random spatial distribution inside the sphere. Within the IRT framework, Smoluchowski's time dependent rate constant was used, whilst in the random flights simulation the scavengers were treated explicitly with no

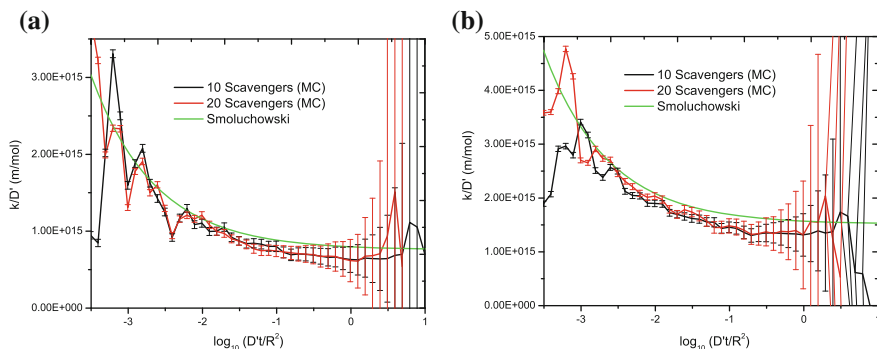


**Fig. 9.10** Rate constant for the scavenging of a particle calculated using Smoluchowski's theory and compared against a micelle with an outer reflective boundary. Scavenging and geminate encounter radii were 2 and 1 Å respectively. **a** Scavengers are stationary and **b** scavengers are mobile with diffusion coefficient of  $0.14 \text{ \AA}^2 \text{ ps}^{-1}$ . Standard error bars are shown to one standard deviation. Here MC refers to random flights simulation

assumption regarding the scavenging rate made (except for the reaction distance). In both simulations an outer reflecting boundary was used for all mobile species. Interestingly, the rate of scavenging (as shown in Fig. 9.10a) was found to be slower inside a micelle in comparison with Smoluchowski. The same was also found to be true if the scavengers were made mobile (Fig. 9.10b). A discussion for the reason why Smoluchowski's rate of scavenging is faster in comparison to scavenging inside a micelle is now presented in the next section.

### 9.5.3.1 Ordered Distances

This section presents the mathematical derivation to calculate the minimum scavenger-particle distance from the viewpoint of Smoluchowski theory to help understand discrepancy in the scavenging rate. To begin with, the probability of scavenger-particle distance  $\gamma$  to be greater than  $r$  is given by

$$\begin{aligned}
 \Pr(\gamma > r) &= \int_r^{r_{\max}} \mathfrak{S}(r) dr \\
 &= P(r_{\max}) - P(r) \\
 &= 1 - P(r)
 \end{aligned} \tag{9.34}$$

where  $\mathfrak{S}(r)$  is the probability density of the scavenger-particle distances and  $P(r)$  is its respective probability distribution function. In a volume containing  $n$  scavengers independently and identically distributed, the probability that the minimum  $\gamma$  is greater than  $r$  is equivalent to all  $\gamma > r$  such that

$$\begin{aligned}
\Pr(\gamma_{\min} > r) &= \Pr(\text{all } \gamma > r) \\
&= [P(r_{\max}) - P(r)]^n \\
&= [1 - P(r)]^n
\end{aligned} \tag{9.35}$$

Let the number of scavengers  $P_n$  have a Poisson distribution of the form

$$P_n = \frac{\mu^n}{n!} \exp(-\mu) \tag{9.36}$$

where  $\mu$  is the mean number of scavengers which is equal to  $cV$ , with  $c$  being the concentration of scavengers in a volume  $V$ . Therefore

$$\begin{aligned}
\Pr(\gamma_{\min} > r) &= \sum_{n=0}^{\infty} \frac{\mu^n}{n!} e^{-\mu} [1 - P(r)]^n \\
&= e^{-\mu} (e^{\mu(1-P(r))}) \\
&= e^{-cV P(r)}
\end{aligned} \tag{9.37}$$

The probability distribution of a typical distance is

$$\begin{aligned}
P(r) &= \frac{4\pi r^2 c(r)}{\int_0^{r_{\max}} 4\pi r^2 c(r) dr} \\
&= \frac{4\pi r^2 c(r)}{V}
\end{aligned} \tag{9.38}$$

where  $c(r)$  is the time dependent concentration of scavengers around any particle, which from Smoluchowski theory is known to be

$$c(r) = \left(1 - \frac{a}{r} \operatorname{erfc}\left(\frac{r-a}{\sqrt{4Dt}}\right)\right) c_0 \tag{9.39}$$

with  $c_0$  being the zero time concentration. Substituting the expression for  $P(r)$  from Eq. (9.38) into Eq. (9.37) gives the probability distribution of  $\gamma_{\min}$  to be

$$\Pr(\gamma_{\min} > r) = e^{-4c\pi \int_0^r r^2 c(r) dr} \tag{9.40}$$

with its respective probability density function being

$$\mathfrak{S}_{\min}(r) = 4\pi c r^2 c(r) e^{-4c\pi \int_0^r r^2 c(r) dr} \tag{9.41}$$

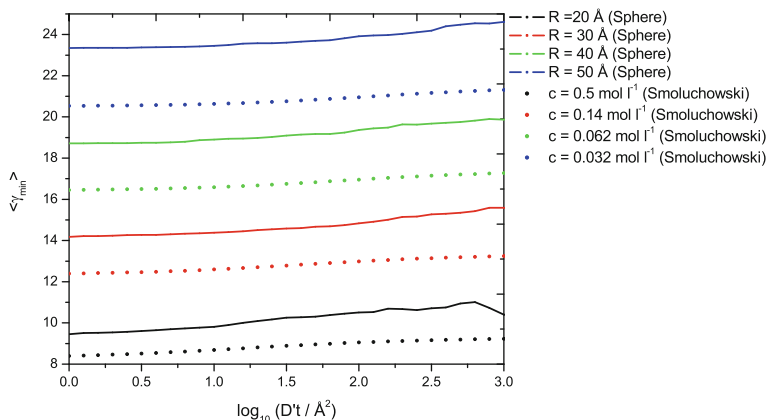


**Fig. 9.11** Mean minimum scavenger-particle distance in Smoluchowski's theory and compared against a closed micelle. 1 particle and 10 scavengers were distributed randomly with the encounter radius set to 2 Å. A diffusion coefficient of 1 Å<sup>2</sup> ps<sup>-1</sup> was used for the particle.  $\langle \gamma_{\min} \rangle$  was numerically calculated for the spherical case. All the results are presented as a function of the sphere radius. Units of the y-axis are in Å

The mean smallest scavenger-particle distance is then readily found to be

$$\langle \gamma_{\min} \rangle = \int_0^{\infty} 4\pi cr^3 c(r) e^{-4c\pi \int_0^r r^2 c(r) dr} dt \quad (9.42)$$

Figure 9.11 shows a plot of Eq. (9.42) and compared with the numerical simulation of  $\langle \gamma_{\min} \rangle$  for one particle and ten scavengers all distributed randomly, with only the particle mobile. It is clearly seen that Smoluchowski's theory places the scavengers much more closely to the particle which ultimately leads to a greater scavenging yield in comparison to a closed micelle. The next section attempts to analyse under what parameter space Smoluchowski's theory might possibly agree with the scavenging kinetics inside a micelle.

### 9.5.3.2 Analysis of the Mean Smallest Distance in Smoluchowski Theory and Inside a Sphere

In this section the probability distribution of  $\langle \gamma_{\min} \rangle$  is examined within the framework of Smoluchowski theory and inside a spherical micelle. From the previous section, it was found that in Smoluchowski theory the minimum radical-scavenger distance is smaller than that inside a spherical micelle; hence if Smoluchowski theory is used to describe scavenging inside a micelle the scavenging yield is overestimated. However, if an 'effective' concentration is used within the framework of Smoluchowski's

theory, it is hypothesised that the scavenging kinetics inside a micelle should be correctly described. This section examines the validity of such a hypothesis.

**Moments of  $\langle \gamma_{\min} \rangle$  in Smoluchowski theory** By using a simple change of variable in Eq. (9.42) such that

$$x = \frac{4}{3}\pi cr^3 \quad (9.43)$$

$$dx = 4\pi r^2 c dr \quad (9.44)$$

the  $n$  moments of the minimum scavenger particle distance in Smoluchowski's theory can be written as

$$\langle \gamma_{\min}^n \rangle = \left( \frac{3}{4\pi c} \right)^{n/3} \int_0^{\infty} x^{n/3} \exp(-x) dx \quad (9.45)$$

The integral in Eq. (9.45) can be evaluated using the definition of a gamma function to give the general expression

$$\langle \gamma_{\min}^n \rangle = \left( \frac{3}{4\pi c} \right)^{n/3} \Gamma\left(\frac{n}{3} + 1\right) \quad (9.46)$$

The corresponding expression for  $\langle \gamma_{\min} \rangle$  conditioned on  $a$  (encounter radius) is found to be

$$\langle \gamma_{\min}^n \rangle = \left( \frac{3}{4\pi c} \right)^{n/3} \Gamma\left(\frac{n}{3} + 1, \frac{4}{3}\pi ca^3\right) \quad (9.47)$$

**Mean scavenger-particle distance inside a sphere** The probability density of the distance  $r$  between two particles inside a spherical micelle of radius  $R$  was found to have the expression

$$f(r) = \frac{3r^2}{R^3} - \frac{9r^3}{4R^4} + \frac{3r^5}{16R^6} \quad (9.48)$$

The expectation distance of  $n$  particles inside a spherical micelle is then simply

$$\langle \gamma_{\min} \rangle = \int_0^{2R} [1 - F(r)]^n dr \quad (9.49)$$

with  $F(r)$  being the cumulative distribution function of Eq. (9.48).

**Comparison of the mean distance in Smoluchowski theory and inside a sphere**

Figure 9.12 shows the variation of  $\langle \gamma_{\min} \rangle$  as a function of  $a/R$  (encounter radius to radius of micelle) obtained by varying the concentration for the survival probability, which is given as

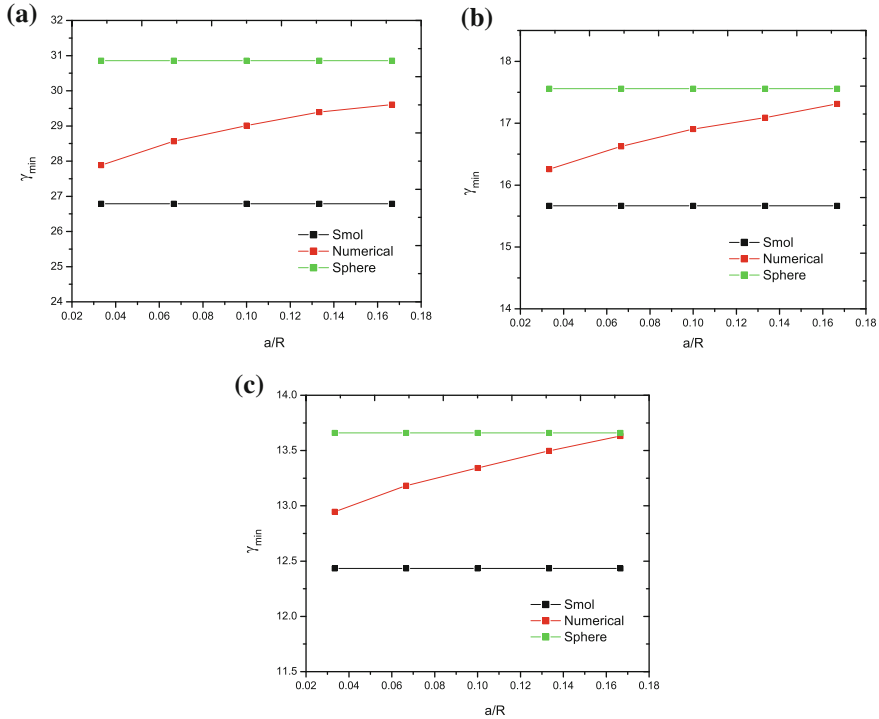


**Fig. 9.12** Variation of  $\langle \gamma_{\min} \rangle$  as a function of  $a/R$  (encounter radius to radius of micelle) at zero time. The micelle contains **a** 1 scavenger, **b** 5 scavengers and **c** 10 scavengers. Encounter distance was varied using a fixed sphere radius of 30  $\text{\AA}$ . Smol and Sphere refer to Eqs. (9.47) and (9.49) respectively. Units of y-axis are in units of  $\text{\AA}$

$$\Omega(t) = \Omega(\infty) \exp\left(-c \left[ k_{\text{smol}} t + \frac{2ck_{\text{smol}}a\sqrt{t}}{\sqrt{\pi D'}} \right]\right) \quad (9.50)$$

with  $\Omega(\infty) = \exp(-k_{\text{smol}}ct)$  where  $k_{\text{smol}}$  is Smoluchowski's steady state rate constant ( $4\pi D'a$ ). By minimising the square of errors between the actual kinetics inside a spherical micelle and that obtained using Smoluchowski's theory, an 'optimum' concentration was found for each case. Using this optimum concentration, the  $\langle \gamma_{\min} \rangle$  value was calculated using Eq. (9.47) (shown in Fig. 9.12 and marked as *Numerical*), to help understand what  $\langle \gamma_{\min} \rangle$  is required in Smoluchowski theory to obtain the correct kinetics inside a sphere. Figure 9.12 also shows the value of  $\langle \gamma_{\min} \rangle$  calculated using Eqs. (9.47) (marked as *Smol*) and (9.49) (marked as *Sphere*) with the unscaled concentration of scavengers.<sup>3</sup> As expected at small values of  $a/R$ ,  $\langle \gamma_{\min} \rangle$  value converges towards Smoluchowski's theory as the encounter radius becomes smaller. As the ratio  $a/R$  increases, the numerical  $\langle \gamma_{\min} \rangle$  approaches the spherical model since

<sup>3</sup> Error bars for the numerical value of  $\langle \gamma_{\min} \rangle$  were calculated using the Jackknife method and found to be negligible.

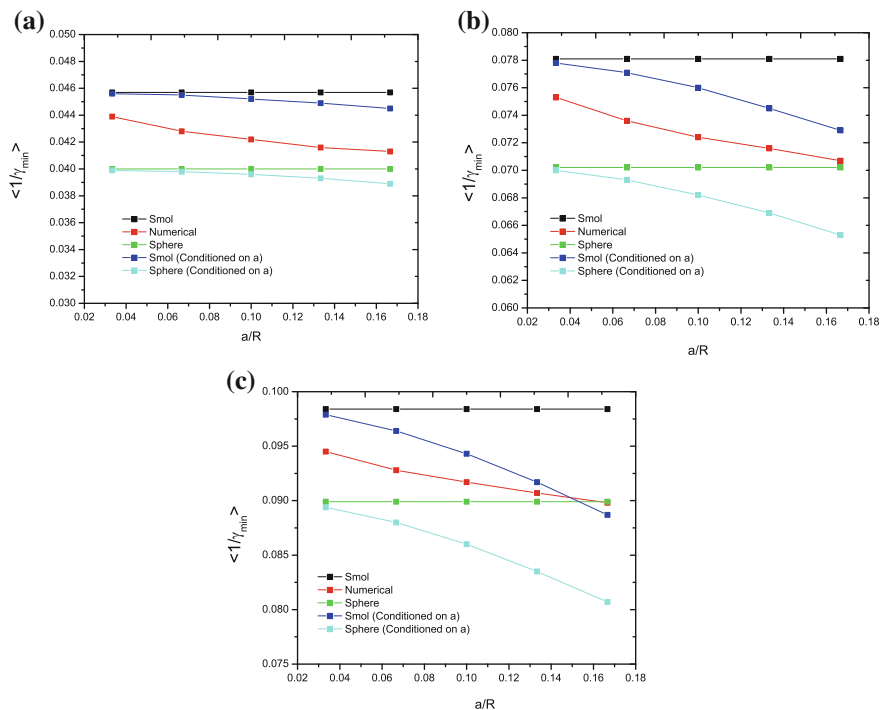


**Fig. 9.13** Variation of  $\langle 1/\gamma_{\min} \rangle$  as a function of  $a/R$  (encounter radius to radius of micelle) at zero time. The micelle contains **a** 1 scavenger, **b** 5 scavengers and **c** 10 scavengers. Encounter distance was varied using a fixed sphere radius of 30  $\text{\AA}$ .  $\langle 1/\gamma_{\min} \rangle$  conditioned on the recombination event in the spherical case was calculated numerically. Smol and Sphere refer to Eqs. (9.47) and (9.49) respectively. Units of y-axis are in units of  $\text{\AA}^{-1}$

Smoluchowski's theory places a greater distribution of scavengers around any one particle leading to a greater probability of scavenging. Hence, within the framework of Smoluchowski's theory by varying the concentration of scavengers the theory should be able to accurately reproduce the correct kinetics of scavenging inside a closed micelle. A similar trend can also be seen in Fig. 9.13 which shows the variation of  $1/\langle \gamma_{\min} \rangle$  (obtained using the same strategy as described above).<sup>4</sup>

#### 9.5.4 Modelling Scavenging Inside a Micelle: Reflecting Outer Boundary

Although the previous section has demonstrated that by using an 'effective' concentration ( $c_{\text{opt}}$ ), Smoluchowski's theory can be used to describe scavenging inside a spherical micelle, it still nonetheless requires a knowledge of  $c_{\text{opt}}$  at the start of the

<sup>4</sup> Error bars for the numerical value of  $1/\langle \gamma_{\min} \rangle$  were calculated using the Jackknife method and found to be negligible.

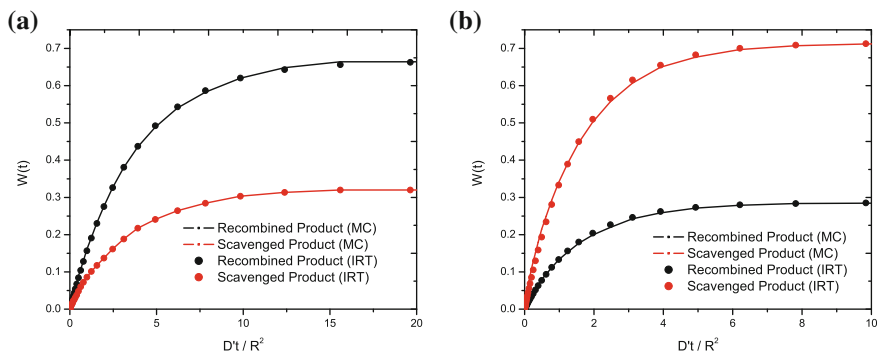


**Fig. 9.14** Scavenging and recombination probability with the two particles mobile and scavengers stationary. Encounter radius for all reactions was set to 2 Å. The micelle contained **a** 1 scavenger and **b** 5 scavengers. Here MC refers to random flights simulation

simulation. An alternative and more flexible approach to treat the scavenging process inside a spherical micelle is to generate  $N_{\text{scav}}$  independent scavenging reaction times (from Eq. 9.10), which have been corrected by using Eq. (9.30). The minimum of the scavenging times is then compared with a generated recombination time [again from Eq. (9.10)] and the corresponding event is executed. The simulation completes once all possible reactions have taken place. In the case where there is one scavengable particle and  $N$  scavengers, the probability of survival can be approximated as  $\exp(-\alpha t)^N$ , where  $\alpha$  is the mean of the process. In this case it is not necessary to generate  $N$  scavenging times, but simply generate a single scavenging time from the probability density  $N\alpha \exp(-\alpha Nt)$ . Unfortunately, this simplification cannot be applied where there are two scavengable particles since one scavenger cannot react with both scavengable particles.

Figures 9.14 shows the recombination/scavenging kinetics using various number of stationary scavengers inside the micelle which are independently and identically distributed (full results can be found in the Appendix Sect. D.1). As expected the agreement between random flights simulation and IRT is excellent. This model can be further extended to model mobile scavengers by simply scaling the mutual diffusion coefficient of the particle and the scavenger; no other modification to the aforementioned pseudo-algorithm is required. As Fig. 9.15 shows good agreement can once again be obtained (full results can be found in the Appendix Sect. D.2). A similar modelling can also be performed should the outer boundary be elastic.

## 9.6 Diffusion on the Surface of a Micelle

In this section diffusion on the surface of a micelle is modelled to verify the feasibility of the exponential approximation for the scavenging and recombination kinetics (within the IRT framework). It has been assumed in the literature that both kinetic

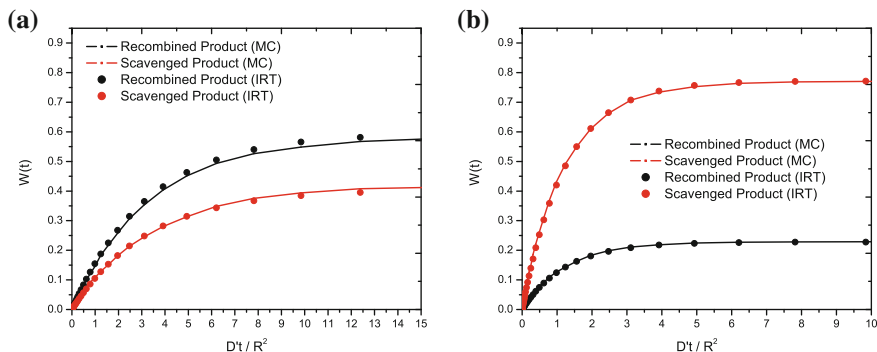


**Fig. 9.15** Scavenging and recombination probability with the scavengers and particle mobile. Scavengers were given a diffusion coefficient of  $0.05 \text{ \AA}^2 \text{ ps}^{-1}$ , and all reactions had an encounter radius of  $2 \text{ \AA}$ . The micelle contains **a** 1 scavenger and **b** 5 scavengers. Here MC refers to random flights simulation

processes follow an exponential decay process since a single pair is well described by this process, and due to the independence of reaction times, so should any number of pairs. However, there are no simulation results in the literature to support this claim. Therefore, the aim of this section is to present a set of results over a wide parameter range which tests the exponential approximation in the IRT program for a single pair and is generalised to many pairs. All values used in this section for the reaction radius are taken from Ref. [13] which are typical to model reactions on the surface of the micelle. As previously done, all IRT simulations are compared with random flights simulations to verify the independent pairs approximation. In order to model the diffusive motion on a spherical surface both the Monte Carlo random flights and IRT algorithms must first be modified for the displacement of the particle's position, which is discussed in the next two sections.

### 9.6.1 Diffusion on a Sphere: Monte Carlo Random Flights Algorithm

To model the diffusive motion on a sphere, the algorithm developed by Krauth [14] was used, in which for a fixed time step  $\Delta t$  a normally distributed 3D vector  $\xi$  of mean zero and standard deviation of one is generated. At every  $\Delta t$  the vector  $\xi$  is made orthogonal to  $x$  (3D vector containing the Cartesian coordinates of the particle's position on the unit sphere) and normalised to unit length, such that

$$\bar{\xi} = \xi - (\xi \cdot x)x \quad (9.51)$$

$$\xi_{\text{ort}} = \frac{\bar{\xi}}{|\bar{\xi}|} \quad (9.52)$$

with  $(\cdot)$  denoting the dot product of the two vectors. The vector  $\xi_{\text{ort}}$  defines the direction of the particles displacement. The new set of coordinates defining the position of the particle ( $x'$ ) is then given as

$$x' = \frac{x + \delta \xi_{\text{ort}}}{|x + \delta \xi_{\text{ort}}|} \quad (9.53)$$

where  $\delta$  is a normally distributed random number with zero mean and a standard deviation  $\sigma = 2\sqrt{D' \Delta t}/R^2$ , with  $D'$  being the diffusion coefficient of the particle and  $R^2$  the square of sphere radius.

### 9.6.2 Diffusion on a Sphere: IRT Algorithm

The relative diffusion equation for two particles (one static and the other mobile) evolves under the influence of an angular diffusion equation of the form

$$\frac{\partial p}{\partial t} = \frac{D'}{R^2} \left[ \frac{1}{\sin \theta} \frac{\partial}{\partial \theta} \left( \sin \theta \frac{\partial p}{\partial \theta} \right) + \frac{1}{\sin^2 \theta} \frac{\partial^2 p}{\partial \phi^2} \right] \quad (9.54)$$

with  $D'$  being the mutual diffusion equation and  $r$  the radius of the sphere. The right hand side of the above equation is simply the angular part of the Laplacian operator expressed in spherical polar coordinates. It should be noticed that the problem of the relative diffusion of a pair is mathematically identical to that of the diffusion of a single particle. Reaction occurs as soon as two particles approach one another within a certain distance on the sphere. As all the points on the sphere are geometrically equivalent, the position of the fixed particle will not influence the kinetics. If one of the particles are fixed at the pole, then the critical angle for reaction is simply an angle of colatitude, and the relative longitude of the particle is of no significance. The density of the longitude  $\phi$  is uniform and equal to  $1/2\pi$  (all great circles have the same circumference), however, the density of the angle of colatitude is not uniform and is given by  $\sin(\theta/2)$ . The relative density is thus independent of  $\phi$  at all times, with the diffusion equation now given by the first term in Eq. (9.54). A final simplification can be performed by a simple change of variable  $z = \cos \theta$ , to give

$$\frac{\partial p}{\partial t} = \frac{D'}{R^2} \frac{\partial}{\partial z} \left( (1 - z^2) \frac{\partial p}{\partial z} \right) \quad (9.55)$$

The required boundary condition is that of Smoluchowski (i.e. particles react instantly on encounter at a critical value  $\zeta$ ) such that

$$p(z = \zeta, t) = 0 \quad (9.56)$$

The initial boundary condition in the transformed coordinate is

$$p(z, t = 0) = \frac{1}{2} \quad (9.57)$$

Using the method of separation of variables, N. J. B. Green (unpublished) has obtained the general solution for the survival probability  $\Omega(t)$  to be

$$\Omega(t) = \sum_i F_i \exp(-v_i(1 + v_i)\tau) \quad (9.58)$$

with  $v_i = \frac{1}{2}(\sqrt{1 + 4\kappa} - 1)$ ,  $\kappa$  being the constant of the separation of variables. The only compatible values for  $v_i$  are those where the Legendre function of the first kind  $P_v(a)$  is zero.  $\tau = D't/R^2$ , which is the natural dimensionless timescale and  $F_i$  is defined to be [15]

$$F_i = \frac{\left[ \int_a^1 P_{v_i}(z) dz \right]^2}{(1 - a) \left[ \int_a^1 P_{v_i}(z) dz \right]^2} \quad (9.59)$$

which can be approximated as [15]

$$F_i \approx \frac{(1 + a)[P_{v_i}^{-1}]^2 \pi^2 (v_i + 1/2)}{\pi^2 - 2 \sin^2(v_i \pi) \psi'(v_i + 1)} \quad (9.60)$$

with  $\psi'$  being the trigamma function. Hence, for a given radical pair with one static at the pole and the other diffusing with the mutual diffusion coefficient, the rate of reaction can be approximated using only the first root as

$$k = \frac{D'}{R^2} v_0 (v_0 + 1) \quad (9.61)$$

where the location of  $v_0$  can be approximated (subject to the constraint that  $a$  is in the vicinity of  $-1$ ) as

$$v_0 \approx \frac{1}{2 \ln(2/\pi - \cos^{-1} a)} \quad (9.62)$$

**One particle and  $n$  scavengers** In the first set of simulations, the scavengers were distributed randomly on the spherical surface (which were made mobile), whilst the particle was fixed at the south pole (which was made stationary). Figure 9.16 shows that the exponential approximation is excellent in describing the scavenging kinetics across the parameter space investigated. The exponential approximation can

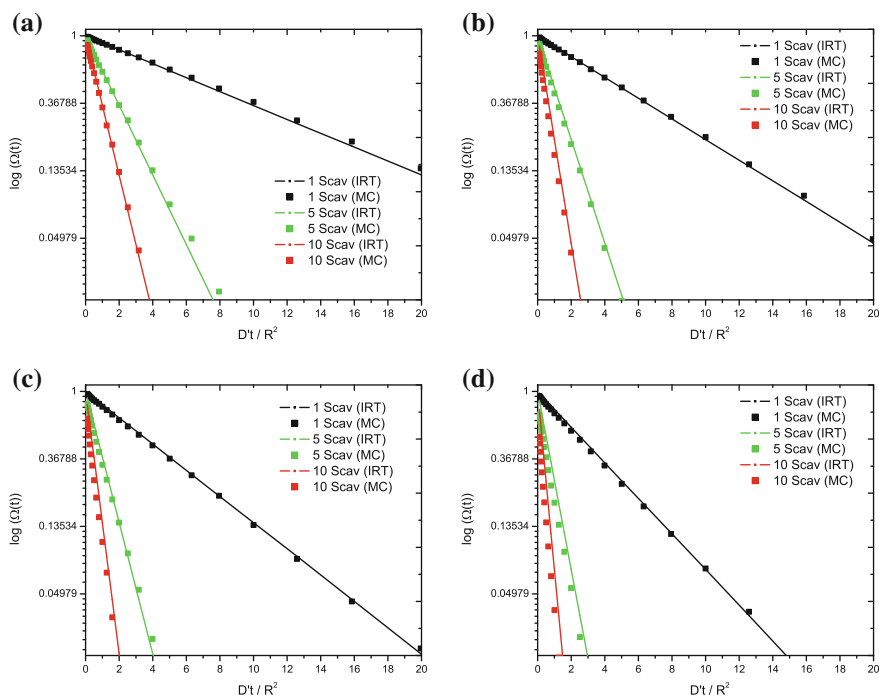


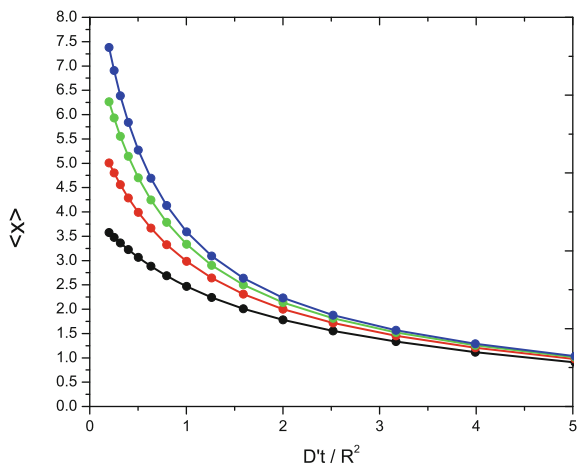
**Fig. 9.16** Survival probability for a single particle (stationary at the south pole) using a different number of scavengers. Scavengers were distributed randomly on the spherical surface. Reaction at a critical value: **a**  $\zeta = -0.99995$ , **b**  $\zeta = -0.99875$ , **c**  $\zeta = -0.995$  and **d**  $\zeta = -0.98$ . Here MC refers to random flights simulation

be generalised in the IRT algorithm to model the scavenging kinetics of  $n$  particles by a simple extension of the one particle and one scavenger case, using the independent pairs approximation.

**Random walk of  $n$  particles** The second set of simulations generalises the algorithm for a single pair on a spherical surface to  $n$  identically distributed radicals on a spherical surface. The simulation is only completed once all the particles have recombined to form stable products. This chemical process has a profound importance in astrophysics and astrochemistry [16, 17], where the bulk formation of molecular hydrogen is thought to occur on interstellar dust grains.<sup>5</sup> In the literature, the recombination process of molecular hydrogen is usually modelled either from a stochastic view point (i.e. random flights simulations[18–21]) or by using the deterministic approach (Master Equation [22, 23]) which solves a set of coupled ordinary differential equations. Both methods have limitations and cannot compare with the flexibility the IRT algorithm has to offer. For example, introducing a more complex

<sup>5</sup> Molecular  $H_2$  cannot form efficiently enough in the gas phase to account for experimental observations.

**Fig. 9.17** Survival yield  $\langle x \rangle$  using 4 (black), 6 (red), 8 (green) and 10 (blue) mobile particles randomly distributed on a unit sphere. Reaction distances relative to the sphere radius  $R$  was  $0.01 R$ . Solid line and circle correspond to analytical calculation and IRT simulation respectively



reaction scheme where some events occur randomly (such as scavenging), would make the Master Equation technique redundant, whilst simulating a larger number of particles will greatly increase the computational time required for random flights simulations.

To ensure firstly that the recombination kinetics was accurately modelled in the IRT framework, the IRT simulation was compared with the analytical expression [24] as obtained by McQuarrie

$$\langle x \rangle = - \sum_{n=2}^{x_0} A_n T_n(t) \quad (9.63)$$

where  $\langle x \rangle$  is the average surviving particles and  $x_0$  the initial number of particles. The coefficients  $A_n$  and  $T_n$  are defined as

$$A_n = \frac{1 - 2n}{2^n} \left[ \frac{\Gamma(x_0 + 1) \Gamma[(x_0 - n + 1)/2]}{\Gamma[(x_0 - n + 1)] \Gamma[(x_0 + n + 1)/2]} \right] \quad (9.64)$$

$$T_n = \exp \left[ -\frac{1}{2} kn(n-1)t \right] \quad (9.65)$$

with  $k$  representing the rate of recombination which is given by Eq. (9.61),  $\Gamma(x)$  is the gamma function and  $n = 2, 4, \dots$ . As seen from Fig. 9.17, both the analytical expression and the IRT produced the same recombination kinetics, which provided the necessary assurance that the IRT algorithm was properly modelling diffusion on a spherical surface.

The second set of simulations involved testing the recombination kinetics of  $n$  particles using the IRT and comparing with random flights simulations using different values for the encounter radius. Figure 9.18 shows that the IRT algorithm accurately

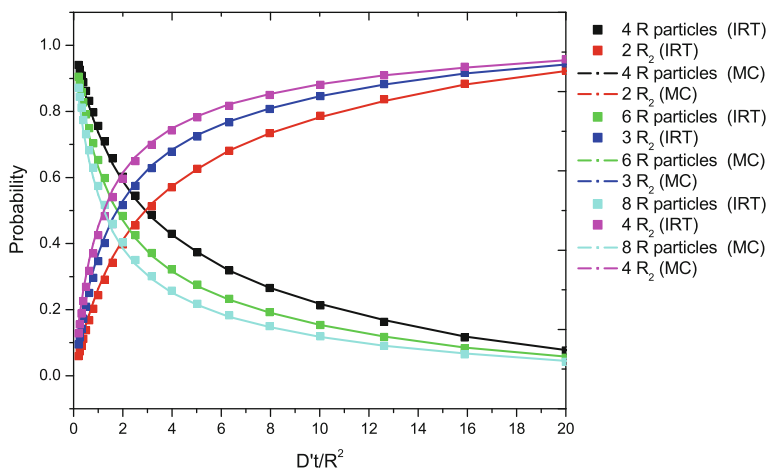


**Fig. 9.18** Survival and recombination probability using 4, 6 and 8 mobile particles randomly distributed on a unit sphere using a reaction distance (relative to the sphere radius  $R$ ) of  $a = 0.01R$ . Here MC refers to random flights simulation

describes the recombination kinetics on a spherical surface using the simple exponential approximation for the case when (i) one particle is fixed and  $n$  scavengers are mobile; (ii) when both the particle and scavengers are mobile and (iii) when  $n$  identical particles are mobile and can recombine with each other (further results can be found in the Appendix Sect. D.3). Obviously, the fast transient period which arises before steady state conditions is not well defined in the IRT. However from the analytical formulation given in Eq. (9.58) it is possible to correctly describe the transient kinetics by generating a uniformly distributed random number  $U(0, 1]$  and finding the value of  $F_i$  such that  $\sum_i F_i > U(0, 1]$ . The corresponding value of  $v_i$  at index  $i$  is then used to calculate the corresponding rate. In the next section, this basic model will be further developed to allow simulation of a more complex chemical system, which involves association and dissociation from the micellar surface.

## 9.7 Reversible Reactions in the IRT Model

A more realistic application of the developed algorithm is for a solute particle to dissociate from the micelle surface and diffuse to the bulk solution. The dissociated particle can then undergo reaction either in the bulk solution or return back to the micelle surface and undergo reaction. This kinetic model has an important application in micelle surface chemistry and reaction kinetics in micellar solutions [25], which serves as the main motivation behind developing such a model within the IRT framework. As previous simulations, all values used in this section for the reaction

radius are taken from Ref. [13] which are typical to model reactions on the surface of the micelle.

Treating reversible reactions within the random flights framework is relatively straightforward since the trajectories of all diffusing particles are tracked. However, within the IRT model if the association reaction is assumed diffusion controlled, then dissociation ultimately never takes place since the encountering pair is formed in contact and react infinitely fast. N. J. B. Green (unpublished) have resolved this error by using a finite reaction on encounter (employing the radiation boundary condition). This ensures that the microscopic rates of barrier crossing in the forward and reverse directions are balanced according to the principle of detailed balance.

The first reaction scheme to be modelled considers a number ( $n$ ) of P particles on the micellar surface which can recombine to form  $P_2$ . More formally stated



The second reaction scheme models the association/dissociation of the P particles to and from the micellar surface. The reaction scheme takes the form



As the position of the adsorbed P on the micelle is not important (since the rate of reaction on the micellar surface is the same at all points), this greatly reduces the complexity of implementing the reaction scheme within the IRT framework, such that no explicit values for  $\phi$  and  $\theta$  are required to describe the kinetics.

**IRT event times** In order to implement this model in the IRT framework, three event times need to be generated from the correct marginal distribution functions to represent the processes: (i) reaction on the surface of the micelle; (ii) escape from the surface and (iii) adsorption back to the micellar surface from the bulk solution. The reaction time for recombination on the surface can readily be generated by employing the pseudo first-order rate constant ( $k$ ) as given in Eq. (9.61) and sampling from the exponential distribution of the form

$$T_{\text{recom}} = -\frac{(\ln U(0, 1])}{k} \quad (9.68)$$

with  $U(0, 1]$  being a uniformly distributed random number between zero and one. The event time to model the escape of the P particle from the micelle surface to the bulk solution can also be generated using Eq. (9.68), using instead the rate constant for the dissociation from the micellar surface  $k_{\text{diss}}$ . The reaction probability for partially diffusion controlled reactions was shown in Sect. 5.3.2 to be

$$W(r, t) = \frac{a}{r} \frac{k_{\text{act}}}{k_{\text{act}} + k_D} \left( \text{erfc}(y) - \exp(x^2 + 2xy) \text{erfc}(x + y) \right) \quad (9.69)$$

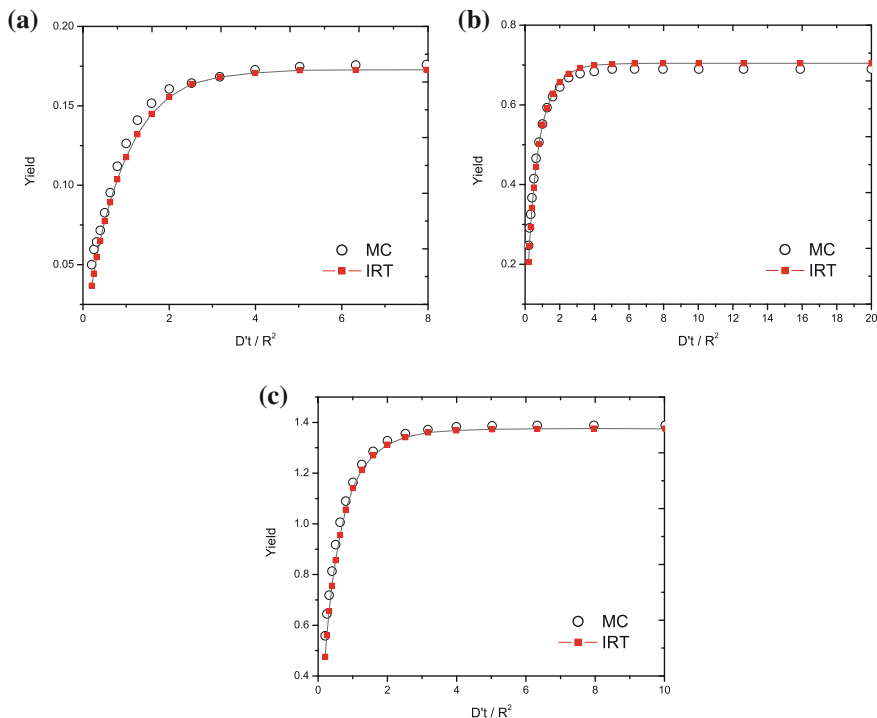


**Fig. 9.19** Recombination probability using **a** 2, **b** 4 and **c** 6 P particles on the spherical surface. A dissociation rate ( $k_{\text{diss}}$ ) of  $0.1 \text{ ps}^{-1}$  was used together with a surface reactivity ( $v/a$  with  $a$  being the encounter distance of the micelle and particle) for the micellar surface of  $0.01 \text{ ps}^{-1}$ . Encounter distance for all reactions on the spherical surface of radius  $R$  was  $a = 0.1R$ . Here MC refers to random flights simulation

where  $y = (r - a)/\sqrt{4D't}$  with  $r$  being the initial separation distance of the pair and  $a$  is the encounter radius.  $x = (1 + k_{\text{act}}/k_{\text{smol}})\sqrt{D't/a^2}$ , with  $k_{\text{act}} = 4\pi a^2 v$  being the rate of association and  $v$  the boundary reactivity.  $k_{\text{smol}}$  is Smoluchowski's steady state rate constant ( $4\pi D'a$ ). Unfortunately, generating a reaction time from Eq. (9.69) must be done numerically for every value of  $r$ , making the method computationally inefficient. However, for reversible reactions, in which the pairs are repeatedly generated at  $a$ , Eq. (9.69) can be simplified to

$$W(a, t) = \frac{k_{\text{act}}}{k_{\text{act}} + k_{\text{smol}}} \left( 1 - \exp(x^2) \text{erfc}(x) \right) \quad (9.70)$$

Hence, in order to generate the event time for the adsorption of P back to the micellar surface ( $T_{\text{esc}}$ ), it is necessary to generate a reaction time with the probability distribution of Eq. (9.70). This can be generated using the algorithm proposed by N. J. B. Green (unpublished), which generates a reaction time from the exponential error distribution as follows:

1. Generate a uniform random number  $U_1(0,1]$  between 0 and 1.
2. If  $U_1(0,1] > (k_{\text{act}}/(k_{\text{act}} + k_{\text{smol}}))$ , the P particle never adsorbs on the surface of the micelle.
3. Otherwise generate a uniformly distributed random number  $N(0,\sqrt{2})$ . Let  $Y = |N(0,\sqrt{2})|$ .
4. Generate a second uniform random number  $U_2$  between 0 and 1 and calculate  $X = -(\ln U_2)/Y$ .
5. Calculate  $T_{\text{esc}} = (Xa)^2/D'$ .

In the simulation, the adsorption on the micellar surface is controlled through the parameter  $v$ . If the P particle is not adsorbed, it diffuses back to the bulk solution as if the boundary were reflecting.

The first step in the analysis involved checking the recombination yield for different number of P particles randomly distributed on a spherical surface using a dissociation rate of  $0.1 \text{ ps}^{-1}$ . From the simulation results presented in Fig. 9.19, both the IRT and random flights results show the same recombination yield for the set of parameters chosen. In order to thoroughly test the algorithm, a wide parameter range was sampled to ensure that no bias was introduced within the IRT framework. The three parameters which most influence the kinetics are (i) the encounter distance on the spherical surface; (ii) rate of association (via the surface reactivity parameter) and (iii) the rate of dissociation. A sample of the results for the recombination probability for each case are shown in the Appendix (Sects. D.4–D.6). In all cases, no significant deviations are noticed in the IRT simulation.

The model developed in this section can easily be generalised to simulate a bulk solution which contains any number of micelles, which in turn contains any number of P particles. Modelling such complex chemical systems in the IRT has not been previously realised, especially for confined systems such as micelles.

## 9.8 Conclusion and Further Work

Through the use of new simulation techniques this chapter has shown that: (i) the recombination kinetics for randomly distributed particles inside the sphere can be corrected by using an ‘effective’ mutual diffusion coefficient. This is found true for complex systems where the micelle can undergo breakage and the particle can escape to the bulk solution. Both scavenging and recombination can be accurately treated using this ‘effective’ mutual diffusion coefficient. (ii) The exponential approximation is valid in modelling the recombination kinetics on the surface of the micelle, with good agreement found with full random flights simulations. (iii) The complex diffusive motion where a solute particle can undergo association and dissociation from the micellar surface can be modelled completely within the IRT framework. Such systems have been previously investigated using random flights simulations, however, with this extension to the IRT algorithm much better statistics can be obtained through the use of many more realisation.

This work has demonstrated that for confined systems such as micelles the IRT algorithm can be used with reasonable accuracy. As mentioned previously, the main motivation of using the IRT is due to the speed and flexibility it offers, as essentially introducing more particles into the reaction scheme does not greatly slow down the algorithm. This is not true for the random flights simulation, where the introduction of a single particle requires a trace of its trajectory. In addition, the IRT does not suffer from time step problems and requires no implementation of a Brownian bridge, making its implementation for confined systems relatively straightforward.

Through the other advances made in the IRT algorithm (as described in Chap. 4 of this work), the micelle model can now be extended to model (i) partially diffusion controlled reactions on a spherical surface, (ii) ionic species and (iii) explicit treatment of spin dynamics. Further work in this area would include investigating whether: (i) the increased scavenging rate of ions is observed in micelles (i.e. whether the correlation between the scavenging and recombination times is still applicable) and (ii) whether cross-recombination between spin correlated radical pairs in micelles accelerates  $T_1$  spin-relaxation due to the Einstein-Rosen-Podolsky effect.

## References

1. P.P. Infelta, M. Gratzel, J.K. Thomas, *J. Phys. Chem.* **78**, 190 (1974)
2. M.A.J. Rodgers, M.F. da Silva, E. Wheeler, *Chem. Phys. Lett.* **53**, 165 (1978)
3. Y. Waka, K. Hamamoto, N. Mataga, *Chem. Phys. Lett.* **53**, 242 (1978)
4. S.S. Atik, L.A. Singer, *Chem. Phys. Lett.* **59**, 519 (1978)
5. M. Tachiya, *Chem. Phys. Lett.* **33**, 289 (1975)
6. A. Yekta, M. Aikawa, N.J. Turro, *Chem. Phys. Lett.* **63**, 543 (1979)
7. R.C. Dorrance, T.F. Hunter, *J. Chem. Soc. Faraday Trans.* **63**, 1312 (1979)
8. H.J. Pownall, L.C. Smith, *J. Am. Chem. Soc.* **95**, 3136 (1973)
9. U. Khuanga, B.K. Selinger, R. McDonald, *Aust. J. Chem.* **29**, 1 (1976)
10. U. Gosele, U.K.A. Klen, M. Hauser, *Chem. Phys. Lett.* **68**, 291 (1979)
11. C.D. Bruce, M.L. Berkowitz, L. Perera, M.D.E. Forbes, *J. Phys. Chem.* **84**, 1853 (1980)
12. M. Tachiya, *Chem. Phys. Lett.* **69**, 605 (1980)
13. H. Sano, M. Tachiya, *J. Chem. Phys.* **75**, 2870 (1981)
14. W. Krauth, *Statistical Mechanics: Algorithms and Computations* (Oxford University Press, Oxford, 2007)
15. A. Erdelyi, W. Magnus, F. Oberhettinger, F.G. Tricomi, *Higher Transcendental Functions*, vols. I, II, III. (McGraw-Hill, New York, 1953)
16. E. Herbst, *Chem. Soc. Rev.* **30**, 168 (2001)
17. D.A. Williams, S. Viti, *Annu. Rep. Prog. Chem. Sect.* **98**, 87 (2002)
18. A.G.G.M. Tielens, L.J. Allamandola, *Interstellar Processes* (Reidel, Dordrecht, 1987)
19. A.G.G.M. Tielens, S.B. Charnley, *Origins Life Evol. Biosphere* **27**, 23 (1997)
20. A.G.G.M. Tielens, S.B. Charnley, S.D. Rodgers, *Astro. J.* **482**, L203 (1997)
21. S.B. Charnley, *Astro. J.* **509**, L121 (1998)
22. D.P. Ruffle, E. Herbst, *Mon. Not. R. Astron. Soc.* **319**, 837 (2000)
23. N.J.B. Green, T. Toniazzo, M.J. Pilling, D.P. Ruffle, N. Bell, T.W. Hartquist, *Astron. Astrophys.* **375**, 1111 (2001)
24. D.A. McQuarrie, *J. Appl. Prob.* **4**, 413 (1967)
25. M. Tachiya, *Can. J. Phys.* **68**, 979 (1990)

# Appendix A

## Theoretical Details

### A.1 Diffusion Centre of Mass (See Sect. 6.3.4)

If the positions of two particles are denoted  $\mathbf{X}_1$  and  $\mathbf{X}_2$  with diffusion coefficients  $D_1$  and  $D_2$  respectively, the interparticle vector  $\mathbf{R}$  is a linear combination of  $\mathbf{X}_1$  and  $\mathbf{X}_2$  as

$$\mathbf{R} = \mathbf{X}_2 - \mathbf{X}_1 \quad (\text{A.1})$$

We wish to find another linear combination vector  $\mathbf{S}$  such that the vectors  $\mathbf{R}$  and  $\mathbf{S}$  diffuse independently (which are made independent via the parameter  $\alpha$ ).

$$\mathbf{S} = \alpha\mathbf{X}_2 + \mathbf{X}_1 \quad (\text{A.2})$$

As a three dimensional normal distribution is spherically symmetric, the three directions of the Cartesian coordinates are independent. The components of the vector  $\mathbf{X}$  can be incremented with a given standard deviation ( $\sigma_i$ ) and a normally distributed random number  $N(0, 1)$ , with mean 0 and variance 1 as

$$x_t = x'_t + \sigma_i N_i \quad (\text{A.3})$$

where  $\sigma_i = \sqrt{2D'_i}$ . The covariance of the vector  $\mathbf{X}_i$  and  $\mathbf{X}'_i$  in the  $x$ -direction is

$$\text{cov}(x_1 - x_2, x_1 + \alpha b_{x_2}) = ((\sigma_1 N_1 - \sigma_2 N_2)(\sigma_1 N_1 - \alpha\sigma_2 N_2)) \quad (\text{A.4})$$

The above expression can be simplified by recognising that  $\mathbb{E}[\sigma_1^2 N_1^2] = \sigma_1^2 \mathbb{E}[N_1^2] = \sigma_1^2$ , since the  $\mathbb{E}[N_1^2] = 1 + \mathbb{E}[N_1]^2$ , with  $\mathbb{E}[N_1] = 0$ . A similar expression can be obtained for  $\langle \alpha\sigma_2^2 N_2^2 \rangle$ . Hence Eq. (A.4) simplifies to

$$\text{cov} = \sigma_1^2 - \alpha\sigma_2^2 \quad (\text{A.5})$$

which gives the value for  $\alpha = \sigma_1^2/\sigma_2^2$ . The centre of diffusion of the vector  $\mathbf{S}$  is then simply

$$\mathbf{C} = \frac{\alpha \mathbf{X}_2 + \mathbf{X}_1}{\alpha + 1} \quad (\text{A.6})$$

$$= \frac{\left(\frac{D_1}{D_2}\right) \mathbf{X}_2 + \mathbf{X}_1}{\left(\frac{D_1}{D_2}\right) + 1} \quad (\text{A.7})$$

$$= \frac{D_1 \mathbf{X}_2 + D_2 \mathbf{X}_1}{D_1 + D_2} \quad (\text{A.8})$$

## A.2 Survival Probability: Diffusion in the Interval $[a, b]$ with Two Absorbing Boundaries (See Sect. 4.6.1)

The backward diffusion equation is of the form

$$\frac{\partial \Omega}{\partial t} = \frac{D'}{r} \frac{d^2}{dr^2} (\Omega r) \quad (\text{A.9})$$

with  $r$  being the separation distance and  $D'$  being the mutual diffusion coefficient. Taking the Laplace transform of Eq. (A.9) and multiplying through by  $\frac{r}{D'}$  gives

$$\frac{s \tilde{\Omega} r}{D'} - \frac{r}{D'} = \frac{d^2}{dr^2} (\tilde{\Omega} r) \quad (\text{A.10})$$

with  $\tilde{\Omega}(r)$  representing the Laplace transform of  $\Omega(r)$  and  $s$  being the Laplace transform variable. Letting  $f$  represent  $\tilde{\Omega} r$ , Eq. (A.10) can be rewritten as

$$\frac{d^2 f}{dr^2} - \frac{s f}{D'} = -\frac{r}{D'} \quad (\text{A.11})$$

which can be solved to provide the general solution

$$f = A e^{-r \sqrt{\frac{s}{D'}}} + B e^{r \sqrt{\frac{s}{D'}}} + \frac{r}{s} \quad (\text{A.12})$$

Substituting back the definition for  $f$  into Eq. (A.12) gives

$$\tilde{\Omega}(r, s) = \frac{A e^{-r \sqrt{\frac{s}{D'}}}}{r} + \frac{B e^{r \sqrt{\frac{s}{D'}}}}{r} + \frac{1}{s} \quad (\text{A.13})$$

The arbitrary constant  $A$  and  $B$  in Eq. (A.12) can be solved using matrices by setting  $r = a$  and  $r = b$ , to give two coupled equations of the form

$$-\frac{a}{s} = Ae^{-a\gamma} + Be^{a\gamma} \quad (\text{A.14})$$

$$-\frac{b}{s} = Ae^{-b\gamma} + Be^{b\gamma} \quad (\text{A.15})$$

where  $\gamma = \sqrt{\frac{s}{D}}$ . Equations (A.14) and (A.15) can be re-expressed in matrix notation to give

$$\begin{pmatrix} -a/s \\ -b/s \end{pmatrix} = \begin{pmatrix} e^{-a\gamma} & e^{a\gamma} \\ e^{-b\gamma} & e^{b\gamma} \end{pmatrix} \begin{pmatrix} A \\ B \end{pmatrix} \quad (\text{A.16})$$

Inverting the matrix gives

$$\begin{pmatrix} A \\ B \end{pmatrix} = \frac{1}{2s \sinh(b-a)\gamma} \begin{pmatrix} -ae^{b\gamma} + be^{a\gamma} \\ ae^{-b\gamma} - be^{-a\gamma} \end{pmatrix} \quad (\text{A.17})$$

From Eq. (A.17), the coefficients  $A$  and  $B$  are found to be

$$\begin{aligned} A &= \frac{-ae^{b\gamma} + be^{a\gamma}}{2s \sinh(b-a)\gamma} \\ B &= \frac{-ae^{-b\gamma} - be^{-a\gamma}}{2s \sinh(b-a)\gamma} \\ \tilde{\Omega}(r, s) &= \frac{-ae^{(b-r)\gamma} + be^{(a-r)\gamma}}{2sr \sinh(b-a)\gamma} + \frac{-ae^{(r-b)\gamma} + be^{(r-a)\gamma}}{2sr \sinh(b-a)\gamma} + \frac{1}{s} \\ \tilde{\Omega}(r, s) &= -\frac{a \sinh(b-r)\gamma}{sr \sinh(b-a)\gamma} - \frac{b \sinh(r-a)\gamma}{sr \sinh(b-a)\gamma} + \frac{1}{s} \end{aligned} \quad (\text{A.18})$$

### A.3 Probability of Hitting One Absorbing Boundary Before the Other in the Interval $[a, b]$ (See Sect. 4.6.4)

The steady state backward diffusion equation takes the form

$$\frac{\partial^2 p}{\partial r^2} + \frac{2}{r} \frac{\partial p}{\partial r} = 0$$

where  $p$  is the probability of hitting the boundary. Setting  $y = \frac{\partial p}{\partial r}$  in the above equation gives

$$\begin{aligned}\frac{dy}{dr} + \frac{2y}{r} &= 0 \\ \therefore y &= \frac{A}{r^2}\end{aligned}\tag{A.19}$$

Substituting back the definition of  $y$  and isolating for  $p$  gives

$$p = B - \frac{A}{r}\tag{A.20}$$

Applying the inner boundary condition ( $p(a) = 0$ ) gives  $B = \frac{A}{a}$ . Similarly using the second boundary condition such that  $p(b) = 1$ , the coefficient  $A$  is obtained as follows

$$\begin{aligned}p &= A \left( \frac{1}{a} - \frac{1}{r} \right) \\ p(b) &= A \left( \frac{1}{a} - \frac{1}{b} \right) = 1 \\ \therefore A &= \frac{ab}{b-a}\end{aligned}\tag{A.21}$$

On substituting back the definition of  $A$  and  $B$ , the probability of exiting at the upper boundary  $b$  is

$$P_b = \frac{b(b-a)}{r(r-a)}\tag{A.22}$$

Similarly, using the boundary condition  $p(a) = 1$  and  $p(b) = 0$  the probability of exiting at the lower boundary is

$$P_a = \frac{a(b-r)}{r(b-a)}\tag{A.23}$$

#### A.4 Transition Density for an Unrestricted 1D Wiener Process (See Sect. 2.3.2.1)

The Laplace transform of the forward diffusion equation is known to be

$$D' \frac{\partial^2 \tilde{p}}{\partial y^2} - s \tilde{p} = -\delta(y-x)\tag{A.24}$$

with the initial condition being  $\delta(y-x)$ . There are no boundaries, but the transition density must approach zero at infinity in both directions. Hence the required lower boundary is of the form  $q_1 = e^{y\sqrt{s/d}}$  and the upper boundary is similarly

$q_2 = e^{-y\sqrt{s/D}}$ . The Wronskian (defined as  $q_1q_2' - q_2q_1'$ ) is found to be  $-2\sqrt{\frac{s}{D}}$ , with the Green's function being

$$G(y, z) = \begin{cases} \frac{1}{\sqrt{4sD'}} e^{-(y-z)\sqrt{s/D'}} & z \leq y \\ \frac{1}{\sqrt{4sD'}} e^{-(z-y)\sqrt{s/D'}} & z \geq y \end{cases} \quad (\text{A.25})$$

which can be written in compact form as  $G(y, z) = \frac{1}{\sqrt{4sD'}} e^{-|y-z|\sqrt{s/D'}}$ . The Laplace transform of the transition density is then simply integrating over the source as

$$\tilde{p}(x, y, s) = \frac{1}{\sqrt{4sD'}} \int_{-\infty}^{\infty} e^{-|y-z|\sqrt{s/D'}} \delta(y-x) dy \quad (\text{A.26})$$

$$= \frac{1}{\sqrt{4sD'}} e^{-|y-x|\sqrt{s/D'}} \quad (\text{A.27})$$

The inverse of the above Laplace transform to the time domain is then

$$p(x, y, t) = \frac{1}{\sqrt{4\pi D't}} e^{-(y-x)^2/4D't} \quad (\text{A.28})$$

An analogous equation can be found with a drift velocity  $\mu$  as

$$p(x, y, t) = \frac{1}{\sqrt{4\pi D't}} e^{-(y-x-\mu t)^2/4D't} \quad (\text{A.29})$$

### A.5 Transition Density for a 1D Wiener Process with an Absorbing Inner Boundary (See Sect. 2.3.2.1)

The transition density for a diffusion process with an inner absorbing boundary can be derived using the same strategy as above. Using Eq. (A.24) together with the complementary functions  $y_1 = \sinh((y-a)\sqrt{s/D'})$  and  $y_2 = e^{-y\sqrt{s/D'}}$ , the Wronskian is found to be  $-\sqrt{s/D'} e^{-a\sqrt{s/D'}}$ . The Green's function is then

$$G(y, z) = \begin{cases} \frac{1}{\sqrt{sD'}} \sinh((z-a)\sqrt{s/D'}) e^{-(y-a)\sqrt{s/D'}} & z \leq y \\ \frac{1}{\sqrt{sD'}} \sinh((y-a)\sqrt{s/D'}) e^{-(z-a)\sqrt{s/D'}} & z \geq y \end{cases} \quad (\text{A.30})$$

which can be rewritten as

$$G(y, z) = \frac{1}{\sqrt{4sD'}} (e^{-|y-z|\sqrt{s/D'}} - e^{-(y+z-2a)\sqrt{s/D'}}) \quad (\text{A.31})$$

The Laplace transform of the transition density is then

$$\tilde{p}(x, y, s) = \frac{1}{\sqrt{4sD'}} (e^{-|y-x|\sqrt{s/D'}} - e^{-(y+x-2a)\sqrt{s/D'}}) \quad (\text{A.32})$$

whose inverse then gives

$$p(x, y, t) = \frac{1}{\sqrt{4\pi D't}} (e^{-(y-x)^2/4D't} - e^{-(y+x-2a)^2/4D't}) \quad (\text{A.33})$$

An analogous equation can be found with a drift velocity  $\mu$  as

$$p(x, y, t) = \frac{1}{\sqrt{4\pi D't}} (e^{-(y-x-\mu t)^2/4D't} - e^{\mu(x-a)/D'} \times e^{-(y+x-2a-\mu t)^2/4D't}) \quad (\text{A.34})$$

## A.6 Transition Density for a 1D Wiener Process with a Reflecting Inner Boundary (See Sect. 2.3.2.1)

The transition density for a 1D diffusion process with a reflecting lower boundary can be obtained by using the renewal process of a diffusion process as

$$p_{\text{ref}}(x, y, t) = p_a(x, y, t) + \int_0^t w(x, a, u) p_{\text{ref}}(a, y, t - u) du \quad (\text{A.35})$$

where  $w(x, a, u)$  is the first passage time density of paths from  $x$  to  $a$  at time  $u$ . The first passage to some point  $a$  can be expressed using the renewal theorem as

$$p(x, y, t) = \int_0^t w(x, a, u) p(a, y, t - u) du \quad (\text{A.36})$$

Taking the Laplace transform of the above equation and rearranging for  $\tilde{w}(x, a, s)$  gives

$$\tilde{w}(x, a, s) = \frac{\tilde{p}(x, y, s)}{\tilde{p}(a, y, s)} \quad (\text{A.37})$$

Equation (A.35) shows that the paths on going from  $x$  to  $y$  can be divided into two categories: (i) those that do not hit  $a$  (first term in the above equation) and (ii) those that hit  $a$  but are reflected to  $y$  (second term in the above equation). The transition density for (i) can be formulated in terms of the renewal process for paths which hit  $a$  and those which do not. The form of the transition density for a path going from  $x$  to  $y$  without hitting  $a$  in Laplace space is known to be of the form

$$\tilde{p}_a(x, y, s) = \tilde{p}_f(x, y, s) - \tilde{w}(x, a, s)\tilde{p}(a, y, s) \quad (\text{A.38})$$

where  $\tilde{p}_f(x, y, s)$  is the transition densities for an unrestricted process. Taking the Laplace transforms of Eq. (A.35) and substituting the expression for  $\tilde{p}_a(x, y, s)$  gives

$$\tilde{p}_{\text{ref}}(x, y, s) = \tilde{p}_f(x, y, s) + \frac{\tilde{p}(x, a, s)}{\tilde{p}(a, a, s)} (\tilde{p}_{\text{ref}}(a, y, s) - \tilde{p}(a, y, s)) \quad (\text{A.39})$$

Using the boundary condition

$$\left. \frac{\partial \tilde{p}_{\text{ref}}(x, y, t)}{\partial x} \right|_{x=a} = 0 \quad (\text{A.40})$$

together with differentiating Eq. (A.39) with respect to  $x$  and taking the limit  $x \rightarrow a$  gives

$$\tilde{p}_{\text{ref}}(x, y, s) = \tilde{p}_f(x, y, s) - \tilde{p}(x, a, s) \frac{\tilde{p}_x(a, y, s)}{\tilde{p}_x(a^+, a, s)} \quad (\text{A.41})$$

where  $p_x(a, y, s)$  and  $p_x(a^+, a, s)$  are the derivative of the transition densities for a diffusion process in the limit that  $x \rightarrow a$ . Substituting the known expressions gives the transition density for the reflected process to be

$$\begin{aligned} \tilde{p}_{\text{ref}}(x, y, s) = & \frac{1}{\sqrt{4D'\gamma}} e^{(y-x)\mu/2D'} e^{-|y-x|\sqrt{\gamma/D'}} - \frac{1}{\sqrt{4D'\gamma}} \frac{(\mu/2\sqrt{D'}) - \sqrt{\gamma}}{(\mu/2\sqrt{D'}) + \sqrt{\gamma}} \\ & \times e^{(y-x)\mu/2D'} e^{-(y+x-2a)\sqrt{\gamma/D'}} \end{aligned} \quad (\text{A.42})$$

where  $\gamma = \sqrt{s/D'}$  and  $\mu$  is the drift velocity. The above expression can be inverted to give

$$\begin{aligned} p_{\text{ref}}(x, y, t) = & \frac{1}{\sqrt{4\pi D't}} e^{-(y-x-\mu t)^2/4D't} + e^{(y-a)\mu/D'} \\ & \times \left[ \frac{1}{\sqrt{4D't}} e^{-(y+x-2a+\mu t)^2/4D't} \right. \\ & \left. - \frac{\mu}{2D'} \operatorname{erfc} \left( \frac{(y+x-2a) + \mu t}{\sqrt{4D't}} \right) \right] \end{aligned} \quad (\text{A.43})$$

## A.7 Transition Density for a 1D Diffusion Process with an Elastic Inner Boundary (See Sect. 2.3.2.1)

Using a similar strategy as above, the transition density with a lower elastic boundary can be formulated using the renewal theorem of a diffusion process as (where the definition for  $\tilde{w}(x, a, s)$  from Eq. (A.37) has been used)

$$\tilde{p}_{\text{rad}}(x, y, s) = \tilde{p}_f(x, y, s) + \frac{\tilde{p}(x, a, s)}{\tilde{p}(a, a, s)} (\tilde{p}_{\text{rad}}(a, y, s) - \tilde{p}(a, y, s)) \quad (\text{A.44})$$

where the first term takes into account all trajectories which do not pass through  $a$ , whilst the second term takes all paths which hit  $a$ , survive reaction and diffuse to  $y$ . Using the lower boundary condition such that

$$\left. \frac{\partial p_{\text{rad}}(x, y, t)}{\partial x} \right|_{x=a} = \beta p(a, y, t) \quad (\text{A.45})$$

and differentiating Eq. (A.44) with the limit  $x \rightarrow a$  gives the expression for the transition density for a path from  $x$  to  $y$  subject to an elastic boundary to be

$$\begin{aligned} \tilde{p}_{\text{rad}}(x, y, s) &= \tilde{p}_{\text{abs}}(x, y, s) + \frac{\tilde{p}(x, a, s)}{\tilde{p}(a, a, s)} \\ &\times \left( \frac{\tilde{p}(a, a, s) \tilde{p}_x(a, y, s) - \tilde{p}_x(a^+, a, s) \tilde{p}(a, y, s)}{\beta \tilde{p}(a, a, s) - \tilde{p}_x(a^+, a, s)} \right) \end{aligned} \quad (\text{A.46})$$

In the above expression  $\beta = v/D'$ , where  $v$  is the parameter which controls the reactivity of the surface,  $p_x(a^+, a, s)$  and  $p_x(a, y, s)$  being the derivative of the transition density for a diffusion process in the limit that  $x \rightarrow a$ . Upon substituting the known transition densities into the above expression, we obtain the explicit form for  $\tilde{p}_{\text{rad}}(x, y, s)$  as

$$\begin{aligned} \tilde{p}_{\text{rad}}(x, y, s) &= \tilde{p}_{\text{abs}}(x, y, s) + \frac{1}{\sqrt{D'}} e^{(y-x)\mu/2D'} e^{-(y+x-2a)\sqrt{\gamma/D'}} \\ &\times \left( \frac{1}{\beta\sqrt{D'} + \frac{\mu}{2\sqrt{D'} + \sqrt{\gamma}}} \right) \end{aligned} \quad (\text{A.47})$$

where  $\gamma = \sqrt{s}D'$  and  $\mu$  is the drift velocity. The above expression can then be readily inverted to give

$$\begin{aligned} p_{\text{rad}}(x, y, t) &= p_{\text{abs}}(x, y, t) + e^{(y-a)\mu/D'} \times \left( \frac{1}{\sqrt{\pi D' t}} e^{-(y+x-2a+\mu t)^2/4D' t} \right. \\ &\quad \left. - \left( \beta + \frac{\mu}{2D'} \right) e^{\beta(y+x-2a+\mu t + \beta D' t)} \right. \\ &\quad \left. \times \operatorname{erfc} \left( \frac{(y+x-2a+\mu t + 2\beta D' t)}{\sqrt{4D' t}} \right) \right) \end{aligned} \quad (\text{A.48})$$

## A.8 Transition Density for a 1D Wiener Process with an Elastic Inner Boundary and Reflective Outer Boundary (See Sect. 9.2.1.2)

Using a similar strategy as above, the transition density for a path from  $x$  to  $y$  subject to an elastic boundary at  $a$  is given by Eq. (A.44). For an upper elastic boundary, the required boundary condition is simply

$$\left. \frac{\partial p_{\text{rad}}(x, y, t)}{\partial x} \right|_{x=a} = -\beta p(a, y, t) \quad (\text{A.49})$$

Differentiating Eq. (A.44) with the limit  $x \rightarrow a$  and using the boundary condition gives the expression for the transition density for a path from  $x$  to  $y$  subject to an upper elastic boundary to be (where the definition for  $\tilde{w}(x, a, s)$  from Eq. (A.37) has been used)

$$\tilde{p}_{\text{rad}}(x, y, s) = \tilde{p}_{\text{abs}}(x, y, s) + \frac{\tilde{p}(x, a, s)}{\tilde{p}(a, a, s)} \left( \frac{\tilde{p}_x(a^-, a, s)\tilde{p}(a, y, s) - \tilde{p}(a, a, s)\tilde{p}_x(a, y, s)}{\beta\tilde{p}(a, a, s) + \tilde{p}_x(a^-, a, s)} \right) \quad (\text{A.50})$$

where  $\beta = v/D'$ , with  $v$  measuring the reactivity of the surface,  $p_x(a^-, a, s)$  and  $p_x(a, y, s)$  being the derivative of the transition density for a diffusion process in the limit that  $x \rightarrow a$ . Upon substituting the known transition densities into the above expression, we obtain the explicit form for  $\tilde{p}_{\text{rad}}(x, y, s)$  as

$$\begin{aligned} \tilde{p}_{\text{rad}}(x, y, s) = & \tilde{p}_{\text{abs}}(x, y, s) + \frac{1}{\sqrt{D'}} e^{(y-x)\mu/D'} e^{-(-y-x+2a)\sqrt{\gamma/D'}} \\ & \times \left( \frac{1}{\beta\sqrt{D'} - \frac{\mu}{2\sqrt{D'} + \sqrt{\gamma}}} \right) \end{aligned} \quad (\text{A.51})$$

where  $\gamma = \sqrt{s}D'$  and  $\mu$  is the drift velocity. The above expression can then be readily inverted to give

$$\begin{aligned} p_{\text{rad}}(x, y, t) = & p_{\text{abs}}(x, y, t) + e^{(a-y)\mu/D'} \times \left( \frac{1}{\sqrt{\pi D' t}} e^{-(-y-x+2a-\mu t)^2/4D' t} \right. \\ & - \left( \beta - \frac{\mu}{2D'} \right) e^{\beta(-y-x+2a-\mu t + \beta D' t)} \\ & \left. \times \operatorname{erfc} \left( \frac{(-y-x+2a-\mu t + 2\beta D' t)}{\sqrt{4D' t}} \right) \right) \end{aligned} \quad (\text{A.52})$$

The transition density for an outer reflective boundary is then easily obtained by making the surface completely unreactive (i.e.  $\beta \rightarrow 0$ ) in Eq. (A.52).

## A.9 Transition Density for an Unrestricted 3D Bessel Process (See Sect. 4.4.2.4)

Before presenting the transition density  $p_a(x, y, t)$  with an absorbing inner boundary condition, a detailed derivation for the transition density for an unrestricted process is first shown using the Green's function method. The result will then be used to derive  $p_a(x, y, t)$  in the next section.

Starting with Laplace transform of the backward diffusion of the form

$$D' \frac{\partial^2 \tilde{p}}{\partial x^2} + \frac{2D'}{x} \frac{\partial \tilde{p}}{\partial x} - s \tilde{p} = -\delta(x - y) \quad (\text{A.53})$$

where  $s$  is the Laplace variable. The complementary function of this backward diffusion equation is  $\frac{A}{x} \exp[x\sqrt{s/D'}] + \frac{B}{x} \exp[-x\sqrt{s/D'}]$ , with constants  $A$  and  $B$  to be determined using the required boundary conditions. A solution obeying the inner boundary condition is of the form  $y_1 = \frac{1}{x} \sinh(x\sqrt{s/D'})$  and the outer is  $y_2 = \frac{1}{x} \exp(-x\sqrt{s/D'})$ . The Wronskian is then

$$W = -\frac{1}{x^2} \sqrt{\frac{s}{D'}} \quad (\text{A.54})$$

The Green's function can then be written as

$$G(x, \gamma) = \begin{cases} \frac{\gamma}{x\sqrt{sD'}} \sinh(\gamma\sqrt{s/D'}) & \gamma \leq y \\ \frac{\gamma}{x\sqrt{sD'}} \sinh(x\sqrt{s/D'}) & \gamma \geq y \end{cases} \quad (\text{A.55})$$

The Green's function can be re-expressed as

$$\tilde{p}(x, y, s) = \frac{1}{\sqrt{4D's}} \frac{y}{x} \left( \exp(-|y - x|\sqrt{s/D'}) - \exp(-(y + x)\sqrt{s/D'}) \right) \quad (\text{A.56})$$

which is the unrestricted transition density for a Bessel process. Its inverse Laplace inverse is the well known form

$$p(x, y, t) = \frac{1}{\sqrt{4\pi D't}} \frac{y}{x} \left( \exp(-(y - x)^2/4D't) - \exp(-(y + x)^2/4D't) \right) \quad (\text{A.57})$$

## A.10 Transition Density for a 3D Bessel Process with an Absorbing Inner Boundary (See Sect. 4.4.2.4)

The transition density for  $p_a(x, y, t)$  can be derived using the above procedure, with appropriate changes made to the inner boundary condition or can be derived by using the renewal theorem. In this appendix, the renewal theorem is used as it demonstrates how  $p_a(x, y, t)$  can be derived without having to solve using the required boundary conditions. Recognising that the transition density  $p_a(x, y, t)$  can be written using the renewal theorem of a diffusion process in Laplace space as

$$\tilde{p}_a(y, s|x) = \tilde{p}(x, s|a) - \tilde{w}(a, s|x)\tilde{p}(y, s|a) \quad (\text{A.58})$$

where  $\tilde{w}(a, s|x)$  is the first passage time density of ‘hitting’  $a$  and  $\tilde{p}(x, s|a)$  and  $\tilde{p}(y, s|a)$  are the unrestricted transition densities as derived earlier. The expression for the density of first passage times has already been derived and is given in Eq. (A.37). Using the fact that  $x \geq a$  and  $y \geq a$  as otherwise the trajectories would be killed, the expressions for  $\tilde{p}(x, s|a)$  and  $\tilde{p}(a, s|a)$  are then

$$\tilde{p}(x, s|a) = \frac{1}{\sqrt{D's}} \frac{x}{a} \exp(-x\sqrt{s/D'}) \sinh(a\sqrt{s/D'}) \quad (\text{A.59})$$

and

$$\tilde{p}(a, s|a) = \frac{1}{\sqrt{D's}} \frac{a}{a} \exp(-a\sqrt{s/D'}) \sinh(a\sqrt{s/D'}) \quad (\text{A.60})$$

$\tilde{w}(a, s|x)$  is then

$$\tilde{w}(a, s|x) = \frac{a}{x} \exp(-(x-a)\sqrt{s/D'}) \quad (\text{A.61})$$

All the terms are now known to calculate Eq. (A.58), which takes the form

$$\begin{aligned} \tilde{p}(x, y, s) = \frac{1}{\sqrt{4D's}} \frac{y}{x} & \left( \exp(-|y-x|\sqrt{s/D'}) \right. \\ & \left. - \exp(-(y+x-2a)\sqrt{s/D'}) \right) \end{aligned} \quad (\text{A.62})$$

which can be inverted to again give the well known Green’s function (using  $\alpha = 4D't$ )

$$p(x, y, t) = \frac{y}{x\sqrt{\pi\alpha}} \left( \exp(-(y-x)^2/\alpha) - \exp(-(y+x-2a)^2/\alpha) \right) \quad (\text{A.63})$$

### A.11 Reflection Algorithm (See Sect. 4.3.3)

The claim is that if  $Y_t$  is a Brownian motion with drift started at  $x$ , with  $a$  being the lower barrier and  $M$  is the infimum of  $Y_t$  at time  $t$ , then  $Z_t = Y_t$  if  $M > a$  and  $Y_t + a - M$  if  $M < a$  is an exact sample of Brownian motion with drift reflected at  $a$ . The infimum on a path from  $x$  to  $y$  can be found as

$$\Pr(M < m|x, y, t) = \frac{p(x, y, t \text{ via } m)}{p(x, y, t)} \quad (\text{A.64})$$

$$= \frac{\int_0^t w(x, m, u)p(m, y, t-u)du}{p(x, y, t)} \quad (\text{A.65})$$

where  $p(x, y, t \text{ via } m)$  are all paths which go through  $m$ ,  $w(w, m, u)$  is the density of first passage times to  $m$  and  $p(x, y, t)$  is the transition density for an unrestricted process. The Laplace transform of the numerator in the above expression is known to be  $\frac{1}{4D's} e^{(y-x)\mu/2D'} e^{-(y+x-2m)\sqrt{s/D'}}$  (with  $s$  being the Laplace variable) whose inverse is  $\frac{1}{4D'\pi t} e^{(y-x)\mu/2D'} e^{-\mu^2 t} e^{-(y+x-2m)^2/4D't}$ . Hence the expression for  $\Pr(M < m|x, y, t)$  simplifies to

$$\Pr(M < m|x, y, t) = \exp[-(y-m)(x-m)/D't] \quad (\text{A.66})$$

with the density of the infimum being

$$f = \frac{x+y-2m}{D't} \exp[-(y-m)(x-m)/D't] \quad (\text{A.67})$$

The joint density of  $Y_t$  and  $M$  is then

$$\xi = \frac{1}{\sqrt{4\pi D't}} \exp[(y-z-\mu t)^2/4D't] \frac{x+y-2m}{D't} \exp[-(y-m)(x-m)/D't] \quad (\text{A.68})$$

If  $M > a$  then  $z = y$ , otherwise  $z = y + a - m$ . Hence the probability density for a path from  $x$  to  $z$  is then

$$\begin{aligned} p(x, z, t) &= \frac{1}{\sqrt{4\pi D't}} e^{-(z-x-\mu t)^2/4D't} \int_a^{\min(x,z)} \frac{x+z-2m}{D't} e^{-(z-m)(x-m)} dm \\ &+ \frac{1}{\sqrt{4\pi D't}} e^{-(z-x-\mu t)^2/4D't} \int_{-\infty}^a e^{-(z+m-a-x-\mu t)^2/4D't} \frac{x+z-a-m}{D't} \\ &\times e^{-(z-a)(x-m)} dm \quad (\text{A.69}) \end{aligned}$$

Evaluating the integrals in the above expression gives

$$\begin{aligned}
 p(x, z, t) = & \frac{1}{\sqrt{4\pi D't}} e^{-(z-x-\mu t)^2/4D't} + e^{(z-a)\mu/D'} \\
 & \times \left[ \frac{1}{\sqrt{4D't}} e^{-(z+x-2a+\mu t)^2/4D't} - \frac{\mu}{2D'} \operatorname{erfc} \left( \frac{(z+x-2a)+\mu t}{\sqrt{4D't}} \right) \right]
 \end{aligned}
 \tag{A.70}$$

which is the solution for the transition density with an inner reflecting boundary.

# Appendix B

## Random Number Statistical Test

### B.1 Random Number Generation (See Sect. 4.2)

#### B.1.1 Chi-Square Method

The Chi-Square method checks for uniformity by dividing a range  $F$  of uniformly distributed random numbers  $a$  into a series of  $k$  adjacent intervals as

$$(a_0, a_1], (a_2, a_2], \dots, (a_{k-1}, a_k] \quad (\text{B.1})$$

Letting  $N_j$  represent the number of  $a$ 's in the interval  $[a_j, a_j)$  and  $p_j$  the probability of outcome  $(a_{j-1}, a_j)$  be

$$p_j = F(a_j) - F(a_{j-1}) \quad (\text{B.2})$$

then the Chi-Squared test statistic is

$$\chi^2 = \sum_{j=1}^k \frac{(N_j - np_j)^2}{np_j} \quad (\text{B.3})$$

where  $np_j$  is the expected number of  $a_i$ 's that fall within the  $j$ -th interval. If the null hypothesis  $H_0$  is true such that each  $a_i$  is randomly distributed with a distribution function  $F$ , then  $\chi^2$  converges to a Chi-Square distribution with  $k - 1$  degrees of freedom as  $n \rightarrow \infty$ . Hence,  $H_0$  is to be rejected if  $\chi^2 > \chi_{k-1, 1-\alpha}^2$ , where  $\chi_{k-1, 1-\alpha}^2$  is the  $1 - \alpha$  quantile of the Chi-Square distribution with  $k - 1$  degrees of freedom. Letting  $k = 10$ ,  $\alpha = 0.05$  and  $n$  equal to  $1 \times 10^3$  and  $1 \times 10^5$ , a chi-squared value of 11.64 and 2.41 was found respectively, both of which are less than the tabulated value of 16.92 suggesting the uniformity of each  $N_i$  within each  $i$ -th interval (i.e. in 95 % of the case the null hypothesis is accepted).

### B.1.2 Kolmogorov-Smirnov Test

In this test the sample empirical cumulative distribution function (cdf)  $S_n(x)$  is compared with a reference probability distribution  $F_n(x)$  to assess the goodness-of-fit. For this test it is assumed that the sample cdf is asymptotically normally distributed. The reference cdf for a uniform distribution is known to be

$$F_n(x) = \frac{1}{n} \sum_{i=1}^n I_{X_i \leq x} \quad (\text{B.4})$$

where  $I_{X_i \leq x}$  is the indicator function and equal to 1 if  $X_i \leq x$  and 0 otherwise. The empirical distribution for a sequence of randomly generated numbers  $a_1, a_2, \dots, a_n$  is

$$S_n(x) = \frac{\text{Number of } a_i \leq x}{n} \quad (\text{B.5})$$

with  $n$  being the length of the series. The Kolmogorov-Smirnov (KS) statistic is then

$$D_n = \sup_x |F_n(x) - S_n(x)| \quad (\text{B.6})$$

The strategy to test the random number generator involves: (i) ranking the i.i.d variables from smallest to largest; (ii) computing the parameters:

$$D^+ = \sup_{1 \leq i \leq n} \left[ \frac{i}{n} - a_i \right] \quad D^- = \sup_{1 \leq i \leq n} \left[ a_i - \frac{i-1}{n} \right] \quad (\text{B.7})$$

and calculating the KS statistic parameter which is the  $\sup[D^+, D^-]$ ; (iii) finding  $D_\alpha$  for the known cdf with significance level  $\alpha$ , which is the probability of rejecting  $H_0$  (null hypothesis) conditioned that  $H_0$  is true. For  $n \geq 100$  the KS statistic can be approximated as  $D_{n,0.95} \approx 1.3581/\sqrt{n}$  with a significance level of 0.95; (iv) if  $D \leq D_\alpha$ , then the initial null hypothesis such that the distribution of  $S_n(x)$  is uniformly distributed is accepted. Using a value of  $n = 50,000$  and  $\alpha = 0.95$  the null hypothesis was accepted since the calculated value for  $D = 4.04 \times 10^{-3} < D_\alpha$  ( $6.074 \times 10^{-3}$ ).

## Appendix C

# Simulation Flow Diagrams

### C.1 General Random Flights Flow Diagram (See Sect. 4.3).

See Fig. C.1.

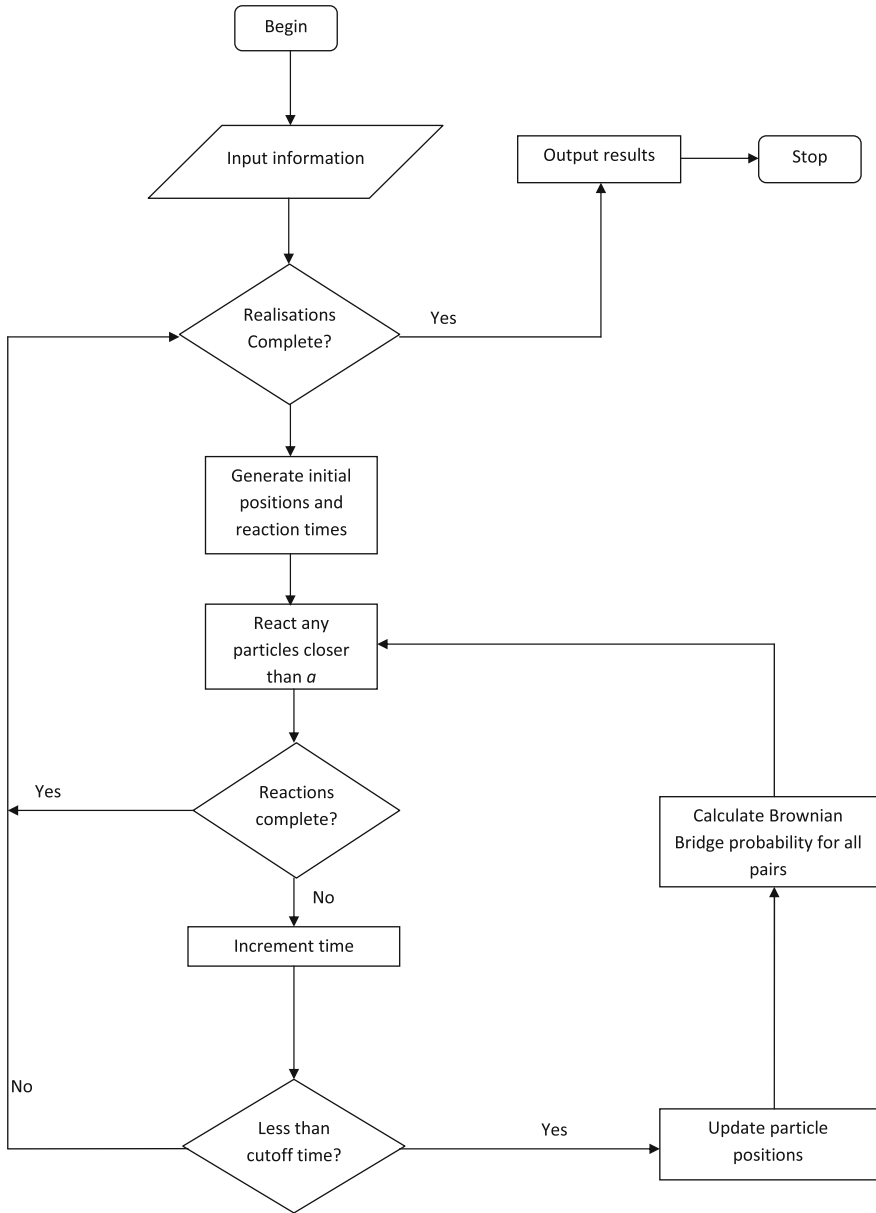


**Fig. C.1** Random flights flow diagram highlighting the basic procedure.  $a$  represents the encounter radius

### C.2 General IRT Flow Diagram (See Sect. 4.4)

See Fig. C.2.

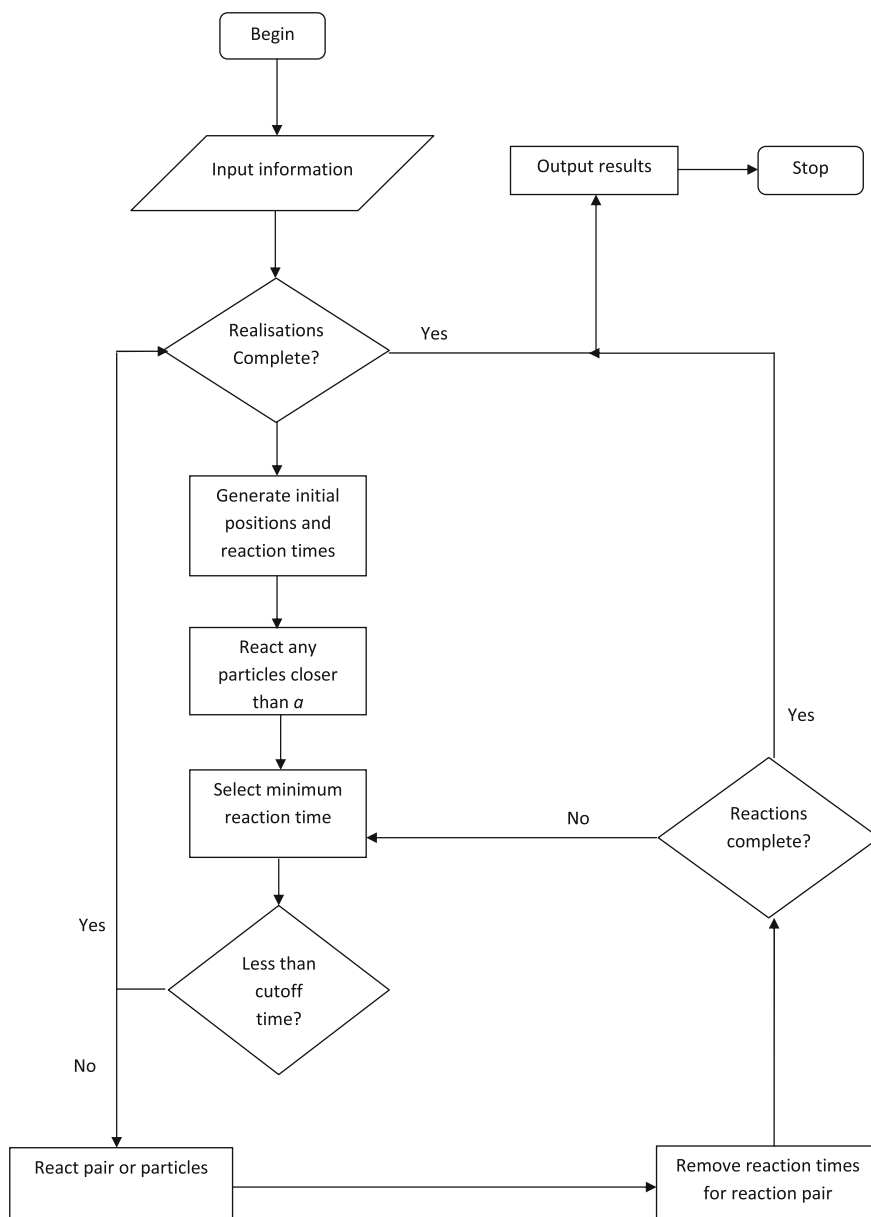


Fig. C.2 IRT flow diagram highlighting the main ingredients of the algorithm

### **C.3 Reflection Flow Diagram (See Sect. 4.4.2.3)**

See Fig. [C.3](#).

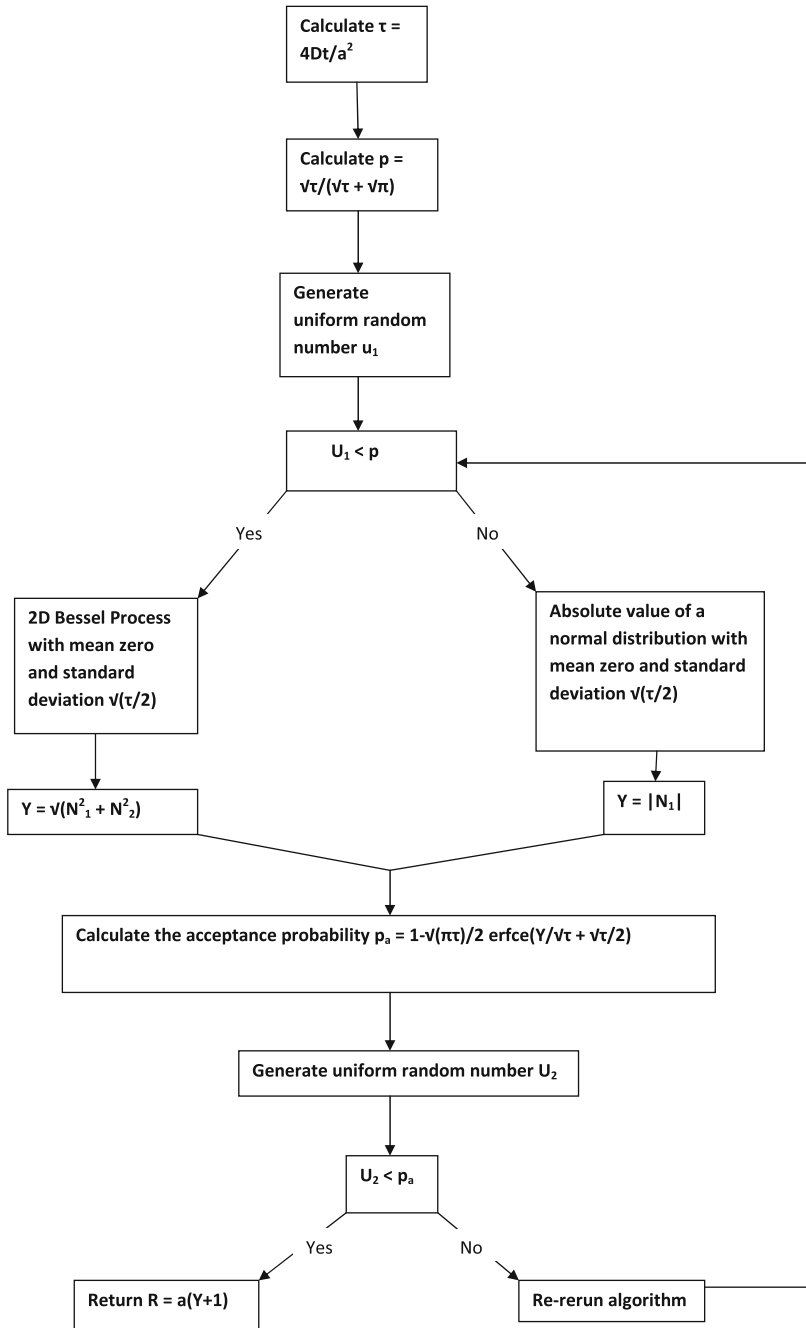
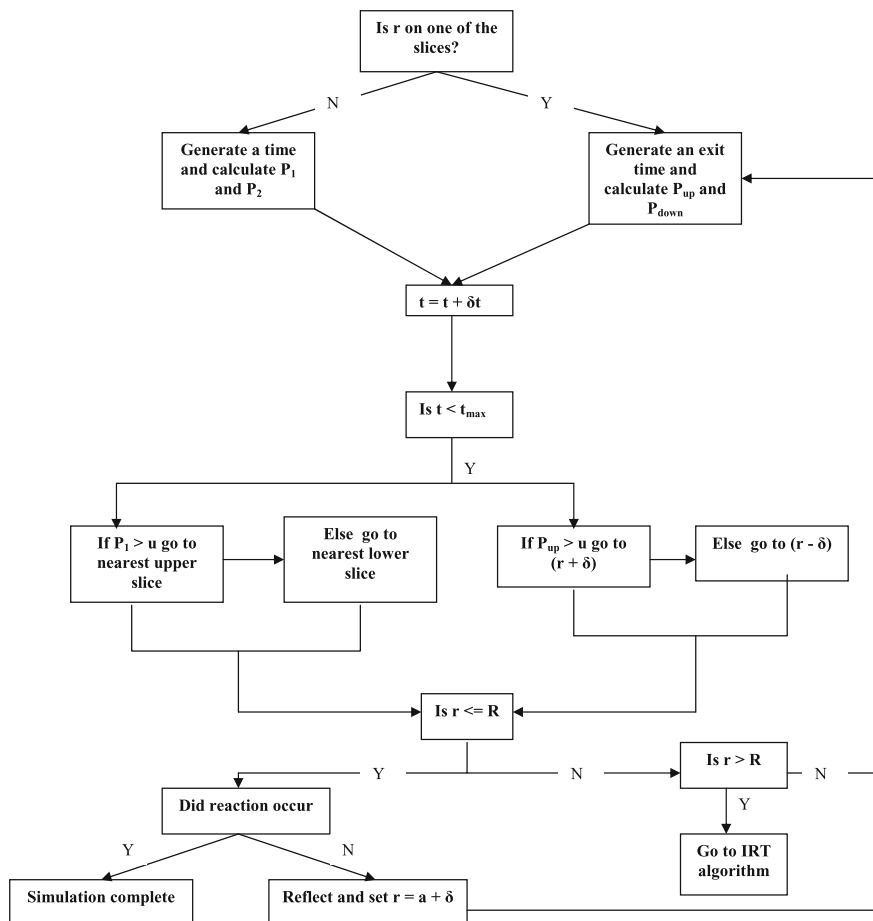


Fig. C.3 Reflection flow diagram, showing the main steps in computing a reflected distance within the IRT framework

## C.4 General Slice Flow Diagram (See Sect. 4.6)

See Fig. C.4.



**Fig. C.4** General flow chart for the Slice program.  $R$  is the maximum distance of the radical pair in which spatial interaction is to be included;  $u$  is a uniform random number between  $(0,1]$  and  $r$  is the current separation distance of the radical pair

## C.5 IRT Flow Diagram Used to Model the $\text{H}_2\text{O}_2$ Chemical System (See Sect. 5.3)

See Fig. C.5.

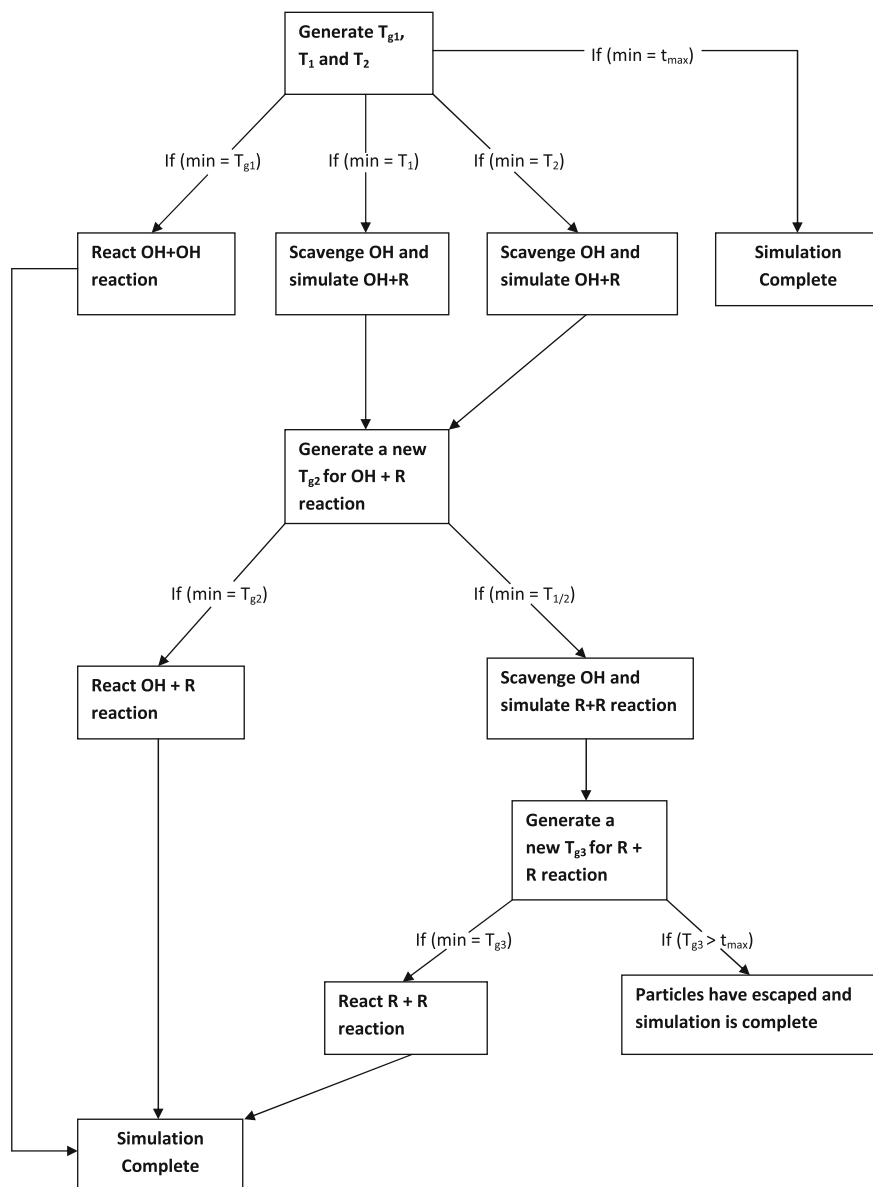
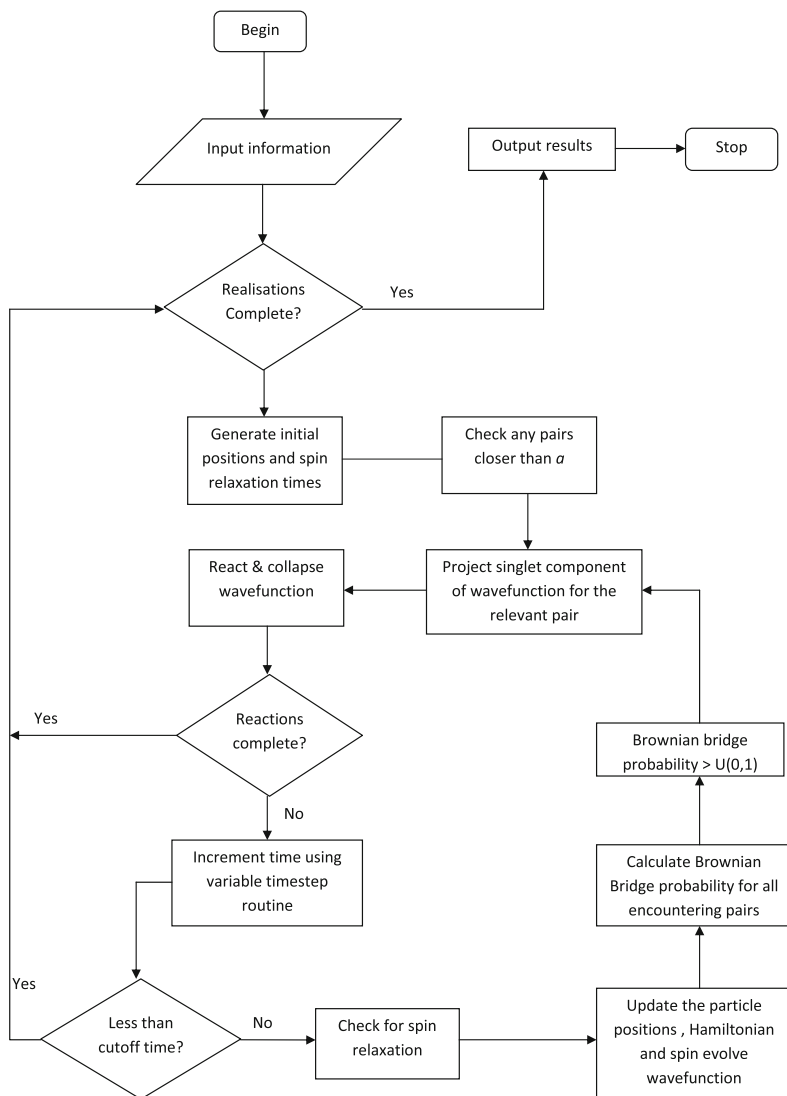


Fig. C.5 Computational flow diagram for the IRT program used to model the kinetics of the system

## C.6 MC Flow Diagram: Radiolysis of Hydrocarbons (See Sect. 8.4.5)

See Fig. C.6.



**Fig. C.6** Monte Carlo flow diagram showing key steps involved.  $U(0, 1]$  in the simulation is a uniformly distributed random number between 0 and 1

## C.7 IRT Flow Diagram: Radiolysis of Hydrocarbons (See Sect. 8.4.5)

See Fig. C.7.

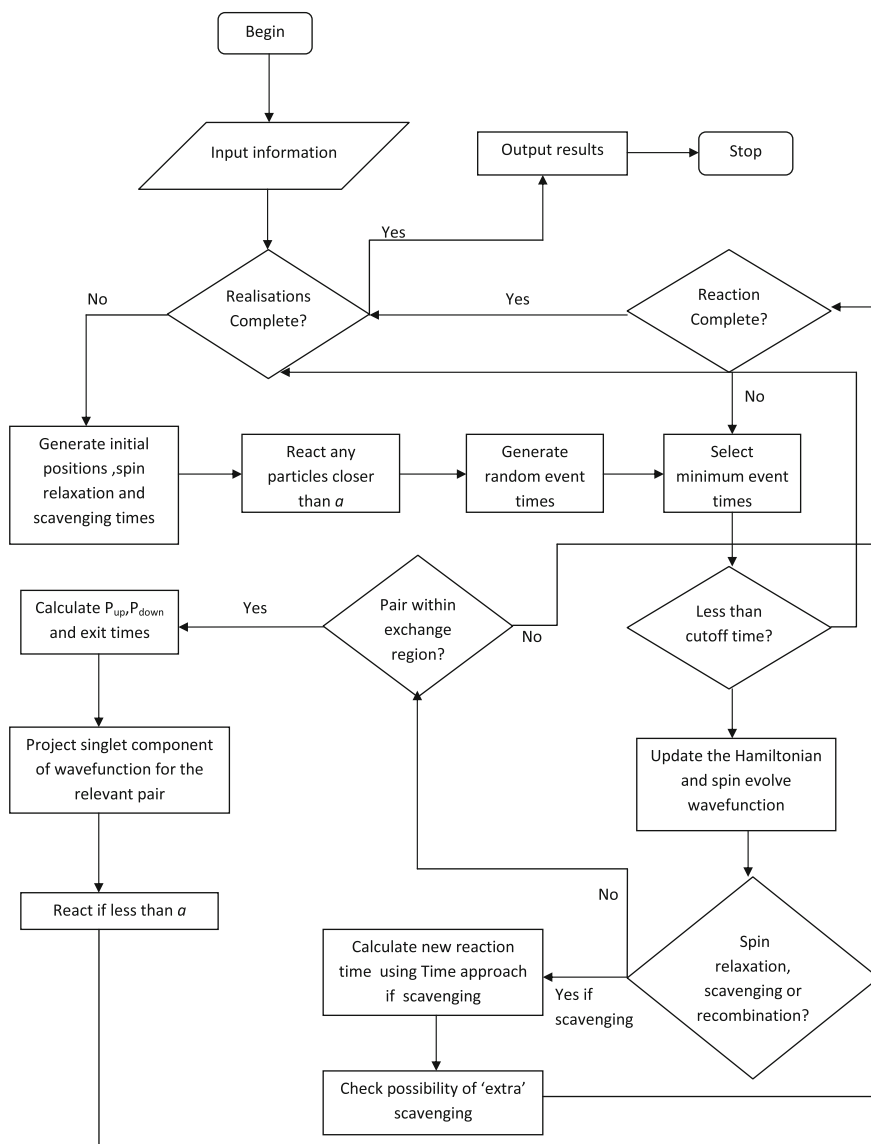


Fig. C.7 IRT flow diagram showing key subroutines involved in the simulation of hydrocarbons

## **Appendix D**

### **Micelle Results**

#### **D.1 Scavenging Inside a Micelle with an Outer Reflecting Boundary: Stationary Scavengers (See Sect. 9.4.4)**

See Figs. [D.1](#) and [D.2](#).

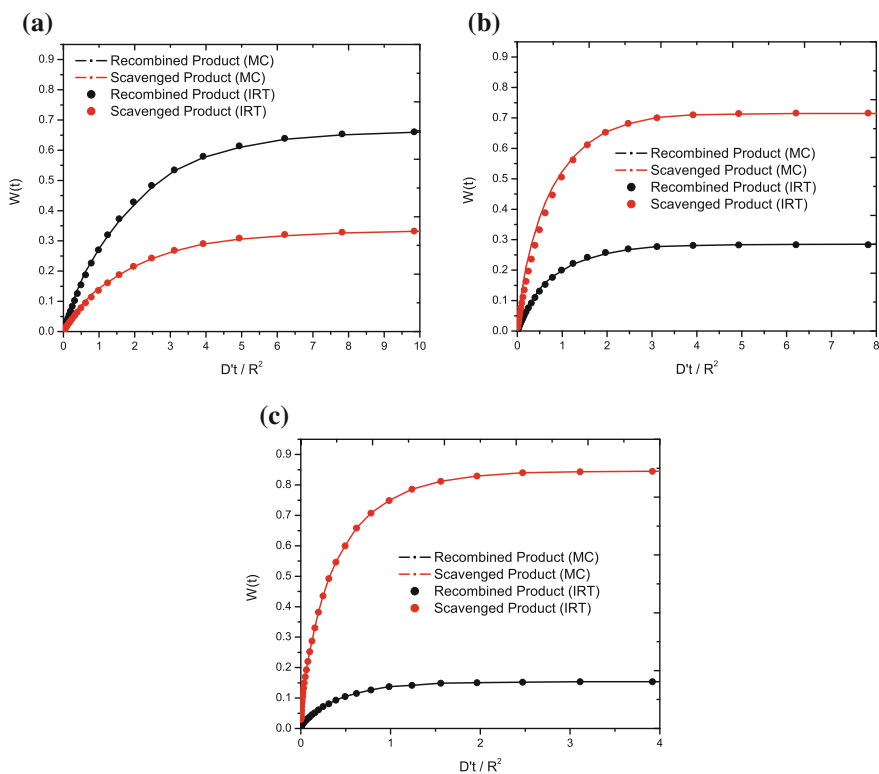


**Fig. D.1** Scavenging and recombination probability with the two particles mobile and scavengers stationary. Encounter radius for all reactions was set to 4 Å. The micelle contained **a** 1 scavenger, **b** 5 scavengers and **c** 10 scavengers

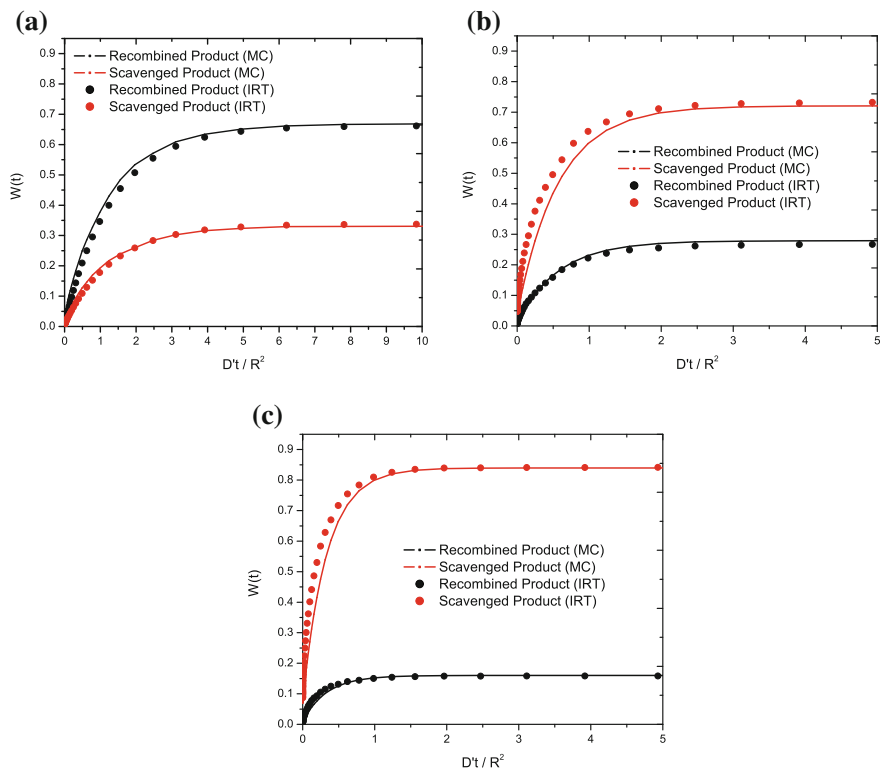


**Fig. D.2** Scavenging and recombination probability with the two particles mobile and scavengers stationary. Encounter radius for all reactions was set to 6 Å. The micelle contained **a** 1 scavenger, **b** 5 scavengers and **c** 10 scavengers

## D.2 Scavenging Inside a Micelle with an Outer Reflecting Boundary: Mobile Scavengers (See Sect. 9.4.4)

See Figs. D.3 and D.4.

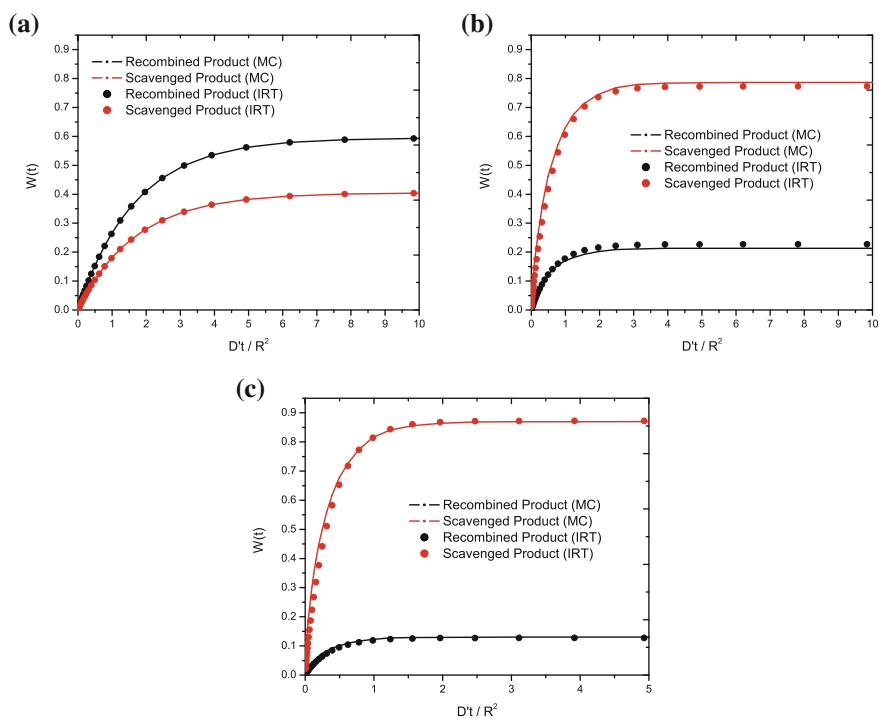


**Fig. D.3** Scavenging and recombination probability with the scavengers and particle mobile. Scavengers were given a diffusion coefficient of  $0.05 \text{ \AA}^2 \text{ ps}^{-1}$ , and all reactions had an encounter radius of  $4 \text{ \AA}$ . The micelle contains **a** 1 scavenger, **b** 5 scavengers and **c** 10 scavengers

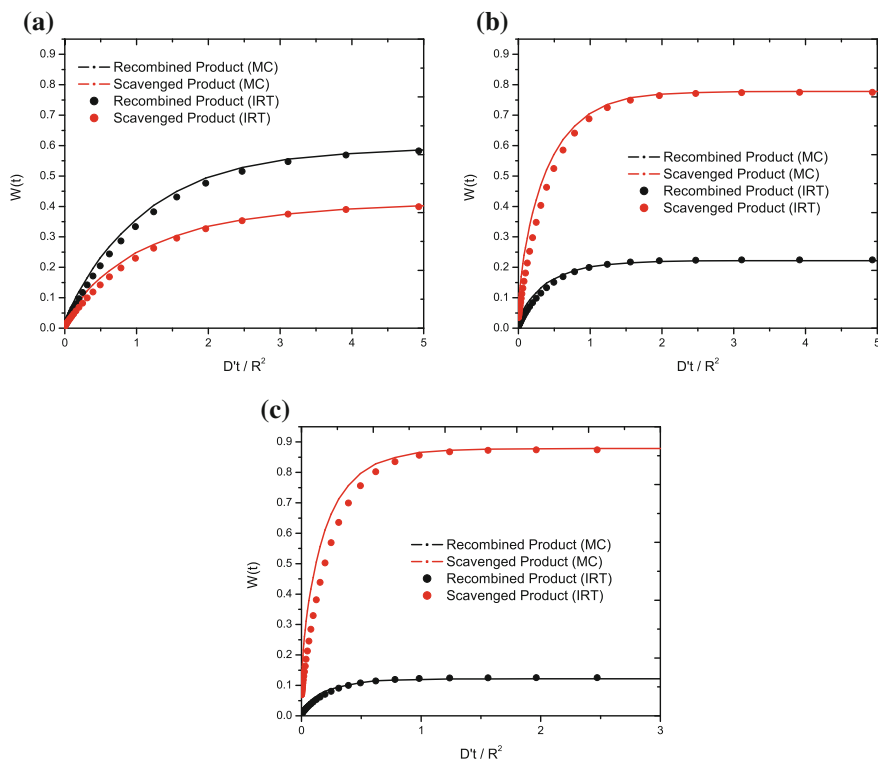
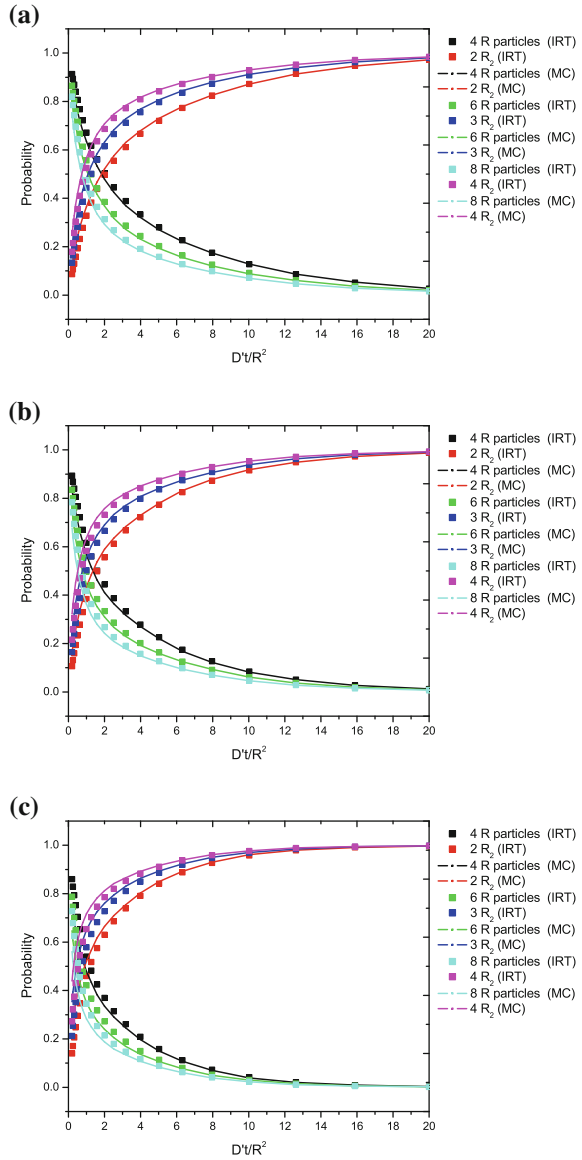


**Fig. D.4** Scavenging and recombination probability with the scavengers and particle mobile. Scavengers were given a diffusion coefficient of  $0.05 \text{ \AA}^2 \text{ ps}^{-1}$ , and all reactions had an encounter radius of  $6 \text{ \AA}$ . The micelle contains **a** 1 scavenger, **b** 5 scavengers and **c** 10 scavengers

### D.3 Recombination Kinetics for $n$ Particles Distributed Randomly on a Sphere (See Sect. 9.5.2)

See Fig. D.5.

**Fig. D.5** Survival and recombination probability using 4, 6 and 8 mobile particles randomly distributed on a unit sphere. Reaction distances relative to the sphere radius  $R$  were: **a**  $a = 0.05R$ , **b**  $a = 0.1R$  and **c**  $a = 0.2R$



## D.4 Results for Reversible Reactions Using 4 P Particles at Different Encounter Distances (See Sect. 9.6)

See Fig. D.6.

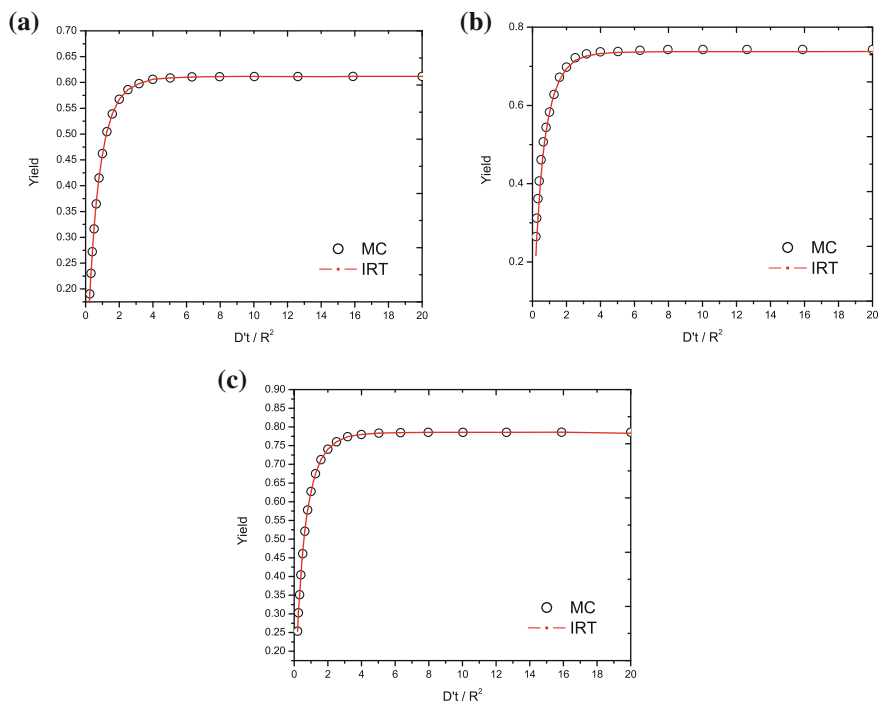


**Fig. D.6** Recombination probability for 4 P particles using a reaction distance of **a**  $0.05R$ , **b**  $0.12R$  and **c**  $0.15R$  on the spherical surface of radius  $R$ . A dissociation rate ( $k_{\text{diss}}$ ) of  $0.1 \text{ ps}^{-1}$  was used together with a surface reactivity ( $k_{\text{act}}/a$  with  $a$  being the encounter distance of micelle and particle) for the micellar surface of  $0.01 \text{ ps}^{-1}$

## D.5 Results for Reversible Reactions Using 4 P Particles at Different Surface Reactivities (See Sect. 9.6)

See Fig. D.7.

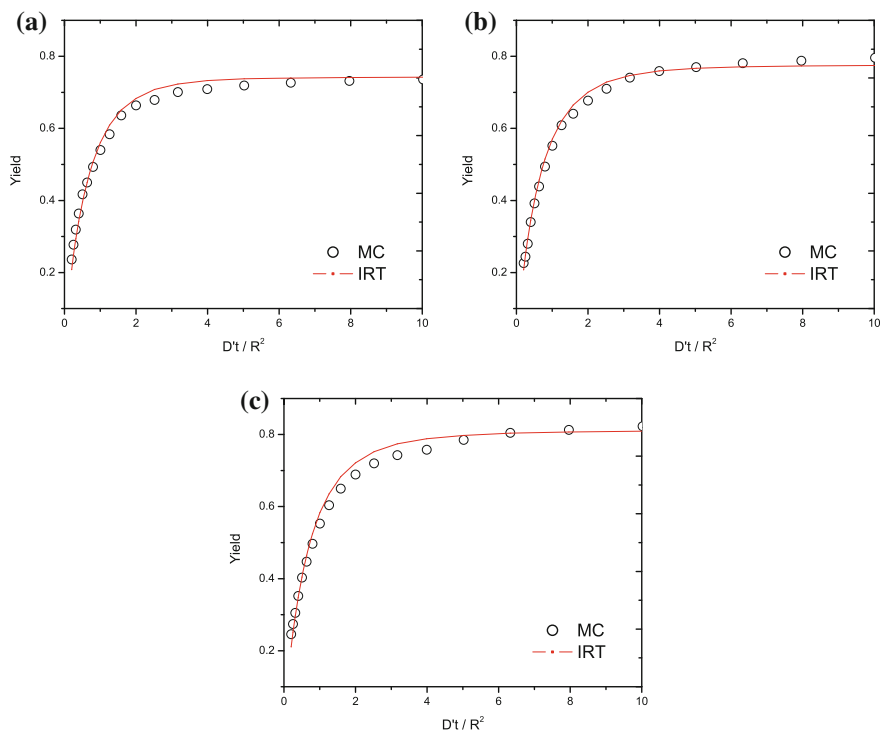


**Fig. D.7** Recombination probability for 4 P particles using a surface reactivity ( $k_{\text{act}}/a$  with  $a$  being the encounter distance of micelle and particle) of **a**  $0.03 \text{ ps}^{-1}$ , **b**  $0.05 \text{ ps}^{-1}$  and **(c)**  $0.07 \text{ ps}^{-1}$ . A dissociation rate ( $k_{\text{diss}}$ ) of  $0.1 \text{ ps}^{-1}$  was used together with a surface reactivity ( $k_{\text{act}}/a$ ) for the micellar surface of  $0.01 \text{ ps}^{-1}$ . Encounter distance for all reactions on the spherical surface of radius  $R$  was  $a = 0.1R$

## D.6 Results for Reversible Reactions Using 4 P Particles at Different Dissociation Rates (See Sect. 9.6)

See Fig. D.8.

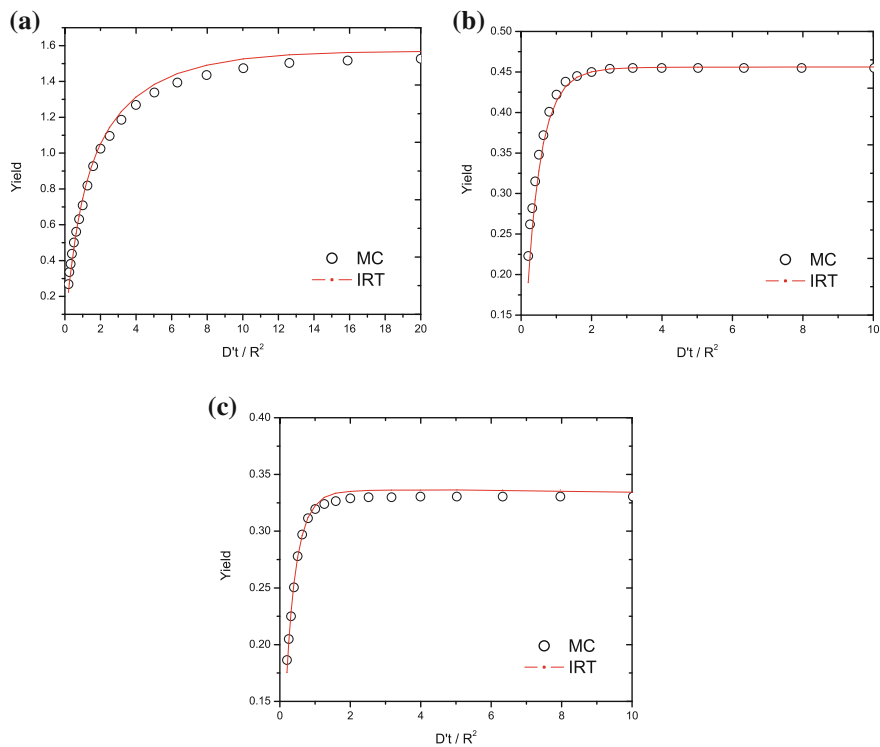


**Fig. D.8** Recombination probability for 4 P particles using a dissociation rate ( $k_{\text{diss}}$ ) of **a**  $0.01 \text{ ps}^{-1}$ , **b**  $0.2 \text{ ps}^{-1}$  and **c**  $0.3 \text{ ps}^{-1}$ . A surface reactivity ( $k_a/a$  with  $a$  being the encounter distance of micelle and particle) of  $0.01 \text{ ps}^{-1}$  was used in all cases. Encounter distance for all reactions on the spherical surface of radius  $R$  was  $a = 0.1R$